Universitat de Girona

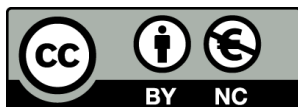# EXPLORING THE BOUNDARIES OF AROMATICITY THROUGH COMPUTATIONAL ANALYSIS OF EXCITED STATES AND COMPLEX MOLECULAR TOPOLOGIES

Sílvia Escayola Gordils

DOCTORAL THESIS

EXPLORING THE BOUNDARIES OF AROMATICITY THROUGH COMPUTATIONAL ANALYSIS OF EXCITED STATES AND COMPLEX MOLECULAR TOPOLOGIES

Sílvia Escayola Gordils

2024

Universitat de Girona

DiPC

DOCTORAL THESIS

EXPLORING THE BOUNDARIES OF AROMATICITY THROUGH COMPUTATIONAL ANALYSIS OF EXCITED STATES AND COMPLEX MOLECULAR TOPOLOGIES

Sílvia Escayola Gordils

2024

DOCTORAL PROGRAMME IN CHEMISTRY

Supervised by:

Prof. Dr. Miquel Solà i Puig
Dr. Albert Poater Teixidor
Prof. Dr. Eduard Matito Gras

Tutor:

Prof. Dr. Miquel Solà i Puig

Presented to obtain the degree of PhD at the University of Girona

"El grill li digué a la cuca Quica:
–T'estic molt agraït.
L'èxit te'l dec a tu...
–És cert. Ho hem fet entre tots dos,
però tu has actuat molt bé"

Empar de Lanuza i Pau Estrada

A tots vosaltres, que heu estat al meu costat

i en especial

a la mama, al papa,
a en Jordi, a la Marina,
a en Drumi, a en Sirius,
a l'avi Lluís,
al meu cutu

Acknowledgements

Aviat farà 10 anys que vaig entrar a l'IQCC, i vull començar els agraïments per aquest punt. Va ser llavors, a mitjans del 2014, quan va començar el meu interès per a fer un doctorat. Recent acabat 2n de grau vaig respondre al correu que ens havia enviat el director, en aquell moment en Lluís Blancafort, per la beca d'estiu. Ell mateix em va ensenyar les comandes de Linux i a fer càlculs CASSCF, això va continuar amb el TFG, TFM, i l'any de pont abans de la tesi. Per això, Lluís, t'estic molt agraïda per tot l'aprenentatge. Des d'aquell estiu vaig anar coneixent la gent que som l'IQCC, alguns d'ells IQCians literalment des que vaig néixer! La primera taula que em van adjudicar va ser la que està esquena per esquena amb en Dani al 177. Ai Dani... quina gràcia pensar que et tenia tant de respecte i que creia que tenies instal·lada una càmera per assegurar que els estudiants ens comportàvem quan no hi eres. Qui m'havia de dir que compartiríem receptes, menjaríem tants pastissos, xerraríem de fricades i que m'ho passaria tan bé. T'aprecio moltíssim i ni amb mil mochis et podria pagar tot el que m'has ajudat durant aquests anys! Vull esmentar també a en Quim i la Carme, encara formaven part de l'IQCC als meus inicis i tot i que només vam coincidir un parell o tres d'anys els tinc molt presents. Un altre record d'aquelles èpoques és el d'assistir als primers seminaris, especialment les presentacions d'en Ferran F. i la Sílvia O., que no feia tant que havien tornat dels postdocs. Fins aquell moment havia llegit, potser, tres papers en la meva vida i no sabia que es podien fer figures tan maques! No és just destacar-los només a ells dos (tot i que certament em van marcar), perquè al llarg d'aquests anys he assistit a moltes xerrades increïbles de molts membres de l'IQCC, UdG, DIPC, i altres ponents que m'han inspirat i motivat. Moltes gràcies a tots de veritat, perquè en algun d'aquells moments de dubte, que et preguntes 'Per què estic fent això?' veure aquestes xerrades era tot el que necessitava. Parlant d'inspiració i suport des dels inicis, he de mencionar a en Pedro. Todas las anécdotas, las salidas en bici, los consejos del camino, 'Pedro, help, ¿cómo funciona esta fórmula?', los apodos, las cenas, Montseny 62, tu técnica del hielo para recoger los restos de café de la taza... te estoy muy agradecida por tantísimas cosas. Vull agrair també a tota la resta de professors per les hores de cafè, els dinars i, en general, el dia a dia compartit. Josep M. i Luis, per ser dels 'sèniors' més propers que fan les coses fàcils i pel teu gran sentit de l'humor. A Sílvia S. i Emili, gràcies per la immensa ajuda amb les pràctiques d'EQF. A Sergei, Germano, Olga i Antony Stasyuk, als Miquels, Albert, a Marc G. i altres professors de la FC com en Pep, Montse H., Mònica I., Anna P., Lidia F., i Anna R., a vosaltres dues en especial, per tota l'ajuda durant el període què heu sigut coordinadores del doctorat en Química. I, sens dubte, a tots els altres que sempre heu estat super amables amb mi, compartint mica en mica moments que no oblidaré.

Com alguns que hem passat amb tu Montse Rodríguez, converses que m'han ajudat moltíssim, dinars, sopars, berenars, barraques o el que faci falta. Moltíssimes gràcies, et fas estimar molt Montse!

Tornant a l'ordre cronològic, vull agrair a en David Casanova per donar-me l'oportunitat de treballar amb ell amb la beca d'estiu del DIPC 2017. Em van encantar les teves explicacions sobre singlet fission, spin-flip... A mes et vull agrair l'esforç i l'interès que vas mostrar ajudant-me a demanar beques de doctorat amb tu, tot sabent que la meva preferència era tornar a Girona. También aprovecho para agradecer a Maru que me supervisó y me ayudo muchísimo con todos los cálculos Q-Chem. Así como Jesús, Gabi, Txoni, Mario, Txema, Edu, Mauricio, Mireia, Irene, Sebastian, Carmelo, y todos con los que tuve el placer de compartir horas del café ese verano, sin saber que en un futuro acabaría volviendo al DIPC.

Després va venir el meu període al Parc científic. Moltíssimes gràcies Ferran no només per permetre'm tornar a Girona durant l'any pre tesi sinó també per la paciència d'ensenyar-me a fer les dinàmiques de l'spinach, juntament amb en Lluís, i ajudar-me a fer que les coses fossin mes fàcils en una epoca que els fails amb les beques de doctorat no ho posaven tan fàcil. D'aquelles èpoques també vull agrair la companyia de les hores de dinar, alguna pujada a St. Miquel, o calçotada, que vam fer amb els membres del CompBioLab: Sílvia O., Adrià, Lorenzo, Eila, Miquel, Christian, Carla, Guillem, Leila, i altres habitants del parc l'Steven, la Vero i l'Ouissam.

Finalment, **Albert** i **Miquel** em vau donar la millor notícia! I al cap d'un temps també t'hi vas sumar tu **Edu**. Moltíssimes gràcies als tres per donar-me la possibilitat de fer el doctorat sota la vostra supervisió. Valoro moltíssim totes les coses que m'heu ensenyat, les oportunitats que m'heu donat i tot el que he pogut aprendre de vosaltres tant en l'àmbit científic com personal. Tinc moltíssimes coses a agrair-vos, però sobretot vull destacar l'empatia que heu mostrat en aquells moments que sentia que estava fallant. Gràcies per simplificar els moments complicats i per totes les correccions de la tesi! Més enllà de la ciència també us vull agrair molt bons moments que he passat anant amb bicicleta, jugant a pàdel, futbol, sopars, sociedades entre d'altres. Gràcies per ser tan propers!

Vull agrair també a tots els col·laboradors amb qui he tingut la sort de treballar, i dels quals alguns dels resultats s'incorporen a aquesta tesi. Gràcies a en Henrik,

del QuantumChemDev Carmelo, Sebastian, Eloy, Luis, Xiang, Markel (moltes gràcies per esperar-me pujant a St. Grau i per assegurar-te que arribes viva a Girona jeje. He d'entrenar mes per la pròxima!), Ruben, y los que todavía no estaban durante esos dos meses pero que nos hemos reunido en los meetings por zoom, RSA-NLOP-workshop, cenas en la sociedad, etc: Javier, Andrei, Guillem, Joan, Mesías, Ander. Moltes gràcies, mila esker, muchas gracias!! También quiero agradecer a Pablo, Raúl, Alejandro, Claudia, Mariarita, Pep, y Davide, porque me lo pase genial con vosotros durante esos dos meses! País Basc em fa pensar inevitablement en la Irene. T'he de donar les gràcies perquè m'has ajudat molt durant tot el doctorat, ja sigui resolent-me dubtes d'ESI, ajudant-me a trobar pis a Donostia, o la mes recent, acceptant ser revisora externa de la tesi. A banda d'això també hem passat bons moments banyant-nos en llacs o piscines en congressos i quedant de tant en tant per fer el cafè quan vens a Girona. Merci per tot :)!

Quantum BTT! Miquel Solà, Miquel Duran han estat molts diumenges de descobrir llocs nous i passar-m'ho genial. Tot un honor formar part d'aquest equip.

A tots els companys i amics de la uni amb els que he compartit despatx, classe, pàdels, futbols, gartiks, congressos, o moltes hores a Can Paco. Gràcies Clara Masdevall, Núria Farró, David, Caixas, Gerard Pareras, Èric Casals, Ernest, Aythami, Pau B., Àlex D., Marc Montilla, Albert Artigas, Anna Vidal, Quique, Gibu, Cristina, Núria, Anju, Abhishek, Jordi S., Guillem, Joan, Helena, Judit (algun dia acabaré un rellotge gràcies a l'amulet grec). Els del QBIS que sempre m'acolliu, Míriam, Valentina, Judith. Sergi Posada, gràcies per ajudar-me sempre que ho he necessitat i per tots els consells, postdoc! Leila, sist, la meva sidekick, el que em pot arribar a emocionar rebre un àudio teu no te sentit! gràcies per entendrem tant bé. Teti, saps treure-li ferro a l'assumpte com ningú i sempre m'alegra parlar amb tu. Joel, un altre bèstia. Ricard, moltíssimes gràcies pels dies de platja i running i els múltiples viatges que hem fet! Martí, gràcies per tota l'ajuda en els primers anys de tesi i sobretot pel Kmino que vam fer junts! Artur, des d'aquell camino també va començar la nostre amistat i aquí seguim, anant a veure balls irlandesos! Roger, miiiau, sens dubte que la teva arribada va millorar molt els últims anys de doctorat i ja trobo a faltar una xerrada infinita amb en Dani en algun parking, truiteria, König (o parking del caprabo fals si cal). Dani, el mestre de l'ML, gràcies de veritat per sopars, voltes, les xerrades infinites, i per organitzar totes les IQCC-activitats dels últims anys, i a tu en Roger i l'Alex merci pel viatge a Toulouse i tots els padels!

Sergio i Pau sou família! Us estimo tant... Amb vosaltres soc feliç prop de París i de qualsevol lloc. Sergio, t'he d'agrair mil milions de coses 'que tu no me juzgues', tots els consells en els moments de dubte, les repassades del teu guess d'examen en el trajecte de 35 minuts en cotxe de Lloret a Montilivi. Pau, tu m'encantes hi ha coses que són així i prou. Aquestes coses se'm dona millor valorar-les i sentir-les que no pas expressar-les, però crec que els dos ja sabeu com us estimo i m'enteneu. Chiraf, ets tan boja, t'estimo tant a tu també. Ets molt important per a mi, gràcies per el teu suport incondicional.

Moltíssimes gràcies, Alex per tot el que fas. L'època d'escriure la tesi, tot i que m'ha agradat, també s'ha fet dura i tu has estat cada dia al meu costat. Encara que hagi sigut en forma d'una petita A de color rosa que apareixia per sorpresa a dalt del document de Latex mentre escrivia. És una sort haver-me trobat amb tu. Gràcies per compartir tantes coses amb mi, des de menjar, les teves infinites aficions, els country i cacaos, i el mes important, la teva família, en Ruben i molts altres amics a qui també vull agrair perquè a tots ells ja me'ls estimo una mica també :)

De Tossa li he de donar les gràcies a la Roser (and family), a l'Anna i en Lluc (i Anna petita), A l'Olga (i a l'Onna), a en Dani, i a la penya Pol, pel viatge a Berlín, cines, i tots els bons records que tinc de vosaltres.

Per acabar, vull agrair a la família. Sou una gran família, he conegut besavis, avis (malauradament em va faltar conèixer l'àvia Carme), un munt de tietes, tiets, cosins, cosines, i els seus fills. De gairebé tots n'he pogut aprendre alguna cosa, us estimo molt, i n'estic realment orgullosa de formar part d'aquesta família amb vosaltres. N'hi ha uns quants als que vull fer una menció especial. Avi Lluís, ja fa uns anys que vas marxar, però sempre et tinc molt present. Sé que ets el meu àngel de la guarda i mira que jo no hi crec en aquestes coses com hi creies tu. Papa, parles poc, però quan ho fas és per dir coses interessants o xistes dels millors jajaja. M'encanta la teva manera calmada d'afrontar les coses i les estones que hem passat al jardí arreglant coses junts són un petit tresor. Tete (Jordi), ets un mimat, però és que costa no fer-ho :) Bromes a part, és una sort tenir-te de germà. M'ho passo genial fent coses amb tu i la Marina. Us estimo molt als dos! A tu mama com ja vaig dir en aquella redacció d'anglès, *you are my favourite person*. També et diré que en el primer capítol d'un dels llibres d'en Feynman, hi ha un apartat que es diu 'així es fa un científic' on parla de l'important rol que va tenir el seu pare en despertar-li la passió per la

ciència. Allà dona uns quants exemples de com sempre procurava traduir-li les dades científiques a realitats properes a ell. Quan ho estava llegint, automàticament ens vaig visualitzar a les dues al pati de darrere de casa donant voltes al Sol (taula de pedra) tu fent de terra i jo orbitant-te fent de lluna. A mi em costava (i em costa) bastant mes entendre les coses que no pas a en Feynman jeje, però tu hi has posat mes esforç que ningú en ajudar-me sempre i encara ara continuo aprenent constantment de tu, del papa i d'en Jordi. No em puc deixar al millor secretari del món, en Sirius. No sé si hauria acabat la tesi sense ell fent-me companyia de dia i de nit, a vegades dormint, però sempre ajudant, t'estimo molt peque. I en falta un, i tant que ens falta! En Drum (drumi gosezno), ens ho fem com podem sense tu i sempre em treus un somriure quan penso en tu. L'altre dia vaig veure Tossa des de l'avió i em vaig emocionar de pensar que en aquell petit poblet tan maco hi viviu tots vosaltres que sou la gent que mes estimo d'aquest món. Només em queda una cosa per dir, UST!!!!

Sílvia

Full List of Publications

This thesis is presented as a compendium of publications:

Chapter 4

1. S. Escayola[†], C. Tonnelé[†], E. Matito, A. Poater, H. Ottosson*, M. Solà*, D. Casanova*, Guidelines for Tuning the Excited State Hückel-Baird Hybrid Aromatic Character of Pro-Aromatic Quinoidal Compounds, *Angew. Chem. Int. Ed.*, **2021**, 60, 10225–10265. [Chemistry, Multidisciplinary, Q1, JCR IF: 15.336]
   [†]These two authors contributed equally to this work
   Classified as a Hot Paper by the editor. Selected to build the Nature Index 2021

2. S. Escayola, M. Callís, A. Poater*, M. Solà*, Effect of Exocyclic Substituents and π-System Length on the Electronic Structure of Chichibabin Diradical(oid)s, *ACS Omega*, **2019**, 4, 10845–10853. [Chemistry, Multidisciplinary, Q2, JCR IF: 2.582]

Chapter 5

3. S. Escayola, J. Labella, D. W. Szczepanik, A. Poater, T. Torres, M. Solà*, E. Matito*, From (Sub)Porphyrin to (Sub)Phthalocyanine: Aromaticity Signatures in the UV-Vis Absorption Spectra, *In preparation.*

4. S. Escayola, A. Poater, A. Muñoz-Castro*, M. Solà*, An Unprecedented π-Electronic Circuit Involving an Odd Number of Carbon Atoms in a Grossly Warped Non-Planar Nanographene, *Chem. Commun.*, **2021**, 57, 3087–3090. [Chemistry, Multidisciplinary, Q1, JCR IF: 6.222]
   Highlighted by Chemistry World and by Anales de Química (*An. Quím.*, **2021**, 117, 74)

5. S. Escayola, N. Proos Vedin, A. Poater, H. Ottosson*, M. Solà*, In the Quest of Hückel–Hückel and Hückel–Baird Double Aromatic Tropylium (tri)Cation and Anion Derivatives, *J. Phys. Org. Chem.*, **2022**, 36, e4447. [Chemistry, Organic, Physical, Q3, JCR IF: 2.155]

   Invited contribution to the Special Issue: Excited State Aromaticity and Antiaromaticity. Top downloaded article in the issue between 1 January 2022—31 December 2022

6. J. Poater, C. Viñas, I. Bennour, S. Escayola, M. Solà*, F. Teixidor*, Too Persistent to Give Up: Aromaticity in Boron Clusters Survives Radical Structural Changes, *J. Am. Chem. Soc.*, **2020**, 142, 9396–9407. [Chemistry, Multidisciplinary, Q1, JCR IF: 15.419]

   Highlighted in "Spotlights on Recent JACS Publications" *J. Am. Chem. Soc.*, **2020**, 142, 10233–10234. Selected to build the Nature Index 2020. Highly cited paper in WoS (2021)

7. J. Poater, C. Viñas, S. Escayola, M. Solà*, F. Teixidor*, Pioneering the Power of Twin Bonds in a Revolutionary Double Bond Formation. Unveiling the True Identity of *o*-Carboryne as *o*-Carborene, *Chem. Eur. J.*, **2023**, 29, e202302448. [Chemistry, Multidisciplinary, Q2, JCR IF: 4.300]

   Classified as a Very Important Paper by the editor

8. J. Poater[†], S. Escayola[†], A. Poater, F. Teixidor, H. Ottosson*, C. Viñas*, M. Solà*, Single—Not Double—3D-Aromaticity in Oxidized *Closo* Icosahedral Dodecaiodo-Dodecaborate Cluster, *J. Am. Chem. Soc.*, **2023**, 145, 22527–22538. [Chemistry, Multidisciplinary, Q1, JCR IF: 15.000]

   [†]These two authors contributed equally to this work

   Highlighted by Sociedad de Biofísica de España

Other published articles not included directly in the compendium of publications for this thesis, but contributing to parts of the discussion:

9. C. J. Richmond, S. Escayola, A. Poater*, Axial Ligand effects of Ru-BDA Complexes in the O-O Bond Formation via the I2M Bimolecular Mechanism in Water Oxidation Catalysis, *Eur. J. Inorg. Chem.*, **2019**, 2019, 2101–2108.

10. S. Escayola, M. Solà*, A. Poater*, Mechanism of the Facile Nitrous Oxide Fixation by Homogeneous Ruthenium Hydride Pincer Catalysts, *Inorg. Chem.*, **2020**, 59, 9374–9383.

11. S. Escayola, A. Brotons, N. Bahri-Laleh, F. Ragone, L. Cavallo*, M. Solà*, A. Poater*, Fluxional Bis(phenoxy-imine) Zr and Ti Catalysts for Polymerization, *Theor. Chem. Acc.*, **2021**, 140, 49.

12. S. Escayola, J. Poater*, M. Ramos, J. A. Luque-Urrutia, J. Duran, S. Simon, M. Solà, L. Cavallo, S. P. Nolan*, A Poater*, Chelation Enforcing a Dual Gold Configuration in the Catalytic Hydroxyphenoxylation of Alkynes, *Appl. Organomet. Chem.*, **2021**, 35, e6362.

13. M. Gimferrer, N. Joly, S. Escayola, E. Viñas, S. Gaillard, M. Solà, J.-L. Renaud*, P. Salvador*, A. Poater*, Knölker Iron Catalysts for Hydrogenation Revisited: Non Spectator Solvent and Fine-Tuning, *Organometallics*, **2022**, 41, 1204–1215.

14. S. Posada-Pérez, S. Escayola, J. Poater*, M. Solà*, A. Poater*, Ni(I)-TPA Stabilization by Hydrogen Bond Formation on the Second Coordination Sphere: a DFT Characterization, *Dalton Trans.*, **2022**, 51, 12585–12595.

15. J. Heitkämper, S. Posada-Pérez*, S. Escayola, M. Solà, J. Kästner, A. Poater*, A Non Expected Alternative Ni(0) Species in the Ni-Catalytic Aldehyde and Alcohol Arylation Reactions Facilitated by a 1,5-Diaza-3,7-diphosphacyclooctane Ligand, *Chem. Eur. J.*, **2023**, 29, e202300193.

16. N. Joly, M. Gimferrer, S. Escayola, M. Cendra, S. Coufourier, J.-F. Lohier, Q. G. Gaillard, S. Gaillard, M. Solà*, J.-F. Renaud*, A. Poater*, Enhancement of Knölker Iron Catalysts for Imine Hydrogenation by Predictive Catalysis: From Calculations to Selective Experiments, *Organometallics*, **2023**, 42, 1784–1792.

17. S. Escayola, N. Bahri-Laleh, A. Poater*, $\%V_{Bur}$ Index and Steric Maps: From Predictive Catalysis to Machine Learning, *Chem. Soc. Rev.*, **2023**, 53, 853–882.

18. M. Orozco-Ic*, L. Soriano-Agueda, S. Escayola, G. Merino, D. Sundholm, E. Matito, Understanding Aromaticity in [5]Helicene-Bridged Cyclophanes: A Comprehensive Study, *J. Org. Chem.*, **2024**, 4, 2459–2466.

19. N. Proos Vedin, S. Escayola, S. Radenković*, M. Solà*, H. Ottosson*, The n,π* States of Heteroaromatics: When are They the Lowest Excited States and in What Way Can They Be Aromatic or Antiaromatic?, *ChemRxiv*, **2024**, DOI: 10.26434/chemrxiv-2023-jx5l5-v3

20. S. Escayola, E. Jimenez-Izal, J. Ugalde, E. Matito, R. Grande-Aztatzi, J. Mercero*, Unveiling the Quantum Secrets of Triel Metal Triangles: A Tale of Stability, Aromaticity, and Relativistic Effects, *Phys. Chem. Chem. Phys.*, **2024** Accepted.

List of Acronyms

A	Aromaticity
AA	Antiaromaticity
ACID	Anisotropy of the Induced Current Density
AIM	Atoms In Molecules
AO	Atomic Orbital
ASE	Aromatic Stabilization Energy
B3LYP	Becke, 3-parameter, Lee-Yang-Parr Functional
BLA	Bond-Length Alternation
BLYP	Becke-Lee-Yang-Parr Functional
BO	Born-Oppenheimer
CAM-B3LYP	Coulomb-Attenuating Method B3LYP
CASPT2	Complete Active Space Perturbation Theory (Second Order)
CASSCF	Complete Active Space Self Consistent Field
CBD	Cyclobutadiene
CCSD(T)	Coupled Cluster Singles, Doubles, and Perturbative Triples
C-DFT	Constrained DFT
CI	Configuration Interaction
CIS	Configuration Interaction Singles
COT	Cyclooctatetraene
CS	Closed-Shell
CT	Charge Transfer
DCM	Dichloromethane
DE	Delocalization Error
$\Delta E_{\text{S-T}}$	Singlet-Triplet Energy Gap (defined as E_{T_1} minus E_{S_1})
$\Delta E_{\text{S}_0\text{-T}}$	Ground State Singlet-Triplet Energy Gap (defined as E_{T_1} minus E_{S_0})
DFA	Density Functional Approximation
DFT	Density Functional Theory

DI	Delocalization Index
DSP	Double Spin Polarization
DZ	Double-ζ
ECP	Effective Core Potential
EDA	Energy Decomposition Analysis
EDDB	Electron Density of Delocalized Bonds
EDG	Electron-Donating Group
ELF	Electron Localization Function
EOM-CCSD	Equation of Motion CCSD
ES	Excited State
EWG	Electron-Withdrawing Group
FCI	Full Configuration Interaction
FLU	Aromatic Fluctuation Index
GGA	Generalised Gradient Approximation
GIAO	Gauge-Independent Atomic Orbital
GIMIC	Gauge-Including Magnetically Induced Current
GS	Ground State
HF	Hartree Fock
HK	Hohenberg-Kohn
HOMA	Harmonic Oscillator Model of Aromaticity
HOMO	Highest Occupied Molecular Orbital
IR	Infrared Spectroscopy
ISC	Intersystem Crossing
KS	Kohn–Sham
LC	Long-Range Corrected
LR	Long-Range
LRes	Linear-Response
LUMO	Lowest Unoccupied Molecular Orbital
M06-2X	Minnesota 2006 Double Exchange Functional
MBO	Mayer Bond Order
MCI	Multicenter Index
MCSCF	Multiconfigurational Self Consistent Field
MO	Molecular Orbital
MP2	Møller-Plesset Perturbation Theory (Second Order)
MRCI	MultiReference Configuration Interaction
MRPT	MultiReference Perturbation Theory

MS-CASPT2	Multi-State CASPT2
n-MR	n-Membered Ring
NBO	Natural Bond Orbital
NICS	Nucleus-Independent Chemical Shift
NLO(P)	Nonlinear Optical (Property)
NMR	Nuclear Magnetic Resonance
NPA	Natural Population Analysis
NTO	Natural Transition Orbital
OS(S)	Open-Shell (Singlet)
OT	Optimally Tuned
P	Porphyrin
Pz	Porphyrazine
PBE	Perdew-Burke-Ernzerhof Functional
Pc	Phthalocyanine
PCM	Polarizable Continuum Model
PES	Potential Energy Surface
ppm	parts-per-million
QTAIM	Quantum Theory of Atoms in Molecules
RHF	Restricted Hartree-Fock
ROHF	Restricted Open-Shell Hartree-Fock
RMSD	Root Mean Square Deviation
SCF	Self Consistent Field
S	Singlet
SIE	Self-Interaction Error
SOMO	Singly Occupied Molecular Orbital
SOC	Spin-Orbit Coupling
SR	Short-Range
STO	Slater-Type Orbital
SubP	SubPorphyrin
SubPc	SubPhthalocyanine
T	Triplet
TBP	TetraBenzoPorphyrin
TBSuP	TriBenzoSubPorphyrin
TD	Time-Dependent
TDDFT	Time-Dependent Density Functional Theory
TDA	Tamm-Dancoff Approximation

TCNQ	TetraCyanoQuinodimethane
TMTQ	TetracyanoMethyleneThiophene[10]annuleneQuinodimethane (2,7-Dicyanomethylene-thiophene-1,6-methano[10]annulene)
TPSS	Tao-Perdew-Staroverov-Scuseria Functional
TZ	Triple-ζ
UV-Vis	Ultraviolet-Visible Spectroscopy
UHF	Unrestricted Hartree Fock
vdW	van der Waals
XC	Exchange-Correlation
X	Halogen Substituent

Contents

Contents

List of figures

List of tables

Summary

Aromaticity is a widely used concept in the prediction, design, and understanding of key aspects related to reactivity, structure, and properties of molecules. Linked to cyclic or three-dimensional molecular systems, it involves electron delocalization within a closed circuit—either a ring or a 3D structure—resulting in enhanced thermodynamic stability, significant magnetic anisotropies, and unusual chemical shifts, among other properties. With nearly two centuries of history and despite not being a physical observable, the analysis of aromaticity and antiaromaticity, the latter leading to increased reactivity and instability, is still of great interest. For instance, aromaticity has applications explaining the behavior of photoexcited molecules, a challenge that prevents the rapid development of new materials or photochemical reactions. The growing use of (anti)aromaticity in excited state chemistry supports the idea that concepts established for the ground state are transferable to excited states. Yet, their inherent complexity demands further exploration, particularly as the applicability of specific aromaticity rules and indicators in certain excited states remains elusive. Furthermore, the discovery of new aromatic compounds extends well beyond simple annulenes, encompassing structures with complex topologies. These include large molecules with multiple delocalization pathways, multifold aromaticity (with the presence of σ-, π-, δ-, and/or φ-aromaticity), three-dimensional, non-planar structures, etc. Such examples necessitate a reevaluation of established boundaries of aromaticity.

In this thesis, we focus on the computational study of aromaticity as a tool for characterizing challenging molecular systems, particularly those in their low-lying excited states or with intricate molecular topologies. Thus, our investigation is divided into two main blocks: Chapter 4, which centers on characterizing pro-aromatic quinoidal systems in their excited states, and Chapter 5, dedicated to examining molecules with complex topologies. Overall, we determine whether aromatic character correlates with specific molecular properties while exploring the utility and limitations of various aromaticity indicators. Additionally, we offer guidelines for molecular design

to achieve specific aromatic features. Through this work, we aim to contribute to the accurate classification of chemical systems, thereby facilitating advancements in practical applications.

Kekulé diradicaloids, with their unique electronic properties and potential applications across various fields, notably in optoelectronics, are a central theme of our investigation. These pro-aromatic molecules exhibit low-lying triplet and singlet excited states, with the open-shell structure having the potential to become the ground state. The stability of these states can be partially ascribed to the transition of the central ring from quinoidal to aromatic forms. The latter, are significantly influenced by resonance structures in which conjugated rings exhibit Hückel-aromatic character. However, structural modifications can induce the central rings to adopt a mixed character between different resonance structures involving $4n + 2$ and $4n$ π-electrons, with hybrid Hückel–Baird-aromatic characteristics. The absence of definitive spectroscopic techniques for elucidating the electronic structure of these molecules in the excited state—key for advancing new material development—underscores the importance of thorough analyses and computational assessments. To explore the applicability of aromaticity rules in characterizing these molecules, we systematically analyzed variously substituted Kekulé diradicaloids. This approach, presented in Chapter 4, has enabled us to establish guidelines for the rational design of molecules with specific singlet–triplet energy gaps and excited state Hückel–Baird aromaticity.

The second block, corresponding to Chapter 5, is composed of four sections devoted to the study of aromaticity in (sub)phthalocyanines and related compounds, $C_{80}H_{30}$ curved nanographene, double aromatic substituted tropylium ions, and polyhedral boranes. Each case faces challenges in evaluating aromaticity due to complex system topologies that limit the applicability of traditional indicators. Yet, determining the aromatic or non-aromatic nature of these systems is crucial for comprehending their inherent properties. Notably, we establish a correlation between the aromaticity of the external conjugated pathways and the Q bands in the UV-Vis absorption spectra of (sub)phthalocyanines. We identified a 75 π-electron conjugated pathway—not following any of the known aromaticity rules—in a grossly warped nanographene, $C_{80}H_{30}$. Besides, we proposed potential σ- and π-doubly aromatic tropylium ion derivatives, noting the challenge of achieving double aromaticity due to electronic and steric effects. Lastly, we examined the aromaticity in 3D boron clusters to explain their stability and gain deeper insights into their chemical bonding.

Resum

L'aromaticitat és un concepte àmpliament utilitzat per predir, dissenyar i entendre els aspectes clau de la reactivitat, estructura i propietats de les molècules. Atribuïda a sistemes moleculars cíclics o tridimensionals, implica la deslocalització d'electrons dins d'un circuit tancat—ja sigui un anell o una estructura 3D—resultant en una major estabilitat termodinàmica, anisotropies magnètiques significatives i desplaçaments químics inusuals, entre d'altres. Amb gairebé dos segles d'història i malgrat no ser un observable, l'anàlisi de l'aromaticitat i antiaromaticitat, la darrera resultant en una major reactivitat i inestabilitat, continua despertant un gran interès. Per exemple, l'aromaticitat té aplicacions explicant el comportament de molècules fotoexcitades, un repte que impedeix el ràpid desenvolupament de nous materials o reaccions foto-químiques. L'ús creixent de l'(anti)aromaticitat i els estudis realitzats en l'àmbit de la química d'estats excitats dóna suport a la idea que els conceptes establerts per l'estat fonamental són transferibles a aquests estats excitats. No obstant, la complexitat inherent a estudiar sistemes excitats exigeix una exploració addicional, especialment si es té en compte que l'aplicabilitat de regles i indicadors específics d'aromaticitat en certs estats excitats encara és elusiva. A més, el descobriment de nous compostos aromàtics s'estén molt més enllà dels annulens simples, abastant estructures amb topologies complexes. Aquests inclouen molècules grans amb diferents camins de deslocalització, aromaticitat múltiple (amb la presència d'aromaticitat σ-, π-, δ-, i/o φ-), estructures tridimensionals, compostos no plans, etc. Els exemples esmentats requereixen una reavaluació dels límits de l'aromaticitat establerts.

Aquesta tesi posa l'accent en l'anàlisi computacional de l'aromaticitat com a eina per caracteritzar sistemes moleculars desafiants, particularment aquells en els seus primers estats excitats (de més baixa energia) o amb topologies moleculars complexes. Així doncs, la nostra investigació es divideix principalment en dos blocs: el Capítol 4, centrat en la caracterització de sistemes quinoidals pro-aromàtics en els seus estats excitats, i el Capítol 5, dedicat a examinar molècules amb topologies

complexes. En general, determinem si el caràcter aromàtic es correlaciona amb propietats moleculars específiques mentre explorem la utilitat i limitacions de diversos indicadors d'aromaticitat. Addicionalment, oferim pautes per al disseny molecular amb l'objectiu d'assolir característiques aromàtiques específiques. Amb aquest treball, aspirem a contribuir a la classificació precisa de sistemes moleculars, facilitant així avenços en aplicacions pràctiques.

Un dels focus d'aquesta investigació són els diradicaloides de Kekulé, els quals presenten propietats electròniques úniques, potencialment aplicables en diversos camps, com l'optoelectrònica. Aquestes molècules, qualificades de pro-aromàtiques, presenten estats excitats triplets i singlets de baixa energia, o fins i tot la possibilitat que l'estat fonamental sigui de capa oberta. L'estabilitat de les formes de capa oberta és deguda al canvi que pateix l'anell central en passar d'una forma quinoidal a una d'aromàtica, generalment, de tipus Hückel. Tanmateix, certs canvis estructurals poden induir l'adopció d'un caràcter mixt entre diferents estructures de ressonància involucrant anells de $4n + 2$ i $4n$ electrons π, amb característiques aromàtiques híbrides de tipus Hückel–Baird. La manca de tècniques espectroscòpiques definitives per a elucidar l'estructura electrònica d'aquestes molècules en l'estat excitat—clau per al desenvolupament de nous materials—, subratlla la importància de dur a terme anàlisis i avaluacions computacionals exhaustives. Tal i com es detalla al Capítol 4, hem analitzat sistemàticament diradicaloides de Kekulé diferentment substituïts definint pautes útils per dissenyar molècules amb les propietats desitjades i aromaticitat Hückel–Baird en estats excitats.

El segon bloc, corresponent al Capítol 5, està repartit en quatre seccions dedicades a l'estudi de l'aromaticitat en (sub)ftalocianines, nanografè corbat $C_{80}H_{30}$, ions tropil·li substituïts doblement aromàtics i borans polièdrics. Cadascun presenta reptes a l'hora d'avaluar l'aromaticitat a causa de les topologies complexes dels sistemes, limitant l'aplicabilitat dels indicadors tradicionals. Malgrat tot, determinar la naturalesa (no-)aromàtica d'aquests sistemes és crucial per comprendre les seves propietats. Notablement, hem establert una correlació entre l'aromaticitat dels camins conjugats externs i les bandes Q en els espectres d'absorció UV-Vis de les (sub)ftalocianines. També hem identificat un camí conjugat de 75 electrons π—que no segueix cap de les regles d'aromaticitat conegudes—en el nanografè deformat, $C_{80}H_{30}$. A més, hem proposat derivats σ- i π-doblement aromàtics de l'ió tropil·li, destacant-ne la dificultat d'assolir doble aromaticitat degut a efectes electrònics i estèrics. Finalment, hem

examinat l'aromaticitat en clústers 3D de bor per explicar la seva estabilitat i generar una comprensió més profunda dels seus enllaços químics.

Resumen

La aromaticidad es un concepto ampliamente utilizado en la predicción, diseño y comprensión de la reactividad, estructura, y propiedades de las moléculas. Vinculado a sistemas moleculares cíclicos o tridimensionales, implica la deslocalización de electrones dentro de un circuito cerrado—ya sea un anillo o una estructura 3D—resultando en una mayor estabilidad termodinámica, anisotropías magnéticas significativas y desplazamientos químicos inusuales, entre otras propiedades. Con casi dos siglos de historia y a pesar de no ser un observable, el análisis de la aromaticidad y antiaromaticidad, esta última dando lugar a una reactividad e inestabilidad incrementadas, sigue siendo de gran interés. Por ejemplo, la aromaticidad permite explicar el comportamiento de moléculas fotoexcitadas, un desafío que impide el rápido desarrollo de nuevos materiales o reacciones fotoquímicas. El uso creciente de la (anti)aromaticidad en química de estados excitados respalda la idea de que los conceptos establecidos para el estado fundamental son transferibles a estados excitados. Sin embargo, la complejidad inherente a estudiar sistemas excitados exige una exploración adicional, particularmente ya que la aplicabilidad de reglas e indicadores específicos de aromaticidad en ciertos estados excitados sigue siendo elusiva. Además, el descubrimiento de nuevos compuestos aromáticos se extiende mucho más allá de los anulenos simples, abarcando estructuras con topologías complejas. Estos incluyen moléculas grandes con diferentes caminos de deslocalización, aromaticidad múltiple (con la presencia de aromaticidad σ-, π-, δ-, y/o φ-), estructuras tridimensionales, compuestos no planos, etc. Tales ejemplos necesitan una reevaluación de los límites de la aromaticidad conocidos.

Esta tesis se centra en el estudio computacional de la aromaticidad como herramienta para caracterizar sistemas moleculares desafiantes, particularmente aquellos en sus primeros estados excitados (de más baja energía) o con topologías moleculares complejas. Así pues, nuestra investigación se divide principalmente en dos bloques: el Capítulo 4, centrado en la caracterización de sistemas quinoidales pro-aromáticos en sus estados excitados, y el Capítulo 5, dedicado a examinar moléculas con topologías complejas. En

general, determinamos si el carácter aromático correlaciona con propiedades moleculares específicas mientras exploramos la utilidad y limitaciones de varios indicadores de aromaticidad. Adicionalmente, ofrecemos pautas para el diseño molecular para lograr características aromáticas específicas. Con este trabajo, nos proponemos contribuir a la clasificación precisa de sistemas moleculares, facilitando así avances en aplicaciones prácticas.

En concreto, los diradicaloides de Kekulé, con propiedades electrónicas únicas y potencialmente aplicables en diversos campos, como la optoelectrónica, son uno de los focos de esta investigación. Estas moléculas pro-aromáticas, con estados excitados tripletes y singletes de baja energía, o incluso la posibilidad de que el estado fundamental sea de capa abierta, muestran estabilidad debido a la transición del anillo central de formas quinoidales a aromáticas, por estructuras de resonancia con anillos aromáticos tipo Hückel. Sin embargo, ciertos cambios estructurales pueden inducir la adopción de un carácter mixto entre diferentes estructuras de resonancia involucrando anillos de $4n + 2$ y $4n$ electrones π, con características aromáticas híbridas de tipo Hückel–Baird. La falta de técnicas espectroscópicas definitivas para elucidar la estructura electrónica de estas moléculas en el estado excitado—clave para el desarrollo de nuevos materiales— subraya la importancia de llevar a cabo análisis y evaluaciones computacionales exhaustivos. Tal y como se detalla en el Capítulo 4, hemos analizado sistemáticamente diradicaloides de Kekulé diferentemente sustituidos proponiendo pautas para diseñar moléculas con las propiedades deseadas y aromaticidad Hückel–Baird en estados excitados.

El segundo bloque, correspondiente al Capítulo 5, está compuesto por cuatro secciones dedicadas al estudio de la aromaticidad en (sub)ftalocianinas, nanografeno curvado $C_{80}H_{30}$, iones tropilio sustituidos doblemente aromáticos y boranos poliédricos. Cada uno presenta desafíos al evaluar la aromaticidad debido a las topologías complejas de los sistemas limitando la aplicabilidad de los indicadores tradicionales. Sin embargo, determinar la naturaleza (no)aromática de estos sistemas es crucial para comprender sus propiedades. Notablemente, establecemos una correlación entre la aromaticidad de los caminos conjugados externos y las bandas Q en los espectros de absorción UV-Vis de las (sub)ftalocianinas. También hemos identificado un camino conjugado de 75 electrones π—que no sigue ninguna de las reglas de aromaticidad conocidas—en el nanografeno deformado, $C_{80}H_{30}$. Además, hemos propuesto derivados σ- y π-doblemente aromáticos del ion tropilio, destacando la dificultad de alcanzar doble aromaticidad debido a efectos electrónicos y estéricos. Finalmente, hemos examinado la aromaticidad en clusters 3D

de boro para explicar su estabilidad y obtener una comprensión más profunda de sus enlaces químicos.

1 Introduction

1.1 Classification in Chemistry

As human beings, we possess an innate drive to understand the world that surrounds us. Whether this drive is motivated by a natural survival instinct or by cultural components, there is an imaginative dimension that sets us apart from other known species. Our investigative attitude and capacity for communication emerged at the end of the Pliocene, about 2.5 million years ago, and has evolved since then. As a result, *homo sapiens* are endowed with great communication capacity, creativity, and the ability to establish intuitive and abstract connections. All these traits truly took off with the transition from prehistory to history, marking the era when the first texts began to document our understanding and experiences. This milestone initiated a continuum of progress and development that continues to the present day.

"*Science is organized knowledge.*"

– attributed to Immanuel Kant (1724-1804)

As knowledge became systematized and more readily disseminated across generations, the foundational elements of contemporary natural sciences started to emerge. Ancient civilizations in Egypt and Mesopotamia initiated structured investigations into physical phenomena. Thinkers and philosophers from Greek, Indian, and other cultures began to ask themselves the big question: '*What really is everything?*'. They hypothesized that matter was composed of small indivisible particles. Indeed, the Greek natural philosophers Leucippus and Democritus introduced the word *atomos*, meaning 'uncuttable', to refer to these elementary particles [1]. However, it was not until the early 1800s that a solid atomic theory gained acceptance within the scientific community after John Dalton's empirical observations led him to propose that common substances always break down into a consistent set of elements in fixed ratios [2].

Introduction

Building upon the foundations of atomic theory, the subsequent discovery of an increasing number of elements called for a systematic way to organize this growing body of knowledge. This led to the creation of the periodic table of elements (Figure 1.1), probably the most iconic symbol of chemistry and an exemplary model of organization within the field. Moseley's periodic table contains the physical elements arranged according to their atomic number, electronic configuration, and properties. This modern periodic table, along with previous arrangements including major contributions by Lavoisier, Döbereiner, Mendeleev, and others [3], provided a coherent framework, which not only facilitated the categorization of known elements during the 19th century but also enabled accurate predictions of the properties of elements that had yet to be discovered.
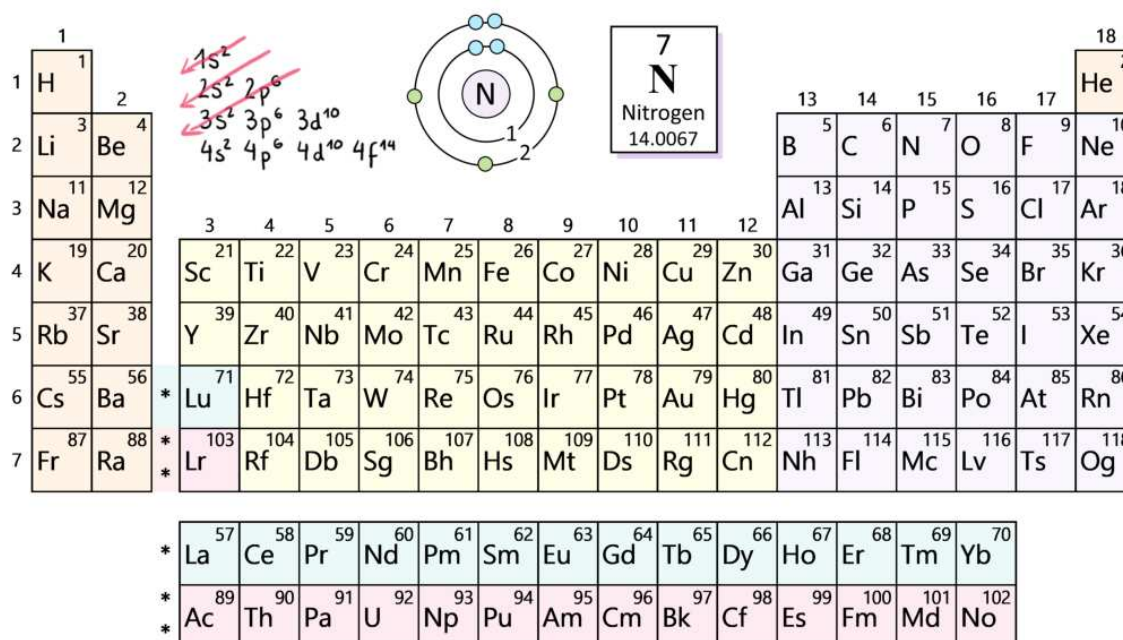
Figure 1.1 Periodic table of the chemical elements. On top are a truncated Moeller diagram and a Bohr-Rutherford diagram for the N atom.

While the periodic table serves as a primary framework for the classification of elements, symmetry provides a fundamental basis for categorizing and understanding molecular structures and reactivity. Importantly, the concept of symmetry extends beyond the chemistry realm; numerous unrelated examples of objects, phenomena, and theories demonstrate the involvement of symmetry. One beautiful case is the discovery of buckminsterfullerene, C_{60}, as shown in Figure 1.2a. In this instance, symmetry served as the link between architecture and chemistry, playing a crucial role in the discovery. In 1985, Kroto, Curl, Smalley, and coworkers made the pivotal

discovery [4] that would lead them to win the Nobel Prize in Chemistry eleven years later. Although C_{60} had previously been detected by mass spectrometry [5], its exact structure remained unidentified until this team related the mass peak of 720 to its icosahedral structure. This identification was inspired by the architectural designs of Buckminster Fuller. Fuller, even not the original inventor, coined and popularized the term *geodesic dome*, and designed several prominent examples, such as the Montreal Biosphère (Figure 1.2b and c) [6].
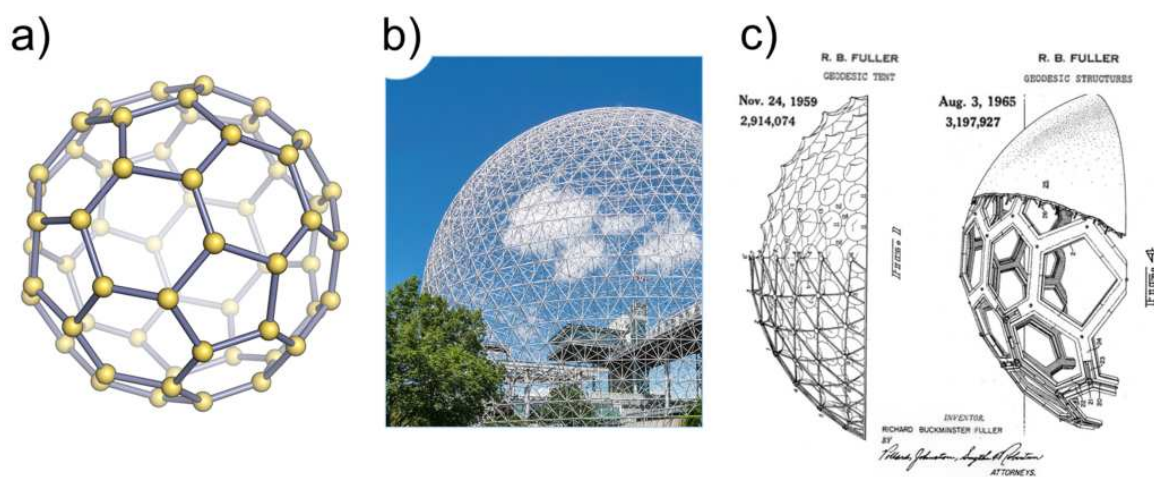
Figure 1.2 Structure of fullerene and geodesic domes. a) The molecular structure of C_{60}. b) The Montreal Biosphère Museum, illustrating geodesic dome architecture, originally constructed in 1967 for the International and Universal Exposition. Image adapted from an original by Ralf Roletschek, 2017. Accessed via http://www.roletschek.at. c) Original drawings of Fuller's geodesic domes. Adapted from reference [7].

This is but one example, highlighting the substantial and extensive role of symmetry in chemistry. Beyond its utility for making predictions based on geometries and Lewis structures, its most critical application resides in the use of group theory in quantum mechanics. The foundational relationship between group theory and quantum mechanics was established in the late 1920s by a group of scientists including Weyl, Wigner, Heisenberg, and others [8]. This became extremely useful with the arrival of computational quantum chemistry in the later half of the 20th century, serving as a practical tool for researchers.

The consideration of molecular symmetry, when present, not only reduces the cost of solving equations but also allows us to get useful information about the properties of molecules from which their structures can be predicted. To achieve this, molecules must be classified according to their *symmetry elements* and *operations*: identity, *n*-fold

rotation axis, plane of symmetry, rotary-reflection axis, and center of symmetry, which are represented as E, C_n, σ, S_n, and i, respectively. Based on the symmetry elements, we can determine the point group to which a molecule belongs. The advantage of this classification is that, once the point group is established, the complexity of the individual molecule becomes less important. Instead, we can focus on a geometric body that exhibits the corresponding symmetry properties [9]. Practically speaking, the systematic approach for determining point groups involves a flow chart, exemplified in Figure 1.3, which, in this case, reveals that the point group of C_{60} is I_h.
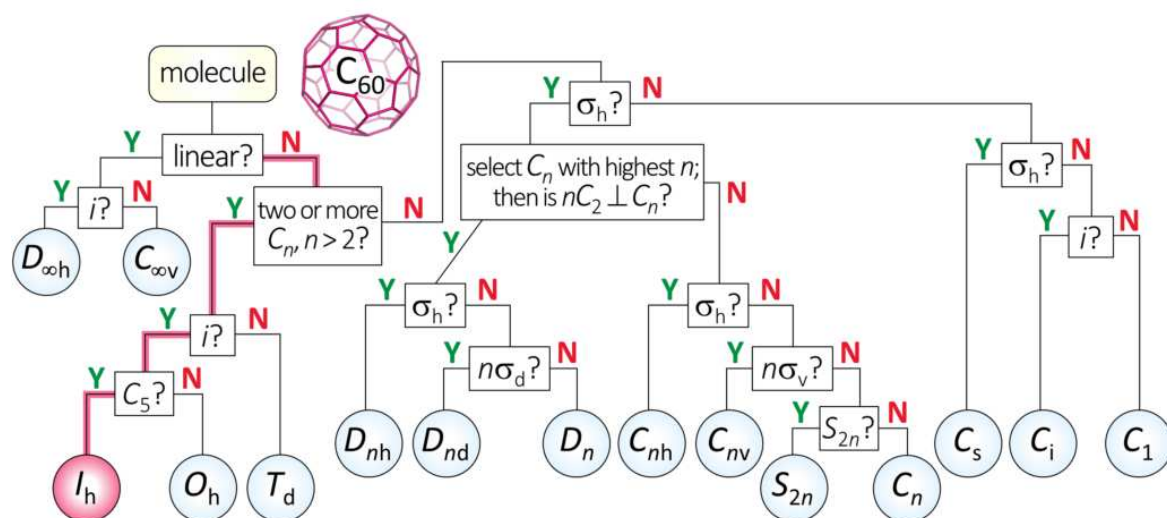
Figure 1.3 Symmetry flow chart for determining the point group of a molecule exemplifying the case of C_{60}.

The previous examples prove that classification is not just a method for imposing order on a chaotic collection of data; it is a tool that drives scientific investigation and enhances our ability to make meaningful advancements.

Considering the importance of organization in science, and since we mentioned computational chemistry, it is noteworthy that the Catalan, Basque, Spanish, and French words for the term computer are derived from the Latin '*ordinator*' «one who orders» [10]. This etymology underscores the role of computers in organizing and systematizing data. Moreover, with artificial intelligence, this capacity for order is evolving and serves also as a feedback mechanism that enhances algorithmic learning [11]. Computers are not only sorting information but are now also discerning patterns and predicting behaviors within chemical systems [12, 13]. This expands the boundaries of classification and helps us to uncover hidden aspects, undetectable by human rationale alone.

This sophisticated level of organization and analysis is particularly crucial in chemistry. The comparative analysis of atoms, molecular fragments, or entire molecules is fundamental for quantifying their distinct characteristics. These comparisons are typically made using simple models or more elaborate computational methods based on classic or quantum mechanics. Whether these quantities are physical observables (*e.g.*, geometries, energies, or dipole moments) or quantities that cannot be directly measured (*e.g.*, covalent radii, bond order, or aromaticity), they are key for understanding the material's nature [14]. Non-observable quantities lack concrete reference values and thus they can have multiple metrics, which may not apply universally. Despite their ambiguity, the practical value of these concepts—enabling communication among researchers in the chemistry community—has been consistently demonstrated [15–18], warranting continued efforts to refine their definitions and broaden their applicability.

As previously mentioned, computational chemistry employs computer simulations, signifying a paradigm shift in the analysis and comprehension of chemical data. It extends beyond traditional boundaries, transforming molecule classification and analysis into predictive and insightful tools. This branch of chemistry encompasses many areas of study, and its influence extends to every domain of chemistry, offering deep insights into both experimental and theoretical aspects. This thesis narrows its focus to one such domain: the study of aromaticity as a tool for characterizing complex molecular systems in their ground and low-lying excited states. We investigate whether aromatic character correlates with specific molecular properties while exploring the utility and limitations of various aromaticity indicators. Additionally, we offer guidelines for molecular design to achieve particular aromatic features. Through this work, we aim to contribute to the accurate classification of chemical systems, thereby facilitating advancements in practical applications within the field.

1.2 Aromaticity

Aromaticity is a long-standing concept in chemistry, useful for understanding both the electronic structure and reactivity of molecules. It is associated to cyclic systems, which show enhanced stability due to electron delocalization and often display distinctive magnetic and electronic properties. Although originally linked to the elucidation of benzene-like compounds and their unique stability, the scope of aromaticity and antiaromaticity has been extended to other domains like heterocycles, saturated

inorganic rings with σ-, π-, δ-, or φ-aromaticity, or any combination thereof, as well as three-dimensional compounds [19]. Moreover, the concept extends beyond ground states to include excited states [20] and it is also used in transition states [21] and not only in stable compounds, presenting unique challenges that have yet to be fully addressed. In light of these complexities, arising from molecular topology or the specific state under consideration, and given the wide variety of existing descriptors and evaluation criteria, a meticulous analysis is needed for an accurate rationalization of experimental evidence [22]. In this section, we review the historical evolution of the concept, the differences between intrinsic and response aromaticity, the state of the art, and today's challenges in the aromaticity areas more related to this thesis—excited states and topologically complex systems.

1.2.1 The Concept's Journey

The history of aromaticity began with the discovery and synthesis of benzene. In 1825, Michael Faraday (Figure 1.4) isolated a compound from the oily mixture used in lamps, which exhibited a simple 1:1 carbon to hydrogen (C/H) ratio, and he termed it 'bicarburet of hydrogen' [23, 24]. A few years later, Eilhard Mitscherlich synthesized the same compound by heating benzoic acid derived from benzoin, naming it 'benzin' [25], and deduced its chemical formula to be C_6H_6. The nineteenth century saw a proliferation of similar findings, with many other compounds showing low C/H ratios and pleasant smells that seemed related to benzene. At that time, August Wilhelm von Hofmann was the first to use the term ***aromatic*** to refer to this group of compounds [26].

In the years after its discovery, the structure of benzene was not clearly understood until 1865, when Friedrich August Kekulé proposed its cyclic structure with alternating

Figure 1.4 Postage stamps from different countries commemorating Faraday and Kekulé for their scientific contributions. Images adapted from [27].

single and double bonds [28]. This significant discovery was later celebrated at the 'Benzolfest', marking 25 years since his seminal contribution. At that event, Kekulé narrated the famous anecdote of his dream about the Ouroboros, the serpent eating its own tail, which inspired his proposal of benzene's cyclic structure [29].

With the increasing number of aromatic compounds discovered, the aromaticity concept continued to evolve, expanding from a focus on benzene derivatives, which were characterized by structural comparison, to encompassing a larger variety of compounds with chemical properties similar to benzene, especially in terms of reactivity. The synthesis of heteroaromatic compounds such as pyridine [30], along with polycyclic hydrocarbons like naphthalene [31], highlighted the need to reevaluate the criteria for aromaticity. Moreover, the original Kekulé's structure had limitations to explain experimental evidence. For instance, such a structure would suggest the existence of two isomers of 1,2-disubstituted benzene, while only one was observed. Kekulé subsequently proposed a model that accounted for the resonance hybrid of two structures, a concept that introduced the idea of delocalized π-electrons [19, 32]. Also from comparing the stability of aromatic compounds to aliphatic analogs, they considered the hypothesis that the unusual stability could be given due to their cyclic resonant structures. However, the discovery and analysis of the properties of cyclooctatetraene (COT), an [8]annulene with two resonant forms (analogous to those of benzene), revealed that this compound had similar properties to a non-cyclic olefinic molecule [33]. Furthermore, this evidence showed that the depiction of benzene as a resonance hybrid does not entirely account for its extraordinary stability.

An important breakthrough came with the advent of quantum mechanics [34] and the development of molecular orbital (MO) theory [35]. These scientific advancements revolutionized the understanding of chemical bonding and molecular structures. Particularly useful was Hückel molecular orbital theory [36], explaining why benzene—a symmetric molecule, with no distinguishable single or double bonds between carbon atoms—exhibits aromaticity, in contrast to COT, which does not. In 1931, Hückel [37–40] proposed his rule stating that monocyclic, planar systems that contain conjugated bonds will be aromatic (A) if they have $4n + 2$ π-electrons and antiaromatic (AA) if they have $4n$ π-electrons (where $n = 0, 1, 2, 3, \dots$).[a] In reality, the most stable

---

[a]Hückel's foundational work demonstrated MO distribution and implicitly established the $4n + 2$ rule for stable compounds with completely filled MO shells, and the $4n$ rule for unstable, incomplete shells. Doering and Detert [41] formulated the $4n + 2$ rule; with the synthesis of $C_7H_7^+$ by Doering and Knox [42] being the first experimental verification of this rule. The term 'antiaromatic' referring to $4n$ π-electron species was first introduced by Breslow [43].
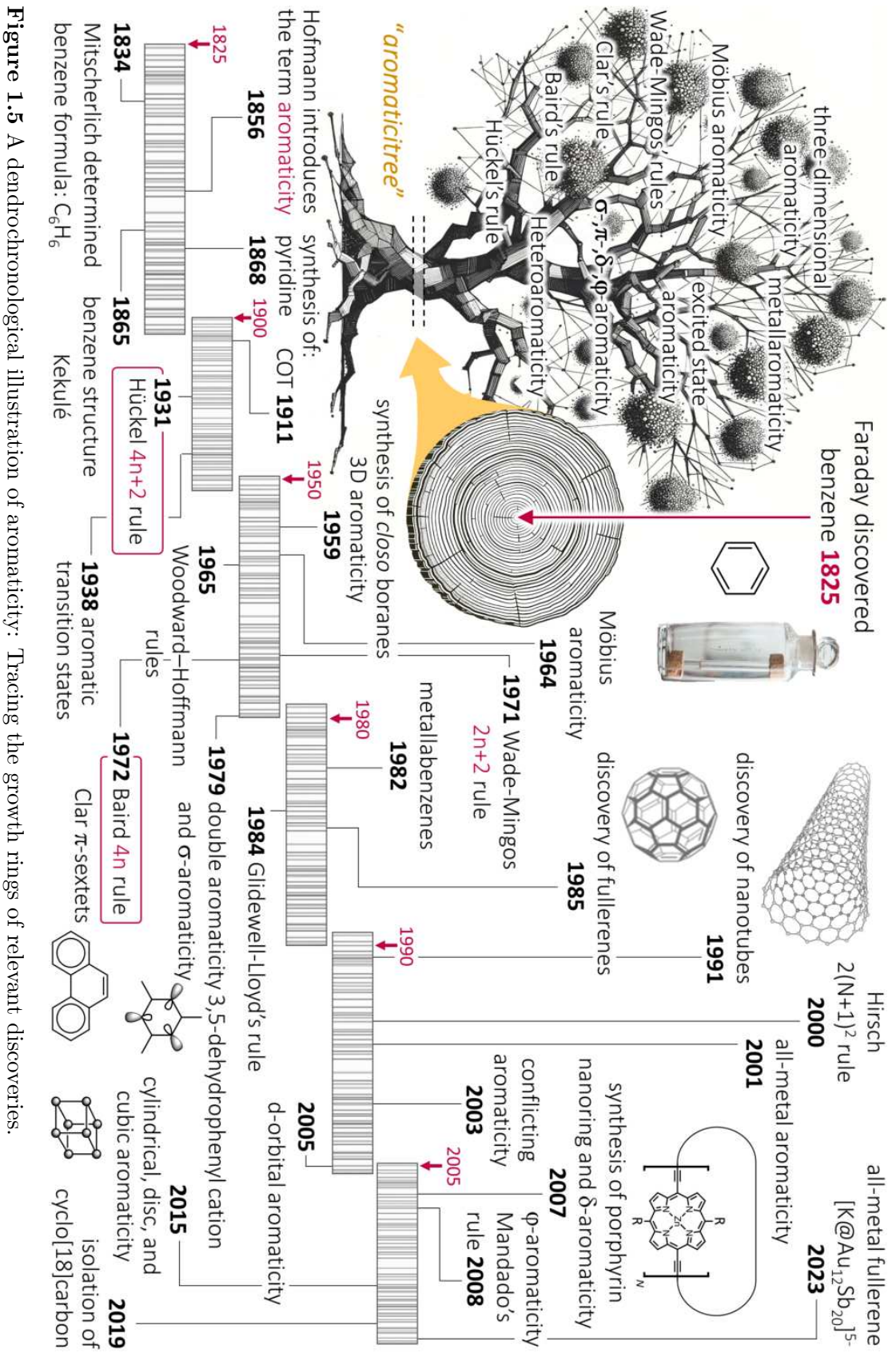
Figure 1.5 A dendrochronological illustration of aromaticity: Tracing the growth rings of relevant discoveries.

conformers of COT and a majority of the larger annulenes do not exhibit antiaromatic characteristics; their substantial ring sizes allow for flexible, puckered geometries that mitigate potential antiaromatic behavior.

The better understanding of electronic structures, promoted by improved experimental techniques and theoretical approaches, broadened significantly the scope of aromaticity. This resulted in a further extension of the concept to macromolecular systems [44–48], inorganic chemistry [49–55], three-dimensional aromaticity [56–60], and aromaticity in different orbital groups, delocalized σ, δ, and φ electrons [54, 61–63]. Even including aromatic excited π, π^* states, as exemplified by the formulation of Baird's rule in 1972 [64] and numerous subsequent studies [20, 65–71], among other discoveries highlighted in Figure 1.5. Nowadays, with nearly two centuries of history, aromaticity is still a crucial concept in chemistry. Despite the lack of a universally accepted definition of it [72], there is consensus on certain characteristic properties. Among these, cyclic electron delocalization and enhanced thermodynamic stability are pivotal [19, 73]. Other common features include bond length equalization, large magnetic anisotropies, which influence the nuclear magnetic resonance (NMR) chemical shifts, and distinctive spectroscopic properties. The indirect manifestations of aromaticity are commonly evaluated by using electronic, energetic, reactivity, geometric, and magnetic aromaticity indices. However, none of these represents a unique and straightforward measurement of aromaticity, and finding a definitive and quantitative measure of aromaticity remains a central challenge in the field.

A summary of the current aromaticity classifications [19] is presented in Figure 1.6. The diagram shows various compound classes, spatial or orbital configuration, electronic states (encompassing the ground, excited, and transition states), and the origin (intrinsic or response) of this aromaticity. Lastly, there are different families of methods used to characterize aromaticity based on electronic, energetic, reactivity, magnetic, and geometric manifestations together with various aromaticity rules [74].

The aromatic character of a molecule can often fall into multiple categories, for example, we can examine the case of a six-porphyrin nanoring (Figure 1.10b). This compound is categorized within the heterocyclic macrocycles, which are a subset of organic compounds. Topologically, it exhibits two-dimensional π-conjugation and the requisite elements for Hückel-type aromaticity. Despite possessing the potential for global aromaticity, it demonstrates only local electron delocalization within each porphyrin unit. This localized aromatic behavior is attributed to the limited delocalization
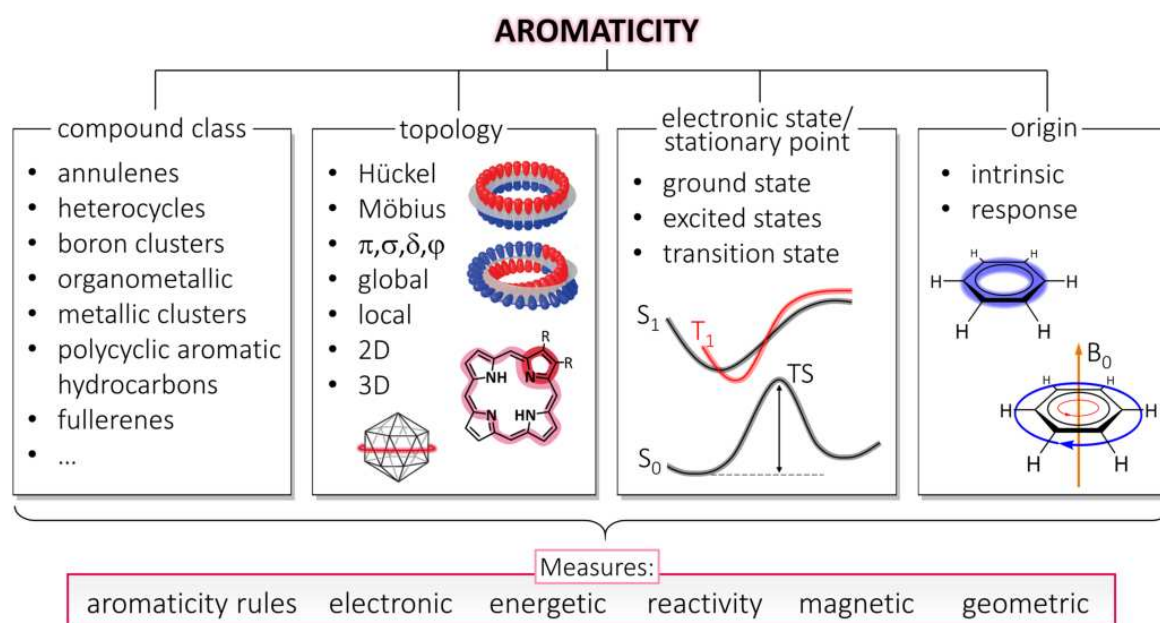
Figure 1.6 Overview of Aromaticity types. The representation of Hückel and Möbius topology has been reproduced with permission from ref. [75].

across the butadiyne linkages [76, 77]. In this case, aromaticity has been primarily investigated for the ground state, although several oxidation states have been analyzed. Finally, it has been noted that certain molecules, while inherently non-aromatic, may acquire aromatic-like properties when interacting with an applied magnetic field (B_0). Consequently, the molecule will only have some of the common aromatic features in the presence of B_0 [78, 79]. The complexity of the previously discussed compound exemplifies very well the intricate nature of molecular systems encountered in contemporary chemistry [77, 80]. It also demonstrates the multiple factors that must be considered for the evaluation of aromaticity, which can bring interesting insights for comprehending the behavior of chemical systems. However, aromaticity can become a complex and potentially misleading concept if not applied judiciously, thus an in-depth analysis is required. Furthermore, leading experts in the field have highlighted a trend towards claiming the discovery of new types of aromaticity. They suggest a shift in focus towards identifying unifying patterns within aromatic systems, which could lead to a broader and more generalized understanding, rather than exclusively pursuing novel forms of aromaticity [22, 81].

In the next sections, we discuss in more detail the differences between intrinsic and response aromaticity, which are crucial aspects for the correct evaluation of this property. Additionally, we address the challenges in characterizing aromaticity in excited states,

macrocyclic, and multidimensional cases including 3D or double aromaticity, for which traditional indices and understandings, originally developed for ground state, and (planar) small molecules, may fall short or are not applicable.

1.2.2 Intrinsic and Response-Based Aromaticity

Magnetic criterion of aromaticity is the most commonly employed when conducting aromaticity analyses [82]. These appear in a significant portion of the research papers published in this area, and are usually used as the exclusive metric for determining a molecule's aromatic character. The popularity of computational tools based on magnetic properties of aromatic rings, especially the nucleus-independent chemical shifts (NICS) [83], is due to its straightforward use (readily available in many quantum chemistry programs) and having more accessible interpretations than those of other methods, particularly from an experimentalist's viewpoint. NICS and other magnetic indices aim to capture the response of delocalized σ-, π-, δ-, or φ-electrons to an external magnetic field. The electrons circulate around the ring generating an induced magnetic field of its own (Figure 1.7a). This circulation of electrons is known as ring current. To specifically capture the magnetic resonance effects attributable to this ring
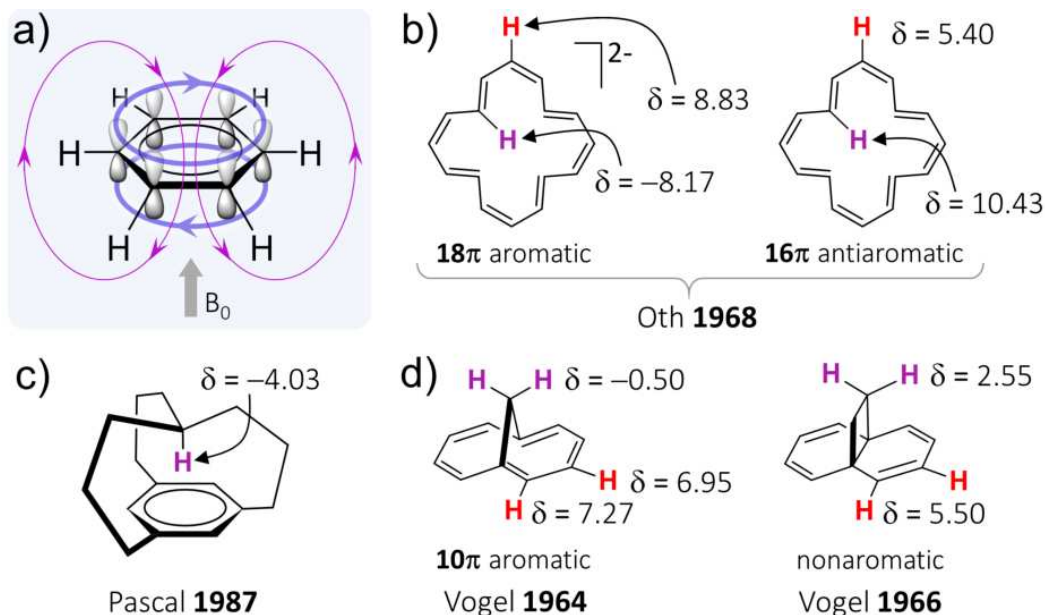
Figure 1.7 a) Ring currents (in violet), induced magnetic field (in magenta), and applied magnetic field (B_0, grey arrow). Chemical shifts (δ) in ppm for various hydrogen atoms in b) [16]annulene in its dianion and neutral forms [84], c) $[3^{4,10}][7]$-metacyclophane [85], and d) 1,6-methano[10]annulene [86] and 1,6-ethano[10]annulene [87]. For clarity, only important hydrogen atoms are shown.

current, NICS measurements are commonly taken at the ring's center. This is typically achieved by placing a 'dummy atom', an artificial point without actual physical presence, at the geometric center of the ring. The NICS value is then calculated at the location of this dummy atom, effectively quantifying the magnetic shielding or deshielding effect caused by the ring current. For more detail, refer to Section 2.4.

Although ring currents are not directly measurable experimentally, their effects are inferred from NMR spectroscopic data, specifically regarding the chemical shifts (denoted by δ) of nuclei in different molecular environments. Aromatic molecules exhibit distinct ^{1}H-NMR chemical shifts, different from the typical values for non-aromatic protons [88], due to diatropic (clockwise) ring currents. External protons in aromatic rings typically resonate at higher chemical shifts (lower field, deshielded) around 6.5 to 9.0 ppm. Conversely, internal protons appear at lower chemical shifts (higher field, shielded), as observed for the H atoms highlighted in magenta in the aromatic molecules presented in Figure 1.7b, c, and d with δ values ranging from -8.17 to -0.50 ppm. In contrast, antiaromatic molecules with paratropic (counterclockwise) net ring currents present an induced magnetic field that opposes B_0 on the outside and reinforces it at the center of the ring. Thus, the amount of (de)shielding can be used to quantify aromatic character experimentally or computationally, as detailed in Section 2.4 of the Methodology.

While magnetic indices used to evaluate aromaticity are focused on the response of the electron density to an external magnetic field, it is crucial to recognize that *aromaticity is an intrinsic characteristic* of certain molecules. Thus, it must exist independently of any external perturbations. For a molecule to be considered aromatic, it must inherently possess specific features: electron delocalization, a particular molecular structure, and increased stability unique to aromatic compounds. Although magnetic indices can, in some cases, correlate well with other measures of aromaticity [82], there are examples where the magnetic aspect of aromaticity diverges from the results obtained with electronic and energetic criteria [62, 78, 89–99].

An increasing number of research studies demonstrate significant differences in the assessments of (anti)aromaticity between magnetic and other classes of aromaticity descriptors. Magnetic measures often exaggerate aromatic or antiaromatic character when compared to energetic, electronic, and/or geometric indices. One example is the overestimation of aromaticity in planar geometries, like in $(N_6H_6)^{2+}$ and $C_2N_4H_6$, which sustain ring currents comparable to benzene but are far less aromatic according

to an electronic criterion [91]. Similarly, the most stable isomer of $B_4N_4H_8$ (azabora-cyclooctatetraene) in the T_1 state shows weak or non-aromatic characteristics based on energetic and electronic indices, but magnetic descriptors suggest considerable Baird-aromaticity [100]. Moreover, the study of radical ions of monocyclic hydrocarbons (including benzene, pyridine, and the three diazines among others) reveals that magnetic descriptors like ring currents are not reliable indicators of energetic stability [78]. Other works also indicate that while magnetic descriptors classify certain systems as highly aromatic, their electronic and energetic evaluations do not corroborate this [101]. This includes findings on expanded porphyrins [102] and porphyrin nanorings [76, 77], where discrepancies between magnetic and energetic or electronic descriptors are even more evidenced due to the complex interplay of local and global macrocyclic ring currents. Additionally, our research on $B_{12}I_{12}$ clusters [101], presented in Section 5.4.3 of Chapter 5, further supports that magnetic descriptors do not consistently align with other descriptors and aromatic stability. These studies collectively underline the need for a careful interpretation of aromaticity results, recognizing the limitations and biases of different descriptors.

In summary, while magnetic indices are widely used and are important tools for aromaticity analysis, they often overestimate molecular aromatic and antiaromatic character. The evidence provided by the aforementioned studies together with other studies pointing to a lack of connection between magnetic properties and energetic stability [103] or electron delocalization [104], calls for a necessary differentiating 'response aromaticity', linked to magnetic aspects, from 'intrinsic aromaticity', associated to electronic, energetic, and structural factors [22]. Therefore, for a complete assessment of aromaticity, we should incorporate multiple descriptors, recognizing that magnetic and electronic or energetic indices, having distinct origins, may not consistently agree in their conclusions about the aromatic nature of the systems.

1.2.3 Challenges in Excited State, Macrocyclic, and Multidimensional Cases

The electronic configuration of a molecule in its excited state(s) is often more complex than in its ground state, presenting hurdles in aromaticity assessment. Similarly, the structures of polycyclic and/or macrocyclic compounds with multiple (and sometimes large) delocalization pathways, are complicated to understand using traditional views of aromaticity. Furthermore, multidimensional molecular systems (*e.g.* double aromatic or three-dimensional systems), where multiple interactions come into play, add more

complexity in understanding and evaluating aromatic properties. This section aims to provide a comprehensive review of the current literature discussing and addressing some of the theories and present challenges of aromaticity evaluation in these complex situations.

Excited State Aromaticity

The extension of the aromaticity concept to excited states took place with the rationalization of the Woodward-Hoffmann rules for pericyclic reactions [105, 106] and the posterior introduction of Baird's rule [64]. In recent years, excited state aromaticity (ESA) has been utilized gradually more to rationalize and interpret experimental and computational findings [20, 107, 108]. Unfortunately, in some cases, Baird's rule has been applied erroneously, leading to misinterpretations [109–111]. In contrast to Hückel's rule, Baird's rule states that annulenes with $4n$ π-electrons are aromatic in their low-lying singlet and triplet excited π, π^* states (S_1 and T_1) while those with $4n + 2$ are antiaromatic (see Figure 1.8).
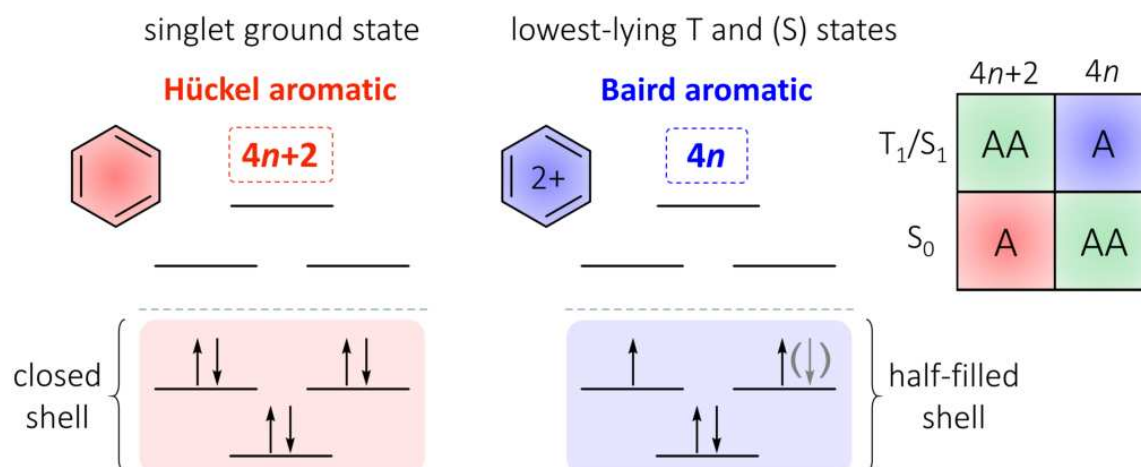
Figure 1.8 Hückel and Baird aromaticity rules exemplified by the distribution of electrons in π-molecular orbitals in S_0 of benzene (left) and low-lying T or S (colored grey in parentheses) excited state of benzene dication (right). Where 'A' = aromaticity; 'AA' = antiaromaticity.

This form of excited state (anti)aromaticity is only applicable in monocyclic cases. It is important to note that Baird's rule was originally developed for π, π^* states and assumes that the excitation is localized within the ring [112]. Moreover, it depends on electronic changes associated with a simple one-electron excitation, usually from the highest occupied molecular orbital (HOMO) to the lowest unoccupied molecular orbital (LUMO) [113]. This excludes other instances such as heteroaromatic molecules with n,π^* S_1 and/or T_1 states [111], and diverse systems where the excitation has

σ, π^*, Rydberg, or metal to ligand charge transfer (MLCT) character, among others. This rule's applicability is further restricted to cases where the electronic excitation does not extend to orbitals outside the ring fragment. Furthermore, the correlation between $4n$ electron count and aromaticity stabilization becomes less pronounced with increasing ring size, thereby restricting the relevance of this rule in macrocyclic rings [114, 115]. Despite this, Baird's rule and extensions of this rule (reformulated versions or in combination with Clar's rule) have been successfully applied in the latter case [70, 115, 116].

A less common but still observed situation is that even in the excited state, the aromatic nature of the molecule must be interpreted in terms of Hückel aromaticity. This occurs when the excitation involves an alteration of the number of π-electrons in the ring, usually due to electron(s) transferred between the ring and exocyclic substituents. This situation is more prevalent in molecules that transition from non-aromatic S_0 to aromatic in higher excited states (S or T). This is the case of the T_1 of Cibalackrot-type compounds [117] and the bright S_2 of a 6-aminosubstituted fulvene-based molecular motor [118]. Or the case of quinoid compounds in their T_1 and S_1 states, which can present a Hückel–Baird hybrid character [109, 110]. The latter systems are an object of study in this thesis presented in Chapter 4.

In all the scenarios previously described, a key aspect is the change in the total electron count, encompassing π, σ, or other orbitals. This change, whether it occurs due to electron transitions between different groups of orbitals (σ, n, $\ldots \rightarrow \pi^*$, and others) or between orbitals localized in the ring and orbitals centered in other parts of the molecule, is critical in determining the applicability of Hückel and Baird aromaticity rules. Thus, it will be useful to use a more general method to characterize aromaticity. To address the challenges of applying these rules in the case of aromatic radical systems (open-shell configurations) Mandado *et al.* [119] proposed the use of the Hückel rule separated into α and β spin contributions, as illustrated in Figure 1.9.

This adaptation, known as Mandado's $2n + 1$ rule for separate spins [119], facilitates the aromaticity assessment in certain cases. Following the examples of S_0 of benzene and T_1 of benzene dication, according to this rule, these states can be interpreted as comprising two Hückel-aromatic subsystems: one with $2n + 1$ π_α-electrons and another with $2m + 1$ π_β-electrons, where $n = m = 1$ for benzene and $n = m + 1$ with $m = 0$ for benzene dication. This partitioning approach is particularly useful for interpreting conflicting aromaticities observed in states such as the ^{1}n,π^* and ^{3}n,π^* excited states
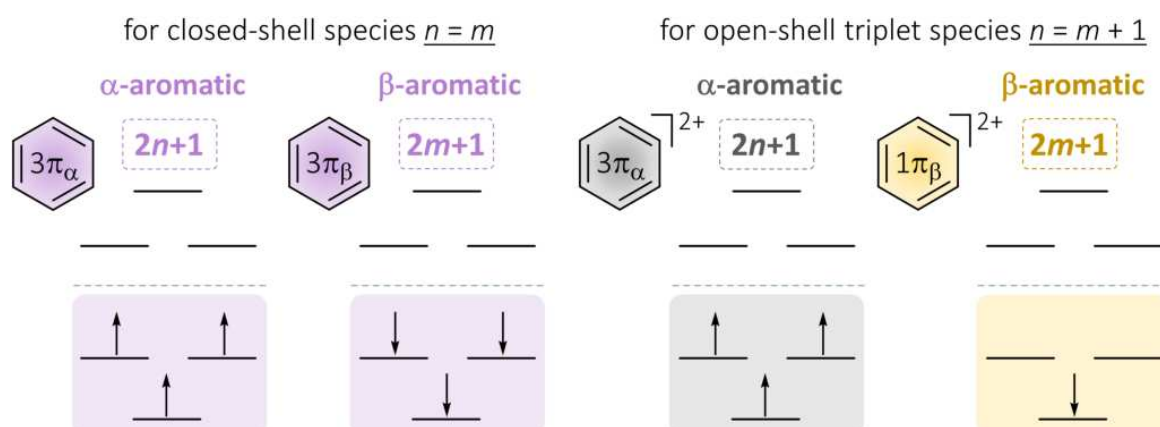
Figure 1.9 Mandado's $2n+1$ rule of aromaticity for separate spins exemplified by the distribution of electrons in π-molecular orbitals in S_0 of benzene (left) and T_1 of benzene dication (right).

of pyridine and other heteroaromatics. These cases often involve one antiaromatic $4\,\pi$-electron subsystem and an aromatic $3\,\pi$-electron subsystem [111]. Additionally, Mandado's rule can effectively distinguish between Baird and Hückel aromatic cycles in computational analyses [109, 110, 117].

Finally, it is important to highlight the difficulty of investigating (anti)aromaticity effects in excited states or open-shell (OS) radical molecules, independently of the excited state character. The study of excited states is more intricate than analyzing properties in the ground state [107]. Standard methods like density functional theory (DFT) may not suffice for accurate electronic structure description in these cases, especially for excited singlet states, often necessitating the use of more advanced techniques like time-dependent DFT or multi-configuration methods such as CASSCF. These methods are more complex to apply and interpret. Moreover, the calculation of certain aromaticity indices, straightforward in the S_0 state, encounters additional complications in excited states. For instance, indices like NICS require specialized CASSCF treatment in the case of singlet excited states [68]. Similarly, other indices such as HOMA or FLU may be less applicable due to the lack of suitable reference systems. Additionally, the calculation of excited states can be constrained by the limitations of available methodologies, making their analysis more challenging.

Similarly, experimental investigation of the electronic structure and behavior of excited-state (anti)aromatic molecules faces significant challenges. For instance, the use of NMR spectroscopy for excited states is uncommon and limited to specific research areas, hindering direct structure examination, unlike with ground-state molecules. Tech-

16

niques like transient absorption spectroscopy [120–122], used for studying electronic state dynamics, only measure the energy difference between states, thus providing ambiguous insights into the properties of individual states. Furthermore, direct structural characterization methods, such as X-ray crystallography, are not available in the excited state, preventing the measurement of changes in bond lengths and other structural parameters upon excitation. These limitations highlight the importance of using theoretical and computational methodologies to understand the excited-state (anti)aromatic systems. However, without meticulous evaluation, computational data on (anti)aromaticity effects in excited states might lead to more confusion than clarity. Hence, a deep understanding and careful application of advanced computational techniques are crucial in deriving meaningful insights from such studies.

Aromaticity in Macrocyclic and Polycyclic Compounds

Understanding the electronic structure of macrocyclic and polycyclic compounds presents unique challenges due to factors such as torsional strain, conformational flexibility, and incorporation of heteroatoms. The study of aromaticity in these compounds, characterized by large cyclic systems and/or multiple interconnected rings, involves understanding both macrocyclic and global aromaticity. Macrocyclic aromaticity is related to individual pathways of π-electron circulation along the macroscopic ring, while global aromaticity refers to electron delocalization across the entire molecule (superposition of multiple pathways). Moreover, these compounds can exhibit macrocyclic electron delocalization, or have aromatic characteristics limited to specific regions (*i.e.* local aromaticity), reflecting the interplay of *local*, *macrocyclic* and *global* aromaticity [48, 123, 124]. To clarify the distinction of these concepts, local and macrocyclic aromaticity are typically assessed computationally with aromaticity indices that require using defined atomic sequences. In contrast, global aromaticity is more effectively evaluated through visualization techniques based on the inspection of the electron density or the magnetic currents obtained with response methods [125]. These different kinds of aromaticity are typically found in certain porphyrins, with locally aromatic pyrrole rings and extended π-conjugated macrocyclic pathways (Figure 1.10a), both contributing to global aromaticity [126]. This was also expected in more complex systems like the previously mentioned porphyrin nanoring [47] (Figure 1.10b), where local aromaticity occurs within each individual porphyrin unit, and potential global aromaticity would be represented by an electron circuit along its entire perimeter.[b]

---

[b]The existence of global aromaticity has not been confirmed by electronic aromaticity measures. Furthermore, their apparent detection using magnetic measures [47, 127] is highly influenced by the choice of density functional approximation, as demonstrated by Casademont-Reig *et al.* [77, 128].
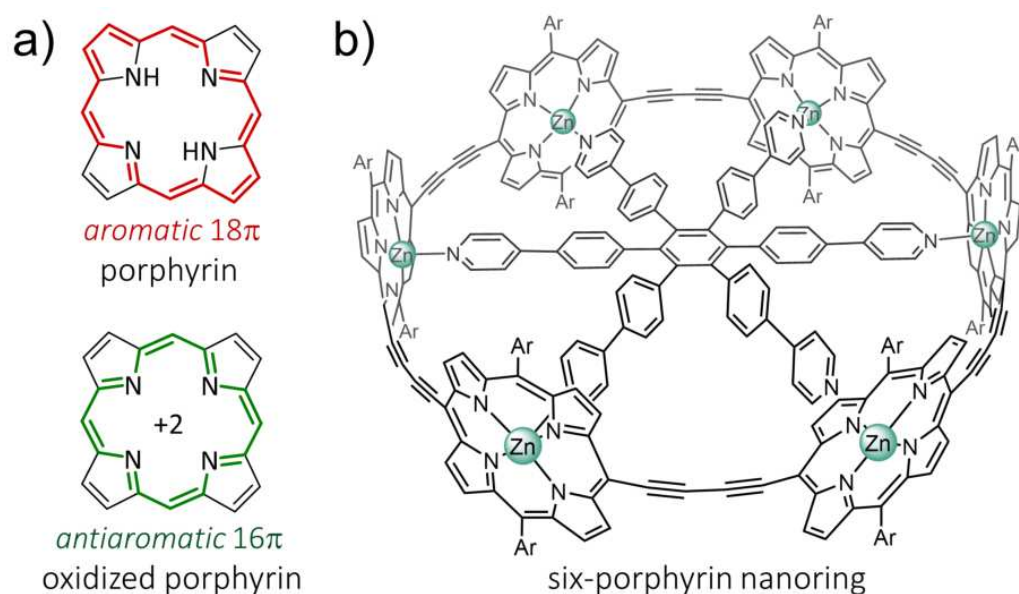
Figure 1.10 Structures of a) porphyrin and oxidized porphyrin with the conjugation pathway, according to the annulene model, highlighted in red (aromatic) and green (antiaromatic). Figure adapted from ref. [129]. And b) six-porphyrin nanoring with the aryl group substituents (Ar) corresponding to 3,5-bis(trihexylsilyl))phenyl. Figure adapted from ref. [76].

To rationalize the aromaticity in these species, the use of empirical rules offers a systematic approach to predict and comprehend their aromatic characteristics. The Hückel rule, initially designed for planar monocyclic molecules such as annulenes, has been adapted or supplemented with new rules for its application to more intricate macrocyclic systems. Continuing with the example of the parent porphyrin, its aromaticity has been traditionally equated to an 18 π-electron aromatic cycle, similar to [18]annulene, thus conforming to the Hückel rule [130]. However, this comparison with analog annulenes is not that simple since many macrocyclic compounds exhibit enhanced conformational flexibility, resulting in non-planar structures. This is seen in examples such as porphyrin derivatives like *p*-benziporphyrins and other Möbius expanded porphyrins, and subphthalocyanines. The former are categorized under Möbius aromaticity [131, 132], a phenomenon observable in large [*n*]annulenes and expanded porphyrins that can be synthesized by inducing a 180º phase shift (topology panel in Figure 1.6 and Figure 1.11a), aligning them with the Möbius symmetry of their hydrocarbon framework and π-molecular orbitals. In these cases, the large size of the ring facilitates adequate π-overlap stabilization and in a closed-shell (CS) configuration they will be Möbius aromatic with $4n$ π-electrons. Subphthalocyanines (Figure 1.11b), on the other hand, are composed of three diiminoisoindole rings N-fused around a central boron core. This arrangement forces the structure into a non-planar, bowl-

shaped geometry, which is a result of the coordination of the central boron atom and the significant degree of ring strain [133, 134]. These cases exemplify the propensity of larger rings to adopt non-planar structures, introducing an additional layer of complexity. Furthermore, it has been observed that in annulenes and other macrocyclic systems, the degree of aromatic character tends to diminish as the ring size increases [135, 136]. This trend complicates the interpretation of aromaticity measures, particularly because distinguishing between different aromatic systems becomes more challenging when dealing with very small values. Additionally, this observation highlights a growing difficulty in identifying larger aromatic molecules, especially when seeking global electron delocalization.

Additional complications arise in the evaluation of polycyclic aromatic hydrocarbons (PAHs), such as coronene (Figure 1.11c), and related nanographene structures with fused rings. While PAHs are not strictly macrocycles, they can feature large aromatic circuits along their perimeters or within other regions. These large circuits can present challenges in assessing aromaticity that are similar to those encountered with macrocycles. For coronene, direct application of the Hückel rule suggests antiaromaticity due to its 24 π-electrons. However, coronene exhibits aromatic behavior [137]. This discrepancy necessitates a modified approach to electron counting, as proposed by Platt and Clar [138–140]. Platt's model treats the π-electrons of the perimeter as an annulene, to which the Hückel rule is applicable, while considering the inner core merely a perturbation. Under this framework, the π-electron count fulfills Hückel's rule with 18 π-electrons. Clar's π-sextet rule, however, provides a more detailed understanding of PAH aromaticity. This rule explains the aromatic character of PAHs in terms of the distribution and resonance stabilization provided by π-sextets, which are localized configurations of six π-electrons in a hexagonal ring. According to Clar, a PAH is most

a) free-base di-p-benzi[28]hexaphyrin
aromatic 28π

b) subphthalocyanine

c) coronene
aromatic 18π
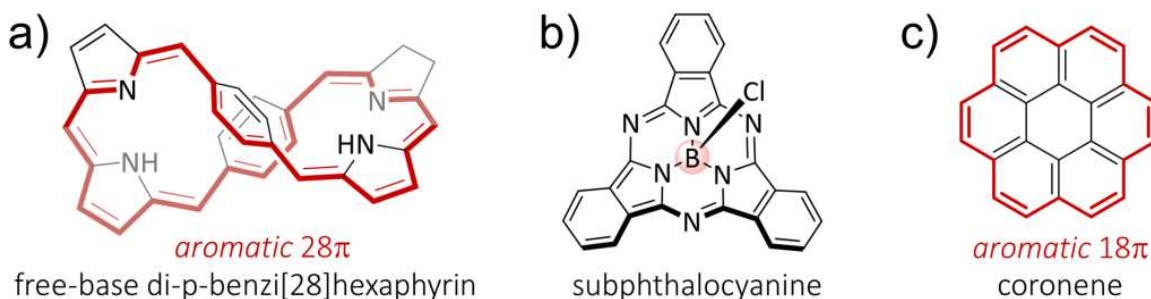
Figure 1.11 Structures of a) free-base di-*p*-benzi[28]hexaphyrin, with the conjugation pathway underlined in red, b) boron subphthalocyanine chloride, and c) coronene, with the perimeter corresponding to the aromatic circuit underlined in red.

stable, and thus most aromatic, when it has the maximum number of disjointed (non-overlapping) π-sextets. This principle is particularly insightful for analyzing the aromatic stability of complex PAHs. It suggests that the aromatic character is not uniformly distributed across the entire molecule but is concentrated in specific regions containing these π-sextets. Clar's rule is limited to molecules formed by six-membered rings (6-MRs), thus Glidewell and Lloyd's proposed an extension allowing the consideration of other ring sizes [141]. The application of these theories has been successfully used to predict the structure and reactivity of PAHs [142]. This rule is particularly useful in identifying areas of concentrated aromatic character, which are often chemically inert. Additionally, assessing aromaticity in polycyclic compounds, especially through magnetic criteria, can be challenging. In larger PAHs with fused rings, it is important to determine whether aromaticity is cumulative or competitive across the rings [143]. The interplay of localized and delocalized electronic states and the coexistence of aromatic and antiaromatic influences in adjacent rings add complexity to the overall evaluation of the molecule's aromatic character.

Alongside the previously discussed complexities, the dimensions of these molecules with large ring sizes introduce a distinct set of challenges. These often lead to a heterogeneous distribution of electron delocalization, which is a critical factor when considering aromatic properties. This variability in electron distribution directly impacts the effectiveness of traditional aromaticity indices based on references (*e.g.* HOMA and FLU), which are typically calibrated for smaller, more homogeneous systems. Furthermore, the implications of this size-related complexity extend to both experimental and computational methods. In the realm of experimental analysis, techniques like Nuclear Magnetic Resonance spectroscopy, essential for aromaticity assessment, may yield complex and overlapping signals due to the varied resonances from different parts of these expansive rings. On the computational side, the preferred method for modeling this systems, *i.e.* DFT, has limitations in accurately modeling the long-range interactions characteristic of these large and flexible molecular structures [76, 144–146]. A careful evaluation of the appropriate level of theory is particularly challenging in aromaticity studies due to the lack of reference values. Additionally, the most reliable electronic aromaticity measure [147, 148], MCI, suffers from size limitations, necessitating the use of approximate methods [18] for evaluating the aromatic character of these compounds (see Methodology for further details).

Experimental techniques are indispensable in assessing the aromaticity of macrocycles. Techniques like X-ray crystallography provide direct insights into molecular

geometry, while methods such as atomic force microscopy, ^{1}H-NMR, UV-Vis, and other spectroscopies offer valuable indirect evidence of aromaticity. The core challenge lies in how aromaticity is characterized rather than in the concept itself, given its multidimensional nature. A key objective is to enhance the correlation between computational ^{1}H-NMR calculations and experimental findings, going beyond functional improvements to more accurately reproduce experimental conditions in computational models. This is crucial for understanding large, flexible molecules like nanorings, where dynamics, aggregation effects, and vibrational considerations are significant. By combining expertise from both fields, we aim to deepen our understanding of complex chemical phenomena and significantly refine our theoretical models. Ultimately, this collaborative approach is poised to offer profound insights into the chemistry of these demanding species, thereby enhancing the accuracy and relevance of computational chemistry in real-world applications.

Double Aromaticity

Aromaticity, traditionally associated with π-delocalized electrons, is also present in all-metal and semimetal clusters through additional forms such as σ, δ, and φ aromaticity [49, 51, 53]. These different types of aromatic characters can coexist, leading to double or triple aromaticity. However, such multiple aromaticity is particularly rare in organic molecules, where π and σ aromaticity are more common, with double aromaticity being an exceptional occurrence [61, 149, 150].

Hückel's and Baird's rules, initially developed for π systems, extend to σ aromaticity as well. This similarity also applies to the indices used for aromaticity evaluation. Consequently, characterizing double aromaticity in principle involves the same challenges that in general aromaticity studies. These include the absence of references, discrepancies among indicators, and the selection of appropriate computational methods. When not considered carefully, these issues can lead to misconceptions about aromaticity. For instance, cyclooctadeca-1,3,5,7,9,11,13,15,17-nonayne (commonly referred to as cyclo[18]carbon or simply C18) with molecular formula C_{18} has been labeled as being strongly aromatic with double Hückel π_{in} and π_{out} character [151–153]. However, in C18, the π-electrons are predominantly localized in the triple bonds [152, 154], with bond-length alternation (BLA), suggesting minimal, if any, aromaticity.

A clear example of double aromaticity in organic systems is the hexaiodobenzene dication ($C_6I_6^{2+}$) [155, 156], which demonstrates both Hückel σ- and π-aromaticity. This is evidenced by 10 delocalized electrons contributing to σ-aromaticity in the ring

formed by iodine atoms, along with six in the benzene ring for π-aromaticity. Other hexahalobenzene dications [157–160] have been computationally explored as potential double aromatic compounds. Moreover, in 2018, Saito *et al.* reported the double σ- and π-aromatic character in hexakis(phenylselenyl)benzene dication, though the σ-aromaticity was found to be weak [161]. Additionally, Fowler and Havenith's studied computationally the double aromaticity in larger 8-MR systems $C_8I_8{}^q$, with different q values from -2 to $+4$, and showed that significant I–I steric repulsion led to highly puckered structures, lacking both σ- and π-aromaticity [162]. This evidence, together with the lack of diversity in the known examples shows that the design of double aromatic organic systems presents a significant challenge (not because it is difficult to characterize but because it is difficult to achieve).

Three Dimensional Aromaticity

The discovery of $[B_{10}H_{10}]^{2-}$ *closo* borane [56] and posterior studies of its electronic structure, along with those of various derivatives [57, 58, 163, 164] meant the extension of the aromaticity concept from two to three dimensions. The stability of some $[B_nH_n]^{2-}$ ions has been attributed to their aromatic nature [165]. Traditional rules for classic organic annulenes are not directly applicable to these systems, prompting Wade to propose a new classification based on valence electron count [166, 167]. His rule considers the polyhedron structures of *closo* boranes and states that *closo* species are aromatic if they have $2n + 2$ valence electrons, excluding those of the B–H bonds, where n represents the number of vertices of the polyhedron (depicted as purple spheres in Figure 1.12). Mingos also proposed a rule including all valence electrons (incorporating the electrons from external B–H bonds), implying that systems with a $4n + 2$ electron count are aromatic [168, 169]. These principles are equivalent and have been integrated into a single rule referred to as the $4n + 2$ Wade-Mingos rule. Both Hückel's and Wade-Mingos' rule use n, but they define it differently. In Hückel's rule, n is a natural number representing the number of π electrons of the ring, while in the Wade-Mingos' rule for boranes, n indicates the number of B atoms, and $4n + 2$ represents the number of valence electrons. In this context, a link has been drawn between Wade-Mingos' and Hückel's rules, considered by some authors as "*two sides of the same coin*" [170–172]. Beyond such electron counting rules, the aromatic character of boron clusters has also been affirmed by computational studies beginning with Aihara's resonance energy calculations in 1978 [165], by the molecular orbitals and their occupations, and supported by numerous subsequent investigations [172, 173].
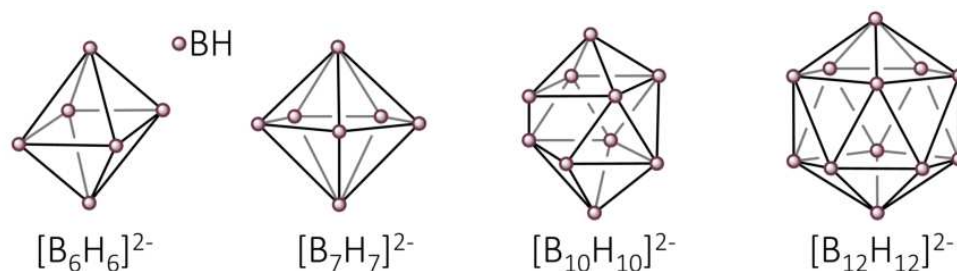
Figure 1.12 Molecular structures of $B_nH_n{}^{2-}$ *closo* boranes whit $n = 6$, 7, 10, and 12.

The concept of 3D aromaticity extends beyond the cage-like aromaticity of icosahedral boron clusters. Other recognized forms include spherical, cylindrical, octahedral, tetrahedral, and cubic aromaticity [19]. Spherical aromaticity, in particular, is widely recognized, having been introduced to explain the stability of fullerenes. These nearly spherical polycyclic structures, endowed with π-conjugated electrons, represent another example of 3D aromatic compounds [174]. For such systems, $2(n+1)^2$ Hirsch's rule [175, 176], offers insights by approximating the π-electron system of fullerenes to a spherical electron gas that envelopes the surface of a sphere, akin to Hückel's rule for planar aromatic compounds [171]. This suggests a broad generalization of aromaticity principles across different molecular topologies.

The exploration of 3D aromaticity challenges traditional models meant for planar systems, offering profound insights into the stability and reactivity of novel molecular architectures with significant implications for material science and nanochemistry. The intricate nature of 3D molecular structures, however, poses substantial challenges to characterization. Occasionally, electron counting rules are insufficient, necessitating comprehensive analyses of the electronic structure. The ill-defined aromaticity concept, as in previous cases, has led to erroneous interpretations. An illustrative example is the mischaracterization of certain systems, *e.g.*, a triphenylamine-based quinoidal bithiophene molecular cage, initially considered 3D aromatic [177], which subsequent research by El Bakouri *et al.* revealed that it exhibits 2D aromaticity within a three-dimensional framework [60]. The latter paper underscores the common misinterpretations and indicates four required conditions for 3D aromaticity: (*i*) significant global π-electron delocalization; (*ii*) a highly symmetrical structure manifesting at least triply degenerate molecular orbitals (MOs); (*iii*) a closed-shell electronic structure, yielding the required electron count for aromaticity; and (*iv*) comparable electronic and magnetic responses in all three xyz dimensions [60].

1.3 Understanding Leads to Design: Materials for Practical Applications

Chemistry has a central role in facing contemporary global challenges: from energy storage and conversion to developing cost-effective pharmaceuticals. The discovery of new molecules and materials—such as catalysts, organic electronic components, and drugs is at the heart of these solutions [178]. For this, we require a deep understanding of matter at the molecular and electronic-structure level, achievable through advanced spectroscopic techniques and quantum chemical computations.

Among all the compounds known by the end of 20th century, it was estimated that about two-thirds are either fully aromatic or have aromatic parts [179]. This substantial proportion along with the additional aromatic compounds discovered during the last two decades, highlights the importance of aromaticity in chemical research. In particular, we are interested in two general categories: (*i*) the excited state properties of aromatic molecules and (*ii*) molecules with complex structures, *e.g.* macrocyclic chemistry, nanomaterials, or boron clusters, having cyclic or 3D electron delocalization.

In this section, we delve into the relevant aspects to understand the practical applications of excited state aromatic molecules and a variety of systems with complex structures. We aim to demonstrate the significance of their molecular features in various technological advancements, connecting our theoretical studies to practical uses of aromatic systems.

1.3.1 Electronic Nature of Systems in the Excited State

Solar radiation is one of the most powerful energy sources in our planet. A large number of phenomena such as photosynthesis, human vision, or global climate are directly dependent on sunlight. This solar energy reaches the Earth in a wide range of wavelengths, from ultraviolet (UV) to infrared (IR), and interacts with aromatic and heteroaromatic molecules that are components of living matter and synthetic materials [180]. Comprehending the interactions between light and matter is not only fundamental for natural processes but also for developing advanced technologies that can harness effectively this abundant energy source.

1.3 Understanding Leads to Design: Materials for Practical Applications

Optimizing the use of solar radiation, as well as alternative light sources, requires a detailed understanding of photophysical and photochemical processes. For the purpose of this thesis, we focus on the interaction with visible and UV light, generally known as *electronic spectroscopy* [181, 182]. In this spectral range, the absorption of light promotes the transition from low-energy states, usually, the ground state (GS), to electronically excited states (ESs). After the excitation of the sample, the excess energy can be dissipated via radiative (with emission of light) and non-radiative mechanisms, illustrated in Figure 1.13b. The occurrence of specific transitions and relaxation pathways can be determined by the selection rules. These rules have their basis in the transition moment integral, which involves the wavefunctions of the initial (Ψ) and final (Ψ') states and the electric dipole moment operator ($\hat{\mu}$). For a transition to be fully allowed, and thus more likely to happen, it must satisfy the spin, orbital, and vibronic selection rules. However, these rules result from a series of approximations (*e.g.* the Born-Oppenheimer or orbital approximations), and in practice, formally forbidden transitions can still occur if the selection rule is relaxed by an appropriate perturbation, albeit always at a lower intensity than fully permitted ones.

To illustrate this point, the Jablonski diagram [183] in Figure 1.13b treats the most common case for organic molecules, where the ground state is a singlet, S_0, and absorption mainly populates S_1 and, to a lesser extent, S_2. Here, T_1 represents a triplet state with the same spatial (orbital) configuration as S_1. This triplet state is generally more stable due to a combination of factors, including the application of Hund's rule, which dictates that higher multiplicities tend to minimize electron-electron repulsion [184]. Despite T_1 being the lowest-energy excited state, it is less likely accessed because of the spin-forbidden nature of the intersystem crossings (ISCs). Nevertheless, if the other competing processes, *i.e.*, fluorescence and internal conversion, occur at low rates, T_1 can achieve a significant population. The primary requirements for an efficient ISC are a small energy difference between states and substantial spin-orbit coupling (SOC), which facilitates the mixing of states with different multiplicities [185, 186]. Ultimately, the kinetics of the different processes will depend on the topology of the potential energy surfaces (PESs) [187] of the different states involved, which will be defined by intrinsic and extrinsic factors. Investigating the evolution of the molecular structure in the GS and ESs is a very important task for understanding a wide range of chemical and physical phenomena, including light-harvesting in photovoltaics [188], reactivity patterns [189, 190], activation in photodynamic therapy [191], quenching of excited states in photoprotection [192], and enzymatic activity [193], to name a few.
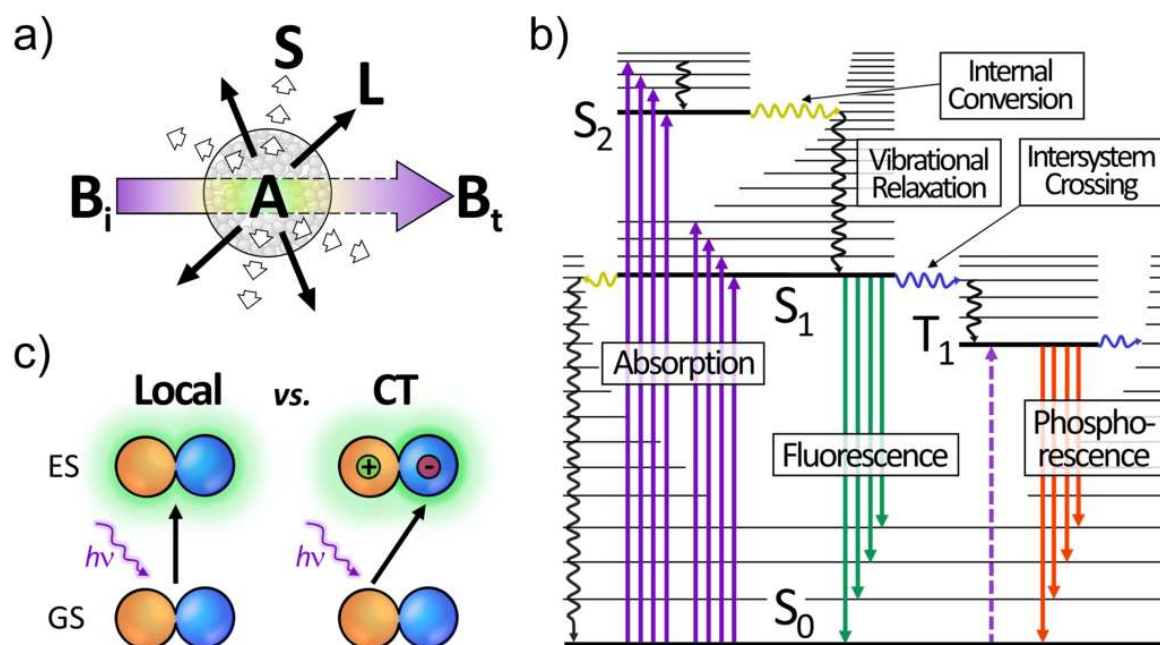
Figure 1.13 Main photophysical molecular events. a) A beam of incident light (B_i) interacting with matter giving: absorption (A), scattering (S), and luminescence (L); the rest is transmitted (B_t). b) Jablonski energy diagram representing the possible events following the absorption of a photon. Straight arrows indicate photon-involved processes, dashed arrow indicates singlet-triplet absorption of very small transition probability, and wiggly arrows represent non-radiative processes. c) Local versus charge transfer (CT) excitation. GS and ES stand for ground and excited state, respectively.

However, the focus of this thesis is to achieve an in-depth understanding of the electronic nature of selected systems. To that end, and despite the significance of dynamic processes, we have concentrated our efforts on the detailed characterization of stationary states, specifically, S_0, S_1, and T_1 states calculated at their corresponding minimum-energy geometries on the PES. Such states are instrumental for the rational development of new materials and can serve as a robust initial approach for a more comprehensive understanding. Yet, it is important to stress that, although valuable, our approach is limited to very few 'snapshots' (S_0, S_1, and T_1 frozen geometries) and thus simplifies the true complexity of the real system behavior. Attaining a complete picture would require the consideration of other factors including molecular dynamics [194], excited-state dynamics [195], and external perturbations, which fall outside the scope of the current work. For the remainder of this thesis, discussions will focus on the stationary approach, leaving aside the deliberation of these limitations.

1.3 Understanding Leads to Design: Materials for Practical Applications

The in-depth characterization of the electronic structure of excited states naturally leads us to explore the changes in the distribution of electrons within the molecule upon excitation. Such changes are reflected in the system wavefunction (Ψ), which in our case is formulated using the orbital approximation, where molecular orbitals (MOs) are built as linear combinations of atomic orbitals (LCAOs). These orbitals are subject to the constraints of the Pauli antisymmetry and exclusion principles. Consequently, our Ψ is represented either by a single Slater determinant or by a combination of Slater determinants (for a detailed methodology, see Section 2.1). It is through this Ψ that we can look closely at the molecular changes induced by electronic transitions. In the context of MO theory, such transitions often involve the promotion of an electron from an occupied to an unoccupied orbital or a rearrangement of electrons within degenerate orbitals leading to an overall increase in energy. These electronic transitions disturb the (GS) molecular forces, potentially altering parameters such as geometry, electron density distribution, bond orders, and even aromaticity in the excited state.

Depending on the distribution of the electron density, electronic transitions can be broadly categorized into two types: local excitations (LE) and charge-transfer (CT) excitations (Figure 1.13c). In LE, one or more electrons—in the case of double excitations—are promoted from one orbital to another within the same region of the system, causing subtle alteration to the electron density distribution. While the electron density does change to some extent, since the electron(s) is now in a different orbital, the overall charge distribution of the molecule remains largely the same. In contrast, CT excitations involve the relocation of at least one electron from one region (donor, D^+) of the molecule or molecular system to another (acceptor, A^-), thereby substantially altering the electron density and inducing a more global change in molecular properties. These CT transitions can have profound effects on molecular properties and reactivity.

Several techniques such as absorption, emission, transient absorption spectroscopy [120], time-resolved photoelectron [121], or two-photon absorption [122] spectroscopies are used to gain information about the chemical structure and molecular properties. Depending on the response of the molecule to the applied perturbation, we can, in certain cases, distinguish between CT and LE, as well as between π, π^* and σ, π^* states. This also provides insights into the molecule's magnetic and optical properties. Molecules that are very sensitive to external electromagnetic fields are especially important for the development of active components in electronic devices.

Next, we will outline the molecular-level requirements for materials to be potentially applied in various fields. These include organic light-emitting diodes (OLEDs), organic solar cells, photocatalysis, systems with nonlinear optical properties (NLOP), photodynamic therapy (PDT), and photothermal therapy (PTT), where the use of chromophores, capable of efficiently absorbing light and energy transfer, is crucial [196]. Other applications include organic field-effect transistors (OFETs), spintronics (spin transport electronics), photodetectors, and biomedical imaging. In the latter cases, other properties like charge transport, magnetic features, and molecular recognition are more central. These fields offer opportunities to explore novel ideas with *para*-quinodimethanes, phthalocyanines, and other macromolecular systems explored in this thesis through computational methodologies. A basic overview of these characteristics is provided in Table 1.1, highlighting the important factors to understand materials from the ground up. Our aim is focused on the exploration of systems and concepts, such as aromaticity, that provide a link between theory and photophysical measurements.

Table 1.1 Summary of requirements for organic materials as potential candidates in various photonic applications and their technological uses.

Field	Key Requirements	Uses
OLEDs	Presence of conjugated π-electrons, which impart semiconductive properties through the overlap of π (bonding) and π^* (antibonding) orbitals. HOMO-LUMO gap within the range of 1 to 4 eV [196].	Displays for multiple devices (smartphones, televisions, automotive components, ...) and solid-state lighting.
Organic Solar Cells	Light-absorbing material with requirements similar to those of OLEDs and the capability to absorb a wide range of the solar spectrum; electron acceptor material with high electron affinity and chemical stability; proper energy alignment driving the electrons from the donor to the acceptor material.	Energy conversion: convert sunlight into electricity.
		Continued on next page

Table 1.1 – continued from previous page

Field	Key Requirements	Uses
Photocatalysis	Ability to undergo efficient and reversible electron transfer processes upon light absorption, facilitating the generation and manipulation of radical intermediates [197].	Key for driving chemical reactions.
NLOPs	Possess a donor-π-acceptor type architecture with a proper separation of frontier molecular orbital facilitating intramolecular charge transfer [198].	Optical switches for molecular-scale memory storage devices.
PDT and PTT	Strong absorption (preferably in the near IR region), easy degradation after use, and long lifetime of the photosensitizer in the T_1 state. In PDT, for improving the generation of chemically reactive species [199]. In PTT, to maximize conversion of the absorbed photons to heat [200].	Medical treatments: destroying diseased cells with minimal damage to surrounding healthy tissues.
OFETs	Aromatic and other π-conjugated small molecules or polymer chains. Organized molecular packing with strong intermolecular couplings, facilitating charge transport driven by delocalization [201].	Sensors, electrical circuits, data storage or light-emitting devices.
Spintronics	Organic semiconductors made of light elements with weak spin-orbit coupling, and therefore, extended spin relaxation times [202].	Magnetic random access memory devices, materials for quantum bits (qubits), transistors, and light-emitting devices.

As demonstrated by various examples of π-conjugated molecules, more specifically aromatic ones, these structures can be highly effective in numerous applications, as the particular properties attributed by the aromatic core in the molecule enable the stabilization of specific electronic states that might otherwise be difficult to achieve. In some cases, we have molecules with pro-aromatic character, meaning that besides not being aromatic in the GS they become aromatic in the excited state [203].

Additionally, there are macrocyclic structures like porphyrinoids and phthalocyanines, whose highly adaptable architectures make them perfect candidates for a diverse array of applications. In the subsequent sections, we will delve deeper into these molecules and their potential uses.

Pro-Aromatic Open-Shell Diradicaloids

In recent years, molecules with electronic structures that deviate from the conventional ordering of electronic states have garnered significant interest. One such example includes systems exhibiting small or even negative singlet-triplet energy gaps (ΔE_{S_0-T}, defined as the E_T minus the E_{S_0}) [48, 147, 204–210] leading, in the latter case, to triplet ground states. Interestingly, in other species, the ground state is a diradical(oid) open-shell singlet (OSS) state, with the same, or almost identical, spatial configuration as the triplet, and thus violating Hund's rule [211–214]. The enhanced stability of the OSS compared to the triplet state can be rationalized using the two-state model, proposed by Zilberg and Haas [215], or the equivalent concept of the double spin polarization (DSP)[216–218] phenomenon. They suggest that for certain geometries the OSS comes from a set of resonance structures, some of which are exclusive to a singlet state and not possible for a triplet configuration. According to the Pauli exclusion principle, the parallel spins of unpaired electrons in the triplet state prevent them from occupying the same spatial orbital, minimizing the electron-electron repulsion. This restriction excludes certain resonance structures that would otherwise contribute to stabilization. Conversely, in the singlet case, the electrons from the HOMO[c] can delocalize into SOMO (singly occupied molecular orbital) vacancies, allowing for two π-delocalization stabilizing effects, one involving the delocalization of a β-electron of the HOMO into the SOMO containing an α-electron, and the other involving an α-electron of the HOMO and a β-electron in the SOMO. This results in a double stabilization for the OSS state compared to a single stabilization (the β-electron of the HOMO into one of the SOMOs containing an α-electron) in the triplet state, explaining why the OSS is often the ground electronic state in many Kekulé diradicals [219].

In addition, systems like heptazine have sparked significant attention due to the occurrence of similar contradictions to Hund's rule in their excited states [220–224]. These systems typically have a closed-shell ground state. In their low-lying excited

---

[c]It must be noted that the HOMO orbital in open-shell singlet configurations do not correspond to the HOMO in closed-shell configurations. In most cases the open-shell HOMO relates with the HOMO-1 of the closed-shell configuration.

states, they exhibit an inverted singlet-triplet gap, especially between the first singlet S_1 and T_1 states ($\Delta E_{S-T} = E_{S_1} - E_{T_1}$). Contrary to what Hund's rule predicts—that the T_1 will be lower in energy than the S_1 state in molecules with a CS ground state—these systems show the opposite when both states share the same spatial configuration. In conventional scenarios, where Hund's rule is obeyed, the overpopulation of the T_1 state hinders the radiative decay from the S_1 state. This, in turn, reduces efficiency in applications reviewed previously such as OLEDs, photovoltaic cells, PDT, and fluorescence imaging and sensing, where radiative decay from the singlet state is crucial. This conventional expectation is challenged in systems exhibiting inverted ΔE_{S-T}, making them ideal candidates for such applications. However, these findings regarding molecules exhibiting inverted ΔE_{S-T} are controversial, as a study employing high-level *ab initio* methods (*i.e.* CCSD(T)/cc-pVTZ) challenges previous results [225]. Regardless, stable open-shell singlet and triplet states are interesting both from a theoretical point of view for understanding chemical bond nature and from a practical one because they show promise in some of the previously mentioned applications such as molecular magnets [226], NLOPs [227–230], and spintronics [231]. Particularly, in this thesis, we are interested in the family of Kekulé diradicaloids, also known as Chichibabin systems, *para*-quinodimethanes, or pro-aromatic quinoidal compounds, among other names. These diradicaloids exhibit aromatic-quinoidal tautomerism [219], characterized by a resonance structure that is intermediate between a closed-shell quinoid, an open-shell diradical[d] benzoid form, and, to a lesser extent, an ionic form (Figure 1.14).
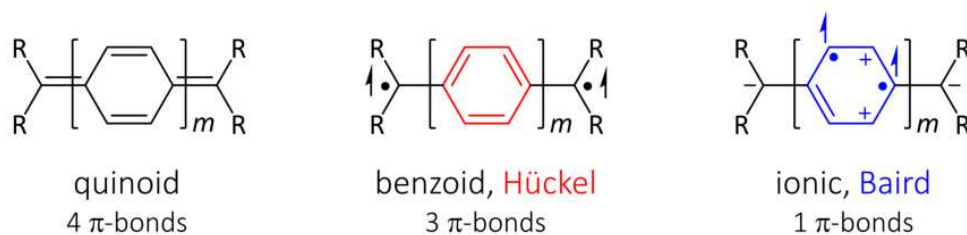
Figure 1.14 Quinoid closed-shell and, benzoid (Hückel) and ionic (Baird) diradical forms of Chichibabin molecules.

In the diradical form, molecules have two separate unpaired electrons, which can align either antiparallel (in OSS) or parallel (in T). These diradicals are characterized

---

[d]The term 'diradical' broadly refers to a molecule with two radical centers. In this thesis, 'diradicaloid' or 'diradical' will denote systems in which the radical centers are capable of interacting. The term 'pure diradical' will be used in the case of fully independent electrons, or what in some contexts is referred to as 'biradical'.

by small HOMO-LUMO gaps, facilitating the manipulation of their electronic properties. Their high reactivity, however, poses a challenge for isolation. To fine-tune these structures for specific technological applications, strategic functionalization, and structural modification are employed. Thus it is crucial to have reliable indicators to monitor the effect of these changes. An important parameter is the diradical character, denoted as y [232–234]. As we mentioned before, Kekulé diradical(oid)s fluctuate between a closed-shell and a pure diradical state, typically with $y \approx 0$ and $y \approx 1$ values, respectively, reflecting the continuum from bonded to dissociated states. This transition from CS to pure radical is further exemplified by H_2 dissociation curve, as shown in Figure 1.15.
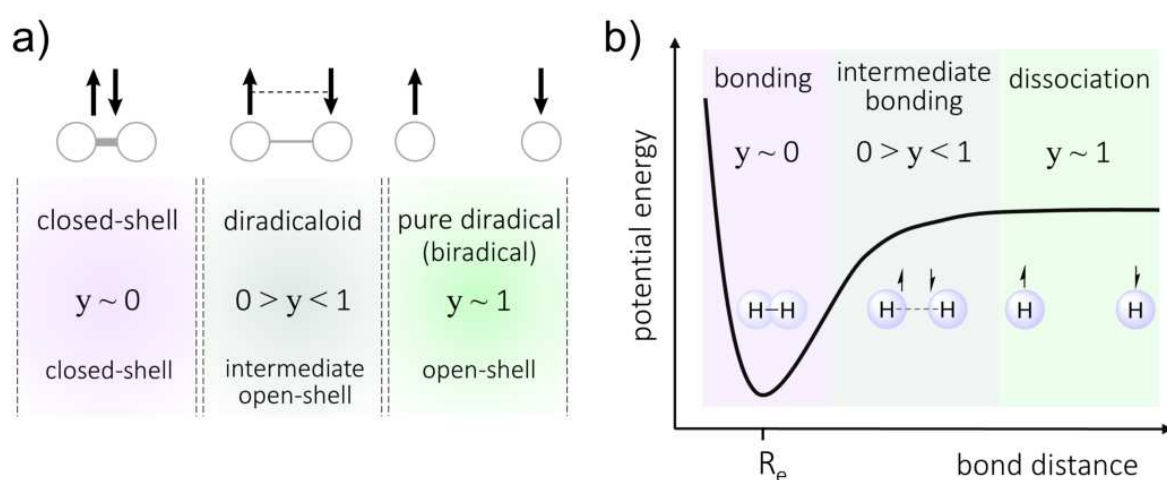
Figure 1.15 Representation of a) singlet configurations of closed-shell, diradicaloid, and diradical species, indicating the diradical character (y) values, and the spheres symbolizing a pair of atoms or molecular fragments. b) homolytic dissociation of H_2.

Elaborating on these ideas, the past decades have seen considerable development in the study of diradical systems, particularly in synthesizing stable, long-lived open-shell molecules. A deeper understanding of the structure-property relationships in diradical(oid) molecular systems has been achieved through quantitative analysis of diradical character and other measures like $\langle \hat{S}^2 \rangle$ or chemical bonding descriptors [235]. A special focus has been given to how structural modifications impact diradical character, thereby influencing the stability of these systems. Among the strategies employed to control diradical character are: (*i*) altering the substitution at terminal positions, either by modifying the functional group or its position [236–241]. As an example, a successful and commonly employed strategy is the use of dicyanomethylene side groups; (*ii*) modifying the oligomer length increasing the number of π-conjugated

spacers, denoted as 'm' [203, 242–246]. Larger chains tend to stabilize the OSS state and amplify diradical character due to increased aromaticity [239, 247]. Classic examples of Kekulé diradicaloids that illustrate this principle include Thiele's ($m = 1$) [248], Chichibabin's ($m = 2$) [249], and Müller's ($m = 3$) [250] hydrocarbons, as demonstrated by the increasing y values in Figure 1.16a; (*iii*) chemical modification of π-bridges or alternative substitutions in the central ring(s) to manipulate electron delocalization or sterics [237, 251–253]; and (*iv*) exploring the effects of isomerism on chemical properties and, consequently, diradical character [254, 255]. These diverse approaches, with some examples illustrated in Figure 1.16, showcase the multifaceted nature of diradical system design.
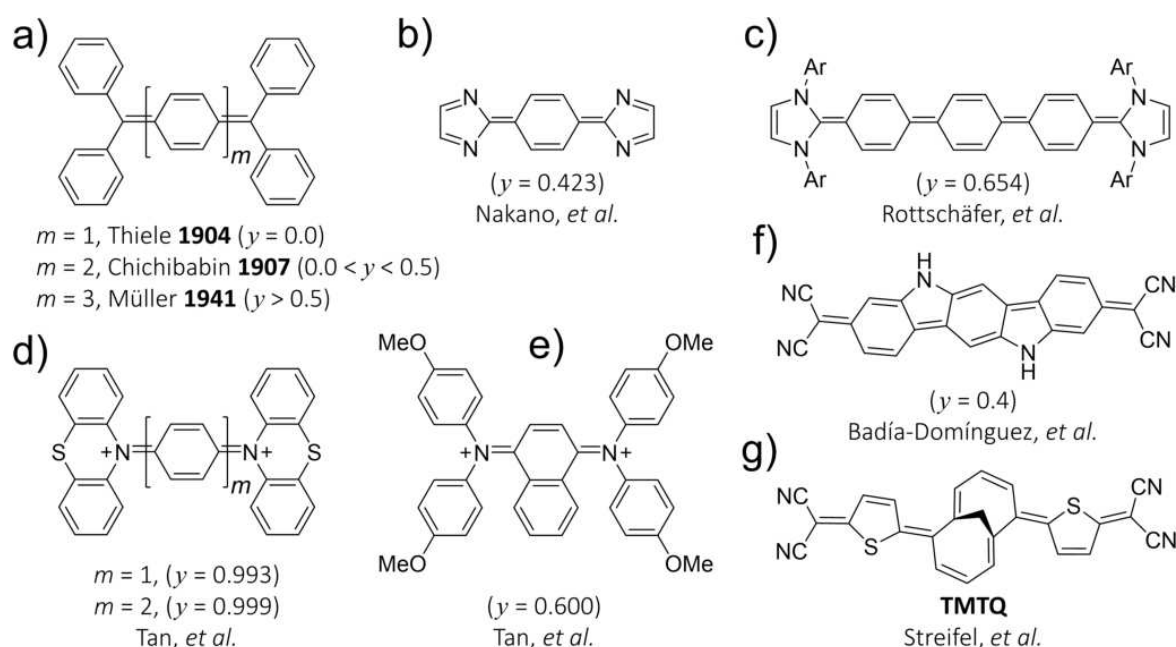
Figure 1.16 Examples of *para*-substituted diradical(oid) systems (quinoidal structures), with their corresponding diradical character (y). a) Thiele's [248], Chichibabin's [249], and Müller's [250] hydrocarbons. N-heterocyclic carbene analog of b) Thiele hydrocarbon, y calculated at UHF/6-31+G** level [236], and c) Müller hydrocarbon, where Ar = 2,6-iPr$_2$C$_6$H$_3$, and y at UHF/6-311G* level [256]. d) and e) bis(triarylamine) dications, y at UBH&HLYP/6-31G* level [237]. f) Indolocarbazole substituted with dicyanomethylene groups, y at UB3LYP/6-31G** level [251]. g) Covalent structure of 2,7-dicyanomethylene-thiophene-1,6-methano[10]annulene (TMTQ) [257].

As we discussed, in aromatic π-conjugated polymers, the diradical becomes increasingly favorable over the closed-shell configuration as the number of ring units grows. This transition to diradical character in larger oligomers correlates with a decrease in the optical band gap and HOMO-LUMO gap. However, it is noteworthy that shorter

oligomers with a single central unit and closed-shell ground states will be more stable and have accessible diradical aromatic excited states. A prime example is TMTQ, a 2,7-dimethylenemethano[10]annulene substituted with two 5-dicyanomethyl-thiophene moieties, shown in Figure 1.16g. TMTQ has a singlet-triplet energy gap of merely 4.9 kcal/mol, and is an interesting subject for the study of excited state aromaticity. Initially, the excited triplet state of TMTQ was described as a Baird aromatic state [257]. However, subsequent analyses revealed that its Baird aromaticity is only partial, about 10-15% and this molecule is better described as a Hückel-Baird hybrid [109]. The evolving understanding of TMTQ's aromatic properties exemplifies the complex nature of excited state diradicals and highlights the importance of rigorous theoretical analysis. Despite the existing evidence, recent results have classified the singlet excited state of TMTQ as a fully Baird aromatic form [258]. Given the lack of comprehensive analysis of the aromaticity to substantiate these claims, we did a detailed (re)investigation of TMTQ's T_1 and S_1 aromatic nature. This project, presented in Chapter 4, aims to provide a clearer understanding of the complex nature of excited state diradicals.

Multiple studies have proven that the characterization of the aromaticity serves as a more comprehensive analysis to explore the influence of the π-system size, exocyclic substituents, among other structural modifications, on different states of *para*-quinodimethanes. The singlet and triplet diradical forms usually exhibit Hückel aromatic character, as shown in Figure 1.14. Thus, aromaticity plays a crucial role in stabilizing these forms. Computational characterization is crucial in facilitating the exploration of new molecules that are difficult to obtain experimentally due to the high reactivity of diradical(oid) molecules. Thus, a theoretical understanding of aromaticity informs the design and synthesis of new molecular systems for specific applications.

UV-Vis Spectra of Porphyrin and (Sub)Phthalocyanines

Another family of molecules that stand out in the realm of electronic properties including excited state applications are porphyrins and similar systems such as phthalocyanines and subphthalocyanines [133, 134, 259, 260]. Porphyrins are heterocyclic macrocycles composed of four pyrrole subunits interconnected via methine bridges (R_1–CH=R_2). This forms a large, conjugated system with a central cavity, typically coordinating a metal ion, which plays a crucial role in their function. These molecules, fundamental in various biological and technological contexts, exhibit distinct absorption spectra. Modified porphyrins, for instance, are responsible for some of the vibrant colors seen

in nature, such as the red of hemoglobin and the green of chlorophyll, where they are involved in oxygen transport and photosynthesis, respectively. This diversity in pigmentation and spectral properties is a direct result of their unique electronic structures.

To understand and predict the π, π^* bands in the UV-Vis spectra of metal porphyrin, in 1961 Gouterman proposed his intuitive four-orbital model [261, 262], which was firmly grounded in previously developed ideas for cyclic polyenes and MO theory. This model explains the electronic transitions within the frontier occupied a_{2u} and a_{1u}, and unoccupied e_g orbitals that give rise to the characteristic Soret (or B) and Q bands observed in the spectra of porphyrin compounds, as shown in Figure 1.17. Accounting for their intensity and spectral positions, the model aids in predicting spectral signatures through monitoring of band shifts and intensity variations in different porphyrin derivatives.
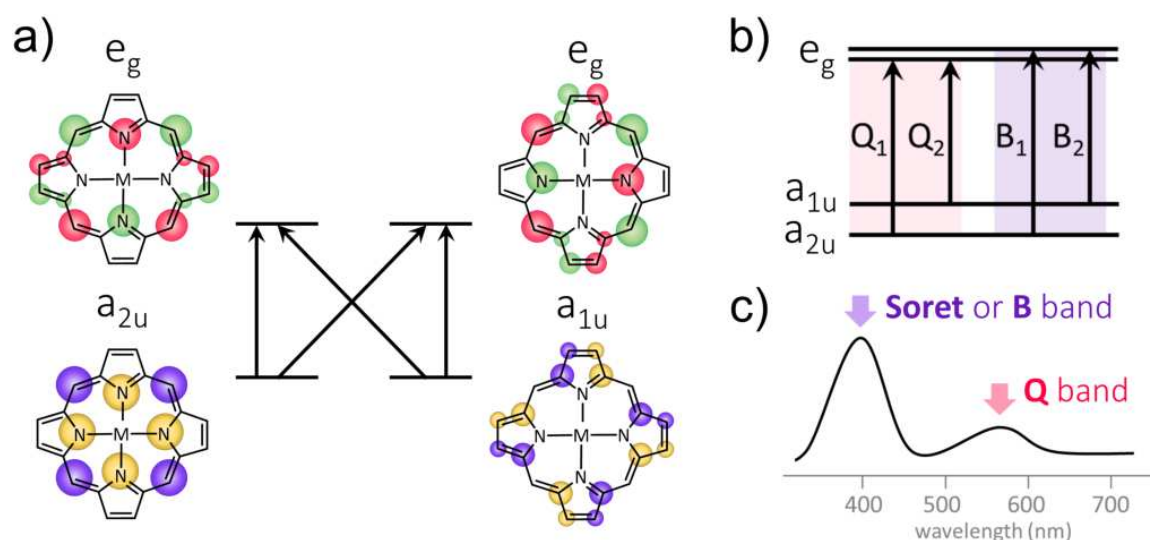
Figure 1.17 Representation of Gouterman's four orbital model for metalloporphyrin: a) HOMOs (a_{2u} and a_{1u} symmetry) and LUMOs (e_g symmetry), b) energy levels of the orbitals and transitions that give rise to Q and B bands, and c) schematic representation of the UV-Vis absorption spectra.

Despite the inherent simplifications in Gouterman's model, it is a straightforward tool for rationalizing spectral features in conjunction with improvements in spectroscopic techniques and computational methods. The better understanding of these optical properties promotes the widespread presence of porphyrins in research and technological applications. There are thousands of examples of porphyrin derivatives, whose structural variations significantly influence their interaction with light, making them highly

tunable [263]. Among these related systems are phthalocyanines, which are larger and more extended than porphyrins, comprising four isoindole units connected by nitrogen atoms to form a planar aromatic macrocycle. Their extended π-conjugated system endows phthalocyanines with unique optical and electronic properties, making them valuable in applications like organic semiconductors, photovoltaics, and photodynamic therapy to treat cancer, among others [260].

Importantly, subphthalocyanines, a contracted analog of phthalocyanines, represent another interesting class of porphyrin-related systems. These molecules are formed by three isoindole units and are typically coordinated to a B-X (where X can be -OH, -F, -Cl, etc.) fragment at the center. They feature a bowl-shaped structure, which favors distinct intermolecular interactions and stacking organizations, leading to different types of assemblies and host-guest chemistry compared to their planar counterparts [264]. Moreover, despite having fewer isoindole units, they maintain a highly conjugated π-system, representing a notable example of non-planar aromatic systems. The curved geometries also influence their electronic and optical characteristics. Like porphyrins and phthalocyanines, they are utilized in a variety of applications, ranging from optoelectronics to medicinal chemistry [134, 265].

The exploration of porphyrin, phthalocyanine, and subphthalocyanine molecules, along with their derivatives, offers a potential pathway for developing compounds with enhanced electronic conductivity, prolonged excitation times, and other desired properties for various applications [134, 260, 266, 267]. As synthetic methodologies advance and new molecules can be developed, understanding the structure-property relationships becomes crucial to achieving these targeted properties. The UV-Vis spectra of these species are particularly insightful, revealing details of their electronic structures. In turn, a deeper understanding of these electronic structures enables us to predict their optical and other properties more effectively.

In this context, the concepts of aromaticity and its counterpart, antiaromaticity, have been useful in deepening our understanding of these relationships. Recently, different authors have spotted connections between the aromaticity of diverse free-base porphyrinoids and their UV-Vis spectra and nonlinear optical properties. This encompasses the evaluation and design of Hückel-Möbius aromaticity switches in expanded porphyrins with superior NLOPs [268, 269], the relationship between (anti)aromaticity and linear and nonlinear optical features [129, 270], and investigations into the most aromatic pathways in charged expanded porphyrin variants [102]. Additionally, another

study showed that it is possible to regulate the properties of silicon(IV) phthalocyanines by changing their aromaticity [271], suggesting a significant interplay between aromaticity and photophysical properties.

Motivated by these findings and taking into account that there is no comparative study including collectively porphyrin, phthalocyanine, subphthalocyanine, and other related species, we decided to analyze the potential relationships between their absorption spectra and aromaticity. Our approach implies the experimental and computational study of the UV-Vis absorption of different species and the use of chemical bonding and aromaticity analyses to characterize the π system to finally identify correlations between these properties. The project is presented in Chapter 5.1.1, where we apply the aromaticity concepts and aromaticity indices discussed earlier in this introduction, and Sections 2.3–2.5, respectively.

1.3.2 Macromolecular, σ, π-Doubly and 3D Aromatic Systems

Carbon-based materials play a pivotal role in diverse scientific fields, including environmental science, energy storage, and materials science. Carbon's electronic configuration, particularly its versatility to adopt sp, sp^2, and sp^3 hybridization, enables a vast array of structural forms, many featuring stable, delocalized electron systems due to the prevalence of π systems. This is further enriched by the potential for heteroatom integration. Aromaticity, a key stabilizing factor, fuels ongoing discoveries in carbon structures, spanning porphyrins, fullerenes, hoop-shaped π systems, nanographenes, and innovative supramolecular complexes like saturnene, which comprises a fullerene surrounded by a [n]cycloparaphenyleneacetylene ring. These structures not only highlight carbon's fascinating chemistry but also exhibit properties critical to their utility, such as enhanced conductivity, tunable optical properties, and remarkable stability [272–274].

In this thesis, we delve into some of these aromatic carbon-based materials. Sections 5.1.1 and 5.2 are dedicated to analyzing the aromaticity in Zn-subphthalocyanines and Zn-phthalocyanines and the study of global aromaticity in nanographene, respectively. Furthermore, exploring new forms of aromaticity, such as double aromaticity featuring both σ- and π-delocalization, represents a thrilling frontier in organic chemistry. This aspect, opens new theoretical avenues, as discussed in Section 5.3.

Additionally, the unique characteristics of icosahedral boron clusters, such as the isomeric icosahedral *closo* $C_2B_{10}H_{12}$ carboranes in their anionic and neutral forms,

represents a fascinating study in aromaticity. Their low nucleophilicity, chemical inertness, and adaptable hydrophilicity are explored in Section 5.4.1. Moreover, we investigate the potential for achieving double aromaticity in boron clusters with an external iodine shell in Section 5.4.3, seeking to rationalize experimental evidence and expand our understanding of aromaticity in these systems.

Porphyrin-related Macrocycles

Having already explored the structure and various applications of porphyrins and phthalocyanines in the previous section, we now turn our attention to the specific structural variations and unique properties of porphyrin-related macrocycles. Common strategies for designing new variants typically involve the following structural modifications to the parent porphyrin: (*i*) substituting CH groups at *meso* positions with nitrogen [133, 275], (*ii*) replacing peripheral hydrogen atoms with functional groups of varying electronic and steric properties [275, 276], or introducing isoindoles and pyrroles fused with different rings instead of pyrrole [275], (*iii*) altering the number of pyrrole/isoindole units to create contracted or expanded porphyrinoids, and (*iv*) changing the central coordination, which includes using different transition metals and axial ligands in metalloporphyrins and phthalocyanines [267, 277], or substituting with boron in contracted porphyrinoids [133]. These modifications significantly impact the physical and chemical properties of the resulting compounds. For instance, changing the nature of peripheral substituents can adjust the solubility [278], electronic absorption spectra [276], and redox properties [279] of the porphyrin complexes. Similarly, the central metal ion, which can range from transition metals like iron and zinc to lanthanides, imparts unique characteristics to the porphyrin's electronic structure and reactivity. This adaptability is crucial in applications ranging from catalysis [280, 281] to photodynamic therapy [191, 260]. Further diversification is seen in the synthesis of phthalocyanine or subphthalocyanine systems, where replacing a pyrrole unit with an isoindole or altering the central metal atom significantly affects their electronic properties. These changes not only enhance light absorption and energy transfer efficiencies but also influence the stability and reactivity of these macrocycles [133, 134]. For example, the introduction of heavier or multiple metal atoms in the core can lead to novel optical and magnetic properties, opening up possibilities for their use in advanced photonic and electronic devices [265]. Moreover, the ability to fine-tune the electronic structure through such modifications enables the tailoring of these compounds for specific functions, ranging from gas sensors to organic semiconductors. The exploration

of these variants offers a rich landscape for developing new materials with enhanced performance and novel functionalities.

A completely different strategy for creating porphyrin-derived systems involves assembling them into tape-like structures [282], or belt-shaped nanorings [46], thereby broadening their application scope. By linking porphyrin units together, the electronic and photophysical properties of the original molecule are significantly altered, enhancing or diversifying their characteristics. In tape-like systems, the extended conjugation across multiple porphyrin units leads to improved light absorption and altered electronic characteristics, making them suitable for applications in photovoltaic cells and sensors [283]. Porphyrin nanorings, formed by a closed-loop arrangement of porphyrins, present a distinct topology that affects their electronic properties, offering potential uses in light harvesting systems [284]. These modifications not only expand the functional capabilities of porphyrins but also provide valuable insights into the interplay between molecular structure and properties in synthetic chemistry.

The aromaticity of porphyrinoids has sometimes been overestimated [108, 146]. Understanding the intricate details of their aromaticity is crucial, as aromaticity plays a pivotal role in determining the electronic, photophysical, and chemical properties of these compounds. This overestimation can lead to misconceptions about their behavior and properties. Therefore, more careful evaluations are essential to improve our understanding and rationalization based on aromaticity estimations.

Nanographenes

In the realm of advanced materials, graphene stands out as a unique carbon allotrope, characterized by its two-dimensional structure composed of a single layer of carbon atoms arranged in a hexagonal lattice. This structure endows graphene with exceptional electronic, mechanical, and thermal properties [285]. One of its defining characteristics is its condition as a zero-gap semiconductor. This is due to the seamless overlap of its conduction and valence bands, which leads to the lack of an optical bandgap. As a result, graphene lacks certain optical properties, limiting its direct application in optoelectronic devices [286]. In contrast, considering smaller segments of graphene—graphene flakes or nanographenes—, typically comprising tens to hundreds of carbon atoms (exceeding 1 nm in size), the electronic confinement within this reduced space generates new energy levels, effectively increasing the band gap [287]. These nanographenes, not only retain

many advantageous properties of pristine graphene but also exhibit photoluminescence, broadening their applicability in various fields.

The absence of chirality in graphene is another notable limitation, but this property can be introduced in nanographenes. Chirality can be achieved by following two strategies: (*i*) a top-down approach involving the addition of chiral element (*i.e.*, supramolecularly or covalently connected to chiral substituent) to the nanographene [288–290], or (*ii*) a bottom-up approach using standard synthetic methodologies to form nanographenes that incorporate topological defects [291–293], thereby making the nanographene inherently chiral. We are particularly interested in the latter case, which is achieved by incorporating non-hexagonal rings within the nanographene's hexagonal honeycomb-like framework. The introduction of rings containing a different number of atoms, such as five- or seven-membered rings, introduces curvature in these molecules. For example, pentagonal rings generate positive curvature, leading to bowl-shaped structures exemplified by corannulene. In contrast, heptagonal rings result in negative curvature, as observed in saddle-shaped structures like [7]circulene [294]. This structural variation significantly expands the functional capabilities of nanographenes, offering new possibilities for their application in various fields [295].

A prominent example of this type of chirality is [6]helicene, depicted in Figure 1.18a. This PAH is three-dimensional due to the steric hindrance between the terminal 6-MRs, forming a 'chiral helix' that imparts spiral chirality to the compound, even in the absence
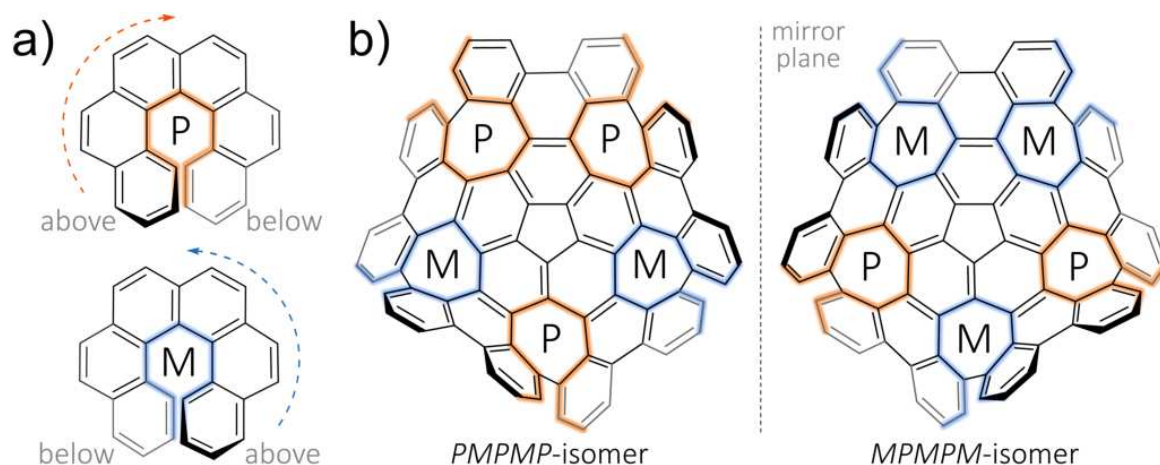
Figure 1.18 Spiral chirality exemplified with the two isomers of a) [6]helicene and b) $C_{80}H_{30}$ nanographene. The *P* (plus) and *M* (minus) nomenclature corresponds to right-handed and left-handed chirality, respectively.

of stereogenic carbons. In spiral chirality, the analogs of R and S configurations, commonly used in regular organic chemistry to describe chirality, are P (plus) and M (minus) configurations. Here, priority is determined by the direction of an arrow drawn from the top ring to the bottom ring, with clockwise (giving P) or counterclockwise (giving M) directions indicating the respective configurations.

The same procedure for determining chirality is applied to more complex systems, such as curved nanographene $C_{80}H_{30}$ [291], which possesses a structure featuring both concave and convex curvatures. This results in the formation of PMPMP- and MPMPM-isomers, as shown in Figure 1.18b, which are enantiomers.

The presence of varying sizes and curvatures in nanographenes allows fine-tuning of their properties [295, 296], including optical characteristics [297] and complexation capabilities with other curved molecules like fullerenes [298]. This adaptability not only holds promise for supramolecular chemistry applications but also for studying electron transfer processes in donor-acceptor complexes. To advance in the development of new materials, it is important to have tools for the characterization of structure-property relationship. A notable example is illustrated in the study by Zhou *et al.* [299], where a corannulene-based helical nanographene coordinated with Na metal exhibited a shift in aromaticity—from aromatic to antiaromatic—upon the two-electron reduction of the system. This observation highlights the role of aromaticity in monitoring and characterizing changes in nanographenes, thus contributing to a deeper understanding of their electronic structure.

Furthermore, the study of aromaticity in such distorted nanographene structures, which encompass multiple fused conjugated rings, presents a significant challenge. Accurate characterization of aromaticity, employing multiple indices, is key for both technical and chemical perspectives. Technically, it helps evaluate the performance of various aromaticity measures, while chemically, it is crucial for understanding the electronic structures and establishing structure-property relationships for these systems. These unique structural features of nanographenes not only serve to test the limits of existing aromaticity indices and rules but also broaden the potential of nanoscale materials. The exploration of these notably distorted geometries in nanographene opens new avenues in material science, paving the way for innovative applications and a deeper comprehension of aromaticity in systems with complex topologies.

Doubly Aromatic Systems

Since the discovery of the first doubly aromatic system, the 3,5-dehydrophenyl cation [61] (see Figure 1.5), there has not been much research on finding organic systems with two orthogonal cyclically delocalized electronic systems. There are examples of σ-,π-doubly aromatic organic and inorganic species [49, 51, 53]. Yet, the examples of the former are reduced to doubly oxidized substituted benzene [155–161]. For instance, in the case of the doubly aromatic $C_6I_6^{2+}$, the dual oxidation of C_6I_6 generates a vacancy in one of the iodine's 5p orbitals. This leads to the formation of six resonance structures, of which only three are depicted in Figure 1.19. The presence of these resonance forms, combined with the fulfilment of Hückel's rule, are required for the system to exhibit σ- and π-aromaticity [300].
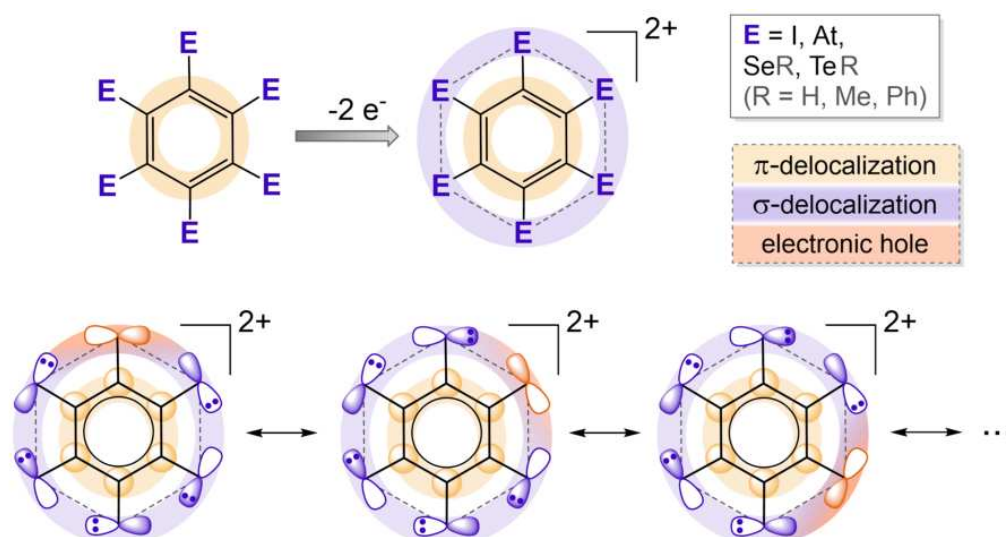
Figure 1.19 Schematic representation of the double aromaticity in dicationic hexahalo- or hexachalcogeno-substituted benzene. The upper part of the figure shows the σ-delocalization, leading to double Hückel π- and σ-aromaticity upon double oxidation of the neutral system. The lower part represents the double aromaticity in $C_6E_6^{2+}$, which requires the formation of an electronic hole to enable σ-delocalization. Adapted from reference [101].

In these cases, the substituted $C_6R_6^{2+}$ (with R being halogen or other functional groups, *e.g.* chalcogen substituents) compounds exhibit double aromaticity, but the large distances between substituents, a consequence of the R–C–C (where C–C represent to adjacent carbon atoms) ~120° angles in hexagonal geometry, result in only weak σ-aromaticity. These double aromaticity instances have led to innovative strategies, such as the strategic positioning of iodine atoms in aromatic systems, where reactive

intermediates and iodinated oligomers can form high-energy in-plane σ-antibonding orbitals, significantly altering the electronic structure [301].

An alternative exploration for double aromaticity was proposed in 8-MRs, specifically $C_8I_8^q$ with charges q $= 0, +1, +2, +4,$ and -2 [151–153]. It has been noted that in 8-MR rings, the increased overlap leads to significant I-I steric repulsion, resulting in puckered geometries. Consequently, and taking into account that aromaticity is observed in substituted benzene we decided to explore the intermediate 7-MR situation as discussed in Section 5.3, substituted tropylium ions are considered potential candidates for double aromatic systems. This consideration stems from both synthetic and structural perspectives, as elaborated in Sections 1.2.3 and 5.3. Our interest in these ions is threefold: (i) in the case of the tropylium cation ($C_7X_7^+$), the X–X distances are intermediate between those in 6- and 8-MR, potentially enhancing conjugation while mitigating repulsion; (ii) the halogen substituents in tropylium cations contribute to a 14 σ-electron system, which conforms to a $4n + 2$ rule, suggesting the possibility of forming a neutral aromatic σ-ring; and (iii) the oxidized form ($C_7X_7^{3+}$)- in the lowest-lying triplet state can potentially show Hückel aromaticity in the benzene ring and Baird aromaticity in the aromatic σ-ring. These ions, therefore, could offer a unique equilibrium, reducing the steric repulsion seen in larger ring systems while preserving significant conjugation.

The tropylium cation, a classic example of a non-benzene aromatic system, adheres to Hückel's rule with its 6 π-electrons. The synthesis and study of these tropylium derivatives could unveil new insights into double aromaticity. Theoretical investigations into these systems would enhance our understanding of electronic structures and stabilization mechanisms in aromatic compounds, especially those exhibiting double aromaticity. This is not only significant for advancing fundamental knowledge in quantum chemistry but also holds potential in the synthesis of complex molecules, where the tropylium ion already plays a crucial role. Moreover, the study of these systems provides a deeper understanding of carbocation chemistry and the behavior of 7-MR systems, which are less common compared to 6-MR rings. Theoretical studies focusing on electronic effects, including hyperconjugation and resonance in these systems, would enrich the theoretical foundations of organic chemistry. The investigation of double aromaticity in such systems could also influence physical properties like UV-Vis absorption, opening new avenues in spectroscopic studies and materials science.

3D Aromatic Systems: Boranes and Carboranes

Boranes, or boron hydrides, are known for their general instability and reactivity. This reactivity is attributed to the fact that they are electron-deficient compounds, with the possibility to form three-center two-electron B–B–B bonds or three-center two-electron B–H–B hydrogen bridges [302]. Despite their substantial reactivity, a subclass known as polyhedral boranes exhibits remarkable stability. These polyhedral boranes, characterized by being made up of triangular faces, are classified into three primary categories: *closo*-, *nido*-, which are stable, and *arachno*-boranes, which are unstable at room temperature. These categories are depicted in Figure 1.20.
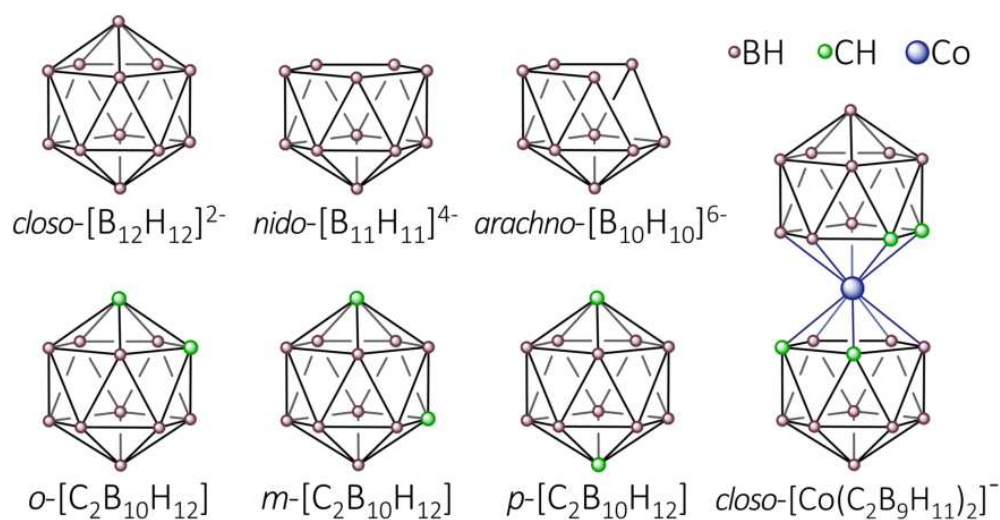
Figure 1.20 Molecular structures of the isoelectronic *closo*-$[B_{12}H_{12}]^{2-}$, *nido*-$[B_{11}H_{11}]^{4-}$, and *arachno*-$[B_{10}H_{10}]^{6-}$ boron clusters (on top, from left to right); *o*-, *m*-, and *p*-isomers of $[C_2B_{10}H_{12}]$ carboranes (bottom, from left to right); and *closo-o*-$[Co(C_2B_9H_{11})_2]^-$ (right part).

The *closo*-boranes class, previously introduced in Section 1.2.3 (see Figure 1.12), presents a highly symmetrical structure. An example is $[B_{12}H_{12}]^{2-}$, which forms a dodecahedron. Next, *nido*-boranes are characterized by their open structures, which result from the *closo* form through various transformations. For example, *nido*-boranes can originate from *closo*-boranes like $[B_{11}H_{11}]^{2-}$ through the addition of two electrons (without the loss of a vertex), resulting in structures like *nido*-$[B_{11}H_{11}]^{4-}$ (in general, $[B_nH_n]^{4-}$), as shown in Figure 1.12. Alternatively, the transition from *closo*- to *nido*-boranes may involve the addition of hydrogen atoms, leading to neutral species such as *nido*-$[B_{11}H_{15}]$ (representing $[B_nH_{n+4}]$). Another rearrangement involves the removal of a vertex (without loss of electrons) from the *closo*-borane with $n + 1$, as exemplified by the conversion of *closo*-$[B_{12}H_{12}]^{2-}$ to *nido*-$[B_{11}H_{11}]^{4-}$. Lastly, *arachno*-boranes are

obtained by further addition of electrons ($[B_nH_n]^{6-}$) or hydrogens ($[B_nH_{n+6}]$); or by removal of one more vertex [303, 304].

The *closo* boranes are the most stable and least reactive among the three classes, characterized by their three-dimensional aromaticity according to the Wade-Mingos' rule [166–169]. It is important to note that while these rules are useful in assessing aromaticity, their primary application is in determining the structural configurations of borane compounds. Similarly, these electron counting rules, along with other systematization schemes [304], are also applicable to heteroboranes and metalloboranes. The extension of these schemes to carboranes and other derivatives is crucial since they serve as tools in synthesis planning, guiding the design of new compounds in the field of borane chemistry, which is relevant from both a theoretical point of view and across various practical fields such as catalysis, medicine, and materials science.

Carboranes, which arise from substituting a BH^- unit with an isoelectronic CH unit in the previously discussed boranes, constitute a distinct class of compounds related to polyhedral boranes. This modification significantly enhances their stability over traditional boranes due to the additional electron density provided by carbon [305, 306]. Their augmented stability makes them important in the realm of weakly coordinating anions. Furthermore, the introduction of a heteroatom[e] facilitates selective functionalization of these compounds. These advancements in boron chemistry paved the way for the development of metallacarboranes, specifically $[M(C_2B_9H_{11})_2]^-$, where M represents a transition metal, also known as metallabis(dicarbollides) [308–310].

Ultimately, the wide range of applications of boranes and related compounds in diverse fields underscores their versatile nature. For instance, hydrogenated versions of *closo* boranes, like B_nH_{n+1}, and their alkali metal derivatives (MB_nH_n), are known for their roles as superhalogens and hyperhalogens, a special class of superatoms that mimic the chemistry of alkali and halogen atoms [311, 312]. The robust three-dimensional structure, aromaticity, and stability of certain polyhedral boranes position them as promising candidates for luminescent and nonlinear optical materials [313]. Boranes also find applications in medicinal chemistry, where compounds like *o*-carborane (referred to as carboranyl when it acts as a ligand) are occasionally viewed as phenyl isosteres[f] because of their comparable stability and lipophilicity, although this is not

---

[e]In carboranes, carbon atoms are treated as heteroatoms, given the electronegativity difference ($\Delta\chi$) of 0.51 between C and B. This value is comparable to $\Delta\chi(N,C)$ of 0.49 [307].

[f](Bio)isosterism is a concept primarily utilized in medicinal chemistry and drug design, referring to molecules with similar chemical and physical properties that also present similar bioactivity [314].

strictly the case [315]. Despite not being isosteres with benzene, carboranes offer unique applications in this field of medicinal chemistry and materials science due to their distinctive properties such as high thermal and chemical stability, and the ability to form structures with varied electronic properties. Their larger volume compared to benzene allows for the exploration of new spatial interactions in molecular design, potentially leading to drugs with novel mechanisms of action [316]. Moreover, the lipophilicity of carboranes can be harnessed to improve the pharmacokinetic profiles of therapeutic agents. Additionally, owing to their high volumetric and gravimetric hydrogen content, boranes are being explored as effective hydrogen storage materials for transportation applications [317, 318]. Extending beyond these applications, the related metallacarboranes have gained attention for their roles in nuclear waste remediation [308, 319–323], advanced material development [324, 325], healthcare [326, 327], and energy production [328], attributed to their unique stability and electron transfer properties.

2 Methodology

As indicated by the title of this thesis—*Exploring the Boundaries of Aromaticity through* ***Computational*** *Analysis of Excited States and Complex Molecular Topologies*—the work done relies on computational approaches to study various systems, primarily using quantum mechanical methods. The following sections are organized to provide an overview of these theoretical approximations. First, we discuss different electronic structure methods. A brief discussion on *ab initio* Hartree-Fock (HF) theory and more sophisticated methods to include electron correlation will be provided. Then, particular emphasis is given to density functional theory (DFT), and time-dependent DFT (TDDFT), which constitute the core methodologies used in the projects of this thesis. Second, we shift our focus to revise the theoretical concepts and tools employed for the study of aromaticity discussing molecular space partitions, electron delocalization indices, magnetic-based aromaticity measures, and finally other analysis techniques that do not fall into the previous categories.

2.1 Electronic Structure Methods

Our primary interest lies in the calculation of quantities of molecular systems in stationary states. In this context, the electronic structure and physical properties of any molecule in any of its states can be determined by solving the time-independent Schrödinger equation [329]:

$$\hat{H}\Psi_i = E_i\Psi_i. \tag{2.1}$$

This is an *eigenvalue problem* characterized by the eigenfunction Ψ_i, which corresponds to the system *wavefunction* of the state i, and contains complete information about both electrons and nuclei within the molecular structure (with M nuclei and N electrons). The eigenvalue, represented by E_i, is the *energy* of this state. Finally, $\hat{H}$ is the

Hamiltonian operator given by

$$\hat{H}(\mathbf{r}, \mathbf{R}) = \hat{T}_{Nu}(\mathbf{R}) + \hat{T}_e(\mathbf{r}) + \hat{V}_{NuNu}(\mathbf{R}) + \hat{V}_{ee}(\mathbf{r}) + \hat{V}_{eNu}(\mathbf{r}, \mathbf{R}), \qquad (2.2)$$

where $\hat{T}$ are the kinetic energy operators of the nuclei (Nu) and the electrons (e), and $\hat{V}$ are the potential energy operators that account for the different attractive and repulsive interactions. The operators are expressed in terms of the $3N$ spatial electronic coordinates ($\mathbf{r} \equiv \{\mathbf{r}_i\}_{i=1,...,N}$), $3M$ spatial nuclear coordinates ($\mathbf{R} \equiv \{\mathbf{R}_i\}_{i=1,...,M}$), or both.

Born and Oppenheimer [330] proposed a physical means of reducing the complexity of $\hat{H}\Psi = E\Psi$, by considering the electrons to be moving in a field of fixed nuclei. This consideration leads to the decoupling of the motions of electrons and nuclei, allowing the splitting of the total Hamiltonian into two simpler equations: the electronic Schrödinger equation $\hat{H}_e\Psi_e = E_e\Psi_e$ and the nuclear Schrödinger equation $\hat{H}_{Nu}\Psi_{Nu} = E_{Nu}\Psi_{Nu}$. The rationale behind this separation is the mass disparity between electrons and nuclei, which allows electrons to adjust rapidly to nuclear motions. The Born-Oppenheimer (BO) approximation proves to be useful for most chemical phenomena; consequently, our focus will be on solving the electronic Schrödinger equation. Under the BO approximation, the Hamiltonian simplifies. The nuclear kinetic energy term $\hat{T}_{Nu}$ is separated and included in the nuclear Hamiltonian, reflecting the motion of nuclei. The $\hat{V}_{NuNu}$ term is a constant for a given nuclear geometry, and the remaining terms form the electronic Hamiltonian ($\hat{H}_e$), that in atomic units is given by:

$$\hat{H}_e = \underbrace{-\sum_{i=1}^{N} \frac{1}{2}\nabla_{r_i}^2}_{\hat{T}_e} \underbrace{-\sum_{i=1}^{N}\sum_{A=1}^{M} \frac{Z_A}{|\mathbf{r}_i - \mathbf{R}_A|}}_{\hat{V}_{eNu}} + \underbrace{\sum_{i=1;j>i}^{N} \frac{1}{|\mathbf{r}_i - \mathbf{r}_j|}}_{\hat{V}_{ee}}, \qquad (2.3)$$

where Z_A and $\mathbf{R}_A$ refer to the charge and position of the Ath nucleus, respectively. In this formulation, the positions of the nuclei $\mathbf{R}$ are treated as parameters, since the nuclei are fixed for the electronic problem. Thus, we can group $\hat{T}_e$ and $\hat{V}_{eNu}$ to rewrite $\hat{H}_e$ in a more compact form

$$\hat{H}_e = \sum_{i=1}^{N} \hat{h}_1(\mathbf{r}_i) + \sum_{i=1;j>i}^{N} \hat{h}_2(\mathbf{r}_i, \mathbf{r}_j). \qquad (2.4)$$

We often refer to $\hat{h}_1$ and $\hat{h}_2$ as the one- and two-electron operators, respectively.

The solutions of the electronic Schrödinger equation include the $\Psi_e(\mathbf{r}, \sigma; \mathbf{R})$ and the corresponding electronic energy. In Ψ_e, $\mathbf{r}$ and σ are the spatial and spin electronic coordinates (collectively indicated as $\mathbf{x}$) that the wavefunction explicitly depends on, and $\mathbf{R}$ are the nuclear coordinates on which it depends parametrically. Consequently, the electronic energy is subject to the fixed $\mathbf{R}$. To obtain the total energy (E_{total}) of the system, one must also consider the nuclear-nuclear repulsion term, given by:

$$E_{total} = E_e + \sum_{\substack{A=1; \\ B>A}}^{M} \frac{Z_A Z_B}{|\mathbf{R}_A - \mathbf{R}_B|}. \tag{2.5}$$

Unless otherwise indicated, from this point forward, we will refer to $\hat{H}_e$, Ψ_e, and E_{total} simply as $\hat{H}$, Ψ, and E, respectively.

The Potential Energy Surface (PES), critical for guiding our understanding of molecular transformation pathways, is constructed by solving the electronic Schrödinger equation repeatedly for a variety of nuclear geometries. However, this equation cannot be solved exactly for most systems, which brings us to the importance of the *variational principle*. The variational principle states that the expectation value of $\hat{H}$ over any well-behaved approximate wavefunction[a], also referred to as a trial wavefunction, will always provide an upper bound to the 'true' ground state energy, E_{true}. This is mathematically expressed as:

$$\frac{\int \Psi^* \hat{H} \Psi d\tau}{\int \Psi^* \Psi d\tau} = E_{trial} \geq E_{true}. \tag{2.6}$$

This principle guarantees that the energy calculated from an approximate Ψ will always be equal to or higher than E_{true}, offering a criterion for evaluating the accuracy of Ψ.

In molecular orbital theory, the approximate molecular wavefunction can be formulated as a determinant of spinorbitals (ϕ), known as the Slater determinant (SD), represented in Equation (2.7). This approach allows for the construction of an anti-symmetrized wavefunction in accordance with the Pauli exclusion principle [34]. In the SD, each row corresponds to an orbital—often an MO written as a linear combination of basis functions, with the shape of the atomic orbitals (LCAOs) [331]—while each

---

[a]A well-behaved, realistic trial wavefunction must be finite, single-valued, and continuous across all space, have a continuous spatial derivative $\frac{d\Psi}{dx}$, and be square-integrable, ensuring that the integral of $|\Psi(x,t)|^2$ over all space is finite.

column represents an electron,

$$\psi(\mathbf{x}_1, \mathbf{x}_2, \dots, \mathbf{x}_N) = \frac{1}{\sqrt{N!}} \begin{vmatrix} \phi_1(\mathbf{x}_1) & \phi_1(\mathbf{x}_2) & \dots & \phi_1(\mathbf{x}_N) \\ \phi_2(\mathbf{x}_1) & \phi_2(\mathbf{x}_2) & \dots & \phi_2(\mathbf{x}_N) \\ \vdots & \vdots & \ddots & \vdots \\ \phi_N(\mathbf{x}_1) & \phi_N(\mathbf{x}_2) & \dots & \phi_N(\mathbf{x}_N) \end{vmatrix}. \tag{2.7}$$

However, in certain cases, the single SD wavefunction is not sufficient to correctly describe the electronic configuration of the molecule, especially for systems with near-degenerate or degenerate orbitals.

For instance, cyclobutadiene (CBD) is an illustrative example. Despite being an apparently simple molecule, CBD exhibits intriguing electronic features. In its planar D_{4h} square structure the last two non-bonding orbitals, e_g, have the same energy [332, 333], as depicted in Figure 2.1. This orbital degeneracy implies that there are multiple ways to distribute the two electrons among the two e_g orbitals.

Given this scenario, a method relying on a single-determinant wavefunction (*e.g.* HF or Kohn-Sham-DFT) would artificially favor one configuration over the others, leading to inaccurate results.[b] In practice, Ψ must be written as a superposition of multiple configurations. The SD, Eq. (2.7), is formulated using N occupied orbitals, forming an $N \times N$ determinant. However, it is worth noting that there are additional unoccupied (virtual) orbitals, making the total set of available spinorbitals larger ($N_{\text{orb}} > N$). These unoccupied orbitals become relevant in methods that go beyond a single-determinant description.

Turning our attention back to the case of D_{4h} CBD, significantly better results can be obtained if Ψ is expressed in terms of two SDs, as it has been done for the two first singlet states in Figure 2.1c. In general, the most practical solution to accurately account for the multiconfigurational character is by describing Ψ as a weighted sum of multiple SDs (ψ_K):

$$\Psi = \sum_{K=1}^{N_c} c_K \psi_K, \tag{2.8}$$

where c_K are the coefficients indicating the contribution of each SD, and N_c is the total number of configurations included. This approach serves as the foundation for

---

[b]KS-DFT, in general, is not well-suited for studying near-degenerate states (*i.e.* including static or nondynamic correlation). Yet, certain exchange-correlation functionals can partially account for a portion of nondynamic electron correlation effects.
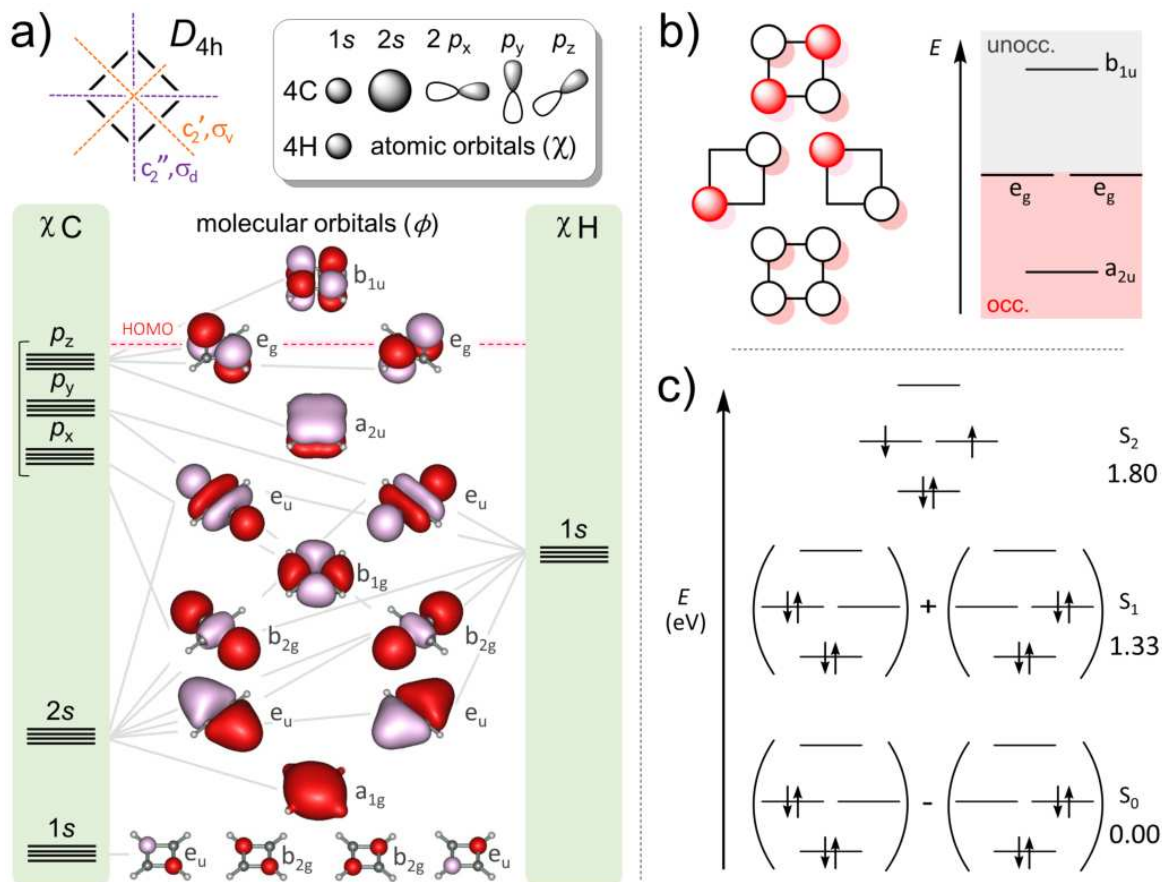
Figure 2.1 Cyclobutadiene in its D_{4h}-square geometry. a) MOs diagram with computed HF/STO-3G orbitals. The AOs of C and H used in the LCAO to generate the MOs are connected via light gray lines. b) The four π-orbitals with their energy diagram. c) The lowest singlet states described by the three possible electronic configurations and their corresponding multireference average-quadratic coupled cluster (MR-AQCC) with aug'-cc-pVTZ basis set (the prime implies that f functions on carbon and d functions on hydrogen were deleted in the augmented set) energies (eV) from reference [334].

methods such as configuration interaction (CI) or the multiconfigurational self-consistent field (MCSCF) family. The best method is the particular case of CI where the combination of all possible determinants, $N_c = \binom{2N_{orb}}{N}$, is used, the so-called full configuration interaction (FCI) [335]. FCI provides the exact solution to the Schrödinger equation within the constraints of a given basis set, under the Born-Oppenheimer approximation, and assuming that the molecular system does not change over time. However, in most cases, the computational cost of this calculation is unaffordable primarily due to the exponential scaling of N_c with the system size. For this reason, we must consider the use of other less demanding post-HF methods to incorporate

electron correlation. A more detailed discussion on electron correlation and post-HF methods will continue in Section 2.1.1.

Following the observation that FCI provides an exact solution within the limitations of a given basis set, it is crucial, not only for FCI but all electronic structure methods, to choose an appropriate basis set for the calculation. Among the various basis set methods available, we used atom-centered functions to represent atomic orbitals. Consequently, we will not discuss alternative options such as plane waves [336] or the auxiliary basis sets used in the resolution of the identity [337, 338]. The use of atomic orbital basis functions is particularly well-suited here, as we focus on non-periodic molecular systems that are computationally manageable in size, and we primarily employ the KS-DFT formulation.

In this context, the term 'basis set' refers basically to a set of one-particle functions centered on atoms. Many different expressions could fit in this category, but in practice, the most common choice is the use of *Gaussian functions* (GF) or *primitives* [339, 340], which are represented as

$$\chi_{abc}^{GF}(\alpha, a, b, c; x, y, z) = Cx^a y^b z^c e^{-\alpha r^2}, \tag{2.9}$$

where C is a normalization constant, α is the Gaussian exponent, and a, b, and c are integral exponents for the x, y, and z Cartesian coordinates. These integral exponents define the shape and orientation of the GF and serve a similar purpose to the angular momentum quantum numbers.[c] Lastly, r represents the radial distance from the nucleus to the point being evaluated.

The basis sets are constructed following specific methodologies and can be classified accordingly. One of the simplest forms is the minimal STO-3G basis. In it, each atom is represented in the same way as in descriptive organic chemistry, using only the occupied atomic orbitals for that atom type (AOs are represented as χ_μ with n = 1, 2, 3, and so on, and $l = s$, p, d, f, and so forth). In turn, each of these orbitals is made up of three primitives (χ_{abc}^{GF}), optimized to closely match a Slater-type orbital (STO).[d] The result of the linear combination (LComb) of primitives is known as contracted Gaussian function (χ_{nl}^{CGF}) and corresponds to χ_μ [341]. Thus, using this basis set, a carbon atom is described by five χ_{nl}^{CGF} corresponding to two *s*-type and three *p*-type

---

[c]While the exponents a, b, c and the angular momentum quantum numbers (l, m) define the shape and orientation of the orbital, they are unrelated and come from different mathematical frameworks.
[d]The name 'STO-3G' comes from using three of these GFs to approximate an STO.

orbitals, illustrated in Figure 2.1a. Therefore, the construction of the MOs will follow the sequence

$$
\overbrace{\chi^{GF}_{abc}}^{primitive} \xrightarrow{\text{LComb GF}} \overbrace{\chi^{CGF}_{nl}}^{AO} \cong \chi_\mu \xrightarrow{\text{LCAO-MO}} \overbrace{\phi_i}^{MO}
$$
$$
\phi_i = \sum_{\mu=1}^{N_{orb}} c_{\mu i} \chi_\mu \tag{2.10}
$$

In general, the addition of more functions can give a better description of the system [342], for instance, a *double zeta* basis set comprises twice the number of χ^{CGF}_{nl} in STO-3G. Basis sets that go beyond STO-3G are known as *extended* basis sets. Additionally, we have *polarization* functions, that correspond to the inclusion of atomic orbitals with an l quantum number greater than the highest required to describe the ground state of the neutral atom [343]. These functions improve the description of the molecular electron density and its response to an external field. For studying phenomena like anions, Rydberg excited states, or any situation where electron density extends far from the nucleus, the basis set benefits from the inclusion of spread-out, or *diffuse*, functions. In commonly used basis sets, these diffuse functions are typically denoted by the prefix 'aug-' or a '+' sign.

Within this thesis, we predominantly employ basis sets of triple-zeta quality. In particular, we use Pople's 6-311G(d,p) [344], occasionally augmented with the + or ++ variants, and cc-pVTZ Dunning's correlation consistent [345, 346] basis sets. This approach is affordable and sufficient for most of the molecules analyzed, which are made of elements up to 3rd period. However, in Sections 5.3.1 and 5.4.3 we studied systems bearing iodines. It is known that relativistic effects can be neglected in most cases for lighter atoms, but have to be included when dealing with heavy elements like iodine [347]. Hence, effective pseudopotentials or core potentials (ECPs) [348] are employed to maintain computational efficiency, capturing key relativistic effects and avoiding the explicit treatment of iodine's 53 electrons.

Switching perspectives: Another way to tackle the electronic Schrödinger equation is by focusing on the *electron density* rather than Ψ. The electron density is an observable, and describes the spatial distribution of electrons in a molecule or atom, quantifying the probability of finding an electron at a specific point in space. It is viable to experimentally obtain high-resolution electron density maps showing the details of the electron density in the chemical bonds [16, 349].

In quantum mechanics, the electron density is derived from the square of Ψ. From this operation, we get the N-order density matrix (DM) as

$$\rho_N(\mathbf{x}_1, \ldots, \mathbf{x}_N; \mathbf{x}'_1, \ldots, \mathbf{x}'_N) = \Psi^*(\mathbf{x}_1, \ldots, \mathbf{x}_N)\Psi(\mathbf{x}'_1, \ldots, \mathbf{x}'_N). \tag{2.11}$$

Given our primary focus on one- and two-electron operators, for example, the terms in $\hat{H}$, as described by Eq. (2.4), we usually only consider two cases: the one-electron reduced density matrix (1RDM or $\rho_1(\mathbf{x}_1; \mathbf{x}'_1)$) and the two-electron reduced density matrix (2RDM or $\rho_2(\mathbf{x}_1, \mathbf{x}_2; \mathbf{x}'_1, \mathbf{x}'_2)$). These are obtained by integrating out the coordinates of $N-1$ or $N-2$ electrons, respectively, from the N-electron wavefunction. From the 1RDM, the electron density $\rho(\mathbf{x}_1)$ corresponds to its diagonal part, *i.e.* $\rho(\mathbf{x}_1) = \rho_1(\mathbf{x}_1; \mathbf{x}_1)$. Similarly, the pair density, $\rho_2(\mathbf{x}_1, \mathbf{x}_2) = \rho_2(\mathbf{x}_1, \mathbf{x}_2; \mathbf{x}_1, \mathbf{x}_2)$, can be obtained from the 2RDM [350, 351]. These matrices not only simplify computational efforts but also provide valuable insights into the electronic structure of molecules and chemical bonding, discussed in more detail in Section 2.2. To do so, it is useful to express both $\rho_1(\mathbf{x}_1)$ and $\rho_2(\mathbf{x}_1, \mathbf{x}_2)$ in terms of molecular spinorbitals

$$\rho_1(\mathbf{x}_1) = \sum_{i,j}^{N_{orb}} {}^1D_j^i \phi_i^*(\mathbf{x}_1)\phi_j(\mathbf{x}_1) \tag{2.12}$$

$$\rho_2(\mathbf{x}_1, \mathbf{x}_2) = \sum_{i,j,k,l}^{N_{orb}} {}^2D_{kl}^{ij} \phi_i^*(\mathbf{x}_1)\phi_j^*(\mathbf{x}_2)\phi_k(\mathbf{x}_1)\phi_l(\mathbf{x}_2). \tag{2.13}$$

These general expressions, valid for both single and multi-determinant wavefunctions, involve ${}^1D_j^i$ and ${}^2D_{kl}^{ij}$, known as the 1-density and 2-density matrices, respectively, which correspond to the tensor representation of the densities. In the particular case of single Slater determinant wavefunctions, although the theoretical framework includes a full basis set of N_{orb} orbitals, the practical calculations exclusively involve the N occupied orbitals. This simplifies the expressions: the 1-density transforms into a diagonal matrix

$$ {}^1D_j^i = \delta_j^i = \begin{cases} 1 & \text{if } i = j \\ 0 & \text{otherwise} \end{cases} \quad \forall i,j \leq N, \text{ and } {}^1D_j^i = 0 \ \forall i > N \vee \forall j > N \tag{2.14}$$

and the 2-density is reduced to

$$ {}^2D_{kl}^{ij} = \begin{vmatrix} {}^1D_k^i & {}^1D_k^j \\ {}^1D_l^i & {}^1D_l^j \end{vmatrix} = \begin{vmatrix} \delta_k^i & \delta_k^j \\ \delta_l^i & \delta_l^j \end{vmatrix}. \tag{2.15}$$

Alternatively, in the case of correlated wavefunctions, the 1- and 2-densities can be simplified by using a different set of orbitals. These are called natural spinorbitals (η_i) and are related to ϕ_i by a unitary transformation, for which the 1-density is diagonal [352]. Then, $\rho_1(\mathbf{x}_1)$ can be expressed as

$$\rho_1(\mathbf{x}_1) = \sum_i^{N_{orb}} n_i \eta_i^*(\mathbf{x}_1)\eta_i(\mathbf{x}_1), \qquad (2.16)$$

where n_i are the natural spinorbital occupation numbers.

Density matrices can serve as the basis for advanced electronic structure methods, including reduced density matrix functional theory (RDMFT) [353]. By focusing on the 1RDM, RDMFT offers an efficient and scalable framework for capturing electron correlation [354]. Despite its efficiency, the large degrees of freedom and computational demands associated with the 1RDM limit the practical use of RDMFT to small-to-moderate systems.

A more popular way for approximating the solution to the N-body Schrödinger equation is *density functional theory* (DFT). The central quantity of DFT is the electron density, $\rho(\mathbf{r})$.[e] In wavefunction theory, one deals with a function of $3N$ variables (ignoring the spin) leading to $3N$ degrees of freedom. Pure DFT instead focuses solely on $\rho(\mathbf{r})$ that depends on just three coordinates, offering a substantial reduction in computational cost. The problem is that, as we will discuss in more detail in Section 2.1.2, the exact expression of the exchange-correlation functional—necessary for solving the Kohn-Sham equations—remains unknown. This is the main reason for the ever-increasing number of density functional approximations (DFAs) available [355]. Among the array of existing DFAs, long-range corrected (or range-separated) functionals have shown consistent accuracy in evaluating aromaticity in systems similar to our focus [76, 144–146]. Hence, these will be our preferred choice. Whenever alternative DFAs are employed, benchmark studies will be conducted to validate the selection.

In reviewing the fundamentals of quantum mechanics, we have noted that the most accurate solutions to the Schrödinger equation, such as FCI with a complete basis set, present excessively high computational requirements. However, various approximations offer a trade-off between computational cost and accuracy. Therefore,

---

[e]Here, $\rho(\mathbf{r})$ is obtained from $\rho(\mathbf{x})$ by integrating out the spin coordinate σ. Moreover, for a normalized wavefunction, $\int \rho(\mathbf{r})\, d\mathbf{r} = N$.

the critical question becomes: *How does one choose the appropriate method?* This decision is further complicated when there is a lack of experimental data to use as a reference. Even when experimental data is available, reproducing the complete experimental setup—including conditions such as temperature, pressure, solvent, and concentration—is often challenging. Additionally, the plethora of electronic structure methods developed over the nearly 100 years since the Schrödinger equation has given rise to a multitude of very sophisticated software packages [356–358]. This diversity in software can introduce variability due to inconsistent implementations of the same theoretical methods, complicating the comparability of results reported in the literature. A deep understanding of the methodologies is essential for mitigating these effects. Such knowledge effectively reduces these issues to minor concerns, especially in non-solid-state calculations.

Despite the advancements in method development, including potential game-changers like quantum Monte Carlo [359], the application of automatic differentiation in machine learning for backpropagation in neural networks [360, 361], and quantum computing [362–364], the field remains open to further optimization. Method selection continues to depend on the specific requirements of the system under study, underscoring the importance of knowing the strengths and limitations of the current methods.

Computational approaches can be categorized according to their accuracy, especially concerning predicted energy results [365]. This is illustrated in the form of a tri-axis in Figure 2.2, emphasizing that more accurate calculations often require simultaneous escalation across these axes, and this improvement comes with a cost.[f] The methods are classified ranging from HF which does not account for electron correlation at all, to methods that include a substantial amount of it. It is worth noting that, in some cases, lower-order methods can yield better descriptions of certain properties due to error cancellation, especially, this can be the case with KS-DFT. Increasing the basis set size typically enhances results [341]. Finally, the third dimension accounts for the Hamiltonian, where higher dimensions correspond to the inclusion of nth-order components in the relativistic Hamiltonian [366]. Relativistic effects become significant primarily for heavy elements, necessitating adjustments to the Hamiltonian. For low-lying (*i.e.* first- and second-row) transition metals, employing ECPs is often sufficient

---

[f]By computational cost, we refer to the combined considerations of computational time (related to the algorithmic scaling with system size, $O(N^x)$), memory requirements, disk space needs, parallel efficiency, and convergence behavior of the method.

to account for these effects [367], offering a practical balance between accuracy and computational demand. For our purposes, we stay at the non-relativistic $\hat{H}$ level, and will only account for relativistic effects employing ECPs.
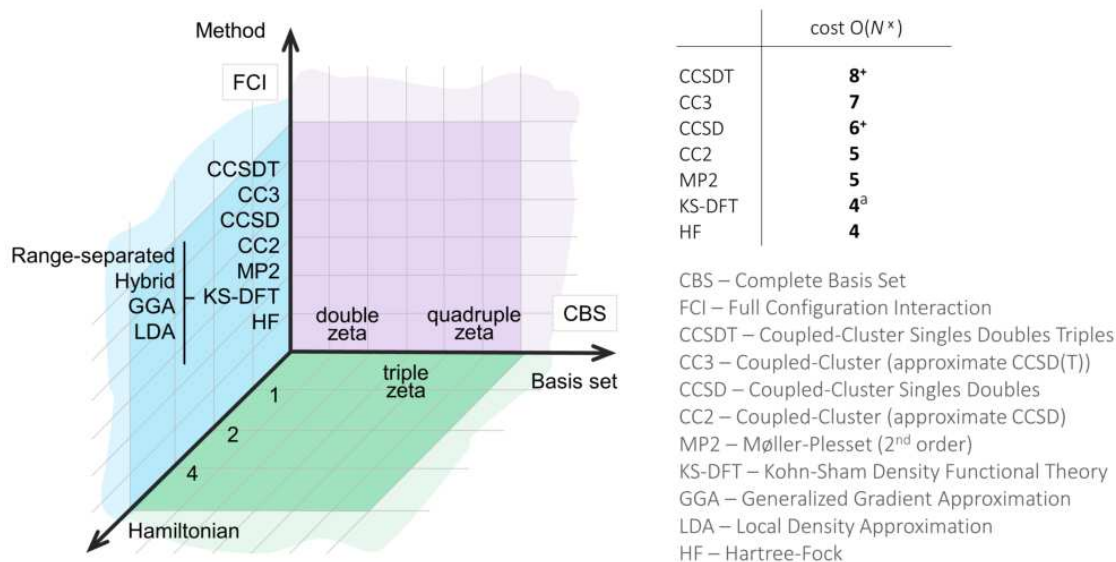
Figure 2.2 Approximate classification of theoretical approaches to electronic structure based on their precision and computational cost. Adapted from reference [366]. The notation '+' indicates iterative processes, which may push computational effort beyond $N^{x^{\text{th}}}$-order due to the convergence demands of the calculation. ^{a}The scaling of KS-DFT can vary from $O(N^2)$ to $O(N^4)$ depending on the exchange-correlation functional.

In summary, understanding the foundational principles of computational methods is crucial for informed decision-making. It is important to find a balanced approximation between cost and accuracy. Thus, benchmarking against established standards, particularly along the method and basis set dimensions, corresponding to the purple region in Figure 2.2, will help to refine our method selection. Following this rationale, we will review in more detail the most prevalent *ab initio* methods and DFT approximations.

2.1.1 Hartree-Fock and Post-HF Methods

The Hartree-Fock (HF) approximation was developed through the collaborative efforts of Hartree, Fock, and Slater. This method is aimed to solve the BO-time-independent Schrödinger equation by applying the variational principle (Eq. (2.6)), and using the independent particle model, which makes the HF method exact for systems of non-interacting electrons. The latter allows us to define a mono-electronic operator ($\hat{F}$). Employing a Slater determinant (Eq. (2.7)) as the wavefunction of the system, the HF

equation for a single-electron orbital (ϕ_i) takes the following form:

$$\hat{F}\phi_i = \varepsilon_i\phi_i, \tag{2.17}$$

where

$$\hat{F} = \hat{h}_1 + \sum_{j=1}^{N}(\hat{J}_j - \hat{K}_j). \tag{2.18}$$

Here, $\hat{J}_j$ and $\hat{K}_j$ are the Coulomb and exchange terms representing the average electron-electron interactions in the mean field approximation. While $\hat{J}_j$ accounts for the electron-electron repulsion by averaging over the positions of all other electrons, $\hat{K}_j$ is a consequence of the Pauli exclusion principle. Acting on ϕ_i, they are expressed as

$$\hat{J}_j\phi_i(\mathbf{x}_1) = \int \frac{|\phi_j(\mathbf{x}_2)|^2}{|\mathbf{r}_2 - \mathbf{r}_1|}\, d\mathbf{x}_2\, \phi_i(\mathbf{x}_1) \tag{2.19}$$

$$\hat{K}_j\phi_i(\mathbf{x}_1) = \int \frac{\phi_j^*(\mathbf{x}_2)\phi_i(\mathbf{x}_2)}{|\mathbf{r}_2 - \mathbf{r}_1|}\, d\mathbf{x}_2\, \phi_j(\mathbf{x}_1). \tag{2.20}$$

These equations are solved using the self-consistent-field (SCF) method; an initial guess for the spinorbitals is used to construct the Fock matrix F, which is diagonalized to produce new orbitals. This new set of spinorbitals is then used for the next iteration, and the process is repeated until the orbital energies ε_i and wavefunctions ϕ_i converge to within a predetermined tolerance.

In the Hartree-Fock approach, the treatment of the spin and occupancy of the orbitals (canonical HF orbitals) is a key factor. Based on that, there are three main formalisms: the restricted (RHF), restricted Open-Shell (ROHF), and unrestricted (UHF) Hartree-Fock. In RHF, designed for closed-shell systems where all electrons are paired, the wavefunction is constructed with restricted spinorbitals. That means orbitals are constrained to have the same spatial parts for α and β electrons, so RHF cannot be applied to triplet or any other states with unpaired electron spins. ROHF utilizes different $\hat{F}$ operators: one for the doubly occupied molecular orbitals, as in RHF, and another for the partially occupied orbitals. Thus, for closed-shell singlet states, ROHF and RHF yield the same results, but ROHF can also be applied to any open-shell situation. Finally, UHF allows all the α and β spinorbitals to vary independently, offering a more flexible approach for handling different spin configurations [368].

As highlighted in Section 1.3.1, we are interested in studying closed-shell singlet, open-shell singlet, and triplet states. Although HF may not be employed directly

in our work, we will utilize single-determinant methods conceptually similar to HF, specifically KS-DFT. We introduced the ROHF method for the sake of completeness; however, our analyses will primarily focus on the restricted and unrestricted formalisms. Hence, we will discuss the main differences between the RHF and UHF approaches, as they are most relevant to our investigations.

Electrons with opposite spin tend to pair and occupy the same spatial orbital. In such scenarios, both UHF and RHF display identical behavior, leading to the CS solution. However, when these electrons are separated, as illustrated by the homolytic cleavage of H_2 depicted in Figure 1.15b on page 32, RHF encounters limitations due to the separability problem, characterized by fictitious self-repulsion, and thus fails to accurately describe the expected energy curve. In contrast, UHF is capable of providing a qualitatively correct description of the energy curve [369, 370]. Thus, only with UHF one will achieve the broken symmetry solution required to describe (bi)radical forms. Unfortunately, the Ψ_{UHF}, *i.e.*, a single SD made of different orbitals for different spins, is not an eigenfunction of the total spin operator, $\hat{S}^2$. And while for an OS singlet state we expect an $\langle\hat{S}^2\rangle$ value of zero ($s(s+1) = 0$, where s denotes the total spin number), higher values ($\langle\hat{S}^2\rangle \neq 0$) are often encountered. This phenomenon is known as spin contamination, and it arises from the fact that UHF does not strictly enforce a correct total spin for the system. As mentioned earlier, it allows the α and β orbitals to vary independently. This flexibility can lead to energetically favorable solutions that incorporate components of other spin states. For a conceptual understanding, we can illustrate the wavefunction as[g]

$$\Psi_{UHF} = C_{2s+1}\Psi_{2s+1} + C_{2s+3}\Psi_{2s+3} + \ldots \tag{2.21}$$

Consequently, our OS state having two unpaired electrons but with an overall zero spin, will contain contributions (C) from a triplet, a quintuplet, etc. with the highest C being the $n_\alpha + n_\beta + 1$ multiplicity (where n_α or n_β correspond to the number of α or β electrons, respectively) [340].

In a 1982 publication, Mayer [370] noted that "*unrestricted Hartree Fock method applying single determinant DODS (different orbitals for different spins) wavefunction is, as well known, probably the simplest one accounting for a part of the correlation energy*". Then again, he discussed the inherent limitations of both RHF and UHF,

---

[g]The Ψ_{UHF} representation in Eq. (2.21) is a simplified illustration to facilitate the understanding of the UHF potential spin contamination. It is not an exact representation.

as they treat electronic motions independently. It is evident that, in reality, the motions of electrons are correlated. When limiting 'reality' to systems studied under non-relativistic Born-Oppenheimer approximations, ***electron correlation*** energy is defined as the energy difference between the exact FCI and the RHF value [371, 372].

$$E_{\text{corr}} = E_{\text{FCI (exact)}} - E_{\text{RHF}} \tag{2.22}$$

There is a more convenient description given by Pines [373], which defines the E_{corr} of a given method as the energy of that method minus the HF energy, so we can consider electron correlation as an intrinsic property of the method. This will be the definition of E_{corr} adopted in this discussion. Additionally, correlation effects can be subdivided into two main categories: nondynamic (also referred to as static) and dynamic correlation [374]. As we have already seen, the former arises from the need to use more than one SD to properly describe the system. In contrast, the latter refers to the correlation effects deriving from the movement of electrons in relation to each other, and it becomes more important with increasing N in the system.

With a set of equations (HF theory) providing the foundational basis for solving the eigenvalue problem, along with an understanding of its limitations in approaching the exact result, the stage was set for the development of methods to obtain E_{corr}, the so-called post-Hartree-Fock methods. Of these, we will briefly discuss the most relevant.

Configuration Interaction

As we have seen, instead of a single SD, we can use a large number of determinants to build Ψ (Eq. (2.8)). Having already introduced FCI, we will now focus on discussing truncated configuration interaction (CI) methods.

Starting from a HF reference, Ψ_{HF}, the way to generate new determinants is to replace the spinorbital ϕ_a by ϕ_r, or the spinorbitals ϕ_a and ϕ_b by ϕ_r and ϕ_s, etc., to obtain Ψ_a^r, Ψ_{ab}^{rs}, or successive excited determinants. These are the singly (S), doubly (D), ..., n-tuply excited determinants, and the order at which we truncate the expansion designates the method: CIS, CISD, and so on. Then, through the linear variational method, we obtain the energies (of both ground and excited states) and the optimal CI coefficients. At this point, the calculation is simplified discarding non-interacting terms based on group theory, Condon-Slater rules, and Brillouin's theorem [341, 375]. It must be noted that, unlike HF, in CI only the expansion coefficients are optimized

while the molecular orbitals are fixed using the ones from the HF solution. Therefore, truncated CI will consistently yield energies closer to the exact solution. At lower truncation levels, such as CISD, the improvement is primarily due to the introduction of dynamic correlation effects. At higher levels, like CISDTQ, the method also captures most nondynamic correlation effects. In many cases, where Ψ_{HF} is already a good approximation to the system true Ψ, truncated CI at accessible orders often represents an optimal approach. However, for systems with orbital degeneracy requiring significant nondynamic correlation treatment, the computational cost of sufficiently high-level CI truncations may be prohibitive, necessitating alternative approaches.

Additionally, truncated CI calculations are more sensitive to the size of the basis set than HF. This increased sensitivity arises because CI methods, unlike HF, use virtual orbitals to construct excited determinants. The quality of the virtual orbitals representation—dictated by the basis set—directly influences the ability to model electron excitations and, consequently, E_{corr}. Hence, it requires larger basis sets to capture E_{corr} more efficiently. In practice, due to the large computational cost and problems like size extensivity and consistency, other CI variations are more used nowadays [376–378].[h]

Multiconfigurational Self-Consistent Field

An alternative approach to reduce the number of excited configurations is to limit the number of spinorbitals where the excitations occur. Typically, excitations from very low-energy orbitals or to very high-energy orbitals contribute less to Ψ compared to those involving frontier orbitals. Given this, we can define a space, 'the active space', that includes the most relevant orbitals for the description of the chemical problem. By allowing excitations only within this active space, we significantly reduce the complexity of the system. The key point is that by reducing the problem to the active space, we enable a treatment involving a combination of a high number of determinants, each representing distinct electron configurations, only within this reduced space. This strategic focus forms the fundamental idea behind multiconfigurational self-consistent field (MCSCF) methods [335, 341, 379].

Among MCSCF methods, the most common is the complete active space self-consistent field (CASSCF). In CASSCF, the orbitals constituting Ψ fall into three classes—orbital subspaces: occupied, active, and virtual orbitals as represented in

---

[h]Size consistency implies that the energy of two non-interacting fragments equals the sum of the energies of the individual fragments. Size extensivity indicates the method's correct scalability with the system size.

Figure 2.3. Similar to the HF method, occupied orbitals remain fully filled, and virtual orbitals are empty. In contrast, active orbitals are treated at the FCI level. This allows for the description of systems with multiconfigurational character (those exhibiting an important amount of nondynamic correlation), *e.g.* bond breaking and formation, diradicals, and conical intersections, provided the active space contains all orbitals relevant to these events.
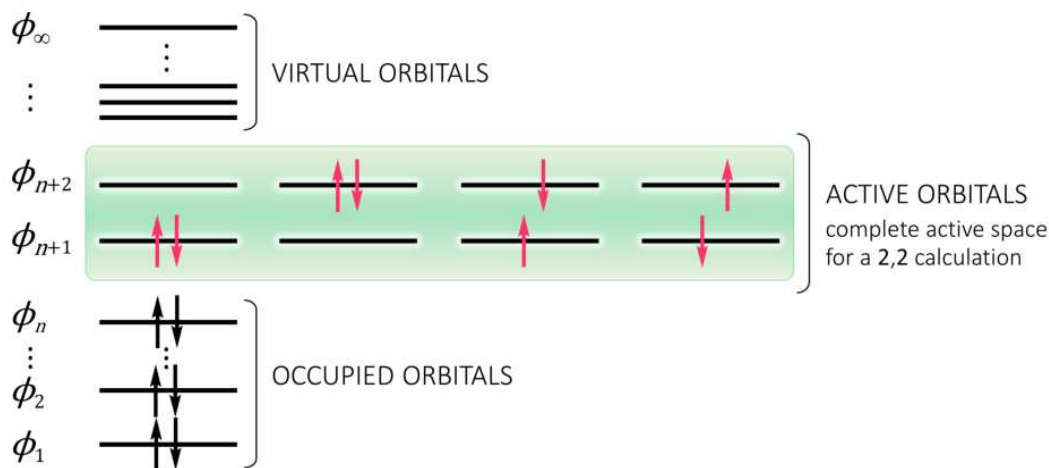
Figure 2.3 Schematic representation of the configurations included in a two electrons in two orbitals (2,2) CASSCF wavefunction for a singlet state. The active space orbitals and electrons are highlighted in green and red, respectively, while the inactive occupied and virtual orbitals are in black.

Moreover, in CASSCF, both the expansion coefficients and the orbitals within the active space are optimized. This can be advantageous for dealing with near-degeneracy effects, where Ψ_{HF} could be biased towards specific covalent or ionic configurations. The flexibility given by the active orbital optimization provides a better representation of these orbitals and allows the description of the electronic state mixing. In this context, it is pertinent to discuss the role of natural orbitals, which are frequently employed in correlated methods. Unlike canonical orbitals that are restricted to integer occupation numbers of 2, 1, or 0, natural orbitals allow for fractional occupation numbers (n_i) ranging between 0 and 2. Natural orbitals are obtained by diagonalizing the 1-density in Eq. (2.12), resulting in Eq. (2.16), where the eigenvalues of the diagonal matrix correspond to n_i. This characteristic of natural orbitals provides a more detailed view of electron distribution.

The most important limitation of CASSCF is the active space dependence. Selecting the type of orbitals and how many must be included in the active space requires

judicious choice. Moreover, CASSCF is often limited to a maximum of 20 orbitals and a comparable number of electrons [380]. This limitation also results in a lack of dynamic correlation, which requires considering a large number of excitations in the whole space. Other MCSCF schemes like the restricted active space (RAS) partially mitigate this by allowing variable excitation levels across more orbital subspaces [381, 382]. Variants of RAS, such as the RAS Spin-Flip configuration interaction approach, and methods like complete active space configuration interaction (CASCI), illustrate the diverse strategies employed to improve results or reduce computational costs by modifying the treatment of orbital optimization and excitation selection [378, 383–385]. Finally, further incorporation of dynamic correlation energy can be achieved by coupling CASSCF with perturbation theory or DFT, resulting in methods such as CAS Møller-Plesset second-order perturbation theory (CASPT2) [386] or multiconfigurational pair-density functional theory (MCPDFT) [387]. While these methods provide accurate descriptions of dynamic correlation effects, it is important to note that CASPT2, in particular, can be computationally more demanding, emphasizing the challenge of balancing computational costs with accuracy.

Coupled Cluster

In coupled cluster (CC), the excited determinants, used to improve the single SD approach, are generated by applying the so-called cluster operator $\hat{T}$ (Eq. (2.23)) on the ground state Slater determinant (Ψ_{HF}),

$$\hat{T} = \hat{T}_1 + \hat{T}_2 + \hat{T}_3 + \cdots + \hat{T}_N. \tag{2.23}$$

The application of $\hat{T}_n$ generates a linear combination of all the excitations of order n. For example, the application of $\hat{T}_2$ gives

$$\hat{T}_2 \Psi_{\text{HF}} = \sum_{i<j}^{\text{occ.}} \sum_{a<b}^{\text{vir.}} t_{ij}^{ab} \Psi_{ij}^{ab} \tag{2.24}$$

where t are the CC amplitudes. The operation of $1 + \hat{T}$ on the Ψ_{HF} produces the FCI wavefunction. The actual CC wavefunction is defined not by the action of $\hat{T}$ but the exponential of $\hat{T}$ on the HF reference,

$$\Psi_{\text{CC}} = e^{\hat{T}} \Psi_{\text{HF}}. \tag{2.25}$$

The application of the exponential generates both connected and disconnected clusters of n-tuply excitations that allow accounting for the interactions more efficiently. One important consequence of the application of the exponential is that the final wavefunction is size-consistent. Similar to truncated CI, there are various levels of CC depending on how many excitations are included. CCSD(T) corresponds to the inclusion of singly and doubly excitations given by $\hat{T}_1$ and $\hat{T}_2$ and the triply excitations estimated using the perturbation theory method [375].

For ground state systems not having multiconfigurational character[i], the coupled cluster method, particularly CCSD(T), is recognized for its high level of accuracy within the range of *ab initio* methods available [388, 389], and CCSD(T) is referred to as the gold standard in computational chemistry. However, the trade-off is a significant increase in computational cost, which scales poorly with the system size. This high computational cost can be mitigated by employing certain approximations that build upon the CCSD methodology [390, 391]. Moreover, these CC methods are not directly applicable to excited states, unlike truncated CI and CASSCF. The most common CC extension used for treating excited states is the equation of motion coupled cluster (EOM-CC) [392].

---

[i]In the case of small systems with multiconfigurational characteristics, such as the dissociation of H_2, with two electrons, CCSD effectively provides an accurate description equivalent to FCI. For such systems, the range of possible excitations is comprehensively covered by the CCSD method. However, for larger systems exhibiting nondynamic correlation effects, the CCSD or CCSD(T) approximation may not capture all relevant configurations, making it insufficient to fully describe these systems' electronic structure.

2.1.2 Density Functional Theory and Time Dependent-DFT

Density functional theory (DFT) stands as one of the most extensively employed electronic structure methods in quantum chemistry, offering a favorable balance between computational efficiency and accuracy [393]. Modern DFT started with the application of the theoretical formalisms resulting from the contributions made by Hohenberg, Kohn, and Sham, which consist of the two Hohenberg-Kohn (HK) theorems [394] and the Kohn-Sham (KS) method [395].

The first theorem establishes that for a given $\rho(\mathbf{r})$ there exists a unique external potential ($V_{ext}(\mathbf{r})$). This unique correspondence between $\rho(\mathbf{r})$ and $V_{\text{ext}}(\mathbf{r})$ ($\rho \leftrightarrow V_{\text{ext}}$) implies the existence of a unique functional, solely dependent on the one-electron density, capable of determining the ground state energy or any other property of the system from $\rho(\mathbf{r})$. For the energy, the electronic energy functional is expressed in terms of the electron density, capturing the essential components necessary for calculating the system's total energy. Thus, it is written as

$$E[\rho(\mathbf{r})] = V_{ext}[\rho(\mathbf{r})] + \underbrace{T[\rho(\mathbf{r})] + V_{ee}[\rho(\mathbf{r})]}_{F_{\text{HK}}[\rho(\mathbf{r})]} = \int \rho(\mathbf{r}) v_{ext}(\mathbf{r}) d\mathbf{r} + F_{\text{HK}}[\rho(\mathbf{r})], \qquad (2.26)$$

where $V_{ext}(\mathbf{r})$ contains the electron-nucleus attraction potential and all other potentials that interact with the *N*-electron system (*e.g.* external electric or magnetic fields) but the electron-electron potential. The other terms are the potential operator ($v_{ext}(\mathbf{r})$) and the *Hohenberg-Kohn functional* ($F_{\text{HK}}[\rho(\mathbf{r})]$), which is universal and it is defined as the sum of the kinetic energy functional ($T[\rho(\mathbf{r})]$) and the electron-electron potential energy functional ($V_{ee}[\rho(\mathbf{r})]$), but its precise expression is *not known.*

The second theorem proves that, for real *N*-electron systems, the ground state $\rho(\mathbf{r})$, which satisfies the conditions of integrating to the total number of electrons $\int \rho(\mathbf{r}) d\mathbf{r} = N$, having $\rho \leftrightarrow V_{\text{ext}}$, and being non-negative $\rho(\mathbf{r}) \geq 0$ everywhere, is the one that minimizes the energy functional. Consequently, any approximate electron density ($\tilde{\rho}(\mathbf{r})$) will result in an energy that is equal to or greater than the energy of the true system. This is analogous to the variational principle in wavefunction-based methods (Eq. (2.6)).

The lack of knowledge about the exact expression of the $F_{\text{HK}}[\rho(\mathbf{r})]$ limited the applicability of DFT until Kohn and Sham proposed their method. They introduced a hypothetical system consisting of *N* non-interacting electrons whose total density is

the same electron density as the real system, where the electrons do interact. For this Kohn-Sham system, the Hamiltonian operator is

$$\hat{H}_s = \sum_{i=1}^{N} \hat{h}_s(\mathbf{r}_i) = \sum_{i=1}^{N}(-\frac{1}{2}\nabla_{r_i}^2 + v_s(\mathbf{r}_i)), \tag{2.27}$$

here $\hat{h}_s$ is the KS one-electron operator and $v_s(\mathbf{r})$ is the KS potential constructed to obtain a ground state electron density that matches the electron density of the real system.

Since we are working with a fictitious non-interacting electrons system, the HF approximation is exact. Thus, the exact Ψ of the KS system can be described as in Eq. (2.17) with the single-electron orbitals fulfilling

$$\hat{h}_s \phi_i = \varepsilon_i \phi_i. \tag{2.28}$$

According to the first HK theorem, the total energy of the KS system will be given by

$$E_s[\rho(\mathbf{r})] = T_s[\rho(\mathbf{r})] + \int \rho(\mathbf{r}) v_s(\mathbf{r}) d\mathbf{r} = \sum_{i=1}^{N} \varepsilon_i, \tag{2.29}$$

and this energy corresponds to the sum of KS orbital energies, ε_i. Additionally, the electron density can be expressed as

$$\rho(\mathbf{r}) = \sum_{i=1}^{N} |\phi_i(\mathbf{r})|^2, \tag{2.30}$$

which is constructed to match the electron density of the real system (Eq. (2.12)), in accordance with the design of the Kohn-Sham approach. Then, we can write the total energy functional (omitting the nucleus-nucleus repulsion therm) of the real system as

$$E[\rho(\mathbf{r})] = T_s[\rho(\mathbf{r})] + V_{ext}[\rho(\mathbf{r})] + \underbrace{\frac{1}{2} \iint \frac{\rho(\mathbf{r}_1)\rho(\mathbf{r}_2)}{|\mathbf{r}_1 - \mathbf{r}_2|} d\mathbf{r}_1 d\mathbf{r}_2}_{J[\rho(\mathbf{r})]} + \underbrace{\Delta T[\rho(\mathbf{r})] + \Delta V_{ee}[\rho(\mathbf{r})]}_{E_{\text{XC}}[\rho(\mathbf{r})]} \tag{2.31}$$

where $T_s[\rho(\mathbf{r})]$ is the kinetic energy functional of the KS system, $V_{ext}[\rho(\mathbf{r})]$ is the external potential containing the electron-nucleus interactions, $J[\rho(\mathbf{r})]$ represents the classical Coulomb electron-electron interaction energy, and $E_{\text{XC}}[\rho(\mathbf{r})]$ is the exchange-correlation functional, which accounts for the non-classical effects of electron-electron interactions, including both exchange and correlation phenomena. This functional incorporates

corrections to the kinetic energy ($\Delta T[\rho(\mathbf{r})]$) and captures the difference between the real $V_{ee}[\rho(\mathbf{r})]$ and $J[\rho(\mathbf{r})]$.

The KS method enables the exact calculation of all terms within the total energy functional except for $E_{\mathrm{XC}}[\rho(\mathbf{r})]$. This functional, describing all non-classical corrections (*i.e.* exchange and correlation) to $V_{ee}[\rho(\mathbf{r})]$ and the kinetic energy beyond the non-interacting model, is unknown. Therefore, to apply the KS method in practical calculations we need to approximate $E_{\mathrm{XC}}[\rho(\mathbf{r})]$.

KS-DFT equations resemble those of HF Eqs. (2.17), (2.18), and (2.19). Both HF and KS-DFT are based on the single-determinant approximation of Ψ. The main difference lies in the fact that HF approximates Ψ of the true interacting electrons system, providing the exact exchange term (Eq. (2.20)), but omitting completely the electron correlation energy. In contrast, KS-DFT represents the Ψ of the non-interacting system whose ground-state density matches that of the real system, thereby incorporating electron correlation effects [375, 396–400].

The undetermined form of $E_{\mathrm{XC}}[\rho(\mathbf{r})]$ necessitates the use of density functional approximations (DFAs) to make the application of the theory feasible in practical scenarios. Some functionals are designed for general use, whereas others are highly parameterized for specific tasks or based on fundamental principles. Perdew's 'Jacob's Ladder' (Figure 2.4) ranks DFAs according to the complexity of their physical ingredients [401]. DFAs include various electron density or kinetic energy descriptors to refine $E_{\mathrm{XC}}[\rho(\mathbf{r})]$. These descriptors account for factors ranging from the occupied orbitals via the density itself [395] to its first ($\nabla\rho(\mathbf{r})$) [402], second derivative ($\nabla^2\rho(\mathbf{r})$) or the kinetic energy density (τ) [403]. Additional refinements consider occupied orbitals through HF exchange ($E_{\mathrm{X}}^{\mathrm{HF}}$) [404, 405] or virtual orbitals via Görling-Levy-based perturbation theory ($E_{\mathrm{C}}^{\mathrm{PT2}}$) [406, 407], among other variations. Before delving into the five primary categories of DFAs based on E_{XC}, it is important to consider that the categories outlined below represent the general frameworks of DFAs, but individual functionals within these categories may diverge from the general formula. Accordingly, the categories are as follows:

- Local Density Approximation (LDA): $E_{\mathrm{XC}} = E_{\mathrm{XC}}\left[\rho(\mathbf{r})\right]$

- Generalized Gradient Approximation (GGA): $E_{\mathrm{XC}} = E_{\mathrm{XC}}\left[\rho(\mathbf{r}), \nabla\rho(\mathbf{r})\right]$

- meta-GGA (mGGA): $E_{\mathrm{XC}} = E_{\mathrm{XC}}\left[\rho(\mathbf{r}), \nabla\rho(\mathbf{r}), \nabla^2\rho(\mathbf{r}), \tau(\mathbf{r})\right]$

- Hybrid: $E_{\mathrm{XC}} = E_{\mathrm{XC}}[\boldsymbol{n}] + \alpha\left[E_{\mathrm{X}}^{\mathrm{HF}} - E_{\mathrm{X}}[\boldsymbol{n}]\right]$, where $\boldsymbol{n} \equiv \rho(\mathbf{r}), \nabla\rho(\mathbf{r}), \nabla^2\rho(\mathbf{r}), \tau(\mathbf{r})$

- Double Hybrid: $E_{XC} = \alpha E_X + (1-\alpha)E_X^{HF} + \beta E_C + (1-\beta)E_C^{PT2}$
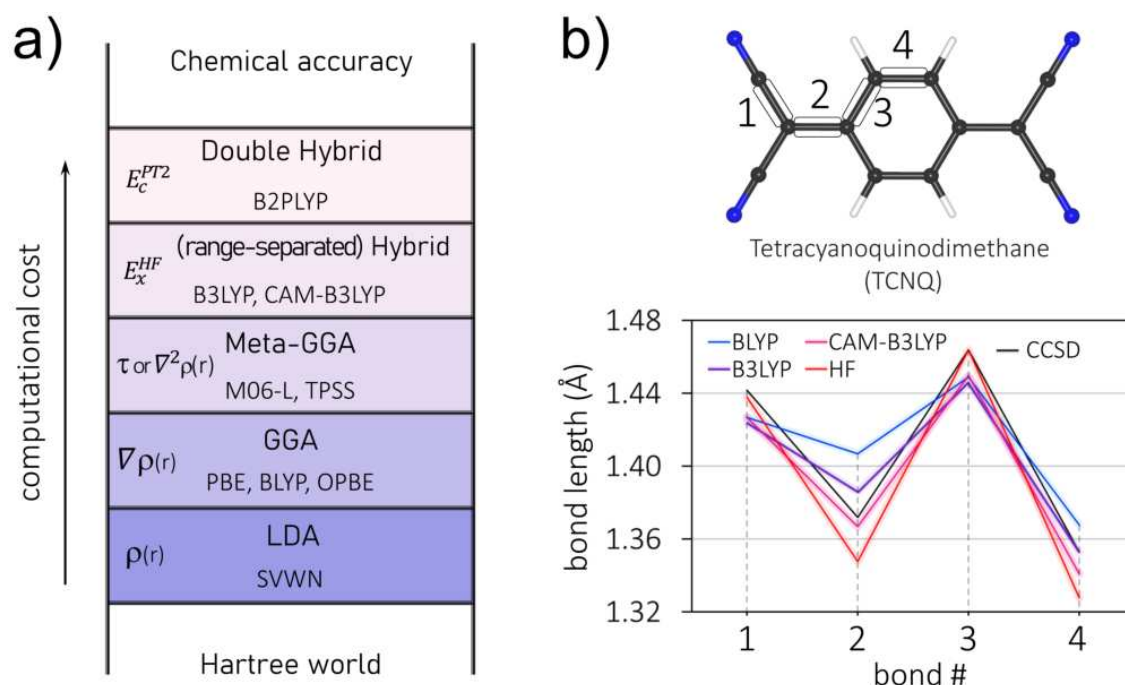
Figure 2.4 a) Jacob's Ladder for DFAs. Adapted from schemes in references: [401, 408, 409]. b) Distribution of carbon-carbon bond lengths (in Å) for the TCNQ molecule, calculated using CCSD, HF, BLYP, B3LYP, and CAM-B3LYP together with 6-311+G(d,p) basis set.

Among these, hybrid functionals are widely employed in quantum chemistry, primarily because they offer improved performance in predicting thermodynamic properties and accurately estimating reaction barriers. For the majority of properties, these functionals show the best performance. On the one hand, it is known that pure functionals (LDA and GGA) suffer from the delocalization error (DE) and self-interaction error (SIE) [410–413]. This is due to their inability to exactly cancel the electron self-interaction, which is the interaction of an electron with itself, leading to over-delocalization of the electron density and incorrect energy level alignments, resulting in underestimated energy barriers. Additionally, accurately reproducing the behavior of electrons at long range, which affects DE, significantly impacts the evaluation of aromaticity in macrocycles [76, 144–146]. On the other hand, HF does not suffer from this DE but neglects electron correlation effects, often leading to highly localized bonds and overestimated energy gaps. These effects can be seen in the plotted bond lengths of tetracyanoquinodimethane, as depicted in Figure 2.4b, which shows that optimization at the HF level leads to the geometry with the greatest bond alternation, while the GGA BLYP functional results in a more delocalized structure with lower bond-length

alternation. Hybrid functionals such as B3LYP and CAM-B3LYP are not exempt from DE but they behave better by including a percentage of E_X^{HF}, the higher the amount of E_X^{HF}, the lower the DE.

A well-known failure of DFAs is the incorrect asymptotic behavior of the functional at long interelectronic distances, which is crucial to account for dispersion forces. These often fail to accurately capture van der Waals (vdW) interactions because they lack the appropriate long-range dynamic correlation. The inadequate representation of dispersion compromises the accuracy of predicted geometrical arrangements. Moreover, these interactions are crucial for accurately modeling excitations to Rydberg states and charge transfer processes [396]. To overcome this deficiency, a common approach is to divide the electron-electron Coulomb operator into short-range (SR) and long-range (LR) terms using an error function (erf)

$$\frac{1}{|\mathbf{r}_1 - \mathbf{r}_2|} \equiv \frac{1}{r_{12}} = \underbrace{\frac{1 - \mathrm{erf}(\omega r_{12})}{r_{12}}}_{\text{SR}} + \underbrace{\frac{\mathrm{erf}(\omega r_{12})}{r_{12}}}_{\text{LR}} . \tag{2.32}$$

Here, ω is the range separation parameter, also called attenuating parameter, which is usually determined empirically and controls the percentage of E_X^{HF} included in the exchange-correlation functional at each interelectronic distance. With this, we achieve a functional that can behave more like a GGA at short range and like HF at long range. Some examples of functionals using a modification of Eq. (2.32) are CAM-B3LYP [414] or ωB97X-D [415].

In certain cases, determining an optimal ω value for each specific system serves to reduce the error in calculated properties (*e.g.*, excitation energies). Among the various optimization strategies, the ΔSCF method [416–418] is frequently utilized. This method aims to fine-tune ω to minimize the discrepancy between calculated and exact values of the ionization potential[j] (IP) and the electron affinity[k] (EA), thus ensuring that the functional adheres as closely as possible to Janak's theorem [421]. The optimization focuses on minimizing the tuning conditions, for which minimizing the $J^*(\omega)$ function, as defined in Eq. (2.33) below, has generally been identified as the

---

[j]Within HF theory, Koopmans's theorem [375, 419] states that the ionization potential of the N-electron system, calculated by subtracting the energy of the N-electron system from the energy of the system with $N-1$ electrons, equals the negative value of the HOMO energy of the neutral system ($\varepsilon_{HOMO}(N)$). According to the IP-theorem [420], this also applies to KS-DFT.

[k]The electron affinity is calculated as the difference between the ground state energies of the system with N electrons and with $N+1$ electrons. According to the IP-theorem [420], the EA of a neutral molecule corresponds to the minus HOMO energy of the anion, $\varepsilon_{HOMO}(N+1)$.

best approach [422, 423].

$$J^*(\omega) = \sqrt{|\varepsilon_{\text{HOMO}}^\omega(N) + \text{IP}(N)|^2(\omega) + |\varepsilon_{\text{HOMO}}^\omega(N+1) + \text{EA}(N)|^2(\omega)}, \qquad (2.33)$$

where $\varepsilon_{\text{HOMO}}^\omega(N)$ and $\varepsilon_{\text{HOMO}}^\omega(N+1)$ are the HOMO energies for systems with N and $N+1$ electrons, respectively. The application of this process to tune ω results in the so-called optimally tuned (OT) range-separated functionals.

Additionally, the poor description of the van der Waals forces can be further corrected by incorporating an extra term accounting for dispersion to the KS equation. This term, designed to account for geometrical effects without imposing significant computational costs, is empirically derived to enhance the treatment of dispersion interactions. One of the most widely adopted approaches for this purpose is the empirical dispersion correction proposed by Grimme [424], with the D3 correction [425], enhanced by the Becke-Johnson (BJ) damping [426–428] for improved accuracy, being particularly popular. The more recent D4 version [429] offers further refinements, extending the applicability and precision of dispersion corrections.

The KS-DFT approach has many advantages, but the most important is the inclusion of electron correlation effects in the electron density and derived properties at a lower computational cost than correlated wavefunction methods. Moreover, the delocalization error and failures at describing long-range interactions can be mitigated by the use of exact exchange and range-separated functionals. Nonetheless, KS-DFT method is still limited to the study of the lowest energy state of a given space-spin symmetry. To address the study of excited states, alternative approaches like time-dependent density functional theory (TDDFT) have been developed, expanding the scope of DFT to excited state chemistry.

Time-dependent density functional theory applies a similar philosophy of the KS method to time-dependent problems. The time-dependent Schrödinger equation is solved for a non-interacting system whose orbitals result in the same time-dependent density $\rho(\mathbf{r}, t)$ as the real system. This can be done because the Runge-Gross theorem [430] establishes that the time-dependent external potential, $v_{ext}(\mathbf{r}, t)$, in a many-electron system is uniquely determined, up to a constant, by the time-dependent electron density. Then, the time-dependent KS equations are defined as

$$i\frac{\partial \phi_j(\mathbf{r}, t)}{\partial t} = \left(-\frac{\nabla^2}{2} + v_s[\rho](\mathbf{r}, t)\right)\phi_j(\mathbf{r}, t), \qquad (2.34)$$

where the first term is the time derivative of the j-th time-dependent KS orbital ϕ_j, multiplied by the imaginary unit i. The v_s is the KS potential, and the density is

$$\rho(\mathbf{r}, t) = \sum_{j=1}^{N} |\phi_j(\mathbf{r}, t)|^2. \tag{2.35}$$

The KS potential can be written as the sum of three terms

$$v_s(\mathbf{r}, t) = v_{ext}(\mathbf{r}, t) + v_{\mathrm{H}}(\mathbf{r}, t) + v_{\mathrm{XC}}(\mathbf{r}, t). \tag{2.36}$$

Here the external potential, v_{ext}, includes contributions from nuclei and any time-varying or constant external fields. v_{H} is the Hartree potential representing the classical electrostatic interaction and v_{XC} is the exchange-correlation functional. The analysis also incorporates the initial wavefunctions of both the interacting system, denoted by Ψ_0, and the Kohn-Sham system, Ψ_0^{KS}. However, in practice, we apply the adiabatic approximation, in which the exchange-correlation potential at a given time is assumed to depend only on the electron density at that exact moment, and not on its past values or the initial wavefunctions. This simplification is generally valid when v_{ext} changes slowly enough for the electron density to adapt instantaneously [431].

While the TDDFT method was originally formulated for systems subject to time-dependent external potentials, it can also be utilized to compute static properties of the system. In this thesis, our primary interest is to employ TDDFT as a tool to obtain mainly vertical excitation energies and the corresponding electron densities of various excited states.

To determine excitation energies and other properties of excited states, the linear-response approach within time-dependent density functional theory (LRes-TDDFT) is most commonly employed. The main idea of LRes-TDDFT is to consider excitations as the system's response to an external electromagnetic field, which is introduced as a perturbation in the KS potential (v_s). In this framework, the vertical excitation energies are obtained as solutions to the Casida equation [396, 432],

$$\begin{pmatrix} A & B \\ B^* & A^* \end{pmatrix} \begin{pmatrix} X \\ Y \end{pmatrix} = \omega \begin{pmatrix} 1 & 0 \\ 0 & -1 \end{pmatrix} \begin{pmatrix} X \\ Y \end{pmatrix}. \tag{2.37}$$

This equation in matrix form represents the eigenvalue problem to be solved to get the excitation energies (denoted by ω), where matrix A contains orbital energy differences and the Coulombic electron-electron interactions, which are crucial for describing the

direct coupling effects between electronic transitions. Matrix B, on the other hand, accounts for the exchange-correlation contributions to these couplings, derived from the exchange-correlation potential within TDDFT. The specific forms of A and B matrices depend on the exchange-correlation functional. For the particular case of a hybrid functional they are given by:

$$A_{ia,jb} = \delta_{ij}\delta_{ab}(\varepsilon_a - \varepsilon_i) + (ia|jb) - \alpha(ia|jb) + (1-\alpha)(ia|f_{\mathrm{XC}}|jb) \quad (2.38)$$

$$B_{ia,jb} = (ia|bj) - \alpha(ij|ab) + (1-\alpha)(ia|f_{\mathrm{XC}}|jb), \quad (2.39)$$

where α determines the percentage of HF exchange in the functional. Then, the exchange-correlation kernel (f_{XC}) on the KS orbitals is written as

$$(ia|f_{\mathrm{XC}}|jb) = \iint \phi_i^*(\mathbf{r})\phi_a(\mathbf{r})\frac{\delta^2 E_{\mathrm{XC}}}{\delta\rho(\mathbf{r})\delta\rho(\mathbf{r}')}\phi_b(\mathbf{r}')\phi_j^*(\mathbf{r}')d\mathbf{r}d\mathbf{r}'. \quad (2.40)$$

As we have discussed previously, computing electronic transitions that feature a significant electron-hole spatial separation (*i.e.* charger transfer states) poses a challenge for DFT. In these cases, it is necessary to employ energy functionals with appropriate long-range behavior, such as range-separated hybrid functionals [225, 433]. One negative aspect of using long-range corrected functionals is that these can lead to significantly underestimated triplet excitation energies [434]. One way to solve this problem is to employ the Tamm-Dancoff approximation (TDA) [435, 436], which corresponds to setting the matrix $B = 0$ in Equation (2.37). Moreover, the use of TDA for those singlet excited states with the same spatial symmetry as the problematic triplets can also improve the singlet excitation energy results, in particular in the case of delocalized electronic structures [437].

2.2   Atoms In Molecules and Electron Sharing Indices

The Schrödinger equation arises from the wave-like properties of particles. These particles do not have a definite position until measured; rather, their probable locations are determined by a probability distribution. This distribution is quantitatively described by the probability density, $|\Psi|^2$, emphasizing their wave nature and the probabilistic description of their presence at any point in space. In this quantum picture, with delocalized electrons and unclear atomic boundaries, most traditional chemical

concepts cannot be firmly established or rigorously defined. Chemistry often involves rationalizing global molecular properties by examining isolated *atoms or functional groups within a molecule.* This understanding also relies on valuable concepts like Lewis structures [438], which help estimate bond strength, molecular stability via resonance forms, and oxidation states to name a few. Therefore, considerable efforts have been invested in developing a theory of atoms in molecules (AIM) bridging traditional chemical intuition and quantum mechanics. Beyond this, examining the atomic contributions of well-defined observables, derived from operators, also helps interpret these quantities. Overall, the theory of AIM offers valuable insights contributing to the understanding and prediction of molecular behavior.

One significant issue is that there is no unique approach to the definition of AIM. In his 1985 seminal paper, Bader [439] posed the following: "*it would appear that to find chemistry within the framework of quantum mechanics one must find a way of determining the values of observables for pieces, that is, subsystems, of a total system. **But how is one to choose the pieces?** Is there only one or are there many ways of dividing a molecule into atoms and its properties into atomic contributions? If there is an answer to this problem then the necessary information must be contained in the state function, for it tells us everything we can know about a system*". This viewpoint highlights the intrinsic difficulties of identifying chemically meaningful quantities from quantum mechanical descriptions.

As previously discussed, our approach to represent the states of a system, Ψ_i, within the Hilbert space[l] involves an expansion in MOs, which, in turn, are built from AOs. This construction allows us to decompose these MOs into their atomic contributions logically. This atomic decomposition is known as *Hilbert space partitioning*, through which the part of an MO associated with a specific atom in the molecule, denoted as *A*, is defined as the set of atomic orbitals centered on *A*. The most popular Hilbert space partition is the Mulliken partition [440]. An alternative is the Natural Bond Orbital (NBO) scheme, which employs NBOs instead of canonical MOs. These NBOs arise from a natural atomic orbital (NAO) basis, which is a set of orthogonal orbitals that maximize electron localization and closely resemble the idealized bonds and lone pairs of Lewis structures [441–443].

---

[l]The Hilbert space is a complete, infinite-dimensional vector space endowed with an inner product operation. It serves as the fundamental framework in quantum mechanics, wherein the states of a quantum system, represented by wavefunctions, are defined as elements of this space.

Alternatively, the atomic contributions can be obtained by partitioning the Cartesian space (real space) occupied by the molecule. These are known as *real space partition* methods. The most popular real space partitioning techniques include the Hirshfeld(-iterative) method [444, 445], Voronoi cells [446], Fuzzy or Becke atoms [447], and Bader's topological analysis in the framework of the quantum theory of atoms in molecules (QTAIM) [439, 448]. Ultimately, the choice between different Hilbert and real space partitioning depends on the balance between its mathematical characteristics and the chemical utility [449]. Throughout this thesis, we will primarily rely on QTAIM, although other methods have been also employed.

The central quantity of QTAIM is the electron density, Equation (2.12). The topological analysis of $\rho_1(\mathbf{x}_1)$ allows us to identify and classify its critical points (CP) through the second derivatives (collected in the Hessian matrix). These CPs are characterized by their rank (r) and signature (s), where the rank represents the number of non-zero curvatures and the signature is the net count of positive ($+1$) and negative (-1) curvatures at the CP. There are four distinct CPs: Attractor Critical Points (ACPs) with (r,s) of $(3, -3)$, Bond Critical Points (BCPs) with $(3, -1)$, Ring Critical Points (RCPs) with $(3, +1)$, and Cage Critical Points (CCPs) with $(3, +3)$. These denote the electron density concentrations (usually matching atomic positions), bonding interactions, ring structures, and cage-like enclosures in a molecule, respectively [450].

In QTAIM, the way to partition a molecule into atoms is based on the behavior of the electron density. The atomic domain is defined by the zero-flux surface around a nucleus, as depicted by the black line in Figure 2.5, or is defined by the limits of the system at infinity. As a result, the atomic basins do not overlap.
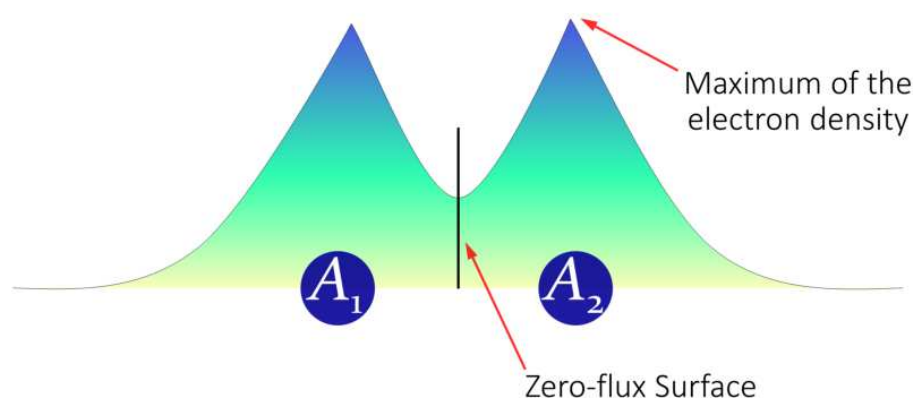
Figure 2.5 Electron density in homonuclear diatomic molecules.

Population Analysis and Delocalization Indices

Among the variety of chemical concepts, atomic populations (N_A), and charges ($Q_A = Z_A - N_A$), provide a quantification of the electron distribution around atoms. This also leads to the concept of the delocalization index (DI), which further describes the nature of electron sharing between atoms, offering insights into molecular structure and reactivity. Simultaneously, bond order, defined as the number of electron pairs shared between a pair of atoms, emerges as another fundamental measure of chemical bonding. Although distinct in their definitions, for simplification, these two concepts are sometimes considered interchangeable. While these concepts are sometimes treated as interchangeable for simplicity, it is crucial to remember their distinct definitions. In particular, the DI offers insights unrelated to direct bonding between atoms [451, 452].

In Hilbert space, the most popular concepts are Mulliken population analysis [440] and Mayer bond order (MBO) [453]. These can be calculated by taking the definition of an MO in terms of AOs (Eq. (2.10)), and determining the MO part that corresponds to atom A as the set of n AOs centered in A. Using also the general definition of the electron density given in Eq. (2.16), the Mulliken population of atom A is

$$N_A = \sum_{\mu \in A} \sum_{\nu}^{n} P_{\mu\nu} S_{\mu\nu}, \qquad (2.41)$$

where $P_{\mu\nu}$ is the density matrix obtained from the MO coefficients (c_μ) and occupation numbers (n_i). The general form of $P_{\mu\nu}$ is

$$P_{\mu\nu} = \sum_{i} n_i c_{\mu i} c_{\nu i}, \qquad (2.42)$$

and $S_{\mu\nu}$ is the overlap between AOs,

$$S_{\mu\nu} = \int \chi_\mu(\mathbf{x_1}) \chi_\nu(\mathbf{x_1}) \, d\mathbf{x_1}. \qquad (2.43)$$

Then, the Mayer bond order between two atoms A and B is given by

$$\text{MBO}_{AB} = \sum_{\mu \in A} \sum_{\nu \in B} (PS)_{\mu\nu} (PS)_{\nu\mu}. \qquad (2.44)$$

We have seen that is pretty straightforward to calculate populations and bond orders from Hilbert space partitioning. Unfortunately, in real space, the calculation of these quantities requires numerical integration over the atomic domain of A, adding

75

computational cost and associated numerical errors. The atomic population in this case is expressed as

$$N_A = \int_A \rho(\mathbf{x}_1)\, d\mathbf{x}_1 = \sum_i n_i S_{ii}(A), \tag{2.45}$$

where

$$S_{ij}(A) = \int_A \phi_i^*(\mathbf{x_1})\phi_j(\mathbf{x_1})\, d\mathbf{x_1}, \tag{2.46}$$

$S_{ij}(A)$ is the overlap between molecular spinorbitals i and j within the basin of A.

To obtain the bond order also referred to as delocalization index ($\delta(A,B)$) or, more generally, when this is extended to n centers ($n \geq 2$), the *electron sharing indices* (ESI) in the real space framework, we will make use of the exchange-correlation density (XCD). The XCD is composed of the $\rho_2(\mathbf{x}_1, \mathbf{x}_2)$ and a fictitious pair density of independent electrons $\rho(\mathbf{x}_1)\rho(\mathbf{x}_2)$ (like in the KS method),

$$\rho_{\text{XC}}(\mathbf{x}_1, \mathbf{x}_2) = \rho(\mathbf{x}_1)\rho(\mathbf{x}_2) - \rho_2(\mathbf{x}_1, \mathbf{x}_2). \tag{2.47}$$

The XCD, which has information about the motion of electron pairs, can be used as a measure of the interactions between electrons in two different regions in space, A and B. By integrating over the space occupied by atoms A and B we get

$$\delta(A,B) = 2\int_B \int_A \rho_{\text{XC}}(\mathbf{x}_1, \mathbf{x}_2) d\mathbf{x}_1 d\mathbf{x}_2. \tag{2.48}$$

For single-determinant wavefunctions (HF and KS-DFT), $\delta(A,B)$ can be written in terms of atomic overlaps (Eq. (2.46)) as:

$$\delta(A,B) = 2\sum_i \sum_j S_{ij}(A)S_{ij}(B). \tag{2.49}$$

Here the sums run over all the occupied molecular spinorbitals.

2.3   Electronic Aromaticity Indices

A fundamental characteristic of aromatic compounds is their cyclic electron delocalization. Consequently, the evaluation of aromaticity can be done from the quantification of this electron delocalization, which, despite not being an eigenvalue of the wavefunction of the system, offers indispensable insights—as discussed in the preceding section. Definitions such as delocalization indices ($\delta(A,B)$), and higher-order electron sharing indices, obtained specially from QTAIM space partitioning have been widely tested and

proved to give proper aromaticity descriptions [95, 128, 454]. Moreover, the electron density of delocalized bonds (EDDB) based on the Hilbert partitioning is also capable of accounting for multicenter bonding at a reasonable cost [455]. Unfortunately, the accuracy of individual aromaticity measures cannot be determined because aromaticity is a property that cannot be measured directly by any physical or chemical experiment, impeding the establishment of unambiguous reference values; therefore, using a variety of indices is recommended. When most indices point in the same direction, it strengthens the confidence in our assessment of aromaticity. Additionally, understanding the specific characteristics of each aromaticity index is crucial, as this can lead to clearer interpretations and alert us to any inconsistencies. Thus, in this section, we will give the definitions and describe the main features of those electronic indices more relevant to this thesis. In the subsequent section (2.4), we will review important aspects of magnetic aromaticity measures. Lastly, geometric, energetic, and other measures, will be briefly described or listed in Section 2.5.

Assessing and interpreting aromaticity results requires comparing the values obtained for the molecule under study with a benchmark aromatic compound, typically benzene. For instance, the fluctuation index (FLU) [17, 456] compares the DI of the atom pairs in a ring ($\mathcal{A} = A_1, A_2, \ldots, A_n$) to the DI of well-known aromatic molecules (*e.g.* benzene for C−C, and pyridine or pyrrole for C−N bonds),

$$\text{FLU}(\mathcal{A}) = \frac{1}{n} \sum_{i=1}^{n} \left[\left(\frac{\delta\left(A_i\right)}{\delta\left(A_{i-1}\right)} \right)^{\alpha} \left(\frac{\delta(A_i, A_{i-1}) - \delta_{\text{ref}}(A_i, A_{i-1})}{\delta_{\text{ref}}(A_i, A_{i-1})} \right) \right]^2, \qquad (2.50)$$

where the function α in the first term corresponds to:

$$\alpha = \begin{cases} 1 & \text{if } \delta(A_{i-1}) \leq \delta(A_i) \\ -1 & \text{if } \delta(A_i) < \delta(A_{i-1}) \end{cases} \qquad (2.51)$$
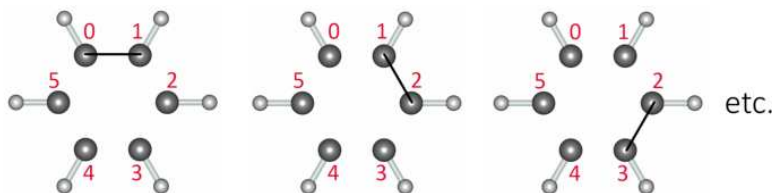
Figure 2.6 Pairs of atoms considered by the FLU index.

Figure 2.6 illustrates the pairs of atoms considered in FLU calculation for the case of benzene. In Equation (2.50), we see that in addition to the second term accounting

for the differences of the delocalization indices, there is a first term where $\delta(A)$ is the atomic valence for a closed-shell system and the α function ensures that the term always takes values greater or equal than one. $\delta(A,B)$ has been previously described in Eq. (2.49). According to FLU, aromatic molecules will present small values, close to zero (and exactly zero in the case of benzene), and larger values for non-aromatic or antiaromatic molecules. It is worth noting that indices based on references are more suited to evaluate the relative aromaticity degree of compounds that resemble its references like substituted benzenes, small annulenes, or small heteroaromatics but fail in other cases like the transition state of the Diels–Alder reaction [95, 457] or the identification of the annulene pathway as the most aromatic in 18H porphyrin [146]. Furthermore, we can only use FLU for molecular systems with available DI reference values. Consequently, it cannot be used in the context of metal aromaticity, systems with halogens, or B–C and B–B bonds, as well as other bond types that deviate from those typically found in classical organic molecules. Yet, this limitation might be addressed by agreeing on DI values for aromaticity in these systems, allowing for a wider use of FLU.

One interesting feature is that from the expression in Eq. (2.49) we can easily obtain the separation of the FLU index into the α and β components, by only considering α and β molecular spinorbitals [109]. The FLU divided into spin components can provide more insight in the evaluation of open-shell electronic structures providing quantitative support to the Mandado's 2n+1 rule [119] for aromaticity of separate spins. The difference between the α and β contributions to the FLU index can be quantitatively assessed using the following expression [109]:

$$\left| \frac{\Delta \text{FLU}}{\text{FLU}} \right| = \frac{\text{FLU}_\alpha - \text{FLU}_\beta}{\text{FLU}}. \tag{2.52}$$

Another aromaticity index based on bond orders is the bond-order alternation (BOA). This index does not rely on references. Instead, it is based on measuring the degree of bond equalization or bond alternation. Thus it evaluates the DI difference of consecutive bonds, represented in red and green in Figure 2.7, indicating a greater or lesser degree of aromaticity when bonds are more or less equalized, respectively [458]. For instance, in benzene, where all δ(C–C) have the same 1.394 value, at the CAM-B3LYP/6-311G(d,p) level of theory, the BOA is zero [128].

The original formula of BOA [459], initially proposed for open fragments, is mainly suited for rings containing an even number of atoms ($n = 4, 6, 8, \ldots$). It is given by the equation:

$$\text{BOA}(\mathcal{A}) = \frac{1}{n_1} \sum_{i=1}^{n_1} \delta(A_{2i-1}, A_{2i}) - \frac{1}{n_2} \sum_{i=1}^{n_2} \delta(A_{2i}, A_{2i+1}), \tag{2.53}$$

here, n_1 and n_2 are determined using the floor function, denoted as $\lfloor x \rfloor$, which returns the largest integer less than or equal to x. Specifically, $n_1 = \lfloor (n+1)/2 \rfloor$ and $n_2 = \lfloor n/2 \rfloor$, applying the floor function to round down to the nearest whole number.
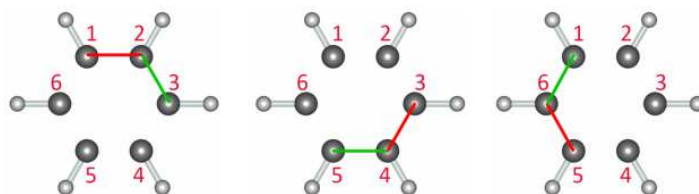
Figure 2.7 Pairs of atoms considered by the BOA index.

For rings with an odd number of atoms, an alternative definition is recommended [135] due to the inadequacy of the original formula. This situation arises because the original approach averages two consecutive bonds, resulting in a value that depends on the atom sequence in the ring. The alternative is formulated as follows:

$$\text{BOA}(\mathcal{A}) = \frac{1}{2n} \sum_{i=1}^{n} |\delta(A_i, A_{i+1}) - \delta(A_{i+1}, A_{i+2})|. \tag{2.54}$$

A different approach based on the evaluation of bond orders is the *para*-delocalization index (PDI). The PDI index consists of the average DI between atoms in *para*-position in a six-membered ring (Figure 2.8) [79]. This was proposed after the observations by Fulton [460] and Bader [461] that benzene has larger DI between the atoms in *para* position than in *meta*.

$$\text{PDI}(\mathcal{A}) = \frac{\delta(A_1, A_4) + \delta(A_2, A_5) + \delta(A_3, A_6)}{3} \tag{2.55}$$

The definition of this index only allows for the evaluation of six-membered rings, giving large values for aromatic molecules (*e.g.* a PDI = 0.103 for benzene and pyridine) and small values close to zero for non-aromatic and antiaromatic molecules. Moreover, PDI can fail to correctly predict the aromatic character of heteroaromatic rings [95].
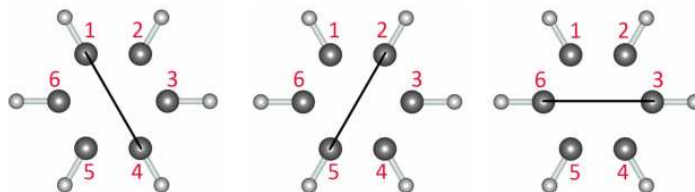
Figure 2.8 Pairs of atoms considered by the PDI index.

A way to improve the evaluation of aromaticity is to extend the two-center index approach and account for the electron delocalization among various atoms simultaneously [462]. The preferred option will be to consider all atoms in the ring, as illustrated in Figure 2.9, which correspond to the I_{ring} [463] and MCI [464] indices, offering a thorough understanding of cyclic and global electron delocalization in the ring, respectively.
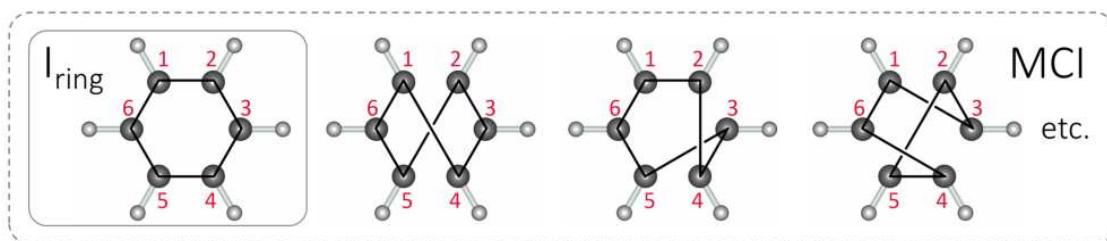
Figure 2.9 Structures considered in I_{ring} and MCI to calculate the n-center indices involved in their calculation.

$I_{\text{ring}}(\mathcal{A})$ measures the electron delocalization between n centers A_1 to A_n by considering overlap integrals across the Kekulé structure, which, in the case of benzene, correspond to a hexagonal ring bonding arrangement. Its expression reads:

$$I_{\text{ring}}(\mathcal{A}) = \sum_{i_1, i_2, \dots, i_n} n_{i_1} \dots n_{i_n} S_{i_1 i_2}(A_1) S_{i_2 i_3}(A_2) \dots S_{i_n i_1}(A_n), \qquad (2.56)$$

where n_i is the orbital occupancy and $S_{ij}(A_n)$ is the overlap of molecular spinorbitals i and j in the atom A_n, defined in Eq. (2.46). The I_{ring} values for reference aromatic (benzene), non-aromatic (cyclohexane), and antiaromatic (cyclohexatriene with a ratio of 0.8 between two consecutive bond distances (a/b)) molecules are 0.048, 0.000, and 0.012, respectively, as calculated using the CAM-B3LYP/6-311G(d,p) level of theory [128].

In contrast, the multicenter index MCI($\mathcal{A}$), introduced by Bultinck and coworkers, measures the amount of electron delocalization present in a ring by averaging the

2.3 Electronic Aromaticity Indices

products of overlap integrals over *all possible permutations* of the n atoms in $\mathcal{A}$,

$$\mathrm{MCI}(\mathcal{A}) = \frac{1}{2n} \sum_{\mathcal{P}(\mathcal{A})} I_{\mathrm{ring}}(\mathcal{A}), \tag{2.57}$$

where $\mathcal{P}(A)$ represents the $n!$ permutations of the elements in $\mathcal{A}$. Thus it considers not only the Kekulé but all structures resulting from taking into account all possible bonding arrangements between the atoms in the ring. These cross-contributions of electron delocalization are particularly important for the description of aromaticity in small rings [465]. This expression of the MCI index (as well as Eq. (2.56)) is ring-size dependent. In most cases, the larger n, the smaller the values. To allow comparisons between rings of different sizes normalized versions of the index were proposed [466, 467], but here we have simply used $\mathrm{MCI}^{1/n}$ [18]. In both unnormalized and normalized cases, aromatic compounds provide large positive numbers, and small or even negative numbers are obtained for non-aromatic and antiaromatic species. For instance, the MCI ($\mathrm{MCI}^{1/n}$) CAM-B3LYP/6-311G(d,p) values are 0.072 (0.646), 0.000 (0.260), and 0.013 (0.484) for benzene, cyclohexane, and cyclohexatriene ($a/b = 0.8$), respectively [128].

Adopting the strategy utilized for the FLU index, it is equally feasible to analyze all other discussed electronic indices (IND) by separating their α and β spin components (IND_α and IND_β). This approach allows for the calculation of $|\Delta\mathrm{IND}|/\mathrm{IND}$ ratios in open-shell systems, providing a metric to assess the Baird contribution in the T_1 state [110]. A low value of $|\Delta\mathrm{IND}|/\mathrm{IND}$ suggests that the ring is predominantly Hückel aromatic with an equal number of α and β π-electrons, whereas a large value points to a Baird aromatic ring unit with two more α than β π-electrons.

An important limitation of multicenter approaches, especially MCI, is that they are only feasible options for rings of small to medium size, with up to 12 members [18]. This size limitation arises from the high computational cost, and the accumulation of numerical integration errors, which are particularly significant in large molecular systems and when using correlated wavefunctions (where the second- or higher-order-density matrices are non-diagonal and the dimensions of the atomic overlap matrix are larger[m]). With the aim to overcome these drawbacks, in 2016 Matito proposed the AV1245 index [18] based on the simultaneous delocalization among four atom fragments. This allows for the evaluation of extended delocalization while maintaining

---

[m]In practical scenarios, approximations to these density matrices are employed, which simplifies the problem to managing the increased size of the atomic overlap matrix.

a reasonable computational cost. AV1245 is calculated as the arithmetic mean of the successive four-center multicenter index (4c-MCI) for the relative atomic positions 1–2 and 4–5 along the perimeter of the ring, as shown within solid line rectangles in Figure 2.10. The dashed lines in the figure represent the $n!$ possible permutations of the elements in the string $\mathcal{A} = \{A_1, A_2, A_4, A_5\}$. Regarding a different yet pertinent detail, the AV1245 index values, which are inherently small, are presented scaled up by a factor of 1000/3 to facilitate the discussion of the results.
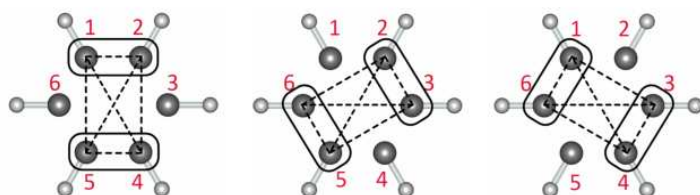
Figure 2.10 Four-center indices considered by AV1245 index.

Examining the results of the AV1245 index, the same as for previously discussed indices, the higher the value, the more aromatic the compound is. For benzene, cyclohexane, and cyclohexatriene ($a/b = 0.8$) the AV1245 CAM-B3LYP/6-311G(d,p) value is 10.72, -0.01, and 2.99, respectively [128]. This index has been specifically created for analyzing large rings, thus AV1245 cannot be calculated for rings of less than six members. It has been used primarily for the study of aromaticity in porphyirinoid systems [102, 129, 146] as well as annulenes [135], porphyrin nanorings [76, 77], and even for exploring the delocalization in polymers [468]. Notably, the AV1245 index values tend to decrease as the size of the system increases, regardless of its aromatic nature. The AV1245 values at CAM-B3LYP/6-311G(d,p) level of theory for aromatic 18H porphyrin and $C_{18}H_{18}$ are 2.16 [146] and 1.80 [135], respectively, which are significantly low compared to the value of benzene. A decrease in the aromaticity values in systems with larger n is inherent to the index's calculation. Mathematically, indices based on n-center-MCIs involve the product of terms, each of which is a number less than unity. As the ring size increases, the number of these multiplicative terms rises, leading to a cumulative effect where the overall product becomes progressively smaller. Moreover, it has been observed that species with extended rings of large sizes can be aromatic but not as aromatic as small cyclic compounds [469]. This trend is explained by the increasing difficulty in maintaining the optimal overlap between orbitals—which favors electron conjugation—as the ring size increases, leading to a reduction in both aromaticity and antiaromaticity [135].

After the application of AV1245 in various studies [77, 102, 135, 146], the authors realized that while for small and highly symmetric rings it provides enough information about the system, for porphyrinoids and other species with large rings and less symmetrical structures, the 4c-MCIs display significant variability. In these systems, subsequent 4c-MCI values along a circuit are not narrowly clustered but can vary widely, sometimes showing large values followed by much smaller ones, thus a single AV1245 value can hide important information. One general limitation of indices based on averaged values (*i.e.* BLA, HOMA, FLU, BOA, or AV1245) is that they can mask the extreme values of electronic delocalization in ring fragments. This is critical to characterize aromaticity since a molecule with one fragment showing very low electronic delocalization is less aromatic than another with the same average value but higher delocalization in its least delocalized fragment. To address this, Casademont-Reig *et al.* recommend to analyze the AV1245 profiles showing sequential 4c-MCI, as depicted in Figure 2.11, and check the minimal absolute value of these 4c-MCIs, the so-called AV_{min} index [468]. For the analysis of AV_{min} results, the authors defined a threshold of $AV_{min} \geq 1$ for a compound to be aromatic, however in many cases is still difficult to differentiate between aromatic, non-aromatic or antiaromatic molecules, thus the use of AV1245 and AV_{min} in conjunction with other aromaticity measures such as BOA is advised [128].
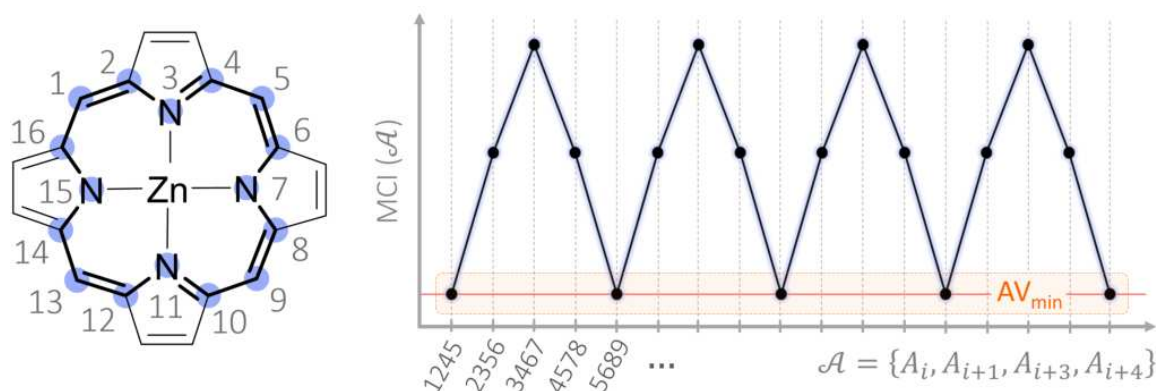
Figure 2.11 AV1245 profile for the inner 16-atom circuit of the Zn-porphyrin.

The Zinc porphyrin example presented in Figure 2.11 allows us to see that delocalization is less effective between atoms at the bridging *meso*-positions. The index distribution profile facilitates a detailed examination of the aromatic nature of different ring fragments. By using it, one can discern variations in aromaticity across a molecule, identifying the most and least aromatic segments. This can be particularly interesting for identifying potential positions to functionalize in order to tune the aromatic charac-

ter or to pinpoint the most reactive positions (unprotected by aromatic delocalization). Additionally, it is useful for differentiating compounds with intermediate aromaticity results, as it offers insights that are not readily apparent through other methods.

The last method based on electronic criteria we review is the electron density of delocalized bonds (EDDB) [455, 470, 471]. It is based on decomposing the one-electron density (ED) in different terms corresponding to the electron density localized on atoms (EDLAs) that includes the core electrons, lone pairs, and so on, the electron density of localized bonds (EDLBs) representing the Lewis-like 2-center 2-electron bonds, and the electron density of delocalized bonds which includes the rest of the density that cannot be assigned to atoms or bonds due to its delocalized nature, as represented in Figure 2.12. The latter term accounts for the conjugation of a bond with the rest of 2c and 3c bonds in the molecule.

$$ED(\mathbf{r}) = EDLA(\mathbf{r}) + EDLB(\mathbf{r}) + EDDB(\mathbf{r}) \tag{2.58}$$
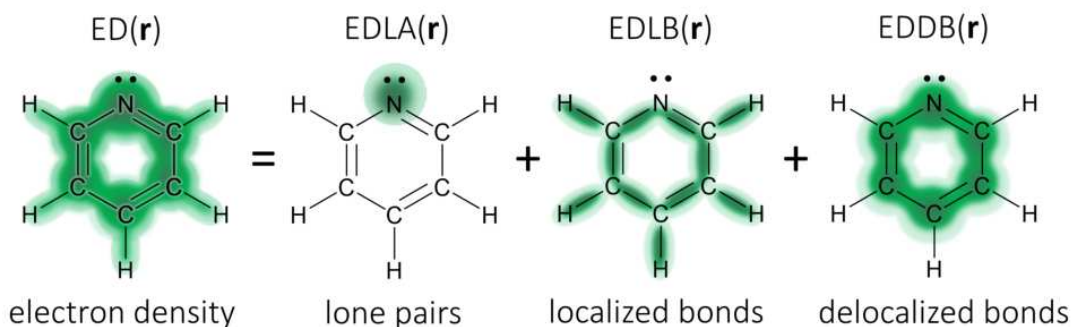
Figure 2.12 Decomposition of the one-electron density in electron density localized on atoms, localized bonds, and delocalized bonds. Adapted from Ref. [125]

The spinless global EDDB function ($EDDB_G(\mathbf{r})$) is expanded in the basis of natural atomic orbitals, θ_i, and for a single determinant Ψ is defined as

$$EDDB_G(\mathbf{r}) = \sum_{ij}^{N_{orb}} \theta_i^*(\mathbf{r}) \mathcal{D}_{i,j}^{\Omega_G} \theta_j(\mathbf{r}), \tag{2.59}$$

where

$$\mathcal{D}^{\Omega_G} = 2 \sum_{\sigma=\alpha,\beta} \mathbf{P}^\sigma \left[\sum_{A,B}^{\Omega_G} C_{A,B}^\sigma \epsilon_{A,B}^{\Omega_G,\sigma} \left(\lambda_{A,B}^\sigma \right)^2 C_{A,B}^{\sigma*} \right] \mathbf{P}^\sigma. \tag{2.60}$$

84

The following list provides a detailed breakdown of the terms and matrices introduced in Equations (2.59) and (2.60):

- $\mathcal{D}^{\Omega_\mathrm{G}}$: Global density matrix, whose trace is interpreted as the population of delocalized electrons across conjugated bonds in the molecule, serving as a measure of global aromaticity. For a system with n atoms, Ω_G represents the set of all $\frac{n(n-1)}{2}$ possible atomic pairs (regardless of whether the atoms are formally bonded or not) [455]. In this context, the subscript 'G' indicates that the full set of atomic pairs present in the molecular system is considered. Details on other sets that can be defined in this context are provided later in the text.

- $\mathbf{P}^\sigma$ (with $\sigma = \alpha, \beta$): σ-spin-resolved charge and bond-order (CBO) matrix that encompasses the charge densities and bond orders for the σ spin state.

- $C^\sigma_{A,B}$: Matrix of linear coefficients for the orthogonalized σ-spin-resolved two-center bond-order orbitals (2cBO) for the bond A–B [472, 473], derived from diagonalizing the appropriate off-diagonal blocks of the CBO matrix [474].

- $\lambda^\sigma_{A,B}$: Diagonal matrix containing the eigenvalues of the 2cBOs, representing the occupation numbers for these orbitals, typically squared in this context.

- $\epsilon^{\Omega_\mathrm{G},\sigma}_{A,B}$: A diagonal matrix of σ-spin bond-conjugation factors [475, 476], indicating the degree of conjugation of each bond based on the bond-orbital projection (BOP) criterion; elements near zero for well-localized bonds, and close to one for conjugated bonds.

Thanks to this description it is easy to restrict the set of atomic pairs in Ω giving rise to different variants of EDDB [125]. The global EDDB$_\mathrm{H}$ function excludes hydrogens to focus on π-aromaticity, avoiding delocalization from σ-subsystem, which can lead to less precise conclusions. Local functions like EDDB$_\mathrm{F}$ and EDDB$_\mathrm{P}$ provide insights into aromaticity within molecular fragments or specific pathways, respectively. The EDDB$_\mathrm{F}$ and EDDB$_\mathrm{P}$ functions serve as local aromaticity descriptors, where EDDB$_\mathrm{F}$ encompasses all atomic interactions within a molecular fragment, while EDDB$_\mathrm{P}$ only considers electron delocalization along a specific pathway (without considering cross-ring conjugation). The distinction between these two indices is equivalent to the relation between MCI and I$_\mathrm{ring}$ indices. Moreover, all these functions can be dissected into α and β spin components, and σ-, π-, and higher-symmetry components, yielding natural orbitals for bond delocalization (NOBD) that facilitate the identification of aromaticity in complex molecular structures, including non-planar compounds. Finally,

it is worth mentioning that these EDDB functions can be graphically depicted as surfaces representing the delocalized electron density. As illustrated in Figure 2.13, the reference values for benzene and CBD offer a clear comparison; aromatic molecules such as benzene show substantial delocalization with a continuous surface and high EDDB values close to six delocalized electrons (almost one delocalized electron per C atom), whereas the antiaromatic S_0 state of CBD has a zero surface and very low delocalized electron values. A limitation to consider is that EDDB, like other electronic aromaticity indices, cannot clearly differentiate between antiaromatic and non-aromatic molecules. This challenge arises because both types of systems may exhibit values close to zero, although with some nuances. Specifically, while non-aromatic compounds are typically characterized by values near zero, antiaromatic systems can sometimes present intermediate values, that fall between those of aromatic and non-aromatic.

a)

$EDDB_G(r)$
6.144 |e| (0.512 |e|/atom)

$EDDB_H(r)$
5.573 |e| (0.929 |e|/atom)

b)

$EDDB_G(r)$
0.419 |e| (0.052 |e|/atom)

$EDDB_H(r)$
0.206 |e| (0.052 |e|/atom)
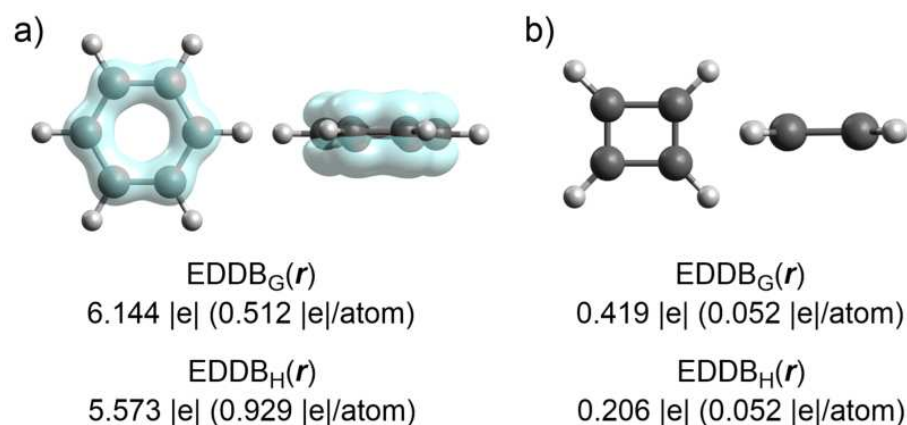
Figure 2.13 Representation of the $EDDB_G$ isosurfaces using an isocontour of 0.02, and $EDDB_G$ and $EDDB_H$ values for a) benzene, and b) cyclobutadiene at CAM-B3LYP-GD3BJ/6-311G(d,p) level of theory.

2.4   Magnetic Aromaticity Indices

Magnetic aromaticity indices serve to evaluate the characteristic response of antiaromatic and aromatic molecules when these interact with an external magnetic field ($\mathbf{B}$ or $\mathbf{B}_0$). This response is distinct from that of non-aromatic species, reflecting the unique nature of their electronic structures. In the case of aromatic and antiaromatic molecules, the application of an external magnetic field perpendicular to the plane of the molecular ring induces an organized response current density. This current flows clockwise, or in a diatropic manner ($\mathbf{J}_d$), around the molecule, and counterclockwise, or

in a paratropic direction ($\mathbf{J}_{\mathrm{p}}$), inside the molecular ring, as represented in Figure 2.14 by the blue and red circular arrows, respectively. The aromatic character of a molecule is discerned by the resultant current strength, which is the sum of the diatropic and paratropic currents of the molecule; a net diatropic current is related to aromaticity, whereas a net paratropic current indicates antiaromaticity. By convention, aromatic, non-aromatic, and antiaromatic molecules have positive, close to zero, and negative, net ring-current strengths, respectively [19, 477].
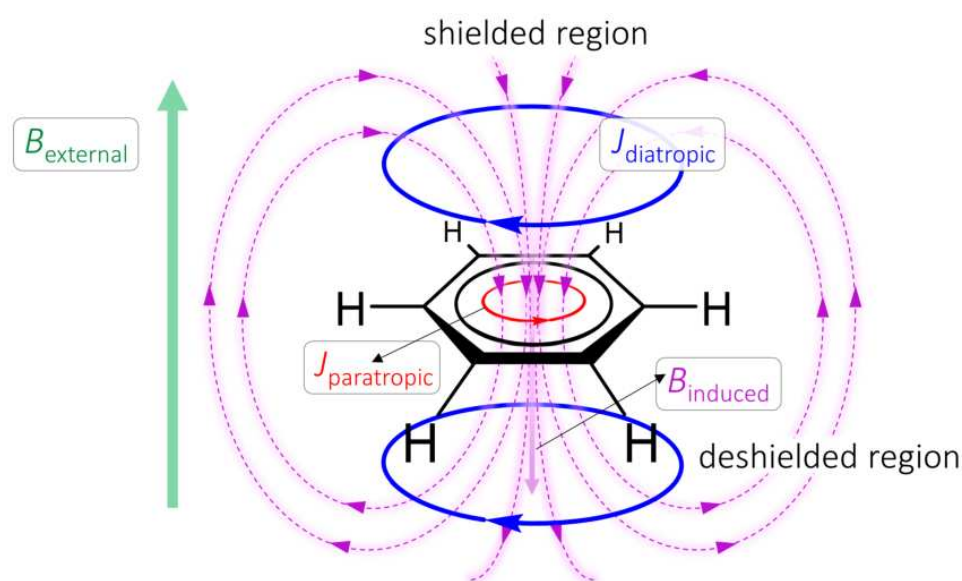
Figure 2.14 Diatropic (blue, clockwise) and paratropic (red, counterclockwise) directions of the induced current flow relative to the external magnetic field (green).

In quantum mechanics, to describe the effect of a uniform magnetic field on a molecule we need to choose the origin of the magnetic vector potential, a point called the 'gauge origin' (**O**). This relates the magnetic vector potential ($\mathbf{A}$)[n] to the magnetic flux (**B**) as

$$\mathbf{A}(\mathbf{r}) = \frac{1}{2}\mathbf{B} \times \mathbf{r_O}, \tag{2.61}$$

where $\mathbf{r_O}$ is the vector between the position $\mathbf{r}$ and the gauge origin.

In the presence of a magnetic field, the molecular Hamiltonian incorporates the vector potential **A** to account for magnetic interactions. The additional terms modify the kinetic energy of the electrons due to the Lorentz force [478]. Consequently, the

---

[n]The magnetic vector potential is defined such that the curl of **A** gives the magnetic field **B**, in accordance with Maxwell's equation for a divergence-free magnetic field.

Hamiltonian $\hat{H}$ in a uniform magnetic field is expanded as:

$$\hat{H} = \hat{H}_0 + \hat{H}_{\text{mag}}, \tag{2.62}$$

where $\hat{H}_0$ is the field-free Hamiltonian, and $\hat{H}_{\text{mag}}$ includes two terms accounting for the interaction with the magnetic field. These terms are: the first-order $\hat{H}^{(1)}$, which has a linear dependence on $\mathbf{A}$, and the second-order $\hat{H}^{(2)}$ with a quadratic dependence on $\mathbf{A}$, see Ref. [477] for the complete formulation of the $\hat{H}_{\text{mag}}$ terms.

While direct measurement of these current densities is at present beyond our experimental capabilities, they are physical subobservables [479] and can be computed as the expected value of an operator. However, this requires solving the Schrödinger equation with the modified Hamiltonian. In practice, $\mathbf{J}(\mathbf{r})$ is calculated using perturbation theory. As a result, we get the total current density with diamagnetic $\mathbf{J}_d$, and paramagnetic $\mathbf{J}_p$ contributions.

The induced current densities, especially the paramagnetic component, are relevant to evaluating molecular aromaticity. These current densities reflect the degree of electron delocalization under an external magnetic field, thereby offering a measure of π-electron movement patterns under an external magnetic field. As outlined earlier in the introduction, the analysis of the current density vectors and the net ring-current strengths contributes to understanding the aromatic characteristics of a molecule. Various computational tools are available for assessing ring-currents in molecular systems [480, 481]. Among them, in our analysis, we employ the gauge-including magnetically induced current (GIMIC) method [482] to conduct these evaluations.

In the current density vector plot of pyridine, in Figure 2.15 (right), we observe distinct ring-currents and bond currents when a magnetic field is applied perpendicular to the molecular plane. There is a clockwise, diatropic current around the molecule's periphery and a counter-clockwise, paratropic current within the pyridine ring (this is not unique to pyridine but characteristic of cyclic systems in general), as well as diatropic circulations around each of the bonds. The orientation of the magnetic field is crucial, as it dictates the presence and direction of these currents.

To quantify the total ring-current strength in a molecule, integration over a defined path or area is necessary. To understand better the current integration we have represented pyridine's illustrative example (Figure 2.15). An integration plane is positioned in pyridine such that it is perpendicular to the molecular plane and crosses
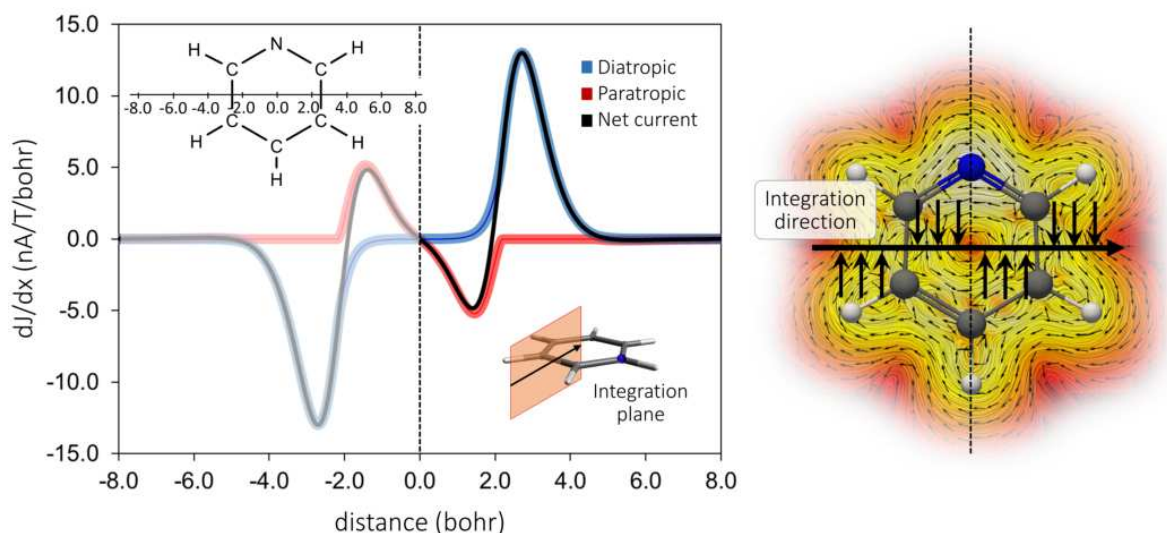
Figure 2.15 On the left, the differential profile of the current density of pyridine obtained by numerical integration of the current density along the integration plane represented in the bottom-right part of the plot. On the right, induced ring-currents at the molecular plane.

any of the bonds (two C–C bonds in this case). Then, the differential profile of the current density is obtained by numerically integrating the current density flux in thin vertical slices of the plane crossing the C–C bonds and through the whole molecule (scanning in the integration direction represented in the right figure). The net ring-current strength of pyridine, represented by a solid black line in the plot, is measured to be significant. The positive and negative contributions refer to the current density flowing downward and upward, respectively, in the right-hand side representation. The vertical dashed bar at $x = 0$ marks the origin of the vortex. The values $x < 0$ correspond to the left side of the integration plane, while the right side of the plane with $x > 0$ is the returning current on the other side of the vortex. Although 2D plots offer detailed visualization of current strengths, they are labor-intensive to generate and analyze. Therefore, in our research, we opt for single-plane integration that provides a direct measure of the current strength of each bond. As a reference, the net current strength obtained for benzene at the B3LYP/def2-TZVP level of theory is 11.8 nA/T (the sum of 16.7 and -4.9 nA/T corresponding to diatropic and paratropic contributions, respectively), while for cyclobutadiene, the net value is -19.9 nA/T [482].

In addition to current strength values, we used qualitative analysis of ring-current such as vector plots, depicted in Figure 2.16 for benzene and CBD references. The plots, especially at the plane 2.0 bohr (1.1 Å) above the molecular plane illustrate the aromatic character of benzene with a predominantly diatropic ring-current (flowing

clockwise when viewed from above). In contrast, the antiaromatic nature of CBD is evidenced by the more intense paratropic ring-current (flowing counterclockwise). Additionally, these current densities can also be visualized using streamline plots [477], which graphically represent the trajectories of particles in the vector field. These plots can be generated with Paraview [483] and help us analyze the directionality of molecular ring currents.
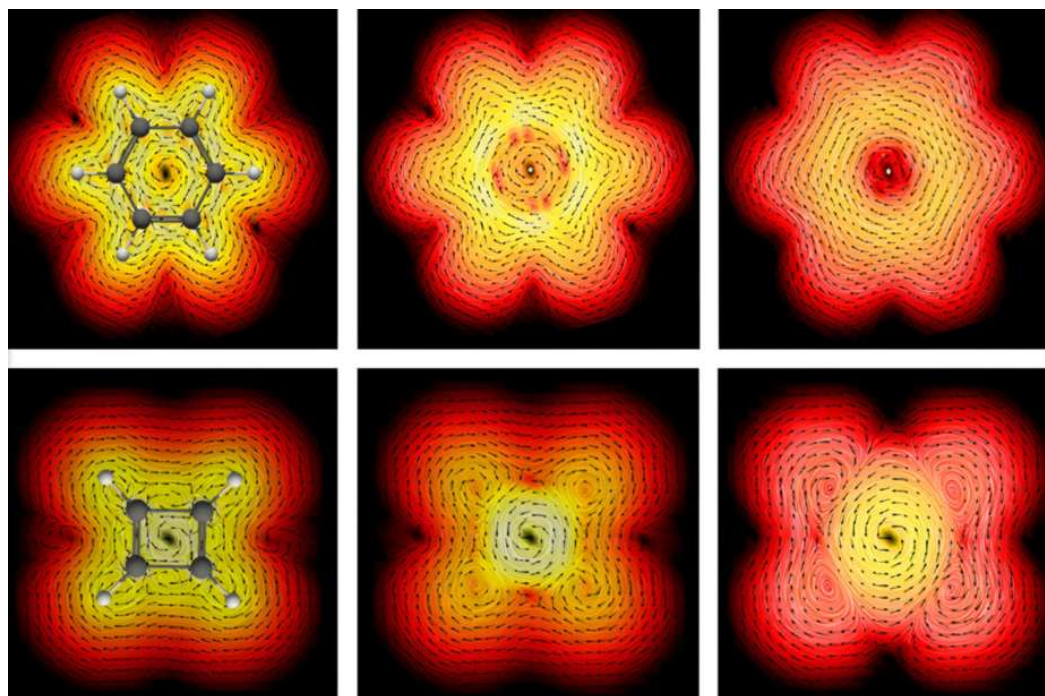
Figure 2.16 Representation of the current density for benzene (top) and cyclobutadiene (bottom) at CAM-B3LYP-GD3BJ/6-311G(d,p) level. Top view of the currents in the molecular plane (0 bohr), and the planes located at 1 and 2 bohr (from left to right, respectively). The color scale gives the modulus of the strength of the current density; white-yellow regions correspond to larger current values (0.4 $nAT^{-1}Å^{-2}$), while dark red corresponds to vanishing current densities ($\leq 10^{-4}$ $nAT^{-1}Å^{-2}$).

Unlike GIMIC, which allowed for the direct evaluation of the induced current density, nucleus-independent chemical shift (NICS) is a scalar quantity, which makes it easy to use, thus it is probably the most popular method for evaluating aromaticity [82]. NICS operates through the relationship between the induced magnetic field $\mathbf{B}_{ind}$ and the external magnetic field $\mathbf{B}_0$, governed by the magnetic shielding tensor $\boldsymbol{\sigma}$ [484].

$$\mathbf{B}_{ind} = -\boldsymbol{\sigma}\mathbf{B}_0, \tag{2.63}$$

where $\boldsymbol{\sigma}$ is defined as

$$\boldsymbol{\sigma} = \begin{pmatrix} \sigma_{xx} & \sigma_{xy} & \sigma_{xz} \\ \sigma_{yx} & \sigma_{yy} & \sigma_{yz} \\ \sigma_{zx} & \sigma_{zy} & \sigma_{zz} \end{pmatrix}, \tag{2.64}$$

and each of its elements corresponds to

$$\sigma_{ij} = \frac{\partial^2 E}{\partial \mu_i \partial B_j}, \tag{2.65}$$

with i and j representing the Cartesian coordinates (x, y, z), E the electronic energy of the molecule, B the external magnetic field, and μ, the magnetic moment (in a loop $\mu = I \cdot A$, where I is the intensity and A is the area). This magnetic shielding tensor is fundamentally related to the NMR spectroscopic chemical shifts, which serve as experimental probes of the local electronic environment around a nucleus [485].

NICS is the average of the diagonal elements of the magnetic shielding tensor [83]:

$$\text{NICS} = -\frac{1}{3}(\sigma_{xx} + \sigma_{yy} + \sigma_{zz}) = -\sigma_{\text{av}}. \tag{2.66}$$

The calculation of NICS requires the strategic placement of a 'ghost' or 'dummy' atom at the center of the ring or positions above or below it at various heights (the evaluation at 1.7 Å from the ring plane is recommended to get better results [486])°, as depicted in Figure 2.17. Moreover, there are several NICS variants consisting of (i) the placement of multiple probe atoms such as NICS scans (also represented in the right-hand side of Figure 2.17) [486, 487], NICS planes or maps [488], or 3D isotropic magnetic shielding mapping [489, 490]; or (ii) limiting the evaluation of NICS to only the σ_{zz} component or the separation into orbital (*e.g.* σ, π, ...) [82] or spin (*i.e.* α and β) [119] contributions. The interpretation of NICS is as follows: large negative NICS values imply aromaticity, characterized by a diatropic ring-current, near-zero values correspond to non-aromatic systems, whereas a positive value indicates antiaromaticity, characterized by a paratropic ring-current.

While the visualization of current density vectors and calculation of NICS values can provide valuable insights into electronic circulations in aromatic systems, it is crucial to recognize the limitations of these methods in defining aromaticity. As such, although

---

°NICS(1.7) should, in principle, capture the presence of π-electron delocalization because the maximum of the p orbitals occurs around these distances. Consequently, this should be a preferred measure of aromaticity in organic molecules
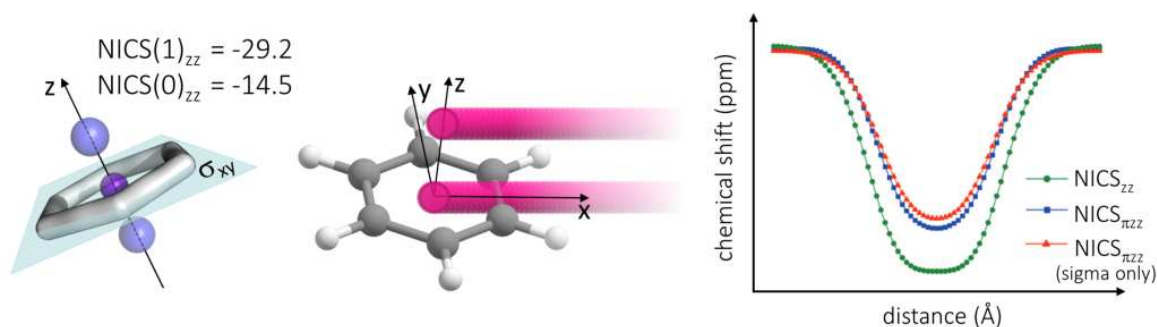
Figure 2.17 On the left, a depiction of the ghost atoms' positions at the center (NICS(0)), and at a distance 'x' (in Å) above and below (NICS($\pm x$)) of a six-membered ring together with the values for benzene in ppm computed with B3LYP/6-311G(d,p). On the right, Ghost atoms and NICS(1.7)-XY-scan. For the latter, the NICS values were determined using three different methods detailed in Ref. [486]; the represented plot has been adapted with permission from the same reference.

aromatic compounds typically exhibit induced ring-current magnetic shielding, *the use of magnetic indicators and, in particular NICS, as a sole measure of aromaticity can be misleading.* The relationship between diatropic ring-currents and aromaticity is complex, where a diatropic current is a necessary, but not sufficient, condition for aromaticity. For this reason, NICS analysis, while helpful, is not definitive for proving aromatic character. This is underscored by an increasing number of studies that highlight pitfalls and failures of NICS [78, 89–95, 491, 492].

2.5 Other Aromaticity Indicators

In addition to the electron delocalization and distinct magnetic responses of aromatic compounds, these are also characterized by specific structural and energetic factors. Geometrically, aromatic species usually exhibit bond length equalization within the ring. Energetically, they are distinguished by having enhanced thermodynamic stability relative to their aliphatic structural analogs, along with a propensity to retain structural integrity during chemical transformations. These characteristics can also be used as indicators of aromaticity.

The degree of bond length equalization can be measured in multiple ways. One geometrical indicator is the bond-length alternation (BLA) [459] which is formulated in the same way as the BOA index, in Equations (2.53) and (2.54), but using bond distances ($R_{Ai,A_{i+1}}$) instead of bond orders. Another popular geometry indicator is the

harmonic oscillator model of aromaticity (HOMA) [493, 494], that can be computed as
follows,

$$\text{HOMA}(\mathcal{A}) = 1 - \frac{\alpha}{n} \sum_{i=1}^{n} (R_{\text{opt}} - R_{Ai,A_{i+1}})^2 \tag{2.67}$$

In this formula, α is an empirical constant chosen to result in values close to one
for aromatic species, and small or negative values for non-aromatic and antiaromatic
molecules. Specifically, for C–C bonds, α is set at 257.7 with R_{opt} being 1.388 Å. For
C–N bonds, α is 93.52 with R_{opt} at 1.334 Å [495]. Therefore, the HOMA values for
benzene, pyridine, cyclohexane, and cyclohexatriene at the CAM-B3LYP/6-311G(d,p)
level of theory are 1.000, 1.000, -4.167, and -31.266, respectively [128].

Another common geometric characteristic of aromatic molecules, complementing the
structural insights provided by BLA and HOMA, is the planarity of the system. While
archetypal aromatic compounds are often perfectly planar rings, it is important to
recognize that not all aromatic rings maintain such planar configurations. In particular,
in larger annulenes, the planarity is lost due to ring strain, which arises either from
steric hindrance between substituents or from the distortion of bond angles. In such
cases, the quantification of the planarity can be a useful aromaticity indicator. To
assess this we used the best-fitted plane π index or root-summed-square (RSS) index
[457]. This method determines the 'best-fitted plane' for a given set of atomic positions
within a molecular ring and calculates the RSS values, which represent the sum of
squared distances of each atom from this optimally fitted plane. Lower RSS values
indicate a higher degree of planarity, which can be related to more aromatic systems.

The energetic aspect of aromaticity is fundamental, where the relative stability
compared to non-aromatic references determines if a compound is aromatic (if it
presents stabilization) or antiaromatic (when it is destabilized). This aspect is an
indispensable quality of aromatic systems. However, the accurate quantification of
(de)stabilization energies in (anti)aromatic systems is a very complex task due to
the dependency on the chosen reference. Among the most prominent energy-based
approaches are the resonance energy (RE) and aromatic stabilization energy (ASE)
[19, 496]. Resonance Energy is calculated as the difference in energy between the actual
molecule and the most stable hypothetical resonance structure (often a single Kekulé
structure). It essentially measures the extra stability gained due to resonance. A higher
RE indicates more delocalization of electrons, contributing to greater stability of the
molecule. Unlike RE, ASE typically compares the energy of the aromatic molecule to
another molecule with the same structural features but with a non-aromatic character.

It is challenging to find appropriate reference compounds with the same ring strain, steric repulsion, hybridization, conjugation, and other characteristics present in the system under study. These factors significantly influence ASE results, as evidenced by the wide range of values (66.9 to 18.4 kcal/mol) obtained from fifteen different reaction schemes for benzene [497]. In trying to mitigate this, hypothetical isodesmic reactions are designed to ensure that the net energy of the proposed process is related to the aromatic stabilization. An isodesmic reaction is a chemical reaction where the types of bonds broken and formed are the same, providing a reliable comparison for energy calculations. The related term, homodesmotic reaction, extends this concept by also considering orbital hybridization and maintaining the same number of carbon to hydrogen bonds. Despite these efforts, applying energetic indices in a generalized way to assess aromaticity remains very challenging.

In addition to the previously mentioned indices for evaluating aromaticity, there are other relevant methods reported in the literature. More exhaustive lists can be found in Refs. [351, 498, 499], and Chapters 5 to 8 of Ref. [19] discussing several indices). These methods, while not mentioned in the previous sections—primarily because they have not been applied in the present thesis—can be encountered in other relevant studies. For instance, the electron localization function (ELF) [500] is an electronic method that offers a way to map electron pair probabilities in multielectronic systems. The anisotropy of the induced current density (ACID) [501], and induced magnetic field maps (B_Z^{ind}) [502] are examples of magnetic-based indices offering perspectives on aromaticity based on magnetic properties. Additionally, the reparameterized HOMA for Excited States (HOMER) [503] represents an adaptation of the traditional HOMA method, fitted to assess molecular geometry in excited states. The isomerization stabilization energy (ISE) [504] is another energetic method calculated through isodesmic reactions that involve a methyl derivative of the aromatic system. Else, a multifaced approach utilizing neural networks, such as self-organizing maps (SOMs) [505]. These methods provide a variety of perspectives and analytical tools for the aromaticity characterization in chemical systems.

3 Objectives

The aim of the present thesis is to explore the concept of aromaticity as a pivotal tool for characterizing challenging situations arising from systems in their excited states, as well as the structure of molecules with complex topologies. In the preceding chapters, we highlighted the broad applicability of aromaticity to comprehend properties at the molecular level. Remarkably, we have explored how Hückel's and Baird's rules, spherical or double aromaticity, and the utilization of aromaticity indices serve as fundamental frameworks for characterizing aspects of π-electron delocalization. Furthermore, we discussed the impact of aromaticity in a range of applications, showing its importance in guiding the design and synthesis of novel compounds with targeted properties. Yet, we also discussed the limitations of existing aromaticity rules and descriptors, identifying cases where new findings do not fit these theories or reveal misapplication, underscoring the need for continuous refinement in our understanding and methodologies. Consequently, we target two areas requiring further investigation: excited state aromaticity and the exploration of systems with complex topologies, with the goal of deepening our knowledge of aromaticity.

The objectives of this thesis are divided into two main blocks. The aim of the first block is to achieve a better characterization of pro-aromatic quinoidal systems in both their ground and excited states, with corresponding investigations detailed in **Chapter 4**; while the aim of the second block is to analyze the aromaticity in compounds with complex electronic structures and molecular topologies, with specific objectives pursued through investigations detailed in **Chapter 5**.

The complex electronic nature of Kekulé diradicals, along with discrepancies found in the literature concerning their aromatic character, motivated us to further investigate their aromaticity in the ground and excited states and highlight their potential use in photonic applications. To achieve this, we have established the following specific objectives for the first block of the present thesis: (**I**) refine the understanding of excited state aromaticity, particularly Baird aromaticity in symmetrically substituted conju-

gated rings using spin-separated indices. (**II**) Investigate the pro-aromatic molecules that exhibit potential Baird aromatic character in their lowest T_1 and S_1 states, focusing on the characterization of these states as either predominantly Hückel-aromatic, Baird-aromatic, or a hybrid of both. (**III**) To establish guidelines for the rational design of molecules that exhibit excited state Hückel/Baird aromaticity, and identify strategies to enhance Baird aromatic character. (**IV**) Understand the relationship between electronic structure, stability, and aromaticity in the GS configurations of poly-*para*-phenylenes; and (**V**) to define aromaticity as a design tool by identifying its correlation with the singlet-triplet energy gap, aiming for precise control in the development of new materials.

In the second block of this thesis, our investigation extends to a wide variety of complex molecules, including large macrocycles, interconnected rings, and three-dimensional structures. A significant portion of these molecules exhibit aromatic characteristics, which aids in applying the concept of aromaticity to rationalize the electronic structure, find structure-property relationships, guide synthesis, and identify new compounds. However, the complexity and large size of these systems limit the use of some aromaticity indices (*e.g.*, MCI for its computationally demanding requirements or FLU for the lack of reference DI values), or unmasks discrepancies between response- and intrinsic-based aromaticity measures, complicating the interpretation of the results. To address these challenges we aim to apply aromaticity indicators, developed in our research groups, suitable for analyzing large molecular systems and apply aromaticity rules tailored to these compound classes, seeking to achieve a meaningful interpretation of the results. Hence, the detailed objectives of this block are divided into four sections, each concentrating on a distinct class of compounds: phthalocyanines and subphthalocyanines, $C_{80}H_{30}$ nanographene, double aromatic tropylium derivatives, and icosahedral boranes and carboranes. Through this evaluation, we aim to deepen our comprehension of their aromatic properties and refine our understanding of the applicability of various aromaticity rules and measures. The objectives for each of these four sections are outlined in the subsequent paragraphs.

Our objectives for investigating the electronic and optical properties of (sub)phthalocyanines and related systems (Section 5.1) are: (**VI**) to characterize the aromaticity of these molecules and (**VII**) determine how it influences the UV-Vis spectrum.

The primary objective in our exploration of the aromaticity in $C_{80}H_{30}$ curved nanographene (Section 5.2) is (**VIII**) to determine the presence and identify which are the most favorable π-aromatic circuits within this uniquely structured nanographene.

In our study detailed in Section 5.3, the focus is on expanding the understanding of double aromatic compounds, exploring $C_7R_7^q$ (where R = F, Cl, Br, and I; and $q = +3$ or -1) systems with separate σ- and π-delocalized currents, the main objective is: (**IX**) to analyze the conditions necessary for achieving double Hückel-Baird aromaticity, including electron counting rules and delocalization requirements.

The main objectives of the last part, devoted to the characterization of the aromaticity of boranes and carboranes (Section 5.4) are the following: (**X**) to understand the isomerization process from o-$C_2B_{10}H_{12}$ to m-$C_2B_{10}H_{12}$ upon heating and relate the ease of deboronation in these structures to their thermodynamic stability and aromaticity; (**XI**) to elucidate the differences in aromaticity between metallabis(dicarbollides) and metallocenes; (**XII**) to assess how aromaticity in boron clusters evolves during structural transformation and electron addition (from *closo* to *nido* forms); (**XIII**) to compare the aromatic nature of *o*-carboryne and *o*-benzyne, focusing on the differences in the C–C bond nature between these two compounds; and (**XIV**) to combine the insights from the study of aromaticity in (car)boranes and the double aromaticity section, to study the possibility of having double aromaticity in iodine-substituted boranes.

4 Understanding the Electronic Nature of Pro-Aromatic Quinoidal Systems in the Ground and Excited States

4.1 Guidelines for Tuning the Excited State Hückel–Baird Hybrid Aromatic Character of Pro-Aromatic Quinoidal Compounds

This section corresponds to the following publication:

S. Escayola[†], C. Tonnelé[†], E. Matito, A. Poater, H. Ottosson*, M. Solà*, D. Casanova*. *Angew. Chem. Int. Ed.*, **2021**, 60, 10225-10265.

[†]*These two authors contributed equally to this work*

Excited State Aromaticity **Hot Paper**

Guidelines for Tuning the Excited State Hückel–Baird Hybrid Aromatic Character of Pro-Aromatic Quinoidal Compounds**

Sílvia Escayola[+], Claire Tonnelé[+], Eduard Matito, Albert Poater, Henrik Ottosson,* Miquel Solà* and David Casanova*

Abstract: Pro-aromatic molecules have higher-energy diradicaloid states that are significantly influenced by resonance structures in which conjugated rings take on Hückel-aromatic character. Recently, it has been argued that there are also pro-aromatic molecules that adopt central units with 4nπ-electron Baird-aromatic character in the T_1 state, although detailed analysis suggests that these compounds are better labelled as T_1 Hückel–Baird hybrid molecules where Hückel-aromaticity dominates. Herein, we consider a series of symmetrically substituted conjugated rings with potential Baird aromaticity in the lowest excited triplet and singlet states. Our computational results allow us to establish general guidelines for the rational design of molecules with excited state Hückel/Baird aromaticity in pro-aromatic quinoidal compounds. We found two main strategies to promote high Baird aromatic character: 1) anionic and small conjugated rings with electron donating groups as substituents and small exocyclic groups with electron withdrawing substituents, or 2) electron deficient conjugated rings with exocyclic electron–donor substitution.

Introduction

Molecules when excited to their lowest electronically excited states often change their electronic structure considerably, which impacts on a range of important molecular properties. For example, the reactivity of a molecule in its excited state often differs markedly from that in its S_0 state.[1] Also, the charge distribution within a molecule is normally altered upon excitation, and consequently, its interaction with the surrounding medium. Excited states can be obtained as electronic transitions with large hole/electron spatial overlap, or alternatively, can involve substantial displacements of the excited electrons.[2] The electronic structure changes upon excitation are influenced by a number of factors; those that are intrinsic to the molecule and those that are extrinsic. The bonding and antibonding features of the orbitals populated in the excited state is one of the most obvious intrinsic factors, whereas the polarity of the surrounding solvent or medium constitutes a typical example of extrinsic factors. An important intrinsic factor is the ability of a molecule to switch its electronic structure from a pro-aromatic structure to an aromatic one.[3]

Aromaticity and antiaromaticity are concepts that come in various forms. Baird's rule[4] for the lowest ππ* triplet state (T_1) tells that $4n\pi$-electron conjugated monocycles are aromatic while $(4n+2)\pi$-electron cycles are antiaromatic, and it often also applies to the lowest singlet excited state (S_1).[5] Yet, Hückel-aromaticity can also impact on features in the excited states.[6] Interestingly, one may even have excited states which are influenced simultaneously by Baird- and Hückel-aromaticity, as has been revealed for a 2,7-dimethylenemethano[10]annulene exo-substituted with two 5-dicyanomethyl-thiophene (DT) moieties at the peripheries (**TMTQ**). Tovar and co-workers explored **TMTQ** in its T_1 state and reasoned that this compound is Baird-aromatic,[7] although it was later shown to be a triplet state Hückel-Baird hybrid aromatic molecule with minor Baird character (vide infra).[8] Recently, the S_1 state of **TMTQ** was argued to display Baird-aromaticity ascribed to photoinduced two-electron charge transfer (CT) from the central ring to the two DT units (Figure 1).[9]

Research on excited state Baird-aromaticity has intensified in the last decade.[10] Yet, comprehensive and critical analyses combined with solid computational assessments are required for the proper interpretation of experimental data as there is presently no spectroscopic technique that can be used as the sole method to evaluate excited state aromaticity in a similar manner as ^{1}H NMR spectroscopy can be used to assess aromaticity in the S_0 state. The correctness of the interpretations is crucial as only then can the Baird-aromaticity concept be developed into a tool that is useful to the design of molecules with targeted optoelectronic properties for potential use in, e.g., organic electronics.[11] Now, can the

[*] S. Escayola,[+] Dr. A. Poater, Prof. M. Solà
Institute of Computational Chemistry and Catalysis and Department of Chemistry, University of Girona
C/ M. Aurèlia Capmany, 69, 17003 Girona, Catalonia (Spain)
E-Mail: miquel.sola@udg.edu

S. Escayola,[+] Dr. C. Tonnelé,[+] Dr. E. Matito, Dr. D. Casanova
Donostia International Physics Center (DIPC)
Donostia, Euskadi (Spain)
E-Mail: david.casanova@ehu.eus

Dr. E. Matito, Dr. D. Casanova
Ikerbasque Foundation for Science
48009 Bilbao, Euskadi (Spain)

Prof. H. Ottosson
Department of ChemistryÑ ÅngstrÁm Laboratory, Uppsala University
75120 Uppsala (Sweden)
E-Mail: henrik.ottosson@kemi.uu.se

[+] These authors contributed equally to this work.
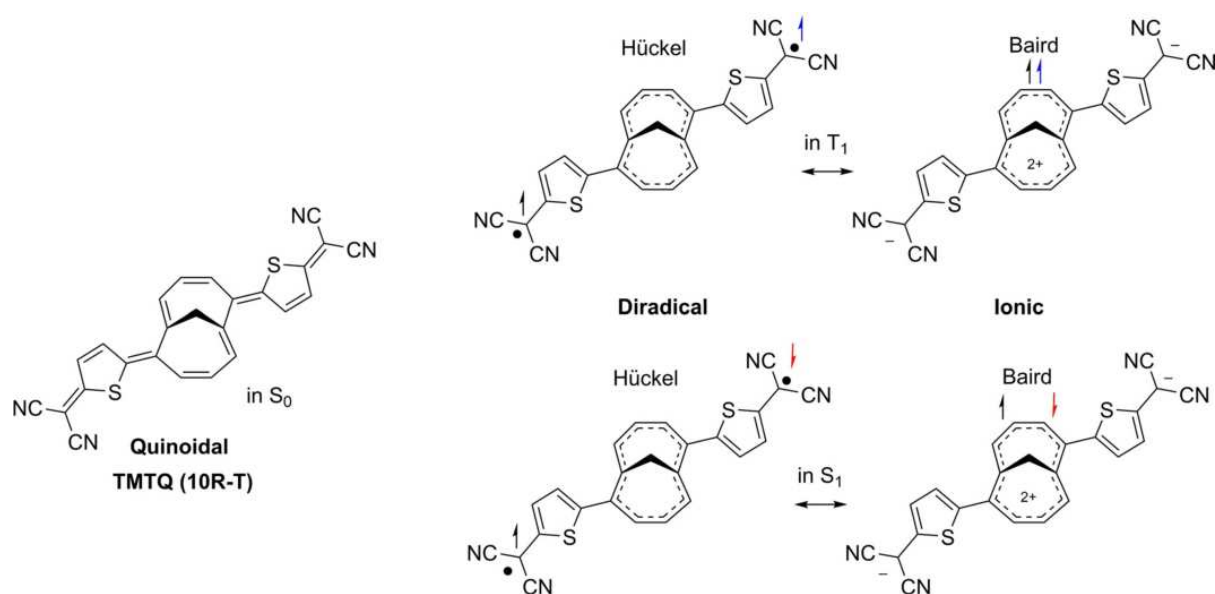
Figure 1. Quinoidal, diradical, and ionic resonance structures of importance for **TMTQ** (**10R-T**) involved in the description of S_0, S_1, and T_1 states.

Baird-aromatic character in (symmetrically) substituted conjugated quinoidal rings be increased either (*i*) by going from the T_1 to the S_1 state, (*ii*) by using different central pro-aromatic units, (*iii*) by considering longer or shorter side groups, and/or (*iv*) by altering their structures in some other way?

Numerous pro-aromatic molecules can be designed which on paper can be labelled as Hückel-Baird hybrids in their lowest triplet states (Figure 2). Here, an interesting aspect is the difference in the number of CC π-bonds between the Hückel-aromatic and the Baird-aromatic resonances. For the neutral pro-aromatic molecules, the difference is two, while for the three charged pro-aromatic molecules the difference is one, indicating that less number of π-bonds formally need to be broken. Hence, an influence of the Baird-aromatic structure in the ionic compounds should imply a smaller energy penalty. Additionally, as the charge separation is larger in the Baird-aromatic resonance structures for the neutral molecules (-1, $+2$, -1) than for the charged ones (either -1, $+1$, -1 or $+1$, -1, $+1$), we postulate that it could be more facile to develop stronger Baird-aromatic character in the T_1 and S_1 states of the latter ones.

Now, why can molecules with excited states having Baird-aromatic instead of Hückel-aromatic character be useful? In the compounds of Figure 2, high involvement of Baird-aromatic character in the triplet states implies a higher CT extent than in the Hückel-aromatic structures, a useful feature for photovoltaics. A molecule with a Baird-aromatic CT state may also exhibit a high photochemical stability, in analogy to other Baird-aromatic molecules.[12]

The present work explores to what extent a range of Hückel-Baird hybrid compounds (Figure 3) have the ability to adopt Baird aromatic character in the lowest singlet and triplet excited states. The study intends to solve several important questions. Are there pro-aromatic Hückel-Baird hybrid compounds for which the Baird aromaticity dominates in the T_1 state? How similar are the S_1 and T_1 states in

character? What is the extent of CT in S_1 and T_1? How can we increase the Baird-aromatic character of the T_1 and S_1 states through different central rings and exocyclic substituents? By answering these questions, we aim to develop general guidelines for the design of hybrid Hückel-Baird pro-aromatic species with strong Baird-aromatic character in their lowest excited states.

Results and Discussions

Excited State Aromaticity in Conjugated Rings

This section has two parts. We first discuss the Hückel-Baird aromatic character in the T_1 and S_1 states of molecules with conjugated rings symmetrically substituted with two dicyanomethylene units labelled as *n*R (Figure 3). In the second part, we explore species in which one thiophene unit has been added in each of the two side-arms (*n*R-T compounds).

The lowest singlet and triplet states of *n*R with $n = 5$, 6, 9, and 10 (*n* being the number of C atoms in the central ring), i.e., **5R**, **6R**, **9R**, and **10R**, are obtained as the single electron occupancy of the highest occupied molecular orbital (HOMO) and the lowest unoccupied molecular orbital (LUMO). Both frontier π-orbitals are well delocalized over the molecule (Figure 4). Triplet vertical excitation energies of *n*R are within the 1.1–1.4 eV range (B3LYP, Table S18), and about twice as large for S_1. Structural relaxation stabilizes the lowest triplet by 0.2–0.3 eV and considerably more in the first excited singlet. The relative energies of T_1 and S_1 states computed with other functionals yield very similar results (Tables S1 and S2).

Minimal energy structures of T_1 and S_1 for the four *n*R molecules exhibit a systematic bond length equalization with respect to the bond alternation pattern in the ground state (Figure 5a), which points out an increase of the aromatic
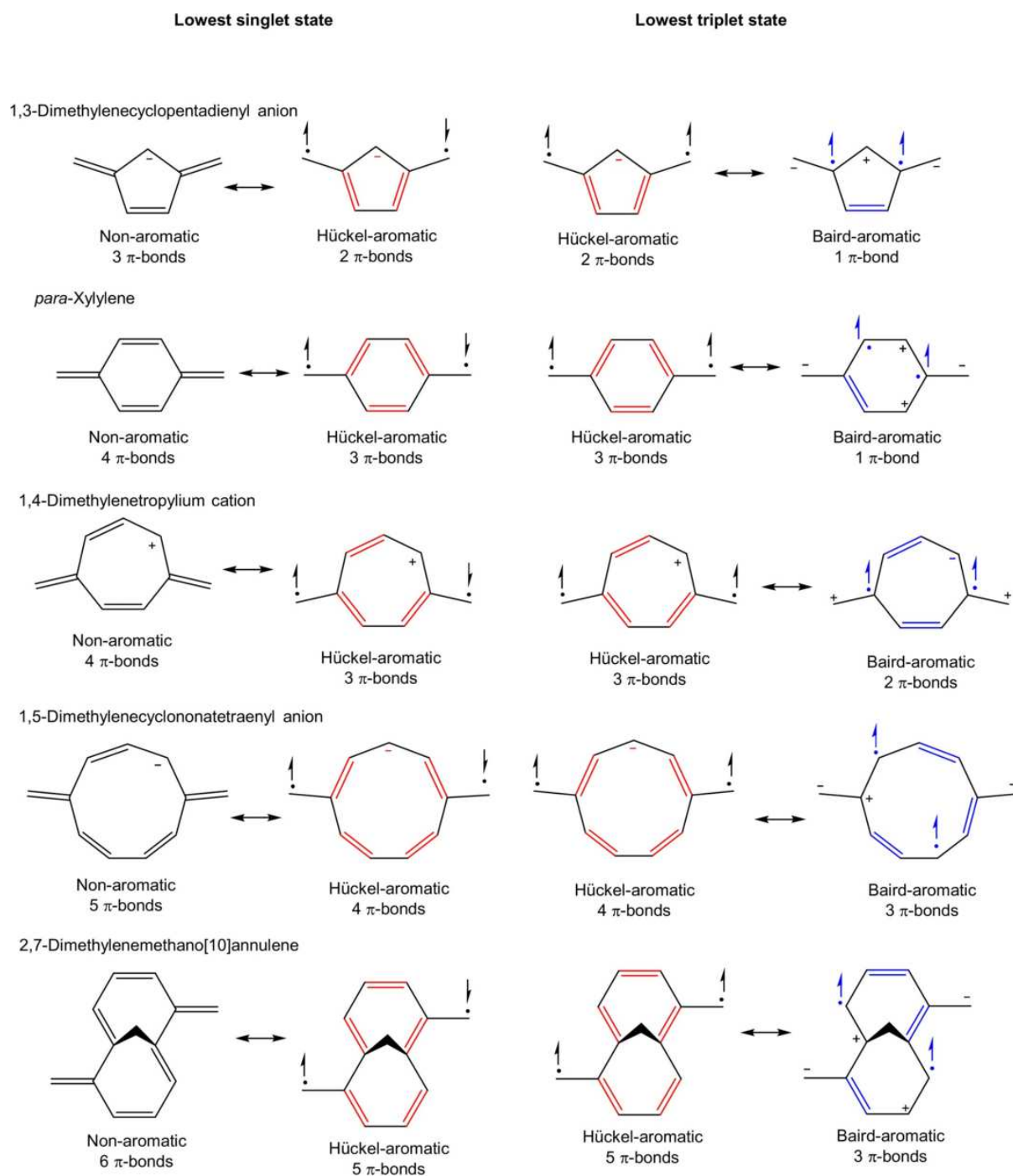
Figure 2. Non-aromatic, Hückel-aromatic (π-bonds in red), and Baird-aromatic (π-bonds in blue) resonance structures of the parent dimethyleneannulenes in their lowest-lying singlet and triplet states.

character of the central rings in the excited states. Bond length changes in **5R** and **9R** when going from S_0 to S_1 are larger than those derived from the transition to T_1, suggesting larger electronic structure rearrangements within the central ring in the excited singlet. The observed bond length equalization is in line with the changes in the bond electron delocalization indices (DIs)[13] (Figure 5b), and are supported by the different methods we have employed to quantify the aromaticity (Tables S86–S101) and GIMIC plots showing a more intense diatropic ring current for the T_1 state than for

S_0 (Figures 6 and S35–S40). Interestingly, all indices suggest a slightly higher aromaticity of the central ring in the S_1 and T_1 states of compounds **6R** and **10R** than in **5R** and **9R**. Besides, structural relaxation on the excited triplet and singlet potential energy surfaces induces an elongation of the two exocyclic CC bonds with a concomitant decrease of the corresponding DIs.

Therefore, structural analysis and (global) aromaticity indices manifest a transition from non-aromatic to aromatic character in the central ring of **nR** upon excitation to T_1 and
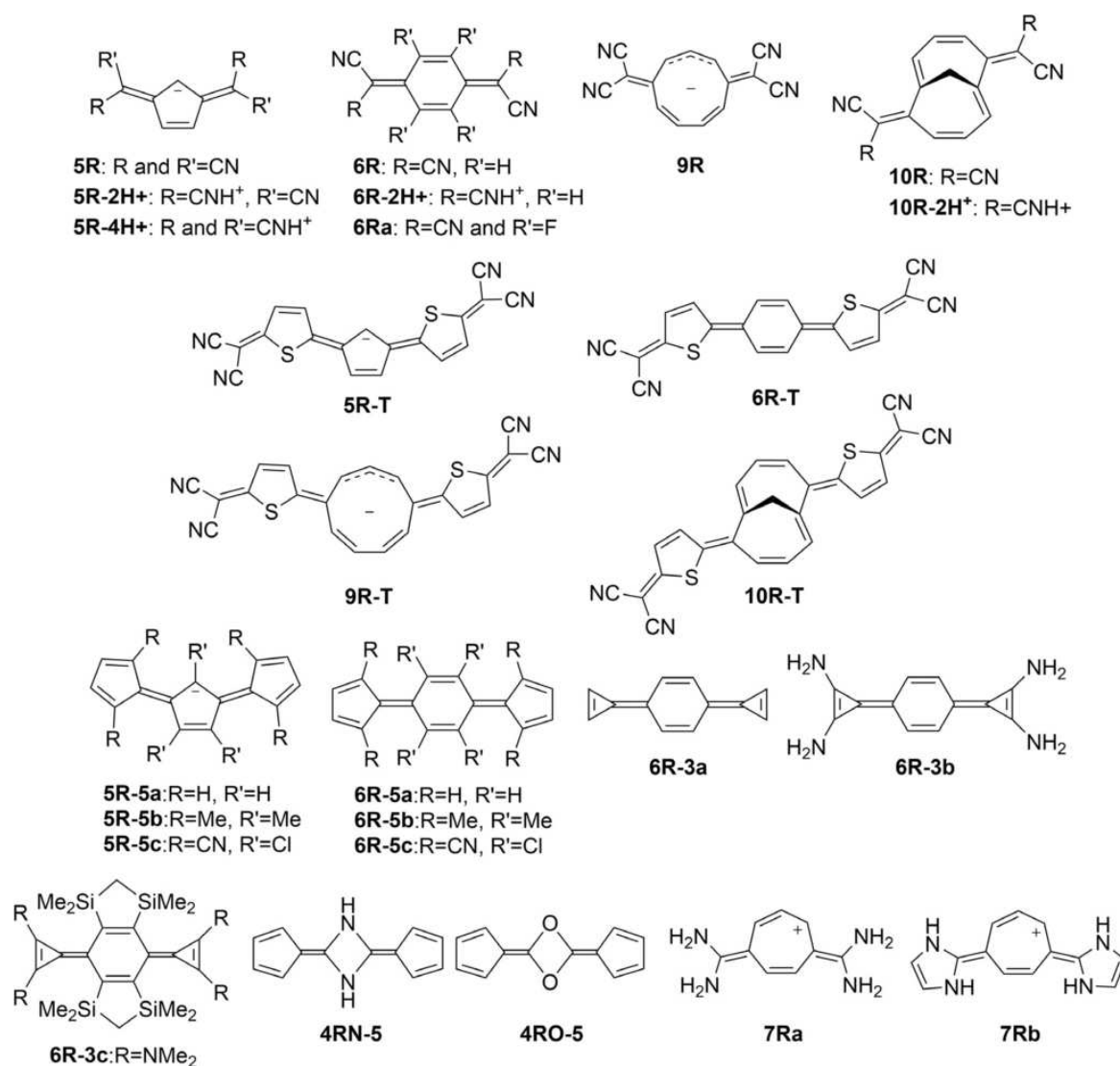
Figure 3. Compounds investigated in this study.

S_1. In the following, we uncover the Hückel, Baird or Hückel-Baird hybrid character of the central ring of the T_1 and S_1 states (Figure 2). Next, we analyze the α and β components of the electron DIs corresponding to the C−C bonds of the central ring in the T_1 state of **5R**, **6R**, **9R**, and **10R**. The difference between α and β components of these DIs is rather small (Tables S54–S85), particularly for **6R** and **10R**, indicating an almost identical contribution of the α and β electrons to the C−C covalent bond order in the conjugated ring. Electronic indices (IND) can be separated into α and β spin components ($IND_α$ and $IND_β$) and one can obtain $|\Delta IND|/IND$ values with $\Delta IND = IND_α - IND_β$ for the T_1 state. These $|\Delta IND|/IND$ values can be used to quantify the Baird contribution to the T_1 state.[8] A low value of $|\Delta IND|/IND$ in the central ring suggests that the central ring is predominantly Hückel aromatic with equal number of α and β π-electrons, whereas a large value points to a Baird aromatic ring unit with two more α than β π-electrons.

In the following, we focus on the results obtained with the FLU index. Values obtained with other electronic indices with

a full list of references are found in the Supporting Information. The percentage of Baird aromaticity is obtained by comparison of the $|\Delta FLU|/FLU$ value of a given system with that of the corresponding fully Baird aromatic species: $^3C_5H_5^+$, $^3C_6H_6^{2+}$, $^3C_9H_9^+$, and $^3C_{11}H_{10}^{2+}$ (Table S105). The relatively low $|\Delta FLU|/FLU$ value denotes strong Hückel character of the central ring in the triplet state of **6R**. For **5R**, **9R**, and **10R**, the Baird character is higher and close to 50% (Table S88). The lower involvement of the Baird form in the neutral **6R** when compared to the anionic **5R** and **9R** compounds is in line with the hypothesis based on the difference in the number of π-bonds between the quinoid and Baird-aromatic zwitterionic resonance structures in charged vs. neutral compounds (Figure 2). The Baird aromatic character of **10R** is probably overestimated by $|\Delta FLU|/FLU$ values (vide infra).

To further quantify the importance of the different resonance structures in the description of the T_1 and S_1 states of ***n*R** and assess the Hückel-Baird aromatic character of the conjugated central ring, we examine the charge and spin

© 2021 Wiley-VCH GmbH
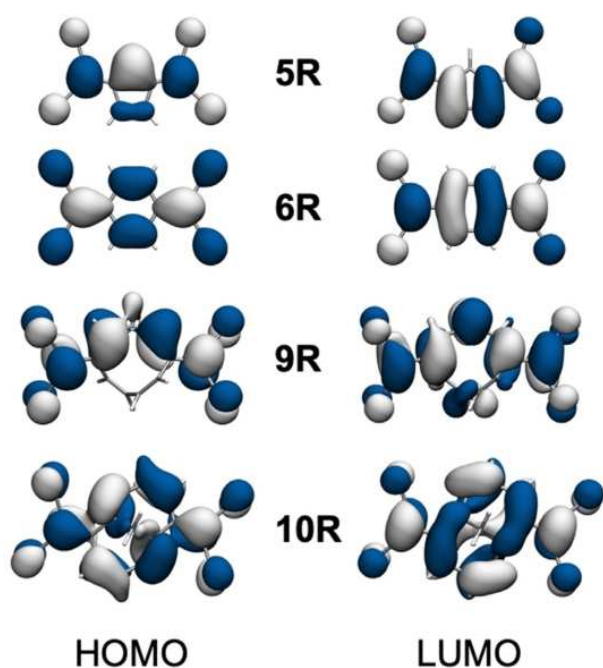
Figure 4. HOMO and LUMO for the *n*R series.
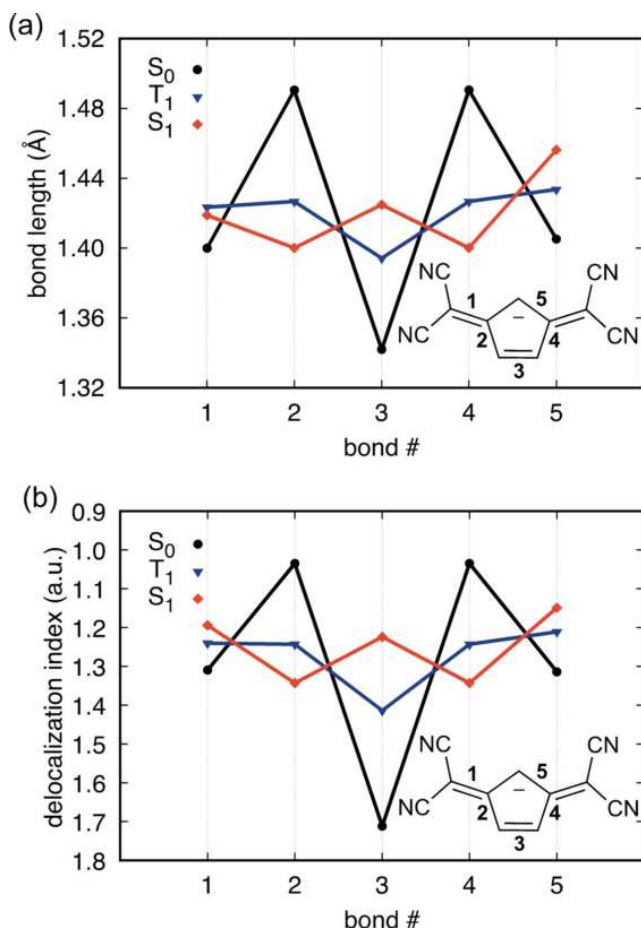
Figure 5. a) Bond lengths (inset with labels) and b) DIs of compound **5R**. Data for all studied molecules are given in the Supporting Information.
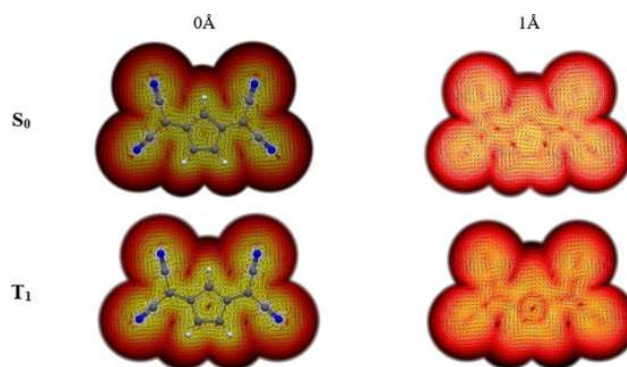
Figure 6. Current-density vector field for S_0 and T_1 states of **5R**. Top view of the currents in the perpendicular plane with respect to the magnetic field vector B_0 located at 0 and 1 Å (left and right, respectively) above the molecular plane. White-yellow regions correspond to larger current values (0.1 nAT^{-1}), while dark red to black correspond to vanishing current densities ($\leq 10^{-6}$ nAT^{-1}).

distributions using different schemes (Mulliken, Hirschfeld, NPA, CHELPG, and QTAIM, Tables S20–S51). We focus here on the QTAIM results, but trends are similar for the rest of the methods. The results differ significantly for anionic (**5R** and **9R**) as compared to neutral (**6R** and **10R**) molecules. For **5R** and **9R**, both T_1 and S_1 states show a similar Baird aromatic character with charges in the 0.01–0.12 e range, indicating that the Baird character in these states is about 50 % (Figure 8), in agreement with T_1 central ring spin densities (1.006 e in **5R** and 0.956 e in **9R**) and $|\Delta$FLU$|$/FLU results. The atomic charges at the six-membered ring (6-MR) obtained for the triplet state of **6R** suggests an 18 % Baird character. The T_1 charge at central ring of **10R** is higher (0.499 e, 25 % Baird), in good agreement with an increase of spin density of **10R** (0.684 e) with respect to **6R** (0.351 e). Spin density plots show that the presence of spin density in the central ring of **6R** and **10R** is small (Figure S32), and we must conclude that there is not enough spin density located in the central rings to consider them fully Baird aromatic. The positive charge at the conjugated rings of **6R** and **10R** in the S_1 state exhibits a small increase with respect to T_1, with 21 % (**6R**) and 29 % (**10R**) Baird character.

Hückel and Baird aromaticity in the central ring could be achieved theoretically by adding to or withdrawing electrons from the ground state configuration, suggesting electron attachment and detachment processes, or by neutral excitations with CT character in which the pro-aromatic ring exchanges electrons with other parts of the system. Here we tackle the latter by evaluating the CT character of low-lying states of the studied molecules. Quantification of electron density gain or loss in the central conjugated ring of molecules *n*R indicates a very small displacement of electrons upon transition to T_1 and S_1 states (Table 1), in line with a HOMO-to-LUMO transition with the two orbitals delocalized over the entire molecule (Figure 4). The computed charge differences between ground and excited state minima are very small, with electron density variations in the central ring smaller than 0.1 e in **5R**, **6R**, and **10R**, and about 0.12–0.13 e increase of electrons in the 9-MR of **9R**. In most cases, there is

© 2021 Wiley-VCH GmbH

Tabelle 1: QTAIM charges (units are e) of the central ring at the S_0, T_1, and S_1 minima of *nR* molecules computed at the B3LYP/6-311+G(d,p) level. $\Delta q(T_1) = q(T_1) - q(S_0)$, $\Delta q(S_1) = q(S_1) - q(S_0)$.

state	5R	6R	9R	10R
S_0	0.066	0.445	0.134	0.551
T_1	0.027	0.359	0.013	0.499
S_1	0.120	0.420	0.006	0.589
$\Delta q(T_1)$	−0.039	−0.086	−0.121	−0.052
$\Delta q(S_1)$	0.054	−0.025	−0.128	0.038

an increase in the negative charge of the central ring when going from S_0 to T_1 and S_1. Charge variations upon $S_0 \rightarrow S_1$ transition at the Franck-Condon geometry are even smaller (Tables S20–S51).

To further understand the CT character (or lack thereof) of the T_1 and S_1 states in relation to their potential Hückel/Baird aromaticity in the central ring, we evaluate the relative energy of the two potential electronic conformers (Hückel and Baird) of the *nR* series within the spin singlet and triplet manifolds. To that aim, we perform electronic structure calculations of the explicit Hückel and Baird configurations with two unpaired electrons, i.e., potentially associated to T_1 and S_1 states, by imposing the required charge and spin restrictions on the central ring and exocyclic groups (indicated in Figure 7 for T_1) by means of constrained DFT calculations.[14] Singlet and triplet Hückel configurations are more stable than the Baird forms in all four *nR* systems. Moreover, the relative stabilization of the Hückel structure (Figure S41) is much larger in the two neutral molecules (**6R**
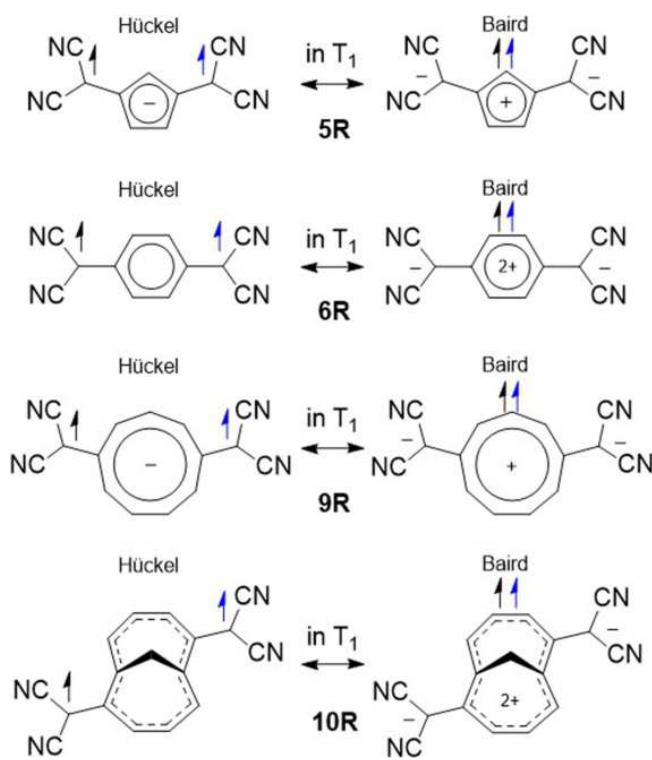
Figure 7. Hückel and Baird triplet state configurations of *nR* molecules.

and **10R**) than in the ionic systems (**5R** and **9R**), in line with our above analysis.

Furthermore, we might approximate the T_1 wave function as a mixing of Hückel (T_H) and Baird (T_B) triplet structures [Eq. (1)]:

$$\Psi_{T_1} \approx c_H \phi_{T_H} \quad c_B \phi_{T_B} \qquad (1)$$

where c_H and c_B amplitudes weight the Hückel and Baird contributions, respectively. The approximation in Eq. (1) allows us to describe the energy of T_1 as the lowest eigenvalue of a 2×2 model Hamiltonian written in the (T_H, T_B) basis [Eq. (2)]:

$$H \begin{pmatrix} \varepsilon_H & \gamma \\ \gamma & \varepsilon_B \end{pmatrix} \qquad (2)$$

where ε_H and ε_B are the energies of the Hückel and Baird triplets, respectively, and γ is the T_H/T_B electronic coupling. Diagonalization of the Hamiltonian for the T_1 state in Eq. (2) can be used to obtain c_H and c_B amplitudes, and quantify the Baird (and Hückel) character of T_1. The participations of the Baird structure in the lowest triplet calculated from T_1, T_H, and T_B energies are shown in Figure 8a. The obtained results follow the same trend as the ones obtained from the analysis derived from QTAIM charges and spins (Figures 8b,c), although with smaller Baird amplitudes. Such energy-based analysis can also be performed for S_1, although in this case the Hückel/Baird deconvolution is more involved than for the triplet state, since in some cases the pristine closed-shell non-aromatic configuration (left structure in Figure 1) might also contribute to the S_1 wave function.

From these results, we conclude that *nR* compounds present central conjugated rings with mixed Hückel/Baird aromatic nature in the T_1 and S_1 states, in which the Baird aromatic character increases for *anionic and small rings*. The Baird aromatic character is slightly larger for S_1 than for T_1 states.

In the following, we consider a new set of compounds derived from the *nR* series, in which we keep the central ring and change the exocyclic groups. Compounds *nR-T* contain the same central conjugated ring as in *nR*, but the *nR-T* molecules accommodate a thiophene ring in each of the two exocyclic moieties. The motivation for this substitution is twofold: (*i*) to explore the impact of increasing the conjugation length of the exocyclic fragments, and (*ii*) to examine the recent experimental characterization of the **10R-T** compound (**TMTQ**) in its singlet excited state.[9]

The presence of the additional thiophenes increases the conjugation and orbital delocalization compared to the *nR* compounds (Figure S5). As a result, excitation energies of *nR-T* are systematically lower (Table S18). The larger conjugation of the two molecular arms stabilizes the two unpaired electrons in the T_1 through radical delocalization, as shown by the spatial representation of the spin density (Figure S32). On the other hand, the total electron density on the central ring of *nR-T* increases with respect to the corresponding counterparts without the thiophene rings, while the spin density on the central ring decreases. As a result, there is a substantial
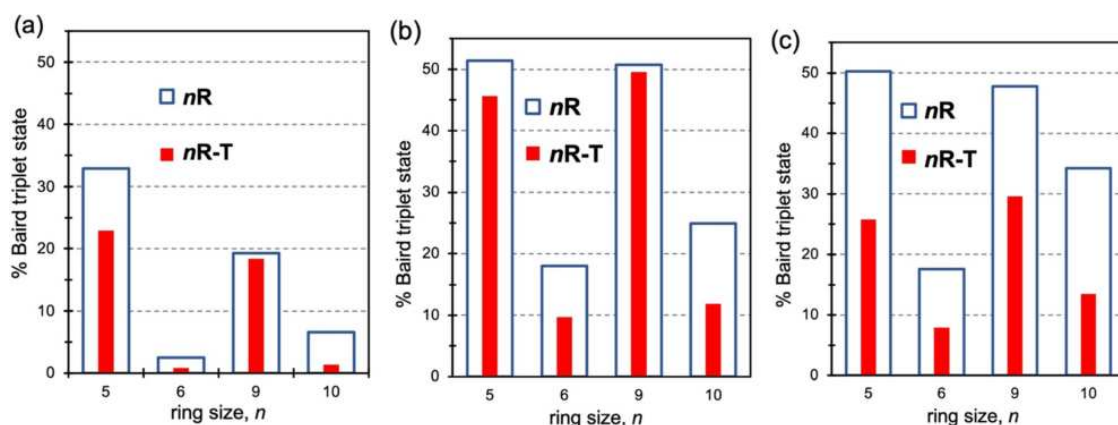
Figure 8. Baird contribution to the T_1 state based on a) relative energies of the constrained Hückel and Baird forms, b) QTAIM charges, and c) spins in *n*R and *n*R-T series.

decrease of the Baird aromatic character in the T_1 and S_1 states of **nR-T** when compared to the neutral and anionic **nR** molecules (Figures 8 b,c). These results are consistent with the systematic decrease of $|\Delta FLU|/FLU$ values (Table S88) and the decrease of the Baird contribution derived from the energy difference between Hückel and Baird configurations (Figure 8 a).

The CT character of the $S_0{\rightarrow}T_1$ and $S_0{\rightarrow}S_1$ transitions in **nR-T** is not larger than in **nR** (Tables S20–S38). These results seem to be in contradiction with recent experimental measurements, in particular for molecule **10R-T** (**TMTQ**), for which photophysical properties were associated to a low-lying (singlet) excited state with two-electron CT character from the central 10-MR to the two exocyclic moieties.[9] This point will be discussed in the next section.

Connection to Experimental Characterization

As discussed in the previous section, computational characterization of the nature of the lowest excited singlet state of **nR** and **nR-T** compounds (and of **10R-T** in particular) indicates that the charge distribution in S_1 barely changes when compared to S_0. All charge analysis schemes employed in the present study indicate no charge displacement upon excitation (Tables 1 and S20–S51), in agreement with a HOMO-to-LUMO transition with the two orbitals delocalized over the entire molecule (Figures 4 and S5). Although these results seem to be in contradiction with the experimental data, in the following we argue that they are perfectly compatible. Conversely, we state that the previous interpretation[9] of the excited state character and aromaticity in **10R-T** needs to be revised.

Shift of the CN Stretching Band

Infrared (IR) spectroscopy measurements on the relative position of the nitrile stretching band in conjugated systems with terminal dicyanomethylene have been used as experimental fingerprint of the CT character of electronic transitions on multiple occasions, since the increase of negative

charge on the $C(CN)_2$ unit produces a redshift of the CN stretching band.[15] Yet, experimental measurements[16] and DFT calculations[8] have suggested that the displacement of the nitrile vibrational frequency towards lower wavenumbers can instead be caused by radical delocalization. To clarify the potential source of the vibrational shift in dicyanomethylenes, we perform benchmarking frequency calculations on one-carbon and three-carbon model systems which are of either neutral saturated, anionic, or radical character (Figure 9). To compare the effect of charge vs. radical delocalization on nitrile frequencies, we quantify the displacement of nitrile vibrations for the anionic and radical forms compared to the neutral molecules (Table 2).

Both charged and radical systems induce a redshift on the computed CN stretching. Moreover, the shift decreases with the conjugation of the system. Dicyanoallyl has the possibility to delocalize the negative charge (**e1**) and the unpaired electron (**e2**), reducing the charge and radical density on the C atom with two cyano substituents, respectively. As a result, the absolute shift of CN frequency is smaller than in dicyanomethyl. Although the negative charge density induces stronger shifts than the unpaired electron density, we
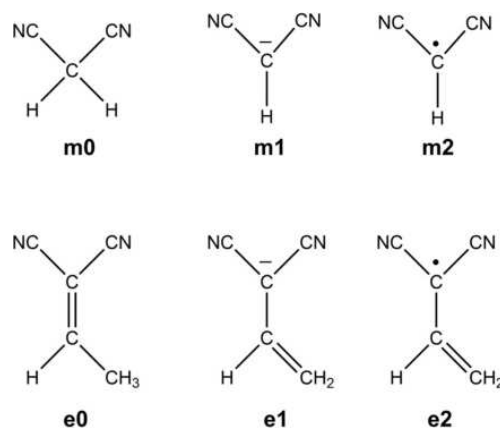
Figure 9. Dicyanomethane (**m0**), dicyanomethyl anion (**m1**) and dicyanomethyl radical (**m2**) (top), and 1,1-dicyanopropene (**e0**), 1,1-dicyanoallyl anion (**e1**), and 1,1-dicyanoallyl radical (**e2**).

Tabelle 2: Average shift of the CN vibration (in cm^{-1}) for the anionic (**m1** and **e1**) and radical (**m2** and **e2**) forms with respect to the neutral species (**m0** and **e0**) for the model compounds in Figure 9 computed at the CCSD and B3LYP levels with the 6-311 + G(d) basis set.

species	CCSD	B3LYP
m1	−143	−166
m2	−149	−179
e1	−104	−111
e2	−57	−75

Tabelle 3: Permanent dipole moments (in Debye) for S$_0$ and S$_1$ and their difference ($\Delta\mu$), and S$_1$ adiabatic energy (ΔE(S$_1$) in eV) of **10R-T** at the B3LYP/6-311 + G(d,p) level in toluene and nitromethane.

solvent	μ(S$_0$)	μ(S$_1$)	$\Delta\mu$	ΔE(S$_1$)
toluene	4.526	7.026	2.500	1.42
nitromethane	5.664	8.521	2.857	1.19

extrapolate that for larger conjugated molecules both effects will be less intense than in the model systems due to lower charge/radical densities, and their differences will diminish. Therefore, we conclude that the excited state redshift in ν(CN) cannot be unequivocally associated to a CT-induced increase of the electron density on the dicyanomethyl anion.

Our calculations predict a redshift of the excited ν(CN) with respect to the ground state frequency in all ***n*R** and ***n*R-T** compounds, which must be attributed to the radical delocalization effect (and not to a CT character, Table S53). Moreover, the displacement towards lower frequencies is larger in ***n*R** (24 cm^{-1} on average) than for the ***n*R-T** series (11 cm^{-1} on average), which can be related to the larger delocalization of the unpaired electrons in S$_1$ provided by the thiophene rings. Concretely, the S$_0$ to S$_1$ redshift in compound **10R-T** (**TMTQ**) is computed at 16 cm^{-1} (experimentally measured at 45 cm^{-1}).[9] The obtained ν(CN) redshifts for the triplet state follow the same trends as in S$_1$ (Table S53).

Photophysical Dependence on the Solvent Polarity

The excited state dependence on the solvent polarity can be rationalized in terms of the different (permanent) dipole moment in the ground and excited states, and by different stabilization of the S$_1$ state with changes in the solvent polarity. Next, we discuss the dependency of the S$_1$ state properties on the solvent's dielectric constant, and we focus on **10R-T** since the dependence of its photophysical behavior on the polarity of the solvent has been experimentally described. Results for other compounds are found in the Supporting Information.

The dipole moments of **10R-T** in S$_0$ and S$_1$ are perpendicularly oriented with respect to the central ring (Figure 10) and increase with the solvent polarity (Table 3). Importantly,

Figure 10. Permanent dipole moments (blue arrows) for the ground (left) and first excited singlet (right) states of **10R-T** at the B3LYP/6-311 + G(d,p) level.

despite the lack of CT character of S$_1$ state in **10R-T**, there is a sizeable increase of the magnitude of the molecular dipole moment upon S$_0$→S$_1$ transition, which might explain the dependence of excited state dynamics on the solvent polarity experimentally observed.[9] Results obtained with different functionals are all in quantitative agreement with B3LYP (Tables S1 and S2).

Moreover, calculations of the S$_1$ excitation in solution with two solvents with very different dielectric constants, i.e., toluene and nitromethane, indicate an increase in the difference between S$_0$ and S$_1$ dipole moments and a decrease of the excitation energies with the solvent polarity (Table 3). All in all, these results reaffirm the dependence of the excited state decay on the polarity of the solvent without the need for strong CT character in the electronic transition.

Searching for Systems with High Baird-Aromatic Character
Cyclopentadienylidene and Cyclopropenylidene Substitution

In this section, we explore the potential increase of Baird-aromaticity by means of cyclopentadienylidene and cyclopropenylidene substitution at the five- and six-membered conjugated rings (**5R-5a–e**, **6R-5a–e**, and **6R-3a–e** in Figure 3). Such substitution provides for terminal (exocyclic) units which themselves can be Hückel-aromatic.

The T$_1$ state of compounds **5R-5a** and **6R-5a**, both having cyclopentadienylidene rings, can display push-pull captodative aromaticity.[17] For this state, QTAIM charges (−0.225 vs. 0.102), spin densities (0.839 vs. 0.325), and |ΔFLU|/FLU values (2.192 vs. 0.642) in the central rings and the relative Hückel/Baird stability (Figure S41) indicate a much large Baird aromatic character in **5R-5a** than in **6R-5a**, although **5R-5a** is less Baird aromatic than **5R**. The same trend is observed for the S$_1$ state. This result is in contradiction with a two-electron transfer from the central ring, which would lead to two external Hückel aromatic cyclopentadienyl anionic rings and one Baird aromatic cyclopentadienyl cationic ring in the middle. In fact, the T$_1$ state in **5R-5a** is obtained as the delocalization of the two unpaired electrons over the three 5-MRs (Figure 11), resulting in partial Baird-aromaticity. Substituting **5R-5a** with methyl groups to impose steric congestion at the planar structure (**5R-5b**), forcing the three rings out of the same plane, results in a minor reduction of the negative charge and spin density in the central ring. On the other hand, a more significant increase of ≈0.26 e is observed in the spin density of the central ring of **5R-5c**, thanks to the electron-donating groups (EDG) attached to the central 5-MR and the electron-withdrawing groups (EWG) at the exocyclic 5-MRs. Interestingly, constrained Hückel/Baird calculations of **5R-5a** produce very similar
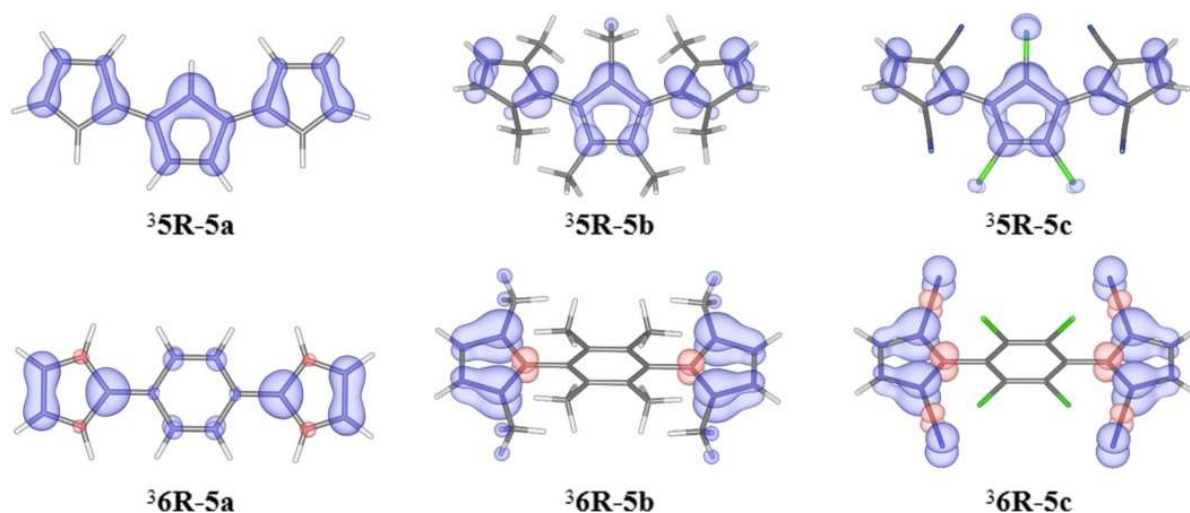
Figure 11. Spin density for the T$_1$ state of **5R-5a–c** and **6R-6a–c** at the B3LYP/6-311+G(d,p) level. Isodensity of 0.005 e⁻ bohr⁻³.

results to those obtained for **5R**, while the singlet and triplet Baird configurations become slightly more stable than the Hückel forms in **5R-5b** and **5R-5c**.

The same substitution series produces rather different results in the 6-MR counterparts (**6R-5a–c**). The three conjugated rings are coplanar in **6R-5a** with minor spin density on the central 6-MR (Figure 11). Steric hindrance in **6R-5b** breaks the molecular planarity with orthogonal disposition of the central and side rings in the triplet state, with the two unpaired electrons localized on the two external cyclopentadienylidene units. Hence, the central ring has a very strong Hückel aromatic character. Substitution with EWG and EDG groups in **6R-5c** does not change the nature of T$_1$ and the central ring remains a local Hückel singlet.

Results on **6R-5a–c** clearly show that the symmetric functionalization of the benzene ring with cyclopentadienylidene is not able to generate significant Baird aromaticity in the central ring. Hence, in order to induce Baird character to the central 6-MR, we consider next the cyclopropenylidene substitution (**6R-3a–c**) which potentially could lead to molecules with CT in the opposite direction compared to those of **6R-5a–c**, i.e., two cationic cyclopropenylidene rings and a dianionic central benzene. Here it is notable that a planar hexasilylbenzene dianion which exhibits a triplet state merely 1.0 kcal mol⁻¹ above the singlet ground state has been reported.[18] For the three compounds, we observe a sizeable triplet state spin density of about 0.5 e on the central ring, which would suggest an increase of the Baird aromatic character (ca. 25%) in **6R-3a–c** with respect to **6R-5a–c**. The order of Baird aromaticity in the central ring is **6R-3b** > **6R-3c** > **6R-3a**, in line with |ΔFLU|/FLU values (Table S88). The relative stability of Hückel/Baird configurations indicate a strong preference for the Hückel form in **6R-3a**, whereas in **6R-3b–c** the gap between the two configurations is much smaller (Figure S41). A close examination of the spin density distribution in the triplet state of cyclopropenylidene substituted 6-MR reveals that the two unpaired electrons mainly localize on the external atoms with delocalization towards the 6-MR moiety (Figure S32). This picture becomes

clear in **6R-3c**, for which the excess of α spin density is perpendicular to the π-system of the central ring, and should be associated with spin delocalization from the external rings rather than a Baird aromatic character of the central ring.

Four-Membered Heterocycles

Next, we explore the use of 4-membered heterocycles with cyclopentadienylidene moieties (**4RN-5** and **4RO-5**). Results based on charges, spin densities, and |ΔFLU|/FLU values of the T$_1$ state do not allow us to conclude which one has the largest Baird aromatic character. Whereas |ΔFLU|/FLU in the central ring is 1.845 in **4RO-5** and 0.870 in **4RN-5**, spin densities indicate that contribution of Baird aromaticity is similar in both systems (21–23%), and electronic charges give more Baird character to **4RN-5** with 0.045 e (S$_1$) and 0.025 e (T$_1$) than to **4RO-5** with −0.203 e (S$_1$) and −0.231 e (T$_1$). Moreover, constrained energies indicate strong preference for the Hückel configuration in the singlet and triplet states of **4RN-5** and **4RO-5**. Hence, although the central ring in **4RN-5** and **4RO-5** is more Baird aromatic than the 6-MR of **6R-5a**, the Baird character is mild at most, and definitely smaller than in the 5-MR of **5R-5a**.

Protonated Systems

We now investigate whether the Baird character can be enhanced by protonation. Concretely, we explore the protonation of two cyano groups in **5R** (**5R-2H⁺**), **6R** (**6R-2H⁺**), and **10R** (**10R-2H⁺**), and four cyano groups in **5R-4H⁺**.

Protonation of two and four cyano groups increases the T$_1$ spin density at the 5-MR to 1.365 e (68% Baird in **5R-2H⁺**) and 1.567 e (78% Baird in **5R-4H⁺**), with respect to **5R** compound (50% Baird). The strong excited state Baird character in **5R-2H⁺** and **5R-4H⁺** is supported by ring charges (Tables S21–S22) and the (triplet and singlet) lower energy obtained for the Baird configurations with respect to the Hückel counterparts ($\varepsilon_B < \varepsilon_H$). Application of Eqs. (1) and (2) reveals Baird aromatic characters of 69% (T$_1$) and 66% (S$_1$)

© 2021 Wiley-VCH GmbH

in **5R-2H**[+], and of 86% (T$_1$) and 82% (S$_1$) in **5R-4H**[+], in very good agreement with charge and spin analysis of T$_1$. Double protonation in **6R** and **10R** also results in a significant increase of about 5–15% in the Baird aromatic character of the central ring.

Seven-Membered Electron-Deficient Central Rings

Finally, instead of trying to pull electrons out of a non-aromatic π-conjugated ring like in many of the systems explored so far, we envisage the possibility of reaching excited state Baird aromaticity by injecting electrons into a conjugated ring which is electron deficient.[19] To that aim, we design two compounds with a cationic 7-MR with exocyclic carbons substituted with EDG (**7Ra** and **7Rb**).

The 7-MR ring in S$_1$ and T$_1$ states of **7Ra** and **7Rb** is effectively neutral, suggesting equal mixing of Hückel and Baird character. The T$_1$ spin density is notably located on the central ring (Figure 12), accounting for ≈1.5 e delocalized on the 7-MR for both molecules. Evaluation of the relative stability of Hückel and Baird configurations confirm the strong Baird character with contributions estimated to be 57% (T$_1$ and S$_1$) in **7Ra** and 68% (T$_1$) and 67% (S$_1$) in **7Rb**. Therefore, the combination of an electron deficient conjugated ring with electron-donor exocyclic substitution seems a good strategy towards Baird aromaticity.


^{3}**7Ra**

^{3}**7Rb**
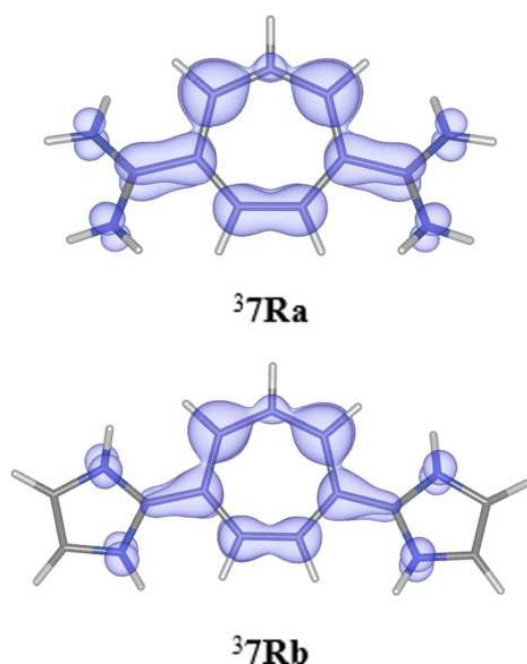
Figure 12. Spin density for the T$_1$ state of **7Ra** and **7Rb** at the B3LYP/6-311 + G(d,p) level. Isodensity of 0.005 e$^-$ bohr^{-3}.

Conclusion

The results of this study stress that characterization of Baird aromaticity needs to be carried out with care and that the labelling of a conjugated ring as Baird aromatic requires a detailed analysis of the excited state electronic structure.

Probably a safe procedure is the one presented here, in which several parameters and computational tools are combined: ring charge, ring spin density, DIs, aromaticity indices, and the newly introduced energy-based analysis of the Hückel and Baird configurations.

The Baird aromaticity of the studied systems can be related to the charge and spin in the central ring. However, while ring charge and spin might be good indicators of the Baird character of electronic states, they do not univocally correspond to a specific type of aromaticity. In other words, it is not possible (in general) to establish a one-to-one map between charge (or spin) and the amount of Baird aromaticity. Therefore, here we take a conservative approach for the quantification of the Baird character of T$_1$ and S$_1$ states by considering the lowest Baird percentage derived from charge and spin analyses (Figure 13). Quantification of Baird aromaticity in S$_1$ has been obtained from ring charges corrected by the charge/spin differences in T$_1$ (Eqs. S8–S11). The use of relative energies between constrained calculations of Hückel and Baird configurations for the systems investigated is, in general, in good agreement with the quantification of Baird character from charge/spin measurements.
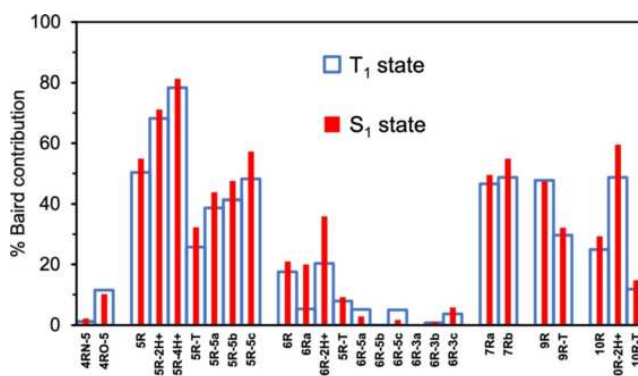
Figure 13. Baird contribution based on QTAIM charges and spins for the T$_1$ and S$_1$ states in all studied systems.

Generation of excited state Baird aromaticity in symmetrically substituted conjugated rings appears rather difficult. High Baird aromatic character (> 50%) in these systems is achieved in molecules with anionic and small central rings with EDG as substituents and small exocyclic groups substituted with EWG. Alternatively, the combination of an electron deficient conjugated ring with electron-donor exocyclic substitution also seems a good strategy towards Baird aromaticity. Interestingly, Baird aromaticity in S$_1$ is typically slightly larger than in T$_1$ (Figure 13), especially for those cases with appreciable Baird character (> 10%).

Overall, our analysis indicates that the symmetric substitution of conjugated rings favors the presence of low-energy excited states with very weak CT character. The coplanarity between the central ring and the two side groups symmetrically arranged facilitates the hole and electron delocalization, resulting in negligible charge separation. In light of the present results, previously assigned excited state Baird aromaticity in symmetrically substituted rings, in

particular for **10R-T**, based on the allegedly strong CT character of the electronic transition needs to be revised. Based on extensive computational results, we have presented an alternative interpretation of the experimental measurements, i.e., the shift in the CN IR stretching band and dependence of excited state decay on the solvent polarity, which does not require charge separation upon excitation and seems, in our opinion, much more feasible.

Acknowledgements

Conflict of interest

The authors declare no conflict of interest.

[1] P. Klan, J. Wirz, *Photochemistry of Organic Compounds: From Concepts to Practice*, Wiley-VCH, Weinheim, **2009**.

[2] a) T. J. Meyer, *Pure Appl. Chem.* **1986**, *58*, 1193–1206; b) J. F. Endicott, in *Electron Transfer in Chemistry* (Ed.: V. Balzani), Wiley-VCH, Weinheim, **2001**, pp. 238–270; c) S. Sasaki, G. P. C. Drummen, G.-i. Konishi, *J. Mater. Chem. C* **2016**, *4*, 2731–2743.

[3] a) X. Shi, E. Quintero, S. Lee, L. Jing, T. S. Herng, B. Zheng, K.-W. Huang, J. T. López Navarrete, J. Ding, D. Kim, J. Casado, C. Chi, *Chem. Sci.* **2016**, *7*, 3036–3046; b) S. Escayola, M. Callís, A. Poater, M. Solà, *ACS Omega* **2019**, *4*, 10845–10853; c) T. Inouchi, T. Nakashima, T. Kawai, *J. Phys. Chem. A* **2014**, *118*, 2591–2598.

[4] a) N. C. Baird, *J. Am. Chem. Soc.* **1972**, *94*, 4941–4948; b) M. Rosenberg, C. Dahlstrand, K. Kilså, H. Ottosson, *Chem. Rev.* **2014**, *114*, 5379–5425; c) H. Ottosson, *Nat. Chem.* **2012**, *4*, 969–971; d) R. Papadakis, H. Ottosson, *Chem. Soc. Rev.* **2015**, *44*, 6472–6493; e) J. Oh, Y. M. Sung, Y. Hong, D. Kim, *Acc. Chem. Res.* **2018**, *51*, 1349–1358; f) B. Durbeej, J. Wang, B. Oruganti, *ChemPlusChem* **2018**, *83*, 958–967; g) C. Liu, Y. Ni, X. Lu, G. Li, J. Wu, *Acc. Chem. Res.* **2019**, *52*, 2309–2321.

[5] a) P. B. Karadakov, *J. Phys. Chem. A* **2008**, *112*, 7303–7309; b) P. B. Karadakov, *J. Phys. Chem. A* **2008**, *112*, 12707–12713; c) F. Feixas, J. Vandenbussche, P. Bultinck, E. Matito, M. Solà, *Phys. Chem. Chem. Phys.* **2011**, *13*, 20690–20703; d) P. B. Karadakov, P. Hearnshaw, K. E. Horner, *J. Org. Chem.* **2016**, *81*, 11346–11352; e) M. Rosenberg, H. Ottosson, K. Kilså, *Phys. Chem. Chem. Phys.* **2011**, *13*, 12912–12919; f) M. Ueda, K. Jorner, Y. M. Sung, T. Mori, Q. Xiao, D. Kim, H. Ottosson, T. Aida, Y. Itoh, *Nat. Commun.* **2017**, *8*, 346; g) R. Kotani, L. Liu, P. Kumar, H. Kuramochi, T. Tahara, P. Liu, A. Osuka, P. B. Karadakov, S. Saito, *J. Am. Chem. Soc.* **2020**, *142*, 14985–14992; h) D. Shukla, P. Wan, *J. Am. Chem. Soc.* **1993**, *115*, 2990–2991; i) J. Toldo, O. El Bakouri, M. Solà, P.-O. Norrby, H. Ottosson, *ChemPlusChem* **2019**, *84*, 712–721.

[6] B. Oruganti, J. Wang, B. Durbeej, *Org. Lett.* **2017**, *19*, 4818–4821.

[7] B. C. Streifel, J. L. Zafra, G. L. Espejo, C. J. Gómez-García, J. Casado, J. D. Tovar, *Angew. Chem. Int. Ed.* **2015**, *54*, 5888–5893; *Angew. Chem.* **2015**, *127*, 5986–5991.

[8] K. Jorner, F. Feixas, R. Ayub, R. Lindh, M. Solà, H. Ottosson, *Chem. Eur. J.* **2016**, *22*, 2793–2800.

[9] J. Kim, J. Oh, S. Park, J. L. Zafra, J. R. DeFrancisco, D. Casanova, M. Lim, J. D. Tovar, J. Casado, D. Kim, *Nat. Commun.* **2019**, *10*, 4983.

[10] a) R. Ayub, O. E. Bakouri, K. Jorner, M. Solà, H. Ottosson, *J. Org. Chem.* **2017**, *82*, 6327–6340; b) C.-H. Wu, L. J. Karas, H. Ottosson, J. I.-C. Wu, *Proc. Natl. Acad. Sci. USA* **2019**, *116*, 20303–20308; c) O. El Bakouri, J. R. Smith, H. Ottosson, *J. Am. Chem. Soc.* **2020**, *142*, 5602–5617; d) D. Chen, D. W. Szczepanik, J. Zhu, M. Solà, *Chem. Commun.* **2020**, *56*, 12522–12525; e) Y. M. Sung, M.-C. Yoon, J. M. Lim, H. Rath, K. Naoda, A. Osuka, D. Kim, *Nat. Chem.* **2015**, *7*, 418–422.

[11] M. Mauksch, S. B. Tsogoeva, *Phys. Chem. Chem. Phys.* **2017**, *19*, 4688–4694.

[12] a) L. A. Paquette, M. Oku, W. E. Heyd, R. H. Meisinger, *J. Am. Chem. Soc.* **1974**, *96*, 5815–5825; b) A. K. Pati, O. El Bakouri, S. Jockusch, Z. Zhou, R. B. Altman, G. A. Fitzgerald, W. B. Asher, D. S. Terry, A. Borgia, M. D. Holsey, J. E. Batchelder, C. Abeywickrama, B. Huddle, D. Rufa, J. A. Javitch, H. Ottosson, S. C. Blanchard, *Proc. Natl. Acad. Sci. USA* **2020**, *117*, 24305–24315.

[13] a) X. Fradera, M. A. Austen, R. F. W. Bader, *J. Phys. Chem. A* **1999**, *103*, 304–314; b) X. Fradera, J. Poater, S. Simon, M. Duran, M. Solà, *Theor. Chem. Acc.* **2002**, *108*, 214–224.

[14] Q. Wu, T. Van Voorhis, *Phys. Rev. A* **2005**, *72*, 024502.

[15] a) J. S. Chappell, A. N. Bloch, W. A. Bryden, M. Maxfield, T. O. Poehler, D. O. Cowan, *J. Am. Chem. Soc.* **1981**, *103*, 2442–2443; b) V. Belova, P. Beyer, E. Meister, T. Linderl, M.-U. Halbich, M. Gerhard, S. Schmidt, T. Zechel, T. Meisel, A. V. Generalov, A. S. Anselmo, R. Scholz, O. Konovalov, A. Gerlach, M. Koch, A. Hinderhofer, A. Opitz, W. Brütting, F. Schreiber, *J. Am. Chem. Soc.* **2017**, *139*, 8474–8486; c) H. Méndez, G. Heimel, S. Winkler, J. Frisch, A. Opitz, K. Sauer, B. Wegner, M. Oehzelt, C. RÁthel, S. Duhm, D. TÁbbens, N. Koch, I. Salzmann, *Nat. Commun.* **2015**, *6*, 8560; d) A. A. Talin, A. Centrone, A. C. Ford, M. E. Foster, V. Stavila, P. Haney, R. A. Kinney, V. Szalai, F. El Gabaly, H. P. Yoon, F. Léonard, M. D. Allendorf, *Science* **2014**, *343*, 66–69; e) D. Yuan, *Chem* **2019**, *5*, 744–745.

[16] T. Takahashi, K.-i. Matsuoka, K. Takimiya, T. Otsubo, Y. Aso, *J. Am. Chem. Soc.* **2005**, *127*, 8928–8929.

[17] B. A. Shainyan, A. Fettke, E. Kleinpeter, *J. Phys. Chem. A* **2008**, *112*, 10895–10903.

[18] K. Ebata, W. Setaka, T. Inoue, C. Kabuto, M. Kira, H. Sakurai, *J. Am. Chem. Soc.* **1998**, *120*, 1335–1336.

[19] L. J. Karas, A. T. Campbell, I. V. Alabugin, J. I. Wu, *Org. Lett.* **2020**, *22*, 7083–7087.

© 2021 Wiley-VCH GmbH

4.2 Effect of Exocyclic Substituents and π-System Length on the Electronic Structure of Chichibabin Diradical(oid)s

This section corresponds to the following publication:

Effect of Exocyclic Substituents and π-System Length on the Electronic Structure of Chichibabin Diradical(oid)s

Sílvia Escayola, Marc Callís, Albert Poater,*[ID] and Miquel Solà*[ID]

Institut de Química Computacional i Catàlisi and Departament de Química, Universitat de Girona, C/Maria Aurèlia Capmany, 69, 17003 Girona, Catalonia, Spain

Ⓢ *Supporting Information*

ABSTRACT: The ground state (GS) of Chichibabin's polycyclic hydrocarbons (CPHs) can be singlet [open- or closed-shell (OSS or CS)] or triplet (T), depending on the elongation of the π-system and the exocyclic substituents. CPHs with either a small singlet−triplet energy gap (ΔE_{ST}) or even a triplet GS have potential applications in optoelectronics. To analyze the effect of the size and exocyclic substituents on the nature of the GS of CPHs, we have selected a number of them with different substituents in the exocyclic carbon atoms and different ring chain lengths. The OPBE/cc-pVTZ level of theory was used for the optimization of the systems. The aromaticity of the resulting electronic structures was evaluated with HOMA, NICS, FLU, PDI, I_{ring}, and MCI aromaticity indices. Our results show that the shortest π-systems (one or two rings) have a singlet GS. However, systems with three to five rings favor OSS GSs. Electron-withdrawing groups (EWGs) and aromatic substituents in the exocyclic carbons tend to stabilize the OSS and T states, whereas electron-donating groups slightly destabilize them. For CS, OSS, and T states, aromaticity measures indicate a gain of aromaticity of the 6-membered rings of the CPHs with the increase in their size and when CPHs incorporate EWGs or aromatic substituents. In general, the CPHs analyzed present small singlet−triplet energy gaps, and in particular, the ones containing EWGs or aromatic substituents present the smallest singlet−triplet energy gaps.
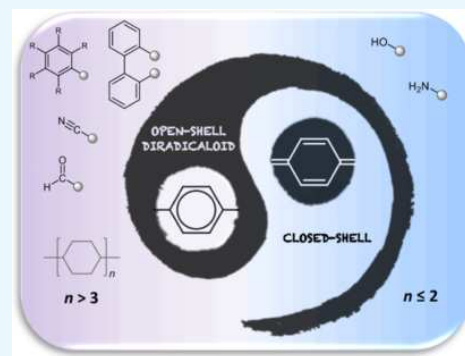
INTRODUCTION

Chichibabin's polycyclic hydrocarbon (CPH), *p,p′*-biphenylene-bis-(diphenylmethyl) (*n* = 2 and R = Ph in Scheme 1a), was synthesized in 1907[1] by Russian chemist Aleksei Yevgen'evich Chichibabin.[2] Three years before, Thiele and Balhorn[3] reported an analogue hydrocarbon with *n* = 1 and R = Ph, whereas Müller and Pfanz[4] produced the species with *n* = 3 and R = Ph in 1941. The electronic structure of Chichibabin's compounds and that of their derivatives

(closed-shell quinoid vs open-shell diradical forms, Scheme 1a) have been a recurring topic of debate for both theoretical and experimental chemists.[5] In 1986, despite the extremely oxygen-sensitive nature of Chichibabin's hydrocarbon, Montgomery et al.[6] determined its molecular structure by X-ray diffraction. In addition, they determined that this molecule has a singlet ground state (GS) with a small singlet−triplet energy gap (ΔE_{ST}) and a large amount of diradical character, i.e., it is a Kekulé diradicaloid. Chichibabin's, Müller's, and related hydrocarbons have usually a diradical or diradicaloid GS and a small ΔE_{ST}.[6−8] These species are getting special attention owing to the tunable character of their GS that can be singlet [open- (OSS) or closed-shell (CS)] or triplet (T), depending on the length of the π-system and the exocyclic substituents.[9−11] In general, the longer the hydrocarbon, the greater the diradical character.[12] Indeed, many investigations support this relationship and also add the fact that the aromaticity is increased in larger CPH systems.[13,14]

π-Conjugated open-shell diradical(oid)s, such as Chichibabin's and Müller's hydrocarbons and analogues, are being intensively investigated as potentially multiple functional organic materials that can be employed as semiconductors in

Scheme 1. (a) Quinoid and Diradical (Benzoid) Resonance Forms of CPHs; (b) Different Substituents Studied in This Work
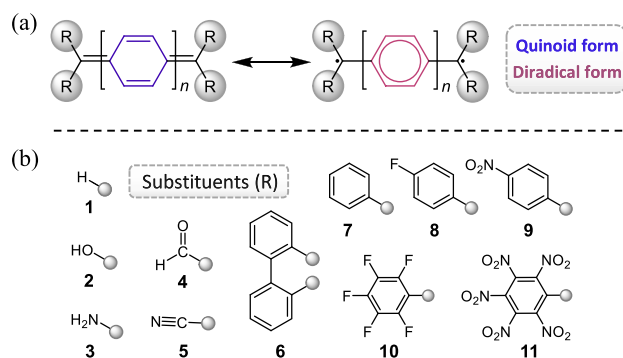
10845

organic field effect transistors,[15,16] as organic light-emitting diodes,[17] as light-harvesting dyes in organic solar cells,[18] as near-infrared fluorescent probes,[19] and as chromophores in nonlinear optics (NLO).[11,20−22] Indeed, NLO properties were shown to be particularly enhanced for systems having intermediate diradical character such as Chichibabin's hydrocarbons.[23−26] Unfortunately, the intrinsic instability of these hydrocarbons prevents their practical applications. For this reason, several related hydrocarbons with increased stability have been synthesized in the last decade.[12,27−36] The quest of thermally stable diradicals arouses considerable interest because these molecules have a great potential for numerous advance applications.[37]

It has been recently shown that substituents on the two biphenylmethylene moieties of tetrabenzo-Chichibabin's hydrocarbons have a significant influence on their chemical bonding and physical properties.[38] From a computational point of view, studies regarding the effect of the substituents on the molecular structure of CPHs or other oligothiophenes analogues are limited to few examples. Most of the studies are mainly focused on the effect of the CPH chain elongation.[26,39] For the case of quinoidal thiophene oligomers, Nakano and co-workers[26,40] examined the effect of the substituent at the terminal positions, by replacing R = H by CN, showing that the effect of this replacement is small. The main aim of this work is to study what is the effect of the exocyclic substitution in Chichibabin's hydrocarbons on their stability and diradical character. We will also analyze the influence of the length of the π-system. In particular, we will consider Chichibabin's hydrocarbons with n in the range of 1−5 and as substituents the set depicted in Scheme 1b. Some of the substituents have π-donor character (2, 3), others have π-acceptor character (4, 5), and some of them have aromatic rings with more or less π-acceptor or π-donor character (6 to 11). Our hope is that the results obtained provide clues that will help designing polycyclic hydrocarbons with enhanced stability and tuned diradical character.

■ RESULTS AND DISCUSSION

Geometry optimizations of different CPHs, with substituents from 1 to 11 (Scheme 1) and chain lengths (n) from 1 to 5 rings (to refer to a specific compound, we will employ the nomenclature: substituent$_n$), were performed at the OPBE/cc-pVTZ level of theory. Three electronic states, namely, closed-shell singlet (CS), open-shell singlet (OSS), and triplet (T), were considered for the calculations. Scheme 2 represents the resonance structures proposed for the $n \geq 2$ systems, which can present from 0 to n aromatic π-sextets.[41,42]

Data in Table 1 show that for 7_1 and 7_2, for which experimental X-ray data is available,[6] the theoretical bond distances are in good agreement with the experimental ones if one considers that the GS of these CPHs is the CS, as experimentally found.[6] From all optimized geometries, only the CS systems 1, 2, and 3 with $n \leq 2$ are planar (dihedral angle values (α) lower than 5°), indicating a huge contribution of the quinoid resonant form in these cases. For the $n = 2$ geometries, the H⋯H distance between neighbor hydrogens of the chain rings is about 1.95 Å, less than the sum of their van der Waals radii. In spite of this, the molecule is planar because the stabilizing effect of the conjugation is strong enough to outweigh the H⋯H repulsion. However, in other systems with $n \leq 2$, the α values can be up to 22° (6), indicating a diminished quinoid contribution to the CS structure in this

Scheme 2. Proposed Resonance Forms for the CS (Top) and OSS/T (Bottom) States of the Chichibabin Polycyclic Hydrocarbons[a]
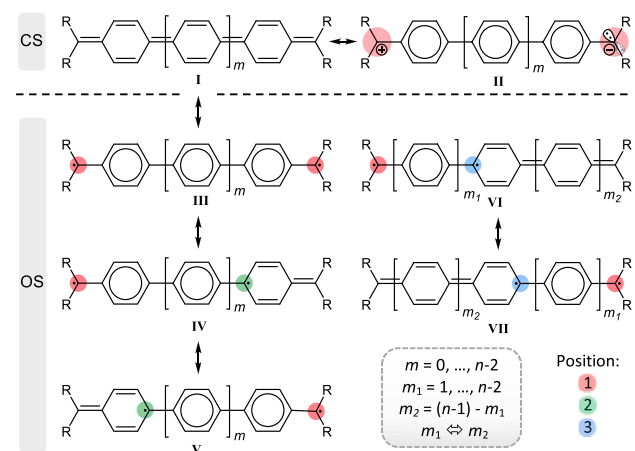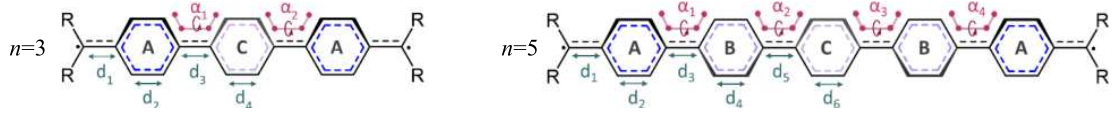
[a]The different radical positions represented for the OSS/T case are also possible for the equivalent CS situation with zwitterionic structure (for instance, structure III is the radical analogue of II; there are zwitterionic structures analogues of IV to VII). n represents the total number of rings.

short-ring-chain cases. Most of these CPHs are nonplanar because of the twisting distortion of the 6-membered rings. The dihedral angle that measures this distortion can be either positive or negative. Because of that, we have a number of possible conformers (see Figure S3). We analyzed all possible conformers for 1_n ($n = 2$ to 5), and our results showed that energy differences between conformers are not larger than 0.003 eV (see Table S2). For this reason, for the rest of the systems, we decided to start the optimization from the planar geometry and to use the final geometry without analyzing whether it corresponds to the most stable conformer. As can be seen from the α values (Table 1), the loss of planarity is smaller in the case of CS than in OSS and T structures, but even so, the distortion in the CS case is still significant. This loss of planarity is also increased by enlarging the chain length. In systems having more neighbor H pairs, the repulsive contribution become more important; for example, in the case of system 1 having $n = 3$ (so, two nonbonded H pairs), α values are around 14°, whereas for $n = 5$ (four H pairs), the α values range from 25 to 32°. H⋯H repulsions decrease with torsion at the cost of reducing conjugation. The degree of distortion is also affected by the nature of the R group; an electron-donating group (EDG) (3) presents smaller α values than EWG and aromatic substituents (5, 6, and 7). This can be related to the fact that EDGs are not efficient in stabilizing the negatively charged C atom (structure II and zwitterionic analogues of IV to VII), thus disfavoring the benzoid forms.

As said before, the twisting distortion is larger in OSS and T states. For these states, the inter-ring C−C bond is a single bond and, therefore, rotation over this bond is easier than in the CS states. For the T states, α is always larger than 35°. This situation reminds that of the biphenyl system that is distorted by 44.4°[43] to avoid steric hindrance with ortho hydrogen atoms.[44] For these systems, there is an interplay between the gain of stabilization due to conjugation in the planar geometry and the reduction of H⋯H repulsions for $\alpha = 90°$. The actual dihedral angle represents the best compromise between these two counteracting forces for each case. EDG (3) presents

Table 1. Selected Bond Distances (Å), Angles (°), and Harmonic Oscillator Model of Aromaticity (HOMA)[a] Values (au) Calculated (OPBE/cc-pVTZ) for 1, 3, 5, 6, and 7 Chichibabin Systems in Closed- and Open-Shell Singlet and Triplet States

system$_n$	state	d_1	d_2	d_3	d_4	d_5	d_6	α_1[b]	α_2[b]	α_3[b]	α_4[b]	HOMA$_A$	HOMA$_B$	HOMA$_C$
1_3	CS	1.373	1.365	1.433	1.372			13.7	13.7			0.576		0.755
	OSS	1.393	1.375	1.460	1.383			28.7	28.7			0.773		0.910
	T	1.401	1.379	1.472	1.387			36.9	36.9			0.833		0.948
1_5	CS	1.381	1.371	1.455	1.382	1.465	1.384	25.0	30.8	31.5	26.1	0.697	0.911	0.928
	OSS	1.399	1.378	1.470	1.387	1.476	1.388	34.8	38.9	39.7	35.3	0.822	0.951	0.957
	T	1.399	1.378	1.470	1.387	1.476	1.388	34.9	40.0	40.0	34.9	0.823	0.950	0.959
3_5	CS	1.409	1.374	1.453	1.382	1.463	1.384	22.4	28.8	29.5	23.2	0.752	0.899	0.918
	OSS	1.413	1.377	1.463	1.386	1.473	1.387	29.1	36.3	36.7	29.5	0.793	0.935	0.949
	T	1.414	1.377	1.464	1.386	1.474	1.388	29.9	37.4	37.8	30.1	0.796	0.938	0.952
5_5	CS	1.427	1.376	1.461	1.383	1.468	1.385	30.3	33.8	32.9	29.1	0.844	0.926	0.936
	OSS	1.435	1.379	1.469	1.386	1.475	1.387	35.0	39.2	38.4	34.3	0.871	0.948	0.956
	T	1.435	1.379	1.469	1.386	1.475	1.388	35.2	39.6	38.9	34.7	0.883	0.949	0.957
6_5	CS	1.446	1.384	1.472	1.387	1.475	1.388	36.2	38.5	38.6	37.6	0.915	0.953	0.955
	OSS	1.454	1.386	1.475	1.388	1.477	1.388	39.0	40.5	40.4	39.7	0.936	0.959	0.960
	T	1.454	1.386	1.475	1.388	1.477	1.388	39.0	40.5	40.4	39.7	0.936	0.959	0.960
7_1	X-ray[c]	1.381	1.346											
	CS	1.397	1.361									0.445		
	T	1.467	1.386									0.918		
7_2	X-ray[c]	1.415	1.371	1.448										
	CS	1.411	1.369	1.431				16.0				0.668		
	T	1.456	1.385	1.474				38.0				0.918		

[a]HOMA indices computed using the ESI-3D program. [b]The dihedral angle results are in absolute values. [c]X-ray values for the **7** compound with n = 2 from ref 6. See the Supporting Information (SI) for other systems results.

smaller α values than EWG and aromatic substituents (**5**, **6**, and **7**), as expected from the fact that EWGs and aromatic substituents can better stabilize the radical centers, thus favoring the benzoid forms.

Similar arguments can be applied to explain the bond distances and harmonic oscillator model of aromaticity (HOMA)[45−47] values. In the previously discussed cases, where the benzoid form is preferred, outer-ring bonds (d_1, d_3, and d_5) are larger and inner-ring bonds (d_2, d_4, and d_6) are closer to the aromatic C−C distance (1.40 Å). HOMA indices are closer to 1 in these cases (an aromatic compound has an HOMA value close to 1, whereas a nonaromatic has value 0 or even lower). Moreover, we can observe that both bond distances and HOMA values are indicating that central rings (C and B) are more aromatic than the external ones (A). This is in good agreement with the existence of the proposed resonant forms (Scheme 2) since in most of the structures the aromatic sextet is maintained in the central rings but not in the external ones. Interestingly, HOMA values in between 0.5 and 0.7 are calculated for CPHs in their CS states, indicating a partial aromatic character of the 6-membered rings that reveals the importance of resonance structure **II** and analogues.

To gain deeper insight into the electronic structure of the Chichibabin diradical(oid)s (OSS and T states), we analyzed the Mulliken spin densities of those carbons contained in the main axis of symmetry of the molecule (see Tables S20−S30 of the SI for more details). We observe that in systems with small n values the spin densities of carbons in position 1 are close to 1 (or −1), whereas the other carbon atoms have values close to 0. By increasing n, the spin population values decrease in position 1 carbons and increase in position 2 carbons; for

example, in the R = H and n = 4 system, the populations of positions 1 and 2 are 0.7 and 0.2, respectively. Alternatively, in all cases, we have found values close to 0 for the position 3 carbons, indicating that the resonance forms with radicals in these positions are not particularly relevant for describing the OSS and T state structures.

The energies (ΔE_{CS-X}, where X = OSS or T) estimated by means of quantum chemical calculations, in most of the cases, suggest that the GS is a CS state for species with $n \leq 2$ and an OSS state for larger n compounds, having a situation like the one depicted in Figure 1 for species **8**. For systems with diradical character, we would expect a T GS according to the Hund rule. However, we found that even though the T state lies close to the OSS singlet, it is always higher in energy.[48,49]
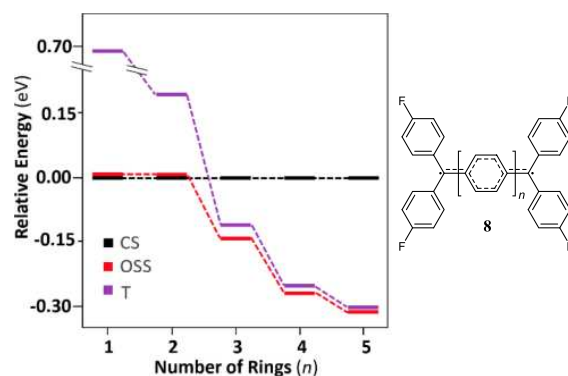
Figure 1. Energy (eV) diagram of the CS, OSS, and T states (referred to CS) depending on n for the R = p-fluorobenzene system (**8**).

This fact can be explained by the two-state model of Zilberg and Haas.[50] They attribute the extra stabilization of the OSS to the possible resonance structures that can exist in the OSS but not in the T form. Since in the T state, the parallel unpaired electrons cannot form a bond, some of the resonance structures are excluded.

Among all systems, there are three exceptions. The first one is system **3**, having a CS GS for $n = 1–3$ (Table 2). Then,

Table 2. Summary of the Calculated Relative Energies (meV) Referred to the CS State for OSS and T States of $n = 2$ and $n = 3$ Systems[a]

	$n = 2$		$n = 3$		
system	OSS	T	OSS	T	y
1	0.00	437.86	−93.82	−24.25	0.31
2	0.00	541.91	−20.00	98.42	0.07
3	0.00	608.17	−0.04	187.39	0.00
4	0.00	155.80	−72.36	−17.44	0.38
5	0.00	272.09	−78.53	−20.32	0.26
6	−60.59	−18.05	−192.30	−186.26	0.73
7	0.00	188.66	−139.32	−118.51	0.53
8	0.00	193.22	−133.72	−112.34	0.52
9	0.00	123.74	−133.37	−123.42	0.57
10	0.00	278.99	−107.44	−71.40	0.42
11	−2.59	130.68	−455.30	−428.07	0.41

[a]For $n = 3$, the diradical character (y) of the OSS systems is also included.

systems **6** and **11**, in which for $n = 1$ the GS is also CS, but in the case of $n = 2$, the OSS solution lies 60.59 and 2.59 meV, respectively, below the CS state. When the OSS solution is lower in energy than the CS, the CS solution can be considered a singlet excited state. In the case of T states, the general trends for the relative energies (with respect to the CS state) are dependent on the substituent nature in a manner similar to the OSS results for $n > 2$. As regards to EDG (**2** and **3**), T state lies above the CS up to $n = 3$. In the case of **6** and **11**, only the T state of $n = 1$ system is higher in energy than the CS, and in the remaining cases, H (**1**), EWG (**4** and **5**) and aromatic (**7**, **8**, **9**, and **10**) substituents, the T is less stable than the CS state for n up to 2. Interestingly, for compounds **6** and **11** with $n \geq 3$, the OSS and T states are much more stable than the CS. Especially, remarkable is the case of **11**$_3$ and **11**$_4$ where the OSS solution is more than 0.40 eV more stable than the CS one. Our study provides evidence that the exocyclic substituents have a direct effect on the nature of the GS of Chichibabin's systems. EDGs favor the CS form, whereas EWGs and aromatic groups stabilize the diradical form, consequently favoring the OSS and T situations. Our calculations indicate that **1**$_3$, **4**$_3$, **5**$_3$, and **6**$_2$ systems have almost degenerated CS and T states (with energy differences not larger than 0.03 eV), whereas almost all systems with $n = 5$ together with **11**$_3$ and **11**$_4$ have particularly stable diradical GS.

For all compounds, we observe a decrease of ΔE_{ST} when n is increased until reaching the degeneracy of the states (Figure 2). This is because at high n values the distance between radical centers increases, and hence, the energy difference between OSS and T states is reduced. There is a clear trend regarding the effect of increasing the chain length, that is the lowering of the singlet−triplet gap with the increasing number of n. Therefore, for small n values, we have CS CPHs; for larger n, CPHs are diradicals; and for intermediate n values,
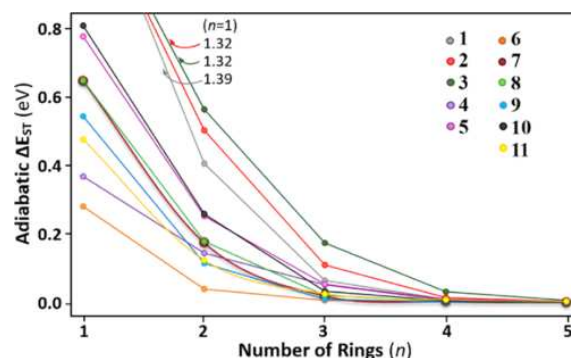
Figure 2. Adiabatic ΔE_{ST} (where S is the lowest singlet state, which can be CS or OS) against the number of rings, for R groups **1**−**11**.

CPHs are diradicaloids,[9] the borders between the different species being somewhat fuzzy and R dependent. This is corroborated by the increase of y values (see Computational Details) from 0 (CS species) to 1 (pure diradical) going from $n = 1$ to 5 (Table S19). Moreover, y is also affected by the exocyclic substituents (Table 2b), and the results are consistent with the structural and energetic measures. Systems **2**$_3$ and **3**$_3$ present CS character, whereas the others are diradicaloids with y values from 0.3 to 0.7, with the aromatic groups being the ones presenting larger y values. Finally, the trends in ΔE_{ST} value differ for small and large systems. For small n values (CS ground state), one can notice that there is a significant difference between the two EWG systems **4** and **5**. In the case of $n = 1$ and 2, the singlet−triplet energy gap for **5**, which has a large electron-accepting character, is larger than for **4**. On the other hand, for the case of EDG, there are no differences between both EDG **3** and **4**. For $n > 2$ (OSS ground state), ΔE_{ST} is almost the same for the two EWG **4** and **5** (see Figure 2), whereas for the two EDG **2** and **3**, there are some differences, ΔE_{ST} being somewhat larger for **3** having the substituent with higher π-donor character (R = NH$_2$).

We performed an exhaustive evaluation of the aromaticity using many electronic indices, MCI, PDI, I$_{ring}$, and FLU; magnetic NICS(0)$_{zz}$ and NICS(1)$_{zz}$ indices; and the previously commented geometric index, HOMA. In the case of MCI, PDI, and I$_{ring}$, positive values close to the result obtained for benzene are indicative of the aromatic character of the analyzed rings, whereas smaller values close to those of cyclohexane correspond to nonaromatic species (Table 3). In the case of FLU, the maximum aromaticity is achieved when FLU = 0. Finally, for the nucleus-independent chemical shift (NICS), negative values indicate that the compound is aromatic, and vice versa.

The trends of aromaticity values given by the different indices correlated with the CS-T energy gaps for compounds **1**, **3**, **5**, and **6** (one substituent belonging to one of the four different groups studied) are presented in Figure 3. In general, we can observe a good agreement between the different indices, showing the following orders from less to more aromatic: **1** < **3** < **5** < **6** in the CS singlet and **3** < **1** < **5** < **6** in the T state, with an exception in the case of NICS, which classifies **3** as the less aromatic compound in both cases, CS and T. For the **1**, **3**, and **5** CS structures, the values obtained resemble those of the nonaromatic cyclohexane and 1,4-cyclohexadiene results. Instead, for most of the T and some of the **6** CS forms, the results are more similar to those of benzene. ΔE_{ST} is small when the difference between the

Table 3. Aromaticity Indices of Reference Systems (Benzene, 1,4-Cyclohexadiene, and Cyclohexane) Calculated at the OPBE/cc-pVTZ Level of Theory

	MCI	PDI	I_{ring}	FLU	NICS(0)$_{zz}$	NICS(1)$_{zz}$
benzene	0.073	0.106	0.049	0.000	−15.2	−29.3
1,4-cyclohexadiene	0.002	0.020	0.002	0.073	26.1	4.4
cyclohexane	0.000	0.010	0.000	0.088	23.3	3.5
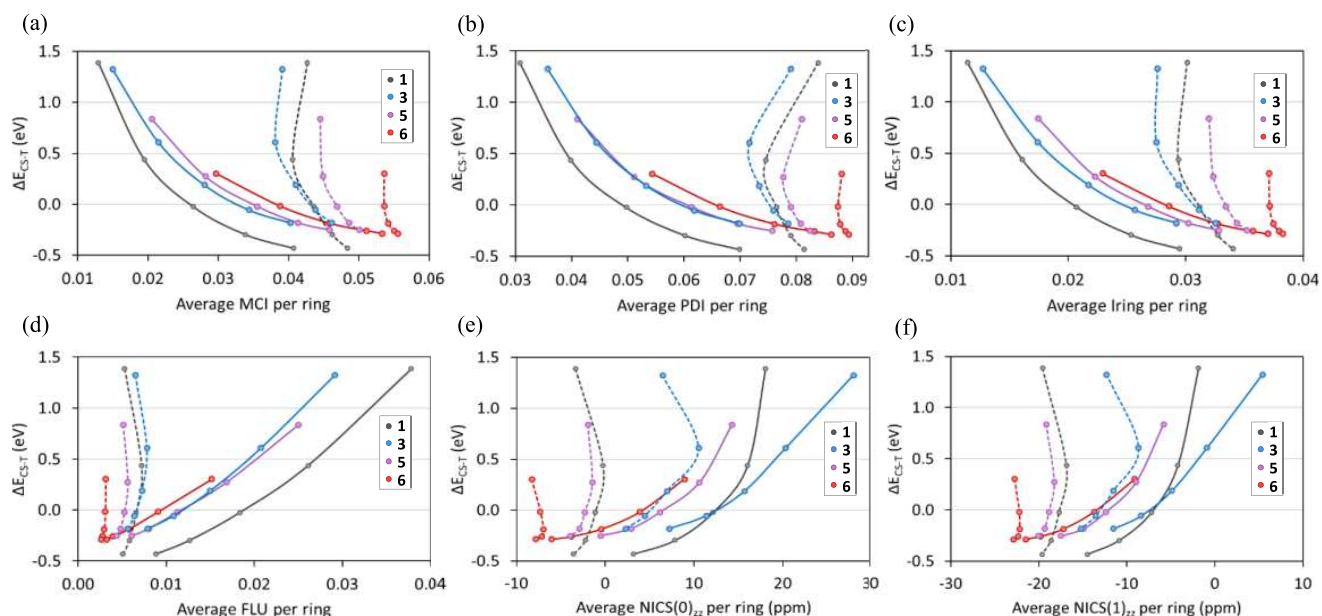
Figure 3. Singlet (CS)−triplet energy gaps as a function of average (a) MCI, (b) PDI, (c) I_{ring}, (d) FLU, (e) NICS(0)$_{zz}$, and (f) NICS(1)$_{zz}$ per ring for systems **1**, **3**, **5**, and **6** with n from 1 to 5. Solid and dashed lines correspond to singlet CS and the triplet values, respectively.

aromaticity of the triplet and CS states is minor and vice versa. Furthermore, it is important to mention that the T and OSS singlet states of CPHs are not 4N e⁻ Baird aromatic species as in the cyclopentadienyl cation but Hückel-type systems having 6π e⁻ per ring.

Figure 3 depicts the average aromaticity measures per ring. Depending on the number of rings and the symmetry and environment of these rings, we have defined four different ring types: A, B, C, and A′ (Figure 4a). A-type rings are located at the ends of the chain, and they are connected to two R groups on one side and another ring on the other side. B-type ones are surrounded by two other ring units but are not in the middle of the molecule. Finally, C and A′ type are in the center of the molecule with symmetric substitution but with the difference that C-type rings are in between two ring units whereas A′-type rings are in a terminal position.

Regarding the electronic aromaticity indices of each specific ring type, we observe that qualitatively MCI, PDI, I_{ring}, and FLU give the same results (see SI). The former four indices indicate that, as expected from resonance structures of Scheme 2, Chichibabin compounds are more aromatic in the T state than in the CS one, in which they are less aromatic (structures of type **II** provide some aromaticity, especially in the central rings) or are even nonaromatic, as can be seen for the case of A and A′ type of rings (Figure 4b). OSS structures are in between CS and T ones with n values from 3 to 5, and the difference between the OSS and T forms become less notable when n increases. The extra stabilization of the OSS comes from the quinoid resonance forms, which is not occurring in
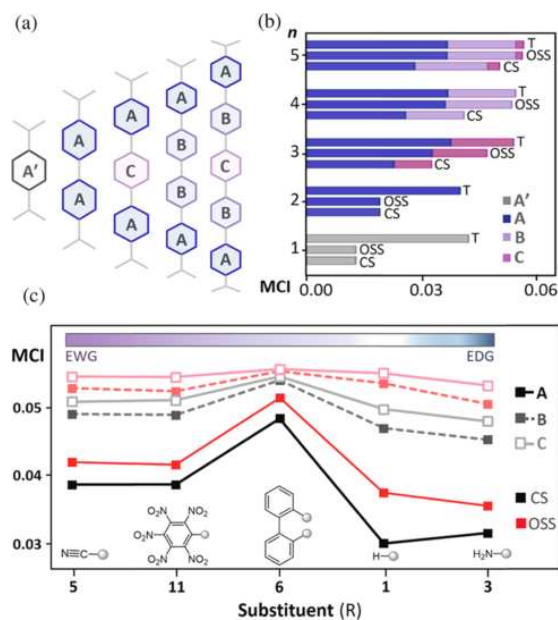
Figure 4. (a) Scheme of different ring types (A, A′, B, and C). MCI aromaticity indices (b) of A-, A′-, B-, and C-type rings for CS, OSS, and T states of system **1**$_n$ with n = 1 to 5 and (c) of A-, B-, and C-type rings for CS and OSS states of the R = **1**, **3**, **5**, **6**, and **11** systems with n = 5.

the case of the T. For this reason, the systems in the T state are more aromatic, as their unique structure is the benzoid form.

Figure 4b shows the behavior of the local aromaticity in 1_n species, which is the general trend found in CPHs. First, the internal rings B and C are more aromatic than the terminal A and A′ ones. Second, there is an increase in the aromaticity of B and C rings with n in both singlet and triplet states. A-type rings show the same trend for CS and OSS states, but in the case of the T state, the increase of aromaticity with increasing n is not observed (Figure 4b).

Results in Figure 4c show that the terminal substituents have an influence on the aromaticity of the compounds, especially on the external rings. EWG favors the T and OSS states stabilizing the diradical character and increasing the aromaticity of the rings. It seems that the aromaticity decreases going from strong EWG as cyanide to strong EDG as amine, with the exception of aromatic substituents, which are poor EWG (the phenyl group has a weak π-donor and inductive withdrawing character) but present the largest aromaticity values. The latter family is especially good in stabilizing the radical forms because it can be delocalized over the π-system, which also explains why the R = aromatic are the systems with the most aromatic rings, especially the A-type ones. We can also observe that the differences between diverse substituted Chichibabin compounds are less noticeable in the central rings than in the external ones. The particular case of **11**, which has the most stable OSS and T state structures, does not present the high aromatic character that we would expect and the values obtained are similar to the ones of **5**.

The evaluation of the aromaticity by means of the NICS index leads to results similar to those yield by the electronic indices (see Tables S34−S36), as it was explained in the general comparison thereby referring to Figure 3. Nevertheless, there are differences when comparing individually the distinct types of rings. For the A type in the CS and OSS cases, the aromaticity increases going from small to large n values and from EDG to EWG. On the contrary, in the T state, the aromaticity decreases significantly when n increases. However, with the electronic indices, we observe that there was no variation in the aromaticity of A rings with changing n and with NICS we found meaningful changes. For example, compound 1_n NICS$(0)_{zz}$ values for $n = 1-5$ are −3.3, −0.3, 1.8, 2.7, and 2.8. In B-type rings, the aromaticity increases with n for the OSS and CS, and it is maintained for the T. Finally, for C-type rings, the aromaticity increases when increasing n in all cases. It is likely that this particular behavior of the NICS indicator of aromaticity is caused by the coupling of the magnetic fields generated by neighboring rings.[51−53]

CONCLUSIONS

The molecular and electronic structures of Chichibabin's polycyclic hydrocarbons have been studied to discuss the effects of elongating the π-system and changing the exocyclic substituents. For large n systems, an increase of the twisting distortion is observed as a consequence of the H···H biphenyl-like repulsions, leading to a loss of planarity and conjugation. All CPHs systems present singlet−triplet energy gaps lower than 1.4 eV. Among them, most of the systems with $n > 2$ have small ΔE_{ST} ranging from 200 to 0.2 meV, thus being potential candidates for the design of new materials with NLO properties. The resonance structures proposed, together with the fact that the energy difference between OSS and the triplet is reduced when the distance between radical centers increases, gives a good explanation for the lowering of the ΔE_{ST} when going from $n = 1$ to 5. Species 1_3, 4_3, 5_3, and 6_2 have almost

degenerated CS and T states (with energy differences lower than 0.03 eV), whereas almost all systems with $n = 5$ as well as 11_3 and 11_4 have particularly stable diradical GS. The aromaticity measures show a gain of aromaticity with the increase of n. Central B and C rings are more aromatic than external A-type rings. Aromatic substituents and EWG tend to stabilize the diradical(oid) forms better than EDG. These findings help in understanding the effect of exocyclic substituents and π-system length on ΔE_{ST} values of Chichibabin diradical(oid)s and may aid in the design of tuned π-electron materials for molecular electronics.

COMPUTATIONAL DETAILS

All geometry optimization, energy, and nucleus-independent chemical shift (NICS) calculations were performed with the Gaussian16 set of programs.[54] To select an appropriate method for the calculations, several DFT functionals were tested and compared against CCSD(T)/cc-pVDZ//QCISD-(T)/cc-pVXZ (X = D, T) results for the R = H and $n = 1$ and 2 systems (see Tables S1−S3 in the SI). As a result of this test and also based on some calculations of spin-state splittings found in the literature,[55−60] we conclude that the best option for these systems is to use the OPBE/cc-pVTZ level of theory.[61,62] In addition, for meta- and para-benzyne, it was shown that pure generalized gradient approximation functionals such as OPBE were superior to hybrid functionals for the description of the open-shell singlet state.[63−65] Moreover, for systems $1_{1−5}$, we compared the OPBE and the range-separated LC-OPBE and ωB97xD results to see how long-range corrections affect the description of the systems with large n values (3−5). The range-separated functionals give larger spin contamination values, with $\langle \hat{S}^2 \rangle$ between 1.2 and 1.8 for the case of OSS and more than 2 for T (see Table S4 of SI). In the case of OSS systems, we perform broken-symmetry calculations giving as a result the collapse on CS species in the cases of $n \leq 2$ and OSS structures in the other cases. We have taken a pragmatic approach and have not applied spin contamination corrections for three reasons: (i) the concept of spin contamination is not completely meaningful at the DFT level because of the absence of a strict definition of the wave function;[66] (ii) when the overlap between open-shell orbitals is small, errors due to spin contamination are minor;[67] and (iii) for benzyne isomers, spin contamination corrections to DFT results lead to worse predictions of ΔE_{ST} as compared to experimental results.[68] We have checked the stability of the approximated DFT wave function for all species. The diradical character (y) of the OS systems has been estimated making use of the spin-unrestricted natural orbitals (UNOs) with the following index proposed by Kamada et al.[69−71]

$$ y = \frac{(1-T)^2}{1+T^2} \text{ and } T = \frac{n_{HOMO} - n_{LUMO}}{2} \quad (1) $$

where n_{HOMO} and n_{LUMO} are the occupation numbers of the bonding and antibonding UNOs.

The aromaticity of the electronic structures was studied using geometric (HOMA),[45−47] electronic[72] (PDI,[73] I$_{ring}$,[74] FLU,[75] and MCI[76]), and magnetic (NICS) aromaticity indices.[77,78] For the latter, we have evaluated three positions of the space NICS (0, 1, and −1) (shown in Figure S5 of SI). The aromaticity indices (except for NICS, which has been calculated with Gaussian16) have been computed using AIMall[79] together with ESI-3D packages.[75,80,81]

■ ASSOCIATED CONTENT

Ⓢ Supporting Information

The Supporting Information is available free of charge on the ACS Publications website at DOI: 10.1021/acsomega.9b00916.

> More detailed computational procedures; analysis of the conformers; and complete aromaticity results, y values, spin densities, and energy results (PDF)
>
> Coordinates of the OPBE/cc-pVTZ optimized geometries (XYZ)

■ AUTHOR INFORMATION

Corresponding Authors

*E-mail: albert.poater@udg.edu (A.P.).
*E-mail: miquel.sola@udg.edu (M.S.).

ORCID ⓘ

Albert Poater: 0000-0002-8997-2599
Miquel Solà: 0000-0002-1917-7450

Notes

The authors declare no competing financial interest.

■ ACKNOWLEDGMENTS

■ REFERENCES

(1) Tschitschibabin, A. E. Über einige phenylierte Derivate des p, p-Ditolyls. *Ber. Dtsch. Chem. Ges.* **1907**, *40*, 1810−1819.

(2) Lewis, D. E. Aleksei Yevgen'evich Chichibabin (1871−1945): A Century of Pyridine Chemistry. *Angew. Chem., Int. Ed.* **2017**, *56*, 9660−9668.

(3) Thiele, J.; Balhorn, H. Ueber einen chinoïden Kohlenwasserstoff. *Ber. Dtsch. Chem. Ges.* **1904**, *37*, 1463−1470.

(4) Müller, E.; Pfanz, H. Über biradikaloide Terphenylderivate. *Ber. Dtsch. Chem. Ges. A/B* **1941**, *74*, 1051−1074.

(5) McConnell, H. M. The Biradical Paradox. *J. Chem. Phys.* **1960**, *33*, 1868−1869.

(6) Montgomery, L. K.; Huffman, J. C.; Jurczak, E. A.; Grendze, M. P. The molecular structures of Thiele's and Chichibabin's hydrocarbons. *J. Am. Chem. Soc.* **1986**, *108*, 6004−6011.

(7) Sloan, G. J.; Vaughan, W. R. Stable Organic Biradicals. *J. Org. Chem.* **1957**, *22*, 750−761.

(8) Morozova, I. D.; Dyatkina, M. E. New data on biradicals. *Russ. Chem. Rev.* **1968**, *37*, 376.

(9) Abe, M. Diradicals. *Chem. Rev.* **2013**, *113*, 7011−7088.

(10) Sun, Z.; Ye, Q.; Chi, C.; Wu, J. Low band gap polycyclic hydrocarbons: from closed-shell near infrared dyes and semiconductors to open-shell radicals. *Chem. Soc. Rev.* **2012**, *41*, 7857−7889.

(11) Zeng, Z.; Shi, X.; Chi, C.; López Navarrete, J. T.; Casado, J.; Wu, J. Pro-aromatic and anti-aromatic π-conjugated molecules: an irresistible wish to be diradicals. *Chem. Soc. Rev.* **2015**, *44*, 6578−6596.

(12) Zeng, Z.; Ishida, M.; Zafra, J. L.; Zhu, X.; Sung, Y. M.; Bao, N.; Webster, R. D.; Lee, B. S.; Li, R.-W.; Zeng, W.; Li, Y.; Chi, C.; Navarrete, J. T. L.; Ding, J.; Casado, J.; Kim, D.; Wu, J. Pushing Extended p-Quinodimethanes to the Limit: Stable Tetracyano-oligo(N-annulated perylene)quinodimethanes with Tunable Ground States. *J. Am. Chem. Soc.* **2013**, *135*, 6363−6371.

(13) Gershoni-Poranne, R.; Rahalkar, A. P.; Stanger, A. The predictive power of aromaticity: quantitative correlation between aromaticity and ionization potentials and HOMO−LUMO gaps in oligomers of benzene, pyrrole, furan, and thiophene. *Phys. Chem. Chem. Phys.* **2018**, *20*, 14808−14817.

(14) Woon, K. L.; Ariffin, A.; Ho, K. W.; Chen, S.-A. Effect of conjugation and aromaticity of 3,6 di-substituted carbazoles on triplet energy and the implication of triplet energy in multiple-cyclic aromatic compounds. *RSC Adv.* **2018**, *8*, 9850−9857.

(15) Casado, J.; Ponce Ortiz, R.; López Navarrete, J. T. Quinoidal oligothiophenes: new properties behind an unconventional electronic structure. *Chem. Soc. Rev.* **2012**, *41*, 5672−5686.

(16) Shi, X.; Lee, S.; Son, M.; Zheng, B.; Chang, J.; Jing, L.; Huang, K.-W.; Kim, D.; Chi, C. Pro-aromatic bisphenaleno-thieno[3,2-b]thiophene versus anti-aromatic bisindeno-thieno[3,2-b]thiophene: different ground-state properties and applications in field-effect transistors. *Chem. Commun.* **2015**, *51*, 13178−13180.

(17) Ai, X.; Evans, E. W.; Dong, S.; Gillett, A. J.; Guo, H.; Chen, Y.; Hele, T. J. H.; Friend, R. H.; Li, F. Efficient radical-based light-emitting diodes with doublet emission. *Nature* **2018**, *563*, 536−540.

(18) Chulanova, E. A.; Pritchina, E. A.; Malaspina, L. A.; Grabowsky, S.; Mostaghimi, F.; Beckmann, J.; Bagryanskaya, I. Y.; Shakhova, M. V.; Konstantinova, L. S.; Rakitin, O. A.; Gritsan, N. P.; Zibarev, A. V. New Charge-Transfer Complexes with 1,2,5-Thiadiazoles as Both Electron Acceptors and Donors Featuring an Unprecedented Addition Reaction. *Chem. - Eur. J.* **2017**, *23*, 852−864.

(19) Burrezo, P. M.; Domínguez, R.; Zafra, J. L.; Pappenfus, T. M.; de la Cruz, P.; Welte, L.; Janzen, D. E.; López Navarrete, J. T.; Langa, F.; Casado, J. Oligomers of cyclopentadithiophene-vinylene in aromatic and quinoidal versions and redox species with intermediate forms. *Chem. Sci.* **2017**, *8*, 8106−8114.

(20) Prabhakar, C.; Yesudas, K.; Bhanuprakash, K.; Rao, V. J.; Santosh Kumar, R. S.; Rao, D. N. Linear and Nonlinear Optical Properties of Mesoionic Oxyallyl Derivatives: Enhanced Non-Resonant Third Order Optical Nonlinearity in Croconate Dyes. *J. Phys. Chem. C* **2008**, *112*, 13272−13280.

(21) Fukuda, K.; Fujiyoshi, J.-y.; Minamida, Y.; Nagami, T.; Matsui, H.; Ito, S.; Kishi, R.; Kitagawa, Y.; Champagne, B.; Nakano, M.; et al. Theoretical investigation of curved π-conjugated fullerene flakes: open-shell character, aromaticity, and third-order nonlinear optical property. *J. Phys. Org. Chem.* **2017**, *30*, No. e3581.

(22) Schoeller, W. W. The Niecke Biradicals and Their Congeners − The Journey from Stable Biradicaloids to Their Utilization for the Design of Nonlinear Optical Properties. *Eur. J. Inorg. Chem.* **2019**, *2019*, 1495−1506.

(23) Nakano, M.; Champagne, B. Nonlinear optical properties in open-shell molecular systems. *Wiley Interdiscip. Rev.: Comput. Mol. Sci.* **2016**, *6*, 198−210.

(24) Muhammad, S.; Nakano, M.; Al-Sehemi, A. G.; Kitagawa, Y.; Irfan, A.; Chaudhry, A. R.; Kishi, R.; Ito, S.; Yoneda, K.; Fukuda, K. Role of a singlet diradical character in carbon nanomaterials: a novel hot spot for efficient nonlinear optical materials. *Nanoscale* **2016**, *8*, 17998−18020.

(25) Fukuda, K.; Suzuki, Y.; Matsui, H.; Nagami, T.; Kitagawa, Y.; Champagne, B.; Kamada, K.; Yamamoto, Y.; Nakano, M. Tuning Nonlinear Optical Properties by Altering the Diradical and Charge-Transfer Characteristics of Chichibabin's Hydrocarbon Derivatives. *ChemPhysChem* **2017**, *18*, 142−148.

(26) Kishi, R.; Dennis, M.; Fukuda, K.; Murata, Y.; Morita, K.; Uenaka, H.; Nakano, M. Theoretical Study on the Electronic Structure and Third-Order Nonlinear Optical Properties of Open-Shell Quinoidal Oligothiophenes. *J. Phys. Chem. C* **2013**, *117*, 21498−21508.

(27) Burrezo, P. M.; Zafra, J. L.; López Navarrete, J. T.; Casado, J. Quinoidal/Aromatic Transformations in π-Conjugated Oligomers: Vibrational Raman studies on the Limits of Rupture for π-Bonds. *Angew. Chem., Int. Ed.* **2017**, *56*, 2250−2259.

(28) Kayahara, E.; Kouyama, T.; Kato, T.; Takaya, H.; Yasuda, N.; Yamago, S. Isolation and Characterization of the Cycloparaphenylene

Radical Cation and Dication. *Angew. Chem., Int. Ed.* **2013**, *52*, 13722−13726.

(29) Kayahara, E.; Kouyama, T.; Kato, T.; Yamago, S. Synthesis and Characterization of [n]CPP (n = 5, 6, 8, 10, and 12) Radical Cation and Dications: Size-Dependent Absorption, Spin, and Charge Delocalization. *J. Am. Chem. Soc.* **2016**, *138*, 338−344.

(30) Rottschäfer, D.; Busch, J.; Neumann, B.; Stammler, H.-G.; van Gastel, M.; Kishi, R.; Nakano, M.; Ghadwal, R. S. Diradical Character Enhancement by Spacing: N-Heterocyclic Carbene Analogues of Müller's Hydrocarbon. *Chem. - Eur. J.* **2018**, *24*, 16537−16542.

(31) Rottschäfer, D.; Ho, N. K. T.; Neumann, B.; Stammler, H.-G.; van Gastel, M.; Andrada, D. M.; Ghadwal, R. S. N-Heterocyclic Carbene Analogues of Thiele and Chichibabin Hydrocarbons. *Angew. Chem., Int. Ed.* **2018**, *57*, 5838−5842.

(32) Rottschäfer, D.; Neumann, B.; Stammler, H.-G.; Andrada, D. M.; Ghadwal, R. S. Kekulé diradicaloids derived from a classical N-heterocyclic carbene. *Chem. Sci.* **2018**, *9*, 4970−4976.

(33) Tan, G.; Wang, X. Isolable Bis(triarylamine) Dications: Analogues of Thiele's, Chichibabin's, and Müller's Hydrocarbons. *Acc. Chem. Res.* **2017**, *50*, 1997−2006.

(34) Wang, J.; Xu, X.; Phan, H.; Herng, T. S.; Gopalakrishna, T. Y.; Li, G.; Ding, J.; Wu, J. Stable Oxindolyl-Based Analogues of Chichibabin's and Müller's Hydrocarbons. *Angew. Chem., Int. Ed.* **2017**, *56*, 14154−14158.

(35) Zeng, Z.; Sung, Y. M.; Bao, N.; Tan, D.; Lee, R.; Zafra, J. L.; Lee, B. S.; Ishida, M.; Ding, J.; López Navarrete, J. T.; Li, Y.; Zeng, W.; Kim, D.; Huang, K.-W.; Webster, R. D.; Casado, J.; Wu, J. Stable Tetrabenzo-Chichibabin's Hydrocarbons: Tunable Ground State and Unusual Transition between Their Closed-Shell and Open-Shell Resonance Forms. *J. Am. Chem. Soc.* **2012**, *134*, 14513−14525.

(36) Majewski, M. A.; Chmielewski, P. J.; Chien, A.; Hong, Y.; Lis, T.; Witwicki, M.; Kim, D.; Zimmerman, P. M.; Stępień, M. 5,10-Dimesityldiindeno[1,2-a:2′,1′-i]phenanthrene: a stable biradicaloid derived from Chichibabin's hydrocarbon. *Chem. Sci.* **2019**, *10*, 3413−3420.

(37) Gallagher, N.; Zhang, H.; Junghoefer, T.; Giangrisostomi, E.; Ovsyannikov, R.; Pink, M.; Rajca, S.; Casu, M. B.; Rajca, A. Thermally and Magnetically Robust Triplet Ground State Diradical. *J. Am. Chem. Soc.* **2019**, *141*, 4764−4774.

(38) Jiang, C.; Bang, Y.; Wang, X.; Lu, X.; Lim, Z.; Wei, H.; El-Hankari, S.; Wu, J.; Zeng, Z. Tetrabenzo-Chichibabin's hydrocarbons: substituent effects and unusual thermochromic and thermomagnetic behaviours. *Chem. Commun.* **2018**, *54*, 2389−2392.

(39) Ponce Ortiz, R.; Casado, J.; Rodríguez González, S.; Hernández, V.; López Navarrete, J. T.; Viruela, P. M.; Ortí, E.; Takimiya, K.; Otsubo, T. Quinoidal Oligothiophenes: Towards Biradical Ground-State Species. *Chem. - Eur. J.* **2010**, *16*, 470−484.

(40) Fukuda, K.; Nakano, M. Intramolecular Charge Transfer Effects on the Diradical Character and Second Hyperpolarizabilities of Open-Shell Singlet X−π−X (X = Donor/Acceptor) Systems. *J. Phys. Chem. A* **2014**, *118*, 3463−3471.

(41) Clar, E. *The Aromatic Sextet*; Wiley: New York, 1972.

(42) Solà, M. Forty years of Clar's aromatic π-sextet rule. *Front. Chem.* **2013**, *1*, 22.

(43) Almenningen, A.; Bastiansen, O.; Fernholt, L.; Cyvin, B. N.; Cyvin, S. J.; Samdal, S. Structure and barrier of internal rotation of biphenyl derivatives in the gaseous state: Part 1. The molecular structure and normal coordinate analysis of normal biphenyl and pedeuterated biphenyl. *J. Mol. Struct.* **1985**, *128*, 59−76.

(44) Poater, J.; Solà, M.; Bickelhaupt, F. M. Hydrogen−Hydrogen Bonding in Planar Biphenyl, Predicted by Atoms-In-Molecules Theory, Does Not Exist. *Chem. - Eur. J.* **2006**, *12*, 2889−2895.

(45) Kruszewski, J.; Krygowski, T. M. Definition of aromaticity basing on the harmonic oscillator model. *Tetrahedron Lett.* **1972**, *13*, 3839−3842.

(46) Krygowski, T. M. Crystallographic studies of Inter- and Intra-Molecular Interactions Reflected in benzenoid Hydrocarbons. Non-equivalence of Indices of Aromaticity. *J. Chem. Inf. Comput. Sci.* **1993**, *33*, 70−78.

(47) Krygowski, T. M.; Cyrański, M. K. Structural Aspects of Aromaticity. *Chem. Rev.* **2001**, *101*, 1385−1420.

(48) Borden, W. T.; Davidson, E. R. Theoretical studies of diradicals containing four π electrons. *Acc. Chem. Res.* **1981**, *14*, 69−76.

(49) Borden, W. T. Diradicals. In *Encyclopedia of Computational Chemistry*; Schleyer, P. v. R.; Allinger, N. L.; Clark, T.; Gasteiger, J.; Kollman, P. A.; Schaefer, H. F., III; Schreiner, P. R., Eds.; John Wiley & Sons: Chichester, 1998; pp 708−722.

(50) Zilberg, S.; Haas, Y. Two-State Model of Antiaromaticity: The Low Lying Singlet States. *J. Phys. Chem. A* **1998**, *102*, 10843−10850.

(51) Poater, J.; Solà, M.; Viglione, R. G.; Zanasi, R. Local Aromaticity of the Six-Membered Rings in Pyracylene. A Difficult Case for the NICS Indicator of Aromaticity. *J. Org. Chem.* **2004**, *69*, 7537−7542.

(52) Osuna, S.; Poater, J.; Bofill, J. M.; Alemany, P.; Solà, M. Are nucleus-independent (NICS) and ^{1}H NMR chemical shifts good indicators of aromaticity in p-stacked polyfluorenes? *Chem. Phys. Lett.* **2006**, *428*, 191−195.

(53) Zhao, L.; Grande-Aztatzi, R.; Foroutan-Nejad, C.; Ugalde, J. M.; Frenking, G. Aromaticity, the Hückel 4n + 2 Rule and Magnetic Current. *ChemistrySelect* **2017**, *2*, 863−870.

(54) Frisch, M. J.; Trucks, G. W.; Schlegel, H. B.; Scuseria, G. E.; Robb, M. A.; Cheeseman, J. R.; Scalmani, G.; Barone, V.; Petersson, G. A.; Nakatsuji, H.; Li, X.; Caricato, M.; Marenich, A. V.; Bloino, J.; Janesko, B. G.; Gomperts, R.; Mennucci, B.; Hratchian, H. P.; Ortiz, J. V.; Izmaylov, A. F.; Sonnenberg, J. L.; Williams-Young, F.; Ding, F.; Lipparini, F.; Egidi, F.; Goings, J.; Peng, B.; Petrone, A.; Henderson, T.; Ranasinghe, D.; Zakrzewski, V. G.; Gao, J.; Rega, N.; Zheng, G.; Liang, W.; Hada, M.; Ehara, M.; Toyota, K.; Fukuda, R.; Hasegawa, J.; Ishida, M.; Nakajima, T.; Honda, Y.; Kitao, O.; Nakai, H.; Vreven, T.; Throssell, K.; Montgomery, J. A., Jr.; Peralta, J. E.; Ogliaro, F.; Bearpark, M. J.; Heyd, J. J.; Brothers, E. N.; Kudin, K. N.; Staroverov, V. N.; Keith, T. A.; Kobayashi, R.; Normand, J.; Raghavachari, K.; Rendell, A. P.; Burant, J. C.; Iyengar, S. S.; Tomasi, J.; Cossi, M.; Millam, J. M.; Klene, M.; Adamo, C.; Cammi, R.; Ochterski, J. W.; Martin, R. L.; Morokuma, K.; Farkas, O.; Foresman, J. B.; Fox, D. J. *Gaussian 16*, revision B.01; Gaussian Inc.: Wallingford, CT, 2016.

(55) Güell, M.; Solà, M.; Swart, M. Spin-state splittings of iron(II) complexes with trispyrazolyl ligands. *Polyhedron* **2010**, *29*, 84−93.

(56) Swart, M.; Güell, M.; Solà, M. A multi-scale approach to spin crossover in Fe(II) compounds. *Phys. Chem. Chem. Phys.* **2011**, *13*, 10449−10456.

(57) Swart, M.; Gruden, M. Spinning around in Transition-Metal Chemistry. *Acc. Chem. Res.* **2016**, *49*, 2690−2697.

(58) Feldt, M.; Phung, Q. M.; Pierloot, K.; Mata, R. A.; Harvey, J. N. Limits of Coupled-Cluster Calculations for Non-Heme Iron Complexes. *J. Chem. Theory Comput.* **2019**, *15*, 922−937.

(59) Radoń, M. Benchmarking quantum chemistry methods for spin-state energetics of iron complexes against quantitative experimental data. *Phys. Chem. Chem. Phys.* **2019**, *21*, 4854−4870.

(60) Chen, H.; Lai, W.; Shaik, S. Exchange-Enhanced H-Abstraction Reactivity of High-Valent Nonheme Iron(IV)-Oxo from Coupled Cluster and Density Functional Theories. *J. Phys. Chem. Lett.* **2010**, *1*, 1533−1540.

(61) Handy, N. C.; Cohen, A. J. Left-right correlation energy. *Mol. Phys.* **2001**, *99*, 403−412.

(62) Dunning, T. H. Gaussian basis sets for use in correlated molecular calculations. I. The atoms boron through neon and hydrogen. *J. Chem. Phys.* **1989**, *90*, 1007−1023.

(63) Winkler, M.; Sander, W. The Structure of meta-Benzyne Revisited. A Close Look into σ-Bond Formation. *J. Phys. Chem. A* **2001**, *105*, 10422−10432.

(64) Schreiner, P. R. Monocyclic Enediynes: Relationships between Ring Sizes, Alkyne Carbon Distances, Cyclization Barriers, and Hydrogen Abstraction Reactions. Singlet−Triplet Separations of Methyl-Substituted p-Benzynes. *J. Am. Chem. Soc.* **1998**, *120*, 4184−4190.

(65) Cramer, C. J. Bergman, Aza-Bergman, and Protonated Aza-Bergman Cyclizations and Intermediate 2,5-Arynes: Chemistry and Challenges to Computation. *J. Am. Chem. Soc.* **1998**, *120*, 6261−6269.

(66) Gräfenstein, J.; Hjerpe, A. M.; Kraka, E.; Cremer, D. An Accurate Description of the Bergman Reaction Using Restricted and Unrestricted DFT: Stability Test, Spin Density, and On-Top Pair Density. *J. Phys. Chem. A* **2000**, *104*, 1748−1761.

(67) Gräfenstein, J.; Kraka, E.; Filatov, M.; Cremer, D. Can Unrestricted Density-Functional Theory Describe Open Shell Singlet Biradicals? *Int. J. Mol. Sci.* **2002**, *3*, 360−394.

(68) Poater, J.; Bickelhaupt, F. M.; Solà, M. Didehydrophenanthrenes: Structure, Singlet−Triplet Splitting, and Aromaticity. *J. Phys. Chem. A* **2007**, *111*, 5063−5070.

(69) Kamada, K.; Ohta, K.; Shimizu, A.; Kubo, T.; Kishi, R.; Takahashi, H.; Botek, E.; Champagne, B.; Nakano, M. Singlet Diradical Character from Experiment. *J. Phys. Chem. Lett.* **2010**, *1*, 937−940.

(70) Nakano, M. Open-Shell-Character-Based Molecular Design Principles: Applications to Nonlinear Optics and Singlet Fission. *Chem. Rec.* **2017**, *17*, 27−62.

(71) Yamaguchi, K. The electronic structures of biradicals in the unrestricted Hartree-Fock approximation. *Chem. Phys. Lett.* **1975**, *33*, 330−335.

(72) Feixas, F.; Matito, E.; Poater, J.; Solà, M. Quantifying aromaticity with electron delocalisation measures. *Chem. Soc. Rev.* **2015**, *44*, 6434−6451.

(73) Poater, J.; Fradera, X.; Duran, M.; Solà, M. The Delocalization Index as an Electronic Aromaticity Criterion. Application to a Series of Planar Polycyclic Aromatic Hydrocarbons. *Chem. - Eur. J.* **2003**, *9*, 400−406.

(74) Giambiagi, M.; de Giambiagi, M. S.; dos Santos, C. D.; de Figueiredo, A. P. Multicenter bond indices as a measure of aromaticity. *Phys. Chem. Chem. Phys.* **2000**, *2*, 3381−3392.

(75) Matito, E.; Duran, M.; Solà, M. The aromatic fluctuation index (FLU): A new aromaticity index based on electron delocalization. *J. Chem. Phys.* **2005**, *122*, No. 014109. Matito, E.; Duran, M.; Solà, M. Erratum: "The aromatic fluctuation index (FLU): A new aromaticity index based on electron delocalization". *J. Chem. Phys.* **2006**, *125*, No. 059901.

(76) Bultinck, P.; Ponec, R.; Van Damme, S. Multicenter bond indices as a new measure of aromaticity in polycyclic aromatic hydrocarbons. *J. Phys. Org. Chem.* **2005**, *18*, 706−718.

(77) Chen, Z.; Wannere, C. S.; Corminboeuf, C.; Puchta, R.; Schleyer, P. v. R. Nucleus-Independent Chemical Shifts (NICS) as an Aromaticity Criterion. *Chem. Rev.* **2005**, *105*, 3842−3888.

(78) Schleyer, P. v. R.; Maerker, C.; Dransfeld, A.; Jiao, H.; van Eikema Hommes, N. J. R. Nucleus-Independent Chemical Shifts: A simple and Efficient Aromaticity Probe. *J. Am. Chem. Soc.* **1996**, *118*, 6317−6318.

(79) Keith, T. A. *AIMAll*, version 14.11.23; TK Gristmill Software: Overland Park KS, 2014.

(80) Matito, E. *ESI-3D: Electron Sharing Indexes Program for 3D Molecular Space Partitioning*; Institute of Computational Chemistry and Catalysis: Girona, Catalonia, Spain, http://iqc.udg.es/~eduard/ESI, 2014.

(81) Matito, E.; Solà, M.; Salvador, P.; Duran, M. Electron Sharing Indexes at the Correlated Level. Application to Aromaticity Measures. *Faraday Discuss.* **2007**, *135*, 325−345.

5 Aromaticity of Systems with Complex Molecular Topologies

5.1 Aromaticity in (Sub)Phthalocyanine and Related Systems

5.1.1 From (Sub)Porphyrin to (Sub)Phthalocyanine: Aromaticity Signatures in the UV-Vis Absorption Spectra

This section corresponds to the following unpublished manuscript:

S. Escayola, J. Labella, D. W. Szczepanik, A. Poater, T. Torres, M. Solà*, E. Matito*. *In preparation.*

From (Sub)Porphyrins to (Sub)Phthalocyanines:
Aromaticity Signatures in the UV-Vis Absorption Spectra

Sílvia Escayola,[a,b] Jorge Labella,[c] Dariusz W. Szczepanik,[d] Albert Poater,[a] Tomas Torres,[c,e,f] Miquel Solà,*[a] Eduard Matito*[b,g]

[a]*Institut de Química Computacional i Catàlisi and Departament de Química, Universitat de Girona, C/ Maria Aurèlia Capmany, 69, 17003 Girona, Catalonia, Spain.*
[b]*Donostia International Physics Center (DIPC), Donostia, Euskadi, Spain.*
[c]*Departamento de Química Orgánica, Universidad Autónoma de Madrid, Madrid 28049, Spain.*
[d]*Department of Theoretical Chemistry, Faculty of Chemistry, Jagiellonian University, 30-387 Kraków, Poland.*
[e]*Institute for Advanced Research in Chemical Sciences (IAdChem), Universidad Autónoma de Madrid, Madrid, 28049, Spain.*
[f]*IMDEA-Nanociencia, Campus de Cantoblanco, Madrid, 28049, Spain.*
[g]*Ikerbasque Foundation for Science, 48011 Bilbao, Euskadi, Spain.*

emails: miquel.sola@udg.edu; ematito@gmail.com

ABSTRACT

The advancement of synthetic methods has significantly enhanced our ability to tailor porphyrin derivatives with specific desired properties. This study examines substituted phthalocyanines and their contracted analogs, subphthalocyanines, which are characterized by nonplanar, bowl-shaped geometries. Central to these macrocycles is their extensive π-conjugated system, which confers distinctive properties, including aromatic ring currents. Metalloporphyrins exhibit characteristic Q and Soret bands within their UV-Vis absorption spectra, the positions of which vary with the molecular structure of each system. Through a combined computational and experimental study, we elucidate the relationship between the spectroscopic features and the degree of aromaticity. Notably, we establish a direct correlation between the aromaticity of the external conjugated pathways and the Q bands. This insight is pivotal for pinpointing modifications in porphyrinoid structures that lead to marked shifts in UV-Vis bands. Our findings offer a strategic framework for designing novel phthalocyanine derivatives with custom-tailored properties.

1

INTRODUCTION

Over the last century, the continuous improvement of synthetic methodologies for generating porphyrin derivatives converged to the point where these can be obtained based on targeted properties.[1] Among the wide variety of systems, some interesting examples are phthalocyanines (Pcs),[2-4] porphyrazines (Pzs),[5,6] tetrabenzoporphyrins (TBPs), and their respective ring-contracted versions, subporphyrins (SubPs),[7] subphthalocyanines (SubPcs),[7-9] subporphyrazines (SubPzs),[8] and tribenzosubporphyrins (TBSubPs),[10] see Scheme 1. The former are aromatic and composed of four isoindole units, interconnected via nitrogen (N) or methine (=CH−) bridges (at the *meso* positions, Scheme 1)[11,12] and tend to be highly planar unless distortion is forced by addition of bulky substituents or large metal ions, as observed in some metal substituted Pcs and TBPs.[13,14] The latter, also aromatic, only have three isoindole moieties and adopt nonplanar bowl-shaped geometries.[15]
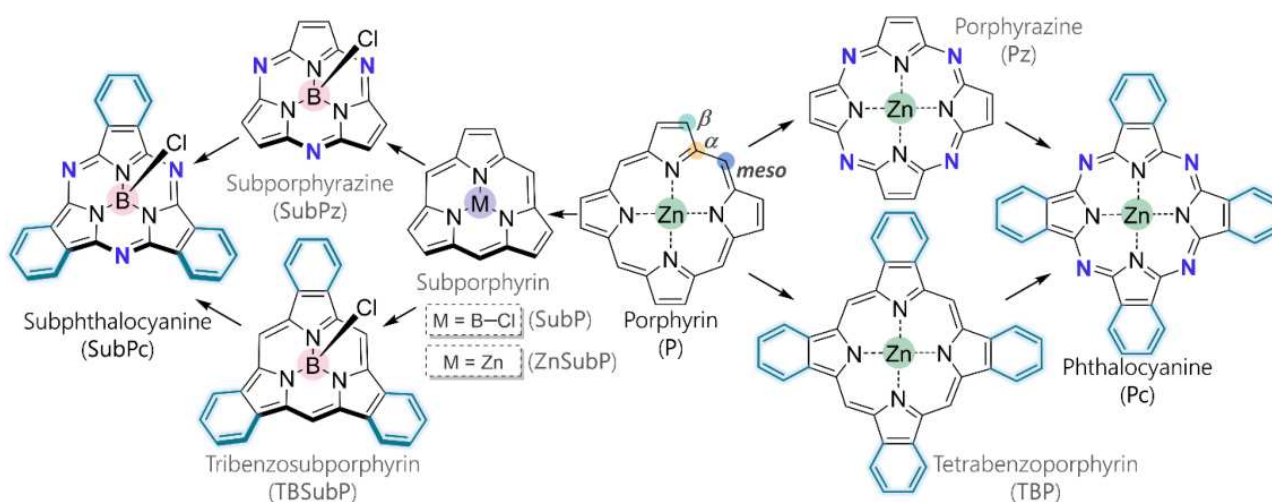
Scheme 1. Metallo or B−X coordinated (sub)porphyrins and (sub)phthalocyanines included in this study. The structural differences that relate porphyrin with phthalocyanine and subphthalocyanine are highlighted in dark blue (N-*meso*) and turquoise (fused 6-MR). In subporphyrin, we considered both central Zn and B−Cl coordination.

A key feature of these macrocyclic compounds is the extended π-conjugated system, which is responsible for their unique properties. Compared to porphyrin, (Sub)Pcs exhibit characteristic Ultraviolet–Visible (UV-Vis) absorption spectra, with (blue)red-shifted Q bands and blue-shifted Soret, or B, bands. According to the Gouterman four-orbital model for porphyrins,[16-18] Q and B bands arise from π–π* transitions and can be understood by considering the four frontier orbitals: a_{2u}, a_{1u}, and two e_g (corresponding to HOMO-1, HOMO, LUMO, and LUMO+1, which will be referred to as H-1, H, L, and L+1, respectively), depicted in Figure 1. The different orbital mixing splits the

resulting excited states into lower-energy, Q bands ($S_0 \rightarrow S_1$), and higher-energy, Soret bands ($S_0 \rightarrow S_2$).[19]
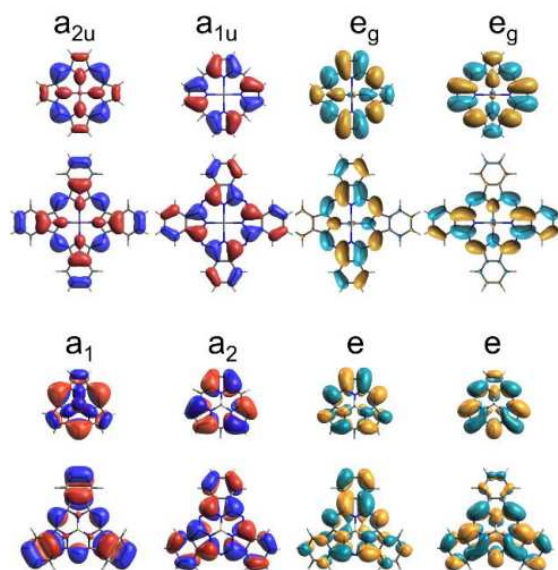
Figure 1. Spatial representation of frontier a_{2u}, a_{1u}, and e_g (or a_1, a_2, and e in C_{3v}) molecular orbitals, with an isocontour of 0.02, from top to bottom for **P**, **Pc**, **SubP**, and **SubPc**. In the case of **SubPc**, the a_1 orbital corresponds to the HOMO-3.

The typical absorption spectra of metalloporphyrins consist of two weak Q bands at 500-650 nm and a Soret intense band at 370−450 nm.[19] In the case of metallophthalocyanines, Q and B bands lie around 600−800 nm and 300−400 nm, respectively, whereas in subphthalocyanines, Q and B bands appear at 460−560 and 260−370 nm regions.[8] In Zn-Phthalocyanine (**Pc**) and Subphthalocyanine (**SubPc**), the relative intensity of Q and Soret bands is reversed compared to Zn-Porphyrin (**P**). This change has been primarily attributed to the N–*meso* substitution that breaks the a_{2u}–a_{1u} near-degeneracy, responsible for the low intensity of Q bands, selectively stabilizing the a_{2u} orbital, thereby making the $S_0 \rightarrow S_1$ transition fully permitted.[20,21] Their characteristic UV–Vis spectra, low-lying singlet (S_1)–triplet (T_1) energy gaps ($\Delta E_{T_1 \rightarrow S_1}$), H–L gaps, and other properties (*e.g.* conductance)[22] make them optimal candidates for solar cells,[3,23-26] nonlinear optics,[27] molecular electronics,[28] and photonics.[29,30] Furthermore, (sub)phthalocyanine derivatives are unique photoactive materials to prepare energy and electron donor-acceptor systems.[31] In this regard, notable is the use of Pcs complexing heavy metals for triplet-triplet annihilation upconversion (TTA-UC),[32-35] and the use of SubPcs and SubPzs for singlet-fission downconversion (SF-DC).[36-38] Overall, these compounds are promising materials for a wide array of applications. However, a clear establishment of structure–property and property–property relationships is crucial to fully exploit their highly tunable potential and applications. Some examples along the lines of identifying these relationships

are the independent studies of Zang *et al*.,[20] Holst *et al*.,[39] and Peterson *et al*.,[40] where they found a correspondence between computed H–L gaps and spectroscopic properties or variations in S_1 and T_1 state energies. The mere calculation of H–L gaps might not be adequate to pinpoint these properties due to potential accuracy issues, as highlighted by Holst and coworkers.[39] There is an ongoing need for streamlined methods that enable quicker screenings through alternative computational analyses. Several authors have unveiled connections between the (anti)aromaticity in diverse free-base porphyrinoids, their UV–Vis spectra, and nonlinear optical properties.[41-46] Ke *et al*. recently introduced a way to regulate the properties of silicon(IV) phthalocyanines by switching their aromaticity.[47] These discoveries hint at a potential interplay between aromaticity and photophysical properties of porphyrinoids. Expanding upon this research, we propose the use of chemical bonding and aromaticity analyses as a systematic procedure to identify π-system–UV–Vis absorption and $\Delta E_{T_1 \to S_1}$ correlations in porphyrin-related compounds.

Aromaticity is widely acknowledged as a pivotal concept in characterizing electronic structures,[48-52] the Hückel rule (4N+2)[53-55] offering the most straightforward approach to predicting the aromatic nature of molecules. While the application of the Hückel rule is primarily focused on planar monocyclic molecules, such as annulenes and their analogues,[56] its simplicity spurred researchers to modify it for intricate systems.[57-60] Traditionally, the aromaticity of porphyrins and Pcs has been ascribed to an 18π–electron aromatic cycle (and a 14π−electron cycle in SubPs and SubPcs) akin to [18]annulene, adhering to the Hückel rule.[61,62] Obviously, this rule cannot differentiate among molecules with an identical number of π–electrons, and falls short when accounting for the aromaticity of some nonplanar systems, other tools becoming essential to comprehensively address aromaticity.[41,42,44,45,63-65] Aromaticity investigations of Pcs and, especially, SubPcs are sparse and primarily restricted to nucleus-independent chemical shift (NICS) and the harmonic oscillator model of aromaticity (HOMA).[66-71] Given the intricacy of these molecules—attributable to their size, topology, and the presence of multiple π-electron circuits—and the inherent limitations of NICS and HOMA as aromaticity gauges,[72-74] there is a compelling case for using more reliable aromaticity descriptors. A more holistic method, integrating both global and local aromaticity metrics, remains desirable to unveil the most favorable pathways for electron delocalization in Pcs and SubPcs.

One of the main challenges in the description of aromaticity in porphyrinoids is the identification of the most conjugated pathway among the complex ring constructed of bridged rings (including but not limited to pyrrole, isoindole, and derivatives), a task which is not suited for some popular aromaticity indicators such as global NICS analysis. The molecule can be divided into different

regions, including *benzo* (b), *outer* (o), and *inner* (i), as defined in Scheme 2. From these regions, potential circuits emerge. Determining the key pathways in such a complex system requires careful analysis and consideration of all possible routes. Over the last few years, significant efforts have been dedicated to the development and application of specific electronic indices to large rings.[63-65,75,76] The latter need emerges from the inadequacy of the most reliable indices of aromaticity[72] for their application to ring structures with more than fourteen atoms.[75]
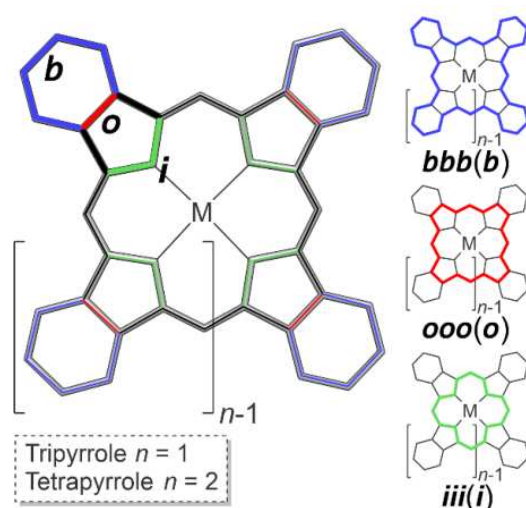
Scheme 2. Possible routes to follow, i *inner*, o *outer*, and b *benzo*, at each pyrrole or isoindole moiety, which define the closed pathways along the molecule. Three examples are the bbb(b), ooo(o), and iii(i) pathways in blue, red, and green, respectively.

In this work, we employ aromaticity indices to identify the key conjugated pathways and discuss the similarities and differences between **P** and **Pc** or **SubPc**. Considering the intrinsic connection between UV–Vis absorption spectrum and H–L gap in these molecules, and the relationship this gap maintains with the aromaticity of π-conjugated systems,[77,78] we will investigate a previously unexplored correlation between UV-Vis absorbance and local pathways, which holds the promise to serve as a powerful tool for property-guided molecular design. Additionally, we also study the relationship between aromaticity in the singlet ground state and the excited-singlet–triplet gap, $\Delta E_{T_1 \rightarrow S_1}$. The latter is particularly pertinent given the rising utility of this compound family in applications like triplet photosensitizers,[79] optoelectronic components,[69] and photodynamic therapy. Our final goal is to establish the connection between aromaticity and UV–Vis absorption spectra or $\Delta E_{T_1 \rightarrow S_1}$, and identify the molecular segments that are key for the control of electron delocalization, offering a promising avenue to suggest specific modifications, leveraging cost-efficient DFT over TDDFT or more accurate wavefunctions methods that require a full study of the excited states.

RESULTS

In the following, we present the results of our investigation comparing the structural differences between **P**, **Pc**, and **SubPc**. These differences (shown in Scheme 1) include (*i*) the replacement of CH at the *meso* position by N, (*ii*) the inclusion of C_4H_4 fragments at the β positions to have isoindoles instead of pyrroles, (*iii*) the reduction in the number of pyrrole or isoindole units from four to three, and (*iv*) the replacement of the central Zn atom by the B-Cl moiety in **SubPc** compared to **P** and **Pc**. This study does not contemplate the role of the central atom and its axial ligation or the effect of peripheral substitutions, which are other common structural changes to tune these molecules. While these modifications can also affect the molecular properties, their impact on the $\pi-$system is typically less pronounced compared to the modifications considered. We focused on Zn (d^{10}) tetrapyrroles to avoid complications associated with axial ligation and the presence of π to d charge transfer and d-d excited states[80,81] in open d-shell species. Apart from **P**, **Pc**, and **SubPc,** we also included other systems, presenting only one (or two, in the case of contracted systems) of the above-mentioned modifications with respect to **P**: Porphyrazine (**Pz**), Tetrabenzoporphyrin (**TBP**), Zn-Subporphyrin (**ZnSubP**), Subporphyrin (**SubP**), Subporphyrazine (**SubPz**), and Tribenzosubporphyrin (**TBSubP**). The study focuses on the changes (*i*)-(*iii*), mentioned above. However, for **SubP**, we also tested the role of the central coordination (*iv*), by considering the **ZnSubP** system, to assess whether the central element affects the aromaticity and whether the comparison between tri- and tetra-pyrrole/isoindoles is consistent. To determine structural changes in the physical properties, we compared the computational and experimental UV-Vis spectra, and analyze the $\Delta E_{T_1 \rightarrow S_1}$, H–L gap, and aromaticity of the different molecules.

UV-Vis absorption spectra, H-L gaps, and $\Delta E_{T_1 \rightarrow S_1}$

A detailed assignment of Q and B bands has been done through TDDFT and UV-Vis spectroscopy. Table 1 presents the vertical absorption energies, oscillator strengths, and TDDFT roots associated with Q and Soret (B) bands for the eight (sub)porphyrinoids under study. Computational absorption maxima (λ_{max}, in nm) are slightly underestimated compared to the experimental counterpart. However, they follow the same trend, presenting an excellent linear correlation with $r^2 = 0.98$ and 0.94 for the Q and B bands, respectively (see Figure S3, SI). While CAM-B3LYP may not reproduce the absolute experimental excitation energies to the highest accuracy, it exhibits consistency in predicting qualitative band shifts. Indeed, the relative band shifts, defined as $\Delta\lambda_{max} = \lambda_{max,X} - \lambda_{max,P}$ (where X represents any system but **P**), show a minimal discrepancy with the experimental values, differences not exceeding 0.2 eV (26.6 nm). For this reason, further discussions will focus on CAM-B3LYP values.

The Q and B bands are represented by a pair of degenerate excited states, resulting from the D_{4h} and C_{3v} symmetries of the tetra- or tri-pyrrole/isoindole systems. For the sake of simplicity, in the ensuing discussion, we will refer to the set of **P**, **Pz**, **TBP**, and **Pc** as phthalocyanines and **ZnSubP**, **SubP**, **SubPz**, **TBSubP**, and **SubPc** as subphthalocyanines. In all cases, the Q band arises from the first two singlet excited states (roots 1 and 2), while the B band originates from higher-lying singlet states. The latter states correspond to roots 3 and 4 in systems having CH at the *meso* position, or higher roots for systems containing N–*meso*. This outcome was expected, given that the a_{2u} (phthalocyanines) and a_1 (subphthalocyanines) orbitals (see Figure 1), are significantly stabilized in the presence of N–*meso*. In the same vein, we could also anticipate the difference in the oscillator strength (*f*) between systems with CH or N *meso*-substitution. **P**, **TBP**, **ZnSubP**, **SubP**, and **TBSubPc** have lower *f* values than their N–*meso* counterparts for the Q band, while the situation is reversed for the B band (see Table 1 and Tables S8 to S16, SI; for instance, compare the results of Tables S13 and S14).

Table 1. Comparison of computational and experimental vertical absorption spectra for **P**, **Pz**, **TBP**, **Pc**, **SubP**, **SubPz**, **TBSubP**, and **SubPc**. TDDFT roots corresponding to the Q and Soret (B) bands, energies (λ_{max} in nm), computed oscillator strengths (*f*), and experimental λ_{max}. Computational results obtained considering the same solvent as that used in experiments.

	Q band				**Soret (B) band**			
	root	λ_{max}	*f*	λ_{max} exp.	root	λ_{max}	*f*	λ_{max} exp.
P	1, 2	520.3	0.010	565[a]	3, 4	354.1	1.370	398[a]
Pz	1, 2	537.9	0.316	596[b]	6, 7	323.2	0.226	343[b]
TBP	1, 2	582.9	0.304	623[a]	3, 4	368.1	1.603	422[a]
Pc	1, 2	636.3	0.675	671[b]	12,13	297.0	1.139	348[b]
SubP	1, 2	403.9	0.025	454[c]	3, 4	304.2	0.855	341[c]
SubPz	1, 2	425.7	0.221	497[b]	9, 10	262.7	0.458	290[b]
TBSubP	1, 2	461.0	0.308	514[d]	3, 4	312.4	1.055	355[d]
SubPc	1, 2	503.3	0.475	565[b]	10, 11	262.9	0.866	305[b]

[a]In ethanol from ref. [111]. [b]These results were generated by our own experimental setup in THF. In the case of **SubPz**, the spectrum corresponds to the *β*-substituted-**SubPz** (see Fig. S2a, SI). In dichloromethane (DCM) from ref. [c][83], and [d][110].
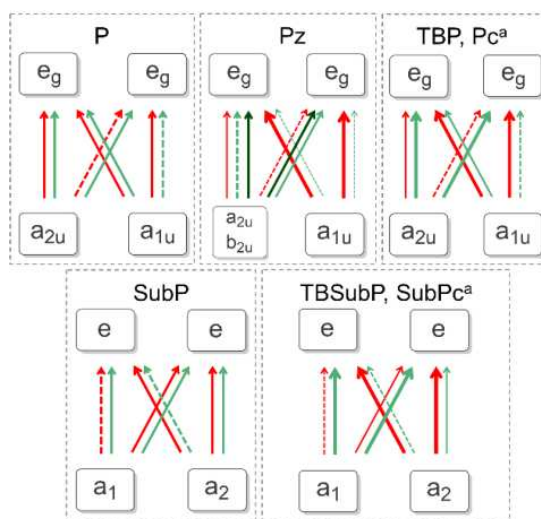
Figure 2. TDDFT-determined transitions between key molecular orbitals contributing to the Q (red) and B (green) bands. Apart from the main transitions, other transitions are included only if they have coefficients with an absolute value exceeding 0.35. Line thickness indicates the coefficient's magnitude, with thicker lines representing larger coefficients. In **Pz**, additional transitions originating from the b_{2u} orbital contributing to the B band are represented by dark green arrows. Orbital transitions with positive TDDFT coefficients are depicted with solid lines, while those with negative coefficients are dashed. [a]For B_1 and B_2 bands in **Pc** and **SubPc**, there are also other transitions with similar weight (< 0.2) to a_{1u} (a_2)→e_g (e). Further details can be found in Tables S8-S19, SI.

The contraction from phthalocyanines and subphthalocyanines results into larger H–L gaps that give rise to the blue shifting of absorption Q bands. Similarly, B bands are also blue shifted upon contraction. The substituted phthalocyanines (**Pz**, **TBP**, and **Pc)** exhibit red and blue shifts in the Q and B bands, respectively, compared to **P**. While the band position is shifted, the intensities (quantified by *f*) of Q and B bands in **Pc** and **SubPc** are also affected. With respect to **P**, the Q band in **Pc** and **SubPc** exhibits an increased intensity, while the B band shows a decrease. However, these variations in intensity, as determined by our computational analysis, do not alter the order of the intensities of these bands, as experimentally found.[2,8] The Q and B band shifts of the substituted subphthalocyanines (**SubPz**, **TBSubP**, and **SubPc)** with respect to **SubP** exhibit the same behavior as the shifts observed in their phthalocyanine counterparts (**Pz**, **TBP**, and **Pc**) when compared to **P**. In fact, the magnitude of these band shifts is comparable between the analogs of both groups, indicating a consistent pattern in the response to substitution. The sole exception to this rule is **TBP,** where the B band is slightly red-shifted owing to the destabilizing influence of the fused benzene in the a_{1u} (H) orbital, coupled with the absence of stabilization in the a_{2u} (H-1) orbital due to the presence of CH–*meso* groups. The latter similarities between phthalocyanines and subphthalocyanines suggest the modifications in *meso* and *β* positions have a similar effect regardless of the molecule's planarity and number of pyrrole or isoindole units. In comparison to **P** reference, **SubP**, **SubPz**, and **TBSubP** show a blue shift in both Q and B bands in agreement with the increase of the spacing between H

and L orbitals in these contracted systems (Figure 3). In the case of **SubPc**, the Q band is observed at wavelengths comparable to those in **P**, while the predicted H-L energy gap is 0.2 eV narrower in **SubPc**. For the B band of this system, a blue shift is observed, consistent with the trend seen in the other subphthalocyanines. Hence, in general, the reduction in the number of pyrrole or isoindole units increases the band gap, as expected from the decrease of the π-conjugated units (the same happens with linear paraphenylenes, for instance).[82] Finally, the comparison between **SubP** and **ZnSubP** confirms that the previously mentioned changes are not due to the central coordination, thereby primarily attributing the blue shifts with respect to **P** to adjustments within the π-system and other differences in the carbon-nitrogen framework.

The optical spectra of **P** and **SubP** are primarily influenced by the frontier orbitals. As seen in Figure 2, the character of the states related to the Q band (red arrows) is determined primarily by the $a_{1u} \rightarrow e_g$ and $a_2 \rightarrow e$ transitions in **P** and **SubP**, respectively. For the B band (green arrows), $a_{2u} \rightarrow e_g$ (**P**) and $a_1 \rightarrow e$ (**SubP**) transitions play a major role. In general, an increase in the $\Delta\varepsilon_{a1u\text{-}eg}$ and $\Delta\varepsilon_{a2u\text{-}eg}$ (or $\Delta\varepsilon_{a2\text{-}e}$ and $\Delta\varepsilon_{a1\text{-}e}$ in C_{3v} systems) leads to higher absorption energies in the Q and B bands, respectively. This role of the frontier orbitals on the absorption spectra aligns with the Gouterman model and is further confirmed by our analysis of the nature of the excitations. There is a particularly good correlation between the Q band and $\Delta\varepsilon_{a1u\text{-}eg}$ ($\Delta\varepsilon_{a2\text{-}e}$), as displayed in Figure 4. It is worth noting that for **SubP**, the energy gap $\Delta\varepsilon_{a1u\text{-}eg}$ of 5.7 eV at the CAM-B3LYP/cc-pVTZ level should be compared with a value of 3.64 eV obtained using B3LYP/6-311G(d).[83] Despite the correlation between the B band and $\Delta\varepsilon_{a2u\text{-}eg}$ ($\Delta\varepsilon_{a1\text{-}e}$), data points tend to cluster based on substitution at the *meso* positions and number of pyrrole and isoindole units, leading to a non-uniform distribution along the regression line. In the case of systems with CH–*meso*, the B and Q bands only have contributions from H-1(a_{2u}), H (a_{1u}), and L (e_g). A similar pattern is observed for the Q band in N–*meso* systems. Yet, the B band in these systems not only has a significant contribution from a_{2u} to e_g but also incorporates transitions from b_{2u} to e_g. Thus, in these cases, the Gouterman model is insufficient to explain the nature of the B band. Given the involvement of additional transitions in the B band, we expanded the Gouterman four-orbital model to consider other orbitals involved in the transitions and their influence on the excitation energy (see section S2.3, SI). The resulting pondered $\Delta\varepsilon$ shows a more uniform distribution of the data, leaving **Pz** as the only outlier (the correlation coefficient r^2 increases from 0.84 to 0.98 upon removing **Pz**; see Figure S4, SI). In **Pz**, the E_u states associated with the B_1 and B_2 bands show a significant contribution (the weight is 0.49; see Table S9 and Figure S5, SI) from the $b_{2u}-e_g$ transition, in contrast to all other systems where the contributions come from the a_{1u} and a_{2u} to e_g transitions.

In **P** (**SubP**), the a_{1u} and a_{2u} (a_2 and a_1) orbitals correspond to H and H-1, respectively. The latter orbitals are nearly degenerate (energy difference below 0.2 eV; see Figure 3), contributing to both Q and B bands. Upon addition of the *benzo* substituents at the *β*-positions, the energy difference between a_{1u} and a_{2u} (a_2 and a_1) orbitals increases to approximately 1 eV, thus eliminating the near degeneracy. The difference is further increased upon the inclusion of the N–*meso* substituent, leading to a near degeneracy of H-1 and H-2 orbitals. The H–L gaps decrease with the inclusion of the *benzo* moieties, primarily due to the destabilization of the H upon addition of the substituents, which give antibonding character to this orbital around the *β*-position. Systems that also have N–*meso* (**Pc** and **SubPc**), exhibit further reduction of the H–L gap due to the stabilization of LUMO orbital. This results in **Pc** having the smallest H–L gap among all systems.
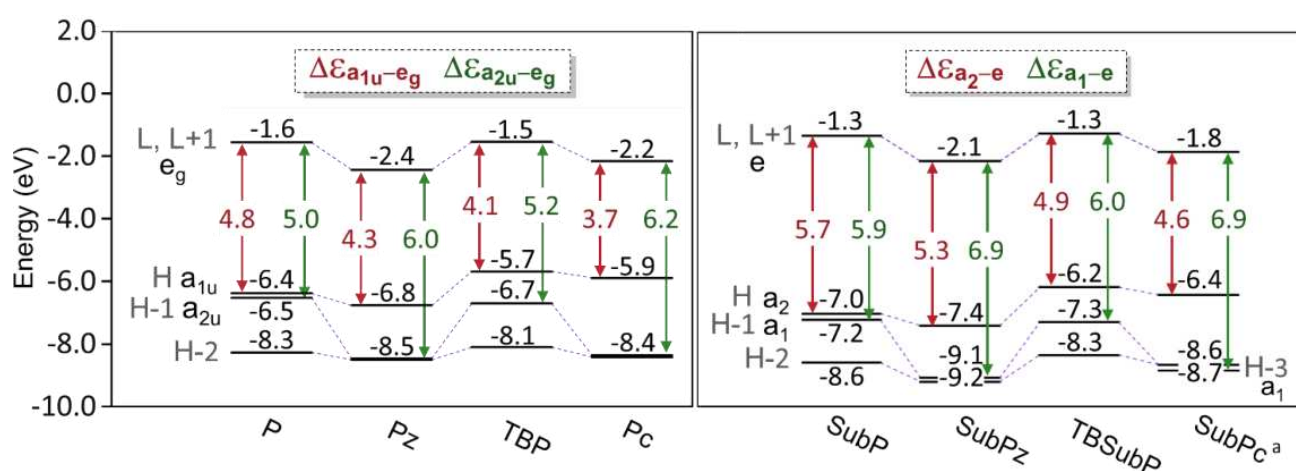
Figure 3. Energy of the frontier orbitals (in eV), and $\Delta\varepsilon_{a1u\text{-}eg}$ and $\Delta\varepsilon_{a2u\text{-}eg}$ (or $\Delta\varepsilon_{a2\text{-}e}$ and $\Delta\varepsilon_{a1\text{-}e}$) (in eV) at CAM-B3LYP/cc-pVTZ level of theory for phthalocyanines (left) and subphthalocyanines (right). [a] In the case of **SubPc**, the orbital with a_1 symmetry is the H-3 instead of H-1. Further details are given in Tables S17-S19, SI.
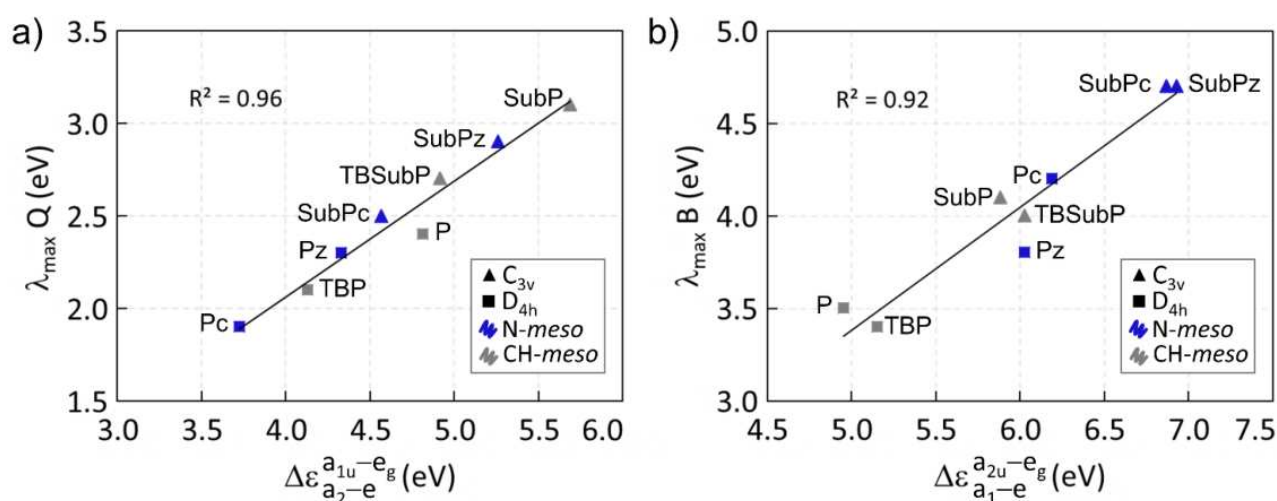
Figure 4. Relationship between a) Q band λ_{max} and $\Delta\varepsilon_{a1u\text{-}eg}$ ($\Delta\varepsilon_{a2\text{-}e}$), and b) B band λ_{max} and $\Delta\varepsilon_{a2u\text{-}eg}$ ($\Delta\varepsilon_{a1\text{-}e}$).

10

Given the similarity between the orbital distribution of S_1 and T_1 states, in the following, we analyze whether the Gouterman model, which is only useful to predict the Q band, can also be used to anticipate the behavior of T_1 and its influence in the $\Delta E_{T_1 \to S_1}$. To this end, we have computed the triplet vertical excited states at the TDDFT level of theory (see Table S21 and Figures S6-S7a for a comparison with TDA, SI). In all cases, the first two roots correspond to two degenerate triplet states (T_1) with a predominant H-1, H→L (a_{2u}, a_{1u} to e_g) transitions and energies 1.04−1.55 eV below the singlet excited states associated with the Q band. In the case of **P** and **SubP**, two additional degenerate triplets (T_2) exist, 0.23 and 0.44 eV beneath the first singlet excited state, respectively. For the remaining systems, T_2 is above S_1, however, there is an inverse relationship between the energies of T_1 and T_2 within each family, phthalocyanines and subphthalocyanines (when T_1 increases, T_2 decreases, and the other way around; see Figure S7c, SI). T_1 presents a positive correlation (see Figures S7b and S7d, SI) with both the energy of S_1 and the $\Delta\varepsilon_{a1u\text{-}eg}$ (or $\Delta\varepsilon_{a2\text{-}e}$). Thus, the observations made earlier in the manuscript regarding the role of frontier orbitals on the Q band can be qualitatively extended to the T_1 state.

Our analysis reveals that the evaluation of $\Delta\varepsilon_{a1u\text{-}eg}$ and $\Delta\varepsilon_{a2u\text{-}eg}$ do not comprehensively describe the absorption spectra, in particular the B band for N–*meso* systems where the Gouterman model falls short. An extended Gouterman model provides a rationale for the trends observed in the B band, but it lacks the simplicity of the original model. To provide a more chemically intuitive explanation, we resort to the study of the aromaticity of these compounds.

Aromaticity of Phthalocyanines and Subphthalocyanines

The aromatic stabilization energy (ASE) is known to diminish with the increasing size of [n]annulenes, a trend that is accompanied by a marked decrease in electron conjugation. Notably, the ASE value for [18]annulene is as low as 2.6 kcal/mol,[84] which stands in stark contrast to that of benzene, approximately 30 kcal/mol,[85] depending on the homodesmotic reaction considered. The local aromaticity of the pyrrole rings is important to explain the overall aromatic stabilization in porphyrinoids.[86] In our case, systems containing *benzo* rings have an MCI value close to 0.050, not far from the value obtained for benzene at the same level of theory (MCI=0.071), while all the five-membered rings display MCI values about half the values of pyrrole or lower (*benzo*-substituted compounds) (see Table S32, SI). Nevertheless, the global aromatic character of the molecule is influenced by the conjugated pathways along the whole molecule which pass through these five and six-membered rings. In simple neutral porphyrinoid systems, the aromatic character expected from straightforward π-electron counting rules is observed, whereas more intricate systems call for a more

profound analysis. Hence, in this study, we opt for various electronic and magnetic aromaticity measures.[45,63]

Among the few aromaticity studies of (sub)phthalocyanines, the use of magnetic criteria, especially NICS, is prevalent.[87] However, the utilization of global NICS measures for systems featuring fused rings has, until now, limited the ability to explore conjugated pathways individually. Additionally, previous studies have not delved into the impact of molecular substitutions. In this work, we embark on a comprehensive two-pronged exploration of aromaticity. This entails an examination of intrinsic electronic aromaticity measures such as AV1245 (and AV_{min})[75] and electron density of delocalized bonds (EDDB),[88,89] complemented by a comprehensive analysis of response aromaticity through the investigation of ring currents.

From the ring current perspective, all systems display diatropic currents with global current strengths exceeding 20 nA·T^{-1}, a value larger than the 12 nA·T^{-1} found in benzene (see Figure S10, SI). Hence, all investigated systems display conjugated pathways and can be considered magnetically global aromatic.

Figure 5. Net current strengths (in nA·T^{-1}) passing through selected bonds in the S_0 state. In the case of subphthalocyanines, the values within parentheses represent the calculated current strengths when an external magnetic field is oriented perpendicular to the plane defined by the pyrrole or isoindole ring (refer to section S4.1 for details, SI).

Although the current density maps show a global diatropic circulation, indicative of aromaticity, the global current is evenly split between the *outer* (o), *inner* (i) and *benzo* (b) pathways (see Scheme 2),

as evidenced by examining the current strength in Figure 5. For instance, consider the case of **Pc**, where the total current of 23.1 nA·T^{-1} is broken down into two components: a 12.4 nA·T^{-1} current passing through the iiii pathway and a 10.8 nA·T^{-1} current passing through the oooo pathway. This pattern is akin to what has been observed in free-base **Pc** and **TBP**. Both N–*meso* and *benzo* substitutions play a role in enhancing the intensity of the inner current, with the N–*meso* substitution exerting a particularly significant influence. This becomes apparent when examining the current strengths across different systems, such as the transition from **P** to **Pz**, where a clear outer pathway dominance over the inner one shifts to a similar preference upon N–*meso* substitution. Similarly, in the transition from **Pz** to **Pc**, the preference from the outer to the inner pathway is entirely reversed upon *benzo* substitution. Similar trends are observed in the case of subphthalocyanines. However, due to the nonplanar nature of these molecules, defining an external magnetic field perpendicular to the system is not straightforward, and the results should be considered as semiquantitative.

In the following, we examine electronic aromaticity indices, specifically AV1245 (and AV$_{min}$), and EDDB$_P$ (and limit of EDDB$_P$), which provide information about the electron delocalization in the conjugated pathways of the molecule in the absence of an external perturbation.[41,42,45,56,60,63-65,90] Unlike the magnetic indices, the nonplanarity of subphthalocyanines does not represent a challenge for electronic indices, which can also be decomposed into contributions from individual groups or fragments. AV1245 is calculated as the average of multiple 4-center multicenter indices (MCI) computed at positions 1, 2, 4, and 5 for each five-atom fragment along the conjugated pathway. In contrast, AV$_{min}$ represents the smallest absolute value among these 4-center MCI values. The EDDB method involves the decomposition of the electron density into three components: electron density localized on the atoms (EDLA), electron density localized on the bonds (EDLB), and the delocalized density, referred to as the electron density of delocalized bonds (EDDB). The latter quantity, when measured within a closed circuit, serves as an indicator of aromaticity. In our study, we focus on the EDDB$_P$(r) function and electron populations (referred to as EDDB$_P$), which specifically consider adjacent chemical bonds along the selected pathway. Additionally, similar to the AV$_{min}$ index, we examine the limit of EDDB$_P$ (lim$_{EDDB}$), which corresponds to the atom in the pathway with the smallest delocalized electron population. For all these indices, large values indicate aromaticity, while small values indicate non-aromaticity or antiaromaticity. AV1245 and EDDB$_P$ consider the *average* delocalization along the pathways and are expected to reflect features connected with the conjugated nature of these molecules, whereas AV$_{min}$ and lim$_{EDDB}$ indicate the *least* delocalized fragment/atom in the pathway and this limiting value has been successfully connected to the aromaticity of the pathway in porphyrinoids.[45,63,64] In practice, both values contribute to the overall assessment of conjugated pathways.

The total number of non-equivalent conjugated pathways depends on the symmetry of the molecules. We identify four in **SubP** and **SubPz**, six in **P** and **Pz**, ten in **TBSubP** and **SubPc**, and 21 in **TBP** and **Pc**, for which we have listed all electronic aromaticity indices in Tables S23-S31, SI. However, in practice, the most important contributions are given by three conjugated pathways: *inner* iii(i), *outer* ooo(o), or *benzo* bbb(b) pathways, the results of which are summarized in Figure 6. AV1245 and AV_{min} show significantly reduced values for the most conjugated pathways in the molecules depicted in Scheme 1. Specifically, the AV1245 values are found to be below 3.0, and AV_{min} values are below 1.5 for all the pathways. The latter figures are markedly lower than the values of 10.50 for both indices in benzene, however, they are in line with the values reported for other porphyrinoid systems.[45,63] AV1245 and AV_{min} values do not agree on which pathway is the most conjugated, indicating that minimal and average multicenter delocalizations differ significantly. This difference is particularly evident for *benzo*-substituted molecules. As discussed in previous publications,[76,91] AV_{min} is the index that better reflects aromatic character, whereas AV1245 provides an average delocalization value that can obscure weakly conjugated fragments.

According to $EDDB_P$ and lim_{EDDB}, iii(i) is always the most aromatic pathway with values lower than 0.75 and 0.59 electrons, respectively. In comparison, benzene demonstrates values of 0.92 electrons for both $EDDB_P$ and lim_{EDDB}. Hence, there is a qualitative consensus regarding the most conjugated pathway in phthalocyanines, with AV_{min}, $EDDB_P$, and lim_{EDDB} consistently identifying the iiii(i) pathway as the most conjugated. The sole exception is observed in **Pz**, where AV_{min} does not show a distinct preference between the ooo(o) and iii(i) pathways. Conversely, AV_{min} identifies the ooo(o) and bbb(b) as the most aromatic pathways in subphthalocyanines, whereas lim_{EDDB} always identifies the iiii(i) pathway as the most aromatic. Nevertheless, in instances where the aromaticity of the ooo(o) and iii(i) pathways is ranked separately for each molecule using AV1245 and $EDDB_P$, both indices consistently produce the same order, from the most to the least aromatic. The only deviation occurs in the ranking of the iii(i) circuit in subphthalocyanines, which is also observed with the electronic-based FLU and geometric-based HOMA indices (Tables S23-S31, SI). In the case of the ooo(o) pathway, there is even a good linear correlation between AV1245 and $EDDB_P$ (see Figure S20, SI). All in all, the most important difference between the electronic indices and the magnetic ring currents is the magnitude of the aromaticity. According to the ring current strengths, all compounds are highly aromatic while electronic indices indicate lower aromaticity.

The aromaticity of each pathway reflects the trends we observed in the UV-Vis absorption energies (see Figure 7). Both AV1245 and $EDDB_P$ show that the aromaticity of the ooo(o) circuit decreases along the **P−Pz−TBP−Pc** and **SubP−SubPz−TBSubP−SubPc** series, as it occurred for the energy

of the Q band and $\Delta\varepsilon_{a1u-eg}$. All aromaticity indices uniformly recognize the oooo circuit in phthalocyanines as being less aromatic than the corresponding ooo pathway in their contracted analogs, namely subphthalocyanines. This observation aligns with the higher excitation energies observed in the Q band of these compounds.

AV_{min} and lim_{EDDB}, while they might reflect the limiting conjugated part of the pathway, they do not show any evident connection with the Q and B bands. Instead, they can be used to identify the least conjugated fragment in the molecule and be instrumental in modifying the pathway's aromaticity and, given their connection to the average counterparts, in the case of the ooo(o) pathway, tuning the Q band. In Figures S16-S19 in SI, we split the information of AV1245 into five-atom fragments, in which we can easily recognize the fragment(s) giving rise to AV_{min}. Interestingly, the values of the fragments in the ooo(o) pathways follow the same distribution for a given phthalocyanine and its analog subphthalocyanine. The least (or the second least) delocalized fragment of the ooo(o) pathways always corresponds to the fragment centered in the *meso*-position. This implies that *meso*-substitution influences the Q bands across all systems studied. To achieve a blue shift of the Q bands, a *meso*-substitution is necessary, but it must be distinct from the N–*meso* substitution. Indeed, the transition from **P** to **Pz** or **Pc** (N–*meso* substitution) results in a reduced AV1245 value, which, in turn, shifts the Q band to the red. The addition of a *benzo*-group affects similarly, reducing the delocalization of other five-atom fragments and red-shifting the Q band. The interplay of these effects results in a three-fold reduction in delocalization for certain fragments in phthalocyanines and a five-fold reduction in subphthalocyanines. This significant decrease in delocalization effectively eliminates any conjugated fragments within the ooo(o) pathway, consequently leading to a red-most shift in the Q bands. While the aforementioned analysis provides a reasonable understanding of the Q band shifts, the correlation between the B band and AV1245 values is less clear (see Figure 7b).
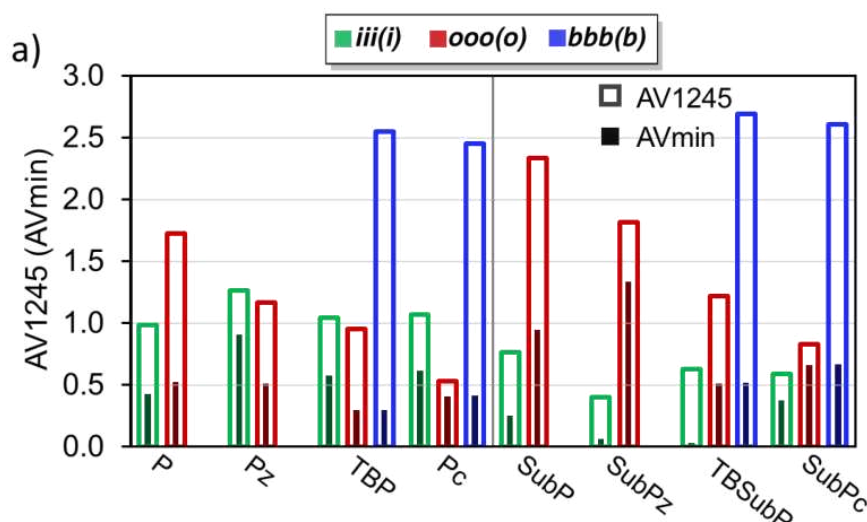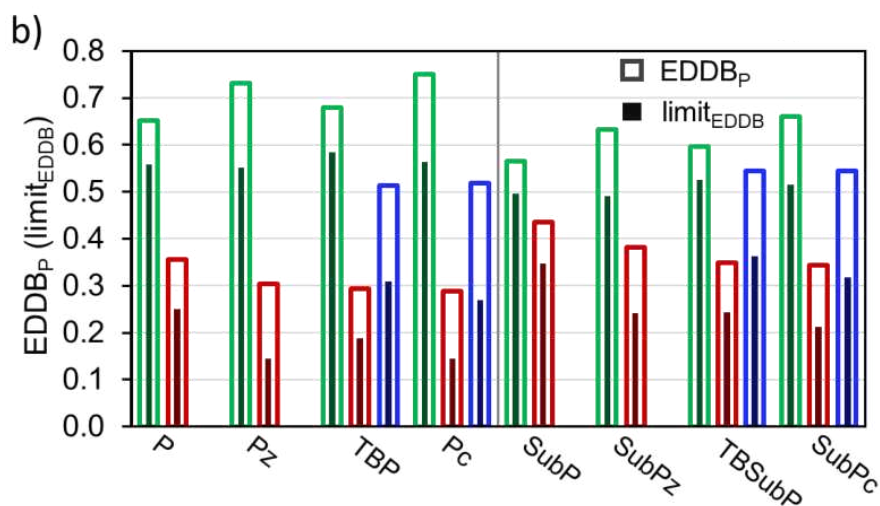
Figure 6. Aromaticity values of iii(i), ooo(o) and bbb(b) circuits in each system according to a) AV1245 and b) EDDB$_P$ (normalized according to the number of atoms in the circuit) aromaticity measures. The darker filled bars represent the a) AV$_{min}$ and b) limit of EDDB$_P$.
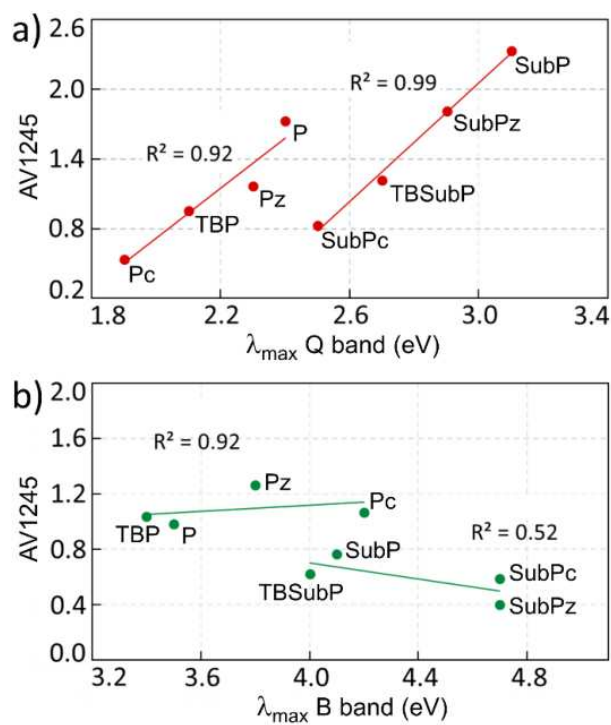
Figure 7. Relationship between a) Q band λ_{max} and AV1245 of ooo(o) pathway, and b) B band λ_{max} and AV1245 of iii(i) pathway.

CONCLUSIONS

This study examines substituted phthalocyanines (**P**, **TBP**, **Pc**, and **Pz**) and their contracted analogs, subphthalocyanines (**SubP**, **TBSubP**, **SubPc**, and **SubPz**), which are characterized by nonplanar, bowl-shaped geometries. The methodology employed in this study, which include CAM-B3LYP/cc-pVTZ calculations, is validated through the comparison of UV-Vis computational and experimental studies. In addition, we rely on the Gouterman four-orbital model for porphyrinoids.

Our analysis reveals that evaluation of the four orbital energies is insufficient to describe the absorption spectra, particularly the B band for N–*meso* systems where deviations from the Gouterman model are apparent. An extension of the Gouterman model, including more orbitals, provides a rationale for the trends observed in the B band, but it sacrifices the simplicity of the original model. Consequently, we turn to the examination of aromaticity of these compounds, providing a more chemically intuitive explanation of their spectral features.

Magnetic response indices characterize all the molecules studied as aromatic, exhibiting important rings currents strengths. Conversely, an analysis of electron delocalization and π-conjugation through AV1245, AV_{min} and EDDB indices, reveals that –despite the important response upon the application of an external magnetic field– the conjugated circuits are much less aromatic than those found in classical organic molecules like benzene, being closer to those already reported in other porphyrinoid systems.[41,63] This evidence adds to the results already reported in the literature, where intrinsic (electronic) and response (magnetic) measures of aromaticity do not align.[64,65,70,90,92,93] However, in general, subphthalocyanines can be considered slightly more aromatic than phthalocyanines, according to the least delocalized fragment of the external-most circuit of these systems, and in agreement with the larger HOMO-LUMO gap observed in subphthalocyanines.

Interestingly, the electronic aromaticity indices help explaining part of the UV-Vis spectrum of (sub)phthalocyanines, giving a direct connection between the aromaticity of the external-most conjugated pathways and the Q bands. Particularly, the substitution at the *meso* position seems to have a large effect on the aromaticity and the position of the Q and B bands. This insight is pivotal for pinpointing modifications in porphyrinoid structures that lead to marked shifts in UV-Vis bands.

Our findings offer a strategic framework for designing novel phthalocyanine derivatives with custom-tailored properties.

COMPUTATIONAL DETAILS

The systems presented in Scheme 1 have been fully optimized and characterized as energy minima in the ground state using harmonic vibrational frequency calculations at the CAM-B3LYP/cc-pVTZ level of theory.[94,95] The choice of the functional, was based on the comparison between optimized **Pc** and **SubPc** using B3LYP, ωB97X, M062X, TPSSH, and LC-ωHPBE together with cc-pVTZ basis set, and the X-Ray structure (Supporting information Tables S1-S4). Additionally, we examined the UV-Vis spectra using different functionals: B3LYP, CAM-B3LYP, ωB97xD, M062X, LC-BLYP and optimally tuned LC-BLYP functionals (Tables S5-S7, SI) to assess the performance of each method. We computed in-solution optical spectra of all systems using CAM-B3LYP functional and cc-pVTZ basis set by means of TDDFT considering the first 20 singlet states solvated in THF, DCM, or ethanol, according to the experimental data available. The effect of the implicit solvent has been accounted with the polarizable continuum model (PCM)[96] approach. For the calculation of the vertical triplet state our choice was to employ time dependent and Tamm-Dancoff approximation (TD and TDA)-DFT (CAM-B3LYP/cc-pVTZ) to calculate the two degenerate triplets resulting from having degenerate L/L+1 orbitals. All calculations have been done with the Gaussian 09 and 16 software packages.[97] For the characterization of the aromaticity, we used a variety of measures including geometrical, electronic, and magnetic indices to determine local and global aromaticity. The 2- (delocalization indices (DIs)), 3- and 4-center indices for each set of atoms in the system and the fluctuation index (FLU),[98,99] bond order alternation (BOA),[56] I_{ring},[100] multicenter index (MCI),[101] AV1245,[75] and AV_{min}[91] electronic indices were computed using AIMAll[102] and ESI-3D (available upon request: ematito@gmail.com) programs. The harmonic oscillator measure of aromaticity (HOMA)[103] and the bond length alternation (BLA) were calculated with ESI-3D using molecular geometries as input.[64] Electron density of delocalized bonds (EDDB)[88,89] results were computed using NBO 6.0[104] software to first obtain the natural atomic orbitals (NAO) and the 1-electron density matrix used as input for the EDDB (v20200925) program (available upon request: dszczpnk@gmail.com). Finally, the magnetic current density and the current strengths were obtained using Gaussian 09 together with GIMIC program.[105,106] Further explanation regarding the calculation of aromaticity indices can be found in the supporting information, section S4.

EXPERIMENTAL DATA

SubPc[107], **Pz**[108], and **SubPz**[109] were synthesized following reported procedures. **Pc** was purchased from Aldrich and used without further purification. The UV-Vis spectra of these compounds were recorded in THF (concentration= 2×10^{-5} M) employing a JASCO-V660 spectrophotometer. **SubPz** has to be prepared as β-substituted-**SubPz** with propyl groups for synthetic reasons.[10] However, since there is no conjugation of the ethyl groups with the pyrroles, their influence on the absorption spectrum is expected to be minor (Q band can be displaced 5-10 nm at most).[10] The data for the remaining molecules has been sourced from the literature. The measured absorption spectra of **SubP** and **TBSubP** were obtained in DCM using derivatives bearing OMe and OH as axial ligands, respectively, in order to avoid hydrolysis.[83,110] It is well known that neither the shape nor displacement of the spectrum is highly affected by the axial ligand. In the case of **P** and **TBP**, presenting very poor solubility, the absorption spectra were obtained in ethanol.[111]

ASSOCIATED CONTENT

The Supporting Information contains detailed computational data including performance assessments of various functionals on geometry optimization, experimental and computational UV-Vis absorption spectra, and electron delocalization and aromaticity analyses. The inputs and outputs of the calculations (including Cartesian coordinates) are available in ioChem-BD[112] and can be accessed via https://doi.org/10.19061/iochem-bd-4-71.

BIBLIOGRAPHY

(1)	Senge, M. O.; Sergeeva, N. N.; Hale, K. J. *Chem. Soc. Rev.* **2021**, *50*, 4730.
(2)	Claessens, C. G.; Hahn U Fau - Torres, T.; Torres, T. *Chem. Rec.* **2008**, *8*, 75.
(3)	Urbani, M.; Ragoussi, M.-E.; Nazeeruddin, M. K.; Torres, T. *Coord. Chem. Rev.* **2019**, *381*, 1.
(4)	Leznoff, C.; Lever, A. *Phthalocyanines: Properties and Applications*; VCH New York, 1989.
(5)	Rodríguez-Morgade, M. S.; Stuzhin, P. A. *J. Porphyr. Phthalocya.* **2004**, *08*, 1129.
(6)	Kudrevich, S. V.; van Lier, J. E. *Coord. Chem. Rev.* **1996**, *156*, 163.
(7)	Shimizu, S. *Chem. Rev.* **2017**, *117*, 2730.
(8)	Claessens, C. G.; González-Rodríguez, D.; Rodríguez-Morgade, M. S.; Medina, A.; Torres, T. *Chem. Rev.* **2014**, *114*, 2192.
(9)	Labella, J.; Torres, T. *Trends Chem.* **2023**, *5*, 353.
(10)	Lavarda, G.; Labella, J.; Martínez-Díaz, M. V.; Rodríguez-Morgade, M. S.; Osuka, A.; Torres, T. *Chem. Soc. Rev.* **2022**, *51*, 9482.
(11)	Smith, K. M. In *Comprehensive Heterocyclic Chemistry*; Katritzky, A. R., Rees, C. W., Eds.; Pergamon: Oxford, 1984, p 377.
(12)	Robertson, J. M.; Woodward, I. *J. Chem. Soc.* **1937**, 219.
(13)	Kobayashi, N.; Fukuda, T.; Ueno, K.; Ogino, H. *J. Am. Chem. Soc.* **2001**, *123*, 10740.
(14)	Kondou, K.; Shiga, M.; Sakamoto, S.; Inuzuka, H.; Nihonyanagi, A.; Araoka, F.; Kobayashi, M.; Miwa, S.; Miyajima, D.; Otani, Y. *J. Am. Chem. Soc.* **2022**, *144*, 7302.
(15)	Torres, T. *Angew. Chem. Int. Ed.* **2006**, *45*, 2834.
(16)	Gouterman, M. *J. Mol. Spectrosc.* **1961**, *6*, 138.
(17)	Gouterman, M. *J. Chem. Phys.* **2004**, *30*, 1139.
(18)	Gouterman, M.; Wagnière, G. H.; Snyder, L. C. *J. Mol. Spectrosc.* **1963**, *11*, 108.
(19)	Simpson, M. C.; Novikova, N. I. In *Fundamentals of Porphyrin Chemistry*; Brothers, P. J.; Senge, M. O, Eds, John Wiley & Sons Inc.: Chichester, 2022, p 505.
(20)	Zhang, A.; Kwan, L.; Stillman, M. J. *Org. Biomol. Chem.* **2017**, *15*, 9081.
(21)	Mack, J.; Asano, Y.; Kobayashi, N.; Stillman, M. J. *J. Am. Chem. Soc.* **2005**, *127*, 17697.
(22)	Breslow, R.; Foss Jr, F. W. *J. Phys.: Condens. Matter* **2008**, *20*, 374104.
(23)	Molina, D.; Follana-Berná, J.; Sastre-Santos, Á. *J. Mater. Chem. C* **2023**.
(24)	Martín-Gomis, L.; Fernández-Lázaro, F.; Sastre-Santos, Á. *J. Mater. Chem. A* **2014**, *2*, 15672.
(25)	Ikeuchi, T.; Nomoto, H.; Masaki, N.; Griffith, M. J.; Mori, S.; Kimura, M. *Chem. Commun.* **2014**, *50*, 1941.

(26)   Urbani, M.; de la Torre, G.; Nazeeruddin, M. K.; Torres, T. *Chem. Soc. Rev.* **2019**, *48*, 2738.

(27)   Yahya, M.; Nural, Y.; Seferoğlu, Z. *Dyes Pigm.* **2022**, *198*, 109960.

(28)   Cranston, R. R.; King, B.; Dindault, C.; Grant, T. M.; Rice, N. A.; Tonnelé, C.; Muccioli, L.; Castet, F.; Swaraj, S.; Lessard, B. H. *J. Mater. Chem. C* **2022**, *10*, 485.

(29)   Martínez-Díaz, M. V.; de la Torre, G.; Torres, T. *Chem. Commun.* **2010**, *46*, 7090.

(30)   Adachi, C. *Jpn. J. Appl. Phys.* **2014**, *53*, 060101.

(31)   See section 2.6 of ref. 9 (*Chem. Soc. Rev.* **2022**, *51*, 9482) and references therein.

(32)   Bharmoria, P.; Bildirir, H.; Moth-Poulsen, K. *Chem. Soc. Rev.* **2020**, *49*, 6529.

(33)   Radiunas, E.; Raišys, S.; Juršėnas, S.; Jozeliūnaitė, A.; Javorskis, T.; Šinkevičiūtė, U.; Orentas, E.; Kazlauskas, K. *J. Mater. Chem. C* **2020**, *8*, 5525.

(34)   Naimovičius, L.; Bharmoria, P.; Moth-Poulsen, K. *Mater. Chem. Front.* **2023**, *7*, 2297.

(35)   Can Karanlık, C.; Aguilar-Galindo, F.; Sobotta, L.; Güzel, E.; Erdoğmuş, A. *J. Phys. Chem. C* **2023**, *127*, 9145.

(36)   Guzmán, D.; Papadopoulos, I.; Lavarda, G.; Rami, P. R.; Tykwinski, R. R.; Rodríguez-Morgade, M. S.; Guldi, D. M.; Torres, T. *Angew. Chem. Int. Ed.* **2021**, *60*, 1474.

(37)   Gotfredsen, H.; Thiel, D.; Greißel, P. M.; Chen, L.; Krug, M.; Papadopoulos, I.; Ferguson, M. J.; Nielsen, M. B.; Torres, T.; Clark, T.; Guldi, D. M.; Tykwinski, R. R. *J. Am. Chem. Soc.* **2023**, *145*, 9548.

(38)   Lavarda, G.; Zirzlmeier, J.; Gruber, M.; Rami, P. R.; Tykwinski, R. R.; Torres, T.; Guldi, D. M. *Angew. Chem. Int. Ed.* **2018**, *57*, 16291.

(39)   Holst, D. P.; Friederich, P.; Aspuru-Guzik, A.; Bender, T. P. *J. Chem. Inf. Model.* **2022**, *62*, 829.

(40)   Peterson, E. J.; Rawson, J.; Beratan, D. N.; Zhang, P.; Therien, M. J. *J. Am. Chem. Soc.* **2022**, *144*, 15457.

(41)   Woller, T.; Geerlings, P.; De Proft, F.; Champagne, B.; Alonso, M. *Molecules* **2018**, *23*, 1333.

(42)   Woller, T.; Geerlings, P.; De Proft, F.; Champagne, B.; Alonso, M. *J. Phys. Chem. C* **2019**, *123*, 7318.

(43)   Torrent-Sucarrat, M.; Anglada, J. M.; Luis, J. M. *J. Chem. Phys.* **2012**, *137*.

(44)   Torrent-Sucarrat, M.; Navarro, S.; Marcos, E.; Anglada, J. M.; Luis, J. M. *J. Phys. Chem. C* **2017**, *121*, 19348.

(45)   Casademont-Reig, I.; Woller, T.; García, V.; Contreras-García, J.; Tiznado, W.; Torrent-Sucarrat, M.; Matito, E.; Alonso, M. *Chem. Eur. J.* **2023**, *29*, e202202264.

(46)   Ko, M.-S.; Roh, T.-H.; Desale, P. P.; Choi, S.-W.; Cho, D.-G. *J. Am. Chem. Soc.* **2024**, *146*, 6266.

(47)   Ke, M.-R.; Chen, Z.; Shi, J.; Wei, Y.; Liu, H.; Huang, S.; Li, X.; Zheng, B.-Y.; Huang, J.-D. *Chem. Commun.* **2023**, *59*, 9832.

(48)   von Schleyer, P. R.; Jiao, H. *Pure Appl. Chem.* **1996**, *68*, 209.

(49)   Solà, M. *Front. Chem.* **2017**, *5*, 22.

(50)   Feixas, F.; Matito, E.; Poater, J.; Solà, M. *Chem. Soc. Rev.* **2015**, *44*, 6434.

(51)   Hoffmann, R. *Am. Sci.* **2015**, *103*, 18.

(52)   Stanger, A. *Chem. Commun.* **2009**, 1939.

(53)   Hückel, E. *Z. Phys.* **1931**, *70*, 204.

(54)   Hückel, E. *Z. Phys.* **1931**, *72*, 310.

(55)   Hückel, E. *Z. Phys.* **1932**, *76*, 628.

(56)   Casademont-Reig, I.; Ramos-Cordoba, E.; Torrent-Sucarrat, M.; Matito, E. *Molecules* **2020**, *25*, 711.

(57)   Feixas, F.; Matito, E.; Solà, M.; Poater, J. *Phys. Chem. Chem. Phys.* **2010**, *12*, 7126.

(58)   Solà, M. *Nature Chem.* **2022**, *14*, 585.

(59)   Feixas, F.; Matito, E.; Poater, J.; Solà, M. In *Applications of Topological Methods in Molecular Chemistry*; Chauvin, R., Lepetit, C., Silvi, B., Alikhani, E., Eds.; Springer International Publishing: Cham, 2016, p 321.

(60)   Escayola, S.; Poater, A.; Muñoz-Castro, A.; Solà, M. *Chem. Commun.* **2021**, *57*, 3087.

(61)   Sondheimer, F.; Wolovsky, R.; Amiel, Y. *J. Am. Chem. Soc.* **1962**, *84*, 274.

(62)   Vogel, E. *Pure Appl. Chem.* **1993**, *65*, 143.

(63)   Casademont-Reig, I.; Woller, T.; Contreras-García, J.; Alonso, M.; Torrent-Sucarrat, M.; Matito, E. *Phys. Chem. Chem. Phys.* **2018**, *20*, 2787.

(64)   Casademont-Reig, I.; Guerrero-Avilés, R.; Ramos-Cordoba, E.; Torrent-Sucarrat, M.; Matito, E. J. *Angew. Chem. Int. Ed.* **2021**, *60*, 24080.

(65)   Casademont-Reig, I.; Soriano-Agueda, L.; Ramos-Cordoba, E.; Torrent-Sucarrat, M.; Matito, E. *Angew. Chem. Int. Ed.* **2022**, *61*, e202206836.

(66)   Kolomeychuk, F. M.; Safonova, E. A.; Polovkova, M. A.; Sinelshchikova, A. A.; Martynov, A. G.; Shokurov, A. V.; Kirakosyan, G. A.; Efimov, N. N.; Tsivadze, A. Y.; Gorbunova, Y. G. *J. Am. Chem. Soc.* **2021**, *143*, 14053.

(67)   Yang, Y. *J. Phys. Chem. A* **2010**, *114*, 13257.

(68)   Yang, Y. *Chem. Phys. Lett.* **2011**, *511*, 51.

(69)   Bartkowski, K.; Pawlicki, M. *Angew. Chem. Int. Ed.* **2021**, *60*, 9063.

(70)   Zhao, L.; Grande-Aztatzi, R.; Foroutan-Nejad, C.; Ugalde, J. M.; Frenking, G. *ChemistrySelect* **2017**, *2*, 863.

(71)   Islas, R.; Martínez-Guajardo, G.; Jiménez-Halla, J. O. C.; Solà, M.; Merino, G. *J. Chem. Theory Comput.* **2010**, *6*, 1131.

(72)   Feixas, F.; Matito, E.; Poater, J.; Solà, M. *J. Comput. Chem.* **2008**, *29*, 1543.

(73)   Feixas, F.; Jiménez-Halla, J. O. C.; Matito, E.; Poater, J.; Solà, M. *J. Chem. Theory Comput.* **2010**, *6*, 1118.

(74)   Pelloni, S.; Monaco, G.; Lazzeretti, P.; Zanasi, R. *Phys. Chem. Chem. Phys.* **2011**, *13*, 20666.

(75)   Matito, E. *Phys. Chem. Chem. Phys.* **2016**, *18*, 11839.

(76)   Casademont-Reig, I.; Ramos-Cordoba, E.; Torrent-Sucarrat, M.; Matito, E. In *Aromaticity*; Fernández, I., Ed.; Elsevier: 2021, p 235.

(77)   Zhou, Z.; Parr, R. G. *J. Am. Chem. Soc.* **1989**, *111*, 7371.

(78)   De Proft, F.; Geerlings, P. *Phys. Chem. Chem. Phys.* **2004**, *6*, 242.

(79)   Kwak, H. S.; David, J. G.; Thomas, F. H.; Alexander, G.; Yixiang, C.; Jacob, G.; Steve, D.; Mathew, D. H. In *Proc.SPIE* 2016; Vol. 9941, p 994119.

(80)   Sorgues, S.; Poisson, L.; Raffael, K.; Krim, L.; Soep, B.; Shafizadeh, N. *J. Chem. Phys.* **2006**, *124*, 114302.

(81)   Bhowmick, R.; Roy Chowdhury, S.; Vlaisavljevich, B. *Inorg. Chem.* **2023**, *62*, 13877.

(82)   Darzi, E. R.; Jasti, R. *Chem. Soc. Rev.* **2015**, *44*, 6401.

(83)   Kise, K.; Yoshida, K.; Kotani, R.; Shimizu, D.; Osuka, A. *Chem. Eur. J.* **2018**, *24*, 19136.

(84)   Jirásek, M.; Rickhaus, M.; Tejerina, L.; Anderson, H. L. *J. Am. Chem. Soc.* **2021**, *143*, 2403.

(85)   Cyrański, M. K. *Chem. Rev.* **2005**, *105*, 3773.

(86)   Pino-Rios, R.; Cárdenas-Jirón, G.; Tiznado, W. *Phys. Chem. Chem. Phys.* **2020**, *22*, 21267.

(87)   Kupka, T.; Gajda, Ł.; Broda, M. *Turk. Comput. Theor. Chem.* **2018**, *2*, 23.

(88)   Szczepanik, D. W.; Andrzejak, M.; Dominikowska, J.; Pawełek, B.; Krygowski, T. M.; Szatylowicz, H.; Solà, M. *Phys. Chem. Chem. Phys.* **2017**, *19*, 28970.

(89)   Szczepanik, D. W.; Andrzejak, M.; Dyduch, K.; Żak, E.; Makowski, M.; Mazur, G.; Mrozek, J. *Phys. Chem. Chem. Phys.* **2014**, *16*, 20514.

(90)   Orozco-Ic, M.; Soriano-Agueda, L.; Escayola, S.; Sundholm, D.; Merino, G.; Matito, E. *J. Org. Chem.* **2024**, *89*, 2459.

(91)   García-Fernández, C.; Sierda, E.; Abadía, M.; Bugenhagen, B.; Prosenc, M. H.; Wiesendanger, R.; Bazarnik, M.; Ortega, J. E.; Brede, J.; Matito, E.; Arnau, A. *J. Phys. Chem. C* **2017**, *121*, 27118.

(92)   Poater, J.; Escayola, S.; Poater, A.; Teixidor, F.; Ottosson, H.; Viñas, C.; Solà, M. *J. Am. Chem. Soc.* **2023**, *145*, 22527.

(93)   Ottosson, H. *Chem. Sci.* **2023**, *14*, 5542.

(94)   Yanai, T.; Tew, D. P.; Handy, N. C. *Chem. Phys. Lett.* **2004**, *393*, 51.

(95)   Dunning, T. H. *J. Chem. Phys.* **1989**, *90*, 1007.

(96)   Tomasi, J.; Mennucci, B.; Cammi, R. *Chem. Rev.* **2005**, *105*, 2999.

(97)   Frisch, M. J.; Trucks, G. W.; Schlegel, H. B.; Scuseria, G. E.; Robb, M. A.; Cheeseman, J. R.; Scalmani, G.; Barone, V.; Petersson, G. A.; Nakatsuji, H.; Li, X.; Caricato, M.; Marenich, A. V.; Bloino, J.; Janesko, B. G.; Gomperts, R.; Mennucci, B.; Hratchian, H. P.; Ortiz, J. V.; Izmaylov, A. F.; Sonnenberg, J. L.; Williams; Ding, F.; Lipparini, F.; Egidi, F.; Goings, J.; Peng, B.; Petrone, A.; Henderson, T.; Ranasinghe, D.; Zakrzewski, V. G.; Gao, J.; Rega, N.; Zheng, G.; Liang, W.; Hada, M.; Ehara, M.; Toyota, K.; Fukuda, R.; Hasegawa, J.; Ishida, M.; Nakajima, T.; Honda, Y.; Kitao, O.; Nakai, H.; Vreven, T.; Throssell, K.; Montgomery Jr., J. A.; Peralta, J. E.; Ogliaro, F.; Bearpark, M. J.; Heyd, J. J.; Brothers, E. N.; Kudin, K. N.; Staroverov, V. N.; Keith, T. A.; Kobayashi, R.; Normand, J.; Raghavachari, K.; Rendell, A. P.; Burant, J. C.; Iyengar, S. S.; Tomasi, J.; Cossi, M.; Millam, J. M.; Klene, M.; Adamo, C.; Cammi, R.; Ochterski, J. W.; Martin, R. L.; Morokuma, K.; Farkas, O.; Foresman, J. B.; Fox, D. J. Gaussian 16, Revision A.03, Wallingford, CT, 2016.

(98)   Matito, E.; Duran, M.; Solà, M. *J. Chem. Phys.* **2004**, *122*, 014109.

(99)   Matito, E.; Duran, M.; Solà, M. *J. Chem. Phys.* **2006**, *125*, 059901.

(100)   Giambiagi, M.; de Giambiagi, M. S.; dos Santos Silva, C. D.; de Figueiredo, A. P. *Phys. Chem. Chem. Phys.* **2000**, *2*, 3381.

(101)   Bultinck, P.; Ponec, R.; Van Damme, S. *J. Phys. Org. Chem.* **2005**, *18*, 706.

(102)   Keith, T. A. TK Gristmill Software, Overland Park KS, USA, 2019.

(103)   Kruszewski, J.; Krygowski, T. M. *Tetrahedron Lett.* **1972**, *13*, 3839.

(104)   Glendening, E. D.; Landis, C. R.; Weinhold, F. *J. Comput. Chem.* **2013**, *34*, 1429.

(105)   Fliegl, H.; Taubert, S.; Lehtonen, O.; Sundholm, D. *Phys. Chem. Chem. Phys.* **2011**, *13*, 20500.

(106)   Sundholm, D.; Fliegl, H.; Berger, R. J. F. *Wiley Interdiscip. Rev. Comput. Mol. Sci.* **2016**, *6*, 639.

(107)   Claessens, C. G.; González-Rodríguez, D.; McCallum, C. M.; Nohr, R. S.; Schuchmann, H.-P.; Torres, T. *J. Porphyr. Phthalocya.* **2007**, *11*, 181.

(108)   Khelevina, O.; Stuzhin, P.; Berezin, B. *Koord. Khim.* **1988**, *14*, 1199.

(109)   Rodríguez-Morgade, M. S.; Claessens, C. G.; Medina, A.; González-Rodríguez, D.; Gutiérrez-Puebla, E.; Monge, A.; Alkorta, I.; Elguero, J.; Torres, T. *Chem. Eur. J.* **2008**, *14*, 1342.

(110)   Inokuma, Y.; Kwon, J. H.; Ahn, T. K.; Yoo, M.-C.; Kim, D.; Osuka, A. *Angew. Chem. Int. Ed.* **2006**, *45*, 961.

(111)   Liu, X.; Yeow, E. K. L.; Velate, S.; Steer, R. P. *Phys. Chem. Chem. Phys.* **2006**, *8*, 1298.

(112)   Álvarez-Moreno, M.; de Graaf, C.; López, N.; Maseras, F.; Poblet, J. M.; Bo, C. *J. Chem. Inf. Model.* **2015**, *55*, 95.

5.2 Global Aromaticity in Nanographene

5.2.1 An Unprecedented π-Electronic Circuit Involving an Odd Number of Carbon Atoms in a Grossly Warped Non-Planar Nanographene

This section corresponds to the following publication:

S. Escayola, A. Poater, A. Muñoz-Castro*, M. Solà*. *Chem. Commun.*, **2021**, 57, 3087-3090.

ChemComm

Check for updates

An unprecedented π-electronic circuit involving an odd number of carbon atoms in a grossly warped non-planar nanographene†

Sílvia Escayola, [ab] Albert Poater, [a] Alvaro Muñoz-Castro [*c] and Miquel Solà [*a]

The formation of π-aromatic circuits along a grossly warped nanographene, $C_{80}H_{30}$, containing five- and seven-membered rings inserted into a six-membered mesh, reveals global π-circuits at the edge of the backbone. Based on DFT calculations, one of the two most favorable circuits for π-electron delocalization formally has 50 π-electrons abiding by Hückel's rule, whereas the second one formally has 75 π-electrons and, remarkably, it does not follow any of the known rules of aromaticity.

Since the early rationalization of a benzene bonding structure depicted by Kekule's seminal work more than a century and a half ago,[1–3] aromatic molecules have attracted the interest of the scientific community.[4–12] Fused ring species, such as polycyclic aromatic hydrocarbons (PAHs), fullerenes, and porphyrins, to name a few, are challenging cases owing to the presence of different aromatic or antiaromatic circuits of local or global character.[13–21]

The incorporation of extended fused rings in a PAH structure following the continuous development of synthetic strategies[22–24] allows further exploration of the chemistry of finite nanographenes with promising shapes, properties, and applications. The hexagonal honeycomb-like arrangements found in benzenoid PAH lead to planar geometries. Defects in the form of non-hexagonal rings in such networks cause distortions away from planarity. Non-planar π-extended PAHs can be achieved with the presence of five- or seven-membered rings in the structural backbone,[25] resulting in a curved surface

to release the strain given by the incorporation of different ring sizes in a hexagonal mesh. In this sense, pentagons induce a positive curvature of the surface, as observed in corannulene with a characteristic bowl-shape,[26] whereas heptagons induce a negative curvature, as denoted in [7]circulene with a saddle-shaped surface.[27,28]

The grossly warped nanographene ($C_{80}H_{30}$, **1**), which was synthesized by Itami and Scott in 2013,[29] exploits the presence of both bowl- and saddle-shaped sections in a 26-ring nanographene proving the consequences of multiple odd defects in the π-extended PAH. This nanographene (**1**) obtained by successive expansion of corannulene ($C_{20}H_{10}$)[29] contains a central pentagon and five peripheral heptagons with a novel π-landscape with enhanced solubility and electronic-related properties. Like corannulene,[30,31] this grossly warped nanographene is prone to undergo a bowl-to-bowl inversion.

Whereas the aromaticity of benzenoid PAHs is usually well-described by Clar's π-sextet model,[32,33] the aromaticity of benzenoid PAHs containing defects in the form of 5- and 7-MRs is much less explored. In this work, we report our findings using density functional theory (DFT) calculations to unravel the electron delocalization characteristics of nanographene **1**. We performed geometry optimizations using the BP86-D3/TZ2P method and we used the geometries obtained to carry out NMR calculations at the OPBE/TZ2P level and electron delocalization studies at the CAM-B3LYP/6-311G(d,p) level (full computational details are given in the ESI†). π-Aromatic circuits are scrutinized by the electron density of delocalized bonds (EDDB),[34,35] gauge-including magnetically induced currents (GIMIC),[36–38] and induced magnetic field[39,40] calculations, besides structural features to get insight into how aromaticity is accommodated in a highly curved and strained sp²-surface. We aim to evaluate whether the presence of different ring-sizes in a nanographene sheet and the resulting curvature decreases or retains the aromatic properties inherent to the presence of local and global (anti)aromatic motifs along the curved π-surface. In addition, ¹³C-NMR patterns (fingerprint) are studied to relate the position

a Institute of Computational Chemistry and Catalysis and Department of Chemistry, University of Girona, C/ M. Aurèlia Capmany, 69, 17003 Girona, Spain. E-mail: miquel.sola@udg.edu

b Donostia International Physics Center (DIPC), Donostia, Euskadi, Spain

c Grupo de Química Inorgánica y Materiales Moleculares, Facultad de Ingeniería, Universidad Autónoma de Chile, El Llano Subercaseaux 2801, Santiago, Chile. E-mail: alvaro.munoz@uautonoma.cl
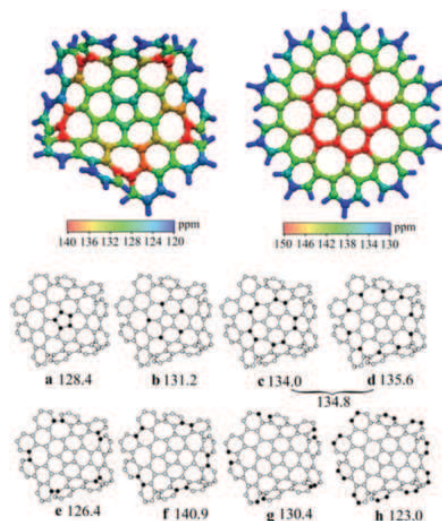
Fig. 1 Calculated ^{13}C-NMR chemical shifts for warped nanographene (**1**) (above-left) and planar (above-right), and averaged calculated ^{13}C-NMR chemical shifts for warped nanographene (**1**), bottom.

of the C atoms at the nanographene sheet with the different shielding/deshielding areas.

The characterized structure for $C_{80}H_{30}$ nanographene (**1**), is based on corannulene, $C_{20}H_{10}$, as a minimal isolated-pentagon-motif[41] providing a central bowl-shaped section, introducing the first curvature to the nanographene π-surface (Fig. 1). The resulting depth at the central section amounts to 0.37 Å,[29] calculated at 0.44 Å in the gas phase, suggesting that the intermolecular aggregation influences the bowl-depth. The bowl-inversion barrier is estimated by the authors to be 18.9 kcal mol^{-1}, 7.4 kcal mol^{-1} larger than that of $C_{20}H_{10}$,[42] owing to the presence of the surrounding heptagons. The resulting warped structure exhibits five chiral seven-membered rings (7-MRs), denoted as *P* and *M*, resulting in two isomers, namely, *PMPMP*- and *MPMPM*-, the former being the one employed in the current work.

^{13}C-NMR analysis[29] provides seven peaks at 139.2, 133.8, 131.7, 129.7, 128.1, 127.5, and 122.5 ppm, as slight wide signals. The calculated values exhibit several peaks (Fig. 1) accounting for the different carbon atom types owing to the fact that the relaxed structure does not possess a five-fold rotation axis, resulting in a differentiation within a carbon of the same type given the variable curvature along the π-surface. More strained carbon atoms around the heptagonal rings appear at lower-field in comparison to the central section. The terminal carbons, C–H, are located at higher-field, similarly to corannulene.[43] The planar nanographene with a five-fold axis shows the "hub" and "rim" atoms from the central corannulene motif in $C_{80}H_{30}$ to be located at lower-field (162.5 and 159.4 ppm, respectively), suggesting a more strained region within such structure.

Further analysis of the calculated ^{13}C-NMR values shows that the average of the similar carbon atom types agrees well with the experimentally characterized values, denoting signals at 128.4 ppm (Exp: 127.5 ppm) for the central pentagon (**a**) and

131.2 ppm for the "hub" atoms (Exp: 131.7 ppm) (**b**). Interestingly, the experimental peak at 133.8 ppm is resolved for carbons **c** and **d** on average, denoting the constant rearrangement provided by the small transition state barrier. Lastly, the signals at 126.4, 140.9, 130.4, and 123.0 ppm account for the peripheral atoms of type **e**, **f**, **g**, and **h** (Fig. 1), respectively. This allows further exploration of the magnetic behavior of **1**.

Moreover, the induced magnetic field (B^{ind}) is calculated to provide characteristics of the resulting shielding or deshielding regions related to the local and global aromatic properties of the individual rings and the overall nanographene structure. B^{ind} is related to the applied field (B^{ext}) via $B_i^{ind} = -\sigma_{ij}B_j^{ext}$, where the isotropic magnetic term is $B_{iso}^{ind} = -(1/3)(\sigma_{xx} + \sigma_{yy} + \sigma_{zz})B_j^{ext}$ accounting for the in-solution molecular tumbling. The resulting isotropic term (B_{iso}^{ind}, Fig. 2) suggests local aromaticity at external hexagons resulting from Clar's π-sextet patterns (see Fig. S2 in the ESI†) owing to the shielding regions, whereas at the central pentagon and peripheral heptagons, a deshielding region is found, signifying a local antiaromatic character, also denoted by NICS(0) calculations (see Fig. S3 in the ESI†). This observation is also denoted from the contour-plot representation (Fig. 2c), showing a shielding region for hexagons and deshielding regions for pentagons and heptagons.

Planar aromatics feature a characteristic long-range shielding response under a perpendicular field (B_z^{ext}), complemented with a perpendicular deshielding region at the ring backbone. This is rationalized as a shielding cone property depicted for different planar aromatic rings,[9,40,44–48] which is similar above and below the π-plane, as obtained for benzene.[40,45,46] For $C_{80}H_{30}$ nanographene, the bowl-shape results in a more shielded region at the concave face, where the shielding cones from aromatic hexagons interact additively, enhancing the strength and long-range characteristics of the overall structure (Fig. 2c). The localized deshielding regions at the pentagon and heptagons

Fig. 2 Induced magnetic field for warped nanographene (**1**), painted over a 0.01 a.u. electron density isosurface (a), shielding and deshielding isosurfaces at ±5.0 ppm (b), and as a cutplane over the *xz*-plane (c). Blue: Shielding; Red: Deshielding. See Fig. S4 (ESI†) for the same plots in the planar nanographene.

suggest that they remain as local antiaromatic (or non-aromatic, *vide infra*) rings, embedded into the extended shielding region enabled by the aromatic hexagons and the overall structure. The planar conformation of **1** (see Fig. S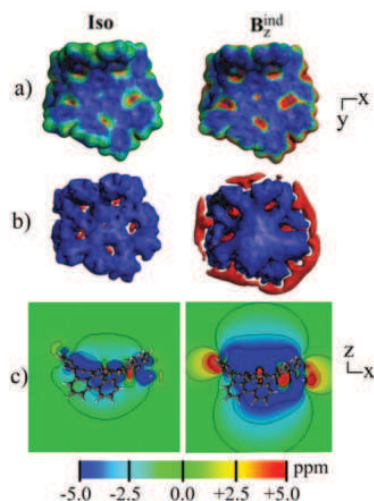4 in the ESI†) enhances the shielding and deshielding regions retaining the characteristics of the induced magnetic field.

To further explore the presence of extended aromatic circuits along the warped nanographene, and the characteristics of each ring locally, we employed different indicators related to geometric and electronic aspects of aromaticity. We used the harmonic oscillator model of aromaticity (HOMA, values close to 1 for aromatic rings)[49] as a geometric-based indicator of aromaticity. As electronic indices we employed the aromatic fluctuation index (FLU, values close to 0 for aromatic rings) and multicenter indices (MCI, see the ESI†), as well as the electron density of delocalized bonds (EDDB),[35,50–55] which measures the electrons delocalized through the system. In addition, the magnetic behavior of induced electronic currents along the molecular backbone is evaluated *via* a magnetically based index obtained from the GIMIC method.[37]

We unraveled the most favorable circuits for π-electronic delocalization in $C_{80}H_{30}$ nanographene, leading to different circuits along the nanographene as denoted in Fig. 3. Interestingly, extended π-circuits involving the external hexagons are the most favorable circuits for π-electron delocalization, according to the different geometrical and electronic aromaticity indices used. The trends remain the same when going from the optimized $C_{80}H_{30}$ nanographene structure to the planar one. Despite a warped π-surface with a challenging non-planar structure, this observation indicates that non-planar nanographenes are also prone to show extended aromatic circuits. The most favorable circuits are (i) the π-circuit that goes through the external rim of the most aromatic external rings (HOMA and FLU indices support this circuit as the most efficient for electronic delocalization) and (ii) the same π-circuit involving the five 7-MRs (EDDB favors this circuit, see Fig. S7 and S8,
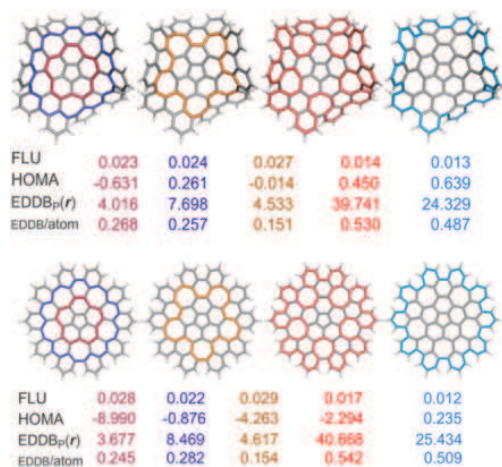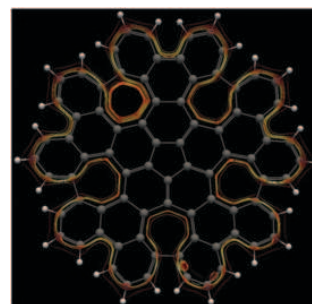
Fig. 4 Streamline representation of the current density in the planar configuration of the $C_{80}H_{30}$ nanographene. The intensity of the current decreases going from white (0.1 nA T^{-1} bohr^{-2}), light yellow, red to black (1 × 10^{-6} nA T^{-1} bohr^{-2}). See Fig. S14 (ESI†) for the same representation in the non-planar *PMPMP*-enantiomer of the $C_{80}H_{30}$ nanographene.

ESI† for EDDB plots). Note that the quantification of aromaticity by HOMA, FLU, and induced currents does not always reproduce the same trends.[56–58] The former circuit involves 50π-electrons and, therefore, follows the 4N + 2 Hückel's rule with N = 12. The latter comprises 75π-electrons, an odd number of electrons, consequently not following any of the known rules of aromaticity. Indeed, the rules usually originate when counting the number of electrons that are required to reach a closed-shell structure.[59] And this is not possible with an odd number of electrons. Interestingly, the most favorable π-circuit based on the GIMIC method[37] is the latter, as can be seen in the streamlined representation of the current density in the planar warped nanographene (Fig. 4 and Fig. S9, ESI† for the calculated net current strengths). This result is also supported by the current density plot in the plane at 2 Bohr above the molecular plane of planar nanographene (see Fig. S12, ESI†). As can be seen, the ring current flows through the π-circuit involving the aromatic external hexagonal rings and the five 7-MRs. Additional representations of the current density plots for the planar and non-planar warped nanographene can be found in Fig. S11–S13 (ESI†).

In conclusion, the grossly warped nanographene, $C_{80}H_{30}$, with a challenging π-landscape shows two most favorable circuits for π-electron delocalization, one with formally 50 π-electrons abiding by Hückel's rule. Interestingly, the second one formally has 75 π-electrons and, therefore, it does not follow any of the known rules of aromaticity. This result represents a change of paradigm in the field of aromaticity. To our knowledge, it is the first time that an efficient π-circuit for electronic delocalization is composed by an odd number of C atoms. Further exploration of larger π-circuits in nanographenes may contribute to the understanding of extended aromatic moieties and their characteristics as the size approaches the largest aromatic species to date involving 162 π-electrons,[13] or even more extended.

FLU	0.023	0.024	0.027	0.014	0.013
HOMA	−0.631	0.261	−0.014	0.450	0.639
EDDB$_P(r)$	4.016	7.698	4.533	39.741	24.329
EDDB/atom	0.268	0.257	0.151	0.530	0.487

|				
FLU	0.028	0.022	0.029	0.017	0.012
HOMA	−8.990	−0.876	−4.263	−2.294	0.235
EDDB$_P(r)$	3.677	8.469	4.617	40.668	25.434
EDDB/atom	0.245	0.282	0.154	0.542	0.509

Fig. 3 Aromaticity results of the selected pathways according to FLU, HOMA, and EDDB$_P(r)$ in the non-planar (above) and planar (below) *PMPMP*-enantiomer of the $C_{80}H_{30}$ nanographene.

Conflicts of interest

There are no conflicts to declare.

References

1 F. A. Kekulé, *Bull. Soc. Chim. Fr.*, 1865, **3**, 98–110.
2 F. A. Kekulé, *Ann. Chem. Pharm.*, 1866, **137**, 129–196.
3 A. Gero, *J. Chem. Educ.*, 1954, **31**, 201–202.
4 T. M. Krygowski, H. Szatylowicz, O. A. Stasyuk, J. Dominikowska and M. Palusiak, *Chem. Rev.*, 2014, **114**, 6383–6422.
5 T. M. Krygowski and M. K. Cyrański, *Chem. Rev.*, 2001, **101**, 1385–1420.
6 T. Heine, C. Corminboeuf and G. Seifert, *Chem. Rev.*, 2005, **105**, 3889–3910.
7 N. Martin and L. T. Scott, *Chem. Soc. Rev.*, 2015, **44**, 6397–6400.
8 G. Merino, A. Vela and T. Heine, *Chem. Rev.*, 2005, **105**, 3812–3841.
9 R. Gershoni-Poranne and A. Stanger, *Chem. Soc. Rev.*, 2015, **44**, 6597–6615.
10 R. Papadakis and H. Ottosson, *Chem. Soc. Rev.*, 2015, **44**, 6472–6493.
11 H. Miyoshi, S. Nobusue, A. Shimizu and Y. Tobe, *Chem. Soc. Rev.*, 2015, **44**, 6560–6577.
12 F. Feixas, E. Matito, J. Poater and M. Solà, *Chem. Soc. Rev.*, 2015, **44**, 6434–6451.
13 M. Rickhaus, M. Jirasek, L. Tejerina, H. Gotfredsen, M. D. Peeks, R. Haver, H.-W. Jiang, T. D. W. Claridge and H. L. Anderson, *Nat. Chem.*, 2020, **12**, 236–241.
14 A. Muñoz-Castro, *Phys. Chem. Chem. Phys.*, 2018, **20**, 3433–3437.
15 E. Vogel, *Angew. Chem., Int. Ed.*, 2011, **50**, 4278–4287.
16 J. I. Wu, I. Fernández and P. v. R. Schleyer, *J. Am. Chem. Soc.*, 2013, **135**, 315–321.
17 D. Chen, D. W. Szczepanik, J. Zhu, A. Muñoz-Castro and M. Solà, *Chem. – Eur. J.*, 2021, **27**, 802–808.
18 D. W. Szczepanik, M. Solà, T. M. Krygowski, H. Szatylowicz, M. Andrzejak, B. Pawełek, J. Dominikowska, M. Kukułka and K. Dyduch, *Phys. Chem. Chem. Phys.*, 2018, **20**, 13430–13436.
19 R. R. Valiev, H. Fliegl and D. Sundholm, *Phys. Chem. Chem. Phys.*, 2018, **20**, 17705–17713.
20 J. Wei, W.-X. Zhang and Z. Xi, *Chem. Sci.*, 2018, **9**, 560–568.
21 G. Naulet, L. Sturm, A. Robert, P. Dechambenoit, F. Röhricht, R. Herges, H. Bock and F. Durola, *Chem. Sci.*, 2018, **9**, 8930–8936.
22 A. Narita, X.-Y. Wang, X. Feng and K. Mullen, *Chem. Soc. Rev.*, 2015, **44**, 6616–6643.
23 A. Shiotari, I. Hamada, T. Nakae, S. Mori, T. Okujima, H. Uno, H. Sakaguchi, Y. Hamamoto, Y. Morikawa and Y. Sugimoto, *Nano Lett.*, 2020, **20**, 8339–8345.
24 X.-Y. Wang, X. Yao and K. Müllen, *Sci. China Chem.*, 2019, **62**, 1099–1144.
25 (*a*) J. Ma, K. Zhang, K. S. Schellhammer, Y. Fu, H. Komber, C. Xu, A. A. Popov, F. Hennersdorf, J. J. Weigand, S. Zhou, W. Pisula, F. Ortmann, R. Berger, J. Liu and X. Feng, *Chem. Sci.*, 2019, **10**, 4025–4031; (*b*) J. M. Fernández-Garcìa, P. J. Evans, S. M. Rivero, I. Fernández, D. Garcìa-Fresnadillo, J. Perles, J. Casado and N. Martìn, *J. Am. Chem. Soc.*, 2018, **140**, 17188–17196.
26 R. G. Lawton and W. E. Barth, *J. Am. Chem. Soc.*, 1971, **93**, 1730–1745.
27 K. Yamamoto, T. Harada, M. Nakazaki, T. Naka, Y. Kai, S. Harada and N. Kasai, *J. Am. Chem. Soc.*, 1983, **105**, 7171–7172.
28 S. H. Pun and Q. Miao, *Acc. Chem. Res.*, 2018, **51**, 1630–1642.
29 K. Kawasumi, Q. Zhang, Y. Segawa, L. T. Scott and K. Itami, *Nat. Chem.*, 2013, **5**, 739–744.
30 L. T. Scott, M. M. Hashemi and M. S. Bratcher, *J. Am. Chem. Soc.*, 1992, **114**, 1920–1921.
31 P. U. Biedermann, S. Pogodin and I. Agranat, *J. Org. Chem.*, 1999, **64**, 3655–3662.
32 V. E. Clar, *The Aromatic Sextet*, John Wiley & Sons Ltd, New York, 1972.
33 M. Solà, *Front. Chem.*, 2013, **1**, 22.
34 D. W. Szczepanik, M. Andrzejak, J. Dominikowska, B. Pawełek, T. M. Krygowski, H. Szatylowicz and M. Solà, *Phys. Chem. Chem. Phys.*, 2017, **19**, 28970–28981.
35 D. W. Szczepanik, M. Andrzejak, K. Dyduch, E. Żak, M. Makowski, G. Mazur and J. Mrozek, *Phys. Chem. Chem. Phys.*, 2014, **16**, 20514–20523.
36 J. Jusélius, D. Sundholm and J. Gauss, *J. Chem. Phys*, 2004, **121**, 3952–3963.
37 H. Fliegl, S. Taubert, O. Lehtonen and D. Sundholm, *Phys. Chem. Chem. Phys.*, 2011, **13**, 20500–20518.
38 D. Sundholm, H. Fliegl and R. J. F. Berger, *Wiley Interdiscip. Rev.: Comput. Mol. Sci.*, 2016, **6**, 639–678.
39 M. Buhl, M. Kaupp, V. G. Malkin and M. Bühl, *Calculation of NMR and EPR Parameters*, Wiley-VCH, Weinheim, FRG, 2004.
40 R. Islas, T. Heine and G. Merino, *Acc. Chem. Res.*, 2012, **45**, 215–228.
41 W. E. Barth and R. G. Lawton, *J. Am. Chem. Soc.*, 1966, **88**, 380–381.
42 T. J. Seiders, K. K. Baldridge, E. L. Elliott, G. H. Grube and J. S. Siegel, *J. Am. Chem. Soc.*, 1999, **121**, 7439–7440.
43 A. M. Orendt, J. C. Facelli, S. Bai, A. Rai, M. Gossett, L. T. Scott, J. Boerio-Goates, R. J. Pugmire and D. M. Grant, *J. Phys. Chem. A*, 2000, **104**, 149–155.
44 P. R. von Schleyer and H. Jiao, *Pure Appl. Chem.*, 1996, **68**, 209–218.
45 G. Merino, T. Heine and G. Seifert, *Chem. – Eur. J.*, 2004, **10**, 4367–4371.
46 A. G. G. Papadopoulos, N. D. D. Charistos and A. Muñoz-Castro, *ChemPhysChem*, 2017, **18**, 1499–1502.
47 P. Lazzeretti, *Prog. Nucl. Magn. Reson. Spectrosc.*, 2000, **36**, 1–88.
48 R. Benassi, P. Lazzeretti and F. Taddei, *J. Phys. Chem.*, 1975, **79**, 848–851.
49 J. Kruszewski and T. M. Krygowski, *Tetrahedron Lett.*, 1972, **13**, 3839–3842.
50 P. Bultinck, R. Ponec and S. Van Damme, *J. Phys. Org. Chem.*, 2005, **18**, 706–718.
51 E. Matito, *Phys. Chem. Chem. Phys.*, 2016, **18**, 11839–11846.
52 E. Matito, M. Duran and M. Solà, *J. Chem. Phys.*, 2005, **122**, 014109.
53 E. Matito, M. Duran and M. Solà, *J. Chem. Phys.*, 2006, **125**, 059901.
54 D. W. Szczepanik, E. Żak, K. Dyduch and J. Mrozek, *Chem. Phys. Lett.*, 2014, **593**, 154–159.
55 D. W. Szczepanik, *Comput. Theor. Chem.*, 2016, **1080**, 33–37.
56 Z. Badri and C. Foroutan-Nejad, *Phys. Chem. Chem. Phys.*, 2016, **18**, 11693–11699.
57 L. Zhao, R. Grande-Aztatzi, C. Foroutan-Nejad, J. M. Ugalde and G. Frenking, *ChemistrySelect*, 2017, **2**, 863–870.
58 J. Poater, I. García-Cruz, F. Illas and M. Solà, *Phys. Chem. Chem. Phys.*, 2004, **6**, 314–318.
59 M. Solà, *Wiley Interdiscip. Rev.: Comput. Mol. Sci.*, 2019, **9**, e1404.

5.3 Double Aromaticity

5.3.1 In the Quest of Hückel–Hückel and Hückel–Baird Double Aromatic Tropylium (tri)Cation and Anion Derivatives

This section corresponds to the following publication:

RESEARCH ARTICLE

Journal of Physical Organic Chemistry WILEY

In the quest of Hückel–Hückel and Hückel–Baird double aromatic tropylium (tri)cation and anion derivatives

Sílvia Escayola[1,2] | Nathalie Proos Vedin[3] | Albert Poater[1] |
Henrik Ottosson[3] | Miquel Solà[1]

[1]Institut de Química Computacional i Catàlisi and Departament de Química, Universitat de Girona, C/ Maria Aurèlia Capmany, 69, Girona, Catalonia, 17003, Spain

[2]Donostia International Physics Center (DIPC), Manuel Lardizabal Ibilbidea, 4, Donostia, Euskadi, 20018, Spain

[3]Department of Chemistry - Ångström Laboratory, Uppsala University, Lägerhyddsvägen, 1, Uppsala, 75120, Sweden

Correspondence
Henrik Ottosson, Department of Chemistry - Ångström Laboratory, Uppsala University, 75120 Uppsala, Sweden.
Email: henrik.ottosson@kemi.uu.se

Miquel Solà, Institut de Química Computacional i Catàlisi and Departament de Química, Universitat de Girona, C/ Maria Aurèlia Capmany, 69, 17003 Girona, Catalonia, Spain.
Email: miquel.sola@udg.edu

Abstract

Besides the most common form of aromaticity involving a π-ring, hexaiodobenzene and hexakis(phenylselenyl)benzene dications also present σ-aromaticity in the outer ring formed by the main group substituents. These two compounds are considered σ- and π-double aromatic, and their characterization is of special interest to the fields of organic and structural chemistry. In this work, we decided to explore the double aromaticity in substituted tropylium cations for three reasons: (i) the seven neutral halogen substituents of the tropylium cations will, without oxidation, lead to 14 σ-electrons (a 4n + 2 Hückel number); (ii) tropylium cations are highly stable and can be easily generated experimentally; and (iii) whereas in substituted benzenes the distances between substituents in the optimized structures or X-ray crystals are too large to allow strong σ-aromaticity, these distances are expected to be shorter in substituted tropylium cations. Yet, instead of the expected σ-aromaticity, we found that the most stable geometries are highly puckered, meaning that delocalization in both π- and σ-systems is lost. Our results, which include also the tropylium anion and trication in the singlet and triplet state, show that there is a need to open a lone pair hole by oxidation to generate σ-aromaticity. Among the systems studied, only triplet $C_7Br_7^{+3}$ with an internal Hückel aromatic tropylium ring and an external incipient Baird aromatic Br_7 ring shows double π- and σ-aromaticity. This result, however, is functional-dependent and reveals that $^3C_7Br_7^{3+}$ is at the borderline for onset of double aromaticity.

KEYWORDS

Baird aromaticity, density functional theory, double aromaticity, excited state aromaticity, theoretical and computational chemistry

1 | INTRODUCTION

Aromaticity has been a central concept in chemistry since the discovery of benzene by Michael Faraday in 1825.[1] It has traditionally been associated with cyclic conjugated organic compounds that present a high π-electron delocalization.[2] For a long time, aromaticity was exclusively associated with π-electrons. However, already in 1979, Dewar introduced the concept of σ-aromaticity to explain the properties of cyclopropane,[3] although, much more recently, Schleyer proved that cyclopropane is not a σ-aromatic molecule.[4] The simplest aromatic molecule, H_3^+, is, in fact, a σ-aromatic molecule.[5] The first doubly aromatic system, the 3,5-dehydrophenyl cation, was identified by Schleyer and coworkers to possess σ- and π-aromaticity.[6] In recent years, the concept of aromaticity has been extended into inorganic chemistry.[7] It turns out that aromaticity in all-metal and semimetal clusters is much more complex than in organic chemistry with several possible combinations of aromaticities and antiaromaticies in the same molecule. The list of molecules with double or triple aromaticity or conflicting aromaticity is large. We briefly mention here four species: $LiAl_4^-$, which is double σ- and π-aromatic,[8] $Li_3Al_4^-$, which in the singlet state is σ-aromatic and π-antiaromatic[9] and in the triplet state is Hückel σ-aromatic and Baird π-aromatic,[10] B_6^{2-}, which is double σ- and π-antiaromatic,[11] and Hf_3, which is triple σ-, π-, and δ-aromatic.[7c,12]

Double aromaticity in classical organic chemistry is much more elusive. Cyclo[18]carbon, recently characterized by high-resolution atomic force microscope, can be considered as one such example of double Hückel π_{in} and π_{out} aromaticities.[13] Another example is the cyclo[16] carbon in its quintet state that was reported to be double Baird π_{in} and π_{out} aromatic.[14] Let us mention here that Baird's rule states that annulenes with $4n$ π-electrons are aromatic and those with $4n + 2$ are antiaromatic in their lowest triplet states.[15] In 1989, Sagl and Martin[16] synthesized the stable singlet ground state dication of hexaiodobenzene, $C_6I_6^{+2}$ (see Scheme 1A, right). Martin et al. provided much evidence on that such a dication had a double Hückel σ-aromaticity (with 10 delocalized electrons through the hexaiodo substituents) and π-aromaticity (with six delocalized electrons in the benzene ring).[16,17] Further theoretical studies supported the double σ- and π-aromaticity of the hexaiodobenzene cation.[18] Other hexahalobenzene dications and the singlet and triplet $C_6(ChH)_6^{2+}$ (Ch = S, Se, Te) species were explored computationally as potential candidates of double aromatic compounds.[19] Sundholm, Liegeois et al.[20] concluded that not only $C_6I_6^{2+}$ but also $C_6At_6^{2+}$, $C_6(SeH)_6^{2+}$, $C_6(SeMe)_6^{2+}$, $C_6(TeH)_6^{2+}$, $C_6(TeMe)_6^{2+}$, and

$C_6(SbH_2)_6^{2+}$ dications are doubly aromatic sustaining spatially separated ring currents in the carbon ring and in the outer ring of the molecule. Borazine analogues of hexaiodobenzene and hexakis (selenyl)benzene dication $B_3N_3I_6^{2+}$ as well as $B_3N_3(TeH)_6^{2+}$ were also reported to be doubly aromatic.[21] Double σ- and π-aromaticity was further claimed in a synthesized bishomotriboriranide[22] and in twisted thienylene-phenylene structures in toroidal and catenated topologies.[23]

Scheme 1 shows different σ- and π-electron counting situations in hexahalo- or hexachalco-substituted benzene and tropylium species in two oxidation states. Substituted benzene (Scheme 1A, left) is Hückel π-aromatic. Despite the fact that it has 12 σ-electrons, a $4n$ number, it cannot be Baird aromatic because one cannot generate a lowest-lying triplet state within the σ-orbital framework formed by the in-plane lone-pairs of the X substituents as these orbitals are fully occupied in the singlet ground state. Doubly oxidized benzene in its singlet ground state with two electrons removed from the σ-system (Scheme 1A, right) is double Hückel σ- and π-aromatic for some X substituents (X = I, At, SeH, TeH, ...). On the other hand, the tropylium cation in its singlet ground state (Scheme 1B, left) could be hypothetically classified as Hückel aromatic in both the σ- and π-systems. Finally, doubly oxidized tropylium cation in a triplet state with two electrons removed from the σ-system and two unpaired σ-electrons could be hypothetically
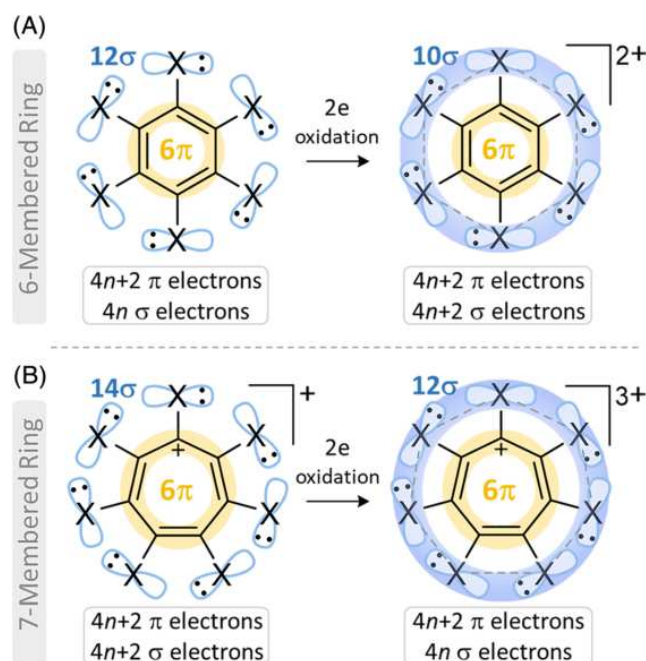
SCHEME 1 (A, B) Representation of different σ- and π-electron counting situations in hexahalo- or hexachalco-substituted (oxidized) benzene and tropylium species

Hückel π-aromatic and Baird σ-aromatic (double Hückel–Baird aromatic, Scheme 1B, right).

In 2018, Saito and co-workers reported in a combined computational and experimental study on the double σ- and π-aromatic character of the bench-stable hexakis(phenylselenyl)benzene dication (**1** in Figure 1).[24] Yet, the distance between the Se atoms in the X-ray crystal structure were 3.24–3.34 Å, and as a result, the σ-aromaticity can only be weak. Recently, with the aim to increase the overlap between the atoms of the outer cycle, Fowler and Havenith performed a computational study of the double aromaticity in larger eight-membered ring model systems $C_8I_8^q$ with charges $q = 0$, $+1$, $+2$, $+4$, -2.[25] However, the large I-I steric repulsion led to highly puckered structures with lack of both σ- and π-aromaticity. The authors demonstrated that in the case of planar constrained geometries with D_{4h} symmetry the systems exhibit double σ- and π-aromaticity. To our knowledge, to date no studies have been performed on substituted tropylium cations and anions (Scheme 1B and **2**, **3**, and **4** in Figure 1) as possible candidates for double σ- and π-aromaticity. Tropylium cations are especially interesting for three reasons: (i) the tropylium cations are highly stable and can be easily generated

experimentally and dissolved in a variety of solvents including methanol; (ii) whereas in the case of substituted benzene the distances between substituents in the optimized structures or X-ray crystal are too large to allow strong σ-aromaticity, these distances are expected to be shorter in substituted tropylium cations, allowing for stronger through-space interaction (however, if the X–X repulsion is too strong the molecule may pucker, losing aromatic character); and (iii) the halogen substituents of the tropylium cations lead to a 14 σ-electrons, a $4n + 2$ Hückel number; that is, we can test the ability to form a σ-aromatic ring when that halogen ring-system is neutral. Apart from the heptahalotropylium cation, several other combinations with tropylium anion and trication (**3** and **4**) with expected Baird/Hückel and Hückel/Baird double aromaticities in their triplet states have been tested (see Figure 1).

The ground state of the heptahalotropylium cation **2** is a singlet state that may be described by a 6π-electron Hückel-aromatic cycle and a 14σ-electron Hückel-aromatic cycle. Yet, for the heptahalotropylium anion **3**, the situation could be different as the singlet state potentially needs to be described as non-aromatic in both the 8π- and 14σ-electron cycles as the 8π-electron ring likely distorts so as to alleviate the Hückel-antiaromaticity at the D_{7h} symmetry, whereby the weak 14σ-electron Hückel aromaticity will be destroyed. In contrast, in the triplet state of **3** one can have a D_{7h} symmetric structure with a Baird-aromatic 8π-electron cycle as well as a 14σ-electron Hückel-aromatic cycle. With this investigation, we would like to answer questions such as the following: To what extent can neutral σ-electron systems sustain σ-aromaticity? Which are the limitations of double aromaticity and which general guiding rules can be given? Which state is the ground state of the heptahalotropylium anions, the singlet or the triplet?
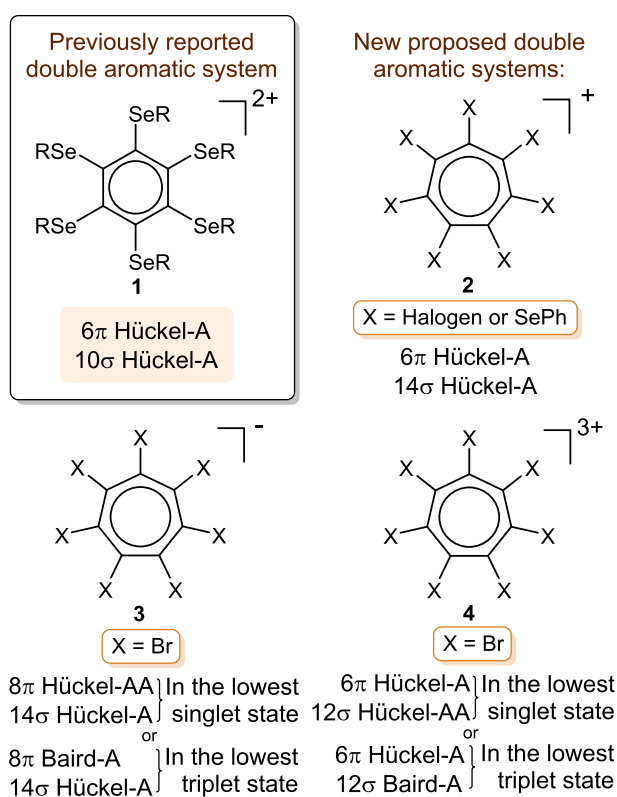
FIGURE 1 Systems with tropylium rings considered in our study (A stands for aromatic and AA for antiaromatic). In cases where the electron count leads to antiaromaticity, we expect the systems to pucker to become non-aromatic.

2 | COMPUTATIONAL DETAILS

All density functional theory (DFT) calculations were performed with Gaussian 16,[26] using BLYP, which combines Becke's 1988 exchange functional with the Lee, Yang, and Parr correlation functional.[27] The electronic configuration of the H, C, F, Cl, and Br atoms was described with the 6-311+G(d,p) basis set of Pople and co-workers,[28] whereas for I atoms the small-core quasi-relativistic Stuttgart/Dresden effective core potential, with an associated valence basis set (SDD), was employed.[29] The geometry optimizations were carried out with D_{7h} (and C_2 when D_{7h} was not possible) symmetry and also without symmetry constraints, and analytical frequency calculations were computed for the

characterization of the located stationary points. It is well known that the BLYP functional exaggerates delocalization in aromatic systems.[30] In our study, we use this functional to exaggerate delocalization so as to not overlook any system that potentially could be in-plane σ-aromatic. However, to check the reliability of our results, in some particular cases, we have evaluated the performance of hybrid, B3LYP[27b,31] and M06-2X,[32] and long range corrected, CAM-B3LYP,[33] functionals (see supporting information, SI, for more details).

The aromaticity has been quantified using structural, electronic, and magnetic probes of aromaticity. As structural measure of aromaticity, the planarity root-summed-square (RSS) index[34] was used. This index measures the deviation of a selection of atoms (in our case the seven or eight C atoms—RSS_C—or the seven or eight halogen atoms—RSS_X) from the best fitted plane and it is related to the fact that small aromatic systems usually prefer to be planar. As electronic indices,[35] we employed the multicenter index (MCI)[36] and the electron density of delocalized bonds (EDDB).[37] MCI measures the electron delocalization between different centers. Because of its size dependency, when comparing MCI of rings of different sizes, it is advisable to use the normalized version, $MCI^{1/N}$, where N is the number of atoms in the ring.[38] The EDDB method decomposes the one-electron density in several "layers" corresponding to different levels of electron delocalization,[39] namely, the density of electrons localized on atoms (EDLA) representing inner shells, lone pairs, and so on; the electron density of localized bonds (EDLB) representing typical (2-center 2-electron) Lewis-like bonds; and EDDB, which represents electron density that cannot be assigned to atoms or bonds due to its (multicenter) delocalized nature. The EDDB population of electrons delocalized through the system of all conjugated bonds in a ring can be used as an indicator of aromaticity.[40] Finally, as magnetic indicator, we used the out-of-plane component of the nucleus-independent chemical shift (NICS), placing the probe at the ring plane and at 1 Å above and below it (NICS[0, 1, and $-1]_{zz}$).[41] In this case, negative values are indicative of aromatic structures, while positive values indicate non- or anti-aromaticity. In all cases, the computational level was the same as for the geometry optimization. Gaussian 16 was employed in the computation of all aromaticity and delocalization indices to get the geometry and wavefunction information used in AIMAll[42] together with ESI-3D[43] packages (for MCI), and NBO 6.0 together with the RunEDDB code for EDDB.[44]

3 | RESULTS AND DISCUSSION

This section is organized as follows. First, we discuss the results for the $C_7X_7^+$ cationic species (X = F, Cl, Br, and I); second, we analyze the singlet and triplet $C_7Br_7^-$ anionic systems; and, finally, we investigate the possibility of having double aromaticity in the singlet and triplet states of the $C_7Br_7^{+3}$ species.

3.1 | The tropylium cation derivatives

Figure 2 and Table 1 contain the most important geometric parameters of the restricted to D_{7h} symmetry and fully optimized (C_1) $C_7X_7^+$ species **2** (X = F, Cl, Br, and I) in their singlet states. As can be seen, the molecule remains planar only in the case of $C_7F_7^+$. For all other systems, the planar geometry is a transition state for ring inversion with at least two out-of-plane distortions that stabilize the molecule. Moving from D_{7h} to C_1 symmetry releases 0.0, 1.3, 8.1, and 34.4 kcal/mol for $C_7F_7^+$, $C_7Cl_7^+$, $C_7Br_7^+$, and $C_7I_7^+$, respectively. According to the RSS values of Figure 2, the loss of planarity for the X_7 ring is much larger than that for the C_7 ring. Except for X = F, the X–X lone pair repulsions are strong enough to force the molecule to pucker losing the potential σ-aromatic character. Through the distortion of the planar geometry, the X–X distance increases from 0.05 for X = Cl to 0.15 Å for X = I. Puckering is not unexpected given that (i) the angle strain in seven-membered rings (7-MRs) can promote puckering as compared to the hexagonal 6-MRs, which are ideal for sp^2 C atoms[45]; (ii) the lowest out-of-plane (oop) frequency changes from 212 cm^{-1} in planar $^1C_7H_7^+$ to 81 cm^{-1} in planar $^1C_7F_7^+$ (see Table S2), showing that increasing the size of X in $^1C_7X_7^+$ increases steric congestion that promotes puckering of the 7-MR; and
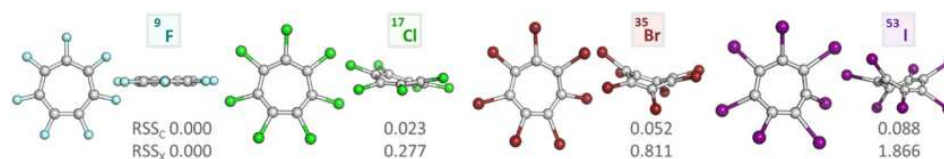
FIGURE 2 Front and side view of the fully optimized $^1C_7X_7^+$ (X = F, Cl, Br, and I) geometries using BLYP/6-311+G(d,p)∼SDD(I) and the planarity root-summed-square (RSS) index computed for the C- and X-rings (RSS_C and RSS_X, respectively)

TABLE 1 R_{C-C}, R_{C-X}, and R_{X-X} distances (Å) and number of imaginary frequencies for the relaxed and D_{7h} constrained geometries of $^1C_7X_7^+$ (X = H, F, Cl, Br, and I) and $^1C_6(SePh)_6^{2+}$ and $^1C_6I_6^{2+}$ compounds optimized at the BLYP/6-311+G(d,p)~SDD (for I) level of theory

System	R_{C-C}	R_{C-X}	R_{X-X}	$n_{imag.}$
$^1C_6(SePh)_6^{2+}$ (D_{2h})[a]	1.402	1.959	3.353 3.358 3.364	0
$^1C_6I_6^{2+}$ (D_{6h})	1.404	2.147	3.551	0
$^1C_7H_7^+$ (D_{7h})	1.406	1.092	2.354	0
$^1C_7F_7^+$ (D_{7h})	1.412	1.326	2.562	0
$^1C_7Cl_7^+$ (D_{7h})	1.432	1.742	2.944	2 (A″)
$^1C_7Cl_7^+$ (C_1)	1.434 1.431 1.426 1.424	1.742 1.740 1.738 1.737	3.007 3.002 2.995 2.992	0
$^1C_7Br_7^+$ (D_{7h})	1.435	1.925	3.106	4 (A″)
$^1C_7Br_7^+$ (C_1)	1.442 1.440 1.436 1.428 1.423 1.415 1.412	1.921 1.919 1.917 1.912 1.909 1.905 1.903	3.290 3.284 3.278 3.263 3.256 3.248 3.247	0
$^1C_7I_7^+$ (D_{7h})	1.440	2.212	3.359	4 (A″)
$^1C_7I_7^+$ (C_1)	1.456 1.454 1.443 1.431 1.407 1.394 1.386	2.172 2.170 2.165 2.160 2.147 2.139 2.131	3.744 3.741 3.738 3.722 3.676 3.666 3.660	0

[a]Optimized geometry at B3LYP-D3/6-31G(d)~SDD level of theory obtained from previous reference.[24]
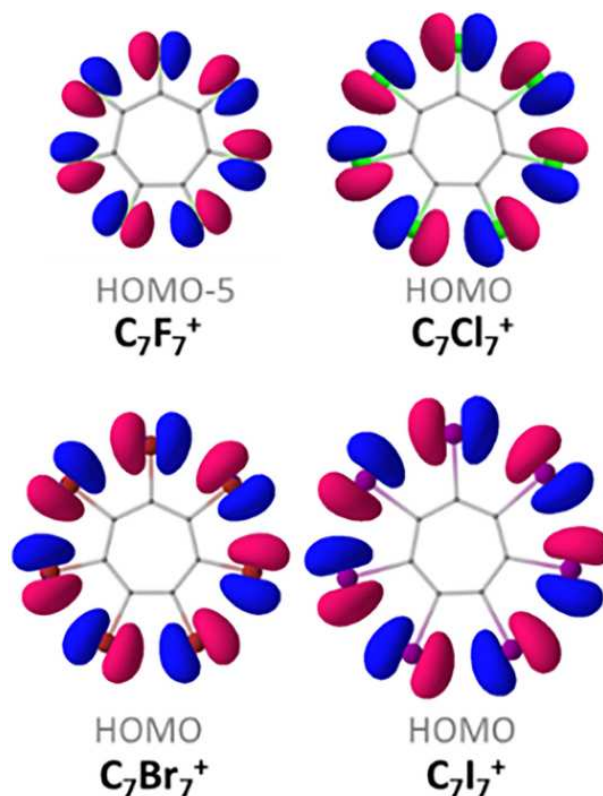
FIGURE 3 The HOMO-5 of D_{7h} $^1C_7F_7^+$ and the HOMO of D_{7h} $^1C_7X_7^+$ (X = Cl, Br, and I)

(iii) the highest occupied molecular orbital (HOMO) of D_{7h} $C_7X_7^+$ (X = Cl, Br, and I) contains seven in-plane antibonding interactions in the ring of X substituents (see Figure 3). The same type of HOMO with maximal in-plane antibonding interaction between the substituents was found by Fowler and Havenith in D_{4h} constrained C_8I_8.[25]

Interestingly, the distortion has a relatively small effect on the aromaticity of the tropylium ring, except in the case of X = I, for which the aromaticity reduction when going from D_{7h} to C_1 is more pronounced (see Table 2). This is in agreement with previous studies showing that π-aromaticity is quite robust with respect to out-of-plane and in-plane distortions.[46] Table 3 provides the aromaticity indices corresponding to the X_7 ring. As can be seen, the MCI is zero and the EDDB points to a residual delocalization in the X_7 ring, marginally larger for compounds with D_{7h} symmetry. In contrast, double aromatic $^1C_6(SePh)_6^{2+}$ and $^1C_6I_6^{2+}$ (especially the latter) have relatively large MCI_X and σ-$EDDB_X$. In the case of planar $^1C_7F_7^+$, the $2p$ orbitals of F are not diffuse enough to generate σ-delocalization. For the rest of the systems, which lose planarity, MCI, EDDB values, small X–X delocalization indices (see Table S3) as well as ring currents (see Figure S6) are in agreement with lack of

TABLE 2 Aromaticity indices (MCI and EDDB in electrons, NICS in ppm) corresponding to the C-ring for the relaxed and D_{7h} constrained geometries of $C_7X_7^+$ (X = H, F, Cl, Br, and I) compounds calculated at the BLYP/6-311+G(d,p)~SDD(I) level of theory

System	MCI_C	σ-$EDDB_C(r)$	π-$EDDB_C(r)$	$NICS(0)_{zz}$	$NICS(1)_{zz}$
$^1C_6(SePh)_6^{2+}$ (D_{2h})[a]	0.0517	0.381	4.683	−25.0	−35.1
$^1C_6I_6^{2+}$ (D_{6h})	0.0548	0.472	4.666	−31.9	−37.3
$^1C_7H_7^+$ (D_{7h})	0.0579	0.385	5.865	−15.9	−25.6
$^1C_7F_7^+$ (D_{7h})	0.0253	0.182	4.698	−13.8	−18.3
$^1C_7Cl_7^+$ (D_{7h})	0.0228	0.306	4.397	−3.4	−12.7
$^1C_7Cl_7^+$ (C_1)	0.0221	0.274	4.228	−4.2	−12.7[b]
$^1C_7Br_7^+$ (D_{7h})	0.0238	0.406	4.505	−4.2	−12.0
$^1C_7Br_7^+$ (C_1)	0.0210	0.310	3.800	−4.0	−10.9[b]
$^1C_7I_7^+$ (D_{7h})	0.0291	0.609	4.733	18.5[c]	27.9[c]
$^1C_7I_7^+$ (C_1)	0.0168	0.432	2.548	−7.8	−11.1[b]

[a]Optimized geometry at B3LYP-D3/6-31G(d)~SDD level of theory obtained from previous reference.[24]
[b]In the case of the non-symmetric systems the NICS(1) corresponds to the average of NICS(1) and (−1).
[c]These positive NICS values are an artifact produced by the exchange between LUMO and LUMO+2 when moving from $^1C_7Br_7^+$ (D_{7h}) to $^1C_7I_7^+$ (D_{7h}) (see Figure S2).

TABLE 3 Aromaticity indices (MCI and EDDB in electrons) corresponding to the X-ring for the relaxed and D_{7h} constrained geometries of $C_7X_7^+$ (X = F, Cl, Br, and I) compounds calculated at the BLYP/6-311+G(d,p)~SDD(I) level of theory

System	MCI_X	σ-$EDDB_X(r)$	π-$EDDB_X(r)$
$^1C_6(SePh)_6^{2+}$ (D_{2h})[a]	0.0055	2.923	0.062
$^1C_6I_6^{2+}$ (D_{6h})	0.0444	5.251	0.087
$^1C_7F_7^+$ (D_{7h})	0.0000	0.103	0.200
$^1C_7Cl_7^+$ (D_{7h})	0.0000	0.210	0.338
$^1C_7Cl_7^+$ (C_1)	0.0000	0.201	0.301
$^1C_7Br_7^+$ (D_{7h})	0.0000	0.217	0.379
$^1C_7Br_7^+$ (C_1)	0.0000	0.230	0.324
$^1C_7I_7^+$ (D_{7h})	0.0000	0.180	0.462
$^1C_7I_7^+$ (C_1)	0.0000	0.299	0.301

[a]Optimized geometry at B3LYP-D3/6-31G(d)~SDD level of theory obtained from previous reference.[24]

σ-aromaticity in $C_7X_7^+$ (X = Cl, Br, and I). The above statement, is reinforced when we compare the MCI and EDDB values (Table 3) of $^1C_7X_7^+$ with $^1C_6(SePh)_6^{2+}$, previously characterized as weakly σ-aromatic, observing that the latter are more than an order of magnitude higher. As to the π-aromaticity, such aromaticity is found in the D_{7h} species and is reduced somewhat when going to the final optimized species. As a whole, despite having a favorable electron counting (Figure 1), $C_7X_7^+$ (X = F, Cl, Br, and I) species are not double σ- and π-aromatic, they are simply π-aromatic. Finally, let us mention that we obtained unexpected positive NICS values for $C_7I_7^+$. These positive NICS values are an artifact produced by the exchange between LUMO and LUMO+2 when

moving from $^1C_7Br_7^+$ (D_{7h}) to $^1C_7I_7^+$ (D_{7h}) (see Figure S2) that results in a change in the direction of the ring current that becomes paramagnetic (see Figure S6), thus explaining the positive NICS values. This is another example of the fact that there is not always a correspondence between ring currents and aromaticity.[47] Since NICS failures are more common in open-shell species,[48] we decided not to include NICS values in the discussion of the coming sections.

3.2 | The tropylium anion derivatives

Next, we decided to analyze compound **3** for X = Br, $C_7Br_7^-$, in the singlet and triplet states. In the singlet state, with 8π-electrons, we do not expect aromaticity in the tropylium ring. For the triplet state, however, it is possible to have Baird π-aromaticity in the tropylium ring and Hückel σ-aromaticity in the external ring through the Br_7 ring (14σ-electrons). We limited our study to $^1C_7Br_7^-$ and $^3C_7Br_7^-$ for two reasons: (i) X = Br is preferred over X = I to avoid excessive steric congestion that will result in ring puckering and (ii) X = Br is preferred to X = Cl because the Br atom has more diffuse $4p$ orbitals that can lead to better overlaps. In the case of the triplet state, the D_{7h} optimization was not possible and instead a planar C_2 optimized geometry was obtained. Going from planar to puckered $C_7Br_7^-$, the molecule is stabilized by 47.2 kcal/mol in the singlet state and by 18.6 kcal/mol in the triplet state. As expected, the stabilization due to puckering in the singlet state is larger because of the release of antiaromaticity when going from planar to puckered structure. According to the RSS values of Table 4, the loss of planarity for the Br_7 ring is

TABLE 4 R_{C-C}, R_{C-Br}, and R_{Br-Br} distances (Å), RSS, and number of imaginary frequencies for the relaxed and D_{7h} (C_2) constrained geometries in the singlet and triplet states of $C_7Br_7^-$ optimized at the BLYP/6-311+G(d,p) level of theory

System	R_{C-C} (Å)	R_{C-Br} (Å)	R_{Br-Br} (Å)	RSS_C	RSS_{Br}	$N_{imag.}$
$^1C_7Br_7^-$ (D_{7h})	1.393	2.114	3.228	0.000	0.000	4(A″)
$^1C_7Br_7^-$ (C_1)	1.391 1.429 1.360 1.451	2.053 1.970 2.030 1.990	3.505 3.578 3.459 3.641	0.077	1.707	0
$^3C_7Br_7^-$ (C_2)	1.374 1.404 1.443 1.461	2.036 2.044 2.049	3.186 3.188 3.190 3.191	0.000	0.000	4(A″) 1(A′)
$^3C_7Br_7^-$ (C_1)	1.396 1.415 1.400 1.358 1.447 1.371 1.422	1.979 1.967 2.428 1.980 1.972 2.073 2.003	3.488 3.459 3.780 3.618 3.462 3.431 3.716	0.061	1.601	0

much larger than that of the C_7 ring. When going from the planar to the non-planar structure, the C–C bond length alternation increases and the Br–Br distance increases by 0.3–0.5 Å.

Taking the values of $^1C_7Br_7^+$ (D_{7h}) in Table 2 as reference, the MCI_C and the $\pi\text{-EDDB}_C(\mathbf{r})$ of the C_7 ring of $^1C_7Br_7^-$ (D_{7h}) in Table 5 are somewhat higher than that of $^1C_7Br_7^+$ (D_{7h}). QTAIM charges in the Br_7 ring of $^1C_7Br_7^+$ (D_{7h}) and $^1C_7Br_7^-$ (D_{7h}) are 1.035 and -1.183 electrons, respectively (see Table S11). Therefore, the two added extra electrons in $^1C_7Br_7^-$ (D_{7h}) are mainly located in the Br atoms. This is why the MCI_C and the $\pi\text{-EDDB}_C(\mathbf{r})$ of the C_7 ring of $^1C_7Br_7^+$ (D_{7h}) and $^1C_7Br_7^-$ (D_{7h}) are similar. Now, moving from D_{7h} $^1C_7Br_7^-$ to C_1 $^1C_7Br_7^-$, MCI and $\pi\text{-EDDB}_C(\mathbf{r})$ decrease due to the increase in the bond length alternation that results in higher π-electron localization. When going from $^1C_7Br_7^-$ (D_{7h}) to $^3C_7Br_7^-$ (C_2), MCI and $\pi\text{-EDDB}_C(\mathbf{r})$ point to a decrease that we attribute to the loss of symmetry and increase in the bond length alternation that leads to a greater π-electron localization. Spin density of $^3C_7Br_7^-$ (C_2) shows that the excess of spin α is distributed among the C_7 and Br_7 rings (see Figure 4). Therefore, the planar C_7 ring cannot be considered fully Baird aromatic. Finally, release of the planarity in $^3C_7Br_7^-$ leads to further reduction of the MCI and $\pi\text{-EDDB}_C(\mathbf{r})$.

TABLE 5 Aromaticity indices (MCI and EDDB in electrons) corresponding to the C-ring for the relaxed (C_1) and constrained (D_{7h} or C_2) geometries in the singlet and triplet states of $C_7Br_7^-$ computed at the BLYP/6-311+G(d,p) level of theory

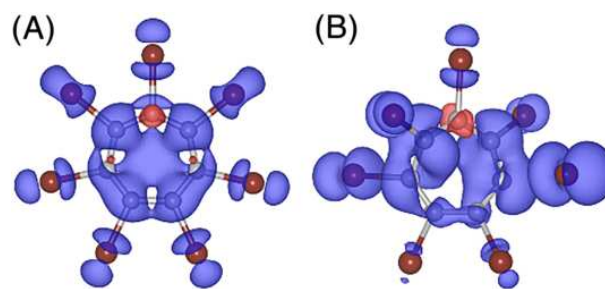| System	MCI_C	$\sigma\text{-EDDB}_C(r)$	$\pi\text{-EDDB}_C(r)$
$^1C_7Br_7^-$ (D_{7h})	0.0381	1.168	4.924
$^1C_7Br_7^-$ (C_1)	0.0080	0.477	2.327
$^3C_7Br_7^-$ (C_2)	0.0172	0.711	3.530
$^3C_7Br_7^-$ (C_1)	0.0121	1.119	2.336

FIGURE 4 Spin density distribution of (A) C_2 and (B) C_1 $^3C_7Br_7^-$. The isodensity corresponds to a value of 0.002 e$^-$/bohr^3. The positive and negative spin densities are represented in blue and red, respectively.

The loss of planarity, the low MCI and EDDB values in Table 6, and the delocalization indices (see Table S4) are in agreement with lack of σ-aromaticity in the Br_7 ring of $^1C_7Br_7^-$ and $^3C_7Br_7^-$. In summary, neither $^1C_7Br_7^-$ nor $^3C_7Br_7^-$, the latter despite having a favorable electron counting for Baird π- and Hückel σ-aromaticity, are double σ- and π-aromatic.

3.3 | The tropylium trication derivatives

As shown in previous subsections, following Hückel or Baird electron counting rules does not warrant the existence of double aromaticity. As pointed out by Schleyer et al.,[41b] aromaticity requires electron delocalization in closed circuits. In the Valence Bond language, this means that we must have a number of resonance structures with same or similar weights. In $C_7X_7^+$, we have seven resonance structures of the same weight, the resonating electrons being the 6π-electrons of the tropylium ring. However, the σ-electrons of the external electrons of X_7 ring are non-resonant localized lone pairs. Without the delocalization of the σ-electrons, in general, the systems cannot be σ-aromatic and they are only π-aromatic. Therefore, not only must the electron counting rules be fulfilled but also the σ-electrons in the external ring have to be delocalized. For instance, in the double aromatic $C_6I_6^{+2}$, double oxidation of C_6I_6 opens a hole in one of the *5p* orbitals of iodine that generates six possible resonance structures (Scheme 2 shows only three) that have the same weight. The existence of these resonance structures and the fulfillment of the Hückel's rule generate the double σ- and π-aromaticity.

TABLE 6 Aromaticity indices (MCI and EDDB in electrons) corresponding to the Br-ring for the relaxed (C_1) and constrained (D_{7h} or C_2) geometries in the singlet and triplet states of $C_7Br_7^-$ computed at the BLYP/6-311+G(d,p) level of theory

System	MCI_{Br}	$\sigma\text{-EDDB}_{Br}(r)$	$\pi\text{-EDDB}_{Br}(r)$
$^1C_7Br_7^-$ (D_{7h})	0.0003	0.742	0.236
$^1C_7Br_7^-$ (C_1)	0.0000	0.180	0.136
$^3C_7Br_7^-$ (C_2)	0.0002	0.406	0.165
$^3C_7Br_7^-$ (C_1)	0.0000	0.091	0.314
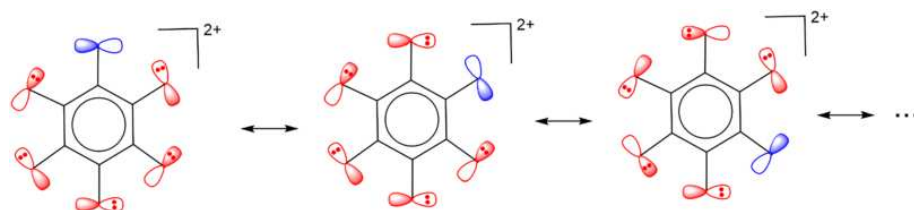
With this idea in mind, we decided to explore the singlet and triplet $C_7Br_7^{+3}$ species (system **4** in Figure 1). We expect that double oxidation of $C_7Br_7^+$ to generate $C_7Br_7^{+3}$ will create the necessary σ-delocalization. For the singlet, with 6π-electrons we expect Hückel aromaticity of the tropylium ring and Hückel antiaromaticity from the 12σ-electrons of the external Br_7 ring. On the other hand, for the triplet, we could have Hückel aromaticity of the tropylium ring and Baird aromaticity from the 12σ-electrons (10 paired and two unpaired electrons) of the outer Br_7 ring.

Interestingly, the $^1C_7Br_7^{+3}$ species is the first of our studied systems (except $^1C_7F_7^+$) that keeps the planarity and the D_{7h} symmetry (see Table 7). For the D_{7h} triplet, we have been unable to converge the self-consistent field (SCF) procedure; this was only possible for the C_2 symmetry. However, we have found a $^3C_7Br_7^{+3}$ species of C_1 symmetry that it is very close to the D_{7h} symmetry, with minor bond length alternation and RSS_C and RSS_{Br} close to zero. The energy difference with respect the C_2 constrained geometry is insignificant, only 0.03 kcal/mol. The singlet is more stable than the triplet by only 13.3 kcal/mol. These two species are good candidates to have both π-aromaticity and σ-(anti)aromaticity.

The MCI and EDDB results of $^1C_7Br_7^{+3}$ and $^3C_7Br_7^{+3}$ in Table 8 are almost identical to those of $^1C_7Br_7^+$, thus confirming the π-aromatic character of the tropylium ring in both states. Indeed, the spin density of Figure 5 is fully located in the outer Br_7 ring. On the other hand, the MCI and EDDB results of Table 9 point out the antiaromatic character of the Br_7 ring in the $^1C_7Br_7^{+3}$ species with a negative and relatively large MCI value. To our knowledge, this is the first example of an organic molecule showing conflicting aromaticity. The aromatic character of the Br_7 ring in C_1 $^3C_7Br_7^{+3}$ with a low MCI value is weak. Still this MCI value is the largest among the series of analyzed systems and is comparable to that of $C_6(SePh)_6^{2+}$ ($MCI_{Br}^{1/7} = 0.583$ as compared to $MCI_{Se}^{1/6} = 0.420$ of $C_6(SePh)_6^{2+}$). In addition, the high stability of the triplet with respect to the singlet is in agreement with the change from antiaromatic to aromatic character of the Br_7 ring when moving from the singlet to the triplet $C_7Br_7^{+3}$. Unfortunately, this double aromaticity is not confirmed by ring currents because of the high paratropic ring currents shown by the β

SCHEME 2 The double aromaticity in $C_6I_6^{2+}$ and similar species requires the opening of an electronic hole to generate σ-delocalization as indicated by the different resonance structures.

TABLE 7 R_{C-C}, R_{C-X}, and R_{X-X} distances (Å), RSS, and number of imaginary frequencies for the relaxed and D_{7h} constrained geometries in the singlet and triplet states of $C_7Br_7^{+3}$ optimized at BLYP/6-311+G(d,p) level of theory

System	R_{C-C} (Å)	R_{C-X} (Å)	R_{X-X} (Å)	RSS_C	RSS_{Br}	$N_{imag.}$
$^1C_7Br_7^{+3}$ (D_{7h})	1.419	1.914	3.080	0.000	0.000	0
$^3C_7Br_7^{+3}$ (C_2)	1.416 1.419 1.425 1.426	1.910 1.924 1.932 1.937	2.965 2.998 3.101 3.237	0.000	0.000	1
$^3C_7Br_7^{+3}$ (C_1)	1.426 1.418 1.421 1.426 1.424 1.416	1.908 1.926 1.936 1.920 1.913 1.933 1.930	3.206 2.984 3.018 3.250 3.074 2.968 3.146	0.001	0.008	0

TABLE 8 Aromaticity indices (MCI and EDDB in electrons) corresponding to the C-ring for the relaxed (C_1) and constrained (D_{7h} or C_2) geometries in the singlet and triplet states of $C_7Br_7^{+3}$ computed at BLYP/6-311+G(d,p) level of theory

System	MCI_C	$\sigma\text{-EDDB}_C(r)$	$\pi\text{-EDDB}_C(r)$
$^1C_7Br_7^{+3}$ (D_{7h})	0.0247	0.477	4.442
$^3C_7Br_7^{+3}$ (C_2)	0.0247	0.427	4.458
$^3C_7Br_7^{+3}$ (C_1)	0.0246	0.541	4.303
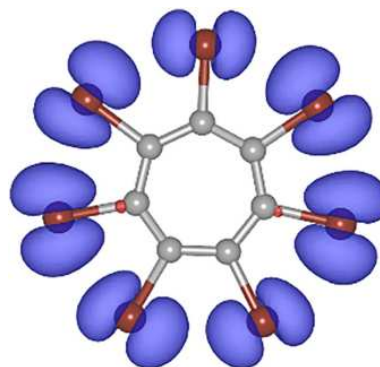
FIGURE 5 Spin density distribution of $^3C_7Br_7^{+3}$. The isodensity corresponds to a value of 0.002 e$^-$/bohr^3. The positive and negative spin densities are represented in blue and red, respectively.

TABLE 9 Aromaticity indices (MCI and EDDB in electrons) corresponding to the Br^7-ring in the singlet and triplet states of $C_7Br_7^{+3}$ computed at BLYP/6-311+G(d,p) level of theory

System	MCI_{Br}	$\sigma\text{-EDDB}_{Br}(r)$	$\pi\text{-EDDB}_{Br}(r)$
$^1C_7Br_7^{+3}$ (D_{7h})	-0.0246	5.484	0.440
$^3C_7Br_7^{+3}$ (C_2)	0.0027	2.787	0.519
$^3C_7Br_7^{+3}$ (C_1)	0.0023	2.626	0.489

electrons in $^3C_7Br_7^{+3}$ (see Figure S7). Still, we think that the results based on electron delocalization measures are more reliable than those derived from magnetic measures.

Finally, as discussed in Section 2, BLYP functional exaggerates delocalization in aromatic systems. Therefore, we expect the lack of double aromaticity in $^1C_7Br_7^+$, $^1C_7Br_7^-$, and $^3C_7Br_7^-$ to be confirmed with the B3LYP or CAM-B3LYP functionals. Less clear is the situation in triplet $C_7Br_7^{+3}$. Indeed, results obtained at the CAM-B3LYP/6-311+G(d,p) level of theory suggest that $^3C_7Br_7^{+3}$ has only π-aromaticity (see Tables S11 and S12). On the other hand, B3LYP results ($MCI_{Br}^{1/7} = 0.296$ and $\sigma\text{-EDDB}_{Br}(r) = 2.313$) are intermediate between those of BLYP and CAM-B3LYP.

In summary, we have found that, first, $^1C_7Br_7^{+3}$ species has conflicting aromaticity,[7a,9] with an internal Hückel aromatic tropylium ring and an external Hückel antiaromatic Br_7 ring; and second, $^3C_7Br_7^{+3}$ has double aromaticity with an internal Hückel π-aromatic tropylium ring and an external weak Baird σ-aromatic Br_7 ring. The presence of double aromaticity in triplet $C_7Br_7^{+3}$, however, depends on the functional used. It is likely that same situation is experienced by most of the so far reported double aromatic compounds.

4 | CONCLUSIONS

Double aromatic classical organic molecules follow two requirements: (i) they must have an electron counting corresponding to the Hückel or Baird rule for both the σ- and the π-systems and (ii) they must have σ- and the π-electron delocalization that in the valence bond language means they need to have more than a single resonance structure to correctly represent the σ- and the π-electron density. These are two necessary but not sufficient conditions. The presence of strong electronic repulsion between the external substituents or substituents with np orbitals that are not diffuse enough may quench the σ-aromaticity by puckering the benzene or tropylium cation rings. Among the species analyzed, the most interesting ones are $^1C_7Br_7^{+3}$, which according to BLYP results has an internal Hückel aromatic tropylium ring and an external Hückel antiaromatic Br_7 ring, and $^3C_7Br_7^{+3}$ with an internal Hückel aromatic tropylium ring and an external weak Baird aromatic Br_7 ring. This result, however, is not confirmed by the B3LYP and CAM-B3LYP functionals. Yet, the functional dependent results on $^3C_7Br_7^{3+}$ indicate that this species is at the borderline for double aromaticity, and it reveals the importance of balancing a number of factors in the design of double aromatic molecules: (*i*) the size of the substituents should allow for close through-space contacts but not overcrowding, (*ii*) the orbital occupancies should be such that orbitals with maximal antibonding in-plane interactions between the substituents must not be occupied (achieved by oxidation), and (*iii*) the inherent angle strain of a compound, which promotes puckering of the carbon framework, should be as low as possible. Hence, for 8-MRs one needs tetraoxidation to achieve double aromaticity,[25] with 7-MRs it is achieved for the trication, and with 6-MRs it is dications that can exhibit double aromaticity.[24]

DATA AVAILABILITY STATEMENT

A data set collection of computational results (Cartesian coordinates, energies, molecular orbitals, etc.) from this work is available in the ioChem-BD repository[49] and can be accessed via https://doi.org/10.19061/iochem-bd-4-43

ORCID

Nathalie Proos Vedin https://orcid.org/0000-0002-9313-3739
Henrik Ottosson https://orcid.org/0000-0001-8076-1165
Miquel Solà https://orcid.org/0000-0002-1917-7450

REFERENCES

[1] M. Faraday, *Philos. Trans. R. Soc. London* **1825**, *115*, 440.

[2] a) Aromaticity, *Modern computational methods and applications*, 1st ed., Elsevier, Dordrecht **2021**; b) M. Solà, A. I. Boldyrev, M. C. Cyrański, T. M. Krygowski, G. Merino, *Aromaticity and Antiaromaticity: Concepts and applications*, Wiley-VCH, Chichester **2022**.

[3] M. J. S. Dewar, *Bull. Soc. Chim. Belg.* **1979**, *88*, 957.

[4] W. Wu, B. Ma, J. I-Chia Wu, P. R. Schleyer, Y. Mo, *Chem. – Eur. J.* **2009**, *15*, 9730.

[5] R. W. A. Havenith, F. De Proft, P. W. Fowler, P. Geerlings, *Chem. Phys. Lett.* **2005**, *407*, 391.

[6] J. Chandrasekhar, E. D. Jemmis, P. V. R. Schleyer, *Tetrahedron Lett.* **1979**, *20*, 3707.

[7] a) A. I. Boldyrev, L.-S. Wang, *Chem. Rev.* **2005**, *105*, 3716; b) C. A. Tsipis, *Coord. Chem. Rev.* **2005**, *249*, 2740; c) F. Feixas, E. Matito, J. Poater, M. Solà, *WIREs Comput. Mol. Sci.* **2013**, *3*, 105.

[8] X. Li, A. E. Kuznetsov, H.-F. Zhang, A. Boldyrev, L.-S. Wang, *Science* **2001**, *291*, 859.

[9] A. E. Kuznetsov, K. A. Birch, A. I. Boldyrev, H.-J. Zhai, L.-S. Wang, *Science* **2003**, *300*, 622.

[10] D. Chen, D. W. Szczepanik, J. Zhu, M. Solà, *Chem. Commun.* **2020**, *56*, 12522.

[11] a) D. Y. Zubarev, A. I. Boldyrev, *Phys. Chem. Chem. Phys.* **2008**, *10*, 5207; b) A. N. Alexandrova, A. I. Boldyrev, H.-J. Zhai, L.-S. Wang, E. Steiner, P. W. Fowler, *J. Phys. Chem. A* **2003**, *107*, 1359.

[12] B. B. Averkiev, A. I. Boldyrev, *J. Phys. Chem. A* **2007**, *111*, 12864.

[13] K. Kaiser, L. M. Scriven, F. Schulz, P. Gawel, L. Gross, H. L. Anderson, *Science* **2019**, *365*, 1299.

[14] D. E. Bean, P. W. Fowler, A. Soncini, *Chem. Phys. Lett.* **2009**, *483*, 193.

[15] N. C. Baird, *J. Am. Chem. Soc.* **1972**, *94*, 4941.

[16] D. J. Sagl, J. C. Martin, *J. Am. Chem. Soc.* **1988**, *110*, 5827.

[17] J. C. Martin, L. J. Schaad, *Pure Appl. Chem.* **1990**, *62*, 547.

[18] I. Ciofini, P. P. Lainé, C. Adamo, *Chem. Phys. Lett.* **2007**, *435*, 171.

[19] a) M. Hatanaka, M. Saito, M. Fujita, K. Morokuma, *J. Org. Chem.* **2014**, *79*, 2640; (b) M. Orozco-Ic, J. Barroso, R. Islas, G. Merino, *ChemistryOpen* **2020**, *9*, 657.

[20] M. Rauhalahti, S. Taubert, D. Sundholm, V. Liégeois, *Phys. Chem. Chem. Phys.* **2017**, *19*, 7124.

[21] R. Pino-Rios, A. Vásquez-Espinal, O. Yañez, W. Tiznado, *RSC Adv.* **2020**, *10*, 29705.

[22] M. Unverzagt, G. Subramanian, M. Hofmann, P. v. R. Schleyer, S. Berger, K. Harms, W. Massa, A. Berndt, *Angew. Chem. Int. Ed. Engl.* **1997**, *36*, 1469.

[23] T. D. Leitner, Y. Gmeinder, F. Röhricht, R. Herges, E. Mena-Osteritz, P. Bäuerle, *Eur. J. Org. Chem.* **2020**, *2020*, 285.

[24] S. Furukawa, M. Fujita, Y. Kanatomi, M. Minoura, M. Hatanaka, K. Morokuma, K. Ishimura, M. Saito, *Commun. Chem.* **2018**, *1*, 60.

[25] P. W. Fowler, R. W. A. Havenith, *J. Phys. Chem. A* **2021**, *125*, 6374.

[26] M. J. Frisch, G. W. Trucks, H. B. Schlegel, G. E. Scuseria, M. A. Robb, J. R. Cheeseman, G. Scalmani, V. Barone, G. A. Petersson, H. Nakatsuji, X. Li, M. Caricato, A. V. Marenich, J. Bloino, B. G. Janesko, R. Gomperts, B. Mennucci, H. P. Hratchian, J. V. Ortiz, A. F. Izmaylov, J. L. Sonnenberg, F. Ding Williams, F. Lipparini, F. Egidi, J. Goings, B. Peng, A. Petrone, T. Henderson, D. Ranasinghe, V. G. Zakrzewski, J. Gao, N. Rega, G. Zheng, W. Liang, M. Hada, M. Ehara, K. Toyota, R. Fukuda, J. Hasegawa, M. Ishida, T. Nakajima, Y. Honda, O. Kitao, H. Nakai, T. Vreven, K. Throssell, J. A. Montgomery Jr., J. E. Peralta, F. Ogliaro, M. J. Bearpark, J. J. Heyd, E. N. Brothers, K. N. Kudin, V. N. Staroverov, T. A. Keith, R. Kobayashi, J. Normand, K. Raghavachari, A. P. Rendell, J. C. Burant, S. S. Iyengar, J. Tomasi, M. Cossi, J. M. Millam, M. Klene, C. Adamo, R. Cammi, J. W. Ochterski, R. L. Martin, K. Morokuma, O. Farkas, J. B. Foresman, D. J. Fox, Gaussian 16 Rev. B.01, Wallingford, CT, **2016**.

[27] a) A. D. Becke, *Phys. Rev. A* **1988**, *38*, 3098; b) C. Lee, W. Yang, R. G. Parr, *Phys. Rev. B* **1988**, *37*, 785.

[28] a) R. Krishnan, J. S. Binkley, R. Seeger, J. A. Pople, *J. Chem. Phys.* **1980**, *72*, 650; b) T. Clark, J. Chandrasekhar, G. W. Spitznagel, P. v. R. Schleyer, *J. Comput. Chem.* **1983**, *4*, 294.

[29] a) U. Häussermann, M. Dolg, H. Stoll, H. Preuss, P. Schwerdtfeger, R. M. Pitzer, *Mol. Phys.* **1993**, *78*, 1211; b) T. Leininger, A. Nicklass, H. Stoll, M. Dolg, P. Schwerdtfeger, *J. Chem. Phys.* **1996**, *105*, 1052.

[30] a) D. W. Szczepanik, M. Solà, M. Andrzejak, B. Pawelek, J. Dominikowska, M. Kukulka, K. Dyduch, T. M. Krygowski, H. Szatylowicz, *J. Comput. Chem.* **2017**, *38*, 1640; b) I. Casademont-Reig, R. Guerrero-Avilés, E. Ramos-Cordoba, M. Torrent-Sucarrat, E. Matito, *Angew. Chem., Int. Ed.* **2021**, *60*, 24080;

[31] a) A. D. Becke, *J. Chem. Phys.* **1993**, *98*, 5648; b) P. J. Stephens, F. J. Devlin, C. F. Chabalowski, M. J. Frisch, *J. Phys. Chem.* **1994**, *98*, 11623.

[32] Y. Zhao, D. G. Truhlar, *Theor. Chem. Acc.* **2008**, *120*, 215.

[33] T. Yanai, D. P. Tew, N. C. Handy, *Chem. Phys. Lett.* **2004**, *393*, 51.

[34] E. Matito, J. Poater, M. Duran, M. Solà, *J. Mol. Struct.: THEO-CHEM* **2005**, *727*, 165.

[35] F. Feixas, E. Matito, J. Poater, M. Solà, *Chem. Soc. Rev.* **2015**, *44*, 6434.

[36] P. Bultinck, R. Ponec, S. Van Damme, *J. Phys. Org. Chem.* **2005**, *18*, 706.

[37] D. W. Szczepanik, M. Andrzejak, J. Dominikowska, B. Pawełek, T. M. Krygowski, H. Szatylowicz, M. Solà, *Phys. Chem. Chem. Phys.* **2017**, *19*, 28970.

[38] J. Cioslowski, E. Matito, M. Solà, *J. Phys. Chem. A* **2007**, *111*, 6521.

[39] D. W. Szczepanik, *Comput. Theor. Chem.* **2016**, *1080*, 33.

[40] D. W. Szczepanik, M. Solà, T. M. Krygowski, H. Szatylowicz, M. Andrzejak, B. Pawelek, J. Dominikowska, M. Kukulka, K. Dyduch, *Phys. Chem. Chem. Phys.* **2018**, *20*, 13430.

[41] a) P. v. R. Schleyer, C. Maerker, A. Dransfeld, H. Jiao, N. J. R. van Eikema Hommes, *J. Am. Chem. Soc.* **1996**, *118*, 6317; b) Z. Chen, C. S. Wannere, C. Corminboeuf, R. Puchta, P. v. R. Schleyer, *Chem. Rev.* **2005**, *105*, 3842; c) P. v. R. Schleyer, M. Manoharan, Z. X. Wang, B. Kiran, H. J. Jiao, R. Puchta, N. J. R. van Eikema Hommes, *Org. Lett.* **2001**, *3*, 2465; d) A. Stanger, *J. Org. Chem.* **2006**, *71*, 883.

[42] T. A. Keith, *AIMAll (Version 19.10.12)*, TK Gristmill Software, Overland Park KS, USA **2014**. http://aim.tkgristmill.com

[43] a) E. Matito, *ESI-3D: Electron sharing indexes program for 3D molecular space partitioning*. http://iqc.udg.es/~eduard/ESI, IQCC (Girona, Catalonia) and DIPC (Donostia, Euskadi), Spain **2015**; b) E. Matito, M. Solà, P. Salvador, M. Duran, *Faraday Discuss.* **2007**, *135*, 325.

[44] D. W. Szczepanik, RunEDDB (version 26-Jun-2021), Krakow, Poland, **2021**. http://www.eddb.pl/runeddb.

[45] P. Preethalayam, N. P. Vedin, S. Radenković, H. Ottosson, *J. Phys. Org. Chem.* **2022**. PMID: submitted.

[46] F. Feixas, E. Matito, J. Poater, M. Solà, *J. Phys. Chem. A* **2007**, *111*, 4513.

[47] L. Zhao, R. Grande-Aztatzi, C. Foroutan-Nejad, J. M. Ugalde, G. Frenking, *ChemistrySelect* **2017**, *2*, 863.

[48] M. Mauksch, S. B. Tsogoeva, *Chem. – Eur. J.* **2021**, *27*, 14660.

[49] M. Álvarez-Moreno, C. de Graaf, N. López, F. Maseras, J. M. Poblet, C. Bo, *J. Chem. Inf. Model.* **2015**, *55*, 95.

SUPPORTING INFORMATION

Additional supporting information can be found online in the Supporting Information section at the end of this article.

5.4   Icosahedral Boron Clusters: 3D Aromaticity

5.4.1   Too Persistent to Give Up: Aromaticity in Boron Clusters Survives Radical Structural Changes

This section corresponds to the following publication:

J. Poater, C. Viñas, I. Bennour, S. Escayola, M. Solà*, F. Teixidor*. *J. Am. Chem. Soc.*, **2020**, 142, 9396-94077.

Too Persistent to Give Up: Aromaticity in Boron Clusters Survives Radical Structural Changes

Jordi Poater, Clara Viñas, Ines Bennour, Sílvia Escayola, Miquel Solà,* and Francesc Teixidor*

ACCESS | Metrics & More | Article Recommendations | Supporting Information

ABSTRACT: o-$C_2B_{10}H_{12}$ isomerizes to m-$C_2B_{10}H_{12}$ upon heating at 400 °C. Deboronation in o-$C_2B_{10}H_{12}$ is a relatively easy process, whereas it is more difficult in m-$C_2B_{10}H_{12}$. These two experimental facts indicate that m-$C_2B_{10}H_{12}$ is thermodynamically more stable than o-$C_2B_{10}H_{12}$. On the other hand, it is widely accepted that *closo*-boranes and -carboranes are aromatic compounds. In this work, we relate the difficulty in the deboronation of the carboranes with their stability and aromaticity. We do this by combining lab work and DFT calculations. Computationally, our results show that the higher thermodynamic stability of m-$C_2B_{10}H_{12}$ is not related to aromaticity differences but to the location of the C atoms in the carborane structure. It is also demonstrated that the aromaticity observed in *closo*-boranes and -carboranes is also present in their *nido* counterparts, and consequently, we conclude that aromaticity in boron clusters survives radical structural changes. Further, sandwich metallocenes (e.g., ferrocene) and sandwich metallabis(dicarbollides) (e.g., $[Co(C_2B_9H_{11})_2]^-$) have traditionally been considered to be similar. Here it is shown that they are not. Metallabis(dicarbollides) display global aromaticity, whereas metallocenes present local aromaticity in the ligands. Remarkable and unique is the double probe given by ^1H and ^{11}B NMR tracing the reciprocally antipodal endocyclic open face H_{ec} and B_1. These magnetic studies have permitted one to correlate both nuclei and relate them to a diatropic current in the plane at the middle of the *nido*-$[C_2B_9H_{12}]^-$. This observation is the first unique evidence that proves experimentally the existence of diatropic currents, and thence aromaticity, in clusters and is comparable to the existence of diatropic currents in planar aromatic compounds. Additionally, heteroboranes with two carbon atoms have been compared to heterocycles with two nitrogen or boron atoms, e.g., $C_2B_{10}H_{12}$ carboranes versus planar $N_2C_4H_4$ diazines or $[B_2C_4H_4]^{2-}$ diboratabenzenes, thereby proving the higher persistence of the aromaticity of the tridimensional compounds in heteroatom-substituted species. This research accounts very well for the "paradigm for the electron requirements of clusters", in which a *closo*-cluster that is aromatic upon addition of $2e^-$ becomes also an aromatic *nido*-species, and explains the informative schemes by Rudolph and Williams.

■ INTRODUCTION

As time goes by, metallacarboranes of the type [M-$(C_2B_9H_{11})_2]^-$ (M = Co, Fe, Ni), named as metallabis-(dicarbollides), have become increasingly important. The first applications were found in nuclear waste remediation[1−10] and, over the years, in advanced materials,[11−13] healthcare,[14] and energy.[15−17] Particularly relevant is their extraordinary stability that features outer-sphere electron transfer, along with the positive consequences that this may have in molecular electronics and aspects related to energy. For any application, but very particularly for nuclear waste remediation and electron transfer related aspects, the stability of the molecule is of utmost relevance. Bench chemists have often resorted to the criterion of aromaticity to account for the high stability of certain molecules. An aromatic molecule generally possesses a higher stability and therefore exhibits lower chemical reactivity in comparison to the associated nonaromatic and antiaromatic systems.

It is known that a very large number of transition-metal sandwich or half-sandwich structures are very stable[18−24] and are described as aromatic because as a molecule they keep the ability to undergo aromatic substitution type reactions while maintaining their cyclic conjugated system. Some appealing examples of these aromatic species are ferrocene and dibenzenechromium, which easily undergo electrophilic substitution but not electrophilic addition. In this sense, for ferrocene, $[Fe(C_5H_5)_2]$, there is scientific consensus that it is an aromatic molecule, but there is controversy over whether it should be considered globally[25,26] or locally[27,28] aromatic. Be it global or local, what is clear is that the aromaticity of these complexes requires the aromaticity of the ligands. This is what happens with $[Cr(\eta^6\text{-}C_6H_6)(CO)_3]$, and it is also the case for cyclobutadieneiron tricarbonyl $[Fe(CO)_3(C_4H_4)]$, which displays electrophilic substitution and thus aromaticity, as

confirmed by its four equal C−C bond lengths, the planarity of the C_4H_4 ring, and its ^1H NMR spectrum.[29] The bonding in this molecule is assumed to involve the triplet state of cyclobutadiene, which is aromatic according to the Baird rule,[30] interacting with two singly occupied Fe(0) orbitals.[31] Remarkably, all these compounds follow the 18 e⁻ rule, which is an additional way to account for the stability or lack of reactivity.

All the former complexes had planar conjugated organic ligands able to perform electrophilic substitution and abiders of the 18 e⁻ rule. At this stage, what is the situation with $[M(C_2B_9H_{11})_2]^-$ (M = Co, Fe, Ni), which do not contain planar conjugated organic ligands and have been described by computation, and with the high stability of $[Co(C_2B_9H_{11})_2]^-$, considered as aromatic,[32] with regard to the aromaticity of their pristine ligands? Metallabis(dicarbollides) $[M-(C_2B_9H_{11})_2]^-$ are commonly mononegative (M = Co, Fe, Ni), but dianionic $[Fe(C_2B_9H_{11})_2]^{2-}$ and neutral Ni-$(C_2B_9H_{11})_2$ are very accessible, too. But all of these metallabis(dicarbollides) $[M(C_2B_9H_{11})_2]^{x-}$ (M = Co, Fe, Ni) have an available 18 e⁻ count molecule: $[Fe(C_2B_9H_{11})_2]^{2-}$, $[Co(C_2B_9H_{11})_2]^-$, and $[Ni(C_2B_9H_{11})_2]$.

Turning now to the issue of the aromaticity of a sandwich complex, which implies that, in general, its ligands are aromatic, the consequence would be that $nido$-$[C_2B_9H_{11}]^{2-}$ is aromatic, too. We demonstrated[33] that $closo$-boranes $[B_nH_n]^{2-}$ abide Wade−Mingos's rule[34−37] and that any of them, with $n \geq 5$, have a polycyclic aromatic hydrocarbon equivalent with an uneven number of π-electron pairs, which obeys Hückel's rule.[38] Taking this into account, what occurs with the $nido$-$[B_nH_n]^{4-}$ series, to which $nido$-$[C_2B_9H_{11}]^{2-}$ belongs?[39] These have one electron pair more of electrons than $closo$-$[B_nH_n]^{2-}$, and therefore, if $closo$-$[B_nH_n]^{2-}$ are aromatic, it is expected that $nido$-$[B_nH_n]^{4-}$ should be nonaromatic or antiaromatic, if the parallelism between $closo$-boranes and flat Hückel's rule abiders holds. This would be the case for typical hydrocarbon aromatic compounds. Is this what is happening with boron clusters? Or, on the contrary, is the change in structure from $closo$ to $nido$ a strategy of the clusters to skip the aromaticity/antiaromaticity transition upon the addition of two extra electrons to keep the aromaticity? If this was the case, their possibilities to maintain a stable structure would be far superior to those of their organic counterparts.

In this paper, we show that the aromatic character of $nido$-$[C_2B_9H_{11}]^{2-}$ is such that it conforms to the sentence "*the aromaticity of a sandwich complex implies that, in general, its ligands have to be also aromatic*". We will also see that the $nido$-$[C_2B_9H_{12}]^-$ precursor of $nido$-$[C_2B_9H_{11}]^{2-}$ is aromatic, too, and that the pentagonal ring C_2B_3 in $nido$-$[C_2B_9H_{11}]^{2-}$ is not more aromatic than the equivalent C_2B_3 ring in $closo$-1,2-$C_2B_{10}H_{12}$, despite having a conjugated open face. The C_2B_3 ring is the one that, following the model of metallocenes, is η^5-coordinated to the metal in $[M(C_2B_9H_{11})_2]^-$. Further, we shall see that the aromatic character of a $closo$ boron cluster depends on the number of electrons and the confined space[40,41] available, defined by the number of atoms in the cluster. Therefore, we shall see that any of the isomers of $closo$-$C_2B_{10}H_{12}$ are aromatic, as are $closo$-$[B_{12}H_{12}]^{2-}$ and $closo$-$[CB_{11}H_{12}]^-$. Moreover, we shall also see that the diatropic current in spheres, as the icosahedral boron clusters can be interpreted, is not geometrically restricted as occurs in p_π systems and can be present at different parallel planes. In addition, we shall observe that metallabis(dicarbollides) are not a surrogate of the metallocenes and that their bulky and spherical ligands play a role in their stability and possibly in their applications, besides their well-documented enhanced electrochemical tuning efficiency and photoredox catalysis properties. Finally, we shall also see that boron clusters have access to a morphological detour to skip the aromaticity → antiaromaticity sequence upon the addition of 2e⁻.

RESULTS AND DISCUSSION

Deboronation of $closo$-1,7-$C_2B_{10}H_{12}$ (m-$C_2B_{10}H_{12}$). The search for the relationship among aromaticity, stability, and lack of reactivity was triggered as a result of the low throughput of the deboronation of $closo$-m-$C_2B_{10}H_{12}$ to yield $nido$-$[7,9$-$C_2B_9H_{12}]^-$. The ease to remove the boron atom bound to the two carbon cluster atoms is well-known in $closo$-1,2-$C_2B_{10}H_{12}$, also represented by o-$C_2B_{10}H_{12}$, despite the electron count of this molecule matching the electron count of $[B_{12}H_{12}]^{2-}$, probably one of the most stable aromatic molecules available, following the $4n + 2$ Wade−Mingos' rule.[34−37] There are several processes to perform the deboronation successfully.[42−50] The most typical one and perhaps the most widely used is the boiling ethanol/KOH procedure. With the aim to produce $[Co(m$-$C_2B_9H_{11})_2]^-$, we investigated the deboronation of $closo$-1,7-$C_2B_{10}H_{12}$ (or m-$C_2B_{10}H_{12}$). However, what seemed to be simple became highly difficult, as was reported by Hawthorne et al., because the reaction must be carried out in an autoclave at 150 °C for 4 h under autogenous pressure to lead to $nido$-$[7,9$-$C_2B_9H_{12}]^-$, in our hands with very low yield.[51] Other methods with other reagents have been developed that produce good yields;[52] however, we were interested in the boiling ethanol/KOH procedure, as m-$C_2B_{10}H_{12}$ deboronation can be directly compared with the deboronation of o-$C_2B_{10}H_{12}$. Why did the two, at this stage of the research, apparently aromatic molecules o-$C_2B_{10}H_{12}$ and m-$C_2B_{10}H_{12}$ behave so differently toward the same reagent to yield so similar $nido$-$[7,8$-$C_2B_9H_{12}]^-$ and $nido$-$[7,9$-$C_2B_9H_{12}]^-$ molecules? Would not these be aromatic? Noticeable is that the same reflux temperature used for the $closo$-o-$C_2B_{10}H_{12}$ to produce $nido$-$[7,8$-$C_2B_9H_{12}]^-$ leaves $closo$-m-$C_2B_{10}H_{12}$ unchanged. For the bench chemist this would indicate that $closo$-m-$C_2B_{10}H_{12}$ is more aromatic than $closo$-o-$C_2B_{10}H_{12}$, but we shall see that this is not the case according to the computed aromaticity indicators. The immediate reaction procedure follow up would be to use a higher temperature. In this case, however, an important fraction of the $closo$-$meta$-cluster is degraded to boric acid esters, which in turn lead to a low yield of $nido$-$[7,9$-$C_2B_9H_{12}]^-$. Is then $nido$-$[7,9$-$C_2B_9H_{12}]^-$ less stable or less aromatic than $nido$-$[7,8$-$C_2B_9H_{12}]^-$? Before answering these questions, we decided to optimize the synthetic procedure, as the ethanol method would be very practical to work up. To do it, we searched for new parameters to improve the yield of $nido$-$[7,9$-$C_2B_9H_{12}]^-$ and lessen the formation of boric acid and boric acid esters during the process. As we have summarized in the Experimental Section and after many trials with this partial degradation altering the temperature and/or time of reaction and/or excess of base (Table 3), the yield of the partial degradation reaction was improved notably to 66%. However, it remains poor in comparison to the yield of $nido$-$[7,8$-$C_2B_9H_{12}]^-$. This anomalous behavior led us to consider that little was known about and much was taken for granted with regard to the stability of the carboranes, their aromaticity, and the stability and aromaticity of their deboronated species. It took us also to revise the old, but still valid, magnificent

scheme shown by Rudolph on the relation among *closo*, *nido*, and *arachno* clusters.[52−55] Therefore, we decided to carry on further research with the aim to learn about ligands that now are relevant and certainly will have an important role in the near future.

Aromaticity of *closo*-Carboranes. The *closo*-$C_2B_{10}H_{12}$ parallels the aromatic *closo*-$[B_{12}H_{12}]^{2-}$.[33] Both share the same number of valence electrons (50) in the same confined space. The *closo*-$C_2B_{10}H_{12}$ has two heteroatoms, which implies three isomers, *ortho*, *meta*, and *para* (Figure 1). Further, the
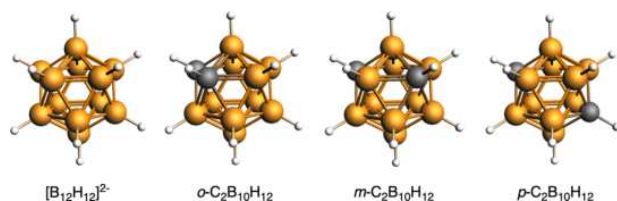

Figure 1. The *closo-o-*, *closo-m-*, and *closo-p-*isomers of $C_2B_{10}H_{12}$, together with $[B_{12}H_{12}]^{2-}$.

difference in electronegativity between the two participating elements in the cluster is $\Delta\chi(C,B) = 0.51$.[56] Thus, considering the 3D and 2D relationship demonstrated earlier,[33] it was sensible to compare these carborane isomers with planar systems with two heteroatoms, also related to a highly aromatic system, and with a $\Delta\chi$ value between those of the participating atoms and as close to $\Delta\chi(C,B)$ as possible. In this regard, C_6H_6 and the three diazines, 1,2-, 1,3-, and 1,4-diazines, commonly known as pyridazine, pyrimidine, and pyrazine, respectively, with $\Delta\chi(N,C) = 0.49$,[57,58] and 1,2-, 1,3-, and 1,4-diboratabenzenes, with $\Delta\chi(C,B) = 0.51$,[59−61] would be the most adequate. It is clear for the bench chemist that both boranes and arenes, as typical aromats, are subject to substitutions restoring the aromaticity; however, the diazines are also keen at additions, which is contrary to strong aromaticity. In line with this, borate[62] or diboratabenzenes are subject to chemical instability, which is also contrary to strong aromaticity. As an example, diazines, upon addition, require rearomatization with oxidizing agents, which is not evidence for strong aromaticity, or when treating the 1-phenyl-boratabenzene anion with an excess of acetic acid, 1,4-pentadiene, *cis*-1,3-pentadiene, and benzene are produced. Noticeably, everything occurs with the three heterosystems *closo*-$C_2B_{10}H_{12}$, diazines, and diboratabenzenes, for which the difference in electronegativity of the constituents is the same, $\Delta\chi(X,Y) \approx 0.50$. All this is supportive of the extraordinary aromaticity of boron clusters, for both homo- or hetero-boranes, whereas it is not so obvious for arenes.

This experimental evidence based on stability and reactivity is supported by theory. We will restrict our Results and Discussion section on the most common 12-vertex carboranes, i.e., *closo*-$C_2B_{10}H_{12}$ and their *nido* derivatives, with the expectation that the results can be extended to other smaller carborane clusters, and will compare the results with those of the diazines and diboratabenzenes.

Relative Stability and Aromaticity of the Dicarboranes. *closo*-$C_2B_{10}H_{12}$ is thermally very stable but tends to isomerize to the more stable isomers (Figure 1). Upon heating at 400 °C, *o*-$C_2B_{10}H_{12}$ isomerizes to *m*-$C_2B_{10}H_{12}$, and near 600 °C, *m*-$C_2B_{10}H_{12}$ isomerizes to *p*-$C_2B_{10}H_{12}$.[63]

The preparative step from *ortho* to *meta* is well-defined, and all *ortho* is converted into *meta*, and no purification is needed. The step from *meta* to *para* is far more difficult, as a long and troublesome purification process is needed due to the generated mixture of the two isomers. Both *m*- and *p*-isomers are converted into each other, preventing an easy isolation. These experimental conditions indicate that a large difference in thermodynamic stability between the *o*- and *m*-isomers is expected, whereas a comparable stability between the *m*- and *p*-isomers is likely. Indeed, this is what is computationally found, as shown in Table 1 (first row). Although these relative

Table 1. Relative Stabilities of *closo*-$C_2B_{10}H_{12}$ and Their *nido* Derivatives (kcal mol^{-1})

	ortho	meta	para
closo-$C_2B_{10}H_{12}$	+19.2	+2.9	0.0
nido-$[C_2B_9H_{12}]^-$	+16.2	0.0	+26.3
nido-$[C_2B_9H_{11}]^{2-}$	+16.6	0.0	+27.5

stabilities are certainly related to the different types of bonds (C−C, B−B, C−B) in the different isomers, they can be more easily explained by considering the relative positions of both carbon atoms in the cluster. As $\chi_C > \chi_B$, C atoms attract higher electron density in their vicinity, inducing a repulsive effect with the adjacent C, which is the case of the *o*-isomer. In contrast, for the *m*-isomer, when one B is inserted in between the two carbon atoms, the repulsive effect is notably diminished, in agreement with Coulomb's inverse-square law. This repulsive effect is even less for the *p*-isomer. These results are easily understood with classical physics, the *p*-isomer being the most stable, in agreement with the calculations (Table 1), but not so different with regard to the *m*-isomer ($\Delta E = 2.9$ kcal mol^{-1}), a factor to be taken into account for practical applications considering the much higher price of the *p*-isomer.

Considering the clear difference in stability between the *o*- and *m*-isomers ($\Delta E = 16.3$ kcal mol^{-1}), does it result in loss of aromaticity between one isomer and the other? The answer is no, if we attend to the magnetically based nucleus-independent chemical shift (NICS) values given in Table 2. If we look at Scheme 1, there are two layers enlightened, the $C_2B_3/CB_4/B_5$ and the CB_4/B_5. This sketch is valid for *closo*-$[B_{12}H_{12}]^{2-}$ and for *closo-o-*, *closo-m-*, and *closo-p-*$C_2B_{10}H_{12}$. In *closo*-$[B_{12}H_{12}]^{2-}$, each B_5 ring displays a NICS of −34.6 ppm, which indicates high aromaticity, and this value is just a little bit lower for C_2B_3

Table 2. NICS (in ppm) of the C_2B_3, CB_4, and B_5 Rings (measured at the center) of *closo*-Carboranes under Analysis[a]

	ring	
carborane	C_2B_3/CB_4	CB_4/B_5
o-$C_2B_{10}H_{12}$	−33.7	−32.7
o-$[C_2B_9H_{12}]^-$	−23.4	−35.4
o-$[C_2B_9H_{11}]^{2-}$	−19.5	−37.0
m-$C_2B_{10}H_{12}$	−34.2	−33.1
m-$[C_2B_9H_{12}]^-$	−21.3	−33.9
m-$[C_2B_9H_{11}]^{2-}$	−18.7	−36.7
p-$C_2B_{10}H_{12}$	−34.6	−34.6
p-$[C_2B_9H_{12}]^-$	−23.2	−36.2
p-$[C_2B_9H_{11}]^{2-}$	−19.6	−37.9

[a]The NICS for the B_5 ring in *closo*-$[B_{12}H_{12}]^{2-}$ is −34.6 ppm.

Scheme 1. Two 5-Membered Rings in 12-Vertex Carboranes and $[B_{12}H_{12}]^{2-}$

C_2B_3 / CB_4 / B_5

CB_4 / B_5
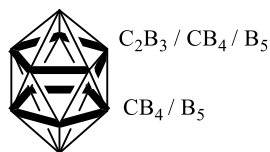
in $closo$-o-$C_2B_{10}H_{12}$ (−33.7 ppm) with −32.7 ppm for B_5 (Table 2). Interestingly, it again increases for $closo$-m-$C_2B_{10}H_{12}$, with −34.2 ppm for C_2B_3 and −33.1 ppm for B_5, and matches the B_5 values found for $closo$-$[B_{12}H_{12}]^{2-}$ and that of CB_4 for $closo$-p-$C_2B_{10}H_{12}$ (−34.6 ppm). For a bench chemist, it is clear that $closo$-$[B_{12}H_{12}]^{2-}$ is by all means more stable or, in other words, less reactive than $closo$-o-$C_2B_{10}H_{12}$, as is also demonstrated in the following

$$[B_{12}H_{12}]^{2-} \rightarrow [B_{11}H_{11}]^{2-} + BH \quad \text{compared to}$$

$$o\text{-}C_2B_{10}H_{12} \rightarrow C_2B_9H_{11} + BH \quad (1)$$
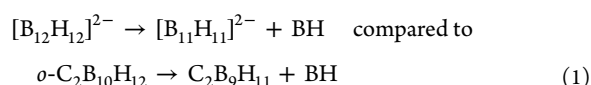
in which all components share the same number of electrons. At the B3LYP/6-311++G(d,p) level of theory, removal of a BH from $closo$-$[B_{12}H_{12}]^{2-}$ requires 29 kcal mol^{-1} more energy than from $closo$-o-$C_2B_{10}H_{12}$ following this scheme. The isoelectronic and isostructural $closo$-$[B_{12}H_{12}]^{2-}$ and $closo$-o-, $closo$-m-, and $closo$-p-$C_2B_{10}H_{12}$ are clear examples that *molecules having similar aromaticity may have very distinct reactivity*.[57,64−66] This was demonstrated in the deboronation of $closo$-o- and $closo$-m-$C_2B_{10}H_{12}$ discussed in the previous section and agrees well with the results of diazines and diborata-benzenes, for which the aromaticity can be compared with those of C_6H_6 [NICS(0) = −8.1 ppm]; the three diazines 1,2-diazine [NICS(0) = −5.4 ppm], 1,3-diazine [NICS(0) = −5.5 ppm], and 1,4-diazine [NICS(0) = −5.4 ppm];[67] and 1,2-diboratabenzene [NICS(0) = −1.9 ppm], 1,3-diboratabenzene [NICS(0) = −2.2 ppm], and 1,4-diboratabenzene [NICS(0) = −1.5 ppm]. It is informative that the percentage discrepancies between the NICS(0) values of the diazine isomer and the benzene reference, which are 33.5% for $closo$-$ortho$, 31.3% for $closo$-$meta$, and 33.4% for $closo$-$para$, are much larger than those for the carboranes with respect to $closo$-$[B_{12}H_{12}]^{2-}$, being 2.6% for $closo$-$ortho$, 1.2% for $closo$-$meta$, and 0% for $closo$-$para$, but smaller than those between the NICS(0) value of the diboratabenzene isomer and the benzene reference, which are 76.4% for $closo$-$ortho$, 72.7% for $closo$-$meta$, and 81.4% for $closo$-$para$. This large percentage difference between NICS(0) values for $closo$-carboranes and diazines is associated with only substitution reactions for the $closo$-carboranes, whereas the diazines are subjected to both additions and substitutions and to purposeful oxidations to restore the aromaticity. When the participating elements are the same, as in the case of $closo$-carboranes and diboratabenzenes, the discrepancy factor has become even more severe, which translates into the chemical instability of the diboratabenzenes. The boratabenzene $[C_5BH_6]^-$ displays a discrepancy index of 28% [NICS(0) = −5.8 ppm], higher than that of pyridine at 17.8%.[68] The discrepancies increase for the homodisubstituted species by about 75% for the diboratabenzenes and 33% for the diazines. Thus, it seems that to keep the aromaticity it is better to have an electronegative element in the planar ring than an electropositive one or, alternatively, an electron-rich element better than an electron-deficient element. This negative

aromatic influence of B in 2D systems is not adhered to in $closo$ 3D-carboranes. The difference is that boron in electron precise compounds (2D) tends to be a Lewis acid, whereas in $closo$ boron clusters (3D) boron compensates for the shortness of electrons with high connectivity.

Aromaticity of the closo-Dicarboranes with Regard to Deboronation. It is known experimentally that $closo$-dicarboranes can lead to deboronation, more easily if the two carbon atoms are adjacent, $ortho$, than if they are separated by a boron atom, $meta$, as described in the above section on the deboronation of m-$C_2B_{10}H_{12}$ and in the Experimental Section, and even more easily than when they are separated by two carbon atoms, $para$, an impractical process. $nido$-Species with the formula $nido$-$[C_2B_9H_{12}]^-$ are produced from $closo$-o- and $closo$-m-$C_2B_{10}H_{12}$ but with different positions of the two carbon atoms. The ease of the deboronation of the $closo$-dicarboranes shall be related to the relative stability and/or reactivity of the $closo$-o-, $closo$-m-, and $closo$-p-$C_2B_{10}H_{12}$ and the kinetics of the involved reaction. Interestingly, it correlates very well with the percentage discrepancy between the NICS(0) values of the $closo$-carborane isomer and the $closo$-$[B_{12}H_{12}]^{2-}$ reference, although their aromatic characters are very similar, as we have demonstrated earlier. The degree of deboronation difficulty of the $closo$-carborane can also be interpreted with classical physics on the grounds of the deboronated compound, $nido$-$[C_2B_9H_{12}]^-$. Simply, one has to consider the relative stabilities of the $nido$-$[C_2B_9H_{12}]^-$ isomer clusters, for which the electron-enriched atoms prefer the edge sites; thus, the positions on the pentagonal open face are preferred to the lateral sites (Figure 2). In this regard, the $nido$-$ortho$- and $nido$-

o-$[C_2B_9H_{12}]^-$ m-$[C_2B_9H_{12}]^-$ p-$[C_2B_9H_{12}]^-$
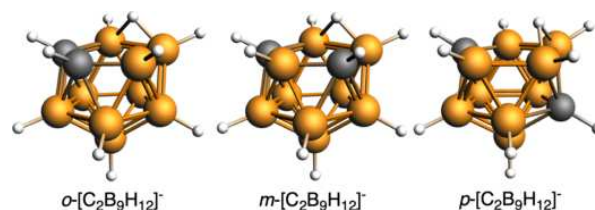
Figure 2. The $nido$-o-, $nido$-m-, and $nido$-p-isomers of $[C_2B_9H_{12}]^-$.

$meta$-isomers should be more stable than the $nido$-$para$ one, and between $nido$-$ortho$ and $nido$-$meta$, $nido$-$meta$ is preferred over $nido$-$ortho$ because of Coulomb's law. This is what is shown in Table 1 for $nido$-isomers o-$[C_2B_9H_{11}]^{2-}$ (ΔE = 16.6 kcal mol^{-1}), m-$[C_2B_9H_{11}]^{2-}$ (ΔE = 0.0 kcal mol^{-1}), and p-$[C_2B_9H_{11}]^{2-}$ (ΔE = 27.5 kcal mol^{-1}). The same argument is valid for the protonated species $nido$-isomers o-, m-, and p-$[C_2B_9H_{12}]^-$. The higher stability of the $nido$-m-$[C_2B_9H_{12}]^-$ vs the $nido$-o-$[C_2B_9H_{12}]^-$ indicates that the difficulty in its formation originates in the much lower reactivity of the corresponding $closo$-species, as evidenced experimentally.

Aromaticity of the nido-Dicarborane Species [7,8-$C_2B_9H_{12}]^-$. Scheme 2 shows the deboronation process leading, in this case, to $nido$-$[7,8$-$C_2B_9H_{12}]^-$. The C_2B_3 open face reminds one closely of cyclopentadiene, the precursor of $[C_5H_5]^-$. We found that the on-top-of-the-face proton (endocyclic, ec)[69] in $[7,8$-$C_2B_9H_{12}]^-$ resonates near −2.5 ppm in the ^{1}H NMR spectrum. As this endocyclic hydrogen can be removed by a strong base, it is certainly acidic, and the question that arises is, how could a proton resonate at such high field? The customary answer is simple; the point is whether it is correct or not. The endocyclic proton (H_{ec}) does

Scheme 2. Deboronation Process of *closo-o*-$C_2B_{10}H_{12}$, Incorrectly Showing a Circle Meaning Aromaticity
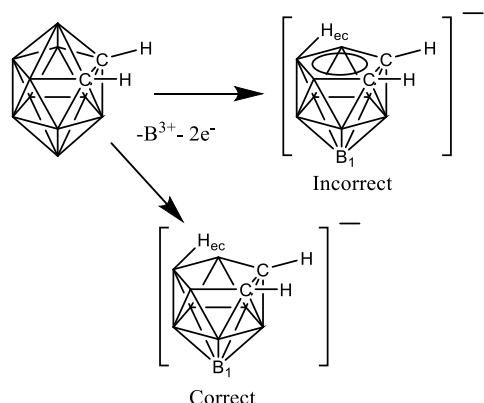
resonate at high magnetic field because there is an induced ring current in the delocalized π-system of the aromatic C_2B_3 ring. Because of this interpretation, it was not uncommon to draw the ring shown in the C_2B_3 face of the *nido*-$[C_2B_9H_{12}]^-$, representing aromaticity (see Scheme 2 Scheme 3). However,

Scheme 3. Possible Location of the Ring Currents in *nido*-$[C_2B_9H_{12}]^-$ and *nido*-$[C_2B_9H_{11}]^{2-}$
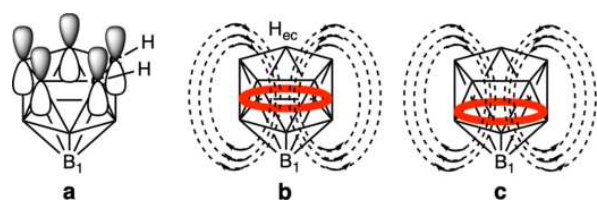
if we think in terms of Hückel aromaticity, there is a major incongruence with this, because to have the conjugation, no p_π open face orbital should be part of a covalent bond (Scheme 3a), as is the B–H_{ec}. Therefore, and contrarily to what has been assumed, the p_π ring in the open face cannot be responsible for the upfield chemical shift of the endocyclic

proton. Further, besides the anomalous chemical shift in the ^1H NMR of the endocyclic proton, there is also another anomalous chemical shift due to B_1 at −37.2 ppm. This is at the highest magnetic field of the spectrum. Again, it can be interpreted to be originating in an induced ring current, but this cannot be due to the supposed delocalized system of π-electrons at the C_2B_3 open face, as it would be too far. Moreover, the anomalous chemical shifts due to the endocyclic proton and the B_1 seem to be related. This indicates that their origin would be the same, supporting the proposition that it is not due to the C_2B_3 open face ring current but to one diatropic current in an intermediate plane equidistant to both nuclei, H and B_1. The ^1H NMR of the upfield endocyclic proton and the upfield ^{11}B NMR of the B_1 resonances prove the existence of diatropic currents and therefore prove the aromaticity of the *nido*-dicarborane.

This relationship between the chemical shift of the endocyclic proton and B_1 can be visualized with Scheme 3b, which explains why H_{ec} and B_1 are related, considering that one is measured with ^1H NMR and the second by ^{11}B NMR. The same Scheme 3b also shows a red circle suggesting a ring current placed in the center of the pentagonal antiprism in which the center of the icosahedron lies. This would explain the anomalous chemical shifts of the endocyclic proton and the apical B_1 and their common origin (vide infra).

Is This View Supported by the NICS of nido-[C₂B₉H₁₂]⁻? Largely, yes. Remarkably, the C_2B_3 layer, although being definitely aromatic according to the NICS value of −27.4 ppm, loses aromaticity with regard to the same layer in *closo*-1,2-$C_2B_{10}H_{12}$ (−33.7 ppm). Conversely, the B_5 layer increases aromaticity (NICS = −35.4 ppm) with regard to B_5 in *closo*-1,2-$C_2B_{10}H_{12}$ (−32.7 ppm). Thus, it is clear that the diatropic loop has descended from the open C_2B_3 face to the B_5 layer, as inferred from the anomalous H_{ec} and B_1 chemical shifts (Scheme 3c).

Aromaticity of the nido-[C₂B₉H₁₁]²⁻ Coordinating Ligand. We have seen that the diatropic ring current in *nido*-$[C_2B_9H_{12}]^-$ has descended from the coordinating face. Does it find its continuation in *nido*-$[C_2B_9H_{11}]^{2-}$, which is the real analogue of $[C_5H_5]^-$, in terms of metal sandwich formation?
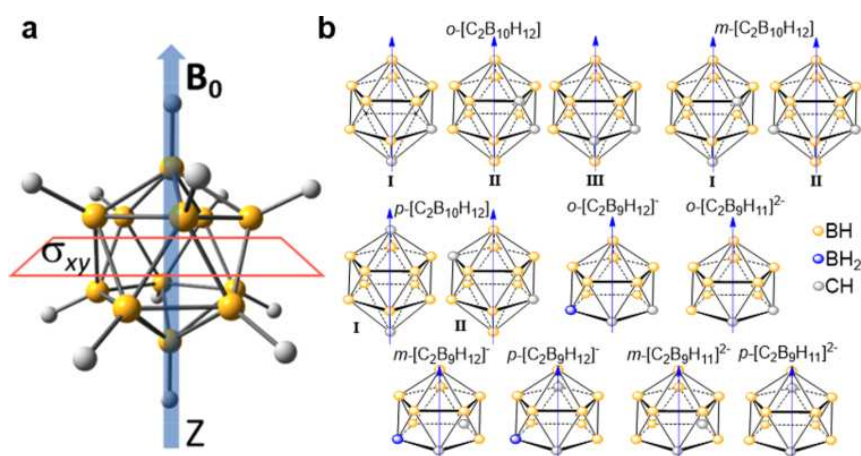
Figure 3. Representation of (a) the integration plane for the calculation of the current density and the magnetic field vector (B_0) for the *closo*-$[B_{12}H_{12}]^{2-}$ system. (b) Representation of the different system orientations with respect to the magnetic field vector B_0 (blue arrow) for the *closo-o*-$C_2B_{10}H_{12}$, *closo-m*-$C_2B_{10}H_{12}$, *closo-p*-$C_2B_{10}H_{12}$, *nido-o*-$[C_2B_9H_{12}]^-$, *nido-o*-$[C_2B_9H_{11}]^{2-}$, *nido-m*-$[C_2B_9H_{12}]^-$, *nido-p*-$[C_2B_9H_{12}]^-$, *nido-m*-$[C_2B_9H_{11}]^{2-}$, and *nido-p*-$[C_2B_9H_{11}]^{2-}$ systems.

Figure 4. Representation of the current density vector field for the *closo*-$[B_{12}H_{12}]^{2-}$ system. Top view of the currents in the perpendicular plane with respect to the magnetic field vector $\mathbf{B}_0$ located at 0, 1, 2, and 3 bohrs (from left to right, respectively) above the central plane. Units are nA T^{-1}. See the Supporting Information for pictures with larger resolution.

Figure 5. Representation of the current density vector field for the *closo-o*-$[C_2B_{10}H_{12}]$ system in orientation **III** (Figure 3). See the Supporting Information for the rest of the orientations of the external magnetic field. Top view of the currents in the σ_{xy} plane located at −2, 0, and 2 bohrs (from left to right, respectively) below or above the plane located in the middle of the two five-membered rings (parallel to the five-membered-ring planes). Color scale given in Figure 4. Units are nA T^{-1}. See the Supporting Information for pictures with larger resolution.
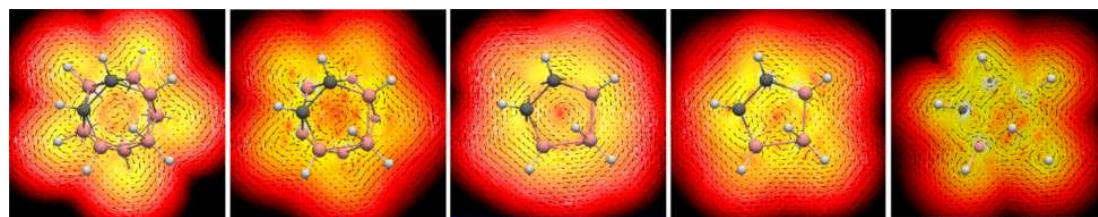
Figure 6. Representation of the current density vector field for the *nido-o*-$[C_2B_9H_{12}]^-$ system. Top view of the currents in the perpendicular plane with respect to the magnetic field vector $\mathbf{B}_0$ located at −2, −1, 0, 1, and 2 bohrs (from left to right, respectively) below or above the plane located in the middle of the two five-membered rings (parallel to the five-membered-ring planes). Color scale given in Figure 4. Units are nA T^{-1}. See the Supporting Information for pictures with larger resolution.

The answer seems to follow the same trend (Table 2). The tendency is the same, as it appears that the B_5 ring is the most aromatic one. We should say unexpectedly because it is contrary to what would be common reasoning for a π-arene system to coordinate to a metal by haptic covalent bonds. The "coordinating face" $C_2B_3/CB_4/B_5$ follows the tendency to lose aromaticity, as manifested in the order *closo*-$[B_{12}H_{12}]^{2-}$ > *closo*-$C_2B_{10}H_{12}$ > *nido*-$[C_2B_9H_{12}]^-$ > *nido*-$[C_2B_9H_{11}]^{2-}$, with NICS values for the *o*-isomer of −34.6, −33.7, −23.4, and −19.5 ppm, respectively. On the contrary, for the B_5/C_4B non-coordinating ring the tendency is reversed—*closo*-$C_2B_{10}H_{12}$ < *nido*-$[C_2B_9H_{12}]^-$ < *nido*-$[C_2B_9H_{11}]^{2-}$—with NICS values of −32.7, −35.4, and −37.0 ppm, respectively. To account for this situation, a similar scheme as this for *nido*-$[C_2B_9H_{12}]^-$ is suggested for *nido*-$[C_2B_9H_{11}]^{2-}$ but with the aromatic ring somehow closer to B_1 (Scheme 3c). And how this should be manifested? If the density of magnetic field lines is higher on B_1 in *nido*-$[C_2B_9H_{11}]^{2-}$ than in *nido*-$[C_2B_9H_{12}]^-$ due to a higher aromaticity of the B_5 ring, then the chemical shift of B_1 in *nido*-$[C_2B_9H_{11}]^{2-}$ shall be more negative than in *nido*-$[C_2B_9H_{12}]^-$, as is the case (δ −46.1 vs −37.2 ppm, respectively).[70]

Ring Currents of *closo*-$[B_{12}H_{12}]^{2-}$, *closo*-$C_2B_{10}H_{12}$, *nido*-$[C_2B_9H_{12}]^-$, and *nido*-$[C_2B_9H_{11}]^{2-}$. The magnetic induced current densities of *closo*-$[B_{12}H_{12}]^{2-}$, *closo-o*-$C_2B_{10}H_{12}$, *nido-o*-$[C_2B_9H_{12}]^-$, and *nido-o*-$[C_2B_9H_{11}]^{2-}$ were computationally obtained by applying an external magnetic field $\mathbf{B}_0$, as shown in Figure 3. The currents for the *meta*- and *para*-isomers are similar to those obtained for the *ortho*-species (see the Supporting Information). As a reference, the Supporting Information contains the magnetic induced current densities of benzene. By convention, it is considered that the direction of the diatropic ring currents indicating aromaticity is clockwise. The magnetic induced current densities of *closo*-$[B_{12}H_{12}]^{2-}$ reach a maximum in the center of the icosahedron (see Figure 4). Interestingly, the most-inner ring current in the center is paratropic. Antiaromatic molecules have paratropic inner and outer ring currents, whereas aromatic molecules present paratropic inner and diatropic outer ring currents.[71] Ring currents perpendicular to the external magnetic field at the center of $[B_{12}H_{12}]^{2-}$ are typical of an aromatic compound. Other planes perpendicular to the external magnetic field located at 1, 2, or 3 bohrs above or below the central plane
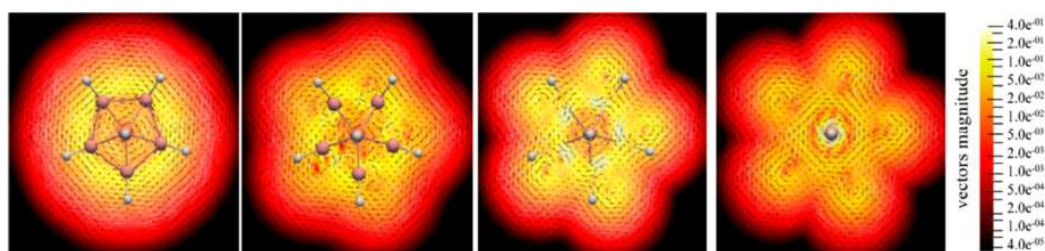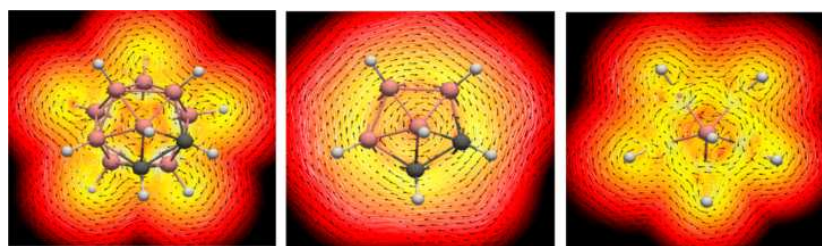
Figure 7. Representation of the current density vector field for the *nido-o*-$[C_2B_9H_{11}]^{2-}$ system. Top view of the currents in the perpendicular plane with respect to the magnetic field vector $\mathbf{B}_0$ located at -2, -1, 0, 1, and 2 bohrs (from left to right, respectively) below or above the plane located in the middle of the two five-membered rings (parallel to the five-membered-ring planes). Color scale given in Figure 4. Units are nA T^{-1}. See the Supporting Information for pictures with larger resolution.
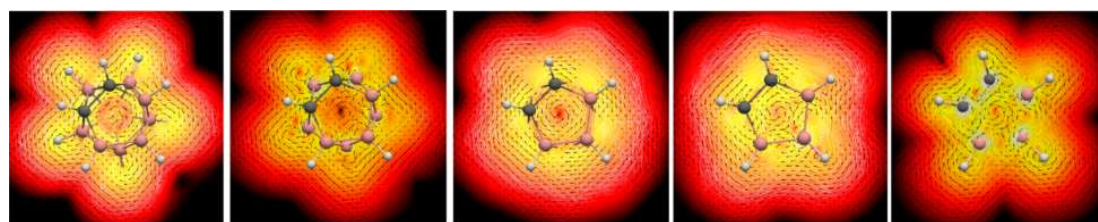
show also the same picture, although the intensity of the ring currents is somewhat reduced.

Figure 5 depicts the magnetic induced current densities of *closo-o*-$C_2B_{10}H_{12}$. Exchanging BH$^-$ for CH does not produce a notable change of the observed ring currents. One can conclude that the aromaticity of the system is affected only slightly by moving from *closo*-$[B_{12}H_{12}]^{2-}$ to *closo-o*-$C_2B_{10}H_{12}$. This is not unexpected, as we keep the *closo* aromatic structure of the borohydride. On the other hand, when we move from *closo-o*-$C_2B_{10}H_{12}$ carborane to *nido-o*-$[C_2B_9H_{12}]^-$, there is a clear decrease of the diatropic intensity in the central part of the polyhedron (the central plane is considered the plane in the middle of the two pentagonal rings), indicating a reduction of the aromatic character of this species (see Figure 6). Still, the picture of the ring currents indicates that we are dealing with an aromatic compound, despite it being less aromatic than the *closo*-$[B_{12}H_{12}]^{2-}$ or *closo-o*-$C_2B_{10}H_{12}$. As we move from the central plane, the currents tend to be more disorganized. Finally, for species *nido-o*-$[C_2B_9H_{11}]^{2-}$, the ring currents are similar to those obtained for *nido-o*-$[C_2B_9H_{12}]^-$ (see Figure 7).

Considerations of the Aromaticity of [Co(C₂B₉H₁₁)₂]⁻ as an Example of Metallabis(dicarbollides) and Their Singularity versus the Metallocenes. Since their discovery, metallabis(dicarbollides) $[M(C_2B_9H_{11})_2]^-$ (M = TM) (Figure 8) have been considered the boron cluster equivalent of the
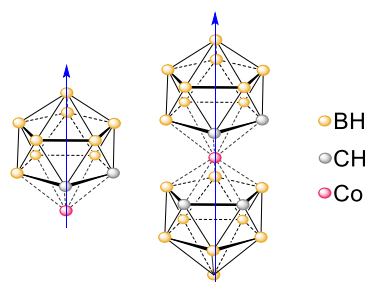

Figure 8. Representation of the orientation of the magnetic field vector $\mathbf{B}_0$ (blue arrow) for the *closo*-$[Co(C_2B_9H_{11})]^+$ and *closo*-$[Co(C_2B_9H_{11})_2]^-$ systems.

metallocenes, but they are not, as we shall demonstrate here. They share the property of having one solid structure that is difficult to reorganize, thus allowing outer-electron transfer that is commonly fast. Both undergo typical aromatic substitution reactions, and both show continuous electron delocalization, at least in part of the molecule. However, inspection of both molecular structures shows a remarkable difference. The word sandwich, which is applied to both molecules, is adequate for the metallocenes because in their

case two parallel planar ligands, to follow the typical aromatic concept, have a metal filling in between. However, the generated pentagonal pyramid does not fit in the classical concept of aromaticity, as in fact what is happening is that coordination to metal by the cyclopentadienyl ligands does not prevent them from exhibiting aromatic properties, although the aromaticity of the ligands can be somewhat reduced, as was demonstrated for the benzene ring of $[Cr(\eta^6\text{-}C_6H_6)(CO)_3]$.[72] Thus, it would seem adequate to say that ferrocene exhibits aromatic properties, rather than refer to it as an aromatic compound. This conclusion is reinforced by the work of Fowler and co-workers showing that the two cyclopentadienyl anions support individual diatropic ring currents.[28] Conversely, the metallabis(dicarbollides) are made of two icosahedra in which the metal occupies one vertex. If we take into account the definition of aromaticity of Chen, Schleyer, and their co-workers, "a manifestation of electron delocalization in closed circuits, either in two or three dimensions",[68] the $[M\text{-}(C_2B_9H_{11})_2]^-$ conforms to a structure, the icosahedron, that is compatible with aromaticity because it can generate a closed circuit. Therefore, metallabis(dicarbollides) are aromatic compounds, whereas metallocenes display aromatic behavior. In other words, metallabis(dicarbollides) display global aromaticity, whereas metallocenes present local aromaticity in the ligands.

This can be well-observed by the ring currents depicted in Figure 9, with the direction of the magnetic field shown in Figure 8. For $[Co(C_2B_9H_{11})]^+$, there is a clear external diatropic ring current from 1 to 5 bohrs with a maximum located at around the center. The intensity of the current density seems to indicate a slight loss of aromaticity when moving from *nido-o*-$[C_2B_9H_{11}]^{2-}$ to *closo*-$[Co(C_2B_9H_{11})]^+$, although care has to be taken when using the ring currents and the NICS as indicators of aromaticity when metal atoms do participate, as paratropic currents are produced in this situation that perturb the diatropic current, leading to misunderstandings.[73] A similar situation is found for *closo*-$[Co(C_2B_9H_{11})_2]^-$ (Figure 10), but now the intensity of the current density seems to be as large as that of *nido-o*-$[C_2B_9H_{11}]^{2-}$. Interestingly, the highest intensity of current density is found inside the icosahedron of the cobaltabis(dicarbollides), not far from the Co atom, whereas in ferrocene the highest intensity of current density is found outside the pentagonal pyramid and far from Fe.[28] We think that this result is a clear indication that we have global aromaticity in metallabis(dicarbollides) and local in ferrocenes.
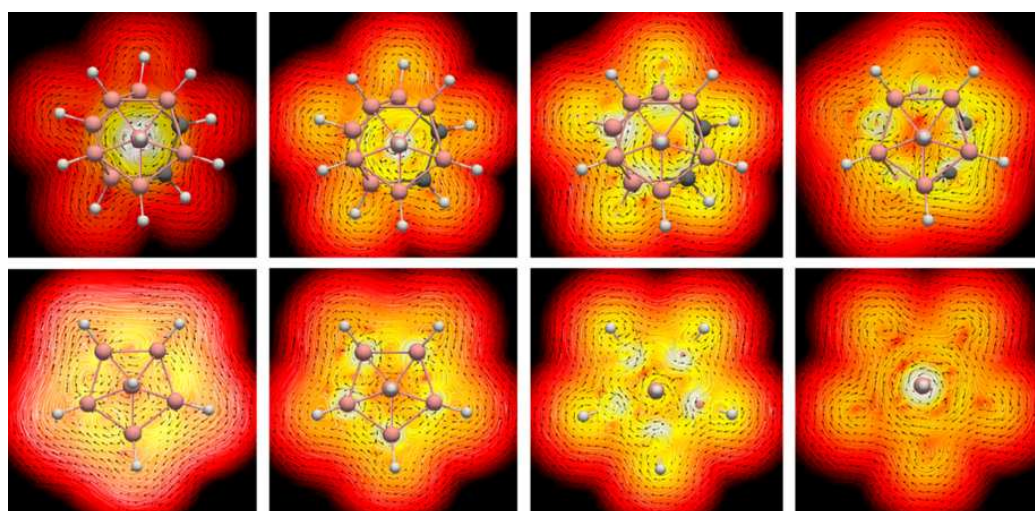
Figure 9. Representation of the current density vector field for the *closo*-[Co(C₂B₉H₁₁)]⁺ system. Top view of the currents in the planes parallel to the five-membered rings located at 0, 1, 2, and 3 bohrs (on top, and from left to right, respectively) and 4, 5, 6, and 7 bohrs (on bottom, and from left to right, respectively). The plane at 0 bohrs is the one containing the Co atom, and the plane at 4 bohrs is the one in the middle of the two five-membered rings. Color scale given in Figure 4. Units are nA T⁻¹. See the Supporting Information for pictures with larger resolution.
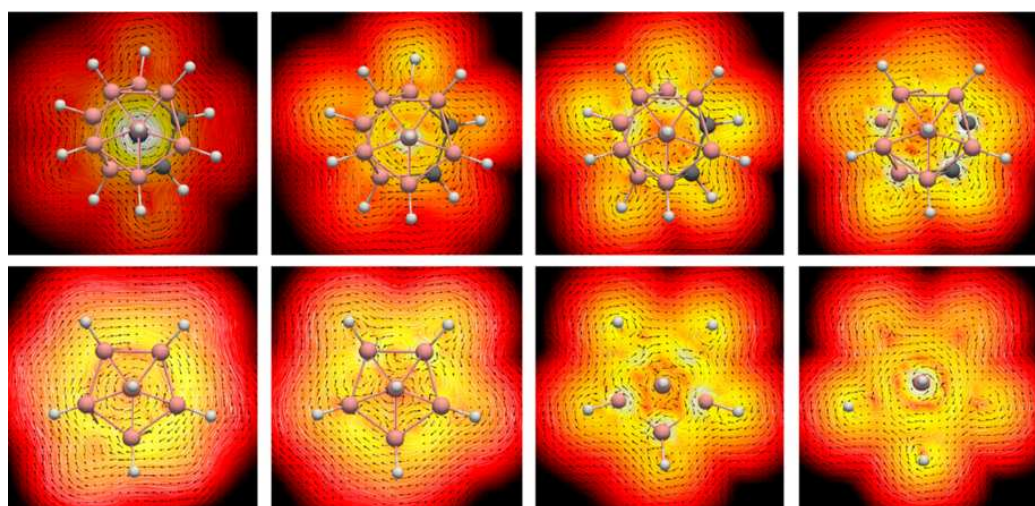
Figure 10. Representation of the current density vector field for the *closo*-[Co(C₂B₉H₁₁)₂]⁻ system. Top view of the currents in the planes parallel to the five-membered rings located at 0, 1, 2, and 3 bohrs (on top, and from left to right, respectively) and 4, 5, 6, and 7 bohrs (on bottom, and from left to right, respectively). The plane at 0 bohrs is the one containing the Co atom, and the plane at 4 bohrs is the one in the middle of the two five-membered rings. Color scale given in Figure 4. Units are nA T⁻¹. See the Supporting Information for pictures with larger resolution.

■ CONCLUSIONS

There are several conclusions that can be drawn from this research; these refer to the aromaticity of *closo*-carboranes, *nido*-carboranes, and sandwich metallabis(dicarbollides) and the relationships between aromaticity and antiaromaticity, aromaticity and reactivity, and planar and spherical aromaticity.

The resistance to deboronation of the *closo-m*-C₂B₁₀H₁₂ as compared to the ease of deboronation of the *closo-o*-C₂B₁₀H₁₂, together with the isomerization of *closo-o*-C₂B₁₀H₁₂ to *closo-m*-C₂B₁₀H₁₂ upon heating, agrees with the B3LYP/6-311+ +G(d,p) results indicating that the *meta*-isomer is 16.3 kcal mol⁻¹ more stable than the *ortho* one. However, this difference is not related to aromaticity but to the location of the C atoms in the carborane structure.

It is to be noticed that the closed or partially closed structure of boranes permits one to draw conclusions on the aromaticity that otherwise would be difficult to observe in other morphologies. Experimentally, it is found that the endocyclic and acid proton on top of a pentagonal C₂B₃ face resonates near −2.5 ppm in the ¹H NMR and its antipodal boron resonates at −37.2 ppm in the ¹¹B NMR. Both are at the highest upfield parts of their respective spectra, proving the existence of diatropic currents in the plane in the middle of the cluster. Upon removal of the endocyclic proton, the C₂B₃ generated plane is not the most aromatic of the possible cluster pentagonal planes according to NICS values. This situation contrasts with that of ferrocene, in which the highest aromaticity is in the Cp⁻ planes. Calculations at the B3LYP/6-311++G(d,p) level of theory also prove that the C₂B₃ ring in *nido*-carborane is not more aromatic than that in *closo*, despite

the former representing a conjugated open face, which coordinates with the metal in metallabis(dicarbollides). More importantly, and different from p_π systems, the strongest diatropic ring currents are not found at ca. 1 Å from the ring plane, but at different parallel planes between the two main five-membered rings of the cluster. The latter is responsible of the anomalous chemical shift in the ^{1}H NMR of the endocyclic proton, as well as that of B_1.

For completeness, comparison to metallocenes allows one to conclude that, whereas metallabis(dicarbollides) are clearly aromatic, as mentioned above, metallocenes display aromatic character. Alternatively, metallabis(dicarbollides) display global aromaticity, whereas metallocenes present local aromaticity in the ligands. *closo*-Boranes, e.g., $[B_{12}H_{12}]^{2-}$, and *closo*-carboranes, e.g., o-, m-, p-$C_2B_{10}H_{12}$, display very similar aromaticity properties, with very large negative NICS values, about −33 ppm, despite the existence of heteroatoms with $\Delta\chi(C,B)$ = 0.51. This contrasts markedly with the planar diazines and diboratabenzenes also having o-, m-, p-$N_2C_4H_4$ and o-, m-, p-$[C_4B_2H_6]^{2-}$ isomers, which can be referenced to C_6H_6. These have similar $\Delta\chi(N,C)$ = 0.49 and precise $\Delta\chi(C,B)$, but the discrepancies with the NICS values between C_6H_6 and the diazines surpass 30%, and those between C_6H_6 and the diboratabenzenes surpass 75%, whereas that between *closo*-$[B_{12}H_{12}]^{2-}$ and *closo*-carboranes is near 1%. The *nido*-carboranes present an aromatic character very similar to that of *closo*-carboranes, despite *nido*-carboranes having lost the spherical shape of the *closo*-carboranes or -boranes. Both NICS magnetic aromaticity criteria and their diatropic ring currents support the aromatic character of *nido*-carboranes.

Thus, the initial hypothesis is proven: if metallabis-(dicarbollides) are aromatic, their ligands must also be aromatic. Unlike aromatic hydrocarbons that become anti-aromatic when two electrons are either added or removed, carboranes keep their aromaticity even when deboronated because they adapt to a different geometry. Therefore, aromaticity in boron clusters survives radical structural changes. When two electrons are added to a *closo* with n vertexes, it becomes a *nido* with $n − 1$ vertexes to preserve the initial aromaticity. This possibility is not feasible for planar conjugated organic molecules with $4n + 2$ π electron counting and highlights the uniqueness of boron clusters with regard to the aromaticity. Further it accounts very well for the "paradigm for the electron requirements of clusters" by Rudolph,[53] in which a *closo* cluster that is aromatic upon addition of $2e^-$ becomes a *nido*-species (actually also aromatic according to this work), and explains the informative schemes by Rudolph and Williams.

EXPERIMENTAL SECTION

Bench Work. Partial degradation or deboronation of *closo*-1,2-$C_2B_{10}H_{12}$ and *closo*-1,7-$C_2B_{10}H_{12}$ has been done in a comparative way to show the differences of the apparently similar but in reality very different isomers (Table 3). Despite there being alternative methods for the partial degradation of *closo*-1,7-$C_2B_{10}H_{12}$, as indicated in the text, the reported autoclave method[51] with KOH in ethanol can be convenient for the simplicity of the working up procedure. All details of the partial degradation procedures done and the NMR characterization are extensively indicated in the Supporting Information.

The reported general procedure is as follows: 200 mg (1.38 mmol) of *closo*-1,7-$C_2B_{10}H_{12}$ and 388 mg (6.94 mmol) of KOH were mixed with 5 mL of ethanol in an autoclave to preserve the solvent at 130 °C for 4 h. The resulting white precipitate was filtered off and the solvent evaporated in vacuum to give *nido*-$[7,9-(C_2B_9H_{11})]^{2-}$. Water (15−20

Table 3. Summary of the Different Parameters Used for the Partial Degradation of the *closo-m*-C$_2$B$_{10}$H$_{12}$ Cluster

working conditions				
T (°C)	time (h)	equiv of KOH	presence of the starting *closo-m*-C$_2$B$_{10}$H$_{12}$ cluster	*nido-m*-[HNMe$_3$][*m*-C$_2$B$_9$H$_{12}$] yield (%)
110	4	5	yes	38.2
115	4	5	yes	40.8
120	4	5	yes	45.3
130	1	5	yes	−
130	2	5	yes	−
130	3	5	yes	−
130	4	5	no	66.1
150	4	3	yes	−
150	4	5	no	47.2
160	4	5	no	−

mL) was added followed by drops of a diluted HCl solution until having the pH equaled 3. Precipitation by adding 132 mg (1.38 mmol) of $[HNMe_3]Cl$ gave 176 mg of $[HNMe_3][7,9$-*nido*-$(C_2B_9H_{12})]$ (66%).

Computational Work. All calculations were performed with the Gaussian 09 package[74] by means of the B3LYP[75−77] hybrid density functional and the 6-311++G(d,p) basis set.[78] The geometry optimizations were carried out without symmetry constraints, and analytical Hessians were computed to characterize the optimized structures as minima (zero imaginary frequencies). Aromaticity was evaluated by means of the nucleus-independent chemical shift (NICS),[33,40,41,68] proposed by Schleyer and co-workers as a magnetic descriptor of aromaticity. NICS is defined as the negative value of the absolute shielding computed at a ring center or at some other point of the system. Rings with large negative NICS values are considered aromatic. NICS values were computed using the gauge-including atomic orbital method (GIAO).[79] The magnetic shielding tensor was calculated for ghost atoms located at the center of the rings (or polyhedra) determined by the nonweighted mean of the heavy atoms coordinates. These values are denoted as NICS(0).[80] Reported ring currents were computed with the GIMIC program[81−83] using the gauge-including atomic orbitals (GIAO) procedure with the B3LYP/6-311++G(d,p) method.[84] A more detailed explanation of the GIMIC calculations is provided in the Supporting Information.

■ ASSOCIATED CONTENT

SI **Supporting Information**

The Supporting Information is available free of charge at https://pubs.acs.org/doi/10.1021/jacs.0c02228.

> An experimental section, including methods, Scheme S1, and Figures S1−S11, and a computational section, including further details of the GIMIC calculations, Table S1, and Figure S12 (PDF)

■ AUTHOR INFORMATION

Corresponding Authors

Miquel Solà − *Institut de Química Computacional i Catàlisi and Departament de Química, Universitat de Girona, 17003 Girona, Catalonia, Spain;* ● orcid.org/0000-0002-1917-7450; Email: miquel.sola@udg.edu

Francesc Teixidor − *Institut de Ciència de Materials de Barcelona, Consejo Superior de Investigaciones Científicas, Campus Universitat Autònoma de Barcelona, 08193 Bellaterra, Spain;* ● orcid.org/0000-0002-3010-2417; Email: teixidor@icmab.es

Authors

Jordi Poater − *Departament de Química Inorgànica i Orgànica & Institut de Quimica Teòrica i Computacional (IQTCUB), Universitat de Barcelona, 08028 Barcelona, Spain; ICREA, 08010 Barcelona, Spain;* orcid.org/0000-0002-0814-5074

Clara Viñas − *Institut de Ciència de Materials de Barcelona, Consejo Superior de Investigaciones Científicas, Campus Universitari Autònoma de Barcelona, 08193 Bellaterra, Spain;* orcid.org/0000-0001-5000-0277

Ines Bennour − *Institut de Ciència de Materials de Barcelona, Consejo Superior de Investigaciones Científicas, Campus Universitari Autònoma de Barcelona, 08193 Bellaterra, Spain*

Sílvia Escayola − *Institut de Química Computacional i Catàlisi and Departament de Química, Universitat de Girona, 17003 Girona, Catalonia, Spain*

Complete contact information is available at:
https://pubs.acs.org/10.1021/jacs.0c02228

Notes

The authors declare no competing financial interest.

■ REFERENCES

(1) Makrlik, E.; Vanura, P. Applications of the Dicarbollylcobaltate-(III) Anion in the Water Nitrobenzene Extraction System. *Talanta* **1985**, *32*, 423−429.

(2) Grimes, R. N. Metallacarboranes in the new millennium. *Coord. Chem. Rev.* **2000**, *200*, 773−811.

(3) Plesek, J. Potential Applications of the Boron Cluster Compounds. *Chem. Rev.* **1992**, *92*, 269−278.

(4) Rais, J.; Selucky, P. New trends in the separation of cesium, strontitum, and transplutonides by extraction methods. *Nucleon (Czechoslovakia)* **1992**, *1*, 17−20.

(5) Rais, J.; Selucky, P.; Kyrs, M. Extraction of Alkali-Metals into Nitrobenzene in Presence of Univalent Polyhedral Borate Anions. *J. Inorg. Nucl. Chem.* **1976**, *38*, 1376−1378.

(6) Reilly, S. D.; Mason, C. F. V.; Smith, P. H. *Cobalt(III) Dicarbollide: A Potential ¹³⁷Cs and ⁹⁰Sr Waste Extraction Agent*; Los Alamos National Laboratory: Los Alamos, NM, 1990.

(7) Sivaev, I. B.; Bregadze, V. I. Chemistry of cobalt bis-(dicarbollides). A review. *Collect. Czech. Chem. Commun.* **1999**, *64*, 783−805.

(8) Viñas, C.; Gómez, S.; Bertrán, J.; Teixidor, F.; Dozol, J. F.; Rouquette, H. New polyether-substituted metallacarboranes as extractants for ¹³⁷Cs and ⁹⁰Sr from nuclear wastes. *Inorg. Chem.* **1998**, *37*, 3640−3643.

(9) Viñas, C.; Gómez, S.; Bertran, J.; Teixidor, F.; Dozol, J. F.; Rouquette, H. Cobaltabis(dicarbollide) derivatives as extractants for europium from nuclear wastes. *Chem. Commun.* **1998**, 191−192.

(10) Gruner, B.; Plesek, J.; Baca, J.; Cisarova, I.; Dozol, J. F.; Rouquette, H.; Viñas, C.; Selucky, P.; Rais, J. Cobalt bis(dicarbollide) ions with covalently bonded CMPO groups as selective extraction agents for lanthanide and actinide cations from highly acidic nuclear waste solutions. *New J. Chem.* **2002**, *26*, 1519−1527.

(11) In *Boron Science: New Technologies and Applications*; Hosmane, N. S., Ed.; CRC Press: Boca Raton, FL, 2012; pp 1−825.

(12) Keener, M.; Hunt, C.; Carroll, T. G.; Kampel, V.; Dobrovetsky, R.; Hayton, T. W.; Menard, G. Redox-switchable carboranes for uranium capture and release. *Nature* **2020**, *577*, 652−655.

(13) Núñez, R.; Romero, I.; Teixidor, F.; Viñas, C. Icosahedral boron clusters: a perfect tool for the enhancement of polymer features. *Chem. Soc. Rev.* **2016**, *45*, 5147−5173.

(14) In *Boron-Based Compounds. Potential and Emerging Applications in Medicine*; Hey-Hawkins, E., Viñas, C., Eds.; John Wiley & Sons Ltd: Chichester, UK, 2018.

(15) Hawthorne, M. F.; Zink, J. I.; Skelton, J. M.; Bayer, M. J.; Liu, C.; Livshits, E.; Baer, R.; Neuhauser, D. Electrical or photocontrol of the rotary motion of a metallacarborane. *Science* **2004**, *303*, 1849−1851.

(16) Li, T. C.; Spokoyny, A. M.; She, C.; Farha, O. K.; Mirkin, C. A.; Marks, T. J.; Hupp, J. T. Ni(III)/(IV) Bis(dicarbollide) as a Fast, Noncorrosive Redox Shuttle for Dye-Sensitized Solar Cells. *J. Am. Chem. Soc.* **2010**, *132*, 4580−4582.

(17) Spokoyny, A. M.; Li, T. C.; Farha, O. K.; Machan, C. W.; She, C.; Stern, C. L.; Marks, T. J.; Hupp, J. T.; Mirkin, C. A. Electronic Tuning of Nickel-Based Bis(dicarbollide) Redox Shuttles in Dye-Sensitized Solar Cells. *Angew. Chem., Int. Ed.* **2010**, *49*, 5339−5343.

(18) Aldridge, S.; Bresner, C. The coordination chemistry of boryl and borate substituted cyclopentadienyl ligands. *Coord. Chem. Rev.* **2003**, *244*, 71−92.

(19) Corsini, M.; de Biani, F. F.; Zanello, P. Mononuclear metallacarboranes of groups 6−10 metals: Analogues of metallocenes - Electrochemical and X-ray structural aspects. *Coord. Chem. Rev.* **2006**, *250*, 1351−1372.

(20) Deck, P. A. Perfluoroaryl-substituted cyclopentadienyl complexes of transition metals. *Coord. Chem. Rev.* **2006**, *250*, 1032−1055.

(21) Nguyen, P.; Gomez-Elipe, P.; Manners, I. Organometallic polymers with transition metals in the main chain. *Chem. Rev.* **1999**, *99*, 1515−1548.

(22) Siemeling, U.; Auch, T. C. 1,1′-Di(heteroatom)-functionalised ferrocenes as [N, N], [O, O] and [S, S] chelate ligands in transition metal chemistry. *Chem. Soc. Rev.* **2005**, *34*, 584−594.

(23) Williams, K. A.; Boydston, A. J.; Bielawski, C. W. Main-chain organometallic polymers: synthetic strategies, applications, and perspectives. *Chem. Soc. Rev.* **2007**, *36*, 729−744.

(24) Yamaguchi, Y.; Ding, W.; Sanderson, C. T.; Borden, M. L.; Morgan, M. J.; Kutal, C. Electronic structure, spectroscopy, and photochemistry of group 8 metallocenes. *Coord. Chem. Rev.* **2007**, *251*, 515−524.

(25) Rausch, M. D.; Fischer, E. O.; Grubert, H. The Aromatic Reactivity of Ferrocene, Ruthenocene and Osmocene¹,². *J. Am. Chem. Soc.* **1960**, *82*, 76−82.

(26) Laskoski, M.; Steffen, W.; Smith, M. D.; Bunz, U. H. F. Is ferrocene more aromatic than benzene? *Chem. Commun.* **2001**, 691−692.

(27) Phillips, L.; Separovic, F.; Aroney, M. J. The aromaticity of ferrocene and some derivatives, ruthenocene and dibenzenechromium as determined via ring current assessment and ¹³C anisotropic contributions to the ¹H NMR shielding. *New J. Chem.* **2003**, *27*, 381−386.

(28) Bean, D. E.; Fowler, P. W.; Morris, M. J. Aromaticity and ring currents in ferrocene and two isomeric sandwich complexes. *J. Organomet. Chem.* **2011**, *696*, 2093−2100.

(29) Seyferth, D. The rise and fall of tetraethyllead. 2. *Organometallics* **2003**, *22*, 5154−5178.

(30) Baird, N. C. Quantum Organic Photochemistry. II. Resonance and Aromaticity in Lowest $3\pi\pi^*$ State of Cyclic Hydrocarbons. *J. Am. Chem. Soc.* **1972**, *94*, 4941−4948.

(31) Seyferth, D. (Cyclobutadiene)iron tricarbonyl - A case of theory before experiment. *Organometallics* **2003**, *22*, 2−20.

(32) Junqueira, G. M. A. Remarkable aromaticity of cobalt bis(dicarbollide) derivatives: a NICS study. *Theor. Chem. Acc.* **2018**, *137*, 92.

(33) Poater, J.; Solà, M.; Vinas, C.; Teixidor, F. π-Aromaticity and Three-Dimensional Aromaticity: Two Sides of the Same Coin? *Angew. Chem., Int. Ed.* **2014**, *53*, 12191−12195.

(34) Mingos, D. M. P. General Theory for Cluster and Ring Compounds of Main Group and Transition-Elements. *Nature Phys. Sci.* **1972**, *236*, 99−102.

(35) Mingos, D. M. P. Polyhedral Skeletal Electron Pair Approach. *Acc. Chem. Res.* **1984**, *17*, 311−319.

(36) Wade, K. Structural Significance of Number of Skeletal Bonding Electron-Pairs in Carboranes, Higher Boranes and Borane Anions, and Various Transition-Metal Carbonyl Cluster Compounds. *J. Chem. Soc. D* **1971**, 792−793.

(37) Wade, K. *Electron-Deficient Compounds*; Nelson and Sons, Ltd.: London, 1971.

(38) Hückel, E. Main feature of the theory of unsaturated and aromatic compounds. *Z. Elektrochemie* **1937**, *43*, 752−788.

(39) McKay, D.; Macgregor, S. A.; Welch, A. J. Isomerisation of nido-$[C_2B_{10}H_{12}]^{2-}$ dianions: unprecedented rearrangements and new structural motifs in carborane cluster chemistry. *Chem. Sci.* **2015**, *6*, 3117−3128.

(40) Poater, J.; Solà, M.; Vinas, C.; Teixidor, F. A Simple Link between Hydrocarbon and Borohydride Chemistries. *Chem. - Eur. J.* **2013**, *19*, 4169−4175.

(41) Poater, J.; Solà, M.; Vinas, C.; Teixidor, F. Hückel's Rule of Aromaticity Categorizes Aromatic closo Boron Hydride Clusters. *Chem. - Eur. J.* **2016**, *22*, 7437−7443.

(42) Davidson, M. G.; Fox, M. A.; Hibbert, T. G.; Howard, J. A. K.; Mackinnon, A.; Neretin, I. S.; Wade, K. Deboronation of *ortho*-carborane by an iminophosphorane: crystal structures of the novel carborane adduct *nido*-$C_2B_{10}H_{12}$.HNP(NMe$_2$)$_3$ and the borenium salt $[(Me_2N)_3PNHBNP(NMe_2)_3]_2O^{2+}$ $(C_2B_9H_{12}^-)_2$. *Chem. Commun.* **1999**, 1649−1650.

(43) Fox, M. A.; Gill, W. R.; Herbertson, P. L.; MacBride, J. A. H.; Wade, K.; Colquhoun, H. M. Deboronation of C-substituted *ortho*- and *meta-closo*-carboranes using "wet" fluoride ion solutions. *Polyhedron* **1996**, *15*, 565−571.

(44) Fox, M. A.; MacBride, J. A. H.; Wade, K. Fluoride-ion deboronation of *p*-fluorophenyl-*ortho*- and -*meta*-carboranes. NMR evidence for the new fluoroborate, HOBHF$_2^-$. *Polyhedron* **1997**, *16*, 2499−2507.

(45) Fox, M. A.; Wade, K. Cage-fluorination during deboronation of *meta*-carboranes. *Polyhedron* **1997**, *16*, 2517−2525.

(46) Taoda, Y.; Sawabe, T.; Endo, Y.; Yamaguchi, K.; Fujii, S.; Kagechika, H. Identification of an intermediate in the deboronation of *ortho*-carborane: an adduct of *ortho*-carborane with two nucleophiles on one boron atom. *Chem. Commun.* **2008**, 2049−2051.

(47) Wiesboeck, R. A.; Hawthorne, M. F. Dicarbaundecaborane(13) and Derivatives. *J. Am. Chem. Soc.* **1964**, *86*, 1642−1643.

(48) Yoo, Y.; Hwang, J. W.; Do, Y. Facile and mild deboronation of o-carboranes using cesium fluoride. *Inorg. Chem.* **2001**, *40*, 568−570.

(49) Zakharkin, L. I.; Kalinin, V. N. On Reaction of Amines with Barenes. *Tetrahedron Lett.* **1965**, *6*, 407-409.

(50) Zakharkin, L. I.; Kirillova, V. S. Cleavage of Ortho-Carboranes to (3)-1,2-Dicarbaundecarborates by Amines. *Bull. Acad. Sci. USSR, Div. Chem. Sci.* **1975**, *24*, 2484−2486.

(51) Hawthorne, M. F.; Young, D. C.; Garrett, P. M.; Owen, D. A.; Schwerin, S. G.; Tebbe, F. N.; Wegner, P. A. Preparation and Characterization of (3)-1,2- and (3)-1,7-Dicarbadodecahydroundecaborate(−1) Ions. *J. Am. Chem. Soc.* **1968**, *90*, 862−868.

(52) Fox, M. A.; Goeta, A. E.; Hughes, A. K.; Johnson, A. L. Crystal and molecular structures of the nido-carborane anions, 7,9- and 2,9-$C_2B_9H_{12}$. *J. Chem. Soc., Dalton Trans.* **2002**, 2132−2141.

(53) Rudolph, R. W. Boranes and Heteroboranes - Paradigm for Electron Requirements of Clusters. *Acc. Chem. Res.* **1976**, *9*, 446−452.

(54) Wade, K. Key to Cluster Shapes. *Chem. Br.* **1975**, *11*, 177−183.

(55) Williams, R. E.; Bender, M. L. Substituent Effects on Chymotrypsin-Catalyzed Hydrolysis of Specific Ester Substrates. *Can. J. Biochem.* **1971**, *49*, 210−217.

(56) Pauling, L. *The Nature of the Chemical Bond*, 3rd ed.; Cornell University Press: Ithaca, NY, 1960.

(57) El-Hamdi, M.; Tiznado, W.; Poater, J.; Solà, M. An Analysis of the Isomerization Energies of 1,2-/1,3-Diazacyclobutadiene, Pyrazole/Imidazole, and Pyridazine/Pyrimidine with the Turn-Upside-Down Approach. *J. Org. Chem.* **2011**, *76*, 8913−8921.

(58) Wang, Y.; Wu, J. I. C.; Li, Q.; Schleyer, P. v. R. Aromaticity and Relative Stabilities of Azines. *Org. Lett.* **2010**, *12*, 4824−4827.

(59) Herberich, G. E.; Hessner, B.; Hostalek, M. A 1,2-Diboratabenzene: Lithium Salt and Transition Metal Complexes. *Angew. Chem., Int. Ed. Engl.* **1986**, *25*, 642−643.

(60) Balzereit, C.; Winkler, H.-J.; Massa, W.; Berndt, A. A 1,3-Diboratabenzene. *Angew. Chem., Int. Ed. Engl.* **1994**, *33*, 2306−2308.

(61) Wörner, K.-F.; Siebert, W. Synthesis of New µ-1,4-Diboracyclohexadiene Triple-Decker Complexes. *Z. Naturforsch., B: J. Chem. Sci.* **1989**, *44*, 1211−1213.

(62) Ashe, A. J.; Shu, P. The 1-Phenylborabenzene Anion. *J. Am. Chem. Soc.* **1971**, *93*, 1804−1805.

(63) Grimes, R. N. *Carboranes*, 3rd ed.; Academic Press, 2016; pp 1−1041.

(64) Hoffmann, R. Perspective The Many Guises of Aromaticity. *Am. Sci.* **2015**, *103*, 18−22.

(65) Matito, E.; Poater, J.; Solà, M.; Schleyer, P. v. R. Aromaticity and Chemical Reactivity. In *Chemical Reactivity Theory*; Chattaraj, P. K., Ed.; Taylor and Francis/CRC Press: Boca Raton, FL, 2009.

(66) Solà, M. Why Aromaticity Is a Suspicious Concept? Why? *Front. Chem.* **2017**, *5*, 22.

(67) Feixas, F.; Matito, E.; Poater, J.; Solà, M. On the performance of some aromaticity indices: A critical assessment using a test set. *J. Comput. Chem.* **2008**, *29*, 1543−1554.

(68) Chen, Z. F.; Wannere, C. S.; Corminboeuf, C.; Puchta, R.; Schleyer, P. v. R. Nucleus-independent chemical shifts (NICS) as an aromaticity criterion. *Chem. Rev.* **2005**, *105*, 3842−3888.

(69) Buchanan, J.; Hamilton, E. J. M.; Reed, D.; Welch, A. J. The structure of $[7,8-C_2B_9H_{12}]^-$; correction of a popular misconception. *J. Chem. Soc., Dalton Trans.* **1990**, 677−680.

(70) Barberà, G.; Viñas, C.; Teixidor, F.; Rosair, G. M.; Welch, A. J. Synthesis and characterisation of the exo-*nido* molybdacarborane complex Mo(-C$_3$H$_5$)(CO)$_2$(7,8-(-SCH$_2$CH$_2$S-7,8-*nido*-C$_2$B$_9$H$_{10}$). Strong B-H-Mo 3-centre bonding. *J. Organomet. Chem.* **2002**, *663*, 221−226.

(71) Fliegl, H.; Sundholm, D.; Taubert, S.; Jusélius, J.; Klopper, W. Magnetically Induced Current Densities in Aromatic, Antiaromatic, Homoaromatic, and Nonaromatic Hydrocarbons. *J. Phys. Chem. A* **2009**, *113*, 8668−8676.

(72) Feixas, F.; Jiménez-Halla, J. O. C.; Matito, E.; Poater, J.; Solà, M. Is the Aromaticity of the Benzene Ring in the (η^6-C$_6$H$_6$)Cr(CO)$_3$ Complex Larger than that of the Isolated Benzene Molecule? *Pol. J. Chem.* **2007**, *81*, 783−797.

(73) Foroutan-Nejad, C. Is NICS a reliable aromaticity index for transition metal clusters? *Theor. Chem. Acc.* **2015**, *134*, 8.

(74) Frisch, M. J.; Trucks, G. W.; Schlegel, H. B.; Scuseria, G. E.; Robb, M. A.; Cheeseman, J. R.; Scalmani, G.; Barone, V.; Mennucci, B.; Petersson, G. A.; Nakatsuji, H.; Caricato, M.; Li, X.; Hratchian, H. P.; Izmaylov, A. F.; Bloino, J.; Zheng, G.; Sonnenberg, J. L.; Hada, M.; Ehara, M.; Toyota, K.; Fukuda, R.; Hasegawa, J.; Ishida, M.; Nakajima, T.; Honda, Y.; Kitao, O.; Nakai, H.; Vreven, T.; Montgomery, J. A., Jr.; Peralta, J. E.; Ogliaro, F.; Bearpark, M.; Heyd, J. J.; Brothers, E.; Kudin, K. N.; Staroverov, V. N.; Kobayashi, R.; Normand, J.; Raghavachari, K.; Rendell, A.; Burant, J. C.; Iyengar, S. S.; Tomasi, J.; Cossi, M.; Rega, N.; Millam, J. M.; Klene, M.; Knox, J. E.; Cross, J. B.; Bakken, V.; Adamo, C.; Jaramillo, J.; Gomperts, R.; Stratmann, R. E.; Yazyev, O.; Austin, A. J.; Cammi, R.; Pomelli, C.; Ochterski, J. W.; Martin, R. L.; Morokuma, K.; Zakrzewski, V. G.; Voth, G. A.; Salvador, P.; Dannenberg, J. J.; Dapprich, S.; Daniels, A. D.; Farkas, Ö.; Foresman, J. B.; Ortiz, J. V.; Cioslowski, J.; Fox, D. J. *Gaussian 09*; Gaussian, Inc.: Pittsburgh, PA, 2009.

(75) Becke, A. D. Density-Functional Thermochemistry. III. The Role of Exact Exchange. *J. Chem. Phys.* **1993**, *98*, 5648−5652.

(76) Lee, C. T.; Yang, W. T.; Parr, R. G. Development of the Colle-Salvetti Correlation-Energy Formula into a Functional of the Electron-Density. *Phys. Rev. B: Condens. Matter Mater. Phys.* **1988**, *37*, 785−789.

(77) Stephens, P. J.; Devlin, F. J.; Chabalowski, C. F.; Frisch, M. J. Ab-Initio Calculation of Vibrational Absorption and Circular-Dichroism Spectra Using Density-Functional Force-Fields. *J. Phys. Chem.* **1994**, *98*, 11623−11627.

(78) Frisch, M. J.; Pople, J. A.; Binkley, J. S. Self-Consistent Molecular-Orbital Methods. 25. Supplementary Functions for Gaussian-Basis Sets. *J. Chem. Phys.* **1984**, *80*, 3265−3269.

(79) Wolinski, K.; Hinton, J. F.; Pulay, P. Efficient Implementation of the Gauge-Independent Atomic Orbital Method for NMR Chemical-Shift Calculations. *J. Am. Chem. Soc.* **1990**, *112*, 8251−8260.

(80) Corminboeuf, C.; Heine, T.; Seifert, G.; Schleyer, P. V.; Weber, J. Induced magnetic fields in aromatic [n]-annulenes - interpretation of NICS tensor components. *Phys. Chem. Chem. Phys.* **2004**, *6*, 273−276.

(81) Fliegl, H.; Taubert, S.; Lehtonen, O.; Sundholm, D. The Gauge Including Magnetically Induced Current Method. *Phys. Chem. Chem. Phys.* **2011**, *13*, 20500−20518.

(82) Jusélius, J.; Sundholm, D.; Gauss, J. Calculation of current densities using gauge-including atomic orbitals. *J. Chem. Phys.* **2004**, *121*, 3952−3963.

(83) Sundholm, D.; Fliegl, H.; Berger, R. J. Calculations of Magnetically Induced Current Densities: Theory and Applications. *WIREs Comput. Mol. Sci.* **2016**, *6*, 639−678.

(84) Gauss, J.; Stanton, J. F. Electron-correlated approaches for the calculation of NMR chemical shifts. In *Advances in Chemical Physics*; Prigogine, I., Rice, S. A., Eds.; John Wiley & Sons, 2002; Vol. *123*, pp 355−422.

(85) Vishnevskiy, Y. V.; Tikhonov, D. S.; Reuter, C. G.; Mitzel, N. W.; Hnyk, D.; Holub, J.; Wann, D. A.; Lane, P. D.; Berger, R. J. F.; Hayes, S. A. Influence of Antipodally Coupled Iodine and Carbon Atoms on the Cage Structure of $9,12\text{-}I_2\text{-}closo\text{-}C_2B_{10}H_{10}$: An Electron Diffraction and Computational Study. *Inorg. Chem.* **2015**, *54*, 11868−11874.

■ NOTE ADDED IN PROOF

Ring currents of $[B_{12}H_{12}]^{2-}$ and of $9,12\text{-}I_2\text{-}closo\text{-}C_2B_{10}H_{10}$ were reported previously in reference 85.

5.4.2 Pioneering the Power of Twin Bonds in a Revolutionary Double Bond Formation. Unveiling the True Identity of *o*-Carboryne as *o*-Carborene

This section corresponds to the following publication:

J. Poater, C. Viñas, S. Escayola, M. Solà*, F. Teixidor*. *Chem. Eur. J.*, **2023**, 29, e202302448.

VIP *Very Important Paper*

Pioneering the Power of Twin Bonds in a Revolutionary Double Bond Formation. Unveiling the True Identity of *o*-Carboryne as *o*-Carborene

Jordi Poater,[a, b] Clara Viñas,[c] Sílvia Escayola,[d, e] Miquel Solà,*[d] and Francesc Teixidor*[c]

Dedicated to Professors Evamarie Hey-Hawkins, Rainer Streubel and Manfred Scheer on the occasion of their retirement, celebrating their exceptional contributions to p-block chemistry through groundbreaking research

The homolytic elimination of two H atoms from two adjacent carbons in benzene results in the aromatic product *o*-benzyne. In a similar way, the homolytic elimination of two H atoms from the two adjacent carbons in $1,2\text{-}C_2B_{10}H_{12}$ results in the aromatic product *o*-carboryne. In this work, we provide experimental and computational evidences that despite the similarity of *o*-carboryne and *o*-benzyne, the nature of the C–C bond generated between two adjacent carbons that lose H atoms is different. While in *o*-benzyne the C–C bond behaves as a triple bond, in *o*-carboryne the C–C bond is a double bond. Therefore, we must stop naming 1,2-dehydro-*o*-carboryne as *o*-carboryne but instead call it *o*-carborene.

Introduction

The phenyl group is present in almost 45% of small molecule-based therapeutic drugs on the market. It is the most abundant aromatic group followed at a distance by the pyridine hetero-cycle. The reasons for the ubiquity of the phenyl group are well defined,[1] but central to this work is that its substituents project outwards along a line passing through the centre of the aromatic cycle and the carbon atom of the ring, thus avoiding stereochemical problems. The *o*-carborane, which has three isomers, i. e., *ortho*- (*o*-), *meta*- (*m*-) and *para*- (*p*-) $C_2B_{10}H_{12}$, has some similarities with the phenyl group. For example, both are very stable as they are aromatic abiding Hückel's rule,[2] and both are also lipophilic, a property of relevance in drug design. As in benzene, the substituents also project radially out of the core by a line passing through the centre of the icosahedron and through a B or C atom at its vertices. Because the projection of the icosahedron on a surface is a hexagon and the benzene itself is a hexagon there is an unfounded assumption that the *o*-carborane occupies the same volume as the phenyl when this latter rotates around one of its axes. This is not the case, as the volume of rotating benzene (vdW) is 102 Å³, while that of the *o*-carborane varies between 141 (*o*-) and 148 (*m*-) Å³.[3] However, this conceptualization of the *o*-carborane/benzene is prevalent among researchers and many compounds have been synthesized in which a phenyl group is replaced by an *o*-carborane. A paradigmatic example is Asborin, which is the carborane analogue of Aspirin,[4] although they do not do the same task. While Aspirin relieves inflammation because it inhibits the enzymes in the body COX-2 and COX-1, Asborin does not inhibit any of the two COX variants but is a potent aldo/keto reductase 1 A1 (AKR1 A1) inhibitor.[5] Other examples of direct substitution of the phenyl group by an *o*-carborane can be found in the literature.[3]

The isosteres concept relates to one of two or more substances that exhibit similarity of some properties as a result of having the same number of total or valence electrons in the same arrangement and that consist of different atoms and not necessarily the same number of atoms. *o*-Carborane and benzene are not isosteres,[6] and in general are not bioisosteres. This does not exclude the possibility that they may give rise to other therapeutic drugs. Among other reasons, the different behavior of the *o*-carborane and the benzene is due to the non-equivalence of a carboranyl with a rotating phenyl. Both are aromatic, which is expressed in several ways, one of them

[a] J. Poater
    Departament de Química Inorgànica i Orgànica & Institut de Química
    Teòrica i Computacional (IQTCUB)
    Universitat de Barcelona
    Martí i Franquès 1–11, 08028 Barcelona (Spain)

[b] J. Poater
    ICREA
    Pg. Lluís Companys 23, 08010 Barcelona (Spain)

[c] C. Viñas, F. Teixidor
    Institut de Ciència de Materials de Barcelona
    Consejo Superior de Investigaciones Científicas
    Campus Universitat Autònoma de Barcelona, 08193 Bellaterra (Spain)
    E-mail: teixidor@icmab.es

[d] S. Escayola, M. Solà
    Institut de Química Computacional i Catàlisi and Departament de Química
    Universitat de Girona
    C/ Maria Aurèlia Capmany, 69, 17003 Girona, Catalonia (Spain)
    E-mail: miquel.sola@udg.edu

[e] S. Escayola
    Donostia International Physics Center (DIPC)
    Donostia, Euskadi (Spain)

Chemistry–A European Journal

Research Article
doi.org/10.1002/chem.202302448

Chemistry Europe
European Chemical
Societies Publishing

preserving the original structure following an electrophilic aromatic substitution. But despite these similarities due to the aromaticity, it is neither conceptually simple to imagine nor experimentally easy to demonstrate that the *o*-carboranyl group is an isostere of the phenyl group. Figure 1 shows a benzene (C_6H_6) and two molecules with the same number of heavy atoms, biphenyl ($C_{12}H_{10}$) and *o*-carborane (1,2-$C_2B_{10}H_{12}$). It is clear that *o*-carborane is not isosteric to biphenyl and much less a mimic to benzene. The dimensions of the connectivities are important and we will see this clearly by discussing two very relevant reagents, *o*-benzyne and *o*-carboryne. The latter is indicated in italics in the following pages in order to maintain the nomenclature adopted so far with respect to *o*-benzyne, but we will finally prove that it is in fact a carborene. Earlier work has already shown that 3D aromaticity does not match 2D aromaticity.[2d,7] And, why is that?

If we take 1,2-$C_2B_{10}H_{12}$ as a 3D aromatic model, we see that the C—C bond distance is far from being the conventional one in organic common structures. The C—C distance in 1,2-$C_2B_{10}H_{12}$ is 1.64 Å, that corresponds to a bond order of 0.74 following the bond distance/bond order correlation established by Linus Pauling $n_x = n_o \exp((r_o - r_x)/c)$, where the bond order n_x of a bond of length r_x is a function of a reference bond of length r_o, whose bond order is defined as n_o. This matches precisely with the Jemmis computed 0.74 bond order.[8] The C—C 0.74 bond order in 1,2-$C_2B_{10}H_{12}$ is definitely much less than a single C—C bond. Conversely the pK_a of 1,2-$C_2B_{10}H_{12}$ is very similar to that of the acetylene ($pK_a \approx 24$). These data are at odds with each other, a triple bond against less than a single bond but similar pK_a is simply a realization that in this case what influences the pK_a is not the bond order between the two carbon atoms but the hybridisation on the carbon, which is sp both in the *o*-carborane and in the acetylene. This may have given rise to mistaken interpretations such as considering that two aromatic units that fuse together give rise to another aromatic unit, although this is valid for two units of the same 2D/2D or 3D/3D aromaticity, but not 2D/3D.[2d]

Results and Discussion

Preliminary discussion. Comparison of *o*-benzyne with *o*-carboryne

o-Benzyne was first introduced as a reactive intermediate in 1927.[9] Since then, many investigations on this reagent have followed. Figure 2 shows three possible models for *o*-benzyne. A nice and competent description is given as "The Benzyne Story".[10] In this work, we will limit ourselves to those aspects that will be relevant to our discussion of *o*-carboryne.[11] In a similar way as the homolytic elimination of two H atoms from two adjacent carbons in benzene generates *o*-benzyne, which is aromatic, the same applies when two H atoms are eliminated from the two adjacent carbons of 1,2-$C_2B_{10}H_{12}$ to make *o*-carboryne, which is also aromatic. Geometric constraints on the triple bond in *o*-benzyne result in diminished overlap of in-plane sp-orbitals, and thus a weak triple bond. Indeed, the vibrational frequency of the triple bond in *o*-benzyne was assigned to be 1846 cm^{-1}, confirming the weaker triple bond than in unstrained alkyne with vibrational frequency of approximately 2150 cm^{-1}. Nevertheless, *o*-benzyne is more like a strained alkyne than a diradical, as seen from the large singlet–triplet gap and alkyne-like reactivity. On the other hand, the 12-vertex *o*-carborane, 1,2-$C_2B_{10}H_{12}$[11-12] (Figure 3), is an outstandingly stable molecule whose strength derives both from its aromatic character and from the fact that it has a base structure, the icosahedron, which is one of the platonic solids.[2f] Although *o*-carborane has 3D-aromaticity,[13] its aromaticity can be related to 2D Hückel aromaticity as was recently demonstrated.[2b]

It is necessary to see whether, despite the similar reactivity between *o*-benzyne and *o*-carboryne, the compounds generated are comparable. In the two cases, the HOMO and the LUMO orbitals are mainly the bonding and antibonding orbitals of the bond formed after removal of two H atoms (Figure S7 in the Supporting Information). However, and taken as an example, the pK_a of the *o*-carborane is very similar to that of acetylene, but the products resulting from the reactivity of the C—H bond have very different properties. Or the reaction of *o*-benzyne (aromatic) with two alkynes [2+2+2] gives rise to naphthalene (global aromatic), while the same reaction but with *o*-carboryne

Figure 2. The different representations of *o*-benzyne.

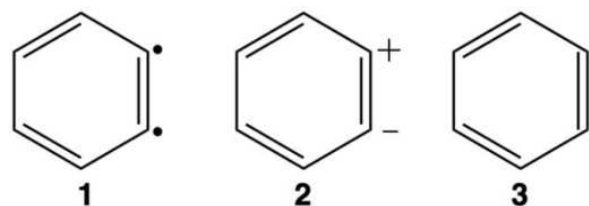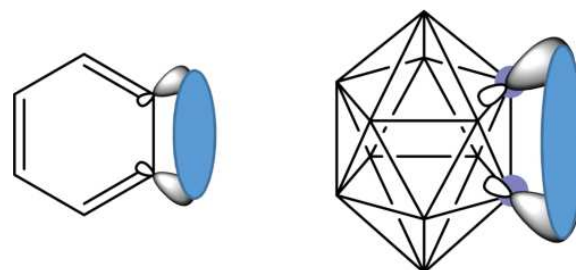**Figure 1.** Structures of benzene, biphenyl and *ortho*-carborane.

Figure 3. The molecular structures of *o*-benzyne (left) and *o*-carboryne (right), stressing that distance matters.

Chemistry–A European Journal

Research Article
doi.org/10.1002/chem.202302448

Chemistry Europe
European Chemical
Societies Publishing

(aromatic) gives rise to benzeno-o-carborane, with local aromaticity on the carborane only.[14] This result highlights the relevance of the main scaffolding bonds in the outcome of the reaction despite having very similar reactivities.

In comparing the o-benzyne and the o-carboryne, it is seen that structurally the length of the o-benzyne's triple bond (1.24 Å) is closer to that of a typical triple bond (1.20 Å, acetylene) than to a double bond (1.34 Å, ethylene) and much less than the C–C in benzene (1.39 Å). If we contemplate again the Pauling's bond distance/bond order, the C≡C triple bond of o-benzyne has a 2.71 bond order, close to a triple bond. If we compare this value (2.71) with the C–C bond order of benzene (1.67), we see that they differ by 1.04 units. Almost a perfect bond order unit. If we make the same comparison between the o-carboryne and the o-carborane, we observe $1.84 - 0.74 = 1.10$. As the bond order should not exceed unity this would suggest that the formation of the sp-sp bond in the o-carborane to yield the o-carboryne exhalts the underlying bond order in the o-carborane from 0.74 to 0.84. This is consistent with a higher contribution of a 2c–2e in the CC, as shown in Figure 4 that bestows a marked C=C character, but definitely not C≡C. The formation of the additional sp-sp bond causes more electron density to build up in the CC connection, pinning a 2c–2e bond thus making it closer to a conventional double bond. It is therefore not surprising that this carboranyl-CC bond acts towards metals as a typical alkene-metal interaction,[15] being $(\eta^2\text{-}C_2B_{10}H_{10})Ni(PPh_3)_2$ and $(\eta^2\text{-}C_2B_{10}H_{10})Cl_2Zr(THF)_3$ remarkable examples.[14a,16] However, upon the coordination of the C–C to metal the bond order in $(\eta^2\text{-}C_2B_{10}H_{10})Ni(PPh_3)_2$ drops to 1.06 from 1.84 in o-carboryne (Figure 4). This is practically a 0.8 loss of bond order. Excessive! Losses between 0.2 and 0.6 in bond order between an alkene and a coordinated alkene are not surprising, but the observed loss of 0.8 is so large that it must be accounted for by the loss of the 2c–2e from which had been pinned between the C–C of the o-carboryne. This suggests that it is the C–C sp-sp bond that interacts with the metal and ultimately the o-carborane returns to the comfort zone provided by its aromatic stabilization energy (ASE). The electron pinning is not only observed in o-carboryne, but also with o-benzyne although in this case it is observed in its complex with a metal, proven with a crystal structure. For o-benzyne in its coordination to Ta, the trapping has been so great that a loss of

aromaticity has been observed with the failing to equalize distances, thus a propensity to cyclohexatriene has been observed. In 1979, Schrock and co-workers reported the synthesis and crystal structure of $Ta(\eta^5\text{-}C_5Me_5)(C_6H_4)Me_2$ in which the C–C distances alternate between 1.36 and 1.41 Å, C_1–C_2 1.364 (linked to Ta), C_2–C_3 1.410, C_3–C_4 1.362, C_4–C_5 1.403, C_5–C_6 1.375, and C_6–C_1 1.408 Å.[17] This definitely proves that although the third bond, the sp-sp, of the triple bond is orthogonal to these π orbitals bestowing aromaticity, its existence affects the aromaticity of the system.

Thus, this process in which the double bond is highly localized before the reaction and reverts to delocalization after the reaction would agree with the statement above on the non-comparable results following reaction between o-benzyne and o-carboryne.[18] And next, what is the difference between o-carboryne and o-benzyne when involved in a cycloaddition reaction that could lead to the fusion of two aromatic halves? In the case of o-benzyne there is a strong scaffolding that does participate in the aromaticity, and two adjacent sp atomic orbitals each one holding a single electron that are orthogonal to the aromatic π-system. There may be pinning but at the moment that the cycloaddition is generated the initial aromatic system is unblocked generating two aromatic units, e.g., naphthalene (Figure 4). What happens to the o-carboryne? o-carboryne does not have a strong scaffolding, it has a system that when the sp-sp bond is formed determines a partial blockage of the aromatic system, favouring a C–C 2c–2e bond ready to participate in cycloaddition reactions.[12,19] Once this takes place, the scaffolding of the o-carborane is unblocked, eliminating the C=C and therefore generating a non-aromatic cyclic system and an aromatic cluster. Therefore, a full 3D/2D aromatic system can never occur, in contradiction to the recently reported experimental results of 3D/2D bonding.[7,19a] Thus we have studied again what could be the causes of the misinterpretation of the NICS and ASE in the o-carborane-fused carbo- and heterocycles.

Comparison of o-benzyne to o-carboryne

The above results support the particularity of the sp-sp generated double bond in o-carboryne, which is not the typical σ or π bond, and it should be of a strength comparable to the third bond in o-benzyne. Therefore, the new bonds in o-benzyne and o-carboryne are not conventional, and not precisely equal. However, the new sp-sp bond either in o-benzyne or o-carboryne does not prevent the aromaticity of $C_2B_{10}H_{12}$ or benzene; and in this way the Wade-Mingos rule[20] continues being fulfilled as the number of electrons of the cage is not affected. Importantly, this aromaticity appears to be strengthened from benzene to o-benzyne according to both electronic-based aromaticity MCI (from 0.072 to 0.077 a.u.), as well as by magnetic-based NICS(0) (from −8.1 to −18.1 ppm, see Table 1). And the same trend is observed from o-carborane to o-carboryne, with an apparent strengthening of aromaticity (Table 1). At this point, it must be pointed out the ring-size dependency of NICS.[21] The NICS values are higher for smaller
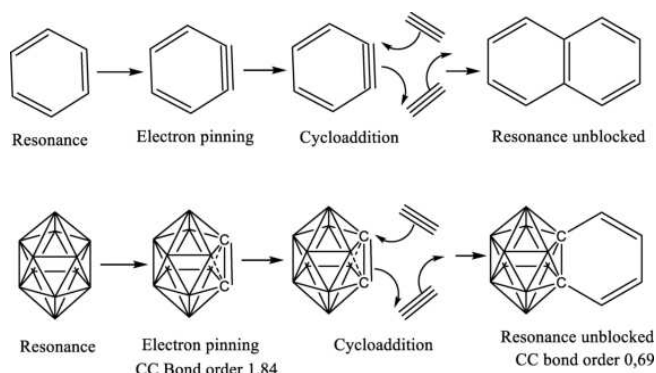
Figure 4. Comparison between o-benzyne and o-carboryne.

In the figure (top row, left to right): Resonance → Electron pinning → Cycloaddition → Resonance unblocked

(bottom row, left to right): Resonance → Electron pinning CC Bond order 1.84 → Cycloaddition → Resonance unblocked CC bond order 0,69

Chemistry–A European Journal

Research Article
doi.org/10.1002/chem.202302448

Chemistry Europe
European Chemical
Societies Publishing

Table 1. NICS (in ppm) and MCI (in au) of benzene and *o*-benzyne, together with NICS of *o*-carborane and *o*-carboryne.

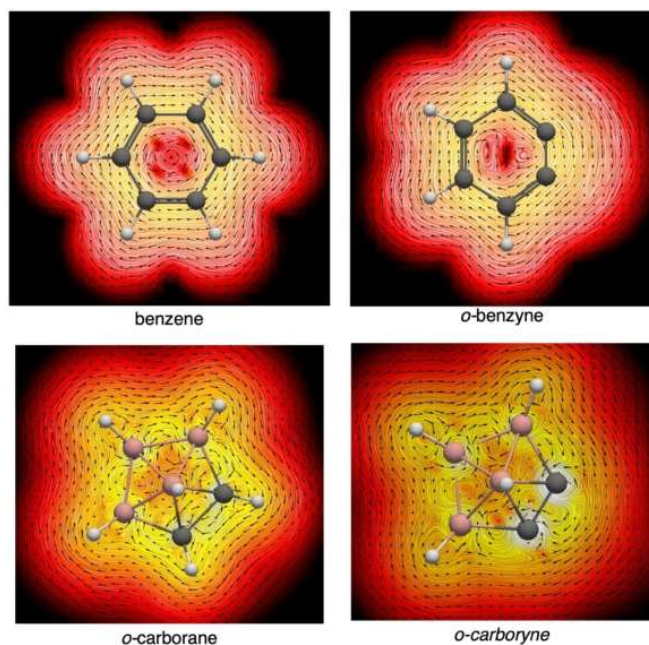|	NICS(0)	NICS(0)$_{zz}$	NICS(1)	NICS(1)$_{zz}$	MCI
benzene	−8.1	−14.6	−10.2	−29.2	0.072
o-benzyne	−18.1	−31.2	−12.8	−33.0	0.077
	NICS(B$_4$C)	NICS(center)			
o-carborane	−33.3	−27.3			
o-carboryne	−40.5	−35.4			

Figure 5. Top: current-density vector field of benzene and *o*-benzyne, with currents at 1 Å above the molecular plane, perpendicular to the magnetic field vector ($\vec{B}$). Bottom: current-density vector field of *o*-carborane and *o*-carboryne, with currents at the central molecular plane (see additional plots in Figures S1–S4 in the Supporting Information), perpendicular to the magnetic field vector ($\vec{B}$). Colour code: dark red – zero intensity; red – low intensity; yellow – high intensity.
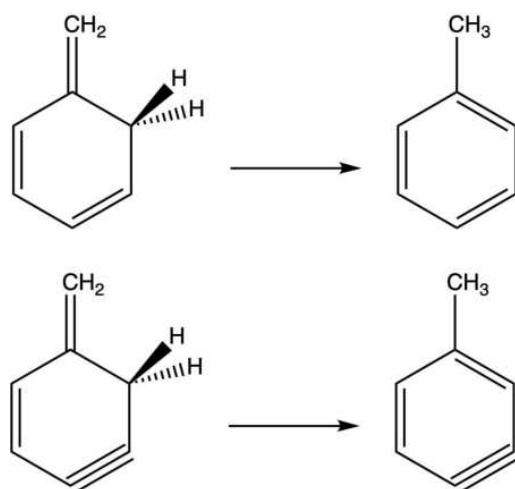
Figure 6. Isomerization stabilization energies of toluene (top) and 4-methyl-benzyne (bottom) are −33.9 and −26.6 kcal mol^{-1}, respectively.

rings, so the more negative NICS of *o*-benzyne and *o*-carboryne could be in part attributed to the ring size shrink. Moreover, the increase in the aromaticity when going from benzene to *o*-benzyne and from *o*-carborane to *o*-carboryne is not observed by means of the computed magnetic induced current densities (Figure 5). It can be observed how the intensity of the currents is similar or somehow reduced when going from benzene to *o*-benzyne, with the main change next to the two carbon atoms from which the H atoms have been removed to form the triple bond. And the same is found when comparing the ring currents of *o*-carborane and *o*-carboryne. Furthermore, isomerization stabilization energies (ISEs) of toluene show a reduction of the aromaticity of the benzene ring when going from toluene to 4-methyl-benzyne (Figure 6). As a whole, various indicators of aromaticity provide different trends, but, in general, it can be concluded that the aromaticity of the ring in benzene and the cage in carborane slightly changes when *o*-benzyne and *o*-carboryne are formed.

Back to the bonds, despite the C–C bond length shortening from *o*-carborane to *o*-carboryne (16.5 %) is larger than from benzene to *o*-benzyne (10.8 %), which might mean a stronger interaction (Table 2 and Figure 7) and is in support of the pinning in electron density in the C–C bond in *o*-carboryne, the delocalization indices[22] support the double bond character of *o*-carboryne (DI = 1.883) versus the triple bond character of *o*-benzyne (DI = 2.249). For completeness, we calculated WBI[23] and MBO[24] bond orders that give the same trends as DI (Table 2). Noticeably, this is further confirmed by computed ^{13}C NMR chemical shifts, with that of *o*-carboryne close to benzene (128.8 and 125.9 ppm, respectively), whereas the chemical shift of *o*-benzyne is much more deshielded (188.4 ppm). In addition, through a fragment analysis (Figure 8), we have computed the overlap between the sp-sp molecular orbitals of *o*-carboryne and compared to the sp-sp of *o*-benzyne to form the corresponding HOMO orbitals. These overlaps further support the stronger interaction present in *o*-benzyne (0.218) than in *o*-carboryne (0.130), despite the bond length shortening in the latter is larger. The reason is the fact that the C–C distance in benzene is already shorter, and thus it is more difficult to shorten it further when generating *o*-benzyne.

Chemistry–A European Journal

Research Article
doi.org/10.1002/chem.202302448

Chemistry
Europe
European Chemical
Societies Publishing

Table 2. C–C bond length (in Å) and C–C delocalization index (in au), together with percentage in which C–C bond length is decreased from *o*-carborane to *o*-carboryne, and from benzene to *o*-benzyne. Wiberg Bond Index[23] and Mayer Bond Order[24] have been included for comparison. Computed ^{13}C NMR chemical shifts (in ppm) are also included. Computed at B3LYP/6-311++G(d,p) level (see Figure S5 in the Supporting Information).

	dist(C=C)	%dist	DI(C=C)	WBI	MBO	[13]C δ
$C_2B_{10}H_{12}$	1.623		0.983	0.735	0.874	58.7[a]
o-carboryne	1.356	16.5	1.813	1.645	2.134	128.8
benzene	1.394		1.389	1.442	1.704	125.9[b]
o-benzyne	1.244	10.8	2.249	2.360	2.447	188.4[c]

[a] Exp. value is 55.5 ppm.[25] [b] Exp. Value in CHCl3 solution is 128.5 ppm.[26] [c] Exp. value of benzyne incarcerated in a molecular container is 181.33 ppm.[27]
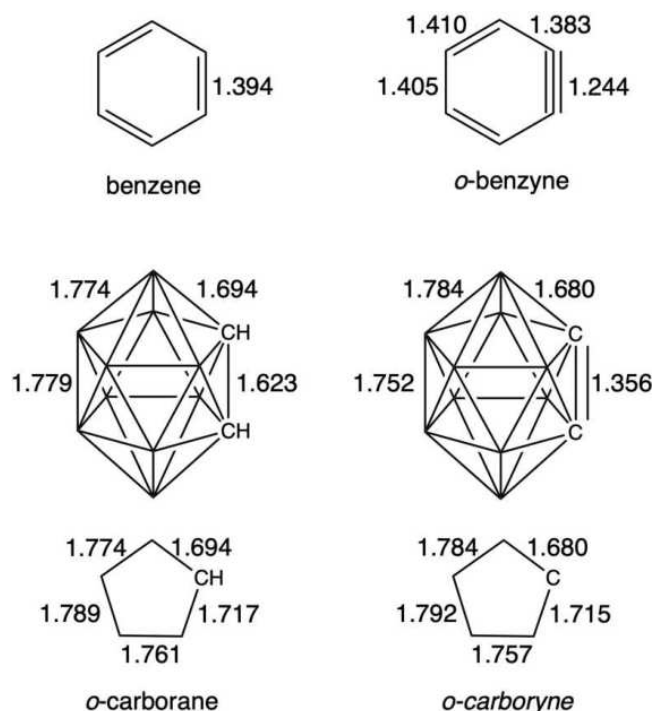
Figure 7. Bond lengths (in Å) for *o*-carborane, *o*-carboryne, benzene, and *o*-benzyne. Computed at B3LYP/6-311++G(d,p) level.
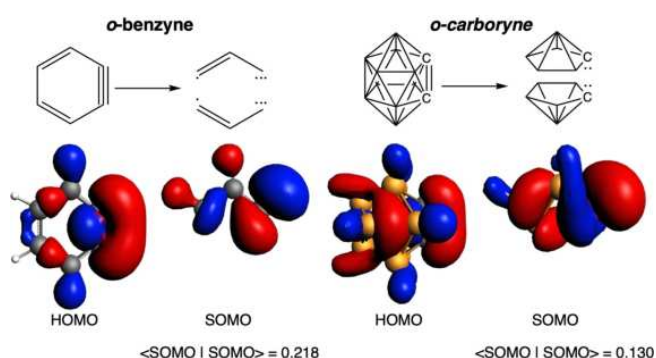
Figure 8. Overlap between single occupied molecular orbitals (SOMOs) of *o*-benzyne (left) and *o*-carboryne (right). Localized MOs are enclosed in Figure S6 in the Supporting Information.

Trimerization of *o*-benzyne and *o*-carboryne

Related to the double vs. triple bond character discussed above, could *o*-carboryne undergo cyclotrimerization as both *o*-benzyne and 9,10-phenanthryne? (Figure 9). First, the cyclo-trimerization is calculated to be thermodynamically favorable for all three systems (−283, −249, and −234 kcal mol^{-1} for *o*-benzyne, 9,10-phenanthryne, and *o*-carboryne, respectively). With respect to aromaticity, both *o*-benzyne and the terminal rings of phenanthryne, as well as *o*-carboryne, keep their aromaticity or it is slightly reduced upon cyclotrimerization (Table 3). But, more importantly, the central ring is non-aromatic for triphenylene and for tri-*o*-carboryne, and just a little bit aromatic for triphenanthryne. The two hydrocarbons not only present smaller bond length alternation in their central ring as compared to *o*-carboryne (0.046 and 0.029 vs. 0.150 Å for *o*-benzyne, 9,10-phenanthryne, and *o*-carboryne, respectively), but the bond lengths are in the order of aromatic bonds. However, that for triphenylene is non-aromatic due to the localization of Clar π-sextets in the three terminal rings and none in the center (Figure 9). Meanwhile, that of triphenan-thryne is slightly aromatic as expected from Clar's π-sextet theory, that locates a π-sextet in the central ring together with a π-sextet on each terminal ring, and despite the non-planarity of this central ring. And finally, the central ring of tri-*o*-carboryne has bond lengths with single-bond character, in agreement with above, and thus it can be considered a cyclohexane. However, it remains planar to reduce the steric repulsion between the three connected *o*-carborane clusters.

Conclusions

This work was motivated by the interest observed in the development of new drugs in substituting the phenyl for the carboranyl group in a lead drug with a view to improving pharmacokinetic or pharmacodynamic properties. It is consid-ered that the phenyl group, which is an aromatic group, could be replaced by a carboranyl group because the latter, by is also aromatic, has a strong resemblance to a phenyl in rotation, the substituents beam out from the center and both are hydro-phobic. Opposite to previous assumption, to us they seem to be far away from the isosteres concept but this is not simple to be demonstrated. In this work, we wanted to refer to the

Chemistry–A European Journal

Research Article
doi.org/10.1002/chem.202302448

Chemistry Europe
European Chemical
Societies Publishing

Figure 9. Cyclotrimerization products of *o*-benzyne, 9,10-phenanthryne, and *o*-carboryne. Bond lengths (in Å) of the central rings are included, together with localization of π-sextets. Naming of rings (in italics) are also included.
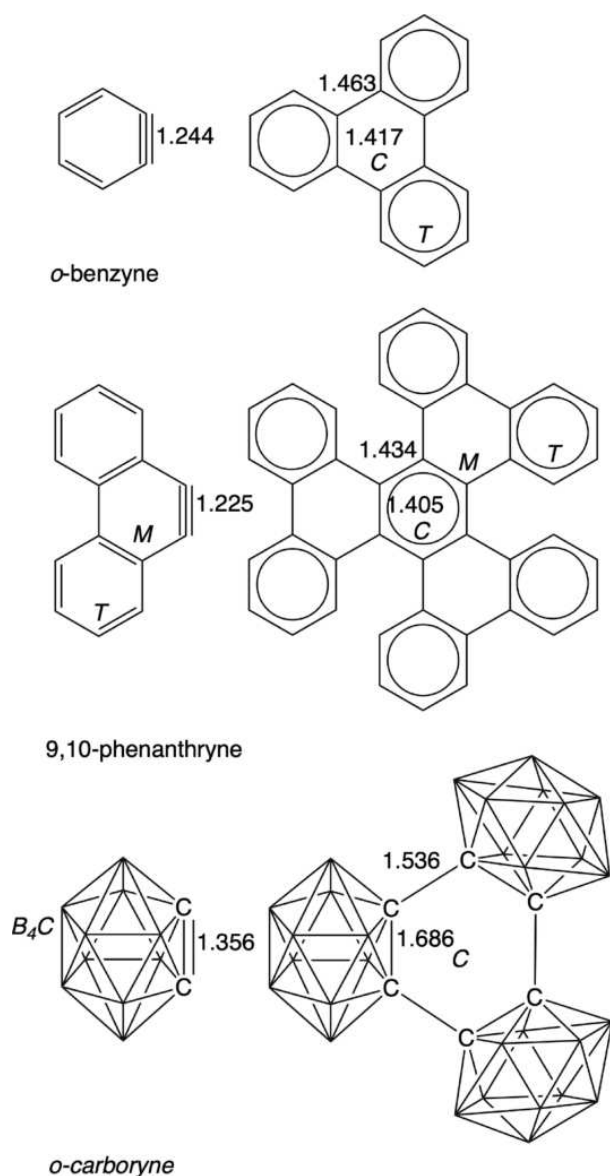
"isosteric" parts, C_6H_6 and $C_2B_{10}H_{12}$, define the electronic and steric differences between the two compounds. Both are aromatic but the C—C distance is very decisive as it also affects the bond order, being in benzene 1.394 Å, BO 1.67, and in carborane 1.623 Å, BO 0.74, but it also influences in *o*-benzyne 1.244 Å, BO 2.71, and *o*-carboryne 1.356 Å, BO 1.84. Upon the reaction with two units of alkyne, the *o*-carboryne and the *o*-benzyne lead to structurally similar cycloaddition compounds but the *o*-carboryne and *o*-benzyne revert to the comfort geometry, the C—C distances and BO of their original parents, *o*-carborane and benzene. Whereas benzene leads to an aromatic compound, the *o*-carborane leads to a local, the carborane, aromatic compound. This has been fully confirmed with cyclo-trimerization of *o*-benzyne, phenanthryne and *o*-carboryne. With no exception, no 3D aromatic *o*-carborane when bonded to four π electron fragments enabled to produce a 6π fragment as a global aromatic compound, only keeping the aromaticity of the original 3D fragment. Conversely, global aromaticity is obtained in similar circumstances with a Hückel[28] 2D original fragment. As said above, this is a consequence of the very dissimilar C—C distance that creates a bond order difference about one unit. Indeed, the *o*-carboryne is in reality an *o*-carborene and therefore should be termed as *o*-carborene. This would explain all reactivity of [2 + 2 + 2] in which the first one is one alkene and the other two alkynes,[29] in this case it would lead to a cyclohexadiene and would express that it is impossible to generate a global aromatic in the fusion of a 3D- and a 2D-aromatic. On the other hand, this study has shown that when a triple bond is produced in benzene or a double bond in *o*-carborane, the aromaticity remains either constant or somehow reduced, that would be due to a pinning of the electronic delocalisation in favour of this triple or double bond, which reverts to total delocalisation once the generated σ is broken. These studies do not seem to support the isosterism of carborane and benzene, but it is another aromatic compound to develop new lead compounds.

concept of a similar number of valence electrons in a similar environment. And the concept of similarity in the number of electrons could be very well related to the concept of aromaticity since both are aromatic and follow either Hückel's or Wade–Mingos rules. And also because of the type of reactivity they offered and the similar environment that could be related to the dimensions, in particular the C—C distance. For this reason, we decided to explore the similarities and differences between one derivative of each the benzene and the *o*-carborane, to say the *o*-benzyne and the *o*-carboryne that are really reactive and produce similar reactions, e.g. the [2 + 2 + 2] cycloaddition. From this, we reached the conclusion that the outcome of each reaction is apparently similar, electronically very different, and similar in terms of their initial stability. The dimensions of the C—C bond and the dimensions of the

Methods

All calculations were performed with the Gaussian 09 package[30] by means of the B3LYP[31] hybrid density functional and the 6–311++G(d,p) basis set.[32] The geometry optimizations were carried out without symmetry constraints (Table S1 in the Supporting Information). Analytical Hessians were computed to characterize the optimized structures as minima (zero imaginary frequencies). Aromaticity was evaluated by means of the nucleus-independent chemical shift (NICS),[2a,b,e,f,33] proposed by Schleyer and co-workers as a magnetic descriptor of aromaticity. NICS is defined as the negative value of the absolute shielding computed at a ring center or at some other point of the system. Rings with large negative NICS values are considered aromatic. NICS values were computed using the gauge-including atomic orbital method (GIAO).[34] Multicenter indices (MCI)[35] and delocalization indices (DI)[22] were computed with the ESI-3D program using Atoms-in-Molecules (AIM) partition of space.[35c,36] Reported ring currents were computed

Chemistry–A European Journal

Research Article
doi.org/10.1002/chem.202302448

**Chemistry
Europe**
European Chemical
Societies Publishing

Table 3. NICS (in ppm) and MCI (in a.u.) of the systems involved in the cyclotrimerization of o-benzyne, 9,10-phenanthryne and o-carboryne. Formation energy (in kcal mol^{-1}) and bond lengths (in Å) are also included.

system	ring	NICS(0)	MCI	$\triangle E$	d(C=C)	d(C–C)^{new}
o-benzyne	6MR	−18.1	0.077		1.244	
o-benzyne^{x3}	6MR$^{central(C)}$	−2.1	0.008	−283.4	1.417	1.463
	6MR$^{terminal(T)}$	−7.5	0.051			
9,10-phenanthryne	6MR$^{mid(M)}$	−13.8	0.018		1.225	
	6MR$^{terminal(T)}$	−8.8	0.048			
9,10-phenanthryne^{x3}	6MR$^{central(C)}$	−1.0	0.025	−248.5	1.405	1.434
	6MR$^{terminal(T)}$	−7.1	0.049			
	6MR$^{mid(M)}$	−0.5	0.009			
o-carboryne	B$_4$C	−40.5			1.356	
	center	−35.4				
o-carboryne^{x3}	6MR$^{central(C)}$	−4.9	0.001	−233.7	1.686	1.536
	B$_4$C	−31.9				
	center	−26.4				

with the GIMIC program using the GIAO procedure at the same level of theory.[37] Canonical and localized molecular orbitals have been depicted with ADF software package.[38]

Acknowledgements

Conflict of Interests

The authors declare no conflict of interest.

Data Availability Statement

The data that support the findings of this study are available from the corresponding author upon reasonable request.

Keywords: benzyne · carboryne · carborane · non-conventional double bond · 3D aromaticity

[1] M. A. M. Subbaiah, N. A. Meanwell, *J. Med. Chem.* **2021**, *64*, 14046–14128.

[2] a) J. Poater, M. Solà, C. Viñas, F. Teixidor, *Chem. Eur. J.* **2013**, *19*, 4169–4175; b) J. Poater, M. Solà, C. Viñas, F. Teixidor, *Angew. Chem. Int. Ed.* **2014**, *53*, 12191–12195; c) J. Poater, C. Viñas, M. Solà, F. Teixidor, *Angew. Chem. Int. Ed.* **2022**, *61*, e202200672; d) J. Poater, C. Viñas, M. Solà, F. Teixidor, *Nat. Commun.* **2022**, *13*, 3844; e) J. Poater, M. Solà, C. Viñas, F. Teixidor, *Chem. Eur. J.* **2016**, *22*, 7437–7443; f) J. Poater, C. Viñas, I. Bennour, S. Escayola Gordils, M. Solà, F. Teixidor, *J. Am. Chem. Soc.* **2020**, *142*, 9396–9407; g) J. Poater, S. Escayola, A. Poater, F. Teixidor, H. Ottosson, C. Viñas, M. Solà, *J. Am. Chem. Soc.* **2023**, *145*, 22527–22538.

[3] M. Scholz, E. Hey-Hawkins, *Chem. Rev.* **2011**, *111*, 7035–7062.

[4] M. Scholz, K. Bensdorf, R. Gust, E. Hey-Hawkins, *ChemMedChem* **2009**, *4*, 746–748.

[5] M. Scholz, M. Steinhagen, J. T. Heiker, A. G. Beck-Sickinger, E. Hey-Hawkins, *ChemMedChem* **2011**, *6*, 89–93.

[6] H. L. Friedman in NAS-NRS, Washington DC, **1951**, p. 295–358.

[7] D. Buzsaki, M. B. Kovacs, E. Humpfner, Z. Harcsa-Pinter, Z. Kelemen, *Chem. Sci.* **2022**, *13*, 11388–11393.

[8] E. D. Jemmis, B. Kiran, *J. Am. Chem. Soc.* **1997**, *119*, 4076–4077.

[9] a) W. E. Bachmann, H. T. Clarke, *J. Am. Chem. Soc.* **1927**, *49*, 2089–2098; b) A. A. Morton, J. T. Massengale, G. M. Richardson, *J. Am. Chem. Soc.* **1940**, *62*, 126–129.

[10] C. Wentrup, *Aus. J. Chem.* **2010**, *63*, 979–986.

[11] H. L. Gingrich, T. Ghosh, Q. Huang, M. Jones, *J. Am. Chem. Soc.* **1990**, *112*, 4082–4083.

[12] J. H. Atkins, D. M. Ho, M. Jones, *Tetrahedron Lett.* **1996**, *37*, 7217–7220.

[13] R. B. King, *Chem. Rev.* **2001**, *101*, 1119–1152.

[14] a) L. Deng, H.-S. Chan, Z. Xie, *J. Am. Chem. Soc.* **2006**, *128*, 7728–7729; b) D. Zhao, Z. W. Xie, *Coord. Chem. Rev.* **2016**, *314*, 14–33.

[15] Z. Z. Qiu, S. K. Ren, Z. W. Xie, *Acc. Chem. Res.* **2011**, *44*, 299–309.

[16] A. A. Sayler, J. F. Sieckhaus, H. Beall, *J. Am. Chem. Soc.* **1973**, *95*, 5790–5792.

[17] S. J. McLain, R. R. Schrock, P. R. Sharp, M. R. Churchill, W. J. Youngs, *J. Am. Chem. Soc.* **1979**, *101*, 263–265.

[18] B. J. Eleazer, D. V. Peryshkov, *Comm. Inorg. Chem.* **2018**, *38*, 79–109.

[19] a) T. L. Chan, Z. W. Xie, *Chem. Sci.* **2018**, *9*, 2284–2289; b) L. BarnettThamattoor, G. X. Zheng, D. M. Ho, M. Jones, J. E. Jackson, *Inorg. Chem.* **1996**, *35*, 7311–7315.

[20] a) K. Wade, *J. Chem. Soc. D Chem. Comm.* **1971**, 792–793; b) D. M. P. Mingos, *Nat. Phys. Sci.* **1972**, *236*, 99–102; c) D. M. P. Mingos, *Acc. Chem. Res.* **1984**, *17*, 311–319.

[21] a) C. Foroutan-Nejad, Z. Badri, S. Shahbazian, P. Rashidi-Ranjbar, *J. Phys. Chem. A* **2011**, *115*, 12708–12714; b) C. Foroutan-Nejad, S. Shahbazian, F. Feixas, P. Rashidi-Ranjbar, M. Solà, *J. Comput. Chem.* **2011**, *32*, 2422–2431; c) C. Foroutan-Nejad, S. Shahbazian, P. Rashidi-Ranjbar, *Phys. Chem. Chem. Phys.* **2010**, *12*, 12630–12637.

[22] a) X. Fradera, M. A. Austen, R. F. W. Bader, *J. Phys. Chem. A* **1999**, *103*, 304–314; b) X. Fradera, J. Poater, S. Simon, M. Duran, M. Solà, *Theor. Chem. Acc.* **2002**, *108*, 214–224.

Chemistry–A European Journal

Research Article
doi.org/10.1002/chem.202302448

Chemistry Europe
European Chemical
Societies Publishing

[23] K. B. Wiberg, *Tetrahedron* **1968**, *24*, 1083–1096.

[24] a) I. Mayer, *Chem. Phys. Lett.* **1983**, *97*, 270–274; b) I. Mayer, *J. Comput. Chem.* **2007**, *28*, 204–221.

[25] M. Diaz, J. Jaballas, J. Arias, H. Lee, T. Onak, *J. Am. Chem. Soc.* **1996**, *118*, 4405–4410.

[26] D. Farcasiu, S. L. Fisk, M. T. Melchior, K. D. Rose, *J. Org. Chem.* **1982**, *47*, 453–457.

[27] R. Warmuth, *Angew. Chem. Int. Ed.* **1997**, *36*, 1347–1350.

[28] E. Hückel, *Z. Elektrochemie* **1937**, *43*, 752–788.

[29] A. Dachs, A. Pla-Quintana, T. Parella, M. Solà, A. Roglans, *Chem. Eur. J.* **2011**, *17*, 14493–14507.

[30] M. J. Frisch, G. W. Trucks, H. B. Schlegel, G. E. Scuseria, M. A. Robb, J. R. Cheeseman, G. Scalmani, V. Barone, B. Mennucci, G. A. Petersson, H. Nakatsuji, M. Caricato, X. Li, H. P. Hratchian, A. F. Izmaylov, J. Bloino, G. Zheng, J. L. Sonnenberg, M. Hada, M. Ehara, K. Toyota, R. Fukuda, J. Hasegawa, M. Ishida, T. Nakajima, Y. Honda, O. Kitao, H. Nakai, T. Vreven, J. A. M. Jr., J. E. Peralta, F. Ogliaro, M. Bearpark, J. J. Heyd, E. Brothers, K. N. Kudin, V. N. Staroverov, R. Kobayashi, J. Normand, K. Raghavachari, A. Rendell, J. C. Burant, S. S. Iyengar, J. Tomasi, M. Cossi, N. Rega, J. M. Millam, M. Klene, J. E. Knox, J. B. Cross, V. Bakken, C. Adamo, J. Jaramillo, R. Gomperts, R. E. Stratmann, O. Yazyev, A. J. Austin, R. Cammi, C. Pomelli, J. W. Ochterski, R. L. Martin, K. Morokuma, V. G. Zakrzewski, G. A. Voth, P. Salvador, J. J. Dannenberg, S. Dapprich, A. D. Daniels, Ö. Farkas, J. B. Foresman, J. V. Ortiz, J. Cioslowski, D. J. Fox in *Gaussian 09, Vol. Revision A.02 ed.* Gaussian, Inc., Pittsburgh, PA, **2009**.

[31] a) A. D. Becke, *J. Chem. Phys.* **1993**, *98*, 5648–5652; b) C. T. Lee, W. T. Yang, R. G. Parr, *Phys. Rev. B* **1988**, *37*, 785–789; c) P. J. Stephens, F. J. Devlin, C. F. Chabalowski, M. J. Frisch, *J. Phys. Chem.* **1994**, *98*, 11623–11627.

[32] M. J. Frisch, J. A. Pople, J. S. Binkley, *J. Chem. Phys.* **1984**, *80*, 3265–3269.

[33] Z. F. Chen, C. S. Wannere, C. Corminboeuf, R. Puchta, P. V. Schleyer, *Chem. Rev.* **2005**, *105*, 3842–3888.

[34] K. Wolinski, J. F. Hinton, P. Pulay, *J. Am. Chem. Soc.* **1990**, *112*, 8251–8260.

[35] a) P. Bultinck, R. Ponec, S. Van Damme, *J. Phys. Org. Chem.* **2005**, *18*, 706–718; b) F. Feixas, E. Matito, J. Poater, M. Solà, *Chem. Soc. Rev.* **2015**, *44*, 6434–6451; c) E. Matito, M. Duran, M. Solà, *J. Chem. Phys.* **2005**, *122*, 014109; d) M. Giambiagi, M. S. de Giambiagi, C. D. D. Silva, A. P. de Figueiredo, *Phys. Chem. Chem. Phys.* **2000**, *2*, 3381–3392.

[36] a) E. Matito in *ESI-3D: Electron Sharing Indices Program for 3D Molecular Space Partitioning, Vol.* Institute of Computational Chemistry and Catalysis (IQCC), University of Girona, Catalonia, Spain, **2006**; b) E. Matito, M. Solà, P. Salvador, M. Duran, *Faraday Discuss.* **2007**, *135*, 325–345; c) R. F. W. Bader, *Chem. Rev.* **1991**, *91*, 893–928.

[37] a) H. Fliegl, S. Taubert, O. Lehtonen, D. Sundholm, *Phys. Chem. Chem. Phys.* **2011**, *13*, 20500–20518; b) J. Juselius, D. Sundholm, J. Gauss, *J. Chem. Phys.* **2004**, *121*, 3952–3963; c) D. Sundholm, H. Fliegl, R. J. F. Berger, *WIREs Comput. Mol. Sci.* **2016**, *6*, 639–678.

[38] G. te Velde, F. M. Bickelhaupt, E. J. Baerends, C. Fonseca Guerra, S. J. A. van Gisbergen, J. G. Snijders, T. Ziegler, *J. Comput. Chem.* **2001**, *22*, 931–967.

5.4.3   Single—Not Double—3D-Aromaticity in Oxidized *Closo* Icosahedral Dodecaiodo-Dodecaborate Cluster

This section corresponds to the following publication:

Article

Single—Not Double—3D-Aromaticity in an Oxidized *Closo* Icosahedral Dodecaiodo-Dodecaborate Cluster

Jordi Poater,[∇] Sílvia Escayola,[∇] Albert Poater, Francesc Teixidor, Henrik Ottosson,* Clara Viñas,* and Miquel Solà*

ACCESS | Metrics & More | Article Recommendations | SI Supporting Information

ABSTRACT: 3D-aromatic molecules with (distorted) tetrahedral, octahedral, or spherical structures are much less common than typical 2D-aromatic species or even 2D-aromatic-in-3D systems. *Closo* boranes, $[B_nH_n]^{2-}$ ($5 \leq n \leq 14$) and carboranes are examples of compounds that are singly 3D-aromatic, and we now explore if there are species that are doubly 3D-aromatic. The most widely known example of a species with double 2D-aromaticity is the hexaiodobenzene dication, $[C_6I_6]^{2+}$. This species shows π-aromaticity in the benzene ring and σ-aromaticity in the outer ring formed by the iodine substituents. Inspired by the hexaiodobenzene dication example, in this work, we explore the potential for double 3D-aromaticity in $[B_{12}I_{12}]^{0/2+}$. Our results based on magnetic and electronic descriptors of aromaticity together with $^{11}B\{^1H\}$ NMR experimental spectra of boron-iodinated *o*-carboranes suggest that these two oxidized forms of a *closo* icosahedral dodecaiodo-dodecaborate cluster, $[B_{12}I_{12}]$ and $[B_{12}I_{12}]^{2+}$, behave as doubly 3D-aromatic compounds. However, an evaluation of the energetic contribution of the potential double 3D-aromaticity through homodesmotic reactions shows that delocalization in the I_{12} shell, in contrast to the 10σ-electron I_6^{2+} ring in the hexaiodobenzene dication, does not contribute to any stabilization of the system. Therefore, the $[B_{12}I_{12}]^{0/2+}$ species cannot be considered as doubly 3D-aromatic.
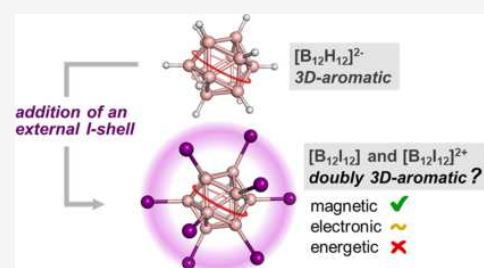
1. INTRODUCTION

Doubly aromatic compounds are species that have two different (nearly) orthogonal types of aromaticity. The discovery of new doubly aromatic systems not only provides new insights into the fundamental principles of chemistry and chemical bonding but may also result in the development of new materials with enhanced stability and unique physicochemical properties. Double and even multiple (anti)-aromaticity is frequent in the field of metallaaromatic compounds.[1−4] For instance, $LiAl_4^-$ is doubly σ- and π-aromatic,[5] $Li_3Al_4^-$ in the singlet state is σ-aromatic and π-antiaromatic[6] and in the triplet state is Hückel σ-aromatic and Baird π-aromatic,[7] B_{12} has double σ- and π-disk aromaticity,[8] B_6^{2-} is doubly σ- and π-antiaromatic,[9,10] Hf_3 has triple σ-, π- and δ-aromaticity,[4,11] $V_2B_7^-$ is doubly σ/π aromatic,[12] and Pa_2B_2 has been recently reported to be σ- and π-Möbius aromatic,[13] among many other examples.

Less common is the double aromaticity in organic compounds. Still, there are already a number of examples. The first reported doubly aromatic system was the 3,5-dehydrophenyl cation with σ- and π-aromaticity.[14] However, the most well-known example of double aromaticity in organic chemistry is the singlet ground-state dication of hexaiodobenzene, $[C_6I_6]^{2+}$ (see Scheme 1a), synthesized by Sagl and Martin.[15] $[C_6I_6]^{2+}$ is doubly Hückel σ- (with 10 delocalized electrons through the hexaiodo substituents) and π-aromatic (with six delocalized electrons in the benzene ring).[15,16]

Theoretical studies support the double σ- and π-aromaticity of $[C_6I_6]^{2+}$[17] as well as that of $[C_6At_6]^{2+}$.[18] For the former, relativistic effects are not so relevant but are essential for the latter.[19] Moreover, several hexaselanylbenzene and hexatellanylbenzene dications $[C_6(ChR)_6]^{2+}$ (Ch = Se, Te; R = H, Me, Ph) were found experimentally and computationally to be doubly aromatic compounds.[18−21] Borazine analogues of hexaiodobenzene and hexakis(selenyl)benzene dication $[B_3N_3I_6]^{2+}$ as well as $[B_3N_3(TeH)_6]^{2+}$ were also reported to be doubly aromatic,[22] although the π-aromaticity of borazine is known to be extensively lower than that of benzene.[23] And very recently, the triplet state of $[C_7Br_7]^{3+}$ has been found to be π-Hückel aromatic (with six π-electrons in the tropylium ring) and weakly σ-Baird aromatic (with 12 delocalized σ-electrons in the Br_7 ring, Scheme 1b).[24] Let us mention that Baird's rule states that annulenes with $4n$ π-electrons are aromatic, and those with $4n+2$ are antiaromatic in their lowest-lying triplet states.[25−27] Other examples are the double σ- and π-aromaticity in bishomotriboriranide[28] and in twisted

A

Scheme 1. (a) Schematic Illustration of the Circular σ-Delocalization in Dicationic Hexahalo- or Hexachalco-Substituted Benzene Leading to Hückel σ-Aromaticity; (b) Schematic Representation of the Circular σ-Delocalization in Tricationic Hexabromotropylium Species in Its Lowest-Lying Triplet State Resulting in Baird σ-Aromaticity; (c) Double Aromaticity in $C_6E_6^{2+}$ Requires the Opening of an Electronic Hole by Double Oxidation to Generate σ-Delocalization
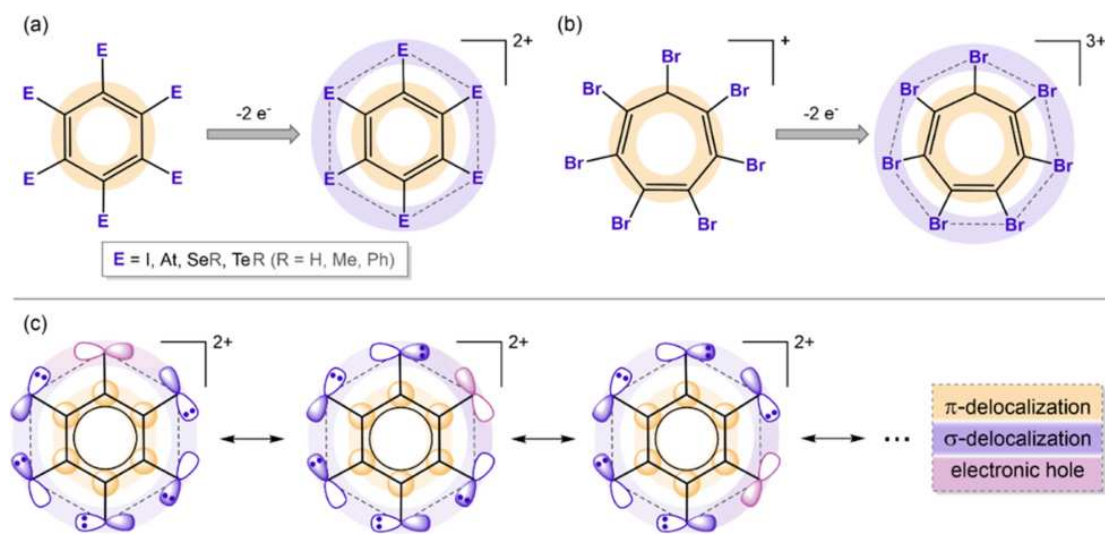
thienylene–phenylene structures in toroidal and catenated topologies.[29,30]

It has to be mentioned that to reach double aromaticity in $[C_6I_6]^{2+}$, double oxidation of C_6I_6 is required to open a hole in one of the 5p orbitals of iodine that generate six possible resonance structures (Scheme 1c depicts only three), if we consider only resonance structures in which the two electrons are removed from the same I atom, all of them with the same weight. The existence of these resonance structures generates the double aromaticity, and the fulfillment of Hückel's rule in both the σ- and π-systems explains it.

Three-dimensional (3D) aromaticity has lately attracted increasing attention.[31–33] The concept of 3D-aromaticity was introduced by King and Rouvray[34] in 1977 and by Aihara[35] in 1978 when they analyzed polyhedral boranes using a Hückel-type molecular orbital (MO) theoretical approach. 2D and 3D-aromaticity were perceived as two independent systems until 2014, when it was shown[36] that the two were related, described as two sides of the same coin. In 2016, it was demonstrated[37] that each aromatic annulene had its aromatic counterpart in the boron *closo* hydrides that could be categorized based on the Hückel's $4n + 2$ rule. Later on, some of us[38] established the conditions that must be fulfilled for a compound to be 3D-aromatic, namely, (i) (at least) triply degenerate MOs as found in tetrahedral or higher symmetry molecules, (ii) a closed-shell electronic structure, which leads to a $6n + 2$ electron count in the case of tetrahedral or octahedral molecules, (iii) extensive electron delocalization involving the complete 3D molecule leading to resonance stabilization, and (iv) similar (optoelectronic and magnetic) properties in the three *xyz* directions. Such conditions are obeyed only by a few compounds. The first known species with 3D-aromaticity were the *closo* boranes, such as $[B_{10}H_{10}]^{2-}$ or $[B_{12}H_{12}]^{2-}$ and derivatives, synthesized at the end of the 1950s.[39,40] Not only *closo* boranes $[B_nH_n]^{2-}$ ($5 \leq n \leq 14$) but also their carboranes counterparts, which result from single or double substitution of BH by isoelectronic CH^+ units in *closo* boranes, are 3D-aromatic compounds.[31] These clusters obey the Wade's $2n + 2$ rule[41] and the equivalent Mingos' $4n + 2$ rule.[42] Their aromaticity is substantiated by results from nucleus-independent chemical shifts (NICS), bond length alternation (BLA) values, resonance energies, and ring currents.[34,35,37,43–46] Moreover, the high thermal stability of these clusters[47–49] further supports their aromatic character.[47,50,51] A number of unique materials and applications were developed based on 3D-aromatic boranes, carboranes, and metallacarboranes due to their enhanced stability.[52–67]

With the present investigation, we would like to provide both evidence and counter-evidence of the potential double 3D-aromaticity of the dodecaiodo-dodecaborate cluster. There are several reasons, more exactly seven, for choosing $[B_{12}I_{12}]^{2-}$. First, $[B_{12}H_{12}]^{2-}$, which has the same boron cage as $[B_{12}I_{12}]^{2-}$, is likely the most aromatic *closo* borane.[37,68] Indeed, it is the one that has the highest heat of formation among $[B_nH_n]^{2-}$ ($5 \leq n \leq 12$) clusters,[69] it has large adiabatic and vertical electron detachment energies, which is an indication of its high stability,[70] it has the lowest average energy on a per-vertex basis,[44] and it has the highest resonance energy.[35] Second, $[B_{12}I_{12}]^{2-}$ (and, in general all *closo* $[B_{12}X_{12}]^{2-}$; X = halogen) has a high structural and electronic stability and chemical inertness, especially in front of electrophilic attacks, as well as superweak basicity.[71,72] Third, $[B_{12}I_{12}]^{2-}$ has the largest oxidation potential among all *closo* $[B_{12}X_{12}]^{2-}$ (X = halogen).[73] Fourth, the second electron in the double oxidation of *closo* $[B_{12}X_{12}]^{2-}$ (X = F, Cl) is taken from the boron cage, whereas for X = I is taken from the halogen shell (for X = Br, we have an intermediate situation with the electron partially removed from the boron cage and the bromide shell).[72] Remember that we need to open a hole in one of the *np* orbitals of perhalogenated *closo* $[B_{12}X_{12}]^{2-}$, and this is possible only in *closo* $[B_{12}I_{12}]^{2-}$. Fifth, because of the X···X distances, we expect to have an appreciable overlap between the *np* orbitals only for $[B_{12}I_{12}]^{2-}$. Such overlap is needed to allow electron delocalization in the I_{12} shell. Sixth, the I···I antibonding HOMO of $[B_{12}I_{12}]^{2-}$ is triply degenerated (see Figure S1) as required for 3D-aromaticity. And finally, the seventh reason, the total number of electrons participating in lone pairs in the I_{12} shell is 72 electrons, a number that follows the $2(n+1)^2$

Hirsch rule[74] for spherical aromaticity, with $n = 5$. However, the required oxidation to open a hole changes this number of electrons.

2. METHODOLOGY

All DFT calculations were performed with the Amsterdam Density Functional (ADF) program[75,76] using dispersion-corrected density functional theory (DFT) with relativistic corrections at the ZORA-BLYP-D3(BJ)/TZ2P level of theory[77−80] for geometry optimizations and energy calculations, with the full electron model for all atoms (no frozen core). All stationary points were verified to be minima on the potential energy surface through vibrational analysis.

The quantification of aromaticity is usually based on the fact that aromatic molecules have most of these properties: (i) an uninterrupted electron delocalization in a 2D or 3D-closed circuit,[81,82] (ii) more stability than a nonaromatic reference compound,[83] (iii) bond length equalization,[84] and (iv) special response in the presence of an external magnetic field.[85−87] It has to be stressed that energetic stabilization and electron delocalization are the two most important requirements for aromaticity, and the two are compulsory conditions, whereas ring currents and bond length equalization are usual conditions followed by most of the aromatic species, but not sufficient to prove aromaticity. We considered magnetic, electronic, and energetic descriptors of aromaticity since it is generally accepted that one should use a set of indices based on different properties to discuss the aromaticity of a given species.[88]

The magnetic properties of aromaticity were first evaluated by means of the nucleus-independent chemical shift (NICS), proposed by Schleyer and co-workers, as a magnetic descriptor of aromaticity.[89] NICS is defined as the negative value of the absolute shielding computed at a ring center or at some other point in the system. Rings with large negative NICS values are considered aromatic. NICS values were computed using the gauge-including atomic orbital method (GIAO).[86,90] NICS scans were carried out with the same ZORA-BLYP-D3(BJ)/TZ2P method. To analyze the importance of relativistic effects, we also computed the NICS scans of $[B_{12}I_{12}]^{2-}$ and singlet $[B_{12}I_{12}]$ clusters as well as those of C_6I_6 and $C_6I_6^{2+}$ with the B3LYP/6-311++G**~LANL2DZ method (Figures S21 and S22). Results show that, except for $C_6I_6^{2+}$, there is an increase in the absolute NICS values (by less than 5 ppm) at the B3LYP/6-311++G**~LANL2DZ level of theory, but when we compared the initial and the oxidized species, the trends remain the same. On the other hand, magnetically induced current-density susceptibility was obtained with gauge-including magnetically induced currents (GIMIC) method.[87,91] GIMIC requires the basis set information, the atomic orbital density matrix, and the perturbed atomic orbital density matrices as input data, which have been obtained by performing NMR shielding calculations with the Gaussian 16 program package.[92] The specific parameters used in the GIMIC calculations are summarized in Table S1. The NMR shielding calculations were performed with the B3LYP functional and the 6-311++G** basis set for boron and LANL2DZ basis set and pseudopotential for iodine using the ZORA-BLYP-D3(BJ)/TZ2P optimized geometries. Finally, the visualization of the current densities was carried out using ParaView 5.9.0.[93]

Second, aromaticity was also assessed through electron delocalization properties with the electron density of delocalized bonds ($EDDB_G$) function.[94−96] The required information on the formatted checkpoint file and the density matrix within the representation of natural atomic orbitals (NAOs) was obtained using NBO 6.0 software coupled to the Gaussian 09 rev. D.01 version. Then, the RunEDDB code (version 26-Jun-2021) was used to perform the EDDB analysis at the B3LYP/6-311++G**~LANL2DZ//ZORA-BLYP-D3(BJ)/TZ2P level of theory.[97] For the visualization of $EDDB_G(\mathbf{r})$ surfaces, we used the Avogadro1.0 molecular editor.[98]

Third, the aromatic stabilization energy was determined through homodesmotic reactions.[99,100] Finally, steric effects were analyzed with the SambVca2.1 package of Cavallo and co-workers, calculating the $\%V_{Bur}$ and depicting steric maps.[101−103]

3. RESULTS AND DISCUSSION

This section begins with the experimental considerations based on $^{11}B\{^1H\}$ NMR spectra of a series of iodinate derivatives that result from the stepwise substitution of hydrogen atoms with iodine atoms in the neutral o-carborane ($1,2$-$C_2B_{10}H_{12}$). Then, the chemical oxidation of halogenated derivatives of icosahedral anionic boranes ($[B_{12}X_{12}]^{2-}$, X = F, Cl, Br, I, with H as the reference) is presented. Subsequently, the discussion delves into the obtained computational results.

3.1. Initial Considerations. The benzene ring is possibly the ideal core to generate an additional ring to produce a concentric and coplanar two-ring system in which the second ring may result in an aromatic ring. Moreover, iodine is easily polarizable, is large, and can be oxidized. Hence, C_6I_6 was the best starting point to build a system with two aromatic rings orthogonal to each other. A perfect structure for double 3D-aromaticity would be a 3D-system whose core is an icosahedron, ideally the periodinated "B_{12}", $[B_{12}I_{12}]^{2-}$, which could give rise to $B_{12}I_{12}$ by oxidation. A similar core structure would be that of the "C_2B_{10}", i.e., periodinate $C_2B_{10}I_{12}$.

To understand the electronic structure and the influence of iodine substitution, one may consider the study of the evolution of $[B_{12}H_{12}]^{2-}$ through the incorporation of iodine groups on the core cluster, step by step. Nevertheless, the step-by-step synthesis of these iodinated compounds cannot be achieved experimentally using the icosahedral cluster $[B_{12}H_{12}]^{2-}$. However, it is feasible to accomplish this synthesis with the o-carborane cluster, as performed by some of us. The presence of two adjacent carbon atoms in the o-carborane cluster leads to variations in the charge density among its different vertices.[104] As a result, it is experimentally feasible to obtain and isolate the step-by-step iodinated compounds derived from o-carborane while modulating both the number and the position of iodine atoms that replace the hydrogen atoms in the o-carborane cluster. The chemistry of mono- to ten-substituted boron-iodinated o-carboranes (I_n-$1,2$-$C_2B_{10}H_{12-n}$, $n = 1-10$) has been widely developed because the usefulness of o-carborane units is dependent upon their functionalization. The 2000s were dominated by the catalyzed reactions under Kumada conditions, and palladium was the sought catalyst for the B−C bond formation from B−I vertices, but more available metals (Ni) as well as the presence of CuI as cocatalyst were also employed to obtain well-defined patterns of o-carborane substitution from different and well-defined iodo-o-carboranes. Conventional reactions in solution as well as new solvent-free methods permitted regioselective control of o-carboranes iodine substitution to generate iodine

C

I_n-1,2-$C_2B_{10}H_{12-n}$ (n = 1−10) derivatives on demand. The synthesis of regioselective B-iodinated *o*-carboranes was achieved; nevertheless, in general, the reactivity of the halogen linked to the boron is low. The $^{11}B\{^1H\}$ NMR spectra of the *o*-carboranes derivatives were used as a probe to analyze the changes in the electron distribution of *o*-carboranes due to substitution.[105−109] Focusing on the $^{11}B\{^1H\}$ NMR spectrum of 9,12-I_2-*o*-carborane (Figure 1b) and comparing it with *o*-carborane (Figure 1a), it can be observed that its appearance is
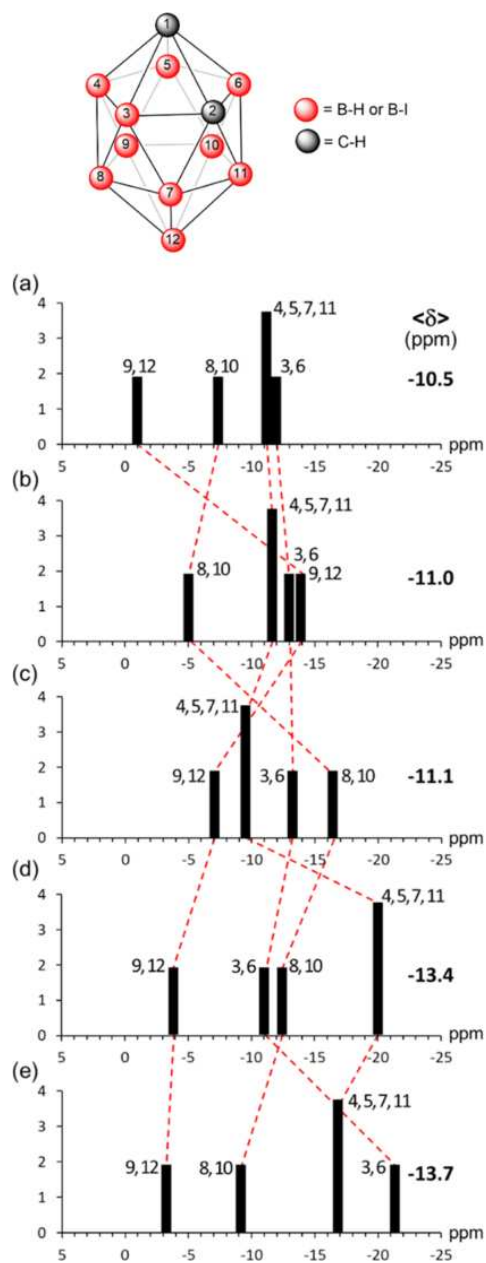

Figure 1. Schematic representation of the ^{11}B NMR spectra from samples in acetone-d_6 solutions with the peak assignments for unsubstituted *o*-carborane (a)[121] and some iodinated derivatives: 9,12-I_2-*o*-carborane (b),[110] 8,9,10,12-I_4-*o*-carborane (c),[122] 4,5,7,8,9,10,11,12-I_8-*o*-carborane (d),[123] and 3,4,5,6,7,8,9,10,11,12-I_{10}-*o*-carborane (e).[113] The peak assignment was unambiguously done by means of a two-dimensional $^{11}B\{^1H\}$−$^{11}B\{^1H\}$ COSY NMR spectrum. On the right is shown the mean $^{11}B\{^1H\}$ NMR chemical shift for each compound. Figure drawn using the data of ref 124.

considerably modified by the presence of iodine atoms on the B(9) and B(12) vertices with respect to pristine *o*-carborane and that the chemical shifts of these boron atoms are especially affected, being largely shifted upfield (from −2.1 ppm in the parent *o*-carborane to −13.8 ppm in the diiodinated *o*-carborane derivative, which corresponds to a $\Delta\delta$ = 11.7 ppm).[110] The explanation that the substitution of hydrogen by iodine causes significant shielding on boron atoms attached to the substituent is that lone pairs of iodine interact efficiently with the *p* orbitals of *ipso* B, which produces a π backdonation from the I atom to the B atom of the substituted vertices. This enriches considerably the electron density at this B vertex, increasing its shielding and consequently shifting its B resonance to a high field.

Important is the fact that the pattern of the $^{11}B\{^1H\}$ NMR spectra of the parent *o*-carborane and the periodinated *o*-carborane from high to low frequency is the same 2:2:4:2, but the mean chemical shift value ($\langle\delta\rangle$) moves slightly upfield from −10.5 to −13.7 ppm as B-iodination of *o*-carborane moves from 0 to 10 atoms, respectively (Figure 1). These results suggest that by increasing the number of I atoms, the π backdonation ability of I atoms decreases, consistent with the formation of intramolecular I···I noncovalent bonding. In other words, the lone pairs of electrons on I are used in backdonation when there is no chance to interact with other neighboring iodine atoms, but when this possibility exists, there is a preference for noncovalent interactions. As a result, these electrons would be less prone for other endeavors, for instance, to be removed (oxidation) from the cluster. To evidence the presence of noncovalent intramolecular interactions in the boron periodinated I_{10}-*o*-carborane, a search at the Cambridge Structural Database (CSD)[111,112] was done. The CSD showed just three hits (CEHWOC, WUNDAL, and WUNDOZ). CEHWOC[113] and WUNDAL[114] have solvents as adducts in the crystal cells, but WUNDOZ was obtained solvent-free.[114] To avoid any interference in measuring the I···I distances, these were measured on the WUNDOZ, giving values in the range 3.946−4.278 Å (the van der Waals radius of the I atom is 1.98 Å,[115] Figure S2) that parallel with the theoretical distances reported by the $C_6H_5I···IC_6H_5$ homo-dimers via type I−IV halogen···halogen interaction (3.96−4.15 Å).[116] The boron periodinated I_{10}-*o*-carborane crystal structure (WUNDOZ) supports the I···I noncovalent bonding formation and the creation of a two adjacent vertices truncated icosahedral (the two adjacent C−H vertices) constituted by the ten connected I atoms.

A similar situation is expected for the periodinated $[B_{12}I_{12}]^{2−}$ that is even a better core than *o*-carborane to form a clustered onion-like structure. Removal of two electrons would seemingly lead to a clustered onion-like structure, but is this what occurs experimentally? When comparing the $^{11}B\{^1H\}$ NMR spectra in acetone of the parent $Na_2[B_{12}H_{12}]$ and its iodinated $Na_2[B_{12}I_{12}]$, it is seen that both display a singlet at the chemical shifts −15.4 ($^1J(B,H)$ = 125 Hz)[48,117] and −15.8 ppm for $Na_2[B_{12}H_{12}]$ and $Na_2[B_{12}I_{12}]$, respectively. This NMR data is consistent with the data obtained for the *o*-carborane, to say that, as in the $[B_{12}H_{12}]^{2−}$, the $[B_{12}I_{12}]^{2−}$ cluster does not generate π backdonation to the *ipso* B atom, but most possibly, the iodine atoms are involved in intramolecular I···I noncovalent bonding interactions. Again, we moved to the CSD to confirm this hypothesis.[111,112] CSD showed just 16 hits for salts of $[B_{12}I_{12}]^{2−}$, but only two hits (QAVVAO and ASIWAC)[118] were found for its sodium salts. QAVVAO

corresponds to a crystal containing $Na_2[B_{12}I_{12}]$, DMF, and γ-cyclodextrin with low-resolution reflections, and ASIWAC corresponds to $Na_2[B_{12}I_{12}] \cdot 8SO_2$ with good resolution. The I⋯I distances in the ASIWAC crystal structure were measured in the 3.982–4.112 Å range, which is consistent with the presence of noncovalent I⋯I bonds between the 12 iodine atoms bonded *exo*-cluster to the B_{12} icosahedron. All of these results support the formation of two concentric layers in a clustered onion-like structure, one made by 12 B atoms connected by multicenter bonds (the inner)[119] and 12 iodine atoms connected by noncovalently bonded halogen bonds (the outer).

If we consider the oxidation of periodobenzene C_6I_6, two methods were utilized. In one method, chlorine is bubbled into a suspension of orange C_6I_6 in a mixture of triflic acid and trifluoroacetyl triflate (TFAT). In this process, besides $[C_6I_6]^{2+}$, the radical $[C_6ClI_5]^{+}$ was obtained. In the same report, an alternative method to produce $[C_6I_6]^{2+}$ involves the use of pertriflic acid (CF_3SO_4H) or H_2O_2 in triflic acid as the oxidizing agent. The mass spectrum displays peaks at m/z 834 corresponding to $[C_6I_6]^{+}$ and at m/z 417 corresponding to $[C_6I_6]^{2+}$. Remarkable was the $^{13}C\{^1H\}$ NMR spectrum that produced a unique ^{13}C resonance, indicating the equivalence of all C atoms and, indeed, that the compound was diamagnetic.[15]

If we now examine the 3D-aromatic core per excellence, the $[B_{12}H_{12}]^{2-}$ and its perhalogenated dianions $[B_{12}X_{12}]^{2-}$ (X= F, Cl, Br, I), it is seen that in liquid sulfur dioxide, they can be oxidized either by chemical or electrochemical methods to give stable radicals.[73] The chemical oxidation is done with the strong oxidizing agent AsF_5 that yields the radical anions $[B_{12}X_{12}]^{-}$ (X = F, Cl, Br), but it fails to produce $[B_{12}I_{12}]^{-}$. When an excess of AsF_5 was used, the neutral *hypercloso*-boranes $B_{12}X_{12}$ (X = Cl, Br) were obtained but failed to produce $B_{12}I_{12}$. The explanation given was the weakness of the B–I bond that would agree with the lack of π backdonation argued above and consistent with the stepwise loss of I⁻ radicals leading to B_{12} demonstrated by electrospray ionization-trap mass spectrometry.[120] $B_{12}Cl_{12}$ and $B_{12}Br_{12}$ were characterized by X-ray diffraction (XRD) and did show unequal B–B bonds characteristic of *hypercloso* species.[73] Electrochemical oxidation of $[B_{12}X_{12}]^{2-}$ (X = F, Cl, Br, I) shows that the first and second oxidation processes are detected for X = F, Cl, Br but not for X = I. Remarkable is the high oxidation potentials required for the oxidation, in the range of +1.68 and +2.29 V vs $Fc^{1+/0}$ for the first process that is quasi reversible while the second process, in the range of +2.63 to +2.71 V vs $Fc^{1+/0}$, is irreversible.

3.2. Molecular Structure. First, we quantum chemically studied the singlet ground state of $[B_{12}I_{12}]^{2-}$ as a possible species with double 3D-aromaticity, the borane cage following the 2N + 2 Wade rule with N = 12, and the I_{12} sphere with 72 electrons as lone pairs following the Hirsch rule. As said before, to reach double aromaticity, a double oxidation may be required to open a hole in one of the 5p orbitals of iodine. Therefore, we analyzed $[B_{12}I_{12}]$ and also $[B_{12}I_{12}]^{2+}$. The first gas-phase ionization Gibbs energy of $[B_{12}I_{12}]^{2-}$ to $[B_{12}I_{12}]^{-}$ is 35.2 kcal/mol, and the second ionization to produce singlet $[B_{12}I_{12}]$ requires 101.3 kcal/mol. It has to be said that the triplet state of $[B_{12}I_{12}]$ is the ground state, and it is more stable than the closed-shell and the open-shell singlet states by 5.7 and 3.7 kcal/mol, respectively. Further oxidation to singlet $[B_{12}I_{12}]^{2+}$ costs 408.2 kcal/mol.[125] The ground state of

$[B_{12}I_{12}]^{2+}$ is a quintet that is more stable than the closed-shell singlet state by 6.9 kcal/mol. The molecular structure of $[B_{12}I_{12}]^{2-}$ has I_h symmetry with B–B bond length of 1.790 Å (see Figure 2) and, therefore, the bond length alternation
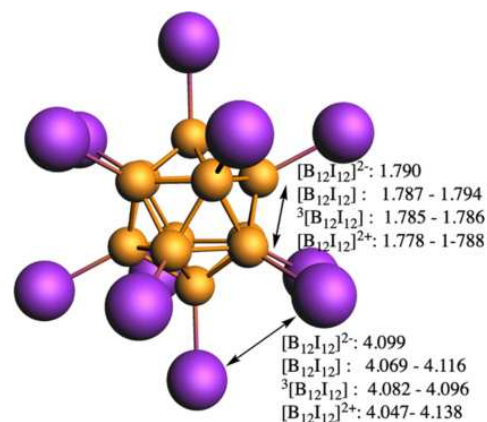

Figure 2. B–B and I⋯I bond distances range (in Å) of closed-shell singlet $[B_{12}I_{12}]^{2-/0/2+}$ and triplet $^3[B_{12}I_{12}]$.

(BLA), i.e., the difference between the shortest and the longest B–B distance, is zero. Our optimized geometries indicate that the shortest I⋯I distance in $[B_{12}I_{12}]^{2-}$ is 4.099 Å, 0.539 Å longer than that of C_6I_6 (3.560 Å). Despite the relatively long I⋯I distance in $[B_{12}I_{12}]^{2-}$, there is almost no space left in the I_{12} crown with a $\%V_{Bur}$ = 91.4% in comparison to $[B_{12}H_{12}]^{2-}$ for which $\%V_{Bur}$ = 41.7% (Figures S23–S26). Double oxidation removes two electrons from the triply degenerated HOMO orbital of $[B_{12}I_{12}]^{2-}$, which is I⋯I antibonding (Figure S1). As a consequence, the I⋯I distance is reduced minutely to 4.082 Å (triplet) or to 4.069 Å (closed-shell singlet), and the B–B bond lengths become also somewhat shorter, ranging from 1.785 to 1.786 Å (triplet) or 1.787 to 1.794 Å (singlet) with a BLA of 0.001 Å for the triplet and 0.007 Å for the singlet. The two electrons are removed from the I_{12} shell, which gets a positive charge of 0.410 (triplet) or 0.408 (singlet) electrons according to Voronoi deformation density (VDD) charges,[126] computed at the ZORA-BLYP-D3(BJ)/TZ2P level of theory. Finally, oxidation to closed-shell singlet $[B_{12}I_{12}]^{2+}$ leads to a minor reduction of the B–B and I⋯I distances (BLA being 0.010 Å). Again, the electrons are removed from the I_{12} shell, which becomes positive by 2.512 electrons (using Hirshfeld charges,[127] we got 0.609 and 2.657 e for the I_{12} unit of $^3B_{12}I_{12}$ and $B_{12}I_{12}{}^{2+}$, respectively). The number of resonance structures that can be built in the I_{12} shell is 12 for $B_{12}I_{12}$ if the doubly positive charge on I_{12} is located in a single I atom and 66 if the two positive charges are placed in two different I atoms. For $[B_{12}I_{12}]^{2+}$, we have 66 resonance structures if the two doubly positive charges are located in two I atoms and 495 resonance structures if the positive charges are placed in four different I atoms. In both cases, the boron core remains with 26 electrons.

3.3. Magnetic Aspects. To determine the magnetic behavior of our systems, we first performed NICS scans moving from the center of the dodecahedron to the center of the closest X_3 (X = H, I) three-membered ring (3-MR). As seen in Figure 3, the NICS scans for $[B_{12}I_{12}]^{2-}$ and $[B_{12}H_{12}]^{2-}$ clusters point out a somewhat higher aromaticity for $[B_{12}H_{12}]^{2-}$. The minimum of the NICS scan in all cases is found around the B_3 plane. NICS scans of $[B_{12}I_{12}]^{2-}$ and
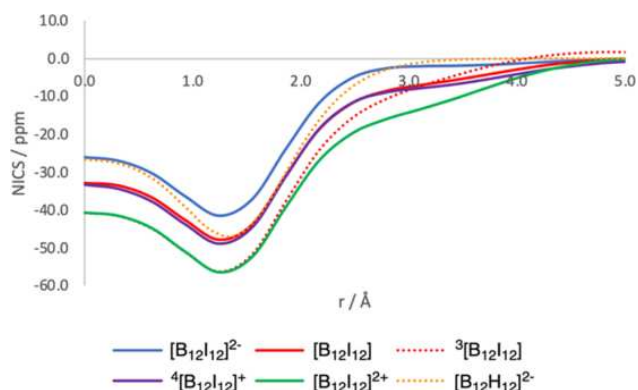
Figure 3. NICS scan (ppm) from the center of the boron cluster to the middle of the closest I_3 (or H_3) three-membered ring for $[B_{12}I_{12}]^{2-}$ (singlet), $[B_{12}I_{12}]$ (singlet and triplet), $[B_{12}I_{12}]^+$ (quartet), and $[B_{12}I_{12}]^{2+}$ (singlet) clusters. Comparison to $[B_{12}H_{12}]^{2-}$ (singlet) is included. Distances in Å.

$[B_{12}H_{12}]^{2-}$ reflect the 3D-aromaticity of the borane cage and the absence of further aromaticity around the X_{12} sphere (X = H, I). When we compare the NICS scans of $[B_{12}I_{12}]^{2-}$ and $[B_{12}I_{12}]$ in their closed-shell singlet and triplet states, the latter show significantly more negative values of about 10 ppm in the closed-shell singlet and 20 ppm in the triplet ground state than $[B_{12}I_{12}]^{2-}$ (for the open-shell singlet, the difference is even higher, of ca. 30 ppm, Figure S3), which is an indication of the presence of magnetic ring currents in the I_{12} shell in closed- and open-shell singlet and triplet states of $B_{12}I_{12}$ despite the fact that now the I_{12} shell has 70 electrons (35 electron pairs) and, consequently, does not follow the Hirsch rule for spherical aromaticity. In contrast, $[B_{12}H_{12}]$ is antiaromatic, as the two electrons are removed from the borane cage (Figure S4). Subsequent oxidation of $[B_{12}I_{12}]$ to yield closed-shell singlet $[B_{12}I_{12}]^{2+}$ produces a further decrease of the NICS values, although differences between closed-shell singlet $[B_{12}I_{12}]$ and $[B_{12}I_{12}]^{2+}$ are now smaller (for the triplet and quintet $[B_{12}I_{12}]^{2+}$, the aromaticity is increased in the former and reduced in the latter, Figures S5 and S6). NICS scans of C_6H_6, C_6I_6, and $[C_6I_6]^{2+}$ follow a trend similar to that found for $[B_{12}H_{12}]^{2-}$, $[B_{12}I_{12}]^{2-}$, and $[B_{12}I_{12}]$ (Figure S7). Based on NICS values, one may therefore consider $[B_{12}I_{12}]$ and $[B_{12}I_{12}]^{2+}$ as doubly 3D-aromatic.

We have also analyzed the quartet state of $[B_{12}I_{12}]^+$ because, in this state, the three orbitals of the triply degenerated HOMO are occupied with a single same spin electron, leading

to an I_h symmetric structure with bond length equalization. So, we expect this state to be particularly doubly aromatic since it reminds the electronic distribution of Baird aromatic species.[38] However, according to the NICS scans of Figure 3, this state has an aromaticity slightly smaller than that of closed-shell singlet $[B_{12}I_{12}]^{2+}$. Other systems with double 3D-aromaticity according to NICS values (Figures S8 and S12) are $[B_{12}Br_{12}]^{0/2+}$ (d_{Br-Br} = 4.069/4.047 Å), $[B_6I_6]^{2+}$ ($d_{I\cdots I}$ = 4.712 Å), and $[B_{14}I_{14}]^{0/2+}$ (longest $d_{I\cdots I}$ = 4.185/4.210 Å) but not $[B_{10}I_{10}]^{0/2+}$ (longest $d_{I\cdots I}$ = 4.693/4.699 Å). The case of $B_{12}Br_{12}$ is important because (i) it shows that efficient overlap between 4p orbitals of Br atoms is possible, and (ii) this species has been detected in the oxidation process of $[B_{12}Br_{12}]^{2-}$.[73]

To confirm that the results of the NICS scan stem from diatropic ring currents, we computed the current-density susceptibility and visualized the current at the plane located in the middle of the two boron 5-MRs (0.0 Å), the plane including one of the boron 5-MR (0.8 Å), and the plane of iodine 5-MR (1.8 Å) for $[B_{12}I_{12}]^{2-}$ for the singlet and triplet states of $[B_{12}I_{12}]$ and $[B_{12}I_{12}]^{2+}$, as well as for $[B_{12}H_{12}]$, C_6I_6, and $[C_6I_6]^{2+}$ (Figures S13−S16). As can be seen, the changes in the current-density susceptibility around the iodine substituents are similar on going from C_6I_6 to $[C_6I_6]^{2+}$ and from $[B_{12}I_{12}]^{2-}$ to $[B_{12}I_{12}]$. This further substantiates the potential double 3D-aromaticity in $[B_{12}I_{12}]$ and $[B_{12}I_{12}]^{2+}$ when evaluated with magnetic aromaticity descriptors. Figure 4 shows the current-density susceptibility of $[B_{12}I_{12}]^{2-}$, singlet and triplet $[B_{12}I_{12}]$, and $[B_{12}I_{12}]^{2+}$ in the 0.8 Å plane, which is ~1 Å above one of the I 5-MR planes. In this plane, differences between the differently oxidized clusters are more evident. From these pictures, one can see the generation of a current density around the iodine substituents when going from $[B_{12}I_{12}]^{2-}$ to $[B_{12}I_{12}]$ and $[B_{12}I_{12}]^{2+}$. This current is particularly intense for $^3[B_{12}I_{12}]$. In addition, we have computed the ring currents for $[C_2B_{10}I_{12}]$ and $[C_2B_{10}I_{12}]^{2+}$ in their singlet and triplet states (Figures S17 and S18), which also show an increase in the current-density around the iodine substituents after oxidation.

3.4. Electronic Aspects. Yet, other aspects of the potential double 3D-aromaticity (electronic, energetic, and geometric) must also be assessed, and next, we have analyzed the electron delocalization using the electron density of delocalized bonds (EDDB) method. The EDDB method decomposes the one-electron density in several "layers" corresponding to different levels of electron delocalization,[128] namely, the density of electrons localized on atoms (EDLA) representing inner shells, lone pairs, etc.; the electron density of localized bonds (EDLB)
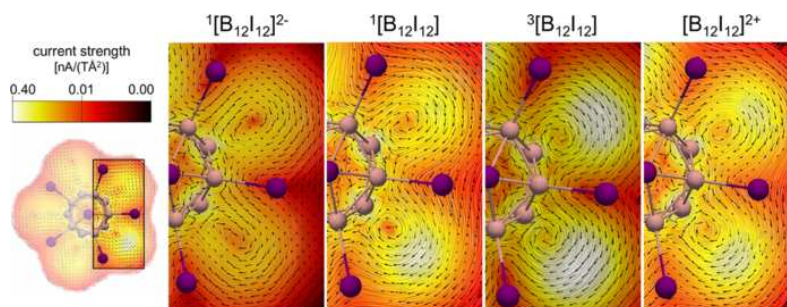

Figure 4. Current-density susceptibility in the magnified area (black rectangle) of the $^1[B_{12}I_{12}]^{2-}$, singlet and triplet $[B_{12}I_{12}]$, and $1[B_{12}I_{12}]^{2+}$ computed in a plane at 0.8 Å (see Figure S13). The color scale corresponds to the strength of the modulus of the current-density susceptibility in the range 0.0001 (dark red) to 0.4 (white) nA/(TÅ²).
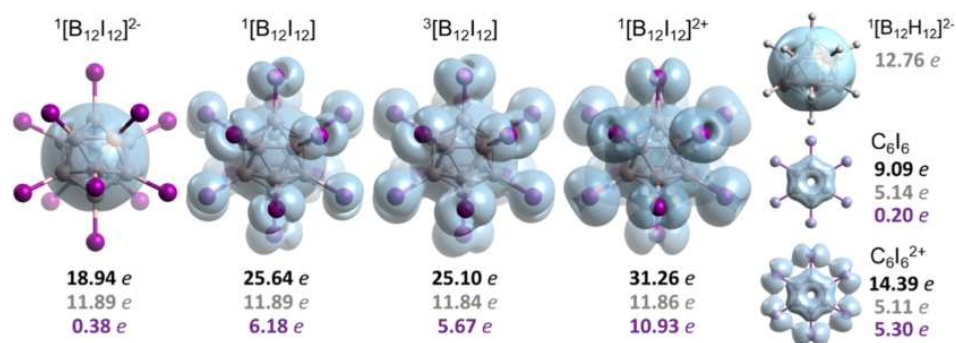
F

Figure 5. Isosurfaces (isocontour 0.007 e) of the electron density of delocalized bonds (EDDB) for $[B_{12}I_{12}]^{2-}$, $[B_{12}I_{12}]$ singlet and triplet states, and $[B_{12}I_{12}]^{2+}$, as well as $[B_{12}H_{12}]^{2-}$, C_6I_6, and $[C_6I_6]^{2+}$ for comparison purposes. Numerical results correspond to the $EDDB_G$ population of the whole system (black), boron/carbon atoms (gray), and iodine (purple) atoms separately.

Table 1. Electronic and Gibbs Reaction Energies (in kcal/mol) of Selected Homodesmotic Reactions[a]

reaction	ΔE	ΔG
$B_{12}I_{12} + [B_{12}H_{12}]^{2-} \rightarrow B_{12}I_6H_6 + [B_{12}H_6I_6]^{2-}$ (1)	−37.5	−40.1
$[B_{12}I_{12}]^{2+} + [B_{12}H_{12}]^{2-} \rightarrow [B_{12}I_6H_6]^{2+} + [B_{12}H_6I_6]^{2-}$ (2)	−2.8	−6.5
$[C_6I_6]^{2+} + C_6H_6 \rightarrow [C_6H_3I_3]^{2+} + C_6H_3I_3$ (3)	37.1	34.1

[a]All species computed in their closed-shell singlet state. In the case of reaction (1), if $B_{12}I_{12}$ and $B_{12}I_6H_6$ are in a triplet state, $\Delta E = -37.9$, and $\Delta G = -40.7$ kcal mol^{-1}.

representing typical (2-center 2-electron) Lewis-like bonds; and EDDB, which represents electron density that cannot be assigned to atoms or bonds due to its (multicenter) delocalized nature. The EDDB population of electrons delocalized in a 2D- or 3D-closed circuit can be used as an indicator of aromaticity.[129] According to the EDDB, the number of delocalized electrons (or holes) increases upon oxidation of $[B_{12}I_{12}]^{2-}$ (Figure 5). The number of delocalized electrons in the borane cage remains more or less similar, while the electron delocalization of the iodine sphere increases from 0.38 e ($[B_{12}I_{12}]^{2-}$) to 6.18 e (singlet $[B_{12}I_{12}]$), 5.67 e (triplet $[B_{12}I_{12}]$), and to 10.93 e ($[B_{12}I_{12}]^{2+}$). In the case of C_6I_6, we also have the delocalization around the I_6 circle going from 0.20 e in C_6I_6 to 5.30 e in $[C_6I_6]^{2+}$. For $[B_{12}I_{12}]^{2+}$, the number of delocalized electrons in the iodine shell (10.93 e out of 48 e coming from the 24 electron pairs located in the spherical surface of I_{12}) is similar to that of the borane cage (11.86 e out of 26 e). However, the percentage of delocalized electrons is still much larger for the borane cage (46 vs 23%). Moreover, the EDDB surface does not cover the entire I_{12} spherical surface. As a whole, the EDDB shows that there is electron delocalization among the I_{12} atoms (as expected from the different resonance structures) but does not fully support the existence of double 3D-aromaticity in $[B_{12}I_{12}]$ and $[B_{12}I_{12}]^{2+}$, especially in the former. EDDB plots for $[C_2B_{10}I_{12}]$ and $[C_2B_{10}I_{12}]^{2+}$ in their singlet and triplet states show very similar behavior (Figure S19), the electron delocalization being clearly higher for $[C_2B_{10}I_{12}]^{2+}$ than for $[C_2B_{10}I_{12}]$, especially in its singlet state.

3.5. Energetic Aspects and the Nature of the I⋯I Chemical Bond. As discussed before, the relatively short I⋯I distances in 3,4,5,6,7,8,9,10,11,12-I_{10}-o-carborane support the existence of noncovalent I⋯I bonding. We expect a similar situation in $[B_{12}I_{12}]^{2-}$. Moreover, we know that the I⋯I distance decreases when we move from $[B_{12}I_{12}]^{2-}$ to $[B_{12}I_{12}]^{0/2+}$. Do we reach a situation that can be defined as

covalent I−I bonding in $[B_{12}I_{12}]^{0/2+}$? To answer this question, we performed a quantum theory of atoms-in-molecules (QTAIM) analysis for these species, and the results show that none of them has a bond critical point (BCP) between the I atoms, thus unambiguously indicating that we have noncovalent I⋯I interaction but not covalent bonding. On the other hand, in the case of $[C_6I_6]^{2+}$, we observe I⋯I BCPs (Figure S20), although the density at these BCPs is very low ($\rho_{BCP,I⋯I} = 0.019$ au), thus precluding the existence of covalent bonding. The highest overlap between lone pair orbitals in two adjacent I atoms in C_6I_6 and $[B_{12}I_{12}]^{2-}$ is 0.165 and 0.097 au, respectively.

Thus, a crucial question is if it is possible to have aromaticity without covalent bonding. The answer from magnetic and electronic indices seems to be yes for $[C_6I_6]^{2+}$ and maybe for $[B_{12}I_{12}]^{0/2+}$. Yet, it is important to emphasize that aromaticity is linked to stability, and we already pointed out that the $[B_{12}I_{12}]^{0/2+}$ compounds have not been isolated. To check whether these molecules are stabilized by the double 3D-aromaticity, we designed several homodesmotic[83] reactions (Tables 1 and S2). We have chosen the position of the H atoms so that in $[B_{12}I_6H_6]^{0/2+}$ or in $[C_6H_3I_3]^{2+}$, the potential double aromaticity is quenched (for instance, in $[C_6H_3I_3]^{2+}$, the three H atoms are located in *meta* positions with respect to each other). As can be seen from reaction (3) in Table 1, there is a stabilization of $[C_6I_6]^{2+}$ because of the double 2D-aromaticity. In contrast, in the case of $[B_{12}I_{12}]^{0/2+}$, such stabilization does not take place (reactions (1) and (2)). Therefore, the energetic indicator of aromaticity does not support the double 3D-aromaticity of $[B_{12}I_{12}]^{0/2+}$, but it reinforces the conclusion that $[C_6I_6]^{2+}$ is doubly 2D-aromatic. So, the answer to the question of whether it is possible to have aromaticity without covalent bonding is that, in some particular cases such as in $[C_6I_6]^{2+}$, it seems possible. Lack of covalent I⋯I bonding in $[C_6I_6]^{2+}$ is substantiated by the low density of I⋯I BCPs, by the population of molecular orbitals

G

with antibonding I···I character, and the large distance between I atoms far outside the sum of the covalent radii of two I atoms (r_I^{cov} = 1.39 Å).[130] In this context, let us mention the synthesized dismutational aromatic isomer of hexa-silabenzene (Si_6R_6),[131] which shows strong diamagnetic response when exposed to an external magnetic field and has two unsubstituted silicon atoms with an interatomic distance that is significantly longer than the common covalent Si−Si single bond.[132]

Furthermore, one can note the pseudo-π method of Steiner and Fowler that replaces CH units in conjugated hydrocarbons by H atoms with a single $1s$ function located at the original C positions.[133] In that way, they reproduce the ring currents of π-conjugated hydrocarbons at a low cost. However, in the pseudo-π model of benzene, there is no H···H covalent bonding or only a very weak one[134] (the H atoms are placed far from each other and $\rho_{BCP,H···H}$ = 0.056 au, whereas for the H_2 molecule, the $\rho_{BCP,H−H}$ is 0.266 au). Moreover, the energy of the cyclic H_6 system is higher than those of the three H_2 molecules by 128.5 kcal/mol. So, there is no aromaticity in these H cycles (lack of stabilization), but there are ring currents and extensive electron delocalization ($EDDB_G$ indicates that 5.43 e out of a total of 6 are delocalized, Figure S27). This situation is akin to that found for $[B_{12}I_{12}]^{0/2+}$.

Finally, a lack of stability of $B_{12}I_{12}$ explains why $[B_{12}I_{12}]^{2-}$ requires such high oxidation potentials or strong oxidizing agents to reach the first oxidation step, the monoanionic radical, and even higher potentials to produce the neutral species.

4. CONCLUSIONS

^{11}B NMR spectra of I_n-o-$C_2B_{10}H_{12-n}$ are consistent with the existence of intramolecular noncovalent I···I bonding when n is large and, in particular, in I_{10}-o-$C_2B_{10}H_2$. It is expected that such a bonding situation is also present in $[B_{12}I_{12}]^{2-}$. Based on the example of double 2D-aromaticity in $[C_6I_6]^{2+}$, we analyzed the possibility of double 3D-aromaticity in $[B_{12}I_{12}]$ and $[B_{12}I_{12}]^{2+}$. Calculations of magnetic and electronic descriptors of aromaticity suggest (the electronic to less extent) that these two oxidized forms of *closo* icosahedral dodecaiodo-dodeca-borate cluster, $[B_{12}I_{12}]$ and $[B_{12}I_{12}]^{2+}$, can be classified as doubly 3D-aromatic compounds, much like $[C_6I_6]^{2+}$ is considered doubly 2D-aromatic. However, consistent with experimentation, homodesmotic reactions rule out the existence of double 3D-aromaticity in $[B_{12}I_{12}]^{0/2+}$ because these reactions are all endothermic and endergonic for these species. Aromaticity is a complex phenomenon; aromatic compounds have many interesting properties, but two are essential, namely, *electron delocalization and energetic stabilization*. A lack of one of these two effects precludes the existence of aromaticity. Although the two species display noticeable magnetic ring currents and electron delocalization (as expected from the multiple existing resonance structures with the same weight), we cannot conclude that there is aromaticity on the I_{12} shell of $[B_{12}I_{12}]^{0/2+}$ because homodesmotic reactions show that there is *no resonance stabilization*, one of the two main conditions required for aromaticity. These systems are good examples illustrating that analyses of aromaticity have to be exhaustive and are not focused only on one of the aspects (usually magnetic properties) that characterize aromatic compounds. $[B_{12}I_{12}]^{0/2+}$ shows that diatropic ring currents and bond length equalization, leading to high symmetry, are

important but not sufficient conditions for claiming aromaticity.

Finally, let us mention that the difficulty of generating $B_{12}I_{12}$ with electrochemical procedures already foreshadowed its lack of double 3D-aromaticity. Aromaticity, which is associated with electron delocalization facilitated by efficient orbital overlap, generally assists the synthesis of aromatic compounds because of their increased stability. However, in the case of $B_{12}I_{12}$, inefficient orbital overlap avoids the formation of a stable compound. This case highlights the potential for alternative approaches to enhancing stability beyond aromaticity. One such possibility is the generation of multiple weak, noncovalent I···I contacts, which, when combined, significantly boost stability.

■ ASSOCIATED CONTENT

ⓢ Supporting Information

The Supporting Information is available free of charge at https://pubs.acs.org/doi/10.1021/jacs.3c07335.

> A detailed description of the computational method, GIMIC calculation parameters used, additional homo-desmotic reactions, additional molecular structures and QTAIM analysis, Cartesian coordinates of all studied species, HOMO and LUMO orbitals of $[B_{12}I_{12}]^{2-}$, together with additional NICS scans, current-density plots, and steric maps (PDF)

■ AUTHOR INFORMATION

Corresponding Authors

Henrik Ottosson − *Department of Chemistry - Ångström Laboratory, Uppsala University, 751 20 Uppsala, Sweden;* ⓞ orcid.org/0000-0001-8076-1165; Email: henrik.ottosson@kemi.uu.se

Clara Viñas − *Institut de Ciència de Materials de Barcelona, Consejo Superior de Investigaciones Científicas, Campus Universitat Autònoma de Barcelona, 08193 Bellaterra, Spain;* ⓞ orcid.org/0000-0001-5000-0277; Email: clara@icmab.es

Miquel Solà − *Departament de Química, Institut de Química Computacional i Catàlisi, Universitat de Girona, 17003 Girona, Catalonia, Spain;* ⓞ orcid.org/0000-0002-1917-7450; Email: miquel.sola@udg.edu

Authors

Jordi Poater − *Departament de Química Inorgànica i Orgànica & IQTCUB, Universitat de Barcelona, 08028 Barcelona, Spain; ICREA, Pg. Lluís Companys 23, 08010 Barcelona, Spain;* ⓞ orcid.org/0000-0002-0814-5074

Sílvia Escayola − *Departament de Química, Institut de Química Computacional i Catàlisi, Universitat de Girona, 17003 Girona, Catalonia, Spain; Donostia International Physics Center (DIPC), 20018 Donostia, Euskadi, Spain;* ⓞ orcid.org/0000-0002-1159-7397

Albert Poater − *Departament de Química, Institut de Química Computacional i Catàlisi, Universitat de Girona, 17003 Girona, Catalonia, Spain;* ⓞ orcid.org/0000-0002-8997-2599

Francesc Teixidor − *Institut de Ciència de Materials de Barcelona, Consejo Superior de Investigaciones Científicas, Campus Universitat Autònoma de Barcelona, 08193 Bellaterra, Spain;* ⓞ orcid.org/0000-0002-3010-2417

Complete contact information is available at:

Author Contributions

∇J.P. and S.E. contributed equally to this work.

Notes

The authors declare no competing financial interest.

■ REFERENCES

(1) Boldyrev, A. I.; Wang, L.-S. All-metal aromaticity and antiaromaticity. *Chem. Rev.* 2005, 105, 3716−3757.

(2) Mercero, J. M.; Boldyrev, A. I.; Merino, G.; Ugalde, J. M. Recent developments and future prospects of all-metal aromatic compounds. *Chem. Soc. Rev.* 2015, 44, 6519−6534.

(3) Tsipis, C. A. DFT Study of "all-metal" aromatic compounds. *Coord. Chem. Rev.* 2005, 249, 2740−2762.

(4) Feixas, F.; Matito, E.; Poater, J.; Solà, M. Metalloaromaticity. *WIREs Comput. Mol. Sci.* 2013, 3, 105−122.

(5) Li, X.; Kuznetsov, A. E.; Zhang, H.-F.; Boldyrev, A.; Wang, L.-S. Observation of All-Metal Aromatic Molecules. *Science* 2001, 291, 859−861.

(6) Kuznetsov, A. E.; Birch, K. A.; Boldyrev, A. I.; Li, X.; Zhai, H.-J.; Wang, L.-S. All-Metal Antiaromatic Molecule: Rectangular Al_4^{4-} in the $Li_3Al_4^-$ Anion. *Science* 2003, 300, 622−625.

(7) Chen, D.; Szczepanik, D. W.; Zhu, J.; Solà, M. All-metal Baird aromaticity. *Chem. Commun.* 2020, 56, 12522−12525.

(8) Islas, R.; Inostroza, D.; Arias-Olivares, D.; Zúñiga-Gutiérrez, B.; Poater, J.; Solà, M. Analysis of the electronic delocalization in some isoelectronic analogues of B_{12} doped with beryllium and/or carbon. *Phys. Chem. Chem. Phys.* 2020, 22, 12245−12259.

(9) Zubarev, D. Y.; Boldyrev, A. I. Developing paradigms of chemical bonding: adaptive natural density partitioning. *Phys. Chem. Chem. Phys.* 2008, 10, 5207−5217.

(10) Alexandrova, A. N.; Boldyrev, A. I.; Zhai, H.-J.; Wang, L.-S.; Steiner, E.; Fowler, P. W. Structure and Bonding in B_6^- and B_6: Planarity and Antiaromaticity. *J. Phys. Chem. A* 2003, 107, 1359−1369.

(11) Averkiev, B. B.; Boldyrev, A. I. Hf_3 Cluster Is Triply (σ-, π-, and δ-) Aromatic in the Lowest D_{3h}, $^1A_1'$ State. *J. Phys. Chem. A* 2007, 111, 12864−12866.

(12) Han, P.-F.; Sun, Q.; Zhai, H.-J. Boron-Based Inverse Sandwich $V_2B_7^-$ Cluster: Double π/σ Aromaticity, Metal−Metal Bonding, and Chemical Analogy to Planar Hypercoordinate Molecular Wheels. *Molecules* 2023, 28, 4721.

(13) Lin, X.; Wu, W.; Mo, Y. Planar Four-Membered Diboron Actinide Compound with Double Möbius Aromaticity. *J. Am. Chem. Soc.* 2023, 145, 8107−8113.

(14) Chandrasekhar, J.; Jemmis, E. D.; Schleyer, P. v. R. Double aromaticity: aromaticity in orthogonal planes. The 3,5-dehydrophenyl cation. *Tetrahedron Lett.* 1979, 20 (39), 3707−3710.

(15) Sagl, D. J.; Martin, J. C. The stable singlet ground state dication of hexaiodobenzene: possibly a σ-delocalized dication. *J. Am. Chem. Soc.* 1988, 110, 5827−5833.

(16) Martin, J. C.; Schaad, L. J. Sigma-delocalized aromatic species formed from cyclic arrays of hypervalent main-group element species. *Pure Appl. Chem.* 1990, 62, 547−550.

(17) Ciofini, I.; Lainé, P. P.; Adamo, C. Quantifying electron delocalization in orthogonal channels: Theoretical investigation of σ and π aromaticity in $[C_6I_6]^{2+}$ and $[C_6Cl_6]^{2+}$. *Chem. Phys. Lett.* 2007, 435, 171−175.

(18) Rauhalahti, M.; Taubert, S.; Sundholm, D.; Liégeois, V. Calculations of current densities for neutral and doubly charged persubstituted benzenes using effective core potentials. *Phys. Chem. Chem. Phys.* 2017, 19, 7124−7131.

(19) Orozco-Ic, M.; Barroso, J.; Islas, R.; Merino, G. Delocalization in Substituted Benzene Dications: A Magnetic Point of View. *ChemistryOpen* 2020, 9, 657−661.

(20) Hatanaka, M.; Saito, M.; Fujita, M.; Morokuma, K. σ-Aromaticity in Hexa-Group 16 Atom-Substituted Benzene Dications: A Theoretical Study. *J. Org. Chem.* 2014, 79, 2640−2646.

(21) Furukawa, S.; Fujita, M.; Kanatomi, Y.; Minoura, M.; Hatanaka, M.; Morokuma, K.; Ishimura, K.; Saito, M. Double aromaticity arising from σ- and π-rings. *Commun. Chem.* 2018, 1, No. 60.

(22) Pino-Rios, R.; Vásquez-Espinal, A.; Yañez, O.; Tiznado, W. Searching for double σ- and π-aromaticity in borazine derivatives. *RSC Adv.* 2020, 10, 29705−29711.

(23) Kiran, B.; Phukan, A. K.; Jemmis, E. D. Is Borazine Aromatic? Unusual Parallel Behavior between Hydrocarbons and Corresponding B−N Analogues. *Inorg. Chem.* 2001, 40, 3615−3618.

(24) Escayola, S.; Proos Vedin, N.; Poater, A.; Ottosson, H.; Solà, M. In the quest of Hückel−Hückel and Hückel−Baird double aromatic tropylium (tri)cation and anion derivatives. *J. Phys. Org. Chem.* 2023, 36, No. e4447.

(25) Baird, N. C. Quantum organic photochemistry. II. Resonance and aromaticity in the lowest $^3\pi\pi^*$ state of cyclic hydrocarbons. *J. Am. Chem. Soc.* 1972, 94, 4941−4948.

(26) Ottosson, H. Organic photochemistry: Exciting excited-state aromaticity. *Nat. Chem.* 2012, 4, 969−971.

(27) Karas, L. J.; Wu, J. I. Baird's rules at the tipping point. *Nat. Chem.* 2022, 14, 723−725.

(28) Unverzagt, M.; Subramanian, G.; Hofmann, M.; Schleyer, P. v. R.; Berger, S.; Harms, K.; Massa, W.; Berndt, A. Carbene Analogues of Boron Stabilized by Neighboring B−B Moieties: Doubly Aromatic Bishomotriboriranides. *Angew. Chem., Int. Ed.* 1997, 36 (13−14), 1469−1472.

(29) Leitner, T. D.; Gmeinder, Y.; Röhricht, F.; Herges, R.; Mena-Osteritz, E.; Bäuerle, P. Twisted Thienylene−Phenylene Structures: Through-Space Orbital Coupling in Toroidal and Catenated Topologies. *Eur. J. Org. Chem.* 2020, 2020, 285−294.

(30) Tanaka, Y.; Koike, T.; Akita, M. 2-Dimensional molecular wiring based on toroidal delocalization of hexaarylbenzene. *Chem. Commun.* 2010, 46, 4529−4531.

(31) King, R. B. Three-Dimensional Aromaticity in Polyhedral Boranes and Related Molecules. *Chem. Rev.* 2001, 101, 1119−1152.

(32) Chen, Z. F.; King, R. Spherical aromaticity: Recent work on fullerenes, polyhedral boranes, and related structures. *Chem. Rev.* 2005, 105, 3613−3642.

(33) Bühl, M.; Hirsch, A. Spherical aromaticity of fullerenes. *Chem. Rev.* 2001, 101, 1153−1183.

(34) King, R. B.; Rouvray, D. H. Chemical applications of group theory and topology. 7. A graph-theoretical interpretation of the bonding topology in polyhedral boranes, carboranes, and metal clusters. *J. Am. Chem. Soc.* 1977, 99, 7834−7840.

(35) Aihara, J. Three-dimensional Aromaticity of Polyhedral Boranes. *J. Am. Chem. Soc.* 1978, 100, 3339−3342.

(36) Poater, J.; Solà, M.; Viñas, C.; Teixidor, F. π Aromaticity and Three-Dimensional Aromaticity: Two sides of the Same Coin? *Angew. Chem., Int. Ed.* 2014, 53, 12191−12195.

(37) Poater, J.; Solà, M.; Viñas, C.; Teixidor, F. Hückel's Rule of Aromaticity Categorizes Aromatic *closo* Boron Hydride Clusters. *Chem.—Eur. J.* 2016, 22, 7437−7443.

(38) El Bakouri, O.; Szczepanik, D. W.; Jorner, K.; Ayub, R.; Bultinck, P.; Solà, M.; Ottosson, H. Three-Dimensional Fully π-Conjugated Macrocycles: When 3D-Aromatic and When 2D-Aromatic-in-3D? *J. Am. Chem. Soc.* 2022, 144, 8560−8575.

(39) Lipscomb, W. N.; Pitochelli, A. R.; Hawthorne, M. F. Probable structure of the $B_{10}H_{10}^{-2}$ ion. *J. Am. Chem. Soc.* **1959**, *81*, 5833−5834.

(40) Pitochelli, A. R.; Hawthorne, F. M. The isolation of the icosahedral $B_{12}H_{12}^{-2}$ ion. *J. Am. Chem. Soc.* **1960**, *82*, 3228−3229.

(41) Wade, K. The Structural Significance of the Number of Skeletal Bonding Electron-Pairs in Carboranes, the Higher Boranes and Borane Anions, and Various Transition-Metal Carbonyl Cluster Compounds. *J. Chem. Soc. D* **1971**, 792−793.

(42) Mingos, D. M. P. A General Theory for Cluster and Ring Compounds of the Main Group and Transition Elements. *Nat. Phys. Sci.* **1972**, *236*, 99−102.

(43) Poater, J.; Viñas, C.; Bennour, I.; Escayola, S.; Solà, M.; Teixidor, F. Too Persistent to Give Up: Aromaticity in Boron Clusters Survives Radical Structural Changes. *J. Am. Chem. Soc.* **2020**, *142*, 9396−9407.

(44) Schleyer, P. v. R.; Najafian, K.; Mebel, A. M. The Large *closo*-Borane Dianions, $B_nH_n^{2-}$ (n = 13−17) Are Aromatic, Why Are They Unknown? *Inorg. Chem.* **1998**, *37*, 6765−6772.

(45) Muñoz-Castro, A. On the magnetic behavior of spherical aromatic compounds. Insights from the *closo*-$[B_{12}H_{12}]^{2-}$ cluster through chemical shift tensor maps. *Chem. Phys. Lett.* **2013**, *555*, 282−285.

(46) Schleyer, P. v. R.; Najafian, K. Stability and Three-Dimensional Aromaticity of *closo*-Monocarbaborane Anions, $CB_{n-1}H_n^-$, and *closo*-Dicarboranes, $C_2B_{n-2}H_n$. *Inorg. Chem.* **1998**, *37*, 3454−3470.

(47) Pitt, M. P.; Paskevicius, M.; Brown, D. H.; Sheppard, D. A.; Buckley, C. E. Thermal Stability of $Li_2B_{12}H_{12}$ and its Role in the Decomposition of $LiBH_4$. *J. Am. Chem. Soc.* **2013**, *135*, 6930−6941.

(48) Caputo, R.; Garroni, S.; Olid, D.; Teixidor, F.; Suriñach, S.; Baró, M. D. Can $Na_2[B_{12}H_{12}]$ be a decomposition product of $NaBH_4$? *Phys. Chem. Chem. Phys.* **2010**, *12*, 15093−15100.

(49) Bonatto Minella, C.; Garroni, S.; Olid, D.; Teixidor, F.; Pistidda, C.; Lindemann, I.; Gutfleisch, O.; Baró, M. D.; Bormann, R.; Klassen, T.; Dornheim, M. Experimental Evidence of $Ca[B_{12}H_{12}]$ Formation During Decomposition of a $Ca(BH_4)_2$ + MgH_2 Based Reactive Hydride Composite. *J. Phys. Chem. C* **2011**, *115*, 18010−18014.

(50) Udovic, T. J.; Matsuo, M.; Unemoto, A.; Verdal, N.; Stavila, V.; Skripov, A. V.; Rush, J. J.; Takamura, H.; Orimo, S.-i. Sodium superionic conduction in $Na_2B_{12}H_{12}$. *Chem. Commun.* **2014**, *50*, 3750−3752.

(51) Wang, R.-Y.; Zhang, J.-X.; Jiang, X.-L.; Ma, N.; Chen, X.; Xu, C.-Q.; Li, J. Understanding the Electronic Structure and Stability of $B_nX_n^{0/2-}$ (n = 4, 6; X = H, F, Cl, Br, I, At, Ts) Clusters†. *Chin. J. Chem.* **2021**, *39*, 1811−1818.

(52) Plesek, J. Potential applications of the boron cluster compounds. *Chem. Rev.* **1992**, *92*, 269−278.

(53) Stauber, J. M.; Schwan, J.; Zhang, X.; Axtell, J. C.; Jung, D.; McNicholas, B. J.; Oyala, P. H.; Martinolich, A. J.; Winkler, J. R.; See, K. A.; Miller, T. F.; Gray, H. B.; Spokoyny, A. M. A Super-Oxidized Radical Cationic Icosahedral Boron Cluster. *J. Am. Chem. Soc.* **2020**, *142*, 12948−12953.

(54) Beck-Sickinger, A. G.; Becker, D. P.; Chepurna, O.; Das, B.; Flieger, S.; Hey-Hawkins, E.; Hosmane, N.; Jalisatgi, S. S.; Nakamura, H.; Patil, R.; Vicente, M. d. G. H.; Viñas, C. New Boron Delivery Agents. *Cancer Biother. Radiopharm.* **2023**, *38*, 160−172.

(55) Qian, E. A.; Han, Y.; Messina, M. S.; Maynard, H. D.; Král, P.; Spokoyny, A. M. Multivalent Cluster Nanomolecules for Inhibiting Protein−Protein Interactions. *Bioconjugate Chem.* **2019**, *30*, 2594−2603.

(56) Barba-Bon, A.; Salluce, G.; Lostalé-Seijo, I.; Assaf, K. I.; Hennig, A.; Montenegro, J.; Nau, W. M. Boron clusters as broadband membrane carriers. *Nature* **2022**, *603*, 637−642.

(57) Jung, D.; Muni, M.; Marin, G.; Ramachandran, R.; El-Kady, M. F.; Balandin, T.; Kaner, R. B.; Spokoyny, A. M. Enhancing cycling stability of tungsten oxide supercapacitor electrodes via a boron cluster-based molecular cross-linking approach. *J. Mater. Chem. A* **2020**, *8*, 18015−18023.

(58) Assaf, K. I.; Nau, W. M. The Chaotropic Effect as an Assembly Motif in Chemistry. *Angew. Chem., Int. Ed.* **2018**, *57*, 13968−13981.

(59) Gentil, S.; Crespo, E.; Rojo, I.; Friang, A.; Viñas, C.; Teixidor, F.; Grüner, B.; Gabel, D. Polypyrrole materials doped with weakly coordinating anions: influence of substituents and the fate of the doping anion during the overoxidation process. *Polymer* **2005**, *46*, 12218−12225.

(60) Schwartz, L.; Eriksson, L.; Lomoth, R.; Teixidor, F.; Viñas, C.; Ott, S. Influence of an electron-deficient bridging *o*-carborane on the electronic properties of an [FeFe] hydrogenase active site model. *Dalton Trans.* **2008**, 2379−2381.

(61) Lerouge, F.; Ferrer-Ugalde, A.; Viñas, C.; Teixidor, F.; Sillanpää, R.; Abreu, A.; Xochitiotzi, E.; Farfán, N.; Santillan, R.; Núñez, R. Synthesis and fluorescence emission of neutral and anionic di- and tetra-carboranyl compounds. *Dalton Trans.* **2011**, *40*, 7541−7550.

(62) Couto, M.; García, M. F.; Alamón, C.; Cabrera, M.; Cabral, P.; Merlino, A.; Teixidor, F.; Cerecetto, H.; Viñas, C. Discovery of Potent EGFR Inhibitors through the Incorporation of a 3D-Aromatic-Boron-Rich-Cluster into the 4-Anilinoquinazoline Scaffold: Potential Drugs for Glioma Treatment. *Chem.—Eur. J.* **2018**, *24*, 3122−3126.

(63) Núñez, R.; Romero, I.; Teixidor, F.; Viñas, C. Icosahedral boron clusters: a perfect tool for the enhancement of polymer features. *Chem. Soc. Rev.* **2016**, *45*, 5147−5173.

(64) Fuentes, I.; Andrio, A.; Teixidor, F.; Viñas, C.; Compañ, V. Enhanced conductivity of sodium versus lithium salts measured by impedance spectroscopy. Sodium cobaltacarboranes as electrolytes of choice. *Phys. Chem. Chem. Phys.* **2017**, *19*, 15177−15186.

(65) Masalles, C.; Llop, J.; Viñas, C.; Teixidor, F. Extraordinary Overoxidation Resistance Increase in Self-Doped Polypyrroles by Using Non-conventional Low Charge-Density Anions. *Adv. Mater.* **2002**, *14*, 826−829.

(66) Grüner, B.; Plešek, J.; Báča, J.; Císařová, I.; Dozol, J. F.; Rouquette, H.; Viñas, C.; Selucký, P.; Rais, J. Cobalt bis(dicarbollide) ions with covalently bonded CMPO groups as selective extraction agents for lanthanide and actinide cations from highly acidic nuclear waste solutions. *New J. Chem.* **2002**, *26*, 1519−1527.

(67) Nuez-Martínez, M.; Queralt-Martín, M.; Muñoz-Juan, A.; Aguilella, V. M.; Laromaine, A.; Teixidor, F.; Viñas, C.; Pinto, C. G.; Pinheiro, T.; Guerreiro, J. F.; Mendes, F.; Roma-Rodrigues, C.; Baptista, P. V.; Fernandes, A. R.; Valic, S.; Marques, F. Boron clusters (ferrabisdicarbollides) shaping the future as radiosensitizers for multimodal (chemo/radio/PBFR) therapy of glioblastoma. *J. Mater. Chem. B* **2022**, *10*, 9794−9815.

(68) Zhao, X.; Yang, Z.; Chen, H.; Wang, Z.; Zhou, X.; Zhang, H. Progress in three-dimensional aromatic-like *closo*-dodecaborate. *Coord. Chem. Rev.* **2021**, *444*, 214042.

(69) Sethio, D.; Daku, L. M. L.; Hagemann, H.; Kraka, E. Quantitative Assessment of B−B−B, B−H_b−B, and B−H_t Bonds: From BH_3 to $B_{12}H_{12}^{2-}$. *ChemPhysChem* **2019**, *20*, 1967−1977.

(70) Aprà, E.; Warneke, J.; Xantheas, S. S.; Wang, X.-B. A benchmark photoelectron spectroscopic and theoretical study of the electronic stability of $[B_{12}H_{12}]^{2-}$. *J. Chem. Phys.* **2019**, *150*, No. 164306.

(71) Warneke, J.; Konieczka, S. Z.; Hou, G.-L.; Aprà, E.; Kerpen, C.; Keppner, F.; Schäfer, T. C.; Deckert, M.; Yang, Z.; Bylaska, E. J.; Johnson, G. E.; Laskin, J.; Xantheas, S. S.; Wang, X.-B.; Finze, M. Properties of perhalogenated {*closo*-B_{10}} and {*closo*-B_{11}} multiply charged anions and a critical comparison with {*closo*-B_{12}} in the gas and the condensed phase. *Phys. Chem. Chem. Phys.* **2019**, *21*, 5903−5915.

(72) Warneke, J.; Hou, G.-L.; Aprà, E.; Jenne, C.; Yang, Z.; Qin, Z.; Kowalski, K.; Wang, X.-B.; Xantheas, S. S. Electronic Structure and Stability of $[B_{12}X_{12}]^{2-}$ (X = F−At): A Combined Photoelectron Spectroscopic and Theoretical Study. *J. Am. Chem. Soc.* **2017**, *139*, 14749−14756.

(73) Boeré, R. T.; Derendorf, J.; Jenne, C.; Kacprzak, S.; Keßler, M.; Riebau, R.; Riedel, S.; Roemmele, T. L.; Rühle, M.; Scherer, H.; Vent-Schmidt, T.; Warneke, J.; Weber, S. On the Oxidation of the Three-

Dimensional Aromatics $[B_{12}X_{12}]^{2-}$ (X = F, Cl, Br, I). *Chem.—Eur. J.* **2014**, *20*, 4447−4459.

(74) Hirsch, A.; Chen, Z.; Jiao, H. Spherical aromaticity in icosahedral fullerenes: The $2(N+1)^2$ rule. *Angew. Chem., Int. Ed.* **2000**, *39*, 3915−3917.

(75) te Velde, G.; Bickelhaupt, F. M.; Baerends, E. J.; Fonseca Guerra, C.; van Gisbergen, S. J. A.; Snijders, J. G.; Ziegler, T. Chemistry with ADF. *J. Comput. Chem.* **2001**, *22*, 931−967.

(76) AMS 2023.1. SCM, Vrije Universiteit, Amsterdam, The Netherlands, 2023, http://www.scm.com (accessed 22nd June 2023).

(77) Lenthe, E. v.; Baerends, E. J.; Snijders, J. G. Relativistic regular two-component Hamiltonians. *J. Chem. Phys.* **1993**, *99*, 4597−4610.

(78) Becke, A. D. Density-functional exchange-energy approximation with correct asymptotic behavior. *Phys. Rev. A* **1988**, *38*, 3098−3100.

(79) Lee, C.; Yang, W.; Parr, R. G. Development of the Colle-Salvetti correlation-energy formula into a functional of the electron density. *Phys. Rev. B* **1988**, *37*, 785−789.

(80) Grimme, S.; Ehrlich, S.; Goerigk, L. Effect of the damping function in dispersion corrected density functional theory. *J. Comput. Chem.* **2011**, *32*, 1456−1465.

(81) Poater, J.; Duran, M.; Solà, M.; Silvi, B. Theoretical Evaluation of Electron Delocalization in Aromatic Molecules by Means of Atoms in Molecules (AIM) and Electron Localization Function (ELF) Topological Approaches. *Chem. Rev.* **2005**, *105*, 3911−3947.

(82) Feixas, F.; Matito, E.; Poater, J.; Solà, M. Quantifying aromaticity with electron delocalisation measures. *Chem. Soc. Rev.* **2015**, *44*, 6434−6451.

(83) Cyrański, M. K. Energetic Aspects of Cyclic π-electron Delocalization: Evaluation of the Methods of Estimating Aromatic Stabilization Energies. *Chem. Rev.* **2005**, *105*, 3773−3811.

(84) Krygowski, T. M.; Szatylowicz, H.; Stasyuk, O. A.; Dominikowska, J.; Palusiak, M. Aromaticity from the Viewpoint of Molecular Geometry: Application to Planar Systems. *Chem. Rev.* **2014**, *114*, 6383−6422.

(85) Lazzeretti, P. Ring Currents. *Prog. Nucl. Magn. Reson. Spectrosc.* **2000**, *36*, 1−88.

(86) Chen, Z.; Wannere, C. S.; Corminboeuf, C.; Puchta, R.; Schleyer, P. v. R. Nucleus-Independent Chemical Shifts (NICS) as an Aromaticity Criterion. *Chem. Rev.* **2005**, *105*, 3842−3888.

(87) Sundholm, D.; Fliegl, H.; Berger, R. J. F. Calculations of magnetically induced current densities: theory and applications. *WIREs Comput. Mol. Sci.* **2016**, *6*, 639−678.

(88) Poater, J.; García-Cruz, I.; Illas, F.; Solà, M. Discrepancy Between Common Local Aromaticity Measures in a Series of Carbazole Derivatives. *Phys. Chem. Chem. Phys.* **2004**, *6*, 314−318.

(89) Schleyer, P. v. R.; Maerker, C.; Dransfeld, A.; Jiao, H.; van Eikema Hommes, N. J. R. Nucleus-Independent Chemical Shifts: A simple and Efficient Aromaticity Probe. *J. Am. Chem. Soc.* **1996**, *118*, 6317−6318.

(90) Wolinski, K.; Hilton, J. F.; Pulay, P. Efficient Implementation of the Gauge-Independent Atomic Orbital Method for NMR Chemical Shift Calculations. *J. Am. Chem. Soc.* **1990**, *112*, 8251−8260.

(91) Fliegl, H.; Sundholm, D.; Taubert, S.; Jusélius, J.; Klopper, W. Magnetically Induced Current Densities in Aromatic, Antiaromatic, Homoaromatic, and Nonaromatic Hydrocarbons. *J. Phys. Chem. A* **2009**, *113*, 8668−8676.

(92) *Gaussian 16 Rev. C.01*; Wallingford, CT, 2016. http://gaussian.com (accessed 22nd June 2023).

(93) Ahrens, J. P.; Geveci, B. *ParaView: An End-User Tool for Large-Data Visualization Handbook*; Elsevier, 2005.

(94) Szczepanik, D. W.; Andrzejak, M.; Dominikowska, J.; Pawełek, B.; Krygowski, T. M.; Szatylowicz, H.; Solà, M. The electron density of delocalized bonds (EDDB) applied for quantifying aromaticity. *Phys. Chem. Chem. Phys.* **2017**, *19*, 28970−28981.

(95) Szczepanik, D. W.; Andrzejak, M.; Dyduch, K.; Żak, E.; Makowski, M.; Mazur, G.; Mrozek, J. A uniform approach to the description of multicenter bonding. *Phys. Chem. Chem. Phys.* **2014**, *16*, 20514−20523.

(96) Szczepanik, D. W.; Żak, E.; Dyduch, K.; Mrozek, J. Electron delocalization index based on bond order orbitals. *Chem. Phys. Lett.* **2014**, *593*, 154−159.

(97) *RunEDDB* Krakow, Poland, 2021. http://www.eddb.pl/runeddb (accessed 22nd June 2023).

(98) Hanwell, M. D.; Curtis, D. E.; Lonie, D. C.; Vandermeersch, T.; Zurek, E.; Hutchison, G. R. Avogadro: an advanced semantic chemical editor, visualization, and analysis platform. *J. Cheminf.* **2012**, *4*, 17.

(99) George, P.; Trachtman, M.; Bock, C. W.; Brett, A. M. Homodesmotic reactions for the assessment of stabilization energies in benzenoid and other conjugated cyclic hydrocarbons. *J. Chem. Soc., Perkin Trans. 2* **1976**, 1222−1227.

(100) George, P.; Trachtman, M.; Brett, A. M.; Bock, C. W. Comparison of various isodesmic and homodesmotic reaction heats with values derived from published ab initio molecular orbital calculations. *J. Chem. Soc., Perkin Trans. 2* **1977**, 1036−1047.

(101) Poater, A.; Cosenza, B.; Correa, A.; Giudice, S.; Ragone, F.; Scarano, V.; Cavallo, L. SambVca: A Web Application for the Calculation of the Buried Volume of N-Heterocyclic Carbene Ligands. *Eur. J. Inorg. Chem.* **2009**, *2009*, 1759−1766.

(102) Falivene, L.; Credendino, R.; Poater, A.; Petta, A.; Serra, L.; Oliva, R.; Scarano, V.; Cavallo, L. SambVca 2. A Web Tool for Analyzing Catalytic Pockets with Topographic Steric Maps. *Organometallics* **2016**, *35*, 2286−2293.

(103) Falivene, L.; Cao, Z.; Petta, A.; Serra, L.; Poater, A.; Oliva, R.; Scarano, V.; Cavallo, L. Towards the online computer-aided design of catalytic pockets. *Nat. Chem.* **2019**, *11*, 872−879.

(104) Teixidor, F.; Barberà, G.; Vaca, A.; Kivekäs, R.; Sillanpää, R.; Oliva, J.; Viñas, C. Are Methyl Groups Electron-Donating or Electron-Withdrawing in Boron Clusters? Permethylation of *o*-Carborane. *J. Am. Chem. Soc.* **2005**, *127*, 10158−10159.

(105) Heřmánek, S.; Gregor, V.; Štíbr, B.; Plešek, J.; Janoušek, Z.; Antonovich, V. A. Antipodal and vicinal shift effects in ^{11}B, ^{13}C, and ^{1}H NMR spectra of substituted dicarba-*closo*-dodecarboranes(12). *Collect. Czech. Chem. Commun.* **1976**, *41*, 1492−1499.

(106) Stanko, V. I.; Babushkina, T. A.; Klimova, T. P.; Goltyapin, Y. V.; Klimova, A. I.; Vasilev, A. M.; Alymov, A. M.; Khrapov, V. V. Transmission of effect of substituents in B-chloro *ortho* carboranes, B-chloro *meta* carboranes and B-chloro *para* carboranes. *Zh. Obshch. Khim.* **1976**, *46*, 1071−1079.

(107) Heřmánek, S.; Plešek, J.; Gregor, V.; Štíbr, B. Background of the nuclear magnetic resonance antipodal shift induced by substituents; an analogy of the mesomeric effect with borane skeletons. *J. Chem. Soc., Chem. Commun.* **1977**, 561−563.

(108) Teixidor, F.; Viñas, C.; Rudolph, R. W. Rules for predicting the boron-11 NMR spectra of closo-boranes and closo-heteroboranes. *Inorg. Chem.* **1986**, *25*, 3339−3345.

(109) Hermanek, S. Boron-11 NMR spectra of boranes, main-group heteroboranes, and substituted derivatives. Factors influencing chemical shifts of skeletal atoms. *Chem. Rev.* **1992**, *92*, 325−362, DOI: 10.1021/cr00010a007.

(110) Barberà, G.; Vaca, A.; Teixidor, F.; Sillanpää, R.; Kivekäs, R.; Viñas, C. Designed Synthesis of New *ortho*-Carborane Derivatives: from Mono- to Polysubstituted Frameworks. *Inorg. Chem.* **2008**, *47*, 7309−7316.

(111) Search performed on May 5th 2023.

(112) Bruno, I. J.; Cole, J. C.; Edgington, P. R.; Kessler, M.; Macrae, C. F.; McCabe, P.; Pearson, J.; Taylor, R. New software for searching the Cambridge Structural Database and visualizing crystal structures. *Acta Crystallogr., Sect. B: Struct. Sci.* **2002**, *58*, 389−397.

(113) Teixidor, F.; Barberà, G.; Viñas, C.; Sillanpää, R.; Kivekäs, R. Synthesis of Boron-Iodinated o-Carborane Derivatives. Water Stability of the Periodinated Monoprotic Salt. *Inorg. Chem.* **2006**, *45*, 3496−3498.

(114) Puga, A. V.; Teixidor, F.; Sillanpää, R.; Kivekäs, R.; Viñas, C. Iodinated *ortho*-Carboranes as Versatile Building Blocks to Design Intermolecular Interactions in Crystal Lattices. *Chem.—Eur. J.* **2009**, *15*, 9764−9772.

K

(115) Bondi, A. van der Waals Volumes and Radii. *J. Phys. Chem. A* **1964**, *68*, 441−451.

(116) Ibrahim, M. A. A.; Saeed, R. R. A.; Shehata, M. N. I.; Ahmed, M. N.; Shawky, A. M.; Khowdiary, M. M.; Elkaeed, E. B.; Soliman, M. E. S.; Moussa, N. A. M. Type I-IV Halogen···Halogen Interactions: A Comparative Theoretical Study in Halobenzene···Halobenzene Homodimers. *Int. J. Mol. Sci.* **2022**, *23*, 3114.

(117) Hwang, S.-J.; Bowman, R. C.; Reiter, J. W.; Rijssenbeek; Soloveichik, G. L.; Zhao, J.-C.; Kabbour, H.; Ahn, C. C. NMR Confirmation for Formation of [B$_{12}$H$_{12}$]$^{2-}$ Complexes during Hydrogen Desorption from Metal Borohydrides. *J. Phys. Chem. C* **2008**, *112*, 3164−3169.

(118) Hollow, S. E.; Johnstone, T. C. Encapsulation of closo-dodecaiododododecaborate in 2-hydroxypropyl-γ-cyclodextrin prevents hemolysis. *Chem. Commun.* **2022**, *58*, 2375−2378.

(119) Shen, Y.-F.; Xu, C.; Cheng, L.-J. Deciphering chemical bonding in B$_n$H$_n$$^{2-}$ (n = 2−17): flexible multicenter bonding. *RSC Adv.* **2017**, *7*, 36755−36764.

(120) Farràs, P.; Vankova, N.; Zeonjuk, L. L.; Warneke, J.; Dülcks, T.; Heine, T.; Viñas, C.; Teixidor, F.; Gabel, D. From an Icosahedron to a Plane: Flattening Dodecaiodo-dodecaborate by Successive Stripping of Iodine. *Chem.—Eur. J.* **2012**, *18*, 13208−13212.

(121) Viñas, C.; Barberà, G.; Oliva, J. M.; Teixidor, F.; Welch, A. J.; Rosair, G. M. Are Halocarboranes Suitable for Substitution Reactions? The Case for 3-I-1,2-*closo*-C$_2$B$_{10}$H$_{11}$: Molecular Orbital Calculations, Aryldehalogenation Reactions, ^{11}B NMR Interpretation of *closo*-Carboranes, and Molecular Structures of 1-Ph-3-Br-1,2-*closo*-C$_2$B$_{10}$H$_{10}$ and 3-Ph-1,2-*closo*-C$_2$B$_{10}$H$_{11}$. *Inorg. Chem.* **2001**, *40*, 6555−6562.

(122) Vaca, A.; Teixidor, F.; Kivekäs, R.; Sillanpää, R.; Viñas, C. A solvent-free regioselective iodination route of *ortho*-carboranes. *Dalton Trans.* **2006**, 4884−4885.

(123) Srivastava, R. R.; Hamlin, D. K.; Wilbur, D. S. Synthesis of Highly Iodinated Icosahedral Mono- and Dicarbon Carboranes. *J. Org. Chem.* **1996**, *61*, 9041−9044.

(124) Sivaev, I. B.; Bregadzea, V. I.; Sjöberg, S. Chemistry of *closo*-Dodecaborate Anion [B$_{12}$H$_{12}$]$^{2-}$: A Review. *Collect. Czech. Chem. Commun.* **2002**, *67*, 679−727.

(125) Multiconfigurational wavefunctions should be used to properly handle oxidized dodecaiodo-dodecaborate clusters. However, a multiconfigurational calculation is not practical because of the quantity of electrons that should be included in the active region (all electron pairs of I atoms).

(126) Fonseca-Guerra, C.; Handgraaf, J.-W.; Baerends, E. J.; Bickelhaupt, F. M. Voronoi Deformation Density (VDD) Charges: Assessment of the Mulliken, Bader, Hirshfeld, Weinhold, and VDD Methods for Charge Analysis. *J. Comput. Chem.* **2004**, *25*, 189−210.

(127) Hirshfeld, F. L. Bonded-atom fragments for describing molecular charge densities. *Theor. Chim. Acta* **1977**, *44*, 129−138.

(128) Szczepanik, D. W. A new perspective on quantifying electron localization and delocalization in molecular systems. *Comput. Theor. Chem.* **2016**, *1080*, 33−37.

(129) Szczepanik, D. W.; Solà, M.; Krygowski, T. M.; Szatylowicz, H.; Andrzejak, M.; Pawelek, B.; Dominikowska, J.; Kukulka, M.; Dyduch, K. Aromaticity of acenes: the model of migrating-circuits. *Phys. Chem. Chem. Phys.* **2018**, *20*, 13430−13436.

(130) Cordero, B.; Gómez, V.; Platero-Prats, A. E.; Revés, M.; Echeverría, J.; Cremades, E.; Barragán, F.; Alvarez, S. Covalent radii revisited. *Dalton Trans.* **2008**, 2832−2838.

(131) Abersfelder, K.; White, A. J. P.; Rzepa, H. S.; Scheschkewitz, D. A Tricyclic Aromatic Isomer of Hexasilabenzene. *Science* **2010**, *327*, 564−566.

(132) Berger, R. J. F.; Rzepa, H. S.; Scheschkewitz, D. Ring Currents in the Dismutational Aromatic Si$_6$R$_6$. *Angew. Chem., Int. Ed.* **2010**, *49*, 10006−10009.

(133) Fowler, P. W.; Steiner, E. Pseudo-π currents: rapid and accurate visualisation of ring currents in conjugated hydrocarbons. *Chem. Phys. Lett.* **2002**, *364*, 259−266.

(134) Wolstenholme, D. J.; Cameron, T. S. Comparative Study of Weak Interactions in Molecular Crystals: H−H Bonds vs Hydrogen Bonds. *J. Phys. Chem. A* **2006**, *110*, 8970−8978.

6 Results and Discussion

In this thesis, the evaluation of aromaticity stands as a unifying and pivotal theme. Following this focus, the critical findings will be revisited and discussed in five sections corresponding to Chapter 4 and the four sections of Chapter 5 (5.1—5.4). Each of these sections begins with an examination of the methodologies utilized and the justification of the selected computational approach. Subsequently, the sections progress to discuss diverse topics: In Section 6.1, we explored the impact of structural changes on the electronic nature of *para*-quinodimethanes in the ground and excited states. The subsequent four sections encompass projects on (sub)phthalocyanine and related compounds, nanographenes, double aromatic substituted tropylium ions, and polyhedral boranes. Each project case faces challenges in evaluating aromaticity due to complex electronic structures and topologies of the systems studied that limit the applicability of traditional indicators. Yet, determining the aromatic or non-aromatic nature of these systems is crucial for comprehending their inherent properties.

6.1 Electronic Nature of S_0, S_1, and T_1 of Pro-Aromatic Quinoidal Systems

The work presented in this Section focuses on the impact of structural changes on the electronic properties of pro-aromatic quinoidal molecules summarizing the insights from two different articles. The first article (Section 4.1) explores the aromatic character, either Hückel or Baird, of the lowest-lying triplet and singlet excited states. The second article (Section 4.2) treats the interplay between structural modifications and the character of the GS, along with alterations in the singlet-triplet energy gap. This GS can manifest either as a closed-shell quinoidal form or an open-shell biradical(oid) depending on the molecular structure. Before proceeding to review the main results of these works, we first comment on the computational benchmarks and criteria that

213

guided the selection of the methodology in each study.

Exchange-Correlation Functional Selection and Comparative Benchmarking

In the articles summarized herein, different density functionals and basis sets—B3LYP/6-311+G(d,p) and OPBE/cc-pVTZ—were employed. For the first article, the choice of B3LYP/6-311+G(d,p) methodology was motivated by the optimal performance shown in the electronic structure study performed by Jorner *et al.* in similar systems [109], as well as its demonstrated efficacy in a study on triplet state Baird aromaticity in macrocycles [506]. Moreover, computed frequencies at this level of theory are in very good agreement with benchmark calculations (CCSD/6-311+G(d,p) in Table 2 of Section 4.1). We are aware of the limitations of hybrid GGA functionals with low % of HF exchange, which consistently underestimate the energy of CT states. Nevertheless, it is important to notice that the low-lying singlet-singlet and singlet-triplet excitations in all the studied compounds do not present significant CT character. This can be confirmed by the well-delocalized over the molecule HOMO and LUMO π-orbitals (Figure 4 in Section 4.1), and the fact that the HOMO$\rightarrow$LUMO transition is the dominant contribution in S_1 according to TDDFT weights. Hence, in this case, we are confident that the electronic character of S_1 and T_1 states is well recovered by a hybrid functional with a 20% of exact exchange, *i.e.*, B3LYP. The suitability of the B3LYP functional has been further confirmed by comparing the results with other functionals (see Table 6.1), and in particular to range-separated functionals (CAM-B3LYP and ωB97X-D). These calculations yield consistent results in terms of energy gaps, bond distances, charges, spin densities, and aromaticity results, as documented in Figures S1-4 and Tables S1-17 in the supplementary information (page 309). Generally, in the aromaticity measurements, even though the S_0 state remains non-aromatic, the results obtained with B3LYP suggest a slightly higher inclination towards aromatic character compared to other functionals. For the T_1 state, which is our primary focus, the differences in aromaticity values across various functionals are minimal. Notably, B3LYP does not exhibit a specific tendency towards higher aromaticity, indicating that the results are quite comparable regardless of the functional used. Lastly, the nature of the lowest excited singlet and triplet states does not change between B3LYP and CAM-B3LYP or ωB97X-D. Besides, the fact that our S_1 and T_1 results computed with B3LYP do not show hole/electron spatial separation, further supports the lack of CT character in these systems, and the appropriateness of the employed methodology.

6.1 Electronic Nature of S_0, S_1, and T_1 of Pro-Aromatic Quinoidal Systems

Table 6.1 TDDFT/6-311+G(d,p) relative energies ($\Delta E_{S_0-X} = E_X - E_{S_0}$, where X = T_1, S_1 or S_2) in eV of adiabatic T_1 and S_1 and vertical T_1, S_1, and S_2 states in gas phase.

	System	T_1 adia	S_1 adia	T_1 vert	S_1 vert	S_2 vert
5R	B3LYP	0.848	1.596	0.957	2.065	3.535
	CAM-B3LYP	0.812	1.733	0.845	2.206	3.931
	ωB97X-D	0.811	1.687	0.828	2.165	3.898
	M06-2X	0.965	1.742	1.038	2.215	3.957
6R	B3LYP	0.778	2.845	0.685	2.983	3.334
	CAM-B3LYP	0.666	3.051	-0.437	3.261	3.885
	ωB97X-D	0.648	3.019	-0.342	3.231	3.832
	M06-2X	0.904	3.094	1.096	3.301	3.956
9R	B3LYP	1.159	0.950	1.263	2.529	3.385
	CAM-B3LYP	1.290	1.744	1.145	2.613	4.004
	ωB97X-D	1.343	1.724	1.165	2.602	4.086
	M06-2X	1.468	1.695	1.285	2.593	3.949
5R-5a	B3LYP	0.718	1.525	0.768	1.895	2.347
	CAM-B3LYP	0.598	1.642	0.332	1.996	3.006
	ωB97X-D	0.581	1.596	0.176	1.956	3.060
	M06-2X	0.736	1.635	0.630	1.994	2.955
10RT$_{trans}$	B3LYP	0.215	1.652	0.393	1.807	2.104
	CAM-B3LYP	0.125	1.977	0.234	2.304	3.097
	ωB97X-D	0.076	1.990	0.384	2.332	3.156
	M06-2X	0.294	1.933	0.960	2.243	2.985

Next, we discuss the computational methodology employed in the second article, specifically the choice of the OPBE/cc-pVTZ functional. This was selected after testing the performance of eleven DFAs, including GGA, meta-GGA, hybrid GGA, and long-range corrected (LC) functionals: BLYP, BP86, PBE, OPBE, M06-L, TPSS, MN15, MN15-L, B3LYP, CAM-B3LYP, and ωB97X-D. We performed benchmark calculations for Thiele, bearing one central unit ($m = 1$), and Chichibabin, $m = 2$, hydrocarbons (Figure 1.16) with hydrogens as terminal substituents. Geometry optimizations were performed for both singlet and triplet states, using DFT/cc-pVTZ and employing QCISD/cc-pVDZ and CCSD(T)//QCISD as references for structural parameters and energies, respectively. Among all tested DFAs, the ones that yield better geometrical (*i.e.* bond distances and angles) results, compared to QCISD/cc-pVDZ geometries, are pure functionals, with only minor discrepancies among them. Moreover, for OPBE, we compared the optimized geometries of *p,p'*-benzene-bis-(diphenylmethylene) and

p,p'-biphenyl-bis-(diphenylmethylene), corresponding to **7₁** and **7₂** in Figure 6.3b, with bond distances from X-Ray available data [211]. The maximum deviations between the calculated and experimental bond distances were found to be $0.016\,\text{Å}$ for **7₁** and $0.004\,\text{Å}$ for **7₂**. Then, in terms of ΔE_{S_0-T}, BP86, BLYP, PBE, OPBE, M06-L, and MN15-L exhibit the smallest deviations compared to CCSD(T)//QCISD results, with errors below 0.13 eV (3 kcal/mol).

Our choice of the OPBE functional is also based on conclusions from previous studies. In 2018 Alexander *et al.* [507] compared the performance of BP86, TPSS, TPSSh, and B3LYP to reproduce structural experimental values of diradical compounds. They concluded that TPSSh (a hybrid functional with 10% exact exchange) provides the best results for two Chichibabin system derivatives. However, they also noted that none of the tested functionals reached optimal performance describing relative bond lengths. Earlier works by M. Swart and co-workers [508, 509] suggest that the OPBE pure functional, characterized by Handy's optimized exchange [510] combined with PBE [511] correlation, performs well in predicting spin states. Additionally, OPBE yields reliable results for calculating magnetic shielding [512], a critical factor in the assessment of NICS values. Therefore, in the absence of a clear best choice, we opted for OPBE due to its balanced performance across multiple criteria, as corroborated by both our data and existing literature.

Additionally, to measure the impact of the long-range corrections in systems with extended chain lengths with $m > 2$, we performed calculations using LC-OPBE and ωB97X-D (Table 6.2). We find that for $m = 1$, all functionals converge to a singlet closed-shell (CS) ground state. For $m = 2$, only OPBE leads to a CS ground state. For larger m values, both the OSS and T are less stabilized by OPBE than by LC-OPBE and ωB97X-D. This can be attributed to the propensity of GGAs like OPBE to artificially stabilize an overall delocalized form [144, 145, 412] resulting from several resonance structures (see Figure 6.1) over the benzoid form. Notice that the benzoid form is represented only by the two resonance structures on the right.
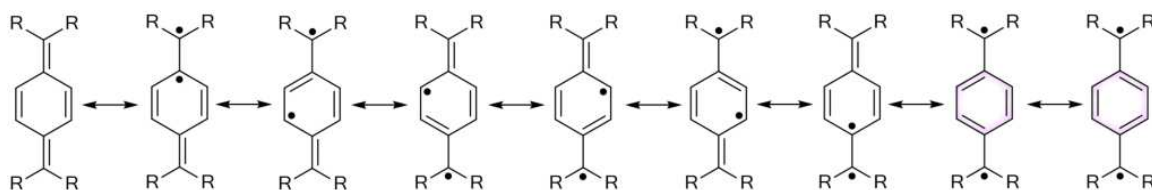

Figure 6.1 Neutral resonance structures of *p*-quinodimethane.

6.1 Electronic Nature of S_0, S_1, and T_1 of Pro-Aromatic Quinoidal Systems

Despite the delocalization error that OPBE may suffer [144, 145, 412], the trends of decreasing energy and increasing $\langle S^2 \rangle$ of the OSS with the increasing value of m are consistent with those obtained from LC-OPBE and ωB97X-D. Hence, while caution is advised for the quantitative interpretation of results from pure functionals, OPBE is still a suitable choice for our study, which primarily focuses on analyzing trends related to the changes in m and peripheral substituents.

Table 6.2 UDFT/cc-pVTZ adiabatic relative energies, $\Delta E_{CS-X} = E_X - E_{CS}$, where CS is the closed-shell singlet solution and X corresponds to the triplet (T) or open-shell singlet (OSS) state (in eV), and $\langle S^2 \rangle$ represented in parenthesis for Chichibabin hydrocarbon derivatives with m from 1 to 5 and H (**1**) as exocyclic substituent.

| | OPBE | | | | LC-OPBE | | | | ωB97X-D | | | |
| | OSS | | T | | OSS | | T | | OSS | | T | |
	ΔE	$\langle S^2 \rangle$	ΔE	$\langle S^2 \rangle$	ΔE	$\langle S^2 \rangle$	ΔE	$\langle S^2 \rangle$	ΔE	$\langle S^2 \rangle$	ΔE	$\langle S^2 \rangle$
$\mathbf{1}_1$	0.00	0.0	1.39	2.0	0.00	0.0	1.25	2.0	0.00	0.0	1.37	2.0
$\mathbf{1}_2$	0.00	0.0	0.44	2.0	−0.40	1.2	−0.16	2.2	−0.14	0.9	0.08	2.1
$\mathbf{1}_3$	−0.09	0.9	−0.02	2.0	−1.20	1.3	−1.15	2.2	−0.84	1.1	−0.81	2.1
$\mathbf{1}_4$	−0.31	1.0	−0.30	2.0	−2.07	1.3	−2.03	2.3	−1.62	1.1	−1.61	2.1
$\mathbf{1}_5$	−0.43	1.0	−0.43	2.0	−2.94	1.3	−2.93	2.3	−2.35	1.1	−2.35	2.1

To further assess the diradical character of the GS of the $m = 2$ system, we compared OPBE and ωB97X-D with CASSCF(6,6)/cc-pVDZ//QCISD/cc-pVDZ results. The frontier orbitals for each of these methods are shown in Figure 6.2. When examining both the planar and distorted optimized QCISD/cc-pVDZ geometries, CASSCF(6,6)[a] indicates that the planar structure is 0.33 eV more stable than the distorted one. Moreover, the dominant configuration is the 111000 with the corresponding occupations being 1.93, 1.91, 1.88, 0.12, 0.09, and 0.06. These findings suggest that the GS likely adopts a closed-shell singlet structure.

As has been discussed, both methodologies are justified in the context of each research article. However, to bridge the findings from both studies, we examined the effect of increasing the oligomer length on the amount of Baird-aromatic character. Thus, for a proper comparison, we repeated the electronic structure single-point calculations for tetracyanoquinodimethane and extended chain derivatives with m = 1 to 5 (hereafter denoted as $\mathbf{5}_{1-5}$, following the nomenclature substituent$_m$) at B3LYP/6-311+G(d,p) level of theory. While the discussion of the results relative

---

[a]A calculation using CASSCF(8,8)/cc-pVTZ basis set was also performed. The results using both active spaces and basis sets showed consistent data.
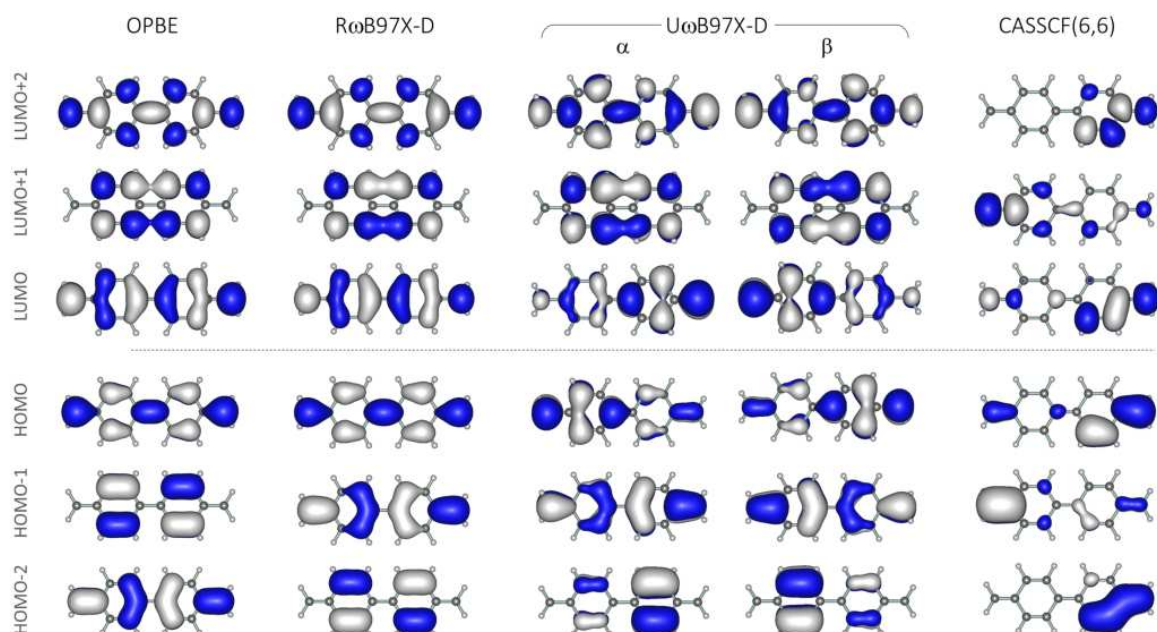
Figure 6.2 Frontier molecular orbitals of system $\mathbf{1}_2$ at OPBE/cc-pVTZ, ωB97X-D/cc-pVTZ, and CASSCF(6,6)/cc-pVDZ//QCISD/cc-pVDZ levels of theory.

to the structure-aromaticity relationship will be done in the next section, these new calculations allow us to assess methodological differences and examine the extent to which conclusions from the second paper (Section 4.2) are also valid when using B3LYP with the 6-311+G(d,p) basis set. Table 6.3 lists the OSS and T state energies relative to CS, along with the MCI values for the central ring in the three electronic states studied. As explained in Section 4.2, centrally located rings are the most aromatic of each system.

Table 6.3 Adiabatic relative energies, $\Delta E_{\text{CS}-\text{X}} = \text{E}_\text{X} - \text{E}_{\text{CS}}$, where CS is the closed-shell singlet and X corresponds to the triplet (T) or open-shell singlet (OSS) state (in eV), and MCI aromaticity values for the CS, OSS, and T states for systems $\mathbf{5}_{\mathbf{1-5}}$.

| | OPBE/cc-pVTZ | | | | | B3LYP/6-311+G(d,p) | | | | |
	OSS	T	MCI_{CS}	MCI_{OSS}	MCI_{T}	OSS	T	MCI_{CS}	MCI_{OSS}	MCI_{T}
$\mathbf{5}_1$	0.00	0.84	0.021	—	0.044	0.00	0.76	0.017	—	0.047
$\mathbf{5}_2$	0.00	0.27	0.028	—	0.045	−0.10	0.06	0.025	0.030	0.046
$\mathbf{5}_3$	−0.08	−0.02	0.040	0.049	0.054	−0.40	−0.37	0.038	0.051	0.056
$\mathbf{5}_4$	−0.19	−0.18	0.046	0.054	0.055	−0.64	−0.63	0.045	0.055	0.056
$\mathbf{5}_5$	−0.26	−0.25	0.052	0.056	0.057	−0.77	−0.76	0.052	0.057	0.058

6.1 Electronic Nature of S_0, S_1, and T_1 of Pro-Aromatic Quinoidal Systems

Interestingly, B3LYP energies have similar behavior to that presented by long-range corrected functionals in systems $\mathbf{1_{1-2}}$, with the switch from having CS to OSS ground state occurring for $m = 2$. Regarding aromaticity, MCI results obtained with both methodologies are in general very similar. The main differences are seen in MCI_{CS} values of systems with $m \leq 3$. For $\mathbf{5_{1-3}}$ systems, the OPBE/cc-pVTZ aromaticity values are slightly higher, and differ less from the corresponding MCI_{T} values, than those of the B3LYP/6-311+G(d,p) approach.

Scope

Overall, including both works, we conducted a thorough investigation into how various structural modifications affect the electronic structure. All of these structural variations are summarized in pannels b-d of Figure 6.3. We examined symmetrically substituted central rings of sizes ranging from four to ten members (n-MRs), focusing on $n = 5$, 6, 9, and 10. Notably, the different sizes come with a variation of the oxidation state of the central moiety, which is neutral for even-numbered rings and charged (either -1 or +1) for odd-numbered rings. The exocyclic substituents were positioned opposite to each other, similar to the *para* position in a 6-MR. Two primary peripheral substitutions were explored: either dicyanomethylene ($\mathbf{nR}$s) or a combination of a thiophene ring with dicyanomethylene, denoted as DT for dicyanomethylene-thiophene ($\mathbf{nRT}$s). With DT, the aim is to create an extended delocalized system. We further diversified our study by incorporating 7-MRs and heterocyclic 4-MRs and varying the exocyclic substitution with different electron-donating groups (EDG) and electron-withdrawing groups (EWG). In the case of 4-, 5-, 6-, and 7-MRs, we considered these groups at the 2,4-, 2,5-, *para*- (1,4-), and 2,5- positions (see blue atom labels in Figure 6.3), respectively. For the 5- and 6-MRs, we also looked into additional exocyclic substitution patterns. Finally, we checked the effects of elongating a 6-MR oligomer with various substituents (X), exploring chain lengths (m) from 1 to 5 units ($\mathbf{X}_m$ systems).

Stability of Singlet and Triplet Open-Shell Forms

As it has been mentioned in the introduction and extensively discussed in Chapter 4, quinoidal pro-aromatic molecules can exhibit small, and even negative, energy gaps between singlet and triplet states, or singlet closed-shell and singlet open-shell states. The latter is calculated either as the difference between the KS-DFT closed-shell (CS) and open-shell (OSS) solutions: $\Delta E_{\text{CS-OSS}}$, or the KS-DFT singlet GS and the TDDFT
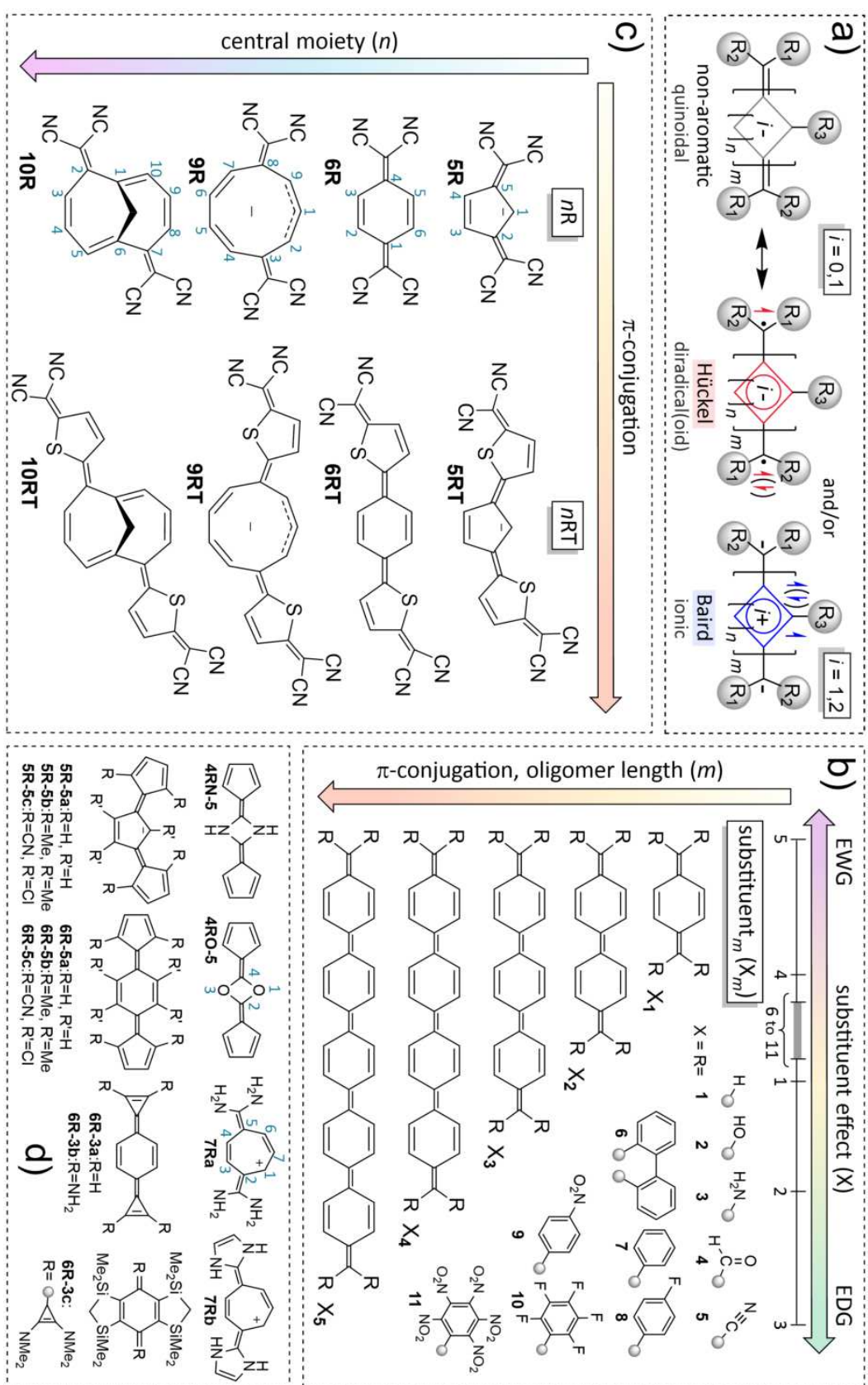
Figure 6.3 Pro-aromatic quinoidal systems. a) Quinoidal, radical, and ionic forms. In b-d) systems are grouped by structural alterations. b) Oligomer length and substitution (Section 4.2). c) and d) 4 to 10-MR with different substitutions (Section 4.1).

6.1 Electronic Nature of S_0, S_1, and T_1 of Pro-Aromatic Quinoidal Systems

S_1 state: ΔE_{S_1}. We focus the discussion on energy differences between minima on the PES, thus all values discussed are adiabatic gaps.

In systems with $n > 4$ and $m = 1$ (including **nRT**s because we consider the thiophene moiety as part of the DT exocyclic substituent), the ΔE_{S_0-T} range from 1.35 eV (31.1 kcal/mol), in **6R-3b**, to -0.78 eV (-18.0 kcal/mol), in **6R-5b** (See Table A.1 in Appendix A for detailed results). In most cases, the ΔE_{S_0-T} consistently remain below 0.85 eV, and the mean value excluding the two systems with negative gaps is 0.70 eV. In the case of **6RT**, **10RT**, **6R-5b**, and **6R-5c**, the ΔE_{S_0-T} is especially low, with values under 0.22 eV (5 kcal/mol), and even negative for the latter two. Regarding the ΔE_{S_1}, for systems with less than two repeated central units, the values tend to be around 1.0 eV higher than those of ΔE_{S_0-T}, except **9R** and **6R-3b** which are 0.2 eV lower (Table A.1). This implies that in general, the triplet state is more stabilized than the optimized singlet excited state obtained at TD-B3LYP level of theory.

A key aspect for the potential applications of these systems is establishing whether they possess CS or OS singlet ground state. For systems with $m \leq 2$, we observed that the S_0 is closed-shell in most of the cases. However, for molecules **6RT**, **6R-5b**, and **6R-5c** the open-shell singlet was found to be lower in energy. For instance, in **6RT**, the $\Delta E_{CS\text{-}OSS}$ is -0.07 eV and this state has an $\langle S^2 \rangle$ value of 0.723. In systems **6R-5b**, and **6R-5c** the $\Delta E_{CS\text{-}OSS}$ are -0.78 and -0.44 eV and $\langle S^2 \rangle$ are 1.033 and 1.062, respectively. In the last two cases, the open-shell singlet and triplet states are degenerate.

In systems with extended π-conjugation, $m \geq 3$, it is observed that generally the ground state is the open-shell singlet (Figure 1 of the article in Section 4.2), with the only exception of the amino substituted **3**$_3$, as shown in Table A.4 in Appendix A. This system has a CS S_0, and the $\Delta E_{CS\text{-}OSS}$ of **3**$_4$ is only -0.09 eV. The NH_2 substituent is the strongest EDG considered in our study and together with the hydroxyl substituted (**2**$_m$), both are the systems showing less stabilization of the diradical forms. In contrast, phenyl-functionalized ligands, in systems **6-11**, help the stabilization of these diradical forms. Beyond the particular effect of each peripheral substituent, a consistent correlation is observed where both the $\Delta E_{CS\text{-}OSS}$ and $\Delta E_{CS\text{-}T}$ decrease as the system length increases. This trend reaffirms the findings from other studies on poly-p-phenylenes, related oligomers, and polyacenes [513–516]. Generally, the OSS is more stabilized than the T state, with $\Delta E_{CS\text{-}OSS}$ taking larger negative values than $\Delta E_{CS\text{-}T}$. This stabilization persists until longer chains with $m = 5$ are

considered, at which point the OSS and T states become degenerate. This degeneracy is attributed to the diradical electrons primarily located at the extremes of the chain, which do not interact over these longer distances. As a result, the singlet and triplet configurations become energetically equivalent.

The trends mentioned in the above text, driven by different substituent types, ring sizes, and chain lengths, clearly illustrate how changes in molecular structure can significantly alter the energies of different states. To better understand the impact of structural modifications on the properties, including ΔE_{S_0-T} or ΔE_{S_1}, we used geometric, spin density, charge distribution, delocalization indices, and aromaticity analyses. Each of these methods led to consistent results regarding the electronic nature of these systems. Therefore, given their agreement, and to avoid repetition, we will focus on the discussion of the aromaticity results. Furthermore, the determination of aromaticity is key to unraveling the potential of these pro-aromatic quinoidal systems for targeted applications.

Determination of Aromatic Character

The low energy gaps exhibited by Kekulé diradicaloids can be partially attributed to the aromatic stabilization of the central ring in the triplet and OSS states. The excited state or open-shell aromaticity of the systems under consideration is often influenced by those resonance structures with Hückel-aromatic character in the central ring, represented by the Lewis structure highlighted in red in Figure 6.3a. Yet, the electronic nature of the excited states of TMTQ (here **10RT**) has been a matter of debate. First, the T_1 state of this molecule was described as Baird aromatic [257]. Later, the detailed computational characterization by Jorner *et al.* [109] pointed instead to a triplet state having a hybrid Hückel-Baird aromatic character, with a low contribution (about 12%) of the Baird form. Despite the existing evidence, more recent investigations [258] claim that the S_1 state, with the same configuration as T_1, of **10RT** is predominantly Baird. Given the conflicting views and motivated by the new experimental evidence, we conducted the study presented in Section 4.1. Additionally, the data from Section 4.2 serves as an extension to 4.1, because it adds an item that was unexplored which is the effect of the chain length.

To characterize the aromaticity and determine the extent of Hückel and Baird character in our systems, we used established reference systems with known aromatic character, represented in Figure 6.4. These model systems resemble either the Hückel

6.1 Electronic Nature of S_0, S_1, and T_1 of Pro-Aromatic Quinoidal Systems

or Baird Lewis structures of the central rings shown in Figure 2 of Section 4.1 and Figure 6.3a). These structures show the differences in electron distribution present in each of these forms: in Hückel structures, unpaired electrons are located outside the central ring, whereas Baird forms are the result of a two-electron transfer from the central ring to peripheral moieties with the unpaired electrons lying in the central ring. This results in electron counts of $4n+2$ or $4n$ in the central ring for Hückel and Baird forms, respectively, both leading to more aromatic structures than closed-shell forms, albeit with distinct electronic configurations. To simulate these Hückel and Baird aromaticities, we considered simple rings and their corresponding doubly oxidized cations or anions in the S_0 and T_1 states. The aromaticity values are listed in Table A.2 in Appendix A.
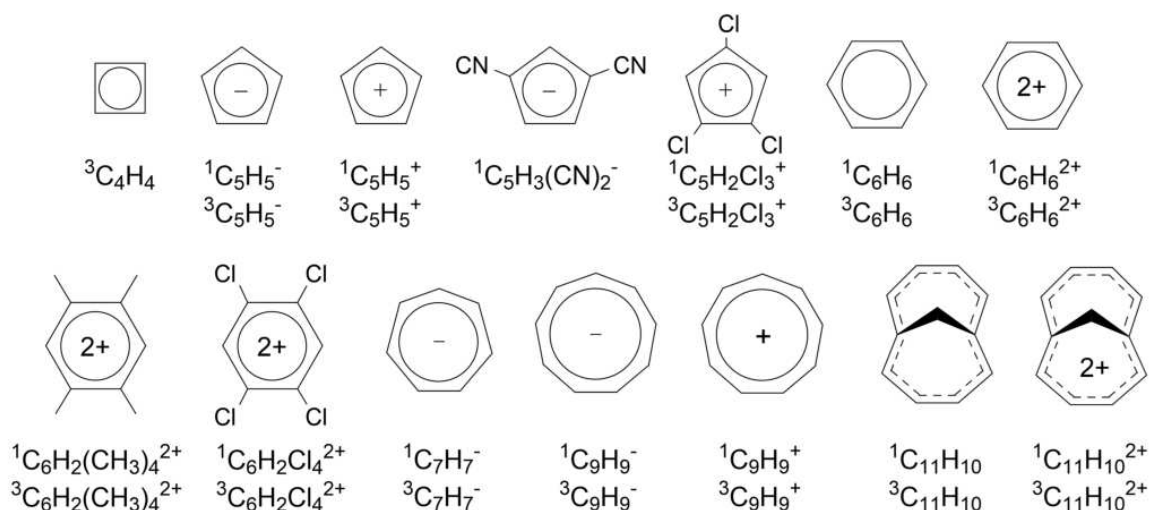

Figure 6.4 Representation of the reference molecules considered in the study.

Unfortunately, the total values (non-spin-separated) of the indices do not offer insightful differentiation between Hückel and Baird forms. For example, the Hückel aromatic $^1C_6H_6$ and Baird aromatic $^3C_6H_6^{2+}$, exhibit FLU values of 0.0000 and 0.0099, and MCI values of 0.0717 and 0.0786, respectively. This indicates that both are aromatic, but does not provide any distinction between the two types of aromaticity. As it has been explained in the introduction and methodology chapters, the aromaticity indices for open-shell wavefunctions can be separated to yield more informative calculations of $|\Delta \mathrm{IND}|/\mathrm{IND}$ as described in Eq. (2.52). Low values of this ratio indicate a predominance of Hückel aromatic character, while larger values suggest a greater Baird aromatic character. Unfortunately, this approach cannot be applied to regular TDDFT calculations. Thus it is not possible to directly determine the Baird character of S_1. Instead, given that the spatial distribution of electrons in S_1 is homologous to

the one in T_1, we focus only on triplet results and consider that the S_1 presents a similar aromatic character. This approximation seems adequate in our case since both states correspond to the same HOMO-LUMO excitation. Moreover, we corroborated that by analyzing the partial charges of the central ring fragment and the energies of Hückel and Baird forms computed with constrained DFT (C-DFT) [517], obtaining consistent results for the S_1 and T_1 states (Figure A.2 in Appendix A).

Focusing on the triplet aromaticity results, there is a good agreement among the various aromaticity indices used in our study, encompassing geometric (HOMA and BLA), electronic (BOA, FLU, I_{ring}, MCI, and AV1245), and magnetic measures (NICS, GIMIC ring currents, and current strengths), as detailed in the supplementary information on page 309. Despite some minor exceptions, the different indices give consistent results (*e.g.* a $R^2 = 0.84$ correlation between FLU and $MCI^{1/n}$, as shown in Figure A.1). Given this, we will center our analysis primarily on the FLU results. The $|\Delta FLU|/FLU$ values for the triplet states, which were used as references for Baird aromaticity, are listed in Table 6.4.

Table 6.4 Dissection of FLU into spin parts for reference systems in the T_1 state computed at the B3LYP/6-311+G(d,p) level of theory.

system	FLU	FLU-α	FLU-β	$|\Delta FLU|$	$|\Delta FLU|/FLU$
C_4H_4	0.0100	0.0032	0.0205	-0.0173	1.7305
$C_5H_5^-$	0.0188	0.0042	0.0465	0.0423	2.2466
$C_5H_5^+$	0.0085	0.0001	0.0373	0.0373	4.3826
$C_5H_2Cl_3^+$	0.0169	0.0020	0.0424	0.0403	2.3916
C_6H_6	0.0238	0.0182	0.0316	0.0134	0.5648
$C_6H_6^{2+}$	0.0099	0.0003	0.0465	0.0462	4.6928
$C_6H_2(CH_3)_4^{2+}$	0.0155	0.0011	0.0469	0.0458	2.9504
$C_6H_2Cl_4^{2+}$	0.0156	0.0029	0.0376	0.0347	2.2265
$C_7H_7^-$	0.0013	0.0014	0.0013	0.0001	0.0499
$C_9H_9^-$	0.0014	0.0011	0.0019	0.0008	0.5758
$C_9H_9^+$	0.0013	0.0003	0.0062	0.0059	4.3868
$C_{10}H_{10}$	0.0180	0.0148	0.0219	0.0070	0.3899
$C_{10}H_{10}^{2+}$	0.0058	0.0029	0.0145	0.0116	1.9993

Most of those systems expected to have Baird character demonstrate significant $|\Delta FLU|/FLU$ values, typically greater than 1.7. In contrast, $^3C_7H_7^-$ (the cyclohepta-trienyl anion in a triplet state), contrary to the expected, shows a near zero value, attributable to the negligible difference between the magnitude of the α and β compo-

nents. Given the anomalous value, we decided to exclude $^3\text{C}_7\text{H}_7^-$ as a reference. Instead, we estimated the Baird percentage not with the $|\Delta\text{FLU}|/\text{FLU}$ but using charges, spin densities, and C-DFT energies.

Now that we have thoroughly reviewed the reference systems and key aspects for interpreting the forthcoming results, we discuss the main findings of publications presented in Chapter 4. For comprehensive details, the reader is referred to the respective sections within that chapter. This discussion will specifically focus on the impact of structural modifications on the electronic structure and aromatic character of quinoidal molecules. A summary of the FLU aromaticity results dissected into its α and β components and $|\Delta\text{FLU}|/\text{FLU}$, along with the computed %Baird character, for the T_1 of the most relevant quinoidal systems studied is presented in Table 6.5.

In the following analysis, we evaluate the FLU values and other pertinent results, categorizing the structural variations into distinct types: the size and charge of central rings, the expansion of the π-system via the addition of DT moieties and the increase in the number of m units in the 6-MR oligomer, as well as the impact of substituents, specifically EDGs and EWGs. Each of these categories provides unique insights into the relationship between molecular structure and the resultant electronic and aromatic properties.

We initiate our examination with the different ring sizes in the **nR** series, comprising compounds with n of 5, 6, 9, and 10 members. Interestingly, no linear trend is observed in the aromatic characteristics as ring size varies. Instead, we noted that Baird character is significantly more pronounced in rings with odd n (**5R** and **9R**), compared to even-numbered ones (**6R** and **10R**), as reflected by their higher %Baird values. A closer look at the values reported in Table 6.5 reveals that **10R** has %Baird based on FLU values comparable to **9R**. However, this observation is not in good agreement with the %Baird calculated from QTAIM charges, spin densities, and C-DFT relative energies. Considering the consistency across multiple indicators, it is plausible that the FLU values for **10R** might be biased. And we potentially attribute that to the relatively low $|\Delta\text{FLU}|/\text{FLU}$ value of 1.9993 for the $\text{C}_{10}\text{H}_{10}^{2+}$ reference, approximately half of the values obtained for other 5, 6, and 9-MR systems, which are around 4.

Simultaneously, the charge of these rings plays a pivotal role in determining their aromaticity. Neutral rings, such as **6R** and **10R**, display a tendency towards Hückel aromaticity. This is contrasted with the charged ring species **5R** and **9R**, which exhibit higher %Baird aromatic character. This differentiation underscores the significant

Table 6.5 FLU, α- and β-FLU, $|\Delta\text{FLU}|/\text{FLU}$ and %Baird values for the quinoidal systems studied in 4.1 and 4.2 in the T_1 state computed at the B3LYP/6-311+G(d,p) level of theory. The labels 'A', 'B', and 'C' in 5_2 to 5_5 denote different ring types: 'A' are the outermost rings, while 'B', and 'C' are the central rings, as illustrated in Figure 6.5, which appears later in this section.

Molecule	FLU	FLU-α	FLU-β	$|\Delta\text{FLU}|$	$|\Delta\text{FLU}|/\text{FLU}$	%Baird[a]
5R	0.0124	0.0026	0.0315	0.0288	2.3312	53.19
6R	0.0034	0.0016	0.0056	0.0040	1.1592	24.70
9R	0.0104	0.0029	0.0224	0.0195	1.8623	42.45
10R	0.0068	0.0044	0.0106	0.0062	0.9112	45.58
5RT	0.0148	0.0058	0.0268	0.0211	1.4177	32.35
6RT	0.0030	0.0025	0.0034	0.0010	0.3201	6.82
9RT	0.0300	0.0270	0.0337	0.0066	0.2214	5.05
10RT	0.0046	0.0041	0.0052	0.0010	0.2225	11.13
5R-5a	0.0123	0.0025	0.0295	0.0269	2.1923	50.02
5R-5b	0.0141	0.0049	0.0288	0.0239	1.6961	38.70
5R-5c	0.0178	0.0070	0.0332	0.0263	1.4766	33.69
6R-5a	0.0034	0.0023	0.0045	0.0021	0.6242	13.30
6R-5b	0.0021	0.0021	0.0021	0.0000	0.0002	0.01
6R-5c	0.0037	0.0035	0.0039	0.0004	0.1114	2.37
6R-3a	0.0120	0.0200	0.0065	0.0135	1.1239	23.95
6R-3b	0.0148	0.0300	0.0052	0.0248	1.6775	35.75
6R-3c	0.0059	0.0114	0.0026	0.0088	1.4777	31.49
4RN-5	0.0101	0.0115	0.0203	0.0088	0.8696	—
4RO-5	0.0180	0.0047	0.0378	0.0331	1.8453	—
7Ra	0.0085	0.0133	0.0061	0.0072	0.8491	—
7Rb	0.0087	0.0125	0.0060	0.0065	0.7431	—
5_2 (A)	0.0049	0.0025	0.0079	0.0054	1.0984	23.41
5_3 (A)	0.0058	0.0028	0.0097	0.0069	1.1946	25.46
5_3 (C)	0.0023	0.0018	0.0027	0.0009	0.3797	8.09
5_4 (A)	0.0062	0.0029	0.0105	0.0076	1.2378	26.38
5_4 (B)	0.0022	0.0018	0.0025	0.0007	0.3223	6.87
5_5 (A)	0.0063	0.0029	0.0109	0.0080	1.2676	27.01
5_5 (B)	0.0022	0.0018	0.0026	0.0008	0.3606	7.68
5_5 (C)	0.0019	0.0017	0.0019	0.0002	0.0969	2.06

[a]Entries where results were not reported are due to unreliability, arising from the reference compound exhibiting a very low $|\Delta\text{FLU}|/\text{FLU}$ value, attributed to closely similar FLU-α and FLU-β values.

influence of the ring's charge on its aromatic nature. We hypothesized that this is due to the less pronounced structural reorganization required in the charged species. In

these cases, it is required a lower variation in the number of π-bonds from quinoidal S_0 to achieve the Baird type T_1/S_1 (see Figure 2 in Section 4.1).

The inclusion of DT units to the original **nR** series leading to **nRT** compounds significantly impacts the aromaticity of these molecules. The addition of external thiophene units leads to an increase in conjugation, thereby stabilizing the unpaired (diradical) electrons at the exocyclic arms. Thus, this extended conjugation results in a reduction of the Baird character in the T_1 and S_1 states, compared to the **nR** counterparts. In the case of %Baird based on FLU values, this reduction ranges from 18 to 37%. This finding highlights a complex interplay between conjugation length and the type of aromaticity exhibited.

An alternative to evaluate the effect of extending the π-system length is the analysis of increasing m in the 6-MR oligomers. For this analysis, we categorized the 6-MRs based on their positions: type A for the outermost rings adjacent to terminal substituents, type B for rings in between terminal and other central rings, and types A' or C for the central rings in systems with odd m. These classifications are illustrated in Figure 6.5. Before examining the Baird character, we first assessed the overall aromatic nature of these Chichibabin systems across the triplet, closed-shell, and open-shell singlet states. We found that for $m \leq 2$, the OSS solution converges to the CSS state, for larger m values we obtained different solutions, so we can only evaluate the OSS states for $m > 2$. In general, a subtle increase or maintenance of aromatic character is observed in each ring type as m increases, as evidenced by marginally higher or similar MCI (see Figure 6.5) and FLU (refer to Table 6.5) values. Focusing on Baird's character, we note a decrease in the %Baird of central rings (types A' and C) with increasing m. Conversely, there is a slight increase in Baird character for type B rings, and a more noticeable enhancement in the outermost type A rings, reaching up to 27% Baird character.

The final aspect of our investigation focuses on various exocyclic substitution patterns. We explored different substitutions using negatively charged 5-MR, neutral 6-MR, and cationic 7-MR central rings, incorporating various electron-withdrawing groups (EWG) and electron-donating groups (EDG) at different positions (as depicted in panels b and d of Figure 6.3). Our modifications fell into two primary categories: substitutions at the lateral positions and substitutions elsewhere on the central ring.

A convenient tool for analyzing the effect of substituents on molecular systems is the inspection of spin density maps, which serve as reliable indicators of Baird

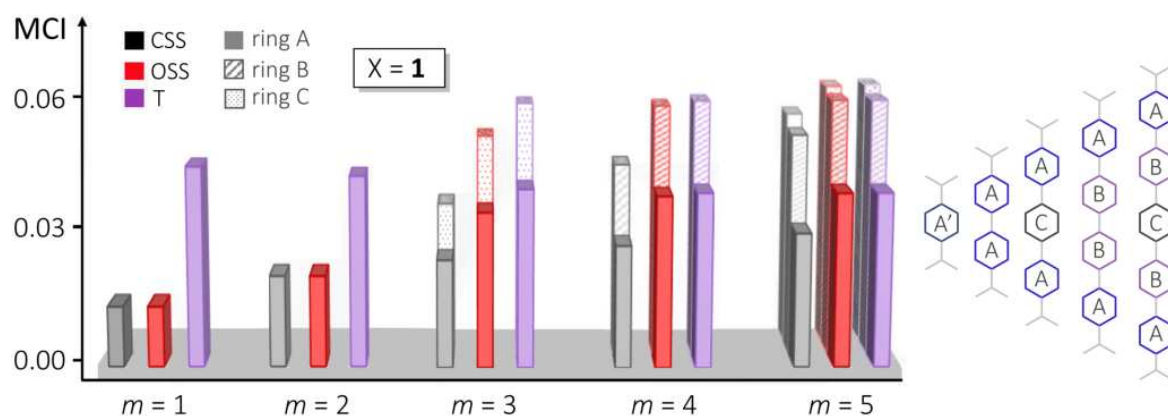**Figure 6.5** MCI aromaticity values for A, B, and C rings of system $\mathbf{1}_m$, with $m = 1\text{-}5$, in the CSS, OSS, and triplet states at the OPBE/cc-pVTZ level of theory.

character. A significant spin density concentrated on the central ring suggests Baird aromaticity. These findings are concisely summarized in Figure 6.6. We observed that attaching EDGs to the central 5-MR and EWGs to the exocyclic 5-MRs (system **5R-5c**) enhanced the Baird character reaching a significant spin density located at the central ring and %Baird value ($> 50\%$). However, this increase was not obtained in the **6R-5c** system, suggesting the difficulty of inducing Baird aromaticity in rings with strong Hückel aromatic characteristics. Shifting the strategy, we considered the possibility of achieving excited-state Baird aromaticity by introducing electrons into an electron-deficient conjugated ring. This led to the design of two compounds with a cationic 7-MR central ring, substituted with EDGs (**7Ra** and **7Rb**). Thus, a combination of an electron-deficient conjugated central ring with electron-donor exocyclic substitutions emerged as a promising approach for achieving Baird aromaticity.

Finally, examining lateral substitutions in 6-MR oligomers revealed that aromatic substituents and EWGs tend to stabilize the diradical(oid) Hückel form over the closed-shell forms, in contrast to EDGs. These systems also show very low spin density values in the central rings indicating strong Hückel aromatic character.

Guidelines for increasing the Baird character or stabilizing the biradical(oid) states

Through our extensive investigation, we have garnered valuable insights into tuning the Baird and Hückel characteristics of quinoidal systems. First, we should note that enhancing the Baird aromatic character in symmetrically substituted quinoidal compounds is challenging. Nevertheless, effective strategies involve designing molecules
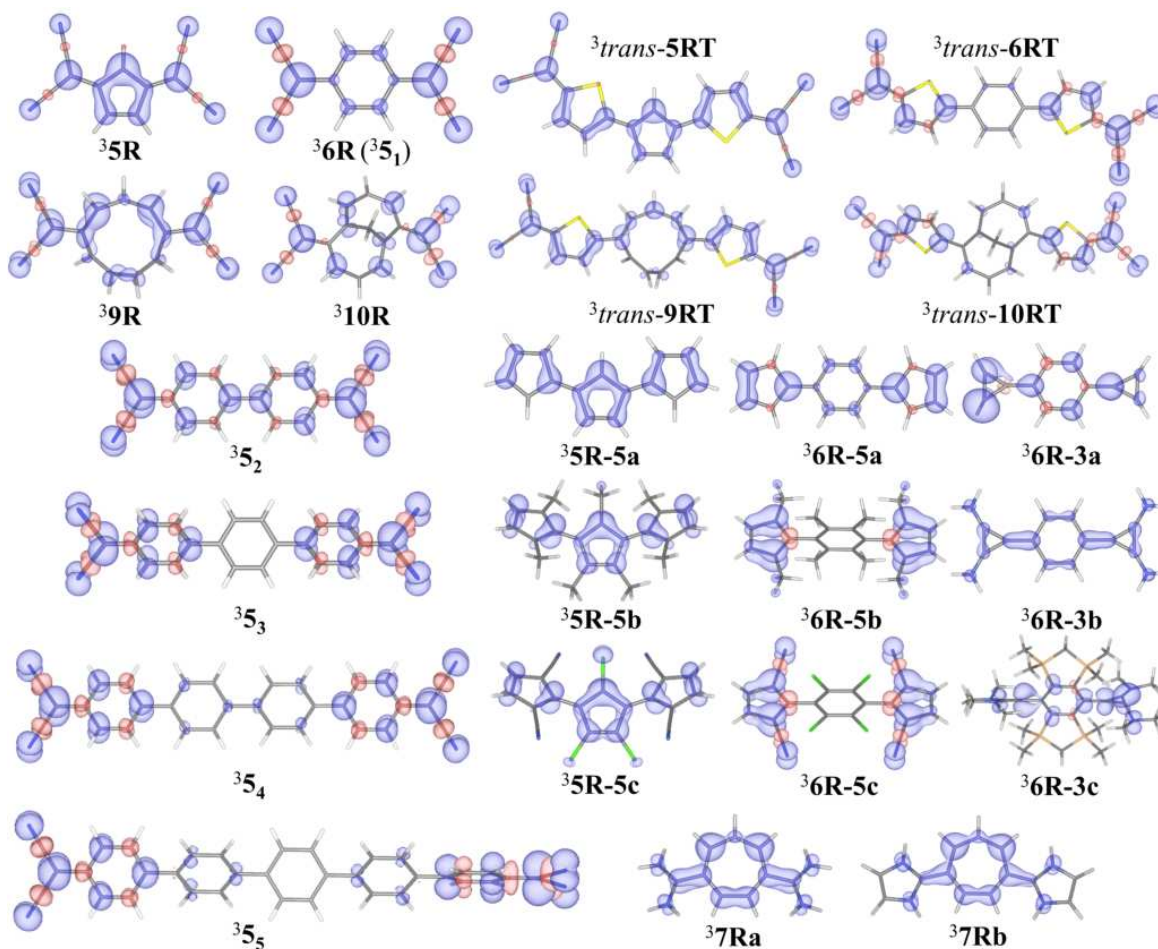
Figure 6.6 Spin density of most relevant studied systems, at B3LYP/6-311+G(d,p) level, in the T_1 state. The isodensity shown corresponds to a value of 0.005 e/bohr^3. The positive and negative spin values are represented in blue and red, respectively.

with a small, negatively charged central ring, coupled with small exocyclic substituents functionalized with EWG and additional EDG attached to the central (Figure 6.7a) ring to compensate for electron density loss in this central ring upon excitation. An alternative approach is the combination of an electron-deficient conjugated central ring with electron-donating groups on the periphery (Figure 6.7b), facilitating charge transfer from the external substituents to the central moiety. Crucially, the choice of exocyclic substituents should not favor the stabilization of the unpaired (biradical or biradicaloid) electrons at these peripheral positions. Therefore, including extended *pi*-conjugated chains is not an effective strategy. Additionally, our observations indicate that Baird aromaticity is generally more pronounced in the S_1 than in the T_1, highlighting subtle differences in their electronic properties.
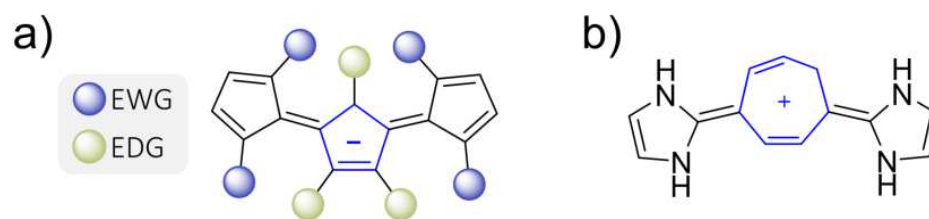
Figure 6.7 Substituents proposed to increase the Baird character.

In contrast, stabilizing the Hückel form and thus fostering stable biradical(oid) states requires longer chain lengths. However, beyond a linear oligomer length of m = 4 units, stabilization reaches a plateau since the unpaired electrons become more localized at the chain ends and interact less over extended distances. The stabilization of unpaired electrons is enhanced by more conjugated external substituents. Additionally, EWGs attract the unpaired electrons also promoting the biradical state. Furthermore, employing non-charged central rings minimizes charge transfer between the central and side moieties, thus facilitating the formation of these states.

6.2   Exploring Aromaticity–Property Relationships in (Sub)Phthalocyanines

This is the first of four sections, each dedicated to systems with topologically challenging features for aromaticity characterization. We begin with the discussion of the study presented in Section 5.1.1, where we analyzed the aromaticity variations within (sub)phthalocyanines and related structures, alongside their correlation with changes in the UV-visible spectra and HOMO-LUMO energy gaps. The investigated systems include: (sub)phthalocyanine, (sub)porphyrin, (sub)porphyrazine, and tri- and tetrabenzoporphyrin. These systems can exhibit multiple pathways with delocalized electrons (see Figure A.3 in Appendix A), offering distinctive electronic and optical properties desirable in various applications.

The characteristics of these systems give rise to two primary challenges in the computational assessment of their aromaticity. First, as highlighted in Section 1.3.2, the choice of the DFA critically impacts the electronic structure predictions. Second, the substantial ring sizes of these molecules hinder the use of MCI, the most reliable electronic aromaticity index [147, 148]. These factors, combined with the chemical complexity of (sub)phthalocyanines, not only complicate the interpretation of the

results but also make it difficult to draw direct structure-property correlations, unlike what is often possible with smaller/simpler aromatic or antiaromatic monocyclic compounds. Our discussion will thus begin by summarizing the methodology used to select the CAM-B3LYP/cc-pVTZ level of theory, proceeding with the research scope, absorption spectra, HOMO-LUMO and singlet-triplet energy gaps, and aromaticity results, concluding with an examination of the correlations among spectroscopic and aromatic properties.

Choice of the DFT Functional

To select an optimal DFA for geometry optimization and the calculation of UV-Vis absorption spectra and aromaticity, we have taken into account findings from previous literature alongside a comparison of selected functionals. Preceding investigations [76, 144–146, 518] highlighted the superior accuracy of range-separated functionals, such as CAM-B3LYP, in characterizing aromatic systems due to reduced delocalization errors when compared to commonly used GGA functionals like B3LYP. Taking this into account, we also examined the performance of various DFAs, including B3LYP, CAM-B3LYP, ωB97X, M06-2X, TPSSh, and LC-ωHPBE functionals for geometry optimization; and B3LYP, CAM-B3LYP, ωB97x-D, M06-2X, and optimally tuned long-range corrected OT-LC-BLYP[b] for the calculation of the UV-Vis spectra. We compared our computational results with available experimental data for phthalocyanine (**Pc**) and subphthalocyanine (**SubPc**). In both—geometry optimizations and UV-Vis calculation—cases, the basis set used was the cc-pVTZ. Moreover, in the case of UV-Vis analysis we employed the polarizable continuum model to include the solvent effect of tetrahydrofuran (THF), using scrf=(pcm,solvent=THF) keyword, to better reproduce experimental conditions.

X-ray crystal structures of **Pc** [520] and **SubPc** [521] were compared with computed values obtained with DFA/cc-pVTZ. For bond lengths, angles, and—in the case of the contracted system, **SubPc**—bowl-depth distances (P1 and P2) the results are collected in Tables A.5 and A.6 (Appendix A). The mean absolute errors (MAE) of these parameters compared to X-ray data are presented in Table 6.6. Analyzing the MAE data, TPSSh stands out with the lowest MAEs for **Pc** and good performance for **SubPc**, tied with CAM-B3LYP for the second place. Despite a higher MAE for

---

[b]In OT-LC-BLYP, the optimized attenuating parameter (ω) has been obtained minimizing J^* as described in Eq. (2.33). For better performance, the calculation of optimized ω was done without the implicit solvent correction [519]. We obtained optimized ω values of 0.1819 and 0.1937 a.u.$^{-1}$ for **Pc** and **SubPc**, respectively.

Pc, CAM-B3LYP is validated as a robust choice. B3LYP consistently shows reliable results for both systems.

Table 6.6 Mean absolute error of the structural parameters with various DFAs for **Pc** and **SubPc**. Distances are in Ångströms and angles in degrees.

	Pc			SubPc			
	bond lengths	angles	total	bond lengths	angles	P1, P2	total
B3LYP	0.006	0.7	0.26	0.009	0.2	0.06	0.05
CAM-B3LYP	0.007	0.7	0.25	0.009	0.5	0.06	0.09
ωB97X	0.007	0.6	0.21	0.010	0.7	0.08	0.13
M06-2X	0.007	0.7	0.25	0.009	0.7	0.08	0.12
TPSSh	0.004	0.5	0.17	0.008	0.5	0.06	0.09
LC-ωHPBE	0.008	0.6	0.20	0.012	1.0	0.07	0.17

The UV-Vis results, corresponding to the characteristic Q and B bands for this class of compounds, obtained with the five functionals have been compared to the experimental values (see Figure 6.8 and Table 6.7). In all cases, the deviations ($\Delta\lambda$) found are below 74 nm (equivalent to 0.3 eV) for the Q band and 53 nm (equivalent to 0.7 eV) for the B band, aligning with values documented in the literature for computed spectra [522, 523]. All functionals tend to overestimate the experimental energies of both Q and B bands, with the exception of the B band in **SubPc** correctly predicted with B3LYP. In the case of OT-LC-BLYP, while we observe an improvement in the accuracy of predicted λ_{max} values for the B band, its performance for the Q band does not show improvement over other long-range corrected functionals. Consequently, the use of OT-LC-BLYP in this context may not constitute a broadly advantageous strategy. Transitioning to the reproduction of band intensity results, which are proportional to the oscillator (f), it is observed that none of the computational methods accurately capture the correct relative intensity of Q and B bands. This discrepancy is clearly exemplified in Figure 6.8 for CAM-B3LYP.

Although B3LYP stands out as the best candidate among the tested functionals for accurately reproducing excitation energies in **Pc** and **SubPc**, Mewes *et al.* [518] proved the limitations of energy benchmarks, since for Mg-porphyrin B3LYP provided good excitation energies but gave a poor description of the wavefunction in terms of exciton size and electron-hole correlation wavefunction descriptors. In contrast, CAM-B3LYP, despite producing slightly less accurate energies, excels in wavefunction accuracy. Further, CAM-B3LYP is favored for aromaticity characterization due to its reduced
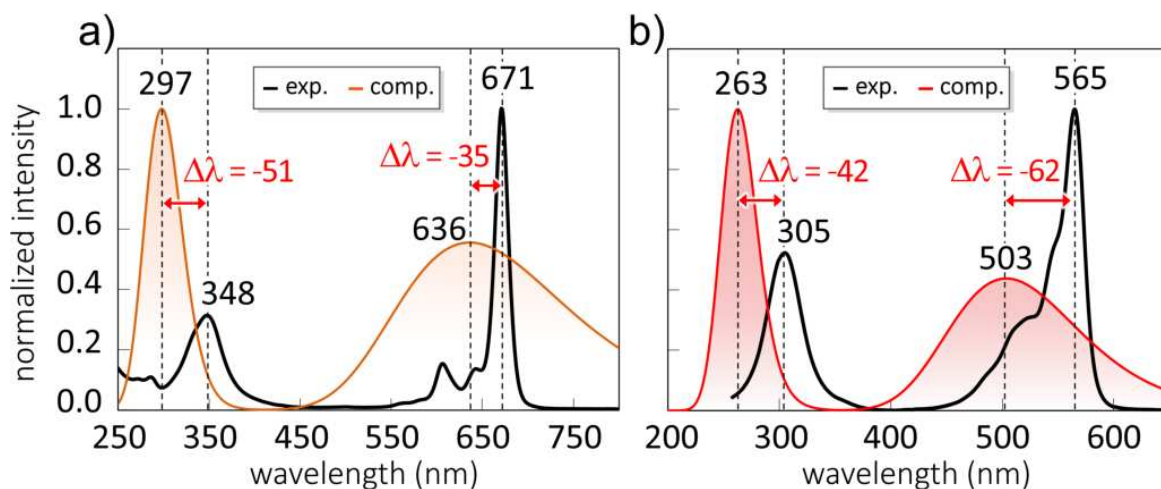
Figure 6.8 Comparison of the computed (CAM-B3LYP/cc-pVTZ) *vs.* experimental absorption spectra for a) **Pc** and b) **SubPc** in THF. See computational and experimental details in Section 5.1.1. The numbers in black correspond to the maximum intensity of the band (λ_{max}), and $\Delta\lambda$, in red, is the difference between experiment and computed values, all in nm.

Table 6.7 Computed wavelengths, λ_{max} (in nm), with the errors compared to experimental data ($\Delta\lambda$), and oscillator strengths (f) for the Q and B bands at DFA/cc-pVTZ PCM=(THF) level of theory, for **Pc** and **SubPc**. The geometries were optimized at CAM-B3LYP/cc-pVTZ level of theory in gas phase.

		Pc			SubPc		
		λ_{max}	$\Delta\lambda$	f	λ_{max}	$\Delta\lambda$	f
Q band	B3LYP	612.8	−58.2	0.619	505.0	−60.0	0.432
	CAM-B3LYP	636.3	−34.7	0.675	503.3	−61.7	0.475
	ωB97x-D	650.0	−21.0	0.667	503.9	−61.1	0.474
	M06-2X	615.3	−55.7	0.698	505.0	−60.0	0.432
	OT-LC-BLYP	630.1	−40.9	0.607	502.8	−62.2	0.434
B band	B3LYP[a]	333.5	−14.5	0.253	304.8	−0.2	0.284
		327.4	−20.6	0.531	—	—	—
	CAM-B3LYP	297.0	−51.0	1.139	262.9	−42.1	0.866
	ωB97x-D	294.8	−53.2	0.956	260.4	−44.6	0.861
	M06-2X	295.2	−52.9	1.124	261.4	−43.6	0.506
	OT-LC-BLYP	316.9	−31.1	0.964	277.7	−27.3	0.557

[a]At B3LYP/cc-pVTZ level of theory, the B_1 and B_2 bands in **Pc** are close in energy, but not degenerate, differing by 6.1 nm (or 0.1 eV).

delocalization errors compared to B3LYP, as supported by other studies [76, 144–146]. Considering these aspects and the acceptable error range of CAM-B3LYP, we opted for CAM-B3LYP/cc-pVTZ approach. Ultimately, this methodology proved to be an

optimal choice in predicting excitation energies as there is a robust correlation between experimental and computed Q and B λ_{max} values across all systems studied, with R^2 values of 0.98 and 0.94, respectively (refer to Figure A.6).

Scope

This study explores the structural variations among Zn coordinated: porphyrin (**P**), porphyrazine (**Pz**), tetrabenzoporphyrin (**TBP**), phthalocyanine (**Pc**), and Zn-subporphyrin (**ZnSubP**); and B-H coordinated: subporphyrin (**SubP**), subporphyrazine (**SubPz**), tribenzosubporphyrin (**TBSubP**), and suphthalocyanine (**SubPc**) systems represented in Figure 6.9b.
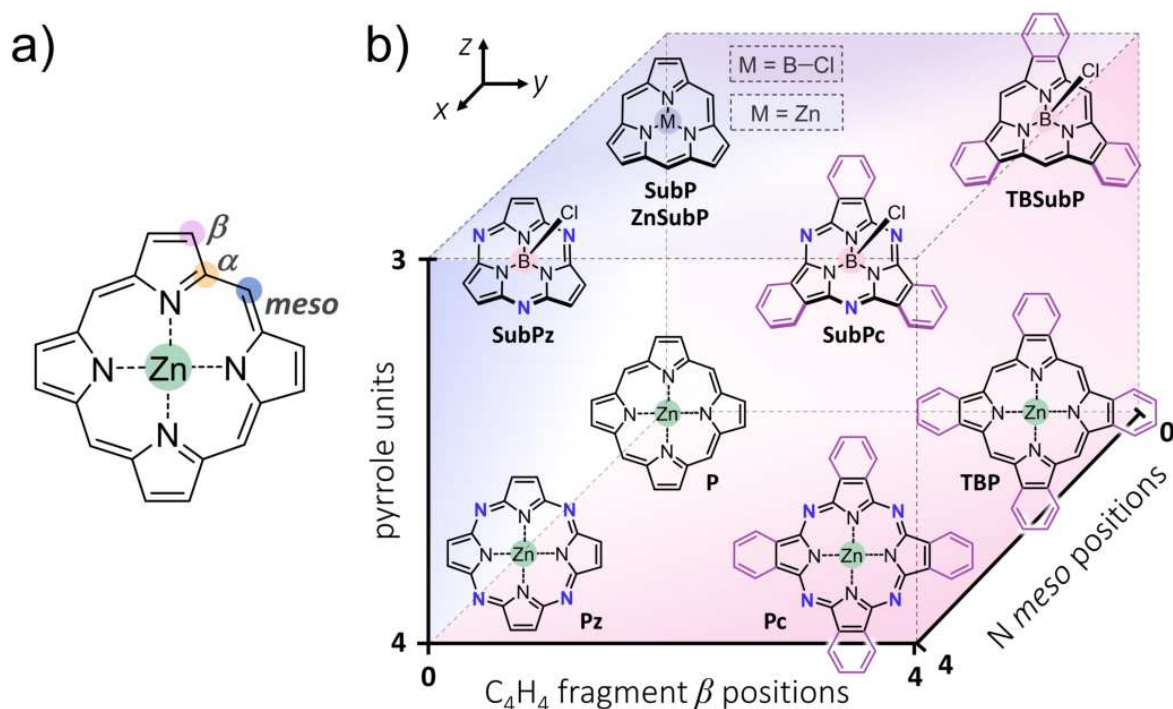
Figure 6.9 Metal- or B-X-coordinated (sub)porphyrin, (sub)phthalocyanine, and variants studied in Section 5.1.1, organized by structural modifications with respect to porphyrin (**P**). The structural differences are highlighted in dark blue (N-*meso*) and magenta (fused 6-MR). In subporphyrin, we considered both central Zn- and B-Cl-coordination.

The selection is based on our aim to elucidate how these key modifications alter the molecules' aromaticity and electronic properties. Specifically, we examine: (*i*) the substitution of CH with N at *meso* positions (x axis in Figure 6.9b); (*ii*) the incorporation of C_4H_4 fragments at β positions to have isoindoles in place of pyrroles (y axis in Figure 6.9b); (*iii*) the reduction of pyrrole or isoindole units from four to three, referred hereafter as 'molecular contraction' (z axis in Figure 6.9b); and (*iv*) the

replacement of a central Zn atom with B-Cl in **SubPc**. This latter modification aims to determine whether the central coordination, different in tetra- or tri-unit systems, plays a critical role in the comparative analysis of these two groups. Our analysis is centered in *i–iii*, intentionally omitting further effects of central atom axial ligation and peripheral substitutions—which affect the π-system, albeit in a more indirect manner—to concentrate on changes directly influencing the π-system.

Absorption Spectra, HOMO-LUMO, and Singlet-Triplet Gaps

In our analysis, we compared the absorption spectra of the different systems considered to reveal the effect of the structural changes discussed earlier. Figure 6.10 represents the computed absorption spectra of a) tetra-unit systems and b) tri-unit systems (with the results for **P** presented in black in both graphs to facilitate a comprehensive comparison). Using **P** as the reference, in panel a) we observe that **Pz**, **TBP**, and **Pc** present a red shift in the Q band, alongside a blue shift in the B band. Conversely, in panel b), the subphthalocyanine derivatives (**SubP**, **SubPz**, **TBSubP**, and **SubPc**) show a blue shift in both the Q and B bands relative to **P**. For a detailed characterization and analysis of the bands, the reader is referred to Section 5.1.1.

The systems explored allow to asses how N-*meso* substitution, the integration of fused benzene rings, and the contraction of the tetra-pyrrole/isoindole forms, influence electronic transitions, leading to observable spectral shifts in Q and B bands. Importantly, as we discussed in Sections 1.3.1 and 5.1.1 these electronic transitions are directly linked to the molecular orbitals involved, as explained by the Gouterman model (Figure 1.17). Specifically, N-*meso* substitution significantly stabilizes the a_{2u} molecular orbital in **Pz** and **Pc**, as well as the a_1 orbital in **SubPz** and **SubPc** (see Figure 1 in Section 5.1.1 and Figures A.7 and A.8). This manifests as a blue shift in the B band of these systems when compared to **P**. Alternatively, the incorporation of C_4H_4 fragments at β positions narrows the gap between the a_{1u} (a_2) and e_g (e) orbitals in **TBP** and **Pc** (**TBSubP** and **SubPc**), which has a greater effect on the Q band, producing a red shift relative to (sub)porphyrin. Finally, all contracted molecules display higher absorption energies in the Q and B bands than their non-contracted counterparts, due to larger energy gaps between their frontier orbitals. These changes affirm the significant role of π-system modifications on their optical properties. Our analysis reveals a robust correlation of the Q λ_{max} with $\Delta\varepsilon_{a_{1u}-e_g}$ ($\Delta\varepsilon_{a_2-e}$), giving an $R^2 = 0.96$; and a relationship between the B λ_{max} and $\Delta\varepsilon_{a_{2u}-e_g}$ ($\Delta\varepsilon_{a_1-e}$) with an $R^2 = 0.92$, as presented in Figure 4 of Section 5.1.1.

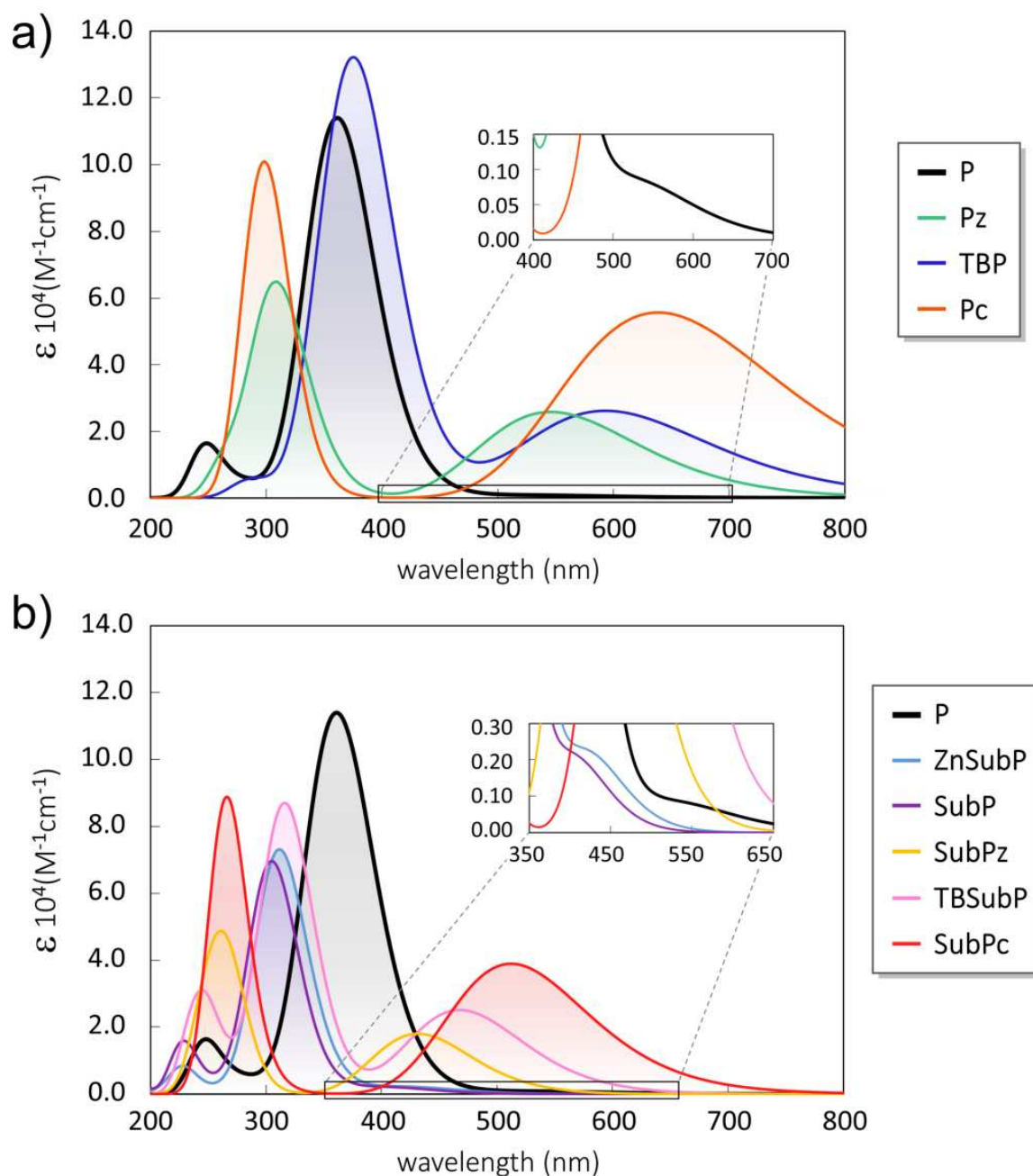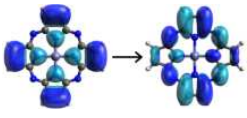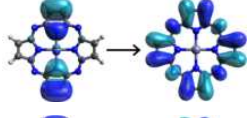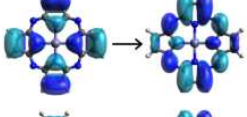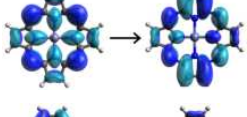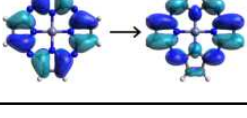**Figure 6.10** CAM-B3LYP/cc-pVTZ absorption spectra of a) tetra- and b) tri-unit systems.

In the case of the B band, although there is a notable correlation, the data points tend to cluster, leading to an uneven distribution across the regression line. This observation highlights the limitations of the Gouterman model, which only focuses on the frontier orbitals (HOMO-1 $\rightarrow$ LUMO, and HOMO $\rightarrow$ LUMO transitions). To address the potential impact of additional transitions, we have extended the Gouterman model to include a broader range of orbitals. Rather than correlating B band's λ_{max}

with $\Delta\varepsilon_{a_{2u}-e_g}$ ($\Delta\varepsilon_{a_1-e}$), we calculated a weighted $\Delta\varepsilon$ that incorporates all orbital transitions involved in the B band. The weighting factors were derived from the transition weights obtained through TDDFT calculations. This approach allowed us to compute a weighted $\Delta\varepsilon$, and the results for all systems, along with the new correlation using this weighted $\Delta\varepsilon$, are presented in Table A.7 and Figure A.9 in Appendix A. In all cases except for **Pz**, the transition with the highest weight corresponded to the $a_{2u} \rightarrow e_g$ ($a_1 \rightarrow e$) excitation. By including not only this main transition but the effect of secondary transitions, we achieved an improved correlation with a more even distribution of data points and an R^2 of 0.98 (excluding **Pz**), as shown in Figure A.9. In the case of **Pz**, the states associated with the B bands exhibit a significant contribution (with a TDDFT weight of 0.49 and a resulting weighting factor of 0.34, see Table 6.8) from the $b_{2u} \rightarrow e_g$ transition. This predominant transition sets **Pz** apart from the other systems and explains its outlier behavior in the correlation.

Table 6.8 Orbital transitions involved in the B band of **Pz**, symmetry and $\Delta\varepsilon$ in eV of the corresponding orbitals, and weighting factor; all computed at CAM-B3LYP/cc-pVTZ (solvent = THF) level of theory. The resulting weighted $\Delta\varepsilon = 6.22$ eV. The isocontour for the orbitals is 0.02.

transition	orbital symmetry	$\Delta\varepsilon$	weighting factor
	a_{2u}, e_g	6.97	0.18
	e_g, b_{1u}	6.54	0.11
	b_{2u}, e_g	6.48	0.34
	a_{2u}, e_g	6.03	0.26
	a_{1u}, e_g	4.32	0.11

Additionally, we explored the ΔE_{ST} to later determine if it holds any relationship with the aromaticity of the systems. For this purpose, we computed the triplet vertical excited states using TDDFT, as detailed in Table 6.9, which also includes a comparison with the TDA results.

237

Table 6.9 $\Delta E_{S_1 T_x}$ (where $x = 1$ or 2) values computed with TD- and TDA-DFT using CAM-B3LYP/cc-pVTZ in gas phase. The reference S_1 energies correspond to the TD formalism. The energies of the first two degenerate roots (labeled T_1) and subsequent degenerate roots 3 and 4 (labeled T_2) have been calculated at both TD and TDA levels.

system	$\Delta E_{S_1 T_1}$ (TD)	$\Delta E_{S_1 T_2}$ (TD)	$\Delta E_{S_1 T_1}$ (TDA)	$\Delta E_{S_1 T_2}$ (TDA)
P	-1.09	-0.23	-0.47	-0.21
Pz	-1.48	0.41	-0.92	0.62
TBP	-1.05	0.10	-0.58	0.23
Pc	-1.55	1.04	-0.91	1.28
SubP	-1.12	-0.44	-0.66	-0.40
SubPz	-1.41	0.14	-1.03	0.24
TBSubP	-1.04	0.04	-0.71	0.18
SubPc	-1.34	0.63	-0.96	0.96

The orbitals involved in the first two degenerate triplet excited states (collectively referred to as T_1), are the same as in S_1 (associated with the Q band). We found that the energy of T_1 presents a positive correlation with S_1 and the $\Delta\varepsilon_{a_{1u}-e_g}$ or $\Delta\varepsilon_{a_2-e}$, with an R^2 of 0.81 and 0.89, respectively. However, we find a poor correlation ($R^2 = 0.39$) between the ΔE_{ST} and the $\Delta\varepsilon$. Thus, by knowing the $\Delta\varepsilon$ we can predict the behavior of the T_1, but not the ΔE_{ST}.

Aromaticity

The characterization of aromaticity in phthalocyanines and subphthalocyanines, as previously introduced in Sections 1.2.3 and 5.1.1, is a complex topic due to their size, topology, and multiple π-electron circuits, necessitating descriptors beyond traditional methods. In this context, it is crucial to employ an approach that integrates both global and local aromaticity metrics to discern the most conjugated pathways. The use of multiple indices, including GIMIC, HOMA, FLU, AV1245, AV_{min}, $EDDB_P$, and limiting value of $EDDB_P$, provides a comprehensive analysis.

In the case of current density maps and net current strengths, it is important to note that for non-planar structures, the orientation of the external magnetic field (usually defined perpendicular to the molecular plane) is not straightforward. To estimate the induced currents we used two different orientations of the magnetic field (Figure 6.11): one perpendicular to the plane formed by the nitrogen atoms of the three pyrroles, and the other perpendicular to the σ_{xy} plane pointing towards the z direction.
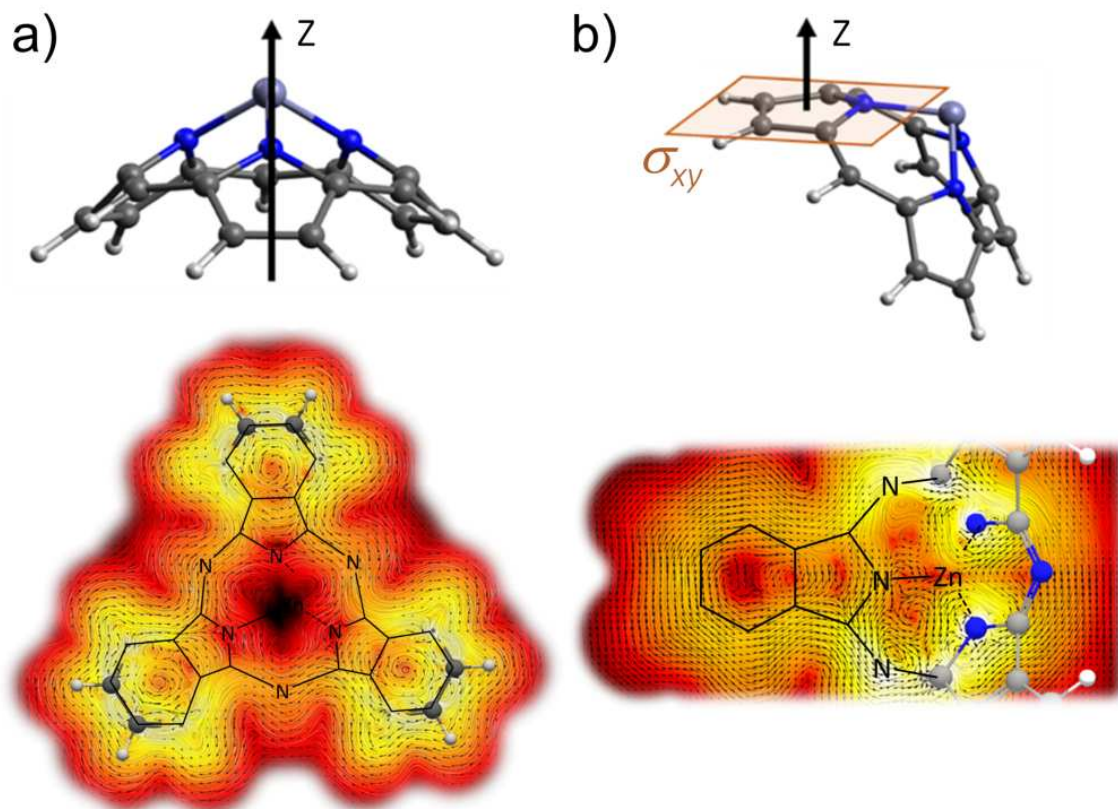
Figure 6.11 Current density in the S_0 state visualized using the LIC representation in **SubPc**. The visualized plane on the left side (a) is located at 2 Å below the Zn/B atom and the plane on the right (b) is 1 Å below the pyrrole/isoindole ring. The color scale corresponds to the strength of the modulus of the current density susceptibility in the range of 0.0001 (red) to 0.4 (white) nA $\cdot$ T^{-1} $\cdot$ Å^{-2}. For illustrative purposes, we depicted the orientation of ZnSubP, which is representative for all the systems under consideration.

From the resulting GIMIC calculations, we obtained both qualitative (current densities) and semiquantitative (current strengths) results. According to the convention, in the current density plots the current flowing clockwise is known as diatropic (and its integrated current density is positive), while a counterclockwise current is paratropic (the integrated current density is negative). All systems present diatropic currents with high current strengths, larger than benzene, indicating aromaticity (see Figure 5 in Section 5.1.1 for the current strengths, and Figure A.10 in Appendix A for current density plots of **P**, **Pz**, **TBP**, and **Pc**). These currents are divided into two fluxes at the α position, resulting in half of this current passing through the i pathway and the other half through the o pathway. The analysis of current densities and strengths in these systems does not offer an unambiguous strategy for distinguishing between the aromaticity of different circuits.
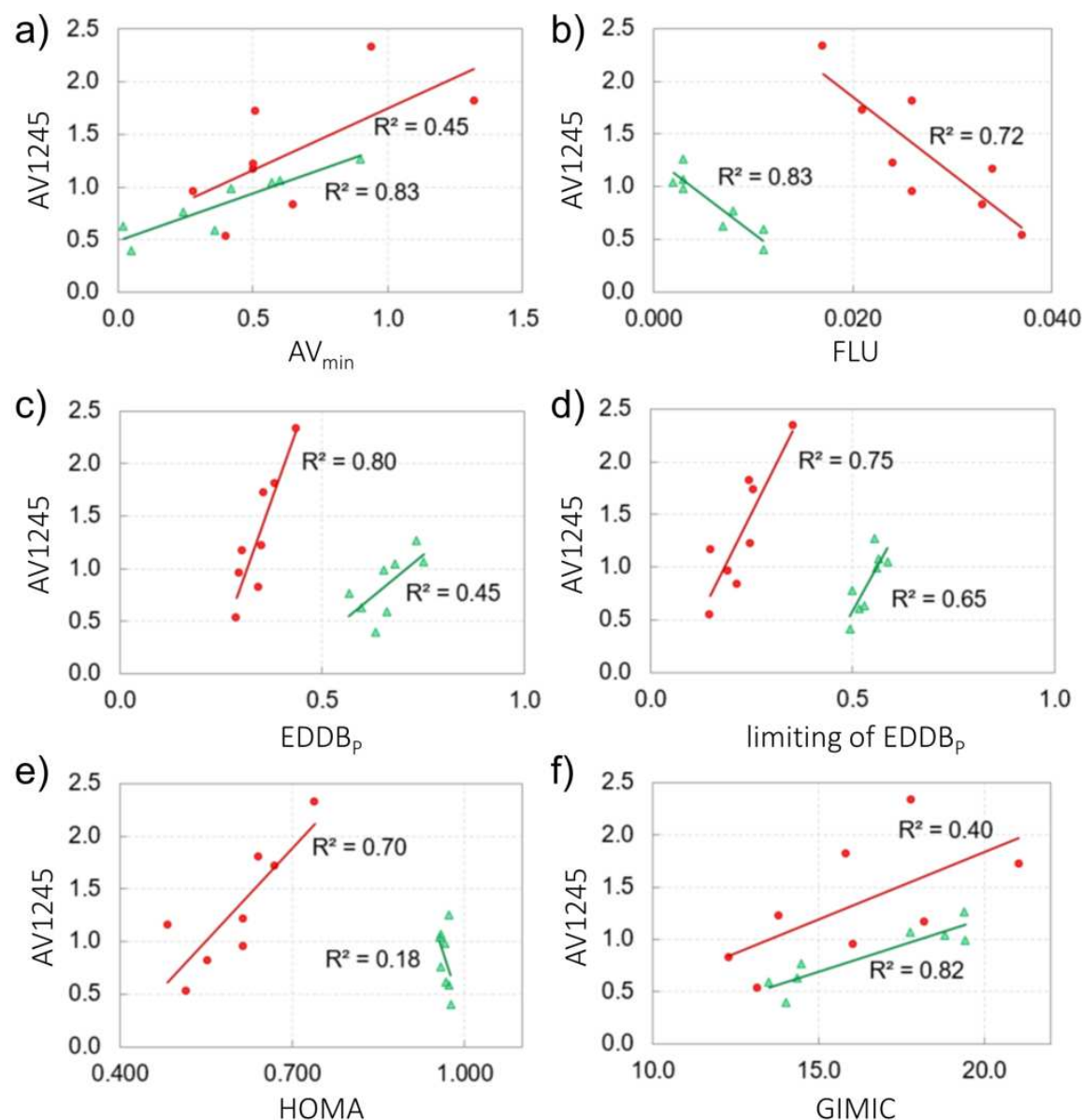
Figure 6.12 Relationships between AV1245 and a range of aromaticity indices for the aromaticity values of the *iii*(*i*) (green triangles) and *ooo*(*o*) (red circles). Each plot represents the correlation with a different aromaticity index as follows: a) AV_{min}, b) FLU, c) $EDDB_p$, d) limiting value of $EDDB_p$ in the atom sequence, e) HOMA, and f) averaged induced current strengths obtained with GIMIC.

Instead, the electronic indices and the HOMA allow for a clearer distinction of the aromaticity in the different pathways. There is a disagreement between different indices when assigning the most aromatic pathway. HOMA, FLU, and $EDDB_P$ always (in all systems) detect the *iii*(*i*) pathway as the most aromatic. On the contrary, AV1245 and AV_{min}, for the contracted systems agree that the most aromatic pathway is the *ooo*,

while for non-contracted systems they differ only in some cases. If we only consider the *i* and *o* pathways, AV1245 and AV$_{\text{min}}$ are agreement with HOMA, FLU, and EDDB$_{\text{P}}$ for **Pz**, **TBP**, and **Pc**, giving the highest values for the *iiii* pathway. However, when we consider also the pathway passing through the fused benzene rings (*bbbb*), AV1245 exhibits the maximum value for this pathway. Then, contrary to the former group of indices, in the case of **P**, both AV1245 and AV$_{\text{min}}$ determine the *oooo* pathway as the most aromatic.

We found that for our purpose, more important than determining the most aromatic pathway, is that the different indices consistently reproduce the variations in aromaticity of a specific pathway (*iii(i)* or *ooo(o)*) with structural modifications. To compare the results of the different indices, we plotted each index against AV1245 to assess their inter-relationships in Figure 6.12. The correlation plot in panel b) reveals a negative relationship in both pathways between FLU and AV1245 values. In this context, considering that a smaller FLU value indicates greater aromaticity, while the opposite is true for AV1245, this suggests a direct proportionality in their variations of aromaticity. In the case of the other indices they present good positive correlations ($R^2 \approx 0.80$) in either the (*iii(i)* or *ooo(o)*) pathway, but show poorer relationship in the other pathway with $R^2 \leq 0.65$. In the latter case, the correlation improves significantly when considering separately the groups of phthalocyanines and subphthalocyanines. This improvement can be attributed to the distinct structural and electronic characteristics inherent to each group, which become more evident in certain cases.

Interplay Between Molecular Properties

The core of our analysis is to understand the relationship between the aromaticity and various properties of the different systems. To synthesize our findings from absorption spectra, $\Delta\varepsilon$, ΔE_{ST}, and aromaticity analyses, we constructed a correlation matrix (Figure 6.13) with the properties examined. This matrix interlinks the results obtained from the AV1245 of *iii(i)*/*ooo(o)* pathways, UV-vis absorption spectra, $\Delta\varepsilon_{\text{H−L}}$ (corresponding to $\Delta\varepsilon_{\text{a}_{1\text{u}}-\text{e}_{\text{g}}}$ and $\Delta\varepsilon_{\text{a}_2-\text{e}}$), $\Delta\varepsilon_{\text{H-1−L}}$ (corresponding to $\Delta\varepsilon_{\text{a}_{2\text{u}}-\text{e}_{\text{g}}}$ and $\Delta\varepsilon_{\text{a}_1-\text{e}}$), and ΔE_{ST}, enabling the collective discussion of these results.

Our analysis underscores that evaluating the four orbital energies (Gouterman model) alone is insufficient for a comprehensive understanding of some optical properties, specially the shifts in the B band and the ΔE_{ST} show somewhat ambiguous correlations with $\Delta\varepsilon$. These findings suggest the need for an extended model that introduces complexity beyond the simplicity of the original approach. In this case, aromaticity
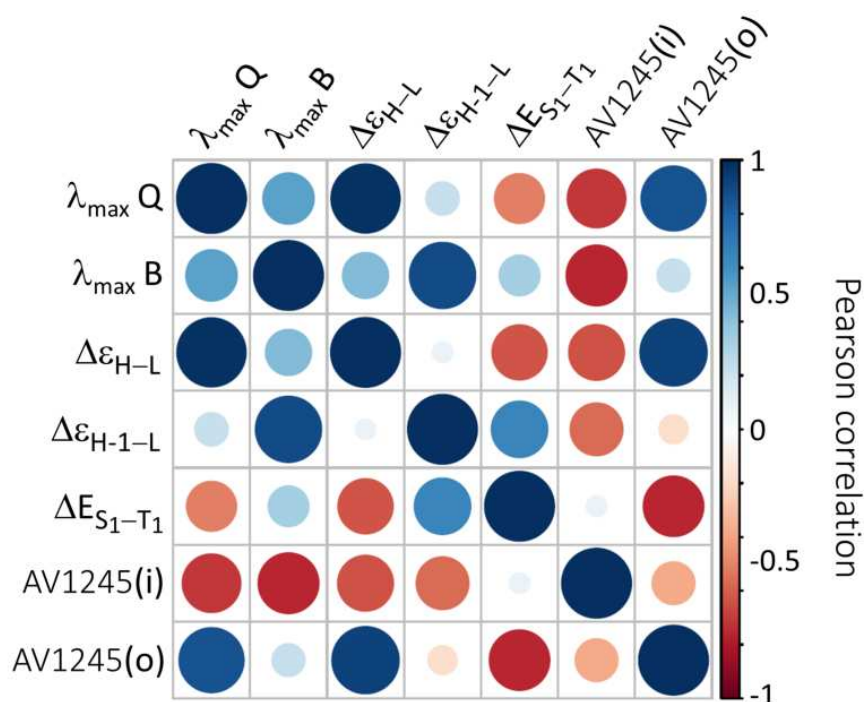
Figure 6.13 Correlation matrix showing the pairwise Pearson correlation coefficients between several molecular properties including λ_{max} for Q and B bands, $\Delta\varepsilon_{a_{1u}-e_g}$ and $\Delta\varepsilon_{a_{2u}-e_g}$ (or $\Delta\varepsilon_{a_2-e}$ and $\Delta\varepsilon_{a_1-e}$), ΔE_{ST}, and the AV1245 values for $iii(i)$ and $ooo(o)$ pathways. The color intensity and circle size are proportional to the absolute value of the correlation coefficient. Positive correlations are displayed in blue and negative correlations in red.

can provide a more complete and chemically intuitive framework for interpreting their spectral features. For the B band, unfortunately, the correlation with AV1245 is of the same order as $\Delta\varepsilon$, indicating no substantial improvement. On the contrary, in the case of ΔE_{ST}, aromaticity (AV1245) shows a stronger correlation. For the Q band λ_{max}, where the correlation with $\Delta\varepsilon$ was already strong, AV1245(o) exhibits comparable correlation.

Overall, we have established a direct correlation between the aromaticity of the $iii(i)$ and $ooo(o)$ pathways in (sub)phthalocyanines and their spectroscopic characteristics. In certain cases, the correlation with AV1245 values improves upon the results obtained with the Gouterman model, while in the worst cases, it matches its performance. These findings enhance our understanding of the structure-property relationship, offering a strategic framework for designing novel phthalocyanine derivatives with custom-tailored properties.

6.3 Global Aromaticity in Nanographene

Turning to a distinct class of macromolecular systems with potential aromatic character, we explored $C_{80}H_{30}$ curved nanographene. Similar to porphyrin-related systems, this molecule has multiple rings that allow for different aromatic or antiaromatic local and/or global delocalization pathways. Additionally, akin to the cases of subphthalocyanines and subporphyrins, the non-planar structure of this system gives it unique electronic features and represents an interesting example of non-planar aromaticity. Therefore, the study of π-electron aromatic circuits in curved nanographenes is not only appealing from a theoretical perspective but also for their potential applications.

In particular, we studied the aromaticity of $C_{80}H_{30}$ warped nanographene (Figure 6.14a), characterized by bowl- and saddle-shaped sections originated by the presence of one 5-MR and five 7-MRs. Experimentally, two isomers were identified in the X-Ray structure: *PMPMP* and *MPMPM* (shown in Section 1.3.2), based on their chirality. Computational analysis at the B3LYP/6-31G(d) level of theory revealed that both isomers are isoenergetic [291]. Given their equal stability, we expect them to also be equivalent in terms of their aromatic properties. Consequently, our analysis is centered on the *PMPMP*-isomer.

To evaluate the aromaticity of this complex system, we consider applying Clar's rule, traditionally used for simpler, planar polycyclic aromatic hydrocarbons (PAHs). While Clar's π-sextet model has been successfully employed to determine π-electron distributions in benzoid PAHs, the non-planar geometry and with the presence of defects (*i.e.* 5- and 7-MRs) in warped nanographene pose a distinct challenge in this context. According to Clar's rule, the molecule is expected to have one π-sextet at each of the external type III 6-MRs, accounting for a total of 60 π-electrons, and two additional migrating Clar sextets at the five 6-MRs (type I) of the corannulene core, contributing an extra 20 π-electrons (Figure 6.14b). However, the considerable distortion of the structure raises questions about how accurately this model reflects the molecule's actual aromaticity. To tackle these complexities, we have tested the applicability of Clar's model to this unconventional structure. We used geometric (HOMA), electronic (FLU and EDDB), and magnetic (NICS, magnetic (de)shielding isosurfaces, and GIMIC) aromaticity indices. Overall, the objective of this project, as elaborated in Section 5.2 of Chapter 5, is to determine the global aromaticity of *PMPMP*-$C_{80}H_{30}$ isomer.
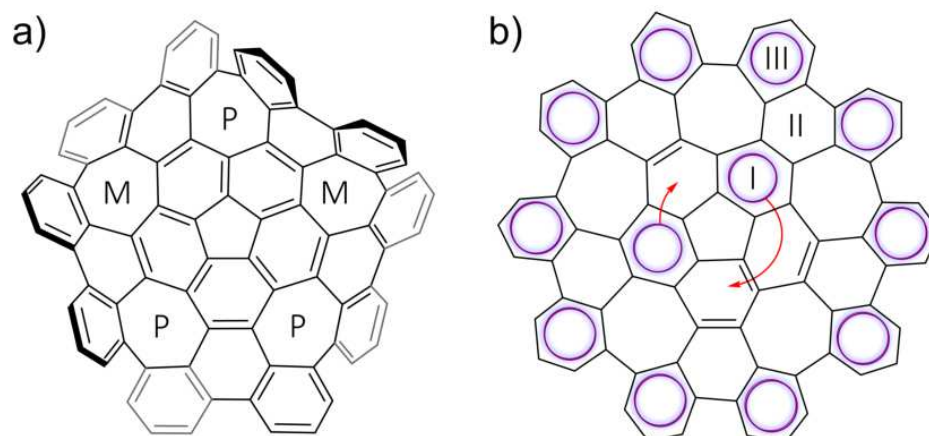
Figure 6.14 Representation of a) *PMPMP*-isomer of $C_{80}H_{30}$ nanographene, and b) Clar sextets depicted as magenta circles. $C_{80}H_{30}$ has 80 π-electrons: 20 in the corannulene core and 60 in type III rings.

Magnetic Aromaticity in Non-Planar Structures

Taking into account the difficulties for magnetic aromaticity indices to be employed for non-planar systems, we opted to explore not only the *PMPMP*-isomer but also a planar structure. The latter was optimized with the constraint of maintaining D_{5h} symmetry. This approach facilitates the use of a model system for characterization, though it is important to note that all indices have been computed for both the planar and non-planar forms, recognizing the significant approximation the planar model represents in comparison to the relaxed structure. Both structures have been optimized at BP86-D3/TZ2P level of theory, as implemented in the ADF package. However, in light of previous studies cited in earlier chapters [76, 144–146], which underscore the limitations of BP86 in describing aromaticity in expanded porphyrins, our analysis shifted towards employing the CAM-B3LYP-GD3BJ/6-311G(d,p) level for electronic structure corrections. This is also supported by the proven accuracy of this methodology in electronic and magnetic properties of similar systems, as reported by Lehtola *et al.* [524].

Just as with our earlier analysis of subporphyrins and subphthalocyanines, the orientation of the magnetic field relative to molecular geometry is a critical factor in accurately assessing the aromaticity of the *PMPMP*-isomer. Especially since our methodology includes a detailed analysis of magnetically induced current densities, utilizing magnetic indices. For the planar constrained structure, we defined the magnetic field perpendicular to the molecular plane. However, the non-planar *PMPMP*-isomer

required different magnetic field orientations due to its distorted structure. Various orientations were examined (shown in Figure 6.15) to accurately assess aromaticity.
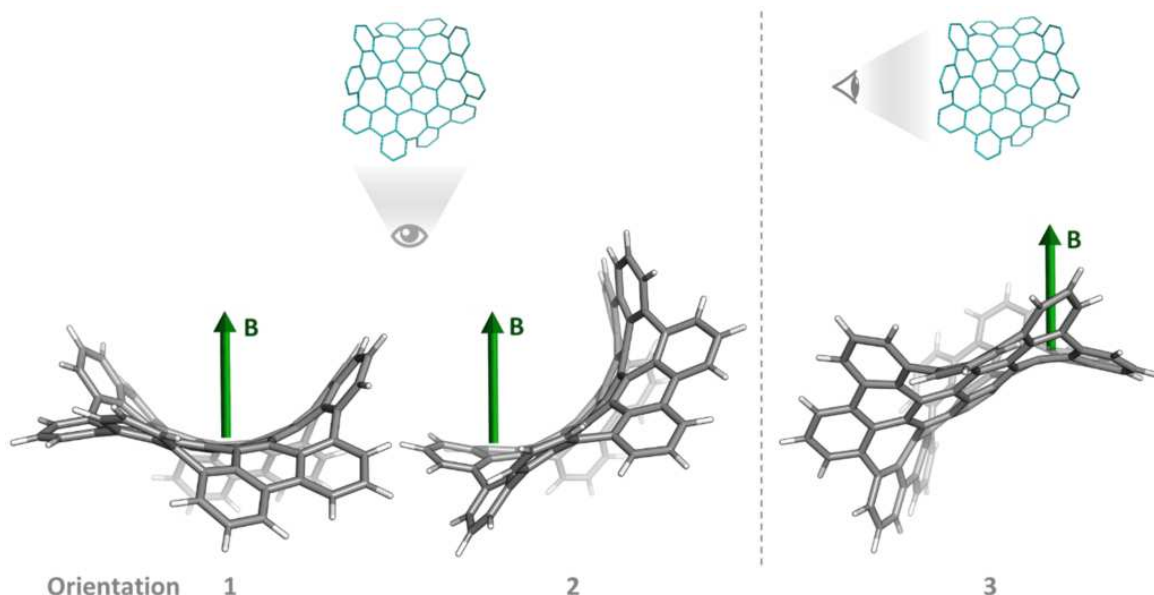

Figure 6.15 Different orientations of the magnetic field vector (**B**) with respect to the molecular structure of the *PMPMP*-isomer of nanographene. Corresponding to Figure S1 in 6.2.1-SI, which can be accessed from the link in Appendix A.

Local Aromaticity

To gain an initial understanding of the system, even though our primary focus is on characterizing the global aromaticity, it is important to also examine the local aromaticity of the individual rings forming the molecule. This approach also helps in identifying the presence of localized π-sextets. The aromatic character of the different ring types has been evaluated using FLU, HOMA, and normalized MCI indices. The results reveal that the external hexagons (rings III to III'''') exhibit the highest local aromaticity, as indicated by higher HOMA values indicating similar C–C distances to isolated benzene (Table 6.10). The small 0.004(5) FLU and large $MCI^{1/n}$ around 0.6 also support the result of having localized π-sextets in rings $III^{('''')}$. In contrast, the 6-MRs of type I and II are aromatic to a lesser extent, with the latter type being the least aromatic. This observation aligns with the Clar structure of nanographene shown in Figure 6.14b.

Having observed the varying degrees of aromaticity in the 6-MRs, we move to the analysis of the remaining 5- and 7-MRs. These rings along with the type II 6-MRs, are categorized as non-aromatic according to Clar's nomenclature. The adjacent 6-MRs

Results and Discussion

Table 6.10 Aromaticity results of the small ring moieties (5-MR, 6-MRs, and 7-MRs, represented in the Scheme on the right side of the table) according to FLU, HOMA, and $MCI^{1/n}$ in *PMPMP*-isomer and constrained planar structure of $C_{80}H_{30}$ nanographene.

PMPMP-isomer	FLU	HOMA	$MCI^{1/n}$	
5-MR	0.033	0.870	0.4029	
6-MR I	0.013	0.383	0.5307	
6-MR I'	0.020	0.054	0.4965	
6-MR I''	0.017	−0.094	0.5141	
6-MR II	0.023	0.135	0.4624	
6-MR II'	0.022	0.254	0.4717	
6-MR II''	0.020	0.125	0.4793	
6-MR III	0.004	0.866	0.6009	
6-MR III'	0.004	0.882	0.6010	
6-MR III''	0.004	0.869	0.5979	
6-MR III'''	0.005	0.844	0.5937	
6-MR III''''	0.005	0.862	0.5923	
7-MR I	0.033	−0.202	0.3900	
7-MR I'	0.033	−0.420	0.3908	
7-MR I''	0.031	−0.480	0.3981	
planar structure				
5-MR	0.037	−1.914	0.4008	
6-MR I	0.020	−4.798	0.5208	
6-MR II	0.024	−3.589	0.4752	
6-MR III	0.005	0.150	0.5973	
7-MR	0.036	−5.947	0.3970	
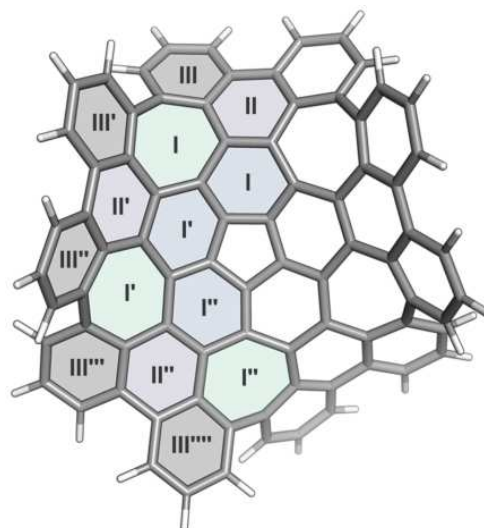
potentially influence the paratropic behavior observed in 5- and 7-MRs, similar to patterns in corannulene and coronene [525, 526]. The five 6-MRs labeled as type I display a migrating π-sextet, resulting in a reduced aromatic character. However, the HOMA values, which suggest aromaticity in 5-MRs and antiaromaticity in 7-MRs, are not consistent with the observed aromaticity in rings II and I. This inconsistency is attributed to the highly strained structure of the nanographene, particularly in its planar form. Such structural strain, as noted in previous studies [527, 528], leads to minor alterations in the cyclic π-electron delocalization in $C_{80}H_{30}$ nanographene.

The nanographene structure features two notable motifs. The 5-MR and adjacent five 6-MRs exhibit a pattern of aromaticity akin to corannulene but with slightly diminished aromaticity in the 6-MRs. This pattern is characterized by a radial structure that prevents double bonds in [5,6] bonds, similar to those observed in C_{60}, where

[5,6] bonds are larger (avg. 1.410 Å) than [6,6] bonds (avg. 1.356 Å). Furthermore, the arrangement of rings I, II, and two adjacent rings III resembles the aromaticity observed in triphenylene, with rings I and III being more aromatic than the central ring II [529]. These trends are consistent even in the planar form of the $C_{80}H_{30}$ nanographene.

Global Aromaticity and Electronic Delocalization

Building upon the examination of local aromaticity, we now shift to global aromaticity and electronic delocalization. Various indices were used to explore the aromatic circuits in the nanographene. Extended π-circuits involving external hexagons, represented in Figure 6.16, were found to be the most favorable for π-electron delocalization.

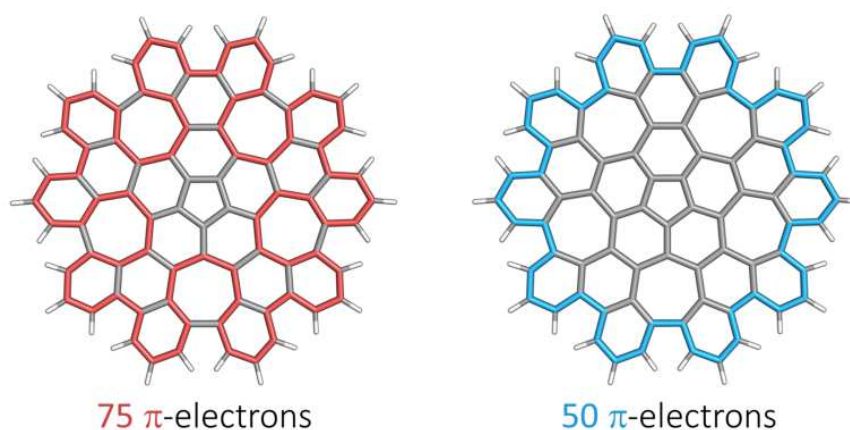75 π-electrons 50 π-electrons

Figure 6.16 Representation of the 75 (in red) and 50 (in blue) π-electron circuits in $C_{80}H_{30}$.

This observation can be related to the previous findings on local aromaticity, where the external benzene-like rings exhibited the highest aromatic character. Despite the non-planar structure of *PMPMP*-$C_{80}H_{30}$, the aromaticity of the extended circuits was comparable to the values obtained for the constrained planar system. Surprisingly, the two most aromatic pathways, according to HOMA, FLU, and EDDB, involve 50 and 75 π-electrons, respectively, and thus the latter circuit does not follow any of the known rules of aromaticity. The normalized EDDB/atom values are approximately 0.5 electrons, roughly half that of benzene. Despite this, these values still fall within the range considered indicative of aromaticity, especially when taking into account the large size of the circuit.

In the case of the warped $C_{80}H_{30}$ nanographene, the quantification of the aromaticity of the different pathways using the integrated current strength could not be done. This is because the distorted geometry, far from the planarity, obstructs the reliable

definition of the integration planes. In the case of the planar structure, we were able to perform these measures, which revealed that the 75 π-electron pathway is the most favorable according to ring currents (Figure. 6.17).
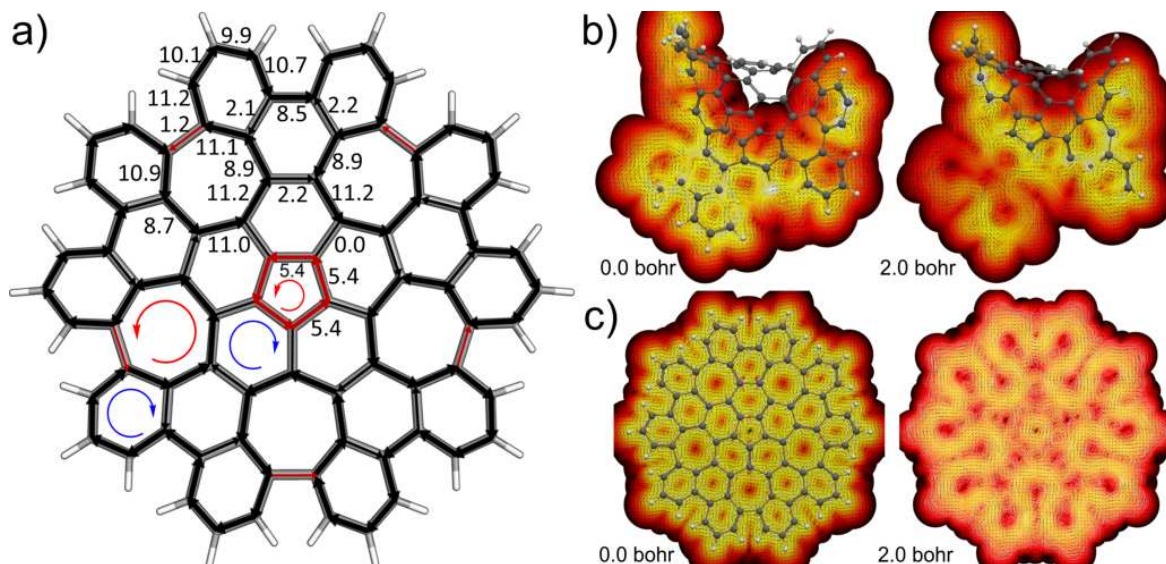

Figure 6.17 a) Calculated net current strengths (in nA $\cdot$ T^{-1}) passing through the selected bonds in planar nanographene. Current density in b) planar and c)*PMPMP*-isomer of nanographene at the molecular plane, and the plane at 2 Bohr above this molecular plane. The magnetic field is placed as in orientation 2, represented in Figure 6.15. For the results using other orientations see S12-15 in 6.2.1-SI (Appendix A).

In the 50 π-electron pathway (highlighted in blue in Figure 6.16) most current strengths range from 11.2 to 8.5 nA $\cdot$ T^{-1}, but there is a small negative current (-1.2 nA $\cdot$ T^{-1}) in the external bond of the 7-MRs. The 75 π-electron pathway (highlighted in red in Figure 6.16) has only positive current strengths and these range from 11.2 to 8.5 nA $\cdot$ T^{-1}.

In summary, the warped nanographene structure, C$_{80}$H$_{30}$, displays two primary circuits for π-electron delocalization, one following Hückel's rule (50 π-electrons) and another with 75 π-electrons, not following traditional aromaticity rules. This finding challenges existing paradigms in aromaticity and suggests that efficient π-electron circuits can be formed with an odd number of C atoms, opening new avenues for understanding extended aromatic systems.

It is important to add that the quantitative magnetic analysis, while providing valuable insights, is limited to planar structures. Furthermore, we must be aware that magnetic aromaticity is considered a response property rather than an intrinsic

property of the molecule. Therefore, it is necessary to employ indices related to other aspects of aromaticity. Upon examining electronic indicators such as FLU and EDDB, we find that the pathways with 50 and 75 π-electron exhibit the highest aromatic values. This supports the presence of the 75 π-electrons circuit, as indicated by the magnetic data, and show the 50 π-electrons one to be similarly aromatic. However, these indicators suggest that the aromaticity is not as pronounced as the ring currents might imply. This leads to the conclusion that the true level of aromaticity, as revealed by these electronic measures, is present but less intense than what might be inferred from magnetic analysis alone.

6.4 Double Aromaticity in Tropylium Ion Derivatives

The following section summarizes the findings on substituted tropylium ions, explored as potential candidates capable of exhibiting double aromatic character. Previous studies, reviewed in Sections 1.3.2 and 5.3.1, have established a foundation for understanding doubly aromatic organic molecules. These studies highlight the difficulty of achieving strong σ-aromaticity in substituted benzene dications ($C_6R_6^{2+}$, where R are halogens or functional moieties containing group 16 or 17 elements), especially with substituents other than iodine where σ-delocalization in the outer ring is generally weaker. Additionally, while larger ring systems like $C_8I_8^q$ with q = 0, +1, +2, +4, −2 were explored to increase substituent proximity and enhance σ-delocalization, the significant steric repulsion between iodine atoms resulted in puckering, thus posing a challenge to this strategy. Our research aims to address these challenges by investigating whether substituted cycloheptatrienyl cation and its anion counterpart, hereinafter referred to as tropylium ions, can exhibit both σ- and π-aromaticity more effectively. Tropylium ion with a D_{7h} symmetry presents R-R distances intermediate between six- and eight-membered rings, which might allow for increased conjugation while controlling steric repulsion, and the presence of $4n + 2$, with $n = 3$, σ-electrons without the need to undergo double oxidation. These structural aspects offer a promising avenue for achieving doubly aromatic character. Here, we detail our results, demonstrating how these ions behave in terms of aromaticity and highlighting how the choice of DFA influences the results.

Results and Discussion

Evaluating DFT Functional and Basis Set Choice

For precise characterization of the ground and triplet states of the selected molecules we need to carefully select a DFT functional able to capture the details of electron delocalization. Given the inherent weak σ-delocalization in these systems, our initial choice was BLYP. We decided to employ a pure GGA functional for its tendency to enhance electron delocalization so as not to overlook any system that could have potential σ-aromaticity.

However, it is well known that by using this approach one can get over-delocalized electrons in cases where the electrons should be well localized. For this reason, we optimized the geometry of $^1C_7Br_7^+$ using three other functionals: B3LYP (hybrid GGA, E_X^{HF}: 20%), CAM-B3LYP (range-separated hybrid with SR E_X^{HF}: 19%, and LR E_X^{HF}: 65%), and M06-2X (hybrid meta-GGA, E_X^{HF}: 54%), all in conjunction with the 6-311+G(d,p) basis set. Following this, we performed single point calculations at the CCSD(T)/6-311+G(d,p) level on each of these optimized geometries (Figure A.11 in Appendix A). The purpose was to compare their energies and determine which functional gave the most stable structure as this is expected to align more closely with the CCSD(T) result.

All functionals resulted in similar somewhat puckered geometries. The BLYP geometry, in general, presented slightly longer bond distances compared to the other functionals. The most stable geometry at the CCSD(T)/6-311+G(d,p) level of theory corresponds to the B3LYP result, followed by M06-2X ($\Delta E = 0.29$ kcal/mol), CAM-B3LYP ($\Delta E = 0.45$ kcal/mol), and BLYP ($\Delta E = 1.34$ kcal/mol). The close energy values among the different functionals suggest that despite the subtle differences in how these handle electron delocalization, they all lead to similar geometrical solutions for $^1C_7Br_7^+$. Thus, we will proceed with the BLYP functional but remain mindful of its tendency to exaggerate electron delocalization, potentially overstating aromaticity.

Our study is centered on halogen-substituted tropylium systems. Yet the study of Saito and co-workers [161], reporting a double aromatic hexakis(phenylselenyl)benzene dication, motivated us to contemplate the inclusion of other ligands, listed in the scope part. Considering the added complexity involved in optimizing structures with larger ligands like SePh or $SeCF_3$, we considered the use of the smaller 6-31G(d,p) basis set. We optimized the $C_7(SeCF_3)_7^+$ molecule using both 6-311+G(d,p) and 6-31G(d,p) basis sets, and we observed significant geometrical differences. To quantify these variations, we employed the root-summed-square (RSS) index giving values of 0.064 and 0.011

for the tropylium carbon ring, and 1.129 and 0.160 for the selenium ring, with the 6-311+G(d,p) and 6-31G(d,p) basis set, respectively. These values indicate a much more puckered geometry (see Figure A.12 in Appendix A) using the larger basis set and suggest that the choice of basis set can significantly influence the predicted molecular structure. Taking into account that the geometries are puckered regardless, indicating a possible non-aromatic-σ ring, as σ-aromaticity can be easily disrupted, we decided against this broader exploration and keep the focus only on halogen substitutions. This focused approach aims to elucidate the fundamental requirements necessary for the formation of a double aromatic system, thereby avoiding the added complexities associated with a multitude of isomers and the intricate nature of substituents involving pnictogens or chalcogens.

Scope

As mentioned earlier, this study aims to identify σ,π-doubly aromatic molecules, with our primary focus on halogen-substituted tropylium ions. As cationic species we considered the singlet state of $C_7X_7^+$ with X = F, Cl, Br, and I; and $C_7Br_7^{3+}$ in the singlet and triplet states. As anionic systems, we analyzed the singlet and triplet states of $C_7Br_7^-$. In the latter cases, the focus on bromine over iodine and chlorine or fluorine is due to its lesser steric congestion and more diffuse 4p orbitals, facilitating better overlaps. Furthermore, we also performed a preliminary investigation of the additional tropylium cations: $C_7R_7^+$ with R = SeH, SeCH$_3$, SeCF$_3$, SePh, SH, SPh, NH$_2$, and N(CH$_3$)$_2$. The hypothetical σ- and π-aromaticity of each ring according to Hückel and Baird rules is indicated in Figure 6.18.
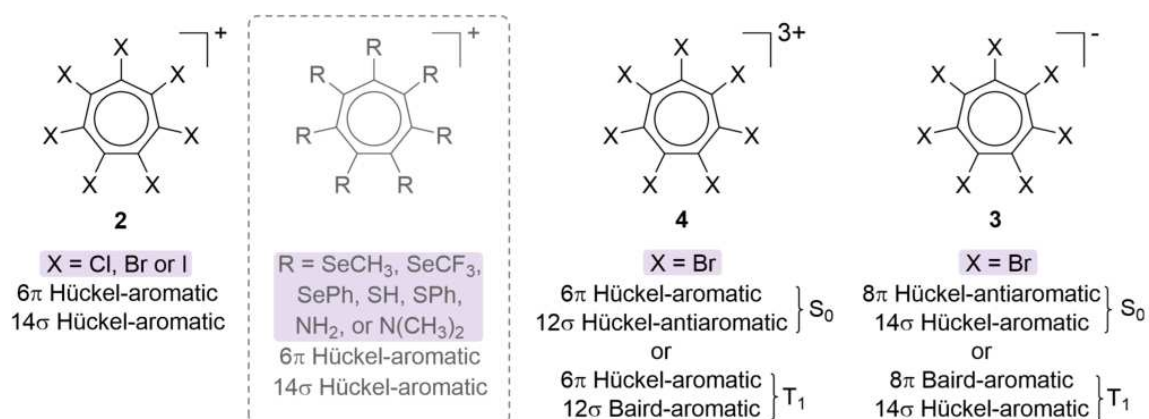

Figure 6.18 Systems with tropylium rings considered in the study of Section 5.3.1.

Results and Discussion

Optimized Geometries and Evaluation of the Planarity

For each system, we allowed for a fully unconstrained geometry optimization. Additionally, we computed geometries constrained to D_{7h} symmetry, serving as a model for aromaticity assessment.

Among all the optimized substituted tropylium monocations (Figure 6.18) in the singlet state, only $C_7F_7^+$ species presents a planar structure without enforcing D_{7h} symmetry. For the other halogen substituted $C_7X_7^+$ and $C_7R_7^+$ systems, with R = $SeCH_3$, $SeCF_3$, SePh, SH, SPh, NH_2 and $N(CH_3)_2$, the tendency is to adopt puckered geometries. This distortion in the geometry indicates an absence of double aromaticity. Consequently, we limited our study to the $C_7X_7^+$ halogen substituted set (including also other oxidized forms: $+3$ and -1, for X = Br). This choice is adopted to evade further complexities arising from bonding scenarios present in molecules with R substituents, allowing us to focus on studying the origins of the preference of this 7-MRs for distorted geometries lacking σ- and in some cases even π-aromaticity in the outer and inner rings, respectively.

In the case of other non-planar $C_7X_7^+$, the energy difference between unconstrained (C_1) and D_{7h} symmetry structures is 1.3, 8.1, and 34.4 kcal/mol for X = Cl, Br, and I, respectively. Moving to the singlet and triplet states of compound **3** ($C_7Br_7^-$), none of them are planar and show distinct stabilization patterns due to puckering, with greater stabilization in the singlet state (47.2 kcal/mol) compared to the triplet state (18.6 kcal/mol). This finding aligns with the expected release of antiaromaticity in the singlet state upon transitioning from a planar to a puckered structure. Finally, we found that for the tropylium trication ($C_7Br_7^{3+}$) in the singlet and triplet states the planarity is kept. Surprisingly, the singlet state is the ground state but being only 13.3 kcal/mol more stable than the triplet.

To gain deeper insight into the stability of these structures, we analyzed their out-of-plane vibrational modes (Table 6.11). These are indicative of the propensity of the system to distort and lose planarity. The two lowest normal modes of the tropylium cation, taken as a reference, demonstrate a much higher frequency compared to the rest of the systems, suggesting a higher stability of the planar configuration for the tropylium cation. The observed increase in the absolute values of the vibrational frequencies from Cl- to I-substituted tropylium monocations aligns with the tendency towards more pronounced puckered geometries. This is directly linked to the increasing size and mass of the halogen, which increments both electrostatic and steric repulsion.

Additionally, variations in the oxidation state from +1 to -1 and +3 have opposite effects on molecular geometry: while the addition of two electrons enhances the distortion tendency, the removal of two electrons appears to stabilize the planar structure.

Table 6.11 Out-of-plane normal modes in cm^{-1} for the D_{7h} $C_7X_7^q$ geometries at the BLYP/6-311+G(d,p) level of theory, with SDD basis set and pseudopotential for I.

system	symmetry	A''_1	A''_2
$^1C_7H_7^+$	(D_{7h})	212.26	212.75
$^1C_7F_7^+$	(D_{7h})	81.69	81.81
$^1C_7Cl_7^+$	(D_{7h})	−27.41	−27.34
$^1C_7Br_7^+$	(D_{7h})	−29.69	−29.69
$^1C_7I_7^+$	(D_{7h})	−40.90	−40.89
$^1C_7Br_7^-$	(D_{7h})	−56.47	−56.41
$^3C_7Br_7^-$	(C_2)	−43.03	−27.95
$^1C_7Br_7^{3+}$	(D_{7h})	31.12	31.13
$^3C_7Br_7^{3+}$	(D_{7h})	−4.84	11.83

Quantification of the Aromaticity

The subsequent discussion centers on the evaluation of the aromatic character of the presented systems. The MCI and EDDB values reported in Tables 2, 3, 5, 6, 8, and 9 of the manuscript in Section 5.3.1 for the relaxed and D_{7h} geometries of $^1C_7X_7^+$, $^{1,3}C_7Br_7^-$, and $^{1,3}C_7Br_7^{3+}$ show that the π-aromaticity of the carbon ring is generally robust against in- and out-of-plane distortions. However, it is noteworthy that in cases with significant distortions, specifically for $^1C_7I_7^+$, $^1C_7Br_7^-$, and $^3C_7Br_7^-$, the MCI and EDDB are reduced to below 0.017 (MCI$^{1/n}$ = 0.559) and 2.55 (EDDB/atom = 0.36) electrons, respectively, indicating a minimal presence of π-delocalization. With these values, it becomes ambiguous whether this can be attributed to residual π-aromaticity or not.

In the case of the ring formed by halogen atoms, both MCI and EDDB show none or marginal σ-delocalization for the tropylium monocationic and anionic species in both singlet and triplet states. Notably, $^1C_7Br_7^{3+}$ and $^3C_7Br_7^{3+}$ are the only ones among the studied systems that potentially exhibit σ-aromaticity. For the singlet state, the normalized MCI (MCI$^{1/n}$) is −0.589, and the σ-EDDB per atom is 0.78 electrons. These values are comparable in magnitude with those of $^1C_6I_6^{2+}$: MCI$^{1/n}$ = 0.595 and σ-EDDB/atom = 0.86 electrons, suggesting a significant extent of σ-aromaticity or antiaromaticity. According to Hückel's rule, the 12σ electron count should correspond

to an antiaromatic σ-ring. While the negative MCI value might suggest antiaromaticity, as expected for a $4n$ ring, it is important to note that electronic indices such as MCI and EDDB are not reliable indicators of antiaromatic character. In particular, for archetypal π-antiaromatic systems, the EDDB/atom values tend to fall between near zero (*e.g.* 0.05 electrons/atom in CBD, see Figure 2.13) and half electron (*e.g.* 0.55 electrons/atom in the antiaromatic π, π^* excited triplet state of benzene at CAM-B3LYP/6-311+G(d,p) level of theory [111]), corresponding to half of the number of expected π-electrons per atom in these small aromatic monocyclic molecules. In our case, the observed EDDB values are higher than this 0.0 to 0.5 electrons range, pointing to an ambiguous aromaticity assessment. Next, considering the triplet state, we observed that the spin density is localized in the halogen ring (Figure 5 in 5.3.1), thus according to Baird's rule we expected the ring with 12 σ-electrons to be aromatic. However, the small values of $\text{MCI}^{1/n} = 0.420$ and σ-EDDB/atom = 0.38 electrons, indicate only a very modest degree of σ-aromaticity.

To gain a more comprehensive understanding, we have evaluated the ring currents, which are shown in Figure 6.19. In the case of the singlet state (a), these are diatropic around both the carbon- and bromine-ring, suggesting that $^1\text{C}_7\text{Br}_7^{3+}$ is both π- and σ-aromatic. In contrast, for the triplet state (b), the current around the Br-ring is flowing counterclockwise, pointing to σ-antiaromaticity. In this latter case, we confirmed the presence of the paratropic current associated with the Br-ring by inspecting the streamline representation of the ring current (Figure A.13 in Appendix A). Remarkably, this representation also reveals significant atomic currents with diatropic circulation around the bromine atoms.

However, interpreting the ring current results in systems with two concentric rings is complex. For a molecule exhibiting double aromaticity, the induced magnetic fields resulting from the delocalized electrons in the inner and outer rings are likely to oppose each other in the region between the carbon and halogen rings as depicted in Figure 6.20. Moreover, the task of assigning aromaticity is further complicated by the presence of bond currents and atomic current vortices around the bromine atoms (more visible at 2.0 Å above the molecular plane in Fig. 6.19), present in both singlet and triplet states. The discrepancies between ring currents and electronic measures point out how complex it is to figure out aromaticity, showing the importance of examining different indicators.
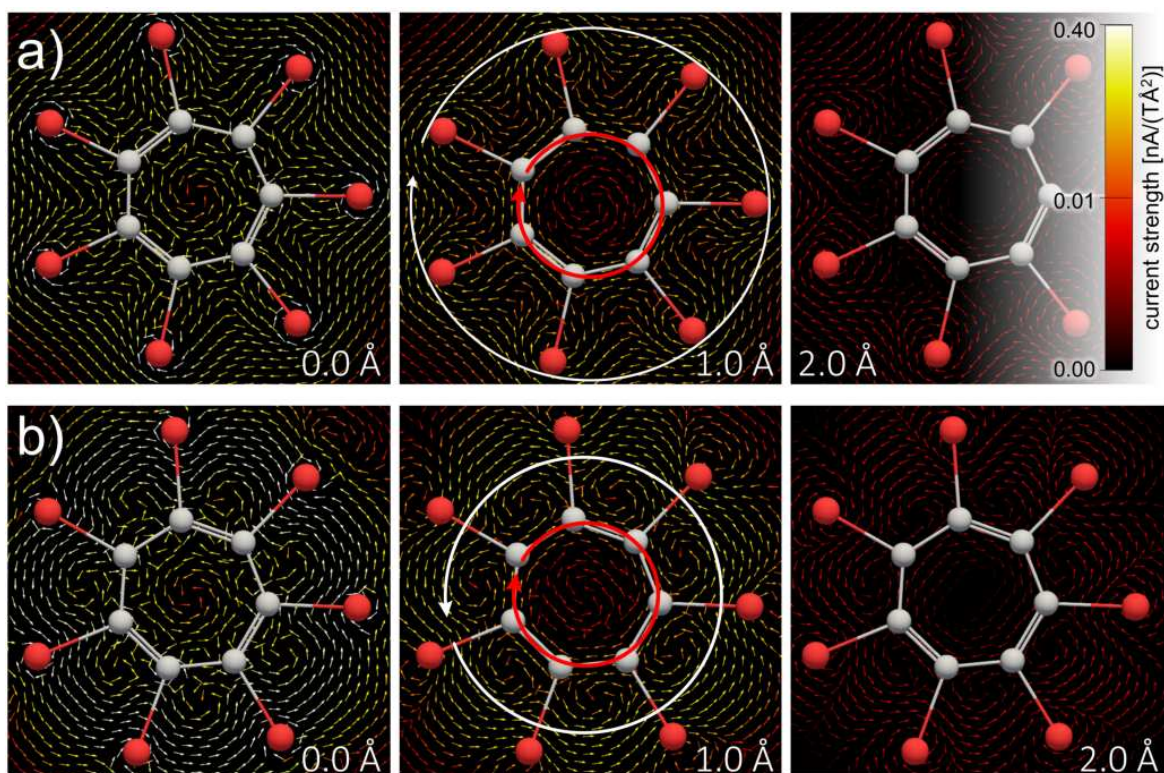
Figure 6.19 Current density of the a) singlet and b) triplet state of $C_7Br_7^{3+}$ at the molecular plane (0.0 Å) and the planes at 1.0 and 2.0 Å above. The color scale corresponds to the strength of the modulus of the current density susceptibility.
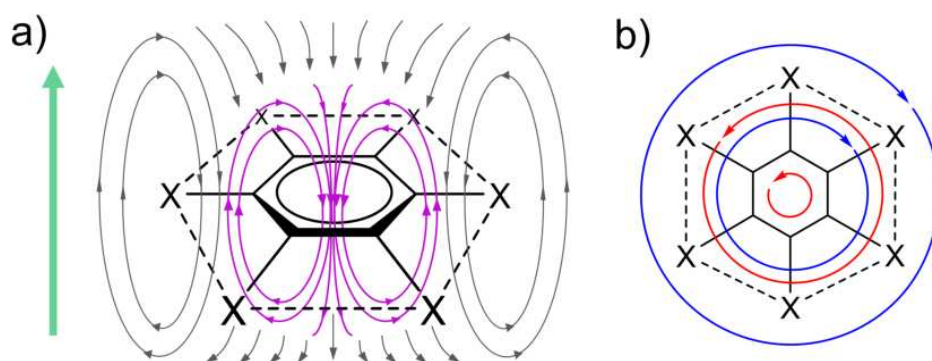

Figure 6.20 Representation of the a) induced magnetic field and b) ring currents in a system of concentric rings. The green straight arrow represents $\mathbf{B}_0$, and the red and blue circular arrows represent the paratropic and diatropic currents, respectively.

To deepen our understanding of aromaticity in the triplet trication, we examined its molecular orbitals (Figure 6.21). With this, we basically aim to understand why the Hückel and Baird rule do not fully explain the aromatic character. It is important to remember that these rules were originally formulated for π electrons in annulenes with

D_{hn} symmetry, and their application to a halogen ring with σ symmetry is, in essence, an extrapolation. Hence, the fulfillment of Hückel and Baird rules does not guarantee aromaticity or antiaromaticity in these systems. As indicated in the figure, the system in the triplet state has seven alpha and five beta σ-electrons, aligning with Mandado's $2n+1$ rule (or rule for separate spins). One must notice that the totally antibonding σ orbital is occupied in the α-part, which could explain the diminished aromaticity in this state. In contrast, in the singlet state, with six alpha and six beta electrons, the σ-antibonding orbital is unoccupied. This configuration is similar to that of $^1C_6I_6^{2+}$. In such a situation, the localization of the halogen lone pairs is prevented, which could potentially explain the ring currents and EDDB values indicative of aromaticity in the singlet state. Such a scenario is not feasible in the case of the tropylium cations and anions, as this orbital is filled, and is only partially achievable in the case of triplet trication, given that only the beta orbital is empty.
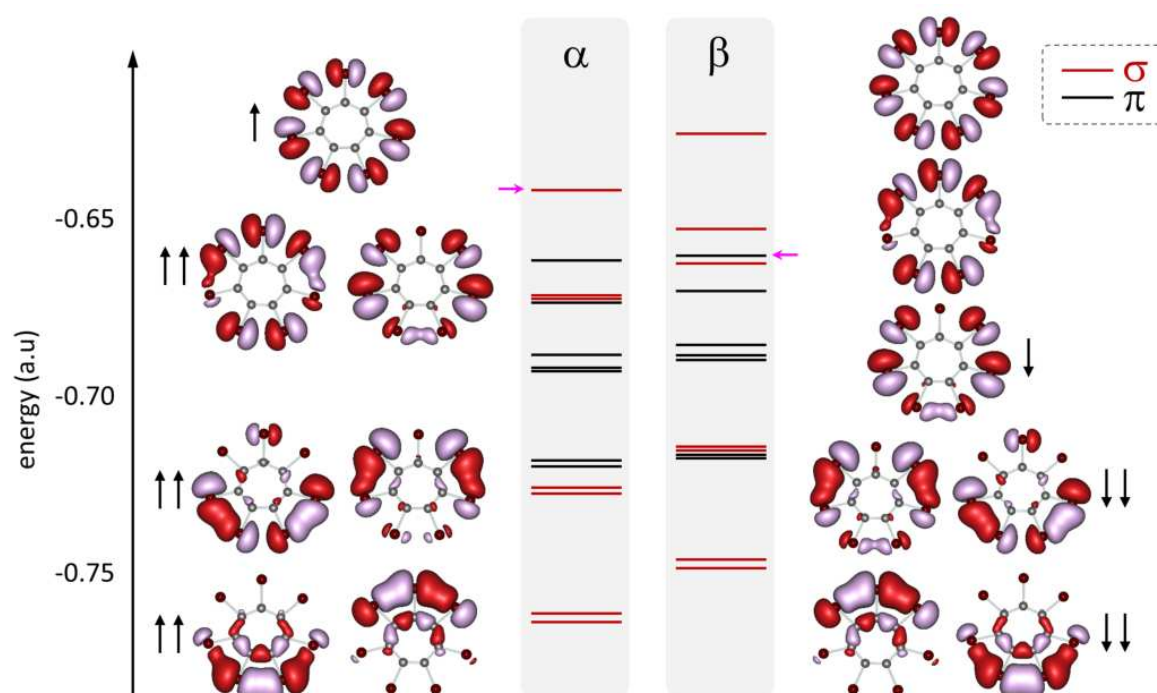

Figure 6.21 Frontier α and β molecular orbitals of the $^3C_7Br_7^{3+}$ system. In the depiction, black and red lines represent the π and σ orbitals, respectively. The pink arrows point to the last singly occupied molecular orbital. The σ orbitals are shown using a 0.02 isosurface, with the black arrows indicating its occupations.

Overall, our results confirm the necessity of creating an electronic hole in the σ-ring to allow electron delocalization, achievable through double oxidation. We detected potential double aromatic character in tropylium trications. However, it is crucial to

note that these observations depend on the DFA used, and the BLYP functional might exaggerate these effects. Nonetheless, this study lays a foundation for future research. It hints at the potential of using substituents that not only favor but also stabilize such higher-charged cationic states, offering new perspectives in the quest for molecules with double aromatic character.

6.5   Icosahedral Boron Clusters: 3D Aromaticity

In this last section of our exploration into topologically complex aromatic systems, we examine the 3D aromaticity within the icosahedral boranes, carboranes, and their derivatives. The present section collects three projects, each using the evaluation of aromaticity to better characterize different boron clusters. In the first project, detailed in Section 5.4.1, the aromaticity is used to evaluate the different carborane structures. We analyze the differences between m-$C_2B_{10}H_{12}$ and o-$C_2B_{10}H_{12}$ to understand their relative the thermodynamic stability, with a particular emphasis on their resistance to deboronation processes. Additionally, we explore how the positioning of carbon atoms within *closo-* and *nido-* carborane structures influences their stability, and we differentiate between the behaviors of sandwich metallabis(dicarbollides) and metallocenes. The second study, corresponding to Section 5.4.2, focuses on examining the nature of C–C bond within 1,2-$C_2B_{10}H_{10}$ (*o-carboryne*). The third and last project, presented in Section 5.4.3, probes the potential for double 3D aromaticity in dodecaiodo-dodecaborate clusters. Moreover, it stresses the need for complete analysis including electron delocalization, and energetic stabilization beyond just magnetic properties. Each project, while all focusing on studying aromaticity, delves into distinct and specific aspects of these boron clusters. Consequently, this section is structured into three parts, with each part dedicated to one of the aforementioned projects.

In contrast to previous sections where we began examining and discussing the performance of various DFAs, in this section, our focus is directly on the aromaticity results, avoiding a detailed exploration of computational methods. To briefly mention our approach: the B3LYP/6-311++G(d,p) level of theory was utilized for the first two projects, while the BLYP/6-311++G(d,p)~LANL2DZ, ZORA-BLYP-D3(BJ)/TZ2P, and B3LYP/6-311++G(d,p)~LANL2DZ//ZORA-BLYP-D3(BJ)/TZ2P were employed in the last project. Notably, B3LYP provides similar optimized geometries with B–B

distances of 1.787 Å for $[B_{12}H_{12}]^{2-}$ when compared to experimental crystallographic data [530], where the distance is 1.780 Å. Furthermore, our calculations regarding the relative stability of *closo*-$[B_{12}H_{12}]^{2-}$ compared to *closo*-*o*-$[C_2B_{10}H_{12}]$ are in agreement with experimental observations [531]. Thus, boron clusters are generally well-described by hybrid or GGA functionals. With this context, we now proceed to summarize our main findings.

Aromaticity and Stability in Boron Clusters: From *closo*-Carboranes to Metallabis(dicarbollides)

Metallabis(dicarbollides) $[M(C_2B_9H_{11})_2]^-$ (where M represents a transition metal), exhibit high stability and reduced chemical reactivity, and are considered aromatic species, equivalent to metallocenes. Metallocenes, such as ferrocene, $[Fe(C_5H_5)_2]$, are organometallic compounds typically consisting of a transition metal sandwiched between two planar aromatic ligands, two cyclopentadienyl anions in the case of ferrocene [532]. In contrast, $[M(C_2B_9H_{11})_2]^-$ do not contain planar conjugated ligands and the aromatic character of their pristine ligands (*nido*-$[C_2B_9H_{11}]^{2-}$) has not been demonstrated. According to Wade-Mingos' rule and their equivalence to PAH obeying Hückel's rule, one would expect *nido*-$[C_2B_9H_{11}]^{2-}$, with two extra electrons compared to the aromatic *closo*-$[B_{11}H_{11}]^{2-}$, to exhibit nonaromatic or antiaromatic character. However, the direct application of these rules in this context has not been proved. Our study aimed to explore the aromaticity of the carboranes shown in Figure 6.22. We also focused on determining the aromaticity of M = Co complex of $[M(C_2B_9H_{11})_2]^-$ and analyze its comparison to ferrocene.

Our discussion is structured around the following key topics: the aromaticity in *closo*- and *nido*-carboranes, the interplay of aromaticity and structural adaptation in boron clusters, a comparative analysis of metallabis(dicarbollides) and metallocenes, and the broader implications these findings have on our understanding of aromaticity in clusters.

In *closo*-$[C_2B_{10}H_{12}]$ structures, the presence of carbon atoms results in three distinct isomers: *ortho*, *meta*, and *para*. Notably, the *meta* and *para* isomers exhibit higher stability, being, respectively, 16.3 and 19.2 kcal/mol more stable than its *ortho* counterpart. Initially, it was hypothesized that this disparity in stability might be attributed to a reduced aromatic character in the *o*-isomer. However, aromaticity results obtained from NICS evaluated at the center of the C_2B_3/CB_4 and CB_4/B_5 rings in the three
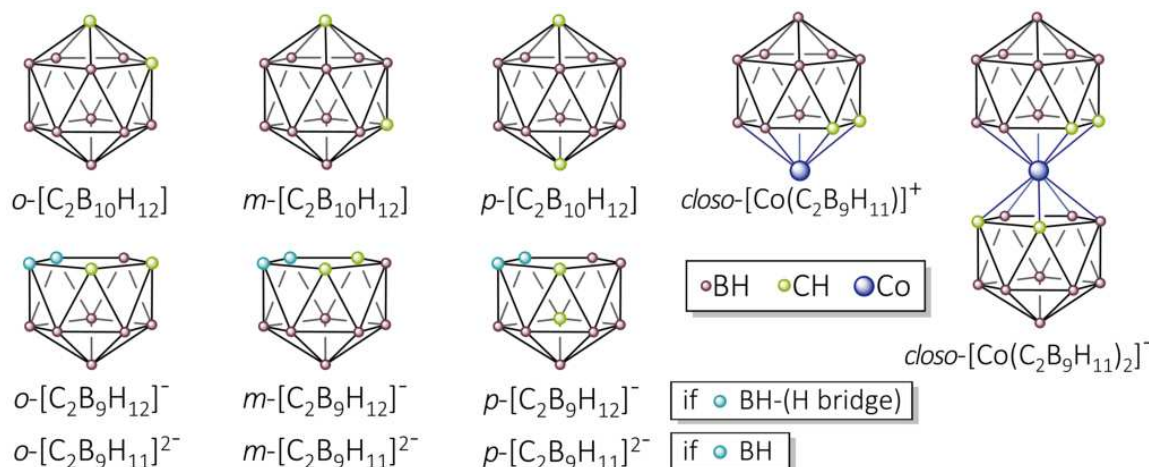
Figure 6.22 Isomers of the different carboranes studied in Section 5.4.1. Top left: the *closo-o-*, *closo-m-*, and *closo-p-*isomers of $[C_2B_9H_{12}]^-$. Bottom left: *nido-o-*, *nido-m-*, and *nido-p-*isomers of $[C_2B_9H_{12}]^-$ and $[C_2B_9H_{11}]^{2-}$. Right: *closo-o-*$[Co(C_2B_9H_{11})]^+$ and *closo-o-*$[Co(C_2B_9H_{11})_2]^-$.

isomers (Table 2 in Section 5.4.1) reveal that all isomers show comparable aromaticity results. This is further confirmed by the presence of similar ring currents in the *o-*, *m-*, and *p-*isomers, as shown in Figure 6.23. Consequently, this result suggests that factors beyond aromaticity, such as the specific structural arrangement of the carbon and boron atoms within the cluster and the resultant electronic distribution, are significant determinants of the clusters' reactivity and stability.

In the case of *nido-*$[C_2B_9H_{11}]^{2-}$, the coordination ligand of metallabis(dicarbollide), there are also three isomers. For all these isomers, the ring currents exhibit similar characteristics, offering limited insights. Notably, a comparison between *nido-*$[C_2B_9H_{11}]^{2-}$ and *closo-*$[C_2B_{10}H_{12}]$ reveals a change in the aromaticity, indicated by distinct NICS values. In the *nido* cluster, the NICS value at the coordination face (5-MR located at the top part of the *nido* systems in Figure 6.22) is -19.5 ppm, which is lower than the *closo* cluster having a NICS $= -33.7$ ppm. Conversely, for the other 5-MR, the NICS at the center is -37.0 ppm in the *nido* form compared to -32.7 ppm in the *closo*. This observation, where the top ring in *nido-*$[C_2B_9H_{11}]^{2-}$ is not the most aromatic, contrasts with the structure of the cyclopentadienyl anion (the ligand in the ferrocene complex). In the ferrocene complex, the metal is directly coordinated to a strongly aromatic ring (cyclopentadienyl). Conversely, in the metallabis(dicarbollide) with *nido-*$[C_2B_9H_{11}]^{2-}$ ligand, the aromaticity of the coordinating face is lower.
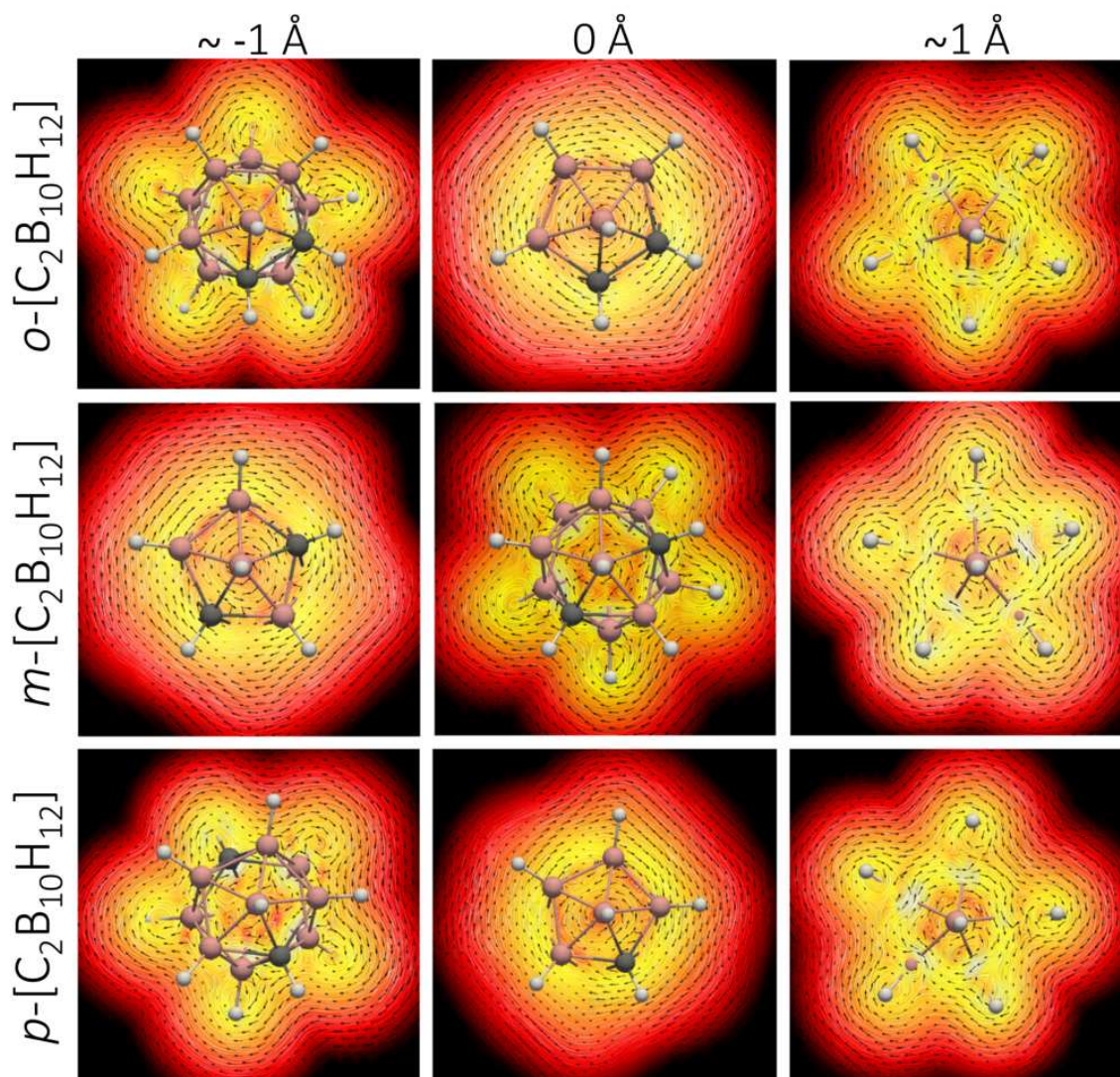
Figure 6.23 Representation of the current density vector field of the *o*-, *m*- and *p*-isomers of *closo*-carborane at the central (0 Å) plane and at planes at 1 and -1 Å, considering the orientations III (for *ortho*) and II (for *meta* and *para*) depicted in Figure 3 of Section 5.4.1, at B3LYP/6-311++G(d,p) level of theory. The color scale corresponds to the strength of the modulus of the current density susceptibility in the range of 0.0001 (dark red) to 0.4 (white) nA · T^{-1} · Å^{-2}.

Building on these insights into the aromaticity within *nido*-clusters, we now discuss the results for metallabis(dicarbollides). Metallabis(dicarbollides) and metallocenes, initially perceived as analogous, exhibit distinct aromatic characteristics upon closer examination. Metallocenes, exemplified by ferrocene, consist of two parallel planar cyclopentadienyl ligands surrounding a metal, forming a pentagonal pyramid that aligns with traditional aromaticity concepts. In contrast, metallabis(dicarbollides) exhibit

global aromaticity, as opposed to the local aromaticity of cyclopentadienyl ligands in ferrocene. Evidence of this is seen in the ring current patterns and current density intensity in $[Co(C_2B_9H_{11})]^+$ and *closo*-$[C_2B_9H_{11})_2]^-$ (Figures 9 and 10 in Section 5.4.1), indicating global aromaticity in metallabis(dicarbollides) and contrasting with the local aromaticity in ferrocene.

The Character of 1,2-$C_2B_{10}H_{10}$ Carbon–Carbon Bond: Double or Triple?

The current project is centered on the study of 1,2-$C_2B_{10}H_{10}$. This *closo*-*o*-carborane derivative, is obtained through the homolytic elimination of two H atoms from adjacent carbons in 1,2-$C_2B_{10}H_{12}$. The same elimination reaction in benzene yields the aromatic product *o*-benzyne. Consequently, by analogy, the *o*-carborane derivative has been named 1,2-dehydro-*o*-carboryne. However, this nomenclature adopted in the chemistry community, implies a triple C≡C in 1,2-$C_2B_{10}H_{10}$. This assumption is primarily based on the comparisons between their parent compounds, *o*-carborane and benzene, both aromatic, and with some similarities in certain reactions, and also between *o*-benzyne and *o*-carboryne themselves, since both show apparently similar reactivity. However, it is crucial to note that *o*-benzyne is a 2D six-membered aromatic ring, while *o*-carboryne has a distinct chemical structure. Therefore, despite their shared features, a detailed characterization of the C–C bond nature and aromaticity was still needed to understand the similarities and differences of these systems.

Given these premises, we examined the geometric and electronic characteristics of the C–C bond in *o*-benzyne and *o*-carboryne. In *o*-benzyne, the C–C bond distance and bond order are closer to those of a typical triple bond. Particularly, the computed—at B3LYP/6-311++G(d,p) level—bond length in *o*-benzyne is 1.244 Å, compared to 1.203 Å in acetylene [307]. Additionally, the delocalization index of this *o*-benzyne C–C bond is 2.249, suggesting a bond character that aligns more closely with a triple bond. In contrast, in *o*-carboryne, the C–C bond distance is 1.356 Å, considerably longer than typical triple bond reference and resembling the distance found in a double bond (*e.g.*, C–C in sp²-hybridized ethylene is 1.339 Å). While a weaker triple bond might be expected in these compounds due to reduced orbital overlap and increased strain, the observed values in *o*-carboryne deviate significantly from typical triple bond characteristics. Furthermore, the smaller delocalization index in *o*-carboryne, being 1.883, also supports the idea of double bond character rather than a triple bond. The above results, together with additional evidence presented in Section 5.4.2, including

the Wiberg bond index, Mayer Bond Order, and fragment analysis of the occupied molecular orbitals, collectively suggest a weaker C–C interaction in *o*-carboryne. This led us to propose renaming this molecule as *o*-carborene, reflecting its unique bonding character.

To further understand the similarities and differences between these systems, we examined the aromatic character of *o*-benzyne and *o*-carboryne, focusing on how this aromaticity is influenced by the formation of specific bonds. To achieve this, we employed magnetic (NICS and GIMIC), electronic (MCI), and energetic (isomerization stabilization energies) aromaticity indices. We determined NICS values at both zero and one Å from the molecular plane of *o*-benzyne and benzene. Similarly, we assessed the NICS values at the center of the 5-MR containing one of the C atoms and the center of mass of the *o*-carboryne and *o*-carborane. The values obtained (see Table 1 in Section 5.4.2) are all negative and in all cases higher in absolute value than the ones found for benzene, suggesting that the aromaticity is not only preserved but increased after the homolytic elimination of the hydrogens. For the evaluation of the induced current densities computed with GIMIC, we defined five planes separated 1.0 Å and considered four different orientations of the external magnetic field (I-IV), represented in Figure 6.24. The resulting current densities are depicted in Figure 6.25. The results for benzene and o-benzyne are shown in Figure 5 in Section 5.4.2.

The current density plots reveal similar induced currents for *o*-carboryne and *o*-carborane, with the global diatropic current in *o*-carboryne marginally diminished due to the presence of local circulations surrounding the carbon atoms. A similar observation is noted for *o*-benzyne in comparison to benzene. These results suggest that the introduction of a stronger C–C bond into the structure does not enhance the aromatic character as much as NICS values might imply. This discrepancy with NICS is further supported by the MCI value of 0.077 for *o*-benzyne, which is quite close to the 0.072 value for benzene (Table 1 in Section 5.4.2). Additionally, the stabilization isomerization energies show values of -26.6 kcal/mol for 4-methyl-benzyne and -33.9 kcal/mol for toluene (see Figure 6 in Section 5.4.2), indicating that benzene has a slightly higher degree of aromaticity compared to *o*-benzyne. Despite some variations among different aromaticity indices, the general conclusion is that there is no substantial alteration in aromaticity following this structural transformation.

In summary, the study on 1,2-$C_2B_{10}H_{10}$ reveals that, contrary to initial assumptions, its C–C bond exhibits characteristics of a double bond rather than a triple bond,
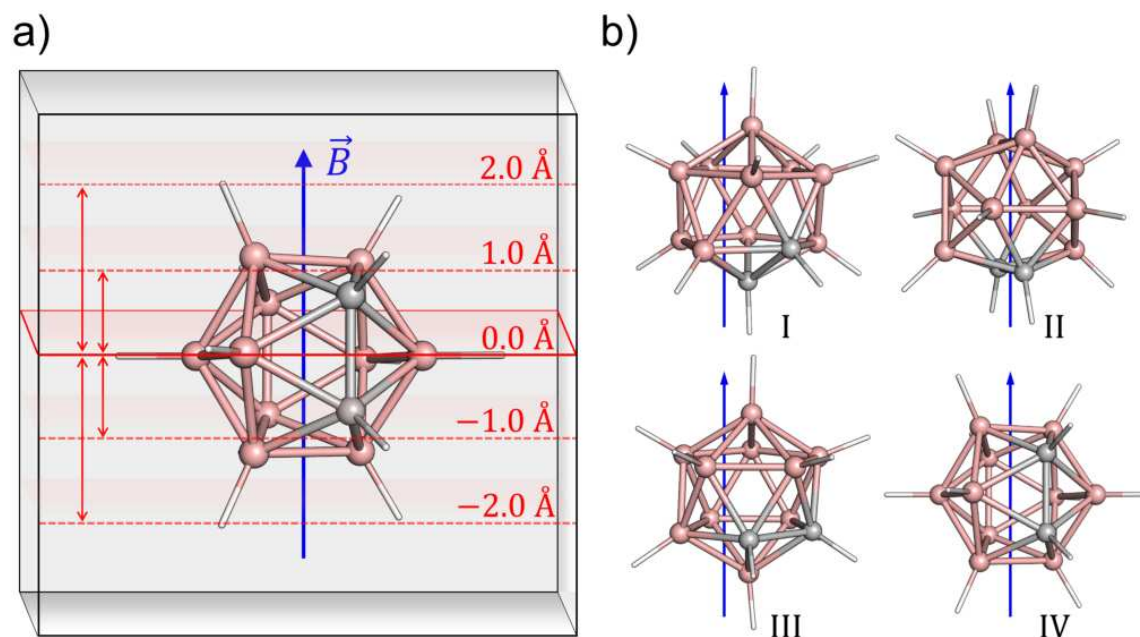
Figure 6.24 a) Representation of the planes selected for the evaluation of the current density and b) different orientations of the magnetic field ($\vec{B}$, blue arrow) considered in *o*-carborane and *o*-carboryne.
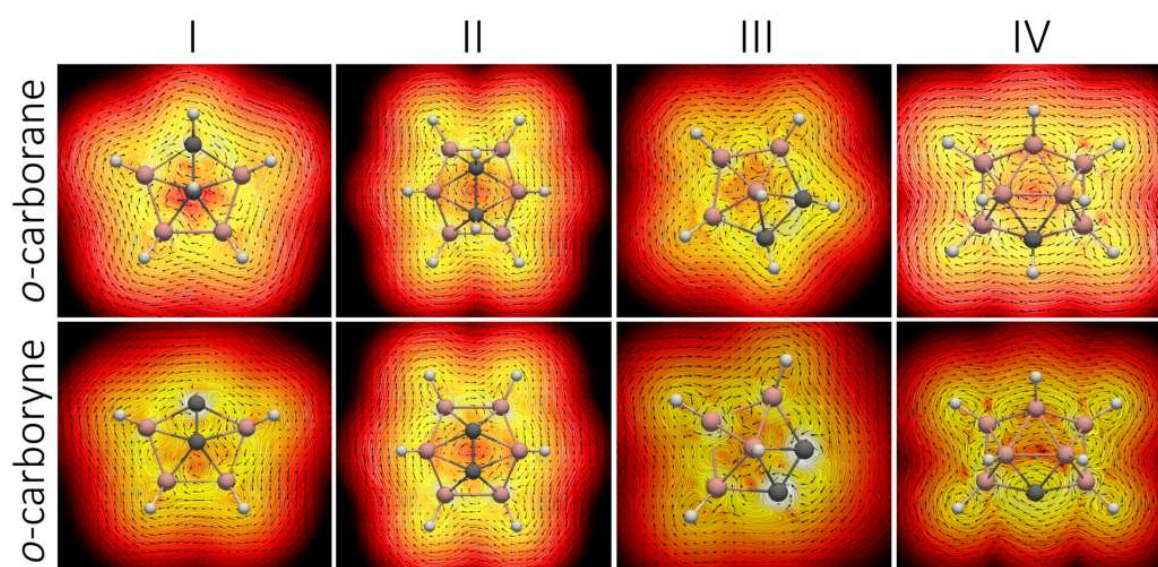

Figure 6.25 Representation of the current density vector field of *o*-carborane (top) and *o*-carboryne (bottom) at the central plane of the four orientations depicted in Figure 6.24 (see additional plots in Figures S1–S4 in the Supporting Information), at B3LYP/6-311++G(d,p) level of theory. The color scale corresponds to the strength of the modulus of the current density susceptibility in the range of 0.0001 (dark red) to 0.4 (white) nA $\cdot$ T^{-1} $\cdot$ Å^{-2}.

leading to the reclassification of the molecule as *o*-carborene. Additionally, we showed that aromaticity assessments indicate that the aromaticity is maintained in *o*-benzyne and *o*-carborene in agreement with the Hückel and Wade-Mingos rule, respectively.

Can the $[\mathbf{B_{12}I_{12}}]^{0/2+}$ Cluster Exhibit Double 3D Aromaticity?

In this project, we used the knowledge from our previous studies on the aromaticity of carboranes (Sections 5.4.1 and 5.4.2) and the exploration of the double aromaticity (Section 5.3) to investigate novel forms of double aromaticity. Motivated by the characteristics of σ, π-double-aromatic $C_6R_6{}^{2+}$ systems, where R represents iodine or chalcogen substituents, we hypothesized that *closo*-dodecaiodo-dodecaborate clusters ($[B_{12}I_{12}]^{0/2+}$) might similarly present double aromaticity. While the practical applications of this phenomenon in these clusters are not yet apparent, our research was motivated by the possibility of discovering a novel interplay between double and 3D aromaticity—a situation not yet explored.

In our study of double aromaticity in tropylium ion derivatives, we determined that to reach double aromaticity it is necessary the oxidation of the system, with the electrons removed from the σ-subsystem. This process opens a vacancy in one of the halogen p orbitals of the external ring. This oxidation introduces various resonance structures that contribute to electron delocalization, as depicted in Figure 1.19 in Section 1.3.2. Additionally, for double aromaticity to manifest, there are other considerations that we must take into account. The oxidized species has to fulfill the Hückel rules in both the σ- and π-subsystems. Another crucial factor is ensuring optimal balance between enough overlap between atoms while avoiding excessive overlap, which leads to repulsion and geometry distortion. Focusing on boron clusters, we chose to investigate the $[B_{12}I_{12}]^{2-}$ cluster due to the known aromaticity of its boron core. The choice of iodine was also strategic since in the iodine-shell that encircles the boron cage, the I$\cdots$I distances are sufficiently extended, making iodine an ideal candidate among halogens. Experimentally, it is observed that *closo*-$[B_{12}X_{12}]^{0/2+}$ clusters, where X represents a halogen, are highly stable and chemically inert [533, 534]. Notably, the X = I variant possesses the highest oxidation potential [535] necessary for creating the hole in the σ-system. Moreover, among all the halogen systems, $[B_{12}I_{12}]^{2-}$ is unique in that the electrons involved in oxidation are taken from the halogen shell [534]. Importantly, this complex also satisfies a key criterion for 3D aromaticity: the presence of a triply degenerate HOMO orbital, corresponding to the I$\cdots$I antibonding orbital (Figure 6.26).
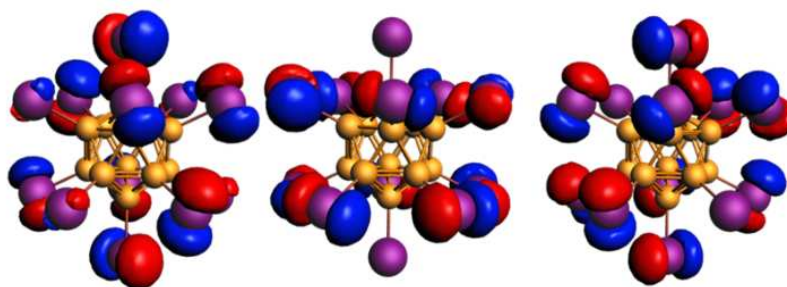
264

Figure 6.26 Triply degenerate HOMO orbital in $[B_{12}I_{12}]^{2-}$. Isocontour at 0.02.

Taking into account the previous considerations, we evaluated the structures of $[B_{12}I_{12}]^{2-}$ as well as its doubly ($[B_{12}I_{12}]$) and tetra ($[B_{12}I_{12}]^{2+}$) oxidized derivatives. The ionization energies to get $[B_{12}I_{12}]$ and $[B_{12}I_{12}]^{2+}$ are greater than 100 kcal/mol, and the ground states of these systems are a triplet and a quintet state, respectively. Interestingly, there is a minute reduction of the $I\cdots I$ bond distances going from the -2 to the neutral cluster and these distances are again slightly reduced with further oxidation to $[B_{12}I_{12}]^{2+}$, justified by the removal of two electrons from the sigma antibonding HOMO orbitals. In the two subsequent 2-electron oxidations the electrons are removed from the I-shell.

Regarding the aromaticity, in the case of $[B_{12}I_{12}]^{2-}$, the borane core adheres to the Wade-Mingos rule, and the I-shell has 72 electrons from the lone pairs following the $2(n+1)^2$ Hirsch rule. In contrast, $[B_{12}I_{12}]$ and $[B_{12}I_{12}]^{2+}$, obey Wade-Mingos rule but do not obey the Hirsch rule. Yet, these systems have vacancies in the 5p orbitals of iodine, which allow for electron delocalization, thereby favoring aromaticity. In order to evaluate the double aromaticity, we used NICS scans, ring currents, EDDB, and homodesmotic reactions.

For the NICS scans, we sampled values along the black arrow represented in Figure 6.27a, which starts at the geometrical center of the boron cage and crosses the 3MR formed by three boron atoms, B_3 plane (at approximately 1.3 Å distance, depending on the system), and also the I_3 plane (at approximately 3.1 Å). These scans reveal significant changes in magnetic ring currents in different electronic/oxidation states of the dodecaiodo-dodecaborate cluster. In all cases the minimum of NICS, corresponding to the most aromatic values, is located around 1.2 Å, close to the B_3 plane. The triplet state of $[B_{12}I_{12}]$ and, to lesser extent the quartet of $[B_{12}I_{12}]^+$, show notably more negative NICS values than $[B_{12}I_{12}]^{2-}$ (Figure 6.28c). Alternatively, the quintet of $[B_{12}I_{12}]^{2+}$ present NICS values close to the parent dianion system. The
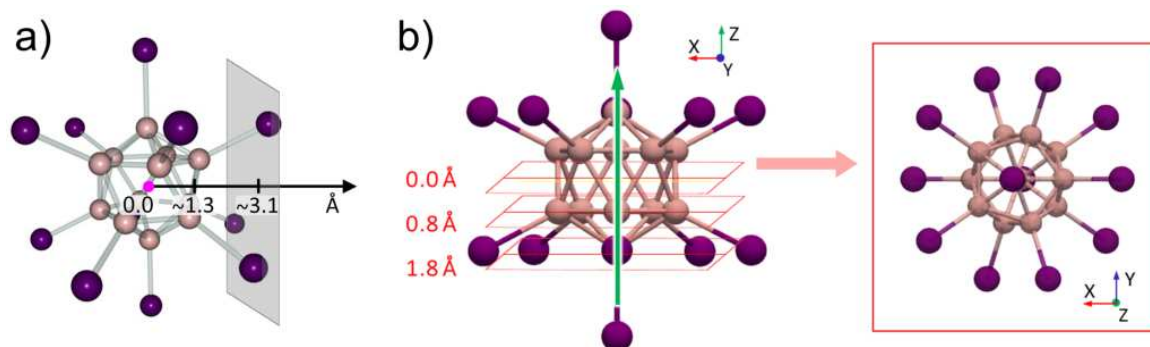
Figure 6.27 Orientation of a) the NICS scan and b) the external magnetic field (green arrow) and perpendicular planes (in red) where the current density susceptibility has been sampled.

singlet (6.9 kcal/mol less stable than the quintuplet) and triplet states of $[B_{12}I_{12}]^{2+}$ are more aromatic than the quintet, and present NICS values below -10 ppm at the region of the I_3 plane. These results indicate that the triplet state of $[B_{12}I_{12}]$, the quartet of $[B_{12}I_{12}]^+$, and the singlet and triplet $[B_{12}I_{12}]^{2+}$ are potentially double 3D aromatic systems.

Current density calculations, evaluated at the planes represented in Figure 6.27b, corroborated NICS scan findings, especially highlighting the generation of current density connecting iodine substituents (comparable to the ring currents in the double aromatic $C_6I_6^{2+}$, see Figure 6.29b) in different oxidation states (Figure 4 in Section 5.4.3), thus substantiating the potential double 3D-aromaticity in these clusters.

Following the current density calculations, the electronic aspects of double 3D aromaticity were explored using the EDDB method. Analysis revealed an increase in the number of delocalized electrons upon oxidation of $[B_{12}I_{12}]^{2-}$, particularly in the iodine sphere, with significant rises from 0.38 e in $[B_{12}I_{12}]^{2-}$ to higher values in the singlet (6.18 e) and triplet (5.67 e) states of $[B_{12}I_{12}]$, and singlet state of $[B_{12}I_{12}]^{2+}$ (10.93 e). However, the proportion of delocalized electrons in the iodine shell, despite being similar to that in the borane cage in the case of $[B_{12}I_{12}]^{2+}$, did not fully cover the I_{12} spherical surface (Figure 5 in Section 5.4.3), indicating incomplete delocalization. This finding, while highlighting electron delocalization among I atoms, does not fully support the double 3D aromaticity in these clusters.

To investigate the stabilization due to double 3D-aromaticity, the homodesmotic reactions presented in Table 1 of Section 5.4.3 were designed. These reactions show stabilization in $C_6I_6^{2+}$ due to double 2D aromaticity, but not in $[B_{12}I_{12}]^{0/2+}$, indicating
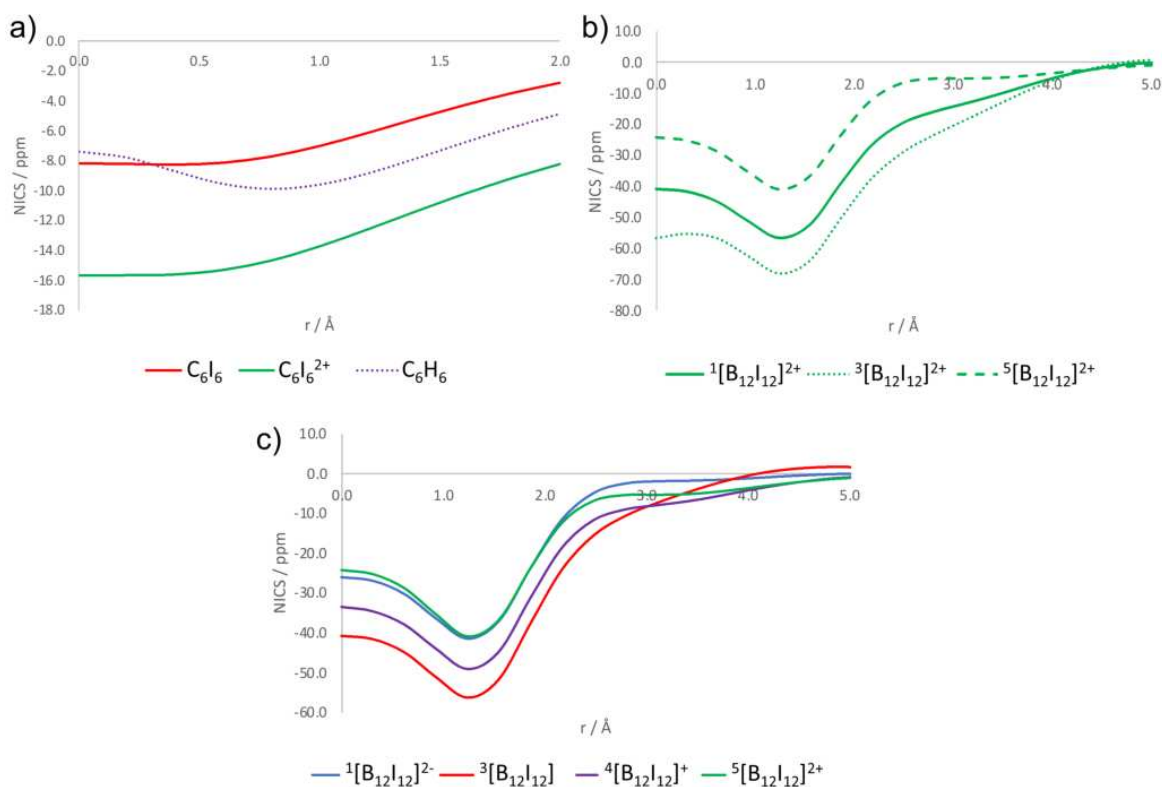
Figure 6.28 NICS scan (ppm) for a) C_6I_6, $C_6I_6^{2+}$, and $C_6I_6^{2+}$, b) singlet, triplet and quintet states of $[B_{12}I_{12}]^{2+}$, and c) singlet $[B_{12}I_{12}]^{2-}$, triplet $[B_{12}I_{12}]$, quartet $[B_{12}I_{12}]^{+}$, and quintet $[B_{12}I_{12}]^{2+}$, at ZORA-BLYP-D3(BJ)/TZ2P level of theory.
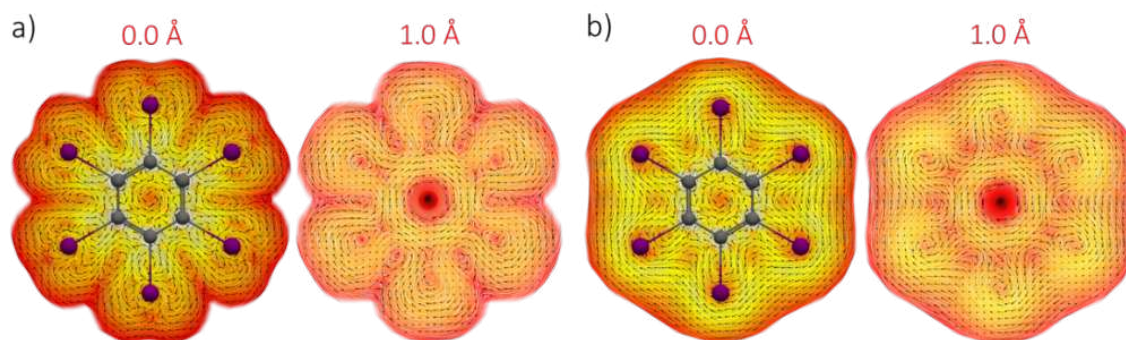
Figure 6.29 Current density susceptibility of a) C_6I_6, and b) $C_6I_6^{2+}$ computed at the molecular plane, and the plane at 1 Å, at the B3LYP/6-311++G(d,p)~LANL2DZ//ZORA-BLYP-D3(BJ)/TZ2P level of theory. The color scale corresponds to the strength of the modulus of the current density susceptibility in the range of 0.0001 (red) to 0.4 (white) $nA \cdot T^{-1} \cdot Å^{-2}$.

that energetic aspects do not support double 3D-aromaticity in $[B_{12}I_{12}]^{0/2+}$. Moreover, there is a lack of covalent bonding as corroborated by the absence of bond critical

points between the I$\cdots$I bonds, large distances between I atoms, and the fact that the occupied HOMOs are of antibonding character.

In summary, the absence of energetic evidence for aromaticity negates the presence of double 3D aromaticity in the studied systems. The discrepancies among the indices evaluating different aspects of aromaticity underscore the need for caution, as relying solely on magnetic indicators like NICS for determining aromaticity can be misleading. Finally, the intricate relationship between aromaticity, electron delocalization, and bonding nature in various iodoborane systems, highlights the complexities in achieving aromaticity without traditional covalent bonding and the implications for molecular stability.

7 Conclusions

In this thesis, we have conducted an extensive exploration of aromaticity in various chemical systems, focusing on complex electronic structures and molecular topologies. The main conclusions drawn from the present thesis are organized in two parts:

Part I: Understanding the Electronic Nature of Pro-Aromatic Quinoidal Systems in the Ground and Excited States

First:

We have revisited the excited state aromaticity of TMTQ and expanded our analysis to include other Kekulé diradicals. In the case of archetypal organic compounds, the aromaticity of the lowest-lying singlet and triplet excited states follows Baird's rule. However, pro-aromatic quinoidal molecules, with a non-aromatic ground state, can become Hückel, Baird, or Hückel-Baird hybrid aromatic following rearrangement of the electron density due to excitation. This distinct behavior has led to misinterpretations when assessing the electronic nature of such systems. A common oversight is the default use of Baird's rule, which does not always apply in excited-state molecules. In fact, our observations indicate that most of these Kekulé diradicals predominantly exhibit Hückel aromaticity. We proved that the combined use of Mandado's rule, spin-separated aromaticity indices, and other chemical descriptors (*e.g.*, charges, DIs, or spin densities) is necessary for a proper interpretation of the electronic structure. Understanding the aromatic character allows for the development of the aromaticity concept in excited states as a practical tool for designing molecules with targeted properties.

Second:

We determined the effect of the structural changes in the excited state properties of pro-aromatic quinoidal systems by analyzing the aromaticity of selected molecules varying in ring sizes and exocyclic substituents. We observed that systems with neutral

central rings and EWG or aromatic exocyclic substituents favor the stabilization of the diradical form, leaning towards the predominant Hückel aromatic character. On the contrary, the combination of EDG-substituted small anionic central rings with electron-acceptor exocyclic substituents presents an increased Baird aromatic character (>50%). On the other hand, the use of an electron-deficient conjugated central ring substituted with electron-donor exocyclic moieties is also a potentially successful strategy in approaching Baird aromaticity. With this, we established guidelines for the design of excited Hückel or Baird aromatic systems.

Third:

In exploring the influence of chain length and exocyclic substituents on pro-aromatic quinoidal systems with 6-MR (Chichibabin diradical(oid)s), we have identified key factors that govern the stabilization of the open-shell singlet (OSS) and triplet (T) states. Poly-*para*-phenylenes with less than three phenylene units, present a quinoid closed-shell (CS) ground state. The elongation of the π-system (by increasing the number of phenylene units) stabilizes the Hückel aromatic OSS, which becomes the ground state in species with three or more phenylene units. This transition is accompanied by a notable decrease in the $\Delta E_{\text{OSS-T}}$ energy gap, reaching near zero for five-unit oligomers. The EDGs at peripheral positions destabilize the presence of diradicals near these positions, thus favoring the CS structure. On the contrary, EWGs and aromatic substituents favor the diradical state, stabilizing the OSS and T states. The aromaticity of the 6-MRs increases with the stabilization of diradical forms. These insights provide a framework for predicting and tuning the aromatic (diradical) character of molecules, informing the development of organic semiconductors, photovoltaics, and other optoelectronic applications.

Part II: Aromaticity of Systems with Complex Molecular Topologies

Fourth:

The investigation of aromatic pathways in complex molecular topologies offers a new dimension in molecular design. It provides a deeper understanding of how alterations in aromatic circuits can directly influence the physical and chemical properties of a molecule. The correlation between aromaticity and optical properties in these complex molecules is particularly striking. In (sub)phthalocyanines, modifications in the aromatic pathways, especially through *meso*-position substitution, significantly influence the positioning of Q and B bands in the UV-Vis spectrum. This insight is crucial for designing novel phthalocyanine derivatives with tailored optical characteristics.

Similarly, in $C_{80}H_{30}$ nanographene, identifying the most aromatic pathways provides a roadmap for strategic modifications. These modifications suggest the potential for fine-tuning molecular properties, which may lead to the development of novel compounds in material science and molecular engineering. The integration of theoretical insights with practical applications hints at the possibility of employing aromaticity indices such as AV1245 and EDDB as potential tools for pinpointing structural modifications that lead to targeted molecular properties.

Fifth:

The exploration of double σ-π-aromaticity in complex molecular systems, extending beyond the realm of substituted benzenes, reveals a series of intricate challenges. Crucial insights from our research reveal that the generation of an electronic 'hole' in the σ framework is a necessary but not a sufficient condition for double aromaticity. There are other critical factors such as abiding the electron counts determined by Hückel and Baird, ensuring extensive electron delocalization, and maintaining the delicate balance between molecular size, orbital interactions, and structural strain. Our studies, particularly on species like the singlet state of $C_7Br_7^{+3}$ and the triplet state of $C_7Br_7^{+3}$, and the exploration of double 3D-aromaticity in $[B_{12}I_{12}]$ species, underscore that double aromaticity necessitates a nuanced, multifaceted approach. This approach must integrate electronic and structural aspects. This comprehensive understanding opens avenues for innovative molecular design, emphasizing the need for a holistic view in the pursuit of double σ-π-aromaticity in complex systems.

Sixth:

The comprehensive study of *closo-*, *nido-*carboranes, and metallabis(dicarbollides) has offered valuable insights into the interplay between aromaticity and molecular geometry, further challenging and expanding our understanding of these concepts in 3D-aromatic systems. Notably, the stability and reactivity of these boron clusters, especially in the context of resistance to deboronation and isomerization, are influenced more significantly by the position of carbon atoms than by their aromatic character. This finding underscores the intricate relationship between atomic positioning and molecular behavior, diverging from the patterns commonly observed in planar aromatic organic compounds. It is also demonstrated that the aromaticity observed in *closo-*boranes and *closo-*carboranes is also present in their *nido* counterparts, and consequently, we conclude that aromaticity in boron clusters survives important structural changes. Furthermore, our investigation of 1,2-$C_2B_{10}H_{10}$ (incorrectly labeled *o*-carboryne), a derivative of *o*-carborane—which is often mistakenly considered an isostere of benzene—

reveals subtle electronic and structural differences between this compound and *o*-benzyne. Understanding these nuances is crucial, as it clarifies the comparability of carboranyl and phenyl groups (as well as between 1,2-$C_2B_{10}H_{10}$ and *o*-benzyne), which is of utmost importance in drug design and molecular engineering. Contrary to initial assumptions, the C–C bond in 1,2-$C_2B_{10}H_{10}$ exhibits characteristics of a double bond rather than a triple bond, leading to the reclassification of the molecule as *o*-carborene. Additionally, we showed that aromaticity assessments indicate that the aromaticity is maintained in *o*-benzyne and *o*-carborene in agreement with the Hückel and Wade-Mingos rule, respectively.

Seventh:

In our observations across various systems, including (sub)phthalocyanines, $C_{80}H_{30}$ curved nanographene, tropylium ion derivatives, and dodecaiodo-dodecaborate clusters, we have found that magnetic indices tend to quantitatively exaggerate the aromatic character of these molecules. Although, in some cases, there is a qualitative agreement between magnetic and other indices (*e.g.*, electronic and geometric), there is a consistent trend of overestimating aromaticity. This raises questions about the reliability of magnetic indices for the quantitative assessment of aromaticity in systems with large rings, σ-aromaticity, or three-dimensional aromatic structures. Importantly, this observation aligns with and further corroborates earlier studies cited in this thesis, highlighting a critical concern: the prevalent reliance on magnetic indices, despite their tendency to exaggerate aromatic character in certain systems, calls for a reassessment of their use in aromaticity evaluation.

Bibliography

[1] J. Barnes, Early Greek Philosophy, Penguin Books, London, **1987**.

[2] P. Ball, In retrospect: A New System of Chemical Philosophy, *Nature*, **2016**, 537, 32–33.

[3] Wikipedia. History of the Periodic Table. https://en.wikipedia.org/wiki/History_ of_the_periodic_table. Accessed: 2024-02-26.

[4] H. W. Kroto, J. R. Heath, S. C. O'Brien, R. F. Curl, R. E. Smalley, C60: Buckminster-fullerene, *Nature*, **1985**, 318, 162–163.

[5] E. A. Rohlfing, D. M. Cox, A. Kaldor, Production and characterization of supersonic carbon cluster beams, *J. Chem. Phys.*, **1984**, 81, 3322–3330.

[6] R.W. Marks, The Dymaxion World of Buckminster Fuller, Anchor Books, New York, **1960**.

[7] R. B. Fuller, Geodesic Tent and Geodesic Structures, Patent No.2914074 and 3197927, New York, **1951**.

[8] E. Scholz, Introducing Groups Into Quantum Theory (1926–1930), *Hist. Math.*, **2006**, 33, 440–490.

[9] D. M. Bishop, Group Theory and Chemistry, Dover Publications, Inc., New York, **1993**.

[10] Gran Diccionari de la Llengua Catalana. Ordinador. https://www.diccionari.cat/ GDLC/ordinador. Accessed: 2023-11-08.

[11] T. Brown, B. Mann, N. Ryder, M. Subbiah, J. D. Kaplan, P. Dhariwal, A. Neelakantan, P. Shyam, G. Sastry, A. Askell, S. Agarwal, A. Herbert-Voss, G. Krueger, T. Henighan, R. Child, A. Ramesh, D. Ziegler, J. Wu, C. Winter, C. Hesse, M. Chen, E. Sigler, M. Litwin, S. Gray, B. Chess, J. Clark, C. Berner, S. McCandlish, A. Radford, I. Sutskever, D. Amodei, Language Models are Few-Shot Learners, *Advances in Neural Information Processing Systems*, **2020**, 33, 1877–1901.

[12] J. Hastings, M. Glauer, A. Memariani, F. Neuhaus, T. Mossakowski, Learning Chemistry: Exploring the Suitability of Machine Learning for the Task of Structure-Based Chemical Ontology Classification, *J. Cheminform.*, **2021**, 13, 1–20.

[13] S. Szymkuć, E. P. Gajewska, T. Klucznik, K. Molga, P. Dittwald, M. Startek, M. Bajczyk, B. A. Grzybowski, Computer-Assisted Synthetic Planning: The End of the Beginning, *Angew. Chem. Int. Ed.*, **2016**, 55, 5904–5937.

[14] P. Mori-Sánchez, A. M. Pendás, V. Luaña, A Classification of Covalent, Ionic, and Metallic Solids Based on the Electron Density, *J. Am. Chem. Soc.*, **2002**, 124, 14721–14723.

[15] E. Ramos-Cordoba, V. Postils, P. Salvador, Oxidation States From Wave Function Analysis, *J. Chem. Theory Comput.*, **2015**, 11, 1501–1508.

[16] C. F. Matta, R. J. Boyd, The Quantum Theory of Atoms in Molecules: From Solid State to DNA and Drug Design, Wiley-VCH, Weinheim, **2007**.

[17] E. Matito, M. Duran, M. Solà, The Aromatic Fluctuation Index (FLU): A New Aromaticity Index Based on Electron Delocalization, *J. Chem. Phys.*, **2005**, 122, 014109–014117.

[18] E. Matito, An Electronic Aromaticity Index for Large Rings, *Phys. Chem. Chem. Phys.*, **2016**, 18, 11839–11846.

[19] M. Solà, A. I. Boldyrev, M. K. Cyrañski, T. M. Krygowski, G. Merino, Aromaticity and Antiaromaticity: concepts and applications, John Wiley & Sons, Ltd., Chichester, **2023**.

[20] M. Rosenberg, C. Dahlstrand, K. Kilsa, H. Ottosson, Excited State Aromaticity and Antiaromaticity: Opportunities for Photophysical and Photochemical Rationalizations, *Chem. Rev.*, **2014**, 114, 5379–5425.

[21] P. v. R. Schleyer, J. I. Wu, F. P. Cossío, I. Fernández, Aromaticity in Transition Structures, *Chem. Soc. Rev.*, **2014**, 43, 4909–4921.

[22] G. Merino, M. Solà, I. Fernández, C. Foroutan-Nejad, P. Lazzeretti, G. Frenking, H. L. Anderson, D. Sundholm, F. P. Cossío, M. A. Petrukhina, J. Wu, J. I. Wu, A. Restrepo, Aromaticity: Quo vadis, *Chem. Sci.*, **2023**, 14, 5569–5576.

[23] M. Faraday, XX. On New Compounds of Carbon and Hydrogen, and on Certain other Products Obtained During the Decomposition of Oil by Heat, *Phil. Trans. R. Soc. Lon.*, **1825**, 440–466.

[24] Royal Institution. Michael Faraday's Sample of Benzene. https://www.rigb.org/explore-science/explore/collection/michael-faradays-sample-benzene. Accessed: 2023-11-08.

[25] E. Mitscherlich, Ueber das Benzol und die Säuren der Oel-und Talgarten, *Annalen der Pharmacie*, **1834**, 9, 39–48.

[26] A. W. V. Hofmann, I. On Insolinic Acid, *Proc. R. Soc. Lond.*, **1857**, 8, 1–3.

[27] M. Thompson, C. Style. Benzene - Molecule of the Month, August 2011. https://www.chm.bris.ac.uk/motm/benzene/benzeneh.htm. Accessed: 2023-11-08.

[28] A. Kekulé, Sur la Constitution des Substances Aromatiques, *Bulletin mensuel de la Société Chimique de Paris*, **1865**, 3, 98.

[29] A. J. Rocke, It began with a daydream: the 150th anniversary of the Kekulé benzene structure, *Angew. Chem. Int. Ed.*, **2015**, 54, 46–50.

[30] G. Koerner, Synthèse d'une Base Isomère à la Toluidíne, *C. R. Acad. Sci. Paris*, **1869**, 5, 111–114.

[31] E. Erlenmeyer, Studien über die sg Aromatischen Säuren, *Liebigs Ann.*, **1866**, 137, 327–359.

[32] L. G. Wade Jr., Química Orgánica: Volumes 1 and 2, Pearson Educación, Mexico, **2011**.

[33] R. Willstätter, E. Waser, Über Cyclo-octatetraen, *Ber. Dtsc. Chem. Ges.*, **1911**, 44, 3423–3445.

[34] W. Pauli, Über den Zusammenhang des Abschlusses der Elektronengruppen im Atom mit der Komplexstruktur der Spektren, *Z. Physik*, **1925**, 31, 765–783.

[35] P. T. Czech, Molecular Orbital Theory, *Encyclopedia Inorg. Bioinorg. Chem.*, **2011**, .

[36] E. Hückel, Grundzüge der Theorie ungesättigter und aromatischer Verbindungen, Verlag Chemie, **1938**.

[37] E. Hückel, Quantentheoretische beiträge zum benzolproblem, *Z. Physik*, **1931**, 70, 204–286.

[38] E. Hückel, Quanstentheoretische Beiträge zum Benzolproblem: II. Quantentheorie der induzierten Polaritäten, *Z. Physik*, **1931**, 72, 310–337.

[39] E. Hückel, Quantentheoretische Beiträge zum Problem der aromatischen und ungesättigten Verbindungen. III, *Z. Physik*, **1932**, 76, 628–648.

[40] E. Hückel, The Theory of Unsaturated and Aromatic Compounds, *Z. Elektrochemie*, **1937**, 43, 752–788.

[41] W. v. E. Doering, F. L. Detert, Cycloheptatrienylium Oxide, *J. Am. Chem. Soc.*, **1951**, 73, 876–877.

[42] W. v. E. Doering, L. H. Knox, The Cycloheptatrienylium (Tropylium) Ion, *J. Am. Chem. Soc.*, **1954**, 76, 3203–3206.

[43] R. Breslow, Antiaromaticity, *Acc. Chem. Res.*, **1973**, 6, 393–398.

[44] M. D. Watson, A. Fechtenkötter, K. Müllen, Big is Beautiful-"Aromaticity" Revisited from the Viewpoint of Macromolecular and Supramolecular Benzene Chemistry, *Chem. Rev.*, **2001**, 101, 1267–1300.

[45] T. Soya, W. Kim, D. Kim, A. Osuka, Stable [48]-,[50]-, and [52] Dodecaphyrins (1.1. 0.1. 1.0. 1.1. 0.1. 1.0): The Largest Hückel Aromatic Molecules, *Chem. Eur. J.*, **2015**, 21, 8341–8346.

[46] M. Hoffmann, C. J. Wilson, B. Odell, H. L. Anderson, Template-Directed Synthesis of a π-Conjugated Porphyrin Nanoring, *Angew. Chem. Int. Ed.*, **2007**, 46, 3122–3125.

[47] M. D. Peeks, T. D. W. Claridge, H. L. Anderson, Aromatic and Antiaromatic Ring Currents in a Molecular Nanoring, *Nature*, **2017**, 541, 200–203.

[48] C. Liu, M. E. Sandoval-Salinas, Y. Hong, T. Y. Gopalakrishna, H. Phan, N. Aratani, T. S. Herng, J. Ding, H. Yamada, D. Kim, D. Casanova, J. Wu, Macrocyclic Polyradicaloids with Unusual Super-Ring Structure and Global Aromaticity, *Chem*, **2018**, 4, 1586–1595.

[49] A. I. Boldyrev, L.-S. Wang, All-Metal Aromaticity and Antiaromaticity, *Chem. Rev.*, **2005**, 105, 3716–3757.

[50] A. N. Alexandrova, A. I. Boldyrev, H.-J. Zhai, L.-S. Wang, All-Boron Aromatic Clusters as Potential New Inorganic Ligands and Building Blocks in Chemistry, *Coord. Chem. Rev.*, **2006**, 250, 2811–2866.

[51] C. A. Tsipis, Aromaticity/Antiaromaticity in "Bare" and "Ligand-Stabilized" Rings of Metal Atoms: in Metal-Metal Bonding, pages 217–274. Springer International Publishing, Cham, **2010**.

[52] M. Mercero, A. I. Boldyrev, G. Merino, J. M. Ugalde, Recent Developments and Future Prospects of All-Metal Aromatic Compounds, *Chem. Soc. Rev.*, **2015**, 44, 6519–6534.

[53] F. Feixas, E. Matito, J. Poater, M. Solà, Metalloaromaticity, *WIREs Comput. Mol. Sci.*, **2013**, 3, 105–122.

[54] A. P. Sergeeva, B. B. Averkiev, A. I. Boldyrev, All-Transition Metal Aromaticity and Antiaromaticity: in Metal-Metal Bonding, pages 275–305. Springer International Publishing, Cham, **2010**.

[55] Y.-H. Xu, W.-J. Tian, A. Muñoz-Castro, G. Frenking, Z.-M. Sun, An all-metal fullerene:$[K@Au_{12}Sb_{20}]^{5-}$, *Science*, **2023**, 382, 840–843.

[56] W. N. Lipscomb, A. R. Pitochelli, M. F. Hawthorne, Probable Structure of the $B_{10}H_{10}{}^{2-}$ Ion, *J. Am. Chem. Soc.*, **1959**, 81, 5833–5834.

[57] A. R. Pitochelli, M. F. Hawthorne, The Isolation of the Icosahedral $B_{12}H_{12}^{-2}$ Ion, *J. Am. Chem. Soc.*, **1960**, 82, 3228–3229.

[58] W. H. Knoth, H. C. Miller, D. C. England, G. W. Parshall, E. L. Muetterties, Derivative Chemistry of $B_{10}H_{10}^{-}$ and $B_{12}H_{12}^{-}$, *J. Am. Chem. Soc.*, **1962**, 84, 1056–1057.

[59] M. Garcia-Borràs, S. Osuna, J. M. Luis, M. Swart, M. Solà, The Role of Aromaticity in Determining the Molecular Structure and Reactivity of (Endohedral Metallo) Fullerenes, *Chem. Soc. Rev.*, **2014**, 43, 5089–5105.

[60] O. El Bakouri, D. W. Szczepanik, K. Jorner, R. Ayub, P. Bultinck, M. Solà, H. Ottosson, Three-Dimensional Fully π-Conjugated Macrocycles: When 3D-Aromatic and When 2D-Aromatic-in-3D?, *J. Am. Chem. Soc.*, **2022**, 144, 8560–8575.

[61] P. v. R. Schleyer, H. Jiao, M. N. Glukhovtsev, J. Chandrasekhar, E. Kraka, Double Aromaticity in the 3,5-Dehydrophenyl Cation and in Cyclo[6]Carbon, *J. Am. Chem. Soc.*, **1994**, 116, 10129–10134.

[62] R. W. A. Havenith, F. De Proft, P. Fowler, P. Geerlings, σ-Aromaticity in H^{3+} and Li^{3+}: Insights from Ring-Current Maps, *Chem. Phys. Lett.*, **2005**, 407, 391–396.

[63] A. C. Tsipis, C. E. Kefalidis, C. A. Tsipis, The Role of the 5f Orbitals in Bonding, Aromaticity, and Reactivity of Planar Isocyclic and Heterocyclic Uranium Clusters, *J. Am. Chem. Soc.*, **2008**, 130, 9144–9155.

[64] N. C. Baird, Quantum Organic Photochemistry. II. Resonance and Aromaticity in the Lowest $^3\pi\pi^*$ State of Cyclic Hydrocarbons, *J. Am. Chem. Soc.*, **1972**, 94, 4941–4948.

[65] J. Aihara, Aromaticity-Based Theory of Pericyclic Reactions, *Bull. Chem. Soc. Jpn.*, **1978**, 51, 1788–1792.

[66] R. Breslow, Stable 4n π Electron Triplet Molecules, *Pure Appl. Chem.*, **1982**, 54, 927–938.

[67] P. B. Karadakov, Ground- and Excited-State Aromaticity and Antiaromaticity in Benzene and Cyclobutadiene, *J. Phys. Chem. A*, **2008**, 112, 7303–7309.

[68] P. B. Karadakov, Aromaticity and Antiaromaticity in the Low-Lying Electronic States of Cyclooctatetraene, *J. Phys. Chem. A*, **2008**, 112, 12707–12713.

[69] F. Feixas, J. Vandenbussche, P. Bultinck, E. Matito, M. Solà, Electron Delocalization and Aromaticity in Low-Lying Excited States of Archetypal Organic Compounds, *Phys. Chem. Chem. Phys.*, **2011**, 13, 20690–20703.

[70] Y. M. Sung, M.-C. Yoon, J. M. Lim, H. Rath, K. Naoda, A. Osuka, D. Kim, Reversal of Hückel (Anti)Aromaticity in the Lowest Triplet States of Hexaphyrins and Spectroscopic Evidence for Baird's Rule, *Nat. Chem.*, **2015**, 7, 418–422.

[71] O. El Bakouri, J. R. Smith, H. Ottosson, Henrik, Strategies for Design of Potential Singlet Fission Chromophores Utilizing a Combination of Ground-State and Excited-State Aromaticity Rules, *J. Am. Chem. Soc.*, **2020**, 142, 5602–5617.

[72] M. Solà, Why Aromaticity is a Suspicious Concept? Why?, *Front. Chem.*, **2017**, 5, 22-26.

[73] A. D. McNaught and A. Wilkinson. IUPAC. Compendium of Chemical Terminology, 2nd ed. (the "Gold Book"): Aromaticity. https://goldbook.iupac.org/terms/view/A00442. Accessed: 2023-11-10.

[74] M. Solà, Aromaticity Rules, *Nat. Chem.*, **2022**, 14, 585–590.

[75] M. Stepien, B. Szyszko, L. Latos-Grażyński, Three-Level Topology Switching in a Molecular Möbius Band, *J. Am. Chem. Soc.*, **2010**, 132, 3140–3152.

[76] I. Casademont-Reig, R. Guerrero-Avilés, E. Ramos-Cordoba, M. Torrent-Sucarrat, E. Matito, How Aromatic Are Molecular Nanorings? The Case of a Six-Porphyrin Nanoring, *Angew. Chem. Int. Ed.*, **2021**, 133, 24282–24290.

[77] I. Casademont-Reig L. Soriano-Agueda, E. Ramos-Cordoba, M. Torrent-Sucarrat, E. Matito, Reply to the Correspondence on "How Aromatic Are Molecular Nanorings? The Case of a Six-Porphyrin Nanoring", *Angew. Chem. Int. Ed.*, **2022**, 61, e202206836.

[78] C. Foroutan-Nejad, Magnetic Antiaromaticity—Paratropicity—Does Not Necessarily Imply Instability, *J. Org. Chem.*, **2023**, 14831—14835.

[79] J. Poater, X. Fradera, M. Duran, M. Solà, The Delocalization Index as an Electronic Aromaticity Criterion: Application to a Series of Planar Polycyclic Aromatic Hydrocarbons, *Chem. Eur. J.*, **2003**, 9, 400–406.

[80] J.-R. Deng, D. Bradley, M. Jirásek, H. L. Anderson, M. D. Peeks, Correspondence on "How Aromatic Are Molecular Nanorings? The Case of a Six-Porphyrin Nanoring", *Angew. Chem. Int. Ed.*, **2022**, 134, e202201231.

[81] H. Ottosson, A Focus on Aromaticity: Fuzzier Than Ever Before?, *Chem. Sci.*, **2023**, 14, 5542–5544.

[82] R. Gershoni-Poranne, A. Stanger, Magnetic criteria of aromaticity, *Chem. Soc. Rev.*, **2015**, 44, 6597–6615.

[83] P. v. R. Schleyer, C. Maerker, A. Dransfeld, H. Jiao, N. J. R. v. E. Hommes, Nucleus-Independent Chemical Shifts: A Simple and Efficient Aromaticity Probe, *J. Am. Chem. Soc.*, **1996**, 118, 6317–6318.

[84] J. F. M. Oth, G. Anthoine, J.-M. Gilles, Le Dianion du [16]Annulene, *Tetrahedron Lett.*, **1968**, 9, 6265–6270.

[85] R. A. Pascal Jr., R. B. Grossman, D. Van Engen, Synthesis of in-$[3^{4,10}][7]$-metacyclophane: Projection of an Aliphatic Hydrogen Toward the Center of an Aromatic Ring, *J. Am. Chem. Soc.*, **1987**, 109, 6878–6880.

[86] E. Vogel, H. D. Roth, The Cyclodecapentaene System, *Angew. Chem. Int. Ed.*, **1964**, 3, 228–229.

[87] E. Vogel, W. Maier, J. Eimer, Über das Valenzisomere System 9.10-dihydro-9.10-äthano-naphthalin-1.6-äthano-cyclodecapentaen, *Tetrahedron Lett.*, **1966**, 7, 655–660.

[88] R. H. Mitchell, Measuring Aromaticity by NMR, *Chem. Rev.*, **2001**, 101, 1301–1316.

[89] S. Fias, P. W. Fowler, J. L. Delgado, U. Hahn, P. Bultinck, Correlation of Delocalization Indices and Current-Density Maps in Polycyclic Aromatic Hydrocarbons, *Chem. Eur. J.*, **2008**, 14, 3093–3099.

[90] S. Fias, S. Van Damme, P. Bultinck, Multidimensionality of Delocalization Indices and Nucleus Independent Chemical Shifts in Polycyclic Aromatic Hydrocarbons, *J. Comput. Chem.*, **2008**, 29, 358–366.

[91] L. Zhao, R. Grande-Aztatzi, C. Foroutan-Nejad, J. M. Ugalde, G. Frenking, Aromaticity, the Hückel 4 n+ 2 Rule and Magnetic Current, *ChemistrySelect*, **2017**, 2, 863–870.

[92] S. Osuna, J. Poater, J. M. Bofill, P. Alemany, M. Solà, Are Nucleus-Independent (NICS) and ^{1}H NMR Chemical Shifts Good Indicators of Aromaticity in π-Stacked Polyfluorenes?, *Chem. Phys. Lett.*, **2006**, 428, 191–195.

[93] J. Poater, J. M. Bofill, P. Alemany, M. Solà, Role of Electron Density and Magnetic Couplings on the Nucleus-Independent Chemical Shift (NICS) Profiles of [2.2]Paracyclophane and Related Species, *J. Org. Chem.*, **2006**, 71, 1700–1702.

[94] J. Poater, M. Solà, R. G. Viglione, R. Zanasi, Local Aromaticity of the Six-Membered Rings in Pyracylene. A Difficult Case for the NICS Indicator of Aromaticity, *J. Org. Chem.*, **2004**, 69, 7537–7542.

[95] F. Feixas, E. Matito, J. Poater, M. Solà, On the Performance of Some Aromaticity Indices: a Critical Assessment Using a Test Set, *J. Comput. Chem.*, **2008**, 29, 1543–1554.

[96] M. Mauksch, S. B. Tsogoeva, Disclosure of Ground-State Zimmerman-Möbius Aromaticity in the Radical Anion of [6] Helicene and Evidence for 4π Periodic Aromatic Ring Currents in a Molecular "Metallic" Möbius Strip, *Chem. Eur. J.*, **2021**, 27, 14660–14671.

[97] J. J. Torres, R. Islas, E. Osorio, J. G. Harrison, W. Tiznado, G. Merino, Is Al_2Cl_6 aromatic? Cautions in Superficial NICS Interpretation, *J. Phys. Chem. A*, **2013**, 117, 5529–5533.

[98] R. Islas, G. Martínez-Guajardo, J. O. C. Jiménez-Halla, M. Solà, G. Merino, Not All that has a Negative NICS is Aromatic: The Case of the H-Bonded Cyclic Trimer of HF, *J. Chem. Theory Comput.*, **2010**, 6, 1131–1135.

[99] A. R. Katritzky, P. Barczynski, G. Musumarra, D. Pisano, M. Szafran, Aromaticity as a Quantitative Concept. 1. A Statistical Demonstration of the Orthogonality of Classical and Magnetic Aromaticity in Five-and Six-Membered Heterocycles, *J. Am. Chem. Soc.*, **1989**, 111, 7–15.

[100] P. Preethalayam, N. Proos-Vedin, S. Radenković, H. Ottosson, Azaboracyclooctatetraenes Reveal that the Different Aspects of Triplet State Baird-Aromaticity are Nothing but Different, *J. Phys. Org. Chem.*, **2023**, 36, e4455–e4469.

[101] J. Poater, S. Escayola, A. Poater, F. Teixidor, H. Ottosson, C. Viñas, M. Solà, Single—Not Double—3D-Aromaticity in an Oxidized Closo Icosahedral Dodecaiodo-Dodecaborate Cluster, *J. Am. Chem. Soc.*, **2023**, 145, 22527–22538.

[102] I. Casademont-Reig, T. Woller, V. García, J. Contreras-García, W. Tiznado, M. Torrent-Sucarrat, E. Matito, M. Alonso, Quest for the Most Aromatic Pathway in Charged Expanded Porphyrins, *Chem. Eur. J.*, **2023**, 29, e2022022.

[103] P. Lazzeretti, Current Density Tensors, *J. Chem. Phys.*, **2018**, 148, 134109.

[104] T. Janda, C. Foroutan-Nejad, Why is Benzene Unique? Screening Magnetic Properties of C_6H_6 Isomers, *ChemPhysChem*, **2018**, 19, 2357–2363.

[105] M. J. S. Dewar, A Molecular Orbital Theory of Organic Chemistry — VIII: Aromaticity and Electrocyclic Reactions, *Tetrahedron*, **1966**, 22, 75–92.

[106] H. E. Zimmerman, On Molecular Orbital Correlation Diagrams, the Occurrence of Möbius Systems in Cyclization Reactions, and Factors Controlling Ground-and Excited-State Reactions. I, *J. Am. Chem. Soc.*, **1966**, 88, 1564–1565.

[107] J. Yan, T. Slanina, J. Bergman, H. Ottosson, Photochemistry Driven by Excited-State Aromaticity Gain or Antiaromaticity Relief, *Chem. Eur. J.*, **2023**, 29, e202203748.

[108] J. Kim, J. Oh, A. Osuka, D. Kim, Porphyrinoids, a Unique Platform for Exploring Excited-State Aromaticity, *Chem. Soc. Rev.*, **2022**, 51, 268–292.

[109] K. Jorner, F. Feixas, R. Ayub, R. Lindh, M. Solà, H. Ottosson, Analysis of a Compound Class with Triplet States Stabilized by Potentially Baird Aromatic [10] Annulenyl Dicationic Rings, *Chem. Eur. J.*, **2016**, 22, 2793–2800.

[110] S. Escayola, C. Tonnelé, E. Matito, A. Poater, H. Ottosson, M. Solà, D. Casanova, Guidelines for Tuning the Excited State Hückel–Baird Hybrid Aromatic Character of Pro-Aromatic Quinoidal Compounds, *Angew. Chem. Int. Ed.*, **2021**, 60, 10255–10265.

[111] N. Proos-Vedin, S. Escayola, S. Radenković, M. Solà, H. Ottosson, The Lowest nπ* States of Heteroaromatics: When are They the Lowest Excited States and in What Way Can They Be Aromatic or Antiaromatic?, *ChemRxiv*, **2024**, .

[112] K. Jorner, Baird Aromaticity in Excited States and Open-Shell Ground States: In Aromaticity Modern Computational Methods and Applications, pages 375–405. Elsevier, Amsterdam, **2021**.

[113] J. Aihara, Graph Theory of Aromatic Stabilization, *Bull. Chem. Soc. Jpn.*, **2016**, 89, 1425–1454.

[114] H. Ottosson, K. Kilså, K. Chajara, M. C. Piqueras, R. Crespo, H. Kato, D. Muthas, Scope and Limitations of Baird's Theory on Triplet State Aromaticity: Application to the Tuning of Singlet–Triplet Energy Gaps in Fulvenes, *Chem. Eur. J.*, **2007**, 13, 6998–7005.

[115] R. Ayub, O. El Bakouri, K. Jorner, M. Solà, H. Ottosson, Can Baird's and Clar's Rules Combined Explain Triplet State Energies of Polycyclic Conjugated Hydrocarbons with Fused 4 n π-and (4 n+ 2) π-Rings?, *J. Org. Chem.*, **2017**, 82, 6327–6340.

[116] Y. M. Sung, J. Oh, W.-Y. Cha, W. Kim, J. M. Lim, M.-C. Yoon, D. Kim, Control and Switching of Aromaticity in Various All-Aza-Expanded Porphyrins: Spectroscopic and Theoretical Analyses, *Chem. Rev.*, **2017**, 117, 2257–2312.

[117] W. Zeng, O. El Bakouri, D. W. Szczepanik, H. Bronstein, H. Ottosson, Excited State Character of Cibalackrot-Type Compounds Interpreted in Terms of Hückel-Aromaticity: A Rationale for Singlet Fission Chromophore Design, *Chem. Sci.*, **2021**, 12, 6159–6171.

[118] B. Oruganti, J. Wang, B.Durbeej, Excited-State Aromaticity Improves Molecular Motors: A Computational Analysis, *Org. Lett.*, **2017**, 19, 4818–4821.

[119] M. Mandado, A. M. Graña, I. Pérez-Juste, Aromaticity in Spin-Polarized Systems: Can Rings be Simultaneously Alpha Aromatic and Beta Antiaromatic?, *J. Chem. Phys.*, **2008**, 129, 164114–164121.

[120] R. Berera, R. van Grondelle, J. T. M. Kennis, Ultrafast Transient Absorption Spectroscopy: Principles and Application to Photosynthetic Systems, *Photosynth. Res.*, **2009**, 101, 105–118.

[121] M. S. Schuurman, V. Blanchet, Time-resolved Photoelectron Spectroscopy: the Continuing Evolution of a Mature Technique, *Phys. Chem. Chem. Phys.*, **2022**, 24, 20012–20024.

[122] W. M. McClain, Two-photon molecular spectroscopy, *Acc. Chem. Res.*, **1974**, 7, 129–135.

[123] J. Aihara, Macrocyclic Conjugation Pathways in Porphyrins, *J. Am. Chem. Soc.*, **2008**, 112, 5305–5311.

[124] Y. Nakagami, R. Sekine, J. Aihara, The Origin of Global and Macrocyclic Aromaticity in Porphyrinoids, *Org. Biomol. Chem.*, **2012**, 10, 5219–5229.

[125] D. Szczepanik, M. Solà, The Electron Density of Delocalized Bonds (EDDBs) as a Measure of Local and Global Aromaticity: In Aromaticity Modern Computational Methods and Applications, pages 260–284. Elsevier, Amsterdam, **2021**.

[126] M. K. Cyrañski, T. M. Krygowski, M. Wisiorowski, N. J. R. van Eikema Hommes, P. v. R. Schleyer, Global and Local Aromaticity in Porphyrins: An Analysis Based on Molecular Geometries and Nucleus-Independent Chemical Shifts, *Angew. Chem. Int. Ed.*, **1998**, 37, 177–180.

[127] D. Bradley, B. K. Hillier, M. D. Peeks, Electronic Delocalization in Charged Macrocycles is Associated with Global Aromaticity, *Chem. Commun.*, **2023**, 59, 13438–13441.

[128] I. Casademont-Reig, E. Ramos-Cordoba, M. Torrent-Sucarrat, E. Matito, Aromaticity Descriptors Based on Electron Delocalization: In Aromaticity Modern Computational Methods and Applications, pages 236–259. Elsevier, Amsterdam, **2021**.

[129] T. Woller, P. Geerlings, F. De Proft, B. Champagne, M. Alonso, Aromaticity as a Guiding Concept for Spectroscopic Features and Nonlinear Optical Properties of Porphyrinoids, *Molecules*, **2018**, 23, 1333–1361.

[130] E. Vogel, The Porphyrins From the "Annulene Chemist's" Perspective, *Pure Appl. Chem.*, **1993**, 65, 143–152.

[131] D. P. Craig, N. L. Paddock, A Novel Type of Aromaticity, *Nature*, **1958**, 181, 1052–1053.

[132] E. Heilbronner, Hűckel Molecular Orbitals of Mőbius-type Conformations of Annulenes, *Tetrahedron Lett.*, **1964**, 5, 1923–1928.

[133] C. G. Claessens, D. Gonzalez-Rodríguez, M. S. Rodríguez-Morgade, A. Medina, T. Torres, Subphthalocyanines, Subporphyrazines, and Subporphyrins: Singular Nonplanar Aromatic Systems, *Chem. Rev.*, **2014**, 114, 2192–2277.

[134] J. Labella, T. Torres, Subphthalocyanines: Contracted Porphyrinoids with Expanded Applications, *Trends Chem.*, **2023**, 5, 353–366.

[135] I. Casademont-Reig, E. Ramos-Cordoba, M. Torrent-Sucarrat, E. Matito, How do the Hückel and Baird Rules Fade Away in Annulenes?, *Molecules*, **2020**, 25, 711–730.

[136] O. Dishi, P. Malakar, L. J. W. Shimon, S. Ruhman, O. Gidron, Ring Size Determines the Conformation, Global Aromaticity and Photophysical Properties of Macrocyclic Oligofurans, *Chem. Eur. J.*, **2021**, 27, 17794–17801.

[137] N. Fedik, A. I. Boldyrev, Insight into The Nature of Rim Bonds in Coronene, *J. Phys. Chem. A*, **2018**, 122, 8585–8590.

[138] J. R. Platt, Classification of Spectra of Cata-Condensed Hydrocarbons, *J. Chem. Phys.*, **1949**, 17, 484–495.

[139] E. Clar, The Aromatic Sextet, John Wiley & Sons, Ltd., New York, **1983**.

[140] M. Solà, Forty Years of Clar's Aromatic π-Sextet Rule, *Front. Chem.*, **2013**, 1, 22–30.

[141] C. Glidewell, D. Lloyd, MNDO Study of Bond Orders in Some Conjugated bi-and tri-Cyclic Hydrocarbons, *Tetrahedron*, **1984**, 40, 4455–4472.

[142] O. El Bakouri, J. Poater, F. Feixas, M. Solà, Exploring the Validity of the Glidewell–Lloyd Extension of Clar's π-sextet Rule: Assessment From Polycyclic Conjugated Hydrocarbons, *Theor. Chem. Acc.*, **2016**, 135, 1–12.

[143] P. Bultinck, S. Fias, R. Ponec, Local Aromaticity in Polycyclic Aromatic Hydrocarbons: Electron Delocalization Versus Magnetic Indices, *Chem. Eur. J.*, **2006**, 12, 8813–8818.

[144] M. Torrent-Sucarrat, S. Navarro, F. P. Cossío, J. M. Anglada, J. M. Luis, Relevance of the DFT Method to Study Expanded Porphyrins with Different Topologies, *J. Comput. Chem.*, **2017**, 38, 2819–2828.

[145] D. W. Szczepanik, M. Solà, M. Andrzejak, B. Pawełek, J. Dominikowska, M. Kukułka, K. Dyduch, T. M. Krygowski and H. Szatylowicz, The Role of the Long-Range Exchange Corrections in the Description of Electron Delocalization in Aromatic Species, *J. Comput. Chem.*, **2017**, 38, 1640–1654.

[146] I. Casademont-Reig, T. Woller, J. Contreras-García, M. Alonso, M. Torrent-Sucarrat, E. Matito, New Electron Delocalization Tools to Describe the Aromaticity in Porphyrinoids, *Phys. Chem. Chem. Phys.*, **2018**, 20, 2787–2796.

[147] F. Feixas, E. Matito, M. Solà, J. Poater, Analysis of Hückel's [4n+2] Rule through Electronic Delocalization Measures, *J. Phys. Chem. A*, **2008**, 112, 13231–13238.

[148] F. Feixas, J. O. Jiménez-Halla, E. Matito, J. Poater, M. Solà, A test to evaluate the performance of aromaticity descriptors in all-metal and semimetal clusters. An appraisal of electronic and magnetic indicators of aromaticity, *J. Chem. Theory Comput.*, **2010**, 6, 1118–1130.

[149] W. Wu, B. Ma, J. I. Wu, P. v. R. Schleyer, Y. Mo, Is Cyclopropane Really the σ-Aromatic Paradigm?, *Chem. Eur. J.*, **2009**, 15, 9730–9736.

[150] J. Chandrasekhar, E. D. Jemmis, P. v. R. Schleyer, Double Aromaticity: Aromaticity in Orthogonal Planes. The 3,5-Dehydrophenyl Cation, *Tetrahedron lett.*, **1979**, 20, 3707–3710.

[151] P. W. Fowler, N. Mizoguchi, D. E. Bean, R. W. A. Havenith, Double Aromaticity and Ring Currents in All-Carbon Rings, *Chem. Eur. J.*, **2009**, 15, 6964–6972.

[152] K. Kaiser, L. M. Scriven, F. Schulz, P. Gawel, L. Gross, H. L. Anderson, An sp-Hybridized Molecular Carbon Allotrope, Cyclo[18]carbon, *Science*, **2019**, 365, 1299–1301.

[153] Z. Liu, T. Lu, Q. Chen, An sp-Hybridized All-Carboatomic Ring, Cyclo[18]Carbon: Bonding Character, Electron Delocalization, and Aromaticity, *Carbon*, **2020**, 165, 461–467.

[154] A. J. Stasyuk, O. A. Stasyuk, M. Solà, A. A. Voityuk, Cyclo[18]Carbon: The Smallest All-Carbon Electron Acceptor, *Chem. Commun.*, **2020**, 56, 352–355.

[155] D. J. Sagl, J. C. Martin, The Stable Singlet Ground State Dication of Hexaiodobenzene: Possibly A sigma-Delocalized Dication, *J. Am. Chem. Soc.*, **1988**, 110, 5827–5833.

[156] J. C. Martin, L. J. Schaad, Sigma-Delocalized Aromatic Species Formed From Cyclic Arrays of Hypervalent Main-Group Element Species, *Pure Appl. Chem.*, **1990**, 62, 547–550.

[157] I. Ciofini, P. P. Lainé, C. Adamo, Quantifying Electron Delocalization in Orthogonal Channels: Theoretical Investigation of σ and π Aromaticity in $[C_6I_6]^{+2}$ and $[C_6Cl_6]^{+2}$, *Chem. Phys. Lett.*, **2007**, 435, 171–175.

[158] M. Hatanaka, M. Saito, M. Fujita, K. Morokuma, σ-Aromaticity in Hexa-Group 16 Atom-Substituted Benzene Dications: A Theoretical Study, *J. Org. Chem.*, **2014**, 79, 2640–2646.

[159] M. Orozco-Ic, J. Barroso, R. Islas, G. Merino, Delocalization in Substituted Benzene Dications: A Magnetic Point of View, *ChemistryOpen*, **2020**, 9, 657–661.

[160] M. Rauhalahti, S. Taubert, D. Sundholm, V. Liégeois, Calculations of Current Densities for Neutral and Doubly Charged Persubstituted Benzenes Using Effective Core Potentials, *Phys. Chem. Chem. Phys.*, **2017**, 19, 7124–7131.

[161] S. Furukawa, M. Fujita, Y. Kanatomi, M. Minoura, M. Hatanaka, K. Morokuma, K. Ishimura, M. Saito, Double Aromaticity Arising From σ-and π-Rings, *Commun. Chem.*, **2018**, 1, 60–67.

[162] P. W. Fowler, R. W. A. Havenith, Per iodoannulenes: A Generalized Annulene-within-an-Annulene Paradigm for Combined σ and π Ring Currents, *J. Phys. Chem. A*, **2021**, 125, 6374–6383.

[163] A. R. Pitochelli, M. F. Hawthorne, The preparation of a new boron hydride $b_{18}h_{22}$, *J. Am. Chem. Soc.*, **1962**, 84, 3218–3218.

[164] F. Klanberg, D. R. Eaton, L. J. Guggenberger, E. L. Muetterties, Chemistry of Boranes. XXVIII. New Polyhedral Borane Anions, $B_8H_8^{2-}$, $B_8H_8^{-}$, and $B_7H_7^{2-}$, *Inorg. Chem.*, **1967**, 6, 1271–1281.

[165] J. Aihara, Three-dimensional aromaticity of polyhedral boranes, *J. Am. Chem. Soc.*, **1978**, 100, 3339–3342.

[166] K. Wade, Electron Deficient Compounds, Nelson & Sons, Ltd, London, **1971**.

[167] K. Wade, The Structural Significance of the Number of Skeletal Bonding Electron-Pairs in Carboranes, the Higher Boranes and Borane Anions, and Various Transition-Metal Carbonyl Cluster Compounds, *J. Chem. Soc. D Chem. Commun.*, **1971**, 792–793.

[168] D. M. P. Mingos, A General Theory for Cluster and Ring Compounds of the Main Group and Transition Elements, *Nat. Phys. Sci.*, **1972**, 236, 99–102.

[169] D. M. P. Mingos, Polyhedral Skeletal Electron Pair Approach, *Acc. Chem. Res.*, **1984**, 17, 311–319.

[170] J. Poater, M. Solà, C. Viñas, F. Teixidor, π Aromaticity and Three-Dimensional Aromaticity: Two sides of the Same Coin?, *Angew. Chem. Int. Ed.*, **2014**, 126, 12387–12391.

[171] M. Solà, Connecting and Combining Rules of Aromaticity. Towards a Unified Theory of Aromaticity, *WIREs Comput. Mol. Sci.*, **2019**, 9, e1404.

[172] J. Poater, M. Solà, C. Viñas, F. Teixidor, Hückel's Rule of Aromaticity Categorizes Aromatic Closo Boron Hydride Clusters, *Chem. Eur. J.*, **2016**, 22, 7437–7443.

[173] R. B. King, Three-dimensional aromaticity in polyhedral boranes and related molecules, *Chem. Rev.*, **2001**, 101, 1119–1152.

[174] H. W. Kroto, A.W. Allaf, S.P. Balm, C60: Buckminsterfullerene, *Chem. Rev.*, **1991**, 91, 1213–1235.

[175] A. Hirsch, Z. Chen, H. Jiao, Spherical Aromaticity in Ih Symmetrical Fullerenes: the 2 (N+ 1) 2 Rule, *Angew. Chem. Int. Ed.*, **2000**, 39, 3915–3917.

[176] Z. Chen, H. Jiao, A. Hirsch, W. Thiel, The 2 $(N+1)^2$ rule for spherical aromaticity: further validation, *Mol. Model.*, **2001**, 7, 161–163.

[177] S. Wu, Y. Ni, Y. Han, X. Hou, C. Wang, W. Hu, J. Wu, Hückel-and Baird-Type Global Aromaticity in a 3D Fully Conjugated Molecular Cage, *Angew. Chem. Int. Ed.*, **2022**, 61, e202115571.

[178] F. Gomollón-Bel, J. García-Martínez, Emerging Chemistry Technologies for a Better World, *Nat. Chem.*, **2022**, 14, 113–114.

[179] A. T. Balaban, D. C. Oniciu, A. R. Katritzky, Aromaticity as a Cornerstone of Heterocyclic Chemistry, *Chem. Rev.*, **2004**, 104, 2777–2812.

[180] P. Suppan, Chemistry and Light, The Royal Society of Chemistry, Cambridge, **1994**.

[181] D. C. Harris, M. D. Bertolucci, Symmetry and Spectroscpy: An Introduction to Vibrational and Electronic Spectroscopy, Dover Publications, Inc., New York, **1989**.

[182] P. Klán, J. Wirz, Photochemistry of Organic Compounds: From Concepts to Practice, John Wiley & Sons, Inc., New Jersey, **2009**.

[183] A. Jablonski, Efficiency of Anti-Stokes Fluorescence in Dyes, *Nature*, **1933**, 131, 839–840.

[184] F. Hund, Zur Deutung Verwickelter Spektren, Insbesondere der Elemente Scandium Bis Nickel, *Z. Physik*, **1925**, 33, 345–371.

[185] M. A. El-Sayed, Triplet State. Its Radiative and Nonradiative Properties, *Acc. Chem. Res.*, **1968**, 1, 8–16.

[186] M. M. Christel, Understanding and Controlling Intersystem Crossing in Molecules, *Annu. Rev. Phys. Chem.*, **2021**, 72, 617–640.

[187] J. C. Tully, Perspective on "Zur Quantentheorie der Molekeln" Born M, Oppenheimer R (1927) Ann Phys 84: 457, *Theor. Chem. Acc.*, **2000**, 103, 173–176.

[188] N. Kandoth, M. Claros, N. Rodriguez, J. Lloret-Fillol, Photoinduced Electron-Transfer in First-Row Transition Metal Complexes: In Springer Handbook of Inorganic Photochemistry, pages 493–546. Springer International Publishing, Cham, **2022**.

[189] J. Zhao, W. Wu, J. Sun, S. Guo, Triplet Photosensitizers: From Molecular Design to Applications, *Chem. Soc. Rev.*, **2013**, 42, 5323–5351.

[190] F. Glaser, O. S. Wenger, Sensitizer-Controlled Photochemical Reactivity via Upconversion of Red Light, *Chem. Sci.*, **2023**, 14, 149–161.

[191] W. Fan, P. Huang, X. Chen, Overcoming the Achilles' heel of photodynamic therapy, *Chem. Soc. Rev.*, **2016**, 45, 6488–6519.

[192] Y. Peperstraete, M. Staniforth, L. A. Baker, N. D. N. Rodrigues, N. C. Cole-Filipiak, W. Quan, V. G. Stavros, Bottom-up Excited State Dynamics of Two Cinnamate-Based Sunscreen Filter Molecules, *Phys. Chem. Chem. Phys.*, **2016**, 18, 28140–28149.

[193] A. Taylor, D. J. Heyes, N. S. Scrutton, Catalysis by Nature's Photoenzymes, *Curr. Opin. Struct. Biol.*, **2022**, 77, 102491–102499.

[194] R. Car, M. Parrinello, Unified Approach for Molecular Dynamics and Density-Functional Theory, *Phys. Rev. Lett.*, **1985**, 55, 2471–2474.

[195] J. C. Tully, Perspective: Nonadiabatic Dynamics Theory, *J. Chem. Phys.*, **2012**, 137, 301–307.

[196] G. Bergamini, S. Silvi, Applied Photochemistry-When Light Meets Molecules, Springer International Publishing, Basel, **2016**.

[197] N. A. Romero, D. A. Nicewicz, Organic Photoredox Catalysis, *Chem. Rev.*, **2016**, 116, 10075–10166.

[198] F. Castet, V. Rodriguez, J.-L. Pozzo, L. Ducasse, A. Plaquet, B. Champagne, Design and Characterization of Molecular Nonlinear Optical Switches, *Acc. Chem. Res.*, **2013**, 46, 2656–2665.

[199] L. Benov, Photodynamic Therapy: Current Status and Future Directions, *Med. Princ. Pract.*, **2014**, 24, 14–28.

[200] H. S. Jung, P. Verwilst, A. Sharma, J. Shin, J. L. Sessler, J. S. Kim, Organic Molecule-Based Photothermal Agents: An Expanding Photothermal Therapy Universe, *Chem. Soc. Rev.*, **2018**, 47, 2280–2297.

[201] Li, Haoyuan and Brédas, Jean-Luc, Developing Molecular-Level Models for Organic Field-Effect Transistors, *Natl. Sci. Rev.*, **2021**, 8, 167–181.

[202] Y. Zhang, L. Guo, X. Zhu, X. Sun, The Application of Organic Semiconductor Materials in Spintronics, *Front. Chem.*, **2020**, 8, 589207.

[203] Z. Zeng, M. Ishida, J. L. Zafra, X. Zhu, Y. M. Sung, N. Bao, R. D. Webster, B. S. Lee, R.-W. Li, W. Zeng, Y. Li, C. Chi, J. T. López Navarrete, J. Ding, J. Casado, D. Kim, J. Wu, Pushing Extended p-Quinodimethanes to the Limit: Stable Tetracyano-oligo (N-annulated Perylene) Quinodimethanes with Tunable Ground States, *J. Am. Chem. Soc.*, **2013**, 135, 6363–6371.

[204] R. Breslow, H. W. Chang, R. Hill, E. Wasserman, Stable Triplet States of Some Cyclopentadienyl Cations, *J. Am. Chem. Soc.*, **1967**, 89, 1112–1119.

[205] M. Saunders, R. Berger, A. Jaffe, J.M. McBride, J. O'Neill, R. Breslow, J.M. Hoffmann, C. Perchonock, E. Wasserman, R.S. Hutton, V.J Kuck, Unsubstituted Cyclopentadienyl Cation, a Ground-State Triplet, *J. Am. Chem. Soc.*, **1973**, 95, 3017–3018.

[206] R. Breslow, B. Jaun, R.Q. Kluttz, C. Xia, Ground State π-Electron Triplet Molecules of Potential Use in the Synthesis of Organic Ferromagnets, *Tetrahedron*, **1982**, 38, 863–867.

[207] J. H. D. Eland, Spectra of the Dications of Benzene, Naphthalene and Azulene, *Chem. Phys.*, **2008**, 345, 82–86.

[208] W.-Y. Cha, T. Kim, A. Ghosh, Z. Zhang, X.-S. Ke, R. Ali, V.M. Lynch, J. Jung, W. Kim, S. Lee, S. Fukuzumi, J.S. Park, J.L. Sessler, T.K. Chandrashekar, D. Kim, Bicyclic Baird-type aromaticity, *Nat. Chem.*, **2017**, 9, 1243–1248.

[209] Y. Ni, T.Y. Gopalakrishna, H. Phan, T. Kim, T.S. Herng, Y. Han, T. Tao, J. Ding, D. Kim, J.Wu, 3D Global Aromaticity in a Fully Conjugated Diradicaloid Cage at Different Oxidation States, *Nat. Chem.*, **2020**, 12, 242–248.

[210] E. Solel, S. Kozuch, Tuning the Spin, Aromaticity, and Quantum Tunneling in Computationally Designed Fulvalenes, *J. Org. Chem.*, **2018**, 83, 10826–10834.

[211] L. K. Montgomery, J. C. Huffman, E. A. Jurczak, M. P. Grendze, The Molecular Structures of Thiele's and Chichibabin's Hydrocarbons, *J. Am. Chem. Soc.*, **1986**, 108, 6004–6011.

[212] M. Bendikov, H. M. Duong, K. Starkey, K. N. Houk, E. A. Carter, F. Wudl, Oligoacenes: Theoretical Prediction of Open-Shell Singlet Diradical Ground States, *J. Am. Chem. Soc.*, **2004**, 126, 7416–7417.

[213] M. Abe, Diradicals, *Chem. Rev.*, **2013**, 113, 7011–7088.

[214] S. Das, J. Wu, Polycyclic Hydrocarbons With an Open-Shell Ground State, *Phys. Sci. Rev.*, **2017**, 2, 1–23.

[215] S. Zilberg, Y. Haas, Two-State Model of Antiaromaticity: the Low-Lying Singlet States, *J. Phys. Chem. A*, **1998**, 102, 10843–10850.

[216] P. Karafiloglou, The Double (or Dynamic) Spin Polarization in π Diradicals, *J. Chem. Educ.*, **1989**, 66, 816–818.

[217] D. A. Dougherty, Spin Control in Organic Molecules, *Acc. Chem. Res.*, **1991**, 24, 88–94.

[218] W. T. Borden, H. Iwamura, J. A. Berson, Violations of Hund's Rule in Non-Kekule Hydrocarbons: Theoretical Prediction and Experimental Verification, *Acc. Chem. Res.*, **1994**, 27, 109–116.

[219] J. Casado, *Para*-Quinodimethanes: A Unified Review of the Quinoidal-Versus-Aromatic Competition and its Implications, *Top. Curr. Chem.*, **2017**, 375, 209–248.

[220] J. Ehrmaier, E. J. Rabe, S. R. Pristash, K. L. Corp, C. W. Schlenker, A. L. Sobolewski, W. Domcke, Singlet–Triplet Inversion in Heptazine and in Polymeric Carbon Nitrides, *J. Phys. Chem. A*, **2019**, 123, 8099–8108.

[221] R. Pollice, P. Friederich, C. Lavigne, G. dos Passos Gomes, A. and Aspuru-Guzik, Organic Molecules with Inverted Gaps Between First Excited Singlet and Triplet States and Appreciable Fluorescence rates, *Matter*, **2021**, 4, 1654–1682.

[222] N. Aizawa, Y.-J. Pu, Y. Harabuchi, A. Nihonyanagi, R. Ibuka, H. Inuzuka, B. Dhara, Y. Koyama, K. Nakayama, S. Maeda, F. Araoka, D. Miyajima, Delayed Fluorescence from Inverted Singlet and Triplet Excited States, *Nature*, **2022**, 609, 502–506.

[223] J. Terence Blaskovits, M. H. Garner, C. Corminboeuf, Symmetry-Induced Singlet-Triplet Inversions in Non-Alternant Hydrocarbons, *Ang. Chem. Int. Ed.*, **2023**, 62, e202218156.

[224] M. H. Garner, J. Terence Blaskovits, C. Corminboeuf, Double-Bond Delocalization in Non-Alternant Hydrocarbons Induces Inverted Singlet-Triplet Gaps, *Chem. Sci.*, **2023**, 14, 10458–10466.

[225] A. Dreuw, J. L. Weisman, M. Head-Gordon, Long-Range Charge-Transfer Excited States in Time-Dependent Density Functional Theory Require Non-Local Exchange, *J. Chem. Phys.*, **2003**, 119, 2943–2946.

[226] J. Veciana, H. Iwamura, Organic Magnets, *MRS Bull.*, **2000**, 25, 41–51.

[227] C. Chi J. T. López-Navarrete J. Casado J. Jishan Z. Zeng, X. Shi, Pro-Aromatic and Anti-Aromatic π-conjugated Molecules: an Irresistible wish to be Diradicals, *Chem. Soc. Rev.*, **2015**, 44, 6578–6596.

[228] M. Nakano, B. Champagne, Nonlinear Optical Properties in Open-Shell Molecular Systems, *Wiley Interdiscip. Rev. Comput. Mol. Sci.*, **2016**, 6, 198–210.

[229] M. Nakano, Open-Shell-Character-Based Molecular Design Principles: Applications to Nonlinear Optics and Singlet Fission, *Chem. Rec.*, **2017**, 17, 27–62.

[230] Z. X. Chen, Y. Li, F. Huang, Persistent and stable organic radicals: Design, synthesis, and applications, *Chem*, **2021**, 7, 288–332.

[231] Y. Shen, G. Xue, Y. Dai, S. Moles-Quintero, H. Chen, D. Wang, F. Miao, F. Negri, Y. Zheng, J. Casado, Normal & Reversed Spin Mobility in a Diradical by Electron-Vibration Coupling, *Nat. Commun*, **2021**, 12, 6262–6270.

[232] K. Takatsuka, T. Fueno, K. Yamaguchi, Distribution of Odd Electrons in Ground-State Molecules, *Theor. Chim. Acta*, **1978**, 48, 175–183.

[233] K. Kamada, K. Ohta, A. Shimizu, T. Kubo, R. Kishi, H. Takahashi, E. Botek, B. Champagne, M. Nakano, Singlet Diradical Character from Experiment, *J. Phys. Chem. Lett.*, **2010**, 1, 937–940.

[234] E. Ramos-Cordoba, P. Salvador, Diradical Character From the Local Spin Analysis, *Phys. Chem. Chem. Phys.*, **2014**, 16, 9565–9571.

[235] M. Nakano, Introduction. In: Excitation Energies and Properties of Open-Shell Singlet Molecules, pages 1–7. Springer, Cham, **2014**.

[236] M. Nakano, R. Kishi, N. Nakagawa, S. Ohta, H. Takahashi, S.-I. Furukawa, K. Kamada, K. Ohta, B. Champagne, E. Botek, S. Yamada, K. Yamaguchi, Second Hyperpolarizabilities (γ) of Bisimidazole and Bistriazole Benzenes: Diradical Character, Charged State, and Spin State Dependences, *J. Phys. Chem. A*, **2006**, 110, 4238–4243.

[237] G. Tan, X. Wang, Isolable Bis(triarylamine) Dications: Analogues of Thiele's, Chichibabin's, and Muller's Hydrocarbons, *Acc. Chem. Res.*, **2017**, 50, 1997–2006.

[238] J. Messelberger, A. Grünwald, P. Pinter, M. M. Hansmann, D. Munz, Carbene Derived Diradicaloids–Building Blocks for Singlet Fission?, *Chem. Sci.*, **2018**, 9, 6107–6117.

[239] S. Escayola, M. Callís, A. Poater, M. Solà, Effect of Exocyclic Substituents and π-system Length on the Electronic Structure of Chichibabin Diradical(oid)s, *ACS Omega*, **2019**, 4, 10845–10853.

[240] Y. Jung, M. Head-Gordon, Controlling the extent of diradical character by utilizing neighboring group interactions, *J. Phys. Chem. A*, **2003**, 107, 7475–7481.

[241] I. Badia-Dominguez, A. Perez-Guardiola, J. C. Sancho-García, J. T. Lopez Navarrete, V. Hernandez Jolin, H. Li, D. Sakamaki, S. Seki, M. C. Ruiz Delgado, Formation of Cyclophane Macrocycles in Carbazole-Based Biradicaloids: Impact of the Dicyanomethylene Substitution Position, *ACS Omega*, **2019**, 4, 4761–4769.

[242] Z. Zeng, S. Lee, M. Son, K. Fukuda, P. Mayorga Burrezo, X. Zhu, Q. Qi, R.-W. Li, J. T. López Navarrete, J. Ding, J. Casado, M. Nakano, D. Kim, J. Wu, Push–Pull Type Oligo(N-annulated perylene)quinodimethanes: Chain Length and Solvent-Dependent Ground States and Physical Properties, *J. Am. Chem. Soc.*, **2015**, 137, 8572–8583.

[243] Z. Zeng, S. Lee, J. L. Zafra, M. Ishida, N. Bao, R. D. Webster, J. T. López Navarrete, J. Ding, J. Casado, D. Kim, J. Wu, Turning on the Biradical State of Tetracyano-Perylene and Quaterrylenequinodimethanes by Incorporation of Additional Thiophene Rings, *Chem. Sci.*, **2014**, 5, 3072–3080.

[244] S. Radenković, M. Antić, J. Đurđević, S. Jeremić, Electronic Structure Study of the Biradical Pleiadene-Like Molecules, *Monatsh. Chem.*, **2014**, 145, 281–290.

[245] S. Ito, M. Nakano, Theoretical Molecular Design of Heteroacenes for Singlet Fission: Tuning the Diradical Character by Modifying π-Conjugation Length and Aromaticity, *J. Phys. Chem. C*, **2015**, 119, 148–157.

[246] T. Stuyver, T. Zeng, Y. Tsuji, P. Geerlings, F. De Proft, Diradical Character as a Guiding Principle for the Insightful Design of Molecular Nanowires with an Increasing Conductance with Length, *Nano lett.*, **2018**, 18, 7298–7304.

[247] P. Ravat, M. Baumgarten, "Tschitschibabin type biradicals": benzenoid or quinoid?, *Phys. Chem. Chem. Phys.*, **2015**, 17, 983–991.

[248] J. Thiele, H. Balhorn, Ueber einen Chinoïden Kohlenwasserstoff, *Ber. Dtsch. Chem. Ges.*, **1904**, 37, 1463–1470.

[249] A. E. Tschitschibabin, Über einige phenylierte derivate des p,p-ditolyls, *Ber. Dtsch. Chem. Ges.*, **1907**, 40, 1810–1819.

[250] E. Müller, H. Pfanz, Über biradikaloide terphenylderivate, *Ber. Dtsch. Chem. Ges.*, **1941**, 74, 1051–1074.

[251] I. Badía-Domínguez, S. Canola, V. Hernandez-Jolin, J. T. López-Navarrete, J. C. Sancho-García, F. Negri, M. C. Ruiz-Delgado, Tuning the Diradical Character of Indolocarbazoles: Impact of Structural Isomerism and Substitution Position, *J. Phys. Chem. Lett.*, **2022**, 13, 6003–6010.

[252] J. M. Anglada, J. Poater, I. P. R. Moreira, J. M. Bofill, Controlling the Diradical Character of Thiele Like Compounds, *J. Org. Chem.*, **2023**, 88, 8553–8562.

[253] X. Hu, H. Chen, L. Zhao, M. Miao, X. Zheng, Y. Zheng, Nitrogen-Coupled Blatter Diradicals: The Fused Versus Unfused Bridges, *J. Mat. Chem. C*, **2019**, 7, 10460–10464.

[254] M. Romain, D. Tondelier, J.-C. Vanel, B. Geffroy, O. Jeannin, J. Rault-Berthelot, R. Métivier, C. Poriel, Dependence of the Properties of Dihydroindenofluorene Derivatives on Positional Isomerism: Influence of the Ring Bridging, *Angew. Chem. Int. Ed.*, **2013**, 52, 14147–14151.

[255] J. E. Barker, J. J. Dressler, A. Cardenas Valdivia, R. Kishi, E. T. Strand, L. N. Zakharov, S. N. MacMillan, C. J. Gómez-García, M. Nakano, J. Casado, M. M. Haley, Molecule Isomerism Modulates the Diradical Properties of Stable Singlet Diradicaloids, *J. Am. Chem. Soc.*, **2019**, 142, 1548–1555.

[256] D. Rottschäfer, J. Busch, B. Neumann, H.-G. Stammler, M. Van Gastel, R. Kishi, M. Nakano, G. Masayoshi, Rajendra S, Diradical Character Enhancement by Spacing: N-Heterocyclic Carbene Analogues of Müller's Hydrocarbon, *Chem. Eur. J.*, **2018**, 24, 16537–16542.

[257] B. C. Streifel, J. L. Zafra, G. L. Espejo, C. J. Gómez-García, J. Casado, J. D. Tovar, An Unusually Small Singlet–Triplet Gap in a Quinoidal 1,6-Methano[10]annulene Resulting from Baird's 4n π-Electron Triplet Stabilization, *Angew. Chem. Int. Ed.*, **2015**, 54, 5888–5893.

[258] J. Kim, J. Oh, S. Park, J. L. Zafra, J. R. DeFrancisco, D. Casanova, M. Lim, J. D. Tovar, J. Casado, D. Kim, Two-Electron Transfer Stabilized by Excited-State Aromatization, *Nat. commun.*, **2019**, 10, 4983–4991.

[259] M. C. Simpson, N. I. Novikova, Porphyrins: Electronic Structure and Ultraviolet/Visible Absorption Spectroscopy: in Fundamentals of Porphyrin Chemistry: A 21st Century Approach, pages 505–586. John Wiley & Sons, Ltd, Chichester, **2022**.

[260] P.-C. Lo, M. S. Rodríguez-Morgade, R. K. Pandey, D. K. P. Ng, T. Torres, F. Dumoulin, The Unique Features and Promises of Phthalocyanines as Advanced Photosensitisers for Photodynamic Therapy of Cancer, *Chem. Soc. Rev.*, **2020**, 49, 1041–1056.

[261] M. Gouterman, Spectra of porphyrins, *J. Mol. Spectrosc.*, **1961**, 6, 138–163.

[262] M. Gouterman, G. H. Wagnière, L. C. Snyder, Spectra of Porphyrins: Part II. Four Orbital Model, *J. Mol. Spectrosc.*, **1963**, 11, 108–127.

[263] Z. Zhou, Z. Shen, Structure Modification and Spectroscopic Properties of Artificial Porphyrinoids, *Isr. J. Chem.*, **2016**, 56, 119–129.

[264] J. Labella, G. Lavarda, L. Hernández-López, F. Aguilar-Galindo, S. Díaz-Tendero, J. Lobo-Checa, T. Torres, Preparation, Supramolecular Organization, and On-Surface Reactivity of Enantiopure Subphthalocyanines: From Bulk to 2D-Polymerization, *J. Am. Chem. Soc.*, **2022**, 144, 16579–16587.

[265] G. Lavarda, J. Labella, M. V. Martínez-Díaz, M. S. Rodríguez-Morgade, A. Osuka, T. Torres, Recent Advances in Subphthalocyanines and related Subporphyrinoids, *Chem. Soc. Rev.*, **2022**, 51, 9482–9619.

[266] R. R. Cranston, B. H. Lessard, Metal Phthalocyanines: Thin-Film Formation, Microstructure, and Physical Properties, *RSC Adv.*, **2021**, 11, 21716–21737.

[267] M. Yahya, Y. Nural, Z. Seferoğlu, Recent Advances in the Nonlinear Optical (NLO) Properties of Phthalocyanines: A Review, *Dyes Pigments*, **2022**, 198, 109960–109974.

[268] M. Torrent-Sucarrat, J. M. Anglada, J. M. Luis, Evaluation of the Nonlinear Optical Properties for an Expanded Porphyrin Hückel-Möbius Aromaticity Switch, *J. Chem. Phys.*, **2012**, 137, 184306–184315.

[269] M. Torrent-Sucarrat, S. Navarro, E. Marcos, J. M. Anglada, J. M. Luis, Design of Hückel–Möbius topological Switches with High Nonlinear Optical Properties, *J. Phys. Chem. C*, **2017**, 121, 19348–19357.

[270] T. Woller, P. Geerlings, F. De Proft, B. Champagne, M. Alonso, Fingerprint of Aromaticity and Molecular Topology on the Photophysical Properties of Octaphyrins, *J. Phys. Chem. C*, **2019**, 123, 7318–7335.

[271] M.-R. Ke, Z. Chen, J. Shi, Y. Wei, H. Liu, S. Huang, X. Li, B.-Y. Zheng, J.-D. Huang, A Smart and Visible Way to Switch the Aromaticity of Silicon (IV) Phthalocyanines, *Chem. Commun.*, **2023**, 59, 9832–9835.

[272] R. Gleiter, G. Haberhauer, Aromaticity and other Conjugation Effects, John Wiley & Sons, Weinheim, **2012**.

[273] M. S. Dresselhaus, Fifty Years in Studying Carbon-Based Materials, *Phys. Scr.*, **2012**, 2012, 14002–14012.

[274] S. Supriya, V. S. Shetti, G. Hegde, Review of conjugated porphyrin systems, *OSF Preprints*, **2020**, 1–43.

[275] C. Azarias, M. Pawelek, D. Jacquemin, Structural and Optical Properties of SubPorphyrinoids: a TD-DFT Study, *J. Phys. Chem. A*, **2017**, 121, 4306–4317.

[276] G. De La Torre, P. Vázquez, F. Agullo-Lopez, T. Torres, Role of Structural Factors in the Nonlinear Optical Properties of Phthalocyanines and Related Compounds, *Chem. Rev.*, **2004**, 104, 3723–3750.

[277] M. M. Montero-Campillo, A. M. Lamsabhi, O. Mo, M. Yanez, UV/Vis Spectra of Subporphyrazines and Subphthalocyanines with Aluminum and Gallium: A Time-Dependent DFT Study, *ChemPhysChem*, **2017**, 14, 915–922.

[278] C. J. P. Monteiro, M. A. F. Faustino, C. Serpa. Porphyrin-Based Compounds: Synthesis and Application, **2023**.

[279] C. Hunt, M. Peterson, C. Anderson, T. Chang, G. Wu, S. Scheiner, G. Ménard, Switchable Aromaticity in an Isostructural Mn Phthalocyanine Series Isolated in Five Separate Redox States, *J. Am. Chem. Soc.*, **2019**, 141, 2604–2613.

[280] A. B. Sorokin, Phthalocyanine Metal Complexes in Catalysis, *Chem. Rev.*, **2013**, 113, 8152–8191.

[281] J. C. Barona-Castaño, C. C. Carmona-Vargas, T. J. Brocksom, K. T. De Oliveira, Porphyrins as Catalysts in Scalable Organic Reactions, *Molecules*, **2016**, 21, 310.

[282] A. Tsuda, H. Furuta, A. Osuka, Syntheses, Structural Characterizations, and Optical and Electrochemical Properties of Directly Fused Diporphyrins, *J. Am. Chem. Soc.*, **2001**, 42, 10304–10321.

[283] R. Paolesse, S. Nardis, D. Monti, M. Stefanelli, C. Di Natale, Porphyrinoids for Chemical Sensor Applications, *Chem. Rev.*, **2017**, 4, 2517–2583.

[284] H. Gotfredsen, J.-R. Deng, J. M. Van Raden, M. Righetto, J. Hergenhahn, M. Clarke, A. Bellamy-Carter, J. Hart, J. O'Shea, T. D. W. Claridge, F. Duarte, A. Saywell, L. M. Herz, H. L. Anderson, Bending a Photonic Wire Into a Ring, *Nat. Chem.*, **2022**, 14, 1436–1442.

[285] A. H. Castro Neto, F. Guinea, N. M. R. Peres, K. S. Novoselov, A. K. Geim, The Electronic Properties of Graphene, *Rev. Mod. Phys.*, **2009**, 81, 109–162.

[286] J. Wang, F. Ma, W. Liang, R. Wang, M. Sun, Optical, Photonic and Optoelectronic Properties of Graphene, h-BN and Their Hybrid Materials, *Nanophotonics*, **2017**, 6, 943–976.

[287] T. Enoki, Y. Kobayashi, K.-I. Fukui, Electronic Structures of Graphene Edges and Nanographene, *Int. Rev. Phys. Chem.*, **2007**, 26, 609–645.

[288] M. Vázquez-Nakagawa, L. Rodríguez-Pérez, M. A. Herranz, N. Martín, Chirality Transfer from Graphene Quantum Dots, *Chem. Commun.*, **2016**, 52, 665–668.

[289] N. Suzuki, Y. Wang, P. Elvati, Z.-B. Qu, K. Kim, S. Jiang, E. Baumeister, J. Lee, B. Yeom, J. H. Bahng, J. Lee, A. Violi, N. A. Kotov, Chiral graphene quantum dots, *ACS Nano*, **2016**, 10, 1744–1755.

[290] M. Vázquez-Nakagawa, L. Rodríguez-Pérez, N. Martín, M. A. Herranz, Supramolecular Assembly of Edge Functionalized Top-Down Chiral Graphene Quantum Dots, *Ang. Chem. Int. Ed.*, **2022**, 61, e202211365.

[291] K. Kawasumi, Q. Zhang, Y. Segawa, L. T. Scott, K. Itami, A Grossly Warped Nanographene and the Consequences of Multiple Odd-Membered-Ring Defects, *Nat. Chem.*, **2013**, 5, 739–744.

[292] J. M. Fernández-García, P. J. Evans, S. Medina Rivero, I. Fernández, D. García-Fresnadillo, J. Perles, J. Casado, N. Martín, π-Extended Corannulene-Based Nanographenes: Selective Formation of Negative Curvature, *J. Am. Chem. Soc.*, **2018**, 140, 17188–17196.

[293] P. Izquierdo-García, J. M. Fernández-García, S. Medina Rivero, M. Šámal, J. Rybáček, L. Bednárová, S. Ramírez-Barroso, F. J. Ramírez, R. Rodríguez, J. Perles, D. García-Fresnadillo, J. Crassous, J. Casado, I. G. Starˊ, N. Martín, Helical Bilayer Nanographenes: Impact of the Helicene Length on the Structural, Electrochemical, Photophysical, and Chiroptical Properties, *J. Am. Chem. Soc.*, **2023**, 145, 11599–11610.

[294] K. Yamamoto, T. Harada, M. Nakazaki, T. Naka, Y. Kai, S. Harada, N. Kasai, Synthesis and Characterization of [7]circulene, *J. Am. Chem. Soc.*, **1983**, 105, 7171–7172.

[295] J. M. Fernández-García, P. J. Evans, S. Filippone, M. A. Herranz, N. Martín, Chiral Molecular Carbon Nanostructures, *Acc. Chem. Res.*, **2019**, 52, 1565–1574.

[296] X.-Y. Wang, A. Narita, K. Müllen, Precision Synthesis Versus Bulk-Scale Fabrication of Graphenes, *Nat. Rev. Chem.*, **2017**, 2, 0100.

[297] C. Wang, H. Dong, W. Hu, Y. Liu, D. Zhu, Semiconducting π-Conjugated Systems in Field-Effect Transistors: a Material Odyssey of Organic Electronics, *Chem. Rev.*, **2012**, 112, 2208–2267.

[298] S. Zank, J. M. Fernández-García, A. J. Stasyuk, A. A. Voityuk, M. Krug, M. Solà, D. M. Guldi, N. Martín, Initiating Electron Transfer in Doubly Curved Nanographene Upon Supramolecular Complexation of C$_{60}$, *Angew. Chem. Int. Ed.*, **2022**, 134, e202112834.

[299] Z. Zhou, Y. Zhu, J. M. Fernández-García, Z. Wei, I. Fernández, M. A. Petrukhina, N. Martín, Stepwise Reduction of a Corannulene-Based Helical Molecular Nanographene with Na Metal, *Chem. Commun.*, **2022**, 58, 5574–5577.

[300] S. Escayola, N. Proos-Vedin, A. Poater, H. Ottosson, M. Solà, In the Quest of Hückel–Hückel and Hückel–Baird Double Aromatic Tropylium(tri) Cation and Anion Derivatives, *J. Phys. Org. Chem.*, **2023**, 36, e4447–e4458.

[301] Y. Qiu, A. H. Winter, Anomalous Electronic Properties of Iodous Materials: Application to High-Spin Reactive Intermediates and Conjugated Polymers, *J. Org. Chem.*, **2020**, 85, 4145–4152.

[302] W. N. Lipscomb, Three-Center Bonds in Electron-Deficient Compounds. Localized Molecular Orbital Approach, *Acc. Chem. Res.*, **1973**, 6, 257–262.

[303] K. Wade. Structural and Bonding Patterns in Cluster Chemistry. In *Adv. Inorg. Chem. Radiochem.*, volume 18, pages 1–66. Elsevier, **1976**.

[304] R. W. Rudolph, Boranes and Heteroboranes: a Paradigm for the Electron Requirements of Clusters?, *Acc. Chem. Res.*, **1976**, 9, 446–452.

[305] B. Stibr, Carboranes other than C$_2$B$_{10}$H$_{12}$, *Chem. Rev.*, **1992**, 92, 225–250.

[306] R. Liao, L. Chai, Y. Zhu, A Theoretical Study on the Stability Difference of the Borane and Carborane C$_2$B$_{n-2}$H$_n$ ($5 \leq n \leq 7$) Clusters, *Int. J. Quantum Chem.*, **2015**, 115, 216–223.

[307] D. R. Lide, CRC Handbook of Chemistry and Physics, CRC press, Cleveland, **2004**.

[308] J. Plesek, Potential Applications of the Boron Cluster Compounds, *Chem. Rev.*, **1992**, 92, 269–278.

[309] M. F. Hawthorne, D. C. Young, P. A. Wegner, Carbametallic Boron Hydride Derivatives. I. Apparent Analogs of Ferrocene and Ferricinium Ion, *J. Am. Chem. Soc.*, **1965**, 87, 1818–1819.

[310] B. A. Barnum, P. J. Carroll, L. G. Sneddon, Syntheses and Structural Characterizations of Metallabis(tricarbadecaboranyl) Sandwiches,(η4-MeC3B7H9) 2M (M= Ni, Pd, Pt): Tricarbadecaboranyl Analogs of (η3-C3H5) 2M Complexes, *Organometallics*, **1996**, 15, 645–654.

[311] G. L. Gutsev, A. I. Boldyrev, DVM-Xα calculations on the ionization potentials of MX$_{k+1}^{-}$ complex anions and the electron affinities of MX$_{k+1}$ "superhalogens", *Chem. Phys.*, **1981**, 56, 277–283.

[312] T. Zhao, Q. Wang, P. Jena, Rational Design of Super-Alkalis and Their Role in CO$_2$ Activation, *Nanoscale*, **2017**, 9, 4891–4897.

[313] B. P. Dash, R. Satapathy, J. A. Maguire, N. S. Hosmane, Polyhedral Boron Clusters in Materials Science, *New J. Chem.*, **2011**, 35, 1955–1972.

[314] R. B. Silverman, M. W. Holladay, The Organic Chemistry of Drug Design and Drug Action, Academic press, San Diego, **2014**.

[315] J. Poater, C. Viñas, S. Escayola, M. Solà, F. Teixidor, Pioneering the Power of Twin Bonds in a Revolutionary Double Bond Formation. Unveiling the True Identity of *o*-Carboryne as *o*-Carborene, *Chem. Eur. J.*, **2023**, 29, e202302448.

[316] M. Scholz, K. Bensdorf, R. Gust, E. Hey-Hawkins, Asborin: the Carbaborane Analogue of Aspirin, *ChemMedChem*, **2009**, 4, 746–748.

[317] M. Felderhoff, C. Weidenthaler, R. von Helmolt, U. Eberle, Hydrogen Storage: the Remaining Scientific and Technological Challenges, *Phys. Chem. Chem. Phys.*, **2007**, 9, 2643–2653.

[318] A. Kumar, N. Vyas, A. K. Ojha, Hydrogen Storage in Magnesium Decorated Boron Clusters (Mg_2B_n, $n = 4$–14): A Density Functional Theory Study, *Int. J. Hydrog. Energy*, **2020**, 45, 12961–12971.

[319] R. N. Grimes, Metallacarboranes in the New Millennium, *Coord. Chem. Rev.*, **2000**, 200, 773–811.

[320] S. D. Reilly, C. F. V. Mason, P. H. Smith, Cobalt(III) dicarbollide: A potential [1]37Cs and [9]0Sr waste extraction agent, Los Alamos National Laboratory, Los Alamos, **1990**.

[321] I. B. Sivaev, V. I. Bregadze, Chemistry of Cobalt bis-(dicarbollides). A Review, *Collect. Czech. Chem. Commun.*, **1999**, 64, 783–805.

[322] C. Viñas, S. Gomez, J. Bertran, F. Teixidor, J.-F. Dozol, H. Rouquette, New Polyether-Substituted Metallacarboranes as Extractants for [1]37Cs and [9]0Sr from Nuclear Wastes, *Inorg. Chem.*, **1998**, 37, 3640–3643.

[323] C. Viñas, S. Gomez, J. Bertran, F. Teixidor, J.-F. Dozol, H. Rouquette, Cobaltabis(dicarbollide) Derivatives as Extractants for Europium from Nuclear Wastes, *Chem. Commun.*, **1998**, 191–192.

[324] N. S. Hosmane, Boron Science: New Technologies and Applications, CRC Press, Boca Raton, **2012**.

[325] R. Núñez, I. Romero, F. Teixidor, C. Viñas, Icosahedral Boron Clusters: a Perfect Tool for the Enhancement of Polymer Features, *Chem. Soc. Rev.*, **2016**, 45, 5147–5173.

[326] M. Scholz, E. Hey-Hawkins, Carbaboranes as Pharmacophores: Properties, Synthesis, and Application Strategies, *Chem. Rev.*, **2011**, 111, 7035–7062.

[327] E. Hey-Hawkins, F. Teixidor, C. Viñas, Boron-Based Compounds: Potential and Emerging Applications in Medicine, John Wiley & Sons, Glasgow, **2018**.

[328] T. C. Li, A. M. Spokoyny, C. She, O. K. Farha, C. A. Mirkin, T. J. Marks, J. T. Hupp, Ni (III)/(IV) Bis(dicarbollide) as a Fast, Noncorrosive Redox Shuttle for Dye-Sensitized Solar Cells, *J. Am. Chem. Soc.*, **2010**, 132, 4580–4582.

[329] E. Schrödinger, An Undulatory Theory of the Mechanics of Atoms and Molecules, *Phys. Rev.*, **1926**, 28, 1049–1070.

Bibliography

[330] M. Born, R. Oppenheimer, Zur Quantentheorie der Molekeln, *Ann. Phys.*, **1927**, 389, 457–484.

[331] R. S. Mulliken, Electronic Structures of Polyatomic Molecules and Valence. II. General Considerations, *Phys. Rev.*, **1932**, 41, 49–71.

[332] L. C. Snyder, A simple Molecular Orbital Study of Aromatic Molecules and Ions Having Orbitally Degenerate Ground States, *J. Chem. Phys.*, **1962**, 66, 2299–2306.

[333] C. Gellini, P. R. Salvi, Structures of Annulenes and Model Annulene Systems in the Ground and Lowest Excited States, *Symmetry*, **2010**, 2, 1846–1924.

[334] M. Eckert-Maksić, M. Vazdar, M. Barbatti, H. Lischka, Z. B. Maksić, Automerization Reaction of Cyclobutadiene and its Barrier Height: An Ab Initio Benchmark Multireference Average-Quadratic Coupled Cluster Study, *J. Chem. Phys.*, **2006**, 125, 064310–064319.

[335] B. O. Roos, Multiconfigurational Self-Consistent Theory: In European Summerschool in Quantum Chemistry 2019: Book II, pages 283–351. S. Reine & T. Saue, Eds., Printed by Fotograph S.R.L., Palermo, **2019**.

[336] J. Ihm, A. Zunger, M. L. Cohen, Momentum-space Formalism for the Total Energy of Solids, *J. Phys. C: Solid State Phys.*, **1979**, 12, 4409–4422.

[337] E. J. Baerends, D. E. Ellis, P. Ros, Self-Consistent Molecular Hartree—Fock—Slater Calculations I. The Computational Procedure, *Chem. Phys.*, **1973**, 2, 41–51.

[338] B. I. Dunlap, J. W. D. Connolly, J. R. Sabin, On Some Approximations in Applications of X-α Theory, *J. Chem. Phys.*, **1979**, 71, 3396–3402.

[339] S. F. Boys, Electronic Wave Functions-I. A General Method of Calculation for the Stationary States of Any Molecular System, *Proc. R. Soc. Lond. Ser. A-Contain. Pap. Math. Phys.*, **1950**, 200, 542–554.

[340] A. Hinchliffe, Computational Quantum Chemistry, John Wiley & Sons, Ltd., Portland, **1988**.

[341] N. S. Ostlund A. Szabo, Modern Quantum Chemistry: Introduction to Advanced Electronic Structure Theory, Dover Publications, Inc., New York, **1996**.

[342] P. C. Hariharan, J. A. Pople, The Influence of Polarization Functions on Molecular Orbital Hydrogenation Energies, *Theor. Chim. Acta*, **1973**, 28, 213–222.

[343] K. I. Ramachandran, D. Gopakumar, K. Namboori, Basis Sets: In Computational Chemistry and Molecular Modeling, pages 115–138. Springer, Basilea, **2008**.

[344] R. Krishnan, J. S. Binkley, R. Seeger, J. A. Pople, Self-Consistent Molecular Orbital Methods. XX. A Basis Set for Correlated Wave Functions, *J. Chem. Phys.*, **1980**, 72, 650–654.

[345] T. H. Dunning Jr, Gaussian Basis Sets for Use in Correlated Molecular Calculations. I. The Atoms Boron Through Neon and Hydrogen, *J. Chem. Phys.*, **1989**, 90, 1007–1023.

[346] R. A. Kendall, T. H. Dunning Jr, R. J. Harrison, Electron Affinities of the First-Row Atoms Revisited. Systematic Basis Sets and Wave Functions, *J. Chem. Phys.*, **1992**, 96, 6796–6806.

[347] P. Pyykko, Relativistic Effects in Structural Chemistry, *Chem. Rev.*, **1988**, 88, 563–594.

[348] M. Dolg, Effective Core Potentials: In Modern methods and algorithms of quantum chemistry, pages 507–540. NIC-Directors, Jülich, **2000**.

[349] T. S. Koritsanszky, P. Coppens, Chemical Applications of X-Ray Charge-Density Analysis, *Chem. Rev.*, **2001**, 101, 1583–1628.

[350] E. Matito, Development, Implementation and Application of Electronic Structural Descriptors to the Analysis of the Chemical Bonding, Aromaticity and Chemical Reactivity, Universitat de Girona, Girona, **2006**.

[351] F. Feixas, Analysis of Chemical Bonding and Aromaticity from Electronic Delocalization Descriptors, Universitat de Girona, Girona, **2011**.

[352] P.-O. Löwdin, Quantum Theory of Many-Particle Systems. I. Physical Interpretations by Means of Density Matrices, Natural Spin-Orbitals, and Convergence Problems in the Method of Configurational Interaction, *Phys. Rev.*, **1955**, 97, 1474–322.

[353] K. Pernal, K. J. H. Giesbertz, Reduced Density Matrix Functional Theory (RDMFT) and Linear Response Time-Dependent RDMFT (TD-RDMFT), *Top. Curr. Chem*, **2016**, 368, 125–183.

[354] M. Piris, Global Method for Electron Correlation, *Phys. Rev. Lett.*, **2017**, 119, 063002–063007.

[355] N. Mardirossian, M. Head-Gordon, Thirty Years of Density Functional Theory in Computational Chemistry: An Overview and Extensive Assessment of 200 Density Functionals, *Mol. Phys.*, **2017**, 115, 2315–2372.

[356] T. Helgaker, P. Jorgensen, J. Olsen, Molecular Electronic-Structure Theory, John Wiley & Sons, Inc., New Jersey, **2013**.

[357] J. Simons, Why Is Quantum Chemistry So Complicated?, *J. Am. Chem. Soc.*, **2023**, 145, 4343–4354.

[358] Wikipedia. List of Quantum Chemistry and Solid-State Physics Software. https://en.wikipedia.org/wiki/List_of_quantum_chemistry_and_solid-state_physics_software. Accessed: 2023-10-27.

[359] D. Ceperley, B. Alder, Quantum Monte Carlo, *Science*, **1986**, 231, 555–560.

[360] M. Sajjan, J. Li, R. Selvarajan, S. H. Sureshbabu, S. S. Kale, R. Gupta, V. Singh, S. Kais, Quantum Machine Learning for Chemistry and Physics, *Chem. Soc. Rev.*, **2022**, 51, 6475–6573.

[361] T. Tamayo-Mendoza, Automatic Differentiation in Quantum Chemistry, Harvard University, Cambridge, **2021**.

[362] R. D'Cunha, T. D. Crawford, M. Motta, J. E. Rice, Challenges in the Use of Quantum Computing Hardware-Efficient Ansätze in Electronic Structure Theory, *J. Phys. Chem. A*, **2023**, 127, 3437–3448.

[363] M. Haidar, M. J. Rančić, T. Ayral, Y. Maday, J.-P. Piquemal, Open Source Variational Quantum Eigensolver Extension of the Quantum Learning Machine for Quantum Chemistry, *Wiley Interdiscip. Rev. Comput. Mol. Sci.*, **2023**, 13, 1664–1690.

[364] J. S. Kottmann, S. Alperin-Lea, T. Tamayo-Mendoza, A. Cervera-Lierta, C. Lavigne, T.-C. Yen, V. Verteletskyi, P. Schleich, A. Anand, M. Degroote, S. Chaney, M. Kesibi, N. G. Curnow, B. Solo, G. Tsilimigkounakis, C. Zendejas-Morales, A. F. Izmaylov, A. Aspuru-Guzik, Tequila: A Platform for Rapid Development of Quantum Algorithms, *Quantum Sci. Technol.*, **2021**, 6, 024009.

[365] K. Raghavachari, J. B. Anderson, Electron Correlation Effects in Molecules, *J. Phys. Chem.*, **1996**, 100, 12960–12973.

[366] O. Fossgaard, O. Gropen, M. Corral Valero, T. Saue, On the Performance of Four-Component Relativistic Density Functional Theory: Spectroscopic Constants and Dipole Moments of the Diatomics HX and XY (X, Y= F, Cl, Br, and I), *J. Chem. Phys.*, **2003**, 118, 10418–10430.

[367] E. Matito, P. Salvador, J. Styszyński, Benchmark Calculations of Metal Carbonyl Cations: Relativistic vs. Electron Correlation Effects, *Phys. Chem. Chem. Phys.*, **2013**, 15, 20080–20090.

[368] J. A. Pople, R. K. Nesbet, Self-Consistent Orbitals for Radicals, *J. Chem. Phys.*, **1954**, 22, 571–572.

[369] C. A. Coulson, I. Fischer, XXXIV. Notes on the Molecular Orbital Treatment of the Hydrogen Molecule, *London Edinburgh Philos. Mag. J. Sci.*, **1949**, 40, 386–393.

[370] I. Mayer, On the Behaviour of the UHF Method Near the "Critical Point", *Acta Phys. Hungarica*, **1983**, 54, 249–266.

[371] E. Wigner, F. Seitz, On The Constitution of Metallic Sodium. II, *Phys. Rev.*, **1934**, 46, 509–524.

[372] P.-O. Löwdin, Correlation Problem in Many-Electron Quantum Mechanics I. Review of Different Approaches and Discussion of Some Current Ideas, *Adv. Chem. Phys.*, **1958**, 2, 207–322.

[373] David Pines. Electron Interaction in Metals. In *Solid State Physics*, volume 1, pages 367–450. Elsevier, **1955**.

[374] E. Ramos-Cordoba, P. Salvador, E. Matito, Separation of Dynamic and Nondynamic Correlation, *Phys. Chem. Chem. Phys.*, **2016**, 18, 24015–24023.

[375] C. J. Cramer, Essentials of Computational Chemistry: Theories and Models, John Wiley & Sons, Ltd., Chichester, **2013**.

[376] J. A. Pople, M. Head-Gordon, K. Raghavachari, Quadratic Configuration Interaction. A general Technique for Determining Electron Correlation Energies, *J. Chem. Phys.*, **1987**, 87, 5968–5975.

[377] A. I. Krylov, Spin-flip Configuration Interaction: an Electronic Structure Model that is Both Variational and Size-Consistent, *Chem. Phys. Lett.*, **2001**, 350, 522–530.

[378] B. G. Levine, A. S. Durden, M. P. Esch, F. Liang, Y. Shu, CAS Without SCF—Why to use CASCI and Where to Get the Orbitals, *J. Chem. Phys.*, **2021**, 154, 090902–090914.

[379] M. W. Schmidt, M. S. Gordon, The Construction and Interpretation of MCSCF Wavefunctions, *Annu. Rev. Phys. Chem.*, **1998**, 49, 233–266.

[380] K. D. Vogiatzis, D. Ma, J. Olsen, L. Gagliardi, W. A de Jong, Pushing Configuration-Interaction to the limit: Towards Massively parallel MCSCF Calculations, *J. Chem. Phys.*, **2017**, 147, 184111-184124.

[381] H. Lischka, D. Nachtigallova, A. J. A. Aquino, P. G. Szalay, F. Plasser, F. B. C. Machado, M. Barbatti, Multireference Approaches for Excited States of Molecules, *Chem. Rev.*, **2018**, 118, 7293–7361.

[382] P.-Å. Malmqvist, A. Rendell, B. O. Roos, The Restricted Active Space Self-Consistent-Field Method, Implemented with a Split Graph Unitary Group Approach, *J. Phys. Chem.*, **1990**, 94, 5477–5482.

[383] D. Casanova, M. Head-Gordon, Restricted Active Space Spin-Flip Configuration Interaction Approach: Theory, Implementation and Examples, *Phys. Chem. Chem. Phys.*, **2009**, 11, 9779–9790.

[384] D. Casanova, Restricted Active Space Configuration Interaction Methods for Strong Correlation: Recent Developments, *Wiley Interdiscip. Rev. Comput. Mol. Sci.*, **2022**, 12, e1561.

[385] B. O. Roos, P. R. Taylor, P. E. M. Sigbahn, A Complete Active Space SCF Method (CASSCF) Using a Density Matrix Formulated Super-CI Approach, *Chem. Phys.*, **1980**, 48, 157–173.

[386] K. Andersson, P.-Å. Malmqvist, B. O. Roos, A. J. Sadlej, K. Wolinski, Second-order Perturbation Theory with a CASSCF Reference Function, *J. Phys. Chem.*, **1990**, 94, 5483–5488.

[387] G. Li Manni, R. K. Carlson, S. Luo, D. Ma, J. Olsen, D. G. Truhlar, L. Gagliardi, Multiconfiguration Pair-Density Functional Theory, *J. Chem. Theory Comput.*, **2014**, 10, 3669–3680.

[388] R. J. Bartlett, M. Musiał, Coupled-Cluster Theory in Quantum Chemistry, *Rev. Mod. Phys.*, **2007**, 79, 291–352.

[389] B. J. Esselman, M. A. Zdanovskaia, A. N. Owen, J. F. Stanton, R. C. Woods, R. J. McMahon, Precise Equilibrium Structure of Benzene, *J. Am. Chem. Soc.*, **2023**, 145, 21785–21797.

[390] M. Saitow, U. Becker, C. Riplinger, E. F. Valeev, F. Neese, A New Near-linear Scaling, Efficient and Accurate, Open-Shell Domain-Based Local Pair Natural Orbital Coupled Cluster Singles and Doubles Theory, *J. Chem. Phys.*, **2017**, 146–176, .

[391] B. Demoulin F. Neese R. Izsak A. K. Dutta S. Haldar, C. Riplinger, Multilayer Approach to the IP-EOM-DLPNO-CCSD Method: Theory, Implementation, and Application, *J. Chem. Theory Comput.*, **2019**, 15, 2265–2277.

[392] M. Musiał, Equation-of-Motion Coupled-Cluster Models: In Quantum Chemistry and Dynamics of Excited States: Methods and Applications, pages 77–108. Wiley Online Library, **2020**.

[393] A. M. Teale, T. Helgaker, A. Savin, C. Adamo, B. Aradi, A. V. Arbuznikov, P. W. Ayers, E. J. Baerends, V. Barone, P. Calaminici, and others, DFT Exchange: Sharing Perspectives on the Workhorse of Quantum Chemistry and Materials Science, *Phys. Chem. Chem. Phys.*, **2022**, 24, 28700–28781.

[394] P. Hohenberg, W. Kohn, Inhomogeneous Electron Gas, *Phys. Rev.*, **1964**, 136, B864–B871.

[395] W. Kohn, L. J. Sham, Self-Consistent Equations Including Exchange and Correlation Effects, *Phys. Rev.*, **1965**, 140, 1133–1138.

[396] D. J. Tozer, Density Functional Theory: In European Summerschool in Quantum Chemistry 2019: Book II, pages 539–580. S. Reine & T. Saue, Eds., Printed by Fotograph S.R.L., Palermo, **2019**.

[397] J. M. Luis, Fundamentals of Computational Chemistry II, Universitat de Girona, Girona, **2017**.

[398] M. Solà, J. M. Ugalde, Quantum Chemistry Methods: II Density Functional Theory: In Theoretical and Computational Chemistry: Foundations, Methods and Techniques, pages 221–277. J. Andrés and J. Bertrán, Eds., Publicacions de la Universitat Jaume I, Castelló de la Plana, **2007**.

[399] T. Ziegler, Approximate Density Functional Theory as a Practical Tool in Molecular Energetics and Dynamics, *Chem. Rev.*, **1991**, 91, 651–667.

[400] P. Geerlings, F. De Proft, W. Langenaeker, Density Functional Theory: a Bridge Between Chemistry and Physics, VUB University Press, Brussels, **1998**.

[401] J. P. Perdew, K. Schmidt, Jacob's Ladder of Density Functional Approximations for the Exchange-Correlation Energy, *AIP Conf. Proc.*, **2001**, 577, 1–20.

[402] A. D. Becke, Density Functional Calculations of Molecular Bond Energies, *J. Chem. Phys.*, **1986**, 84, 4524-–4529.

[403] S. Kurth, J. P. Perdew, P. Blaha, Molecular and Solid-State Tests of Density Functional Approximations: LSD, GGAs, and meta-GGAs, *Int. J. Quant. Chem.*, **1999**, 75, 889–909.

[404] A. D. Becke, A New Mixing of Hartree–Fock and Local Density-Functional Theories, *J. Chem. Phys.*, **1993**, 98, 1372–1377.

[405] C. Lee, W. Yang, R. G. Parr, Development of the Colle-Salvetti Correlation-Energy Formula into a Functional of the Electron Density, *Phys. Rev. B*, **1988**, 37, 785–789.

[406] A. Görling, M. Levy, Correlation-Energy Functional and its High-Density Limit Obtained from a Coupling-Constant Perturbation Expansion, *Phys. Rev. B*, **1993**, 47, 13105–13113.

[407] S. Grimme, Semiempirical Hybrid Density Functional with Perturbative Second-order Correlation, *J. Chem. Phys.*, **2006**, 124, 034108–034124.

[408] M. Jaeger, L. Freitag, L. Gonzalez, Using Computational Chemistry to Design Ru Photosensitizers with Directional Charge Transfer, *Coord. Chem. Rev.*, **2015**, 304, 146–165.

[409] J. R. B. Gomes, J. L. Cagide Fajín, M. N. D. S. Cordeiro, C. Teixeira, P. Gomes, R. S. Pillai, G. Novell-Leruth, J. Toda, M. Jorge, Density Functional Treatment of Interactions and Chemical Reactions at Interfaces: In Density Functional Theory: Principles, Applications and Analysis, pages 1–56. Nova Science Publishers, Inc., New York, **2013**.

[410] K. R. Bryenton, A. A. Adeleke, S. G. Dale, E. R. Johnson, Delocalization Error: The Greatest Outstanding Challenge in Density-Functional Theory, *Wiley Interdiscip. Rev. Comput. Mol. Sci.*, **2023**, 13, e1631–e1659.

[411] Y. Zhang, W. Yang, A Challenge for Density Functionals: Self-Interaction Error Increases for Systems With a Noninteger Number of Electrons, *J. Chem. Phys.*, **1998**, 109, 2604–2608.

[412] A. J. Cohen, P. Mori-Sánchez, W. Yang, Insights into Current Limitations of Density Functional Theory, *Science*, **2008**, 321, 792–794.

[413] P. Mori-Sánchez, A. J. Cohen, W. Yang, Many-Electron Self-Interaction Error in Approximate Density Functionals, *J. Chem. Phys.*, **2006**, 125, 201102-201106.

[414] T. Yanai, D. P. Tew, N. C. Handy, A New Hybrid Exchange-Correlation Functional using the Coulomb-Attenuating Method (CAM-B3LYP), *Chem. Phys. Lett.*, **2004**, 393, 51–57.

[415] J.-D. Chai, M. Head-Gordon, Long-Range Corrected Hybrid Density Functionals with Damped Atom-Atom Dispersion Corrections, *Phys. Chem. Chem. Phys.*, **2008**, 10, 6615–6620.

[416] E. Livshits, R. Baer, A Well-Tempered Density Functional Theory of Electrons in Molecules, *Phys. Chem. Chem. Phys.*, **2007**, 9, 2932–2941.

[417] T. Stein, L. Kronik, R. Baer, Prediction of Charge-Transfer Excitations in Coumarin-Based Dyes Using a Range-Separated Functional Tuned from First Principles, *J. Chem. Phys.*, **2009**, 131, 244119–244124.

[418] T. Stein, L. Kronik, R. Baer, Reliable Prediction of Charge Transfer Excitations in Molecular Complexes Using Time-Dependent Density Functional Theory, *J. Am. Chem. Soc.*, **2009**, 131, 2818–2820.

[419] T. Koopmans, Über die Zuordnung von Wellenfunktionen und Eigenwerten zu den einzelnen Elektronen eines Atoms, *Mitteilung aus der Arbeitsgemeinschaft für theoretische Physik der Utrechter Universität*, **1933**, 1, 104–113.

[420] V. U. Nazarov, Breakdown of the Ionization Potential Theorem of Density Functional Theory in Mesoscopic Systems, *J. Chem. Phys.*, **2021**, 155, 194105–194113.

[421] J. F. Janak, Proof that $\frac{\partial E}{\partial n_i} = \varepsilon$ in Density-Functional Theory, *Phys. Rev. B*, **1978**, 18, 7165–7168.

Bibliography

[422] O. S. Bokareva, G. Grell, S. I. Bokarev, O. Kühn, Tuning Range-Separated Density Functional Theory for Photocatalytic Water Splitting Systems, *J. Chem. Theory Comput.*, **2015**, 11, 1700–1709.

[423] O. S. Bokareva, M. F. Shibl, M. J. Al-Marri, T. Pullerits, O. Kühn, Optimized Long-Range Corrected Density Functionals for Electronic and Optical Properties of Bare and Ligated CdSe Quantum Dots, *J. Chem. Theory Comput.*, **2017**, 13, 110–116.

[424] S. Grimme, Accurate Description of van der Waals Complexes by Density Functional Theory Including Empirical Corrections, *J. Comput. Chem.*, **2004**, 25, 1463–1473.

[425] S. Grimme, J. Antony, S. Ehrlich, H. Krieg, A Consistent and Accurate *ab initio* Parametrization of Density Functional Dispersion Correction (DFT-D) for the 94 Elements H-Pu, *J. Chem. Phys.*, **2010**, 132, 154104–154123.

[426] A. D. Becke, E. R. Johnson, Exchange-hole dipole moment and the dispersion interaction, *J. Chem. Phys.*, **2005**, 122, 154104–154109.

[427] A. D. Becke, E. R. Johnson, A Density-Functional Model of the Dispersion Interaction, *J. Chem. Phys.*, **2005**, 123, 154101–154110.

[428] S. Grimme, S. Ehrlich, L. Goerigk, Effect of the Damping Function in Dispersion Corrected Density Functional Theory, *J. Comput. Chem.*, **2011**, 32, 1456–1465.

[429] E. Caldeweyher, S. Ehlert, A. Hansen, H. Neugebauer, S. Spicher, C. Bannwarth, S. Grimme, A Generally Applicable Atomic-Charge Dependent London Dispersion Correction, *J. Chem. Phys.*, **2019**, 150, 154122–154141.

[430] E. Runge, E. K. U. Gross, Density-Functional Theory for Time-Dependent Systems, *Phys. Rev. Lett.*, **1984**, 52, 977-1000.

[431] K. Burke, J. Werschnik, E. K. U. Gross, Time-Dependent Density Functional Theory: Past, Present, and Future, *J. Chem. Phys.*, **2005**, 123, 062206–062215.

[432] M. E. Casida, Time-Dependent Density Functional Response Theory of Molecular Systems: Theory, Computational Methods, and Functionals; In Recent Developments and Applications in Density Functional Theory, pages 391–439. Elsevier, Amsterdam, **1996**.

[433] A. Dreuw, M. Head-Gordon, Failure of Time-Dependent Density Functional Theory for Long-Range Charge-Transfer Excited States: The Zincbacteriochlorin-Bacteriochlorin and Bacteriochlorophyll-Spheroidene Complexes, *J. Am. Chem. Soc.*, **2004**, 126, 4007–4016.

[434] C. Hirata, M. Head-Gordon, Time-Dependent Density Functional Theory for Radicals: An Improved Description of Excited States with Substantial Double Excitation Character, *Chem. Phys. Lett.*, **1999**, 302, 375–382.

[435] I. Tamm, Energy-Time Uncertainty Relationship in Nonrelativistic Quantum mechanics, *J. Phys.*, **1945**, 9, 449.

[436] S. M. Dancoff, Non-Adiabatic Meson Theory of Nuclear Forces, *Phys. Rev.*, **1950**, 78, 382-385.

[437] M. J. G. Peach, D. J. Tozer, Overcoming Low Orbital Overlap and Triplet Instability Problems in TDDFT, *J. Phys. Chem. A*, **2012**, 116, 9783–9789.

[438] G. N. Lewis, The Atom and the Molecule, *J. Am. Chem. Soc.*, **1916**, 38, 762–785.

[439] R. F. W. Bader, Atoms in Molecules, *Acc. Chem. Res.*, **1985**, 18, 9–15.

[440] R. S. Mulliken, Electronic Population Analysis on LCAO–MO Molecular Wave Functions. I, *J. Chem. Phys.*, **1955**, 23, 1833–1840.

[441] J. E. Carpenter, F. Weinhold, Analysis of the Geometry of the Hydroxymethyl Radical by the "Different Hybrids for Different Spins" Natural Bond Orbital Procedure, *J. Mol. Struct. (Theochem)*, **1988**, 169, 41–62.

[442] A. E. Reed, L. A. Curtiss, F. Weinhold, Intermolecular Interactions from a Natural Bond Orbital, Donor-Acceptor Viewpoint, *Chem. Rev.*, **1988**, 88, 899–926.

[443] F. Weinhold, C. R. Landis, E. D. Glendening, What is NBO analysis and how is it useful?, *Int. Rev. Phys. Chem.*, **2016**, 35, 399–440.

[444] F. L. Hirshfeld, Bonded-Atom Fragments for Describing Molecular Charge Densities, *Theor. Chim. Acta*, **1977**, 44, 129–138.

[445] P. Bultinck, C. P. Van Alsenoy, W. Ayers, R. Carbó-Dorca, Critical analysis and extension of the Hirshfeld atoms in molecules, *J. Chem. Phys.*, **2007**, 126, 144111–144120.

[446] C. Fonseca Guerra, J.-W. Handgraaf, E. J. Baerends, F. M. Bickelhaupt, Voronoi deformation density (VDD) charges: Assessment of the Mulliken, Bader, Hirshfeld, Weinhold, and VDD methods for charge analysis, *J. Comput. Chem.*, **2004**, 25, 189–210.

[447] P. Salvador, I. Mayer, Energy Partitioning for "Fuzzy" Atoms, *J. Chem. Phys.*, **2004**, 120, 5046–5052.

[448] R. F. W. Bader, A Quantum Theory of Molecular Structure and its Applications, *Chem. Rev.*, **1991**, 91, 893–928.

[449] A. M. Pendás, M. A. Blanco, E. Francisco, Chemical Fragments in Real Space: Definitions, Properties, and Energetic Decompositions, *J. Comput. Chem.*, **2007**, 28, 161–184.

[450] E. Matito, New Tools for Chemical Bonding Analysis, Donostia International Physics Center, Donostia, **2021**.

[451] X. Fradera, M. A. Austen, R. F. W. Bader, The Lewis Model and Beyond, *J. Phys. Chem. A*, **1999**, 103, 304–314.

[452] X. Fradera, J. Poater, S. Simon, M. Duran, M. Solà, Electron-Pairing Analysis from Localization and Delocalization Indices in the Framework of the Atoms-In-Molecules Theory, *Theor. Chem. Acc.*, **2002**, 108, 214–224.

[453] I. Mayer, Charge, Bond Order and Valence in the Ab Initio SCF Theory, *Chem. Phys. Lett.*, **1983**, 97, 270–274.

301

[454] F. Feixas, E. Matito, J. Poater, M. Solà, Quantifying Aromaticity with Electron Delocalisation Measures, *Chem. Soc. Rev.*, **2015**, 44, 6434–6451.

[455] D. W. Szczepanik, M. Andrzejak, J. Dominikowska, B. PawełekE, T. Krygowski, H. Szatylowicz, M. Solà, The Electron Density of Delocalized Bonds (EDDB) Applied for Quantifying Aromaticity, *Phys. Chem. Chem. Phys.*, **2017**, 19, 28970–28981.

[456] E. Matito, M. Duran, M. Solà, Erratum:"The Aromatic Fluctuation Index (FLU): A New Aromaticity Index Based on Electron Delocalization"[J. Chem Phys. 122, 014109 (2005)], *J. Chem. Phys.*, **2006**, 125, 059901.

[457] E. Matito, J. Poater, M. Duran, M. Solà, An Analysis of the Changes in Aromaticity and Planarity Along the Reaction Path of the Simplest Diels–Alder Reaction. Exploring the Validity of Different Indicators of Aromaticity, *J. Mol. Struct.*, **2005**, 727, 165–171.

[458] E. Matito, M. Solà, P. Salvador, M. Duran, Electron Sharing Indexes at the Correlated Level. Application to Aromaticity Calculations, *Faraday Discuss.*, **2007**, 135, 325–345.

[459] J.-L. Brédas, Relationship Between Band Gap and Bond Length Alternation in Organic Conjugated Polymers, *J. Chem. Phys.*, **1985**, 82, 3808–3811.

[460] R. L. Fulton, Sharing of Electrons in Molecules, *J. Phys. Chem.*, **1993**, 97, 7516–7529.

[461] R. F. W. Bader, A. Streitwieser, A. Neuhaus, K. E. Laidig, P. Speers, Electron Delocalization and the Fermi Hole, *J. Am. Chem. Soc.*, **1996**, 118, 4959–4965.

[462] M. Giambiagi, M. S. de Giambiagi, K. C. Mundim, Definition of a Multicenter Bond Index, *Struct. Chem.*, **1990**, 1, 423–427.

[463] M. Giambiagi, M. S. de Giambiagi, C. D. dos Santos Silva, A. P. de Figueiredo, Multicenter Bond Indices as a Measure of Aromaticity, *Phys. Chem. Chem. Phys.*, **2000**, 2, 3381–3392.

[464] P. Bultinck, R. Ponec, S. Van Damme, Multicenter Bond Indices as a New Measure of Aromaticity in Polycyclic Aromatic Hydrocarbons, *J. Phys. Org. Chem.*, **2005**, 18, 706–718.

[465] A. C. Castro, E. Osorio, J. L. Cabellos, E. Cerpa, E. Matito, M. Solà, M. Swart, G. Merino, Exploring the Potential Energy Surface of E_2P_4 Clusters (E= Group 13 Element): the Quest for Inverse Carbon-Free Sandwiches, *Chem. Eur. J.*, **2014**, 20, 4583–4590.

[466] I. Gutman, M. Milun, N. Trinajstic, Graph Theory and Molecular Orbitals. 19. Nonparametric Resonance Energies of Arbitrary Conjugated Systems, *J. Am. Chem. Soc.*, **1977**, 99, 1692–1704.

[467] J. Cioslowski, E. Matito, M. Solà, Properties of Aromaticity Indices Based on the One-Electron Density Matrix, *J. Phys. Chem. A*, **2007**, 111, 6521–6525.

[468] C. García-Fernández, E. Sierda, M. Abadía, B. Bugenhagen, M. H. Prosenc, R. Wiesendanger, M. Bazarnik, J. E. Ortega, J. Brede, E. Matito, A. Arnau, Exploring the Relation Between Intramolecular Conjugation and Band Dispersion in One-Dimensional Polymers, *J. Phys. Chem. C*, **2017**, 121, 27118–27125.

[469] M. Jirásek, M. Rickhaus, L. Tejerina, H. L. Anderson, Experimental and Theoretical Evidence for Aromatic Stabilization Energy in Large Macrocycles, *J. Am. Chem. Soc.*, **2021**, 143, 2403–2412.

[470] D. W. Szczepanik, M. Andrzejak, K. Dyduch, E. Żak, M. Makowski, G. Mazur, J. Mrozek, A Uniform Approach to the Description of Multicenter Bonding, *Phys. Chem. Chem. Phys.*, **2014**, 16, 20514–20523.

[471] D. W. Szczepanik, A new Perspective on Quantifying Electron Localization and Delocalization in Molecular Systems, *Comput. Theor. Chem.*, **2016**, 1080, 33–37.

[472] D. W. Szczepanik, J. Mrozek, Symmetrical Orthogonalization within Linear Space of Molecular Orbitals, *Chem. Phys. Lett.*, **2012**, 521, 157–160.

[473] D. W. Szczepanik, J. Mrozek, On Several Alternatives for Löwdin Orthogonalization, *Comput. Theor. Chem.*, **2013**, 1008, 15–19.

[474] D. W. Szczepanik, J. Mrozek, On Quadratic Bond-Order Decomposition within Molecular Orbital Space, *J. Math. Chem.*, **2013**, 51, 1619–1633.

[475] D. W. Szczepanik, On the Three-Center Orbital Projection Formalism within the Electron Density of Delocalized Bonds Method, *Comput. Theor. Chem.*, **2017**, 1100, 13–17.

[476] D. W. Szczepanik, E. Żak, K. Dyduch, Mrozek, J. Mrozek, Electron Delocalization Index Based on Bond Order Orbitals, *Chem. Phys. Lett.*, **2014**, 593, 154–159.

[477] M. Dimitrova, D. Sundholm, Current Density, Current-Density Pathways, and Molecular Aromaticity: In Aromaticity Modern Computational Methods and Applications, pages 155–194. Elsevier, Amsterdam, **2021**.

[478] S. Bais, Equations: Icons of knowledge, Amsterdam University Press, Amsterdam, **2005**.

[479] J. O. Hirschfelder, Quantum Mechanical Equations of Change. I, *J. Chem. Phys.*, **1978**, 68, 5151–5162.

[480] E. Steiner, P. W. Fowler, Patterns of Ring Currents in Conjugated Molecules: A Few-Electron Model Based on Orbital Contributions, *J. Phys. Chem. A*, **2001**, 105, 9553–9562.

[481] R. Herges, D. Geuenich, Delocalization of Electrons in Molecules, *J. Phys. Chem. A*, **2001**, 105, 3214–3220.

[482] H. Fliegl, S. Taubert, O. Lehtonen, D. Sundholm, The Gauge Including Magnetically Induced Current Method, *Phys. Chem. Chem. Phys.*, **2011**, 13, 20500–20518.

[483] J. Ahrens, B. Geveci, C. Law, C. Hansen, C. Johnson, Paraview: An End-User Tool for Large-Data Visualization, *The visualization handbook*, **2005**, 717, 50038.

[484] P. W. Atkins, R. S. Friedman, Molecular Quantum Mechanics, Oxford University Press, Oxford, **1997**.

[485] J. Gauss, Calculation of NMR Chemical Shifts at Second-Order Many-Body Perturbation Theory using Gauge-Including Atomic Orbitals, *Chem. Phys. Lett.*, **1992**, 191, 614–620.

[486] R. Gershoni-Poranne, A. Stanger, The NICS-XY-Scan: Identification of Local and Global Ring Currents in Multi-Ring Systems, *Chem. Eur. J.*, **2014**, 20, 5673–5688.

[487] I. Morao, F. Cossio, A Simple Ring Current Model for Describing in-plane Aromaticity in Pericyclic Reactions, *J. Org. Chem.*, **1999**, 64, 1868–1874.

[488] F. Alvarez-Ramírez, Y. Ruiz-Morales, Database of Nuclear Independent Chemical Shifts (NICS) Versus NICS$_{ZZ}$ of Polycyclic Aromatic Hydrocarbons (PAHs), *J. Chem. Inf. Model.*, **2019**, 60, 611–620.

[489] T. Heine, C. Corminboeuf, G. Seifert, The Magnetic Shielding Function of Molecules and π-Electron Delocalization, *Chem. Rev.*, **2005**, 105, 3889–3910.

[490] A. Artigas, D. Hagebaum-Reignier, Y. Carissan, Y. Coquerel, Visualizing Electron Delocalization in Contorted Polycyclic Aromatic Hydrocarbons, *Chem. Sci.*, **2021**, 12, 13092–13100.

[491] S. Van Damme, G. Acke, R. W. A. Havenith, P. Bultinck, Can the Current Density Map Topology be Extracted from the Nucleus Independent Chemical Shifts?, *Phys. Chem. Chem. Phys.*, **2016**, 18, 11746–11755.

[492] Y.-C. Lin, D. Sundholm, J. Jusélius, On the Aromaticity of the Planar Hydrogen-Bonded (HF)$_3$ Trimer, *J. Chem. Theory Comput.*, **2006**, 2, 761–764.

[493] J. Kruszewski, T. M. Krygowski, Definition of Aromaticity Basing on the Harmonic Oscillator Model, *Tetrahedron Lett.*, **1972**, 13, 3839–3842.

[494] T. M. Krygowski, M. K. Cyrański, Structural Aspects of Aromaticity, *Chem. Rev.*, **2001**, 101, 1385–1420.

[495] T. M. Krygowski, Crystallographic Studies of Inter- and Intramolecular Interactions Reflected in Aromatic Character of π-Electron Systems, *J. Chem. Inf. Comput. Sci.*, **1993**, 33, 70–78.

[496] M. Alonso, I. Fernández, Quantifying Aromaticity According to the Energetic Criterion: In Aromaticity Modern Computational Methods and Applications, pages 195–235. Elsevier, Amsterdam, **2021**.

[497] M. K. Cyrański, Energetic Aspects of Cyclic π-Electron Delocalization: Evaluation of the Methods of Estimating Aromatic Stabilization Energies, *Chem. Rev.*, **2005**, 105, 3773–3811.

[498] R. Gershoni-Poranne, A. Stanger, NICS–Nucleus Independent Chemical Shift: In Aromaticity Modern Computational Methods and Applications, pages 99–154. Elsevier, Amsterdam, **2021**.

[499] Z. Chen, C. S. Wannere, C. Corminboeuf, R. Puchta, P. v. R. Schleyer, Nucleus-independent chemical shifts (NICS) as an aromaticity criterion, *Chem. Rev.*, **2005**, 105, 3842–3888.

[500] A. D. Becke, K. E. Edgecombe, A Simple Measure of Electron Localization in Atomic and Molecular Systems, *Chem. Phys.*, **1990**, 92, 5397–5403.

[501] D. Geuenich, K. Hess, F. Köhler, R. Herges, Anisotropy of the Induced Current Density (ACID), a General Method to Quantify and Visualize Electronic Delocalization, *Chem. Rev.*, **2005**, 105, 3758–3772.

[502] N. D. Charistos, A. Munoz-Castro, Induced Magnetic Field of Fullerenes: Role of σ-and π-Contributions to Spherical Aromatic, Nonaromatic, and Antiaromatic Character in C_{60}^q (q = +10, 0, -6, -12), and Related Alkali-Metal Decorated Building Blocks, $Li_{12}C_{60}$ and Na_6C_{60}, *J. Phys. Chem. C*, **2018**, 122, 9688–9698.

[503] E. M. Arpa, B. Durbeej, HOMER: A Reparameterization of the Harmonic Oscillator Model of Aromaticity (HOMA) for Excited States, *Phys. Chem. Chem. Phys.*, **2023**, 25, 16763–16771.

[504] P. v. R. Schleyer, F. Pühlhofer, Recommendations for the Evaluation of Aromatic Stabilization Energies, *Org. Lett.*, **2002**, 4, 2873–2876.

[505] M. Alonso, B. Herradón, A Universal Scale of Aromaticity for π-Organic Compounds, *J. Comput. Chem.*, **2010**, 31, 917–928.

[506] R. Ayub, O. El Bakouri, J. R. Smith, K. Jorner, H. Ottosson, Triplet State Baird Aromaticity in Macrocycles: Scope, Limitations, and Complications, *J. Phys. Chem. A*, **2021**, 125, 570–584.

[507] B. A. Voigt, T. Steenbock, C. Herrmann, Structural Diradical Character, *J. Comput. Chem.*, **2019**, 40, 854–865.

[508] M. Güell, M. Solà, M. Swart, Spin-State Splittings of Iron (II) Complexes with Trispyrazolyl Ligands, *Polyhedron*, **2010**, 29, 84–93.

[509] M. Swart, M. Güell, M. Solà, A Multi-Scale Approach to Spin Crossover in Fe (II) Compounds, *Phys. Chem. Chem. Phys.*, **2011**, 13, 10449–10456.

[510] N. C. Handy, A. J. Cohen, Left-Right Correlation Energy, *Mol. Phys.*, **2001**, 99, 403–412.

[511] J. P. Perdew, K. Burke, M. Ernzerhof, Generalized Gradient Approximation Made Simple, *Phys. Rev. Lett.*, **1996**, 77, 3865–3868.

[512] Y. Zhang, A. Wu, X. Xu, Y. Yan, OPBE: A Promising Density Functional for the Calculation of Nuclear Shielding Constants, *Chem. Phys. Lett.*, **2006**, 421, 383–388.

[513] J. Gierschner, J. Cornil, H.-J. Egelhaaf, Optical Bandgaps of π-conjugated Organic Materials at the Polymer Limit: Experiment and Theory, *Adv. Mater.*, **2007**, 19, 173–191.

[514] D. Beljonne, J. Cornil, R. H. Friend, R. A. J. Janssen, J.-L. Brédas, Influence of Chain Length and Derivatization on the Lowest Singlet and Triplet States and Intersystem Crossing in Oligothiophenes, *J. Am. Chem. Soc.*, **1996**, 118, 6453–6461.

[515] Y. Yang, E. R. Davidson, W. Yang, Nature of Ground and Electronic Excited States of Higher Acenes, *Proc. Natl. Acad. Sci.*, **2016**, 113, E5098–E5107.

[516] R. Pino-Rios, R. Báez-Grez, M. Solà, Acenes and Phenacenes in their Lowest-Lying Triplet States. Does Kinked Remain more Stable than Straight?, *Phys. Chem. Chem. Phys.*, **2021**, 23, 13574–13582.

[517] Q. Wu, T. Van Voorhis, Direct Optimization Method to Study Constrained Systems Within Density-Functional Theory, *Phys. Rev. A*, **2005**, 72, 024502–024506.

[518] S. A. Mewes, R. Plasser, A. Krylov, A. Dreuw, Benchmarking Excited-State Calculations Using Exciton Properties, *J. Chem. Theory Comput.*, **2018**, 14, 710–725.

[519] A. Karolewski, L. Kronik, S. Kümmel, Using Optimally Tuned Range Separated Hybrid Functionals in Ground-State Calculations: Consequences and Caveats, *J. Chem. Phys.*, **2013**, 138, 204115–204127.

[520] W. R. Scheidt, W. Dow, Molecular Stereochemistry of Phthalocyanatozinc (II), *J. Am. Chem. Soc.*, **1977**, 99, 1101–1104.

[521] H. Kietaibl, Die Kristall-und Molek lstruktur eines neuratigen phthalocyanin hnlichen Borkomplexes, *Monatsh. Chem.*, **1974**, 105, 405–418.

[522] J. Mack, J. Stone, T. Nyokong, Trends in the TD-DFT Calculations of Porphyrin and Phthalocyanine Analogs, *J. Porphyr. Phthalocyanines*, **2014**, 18, 630–641.

[523] A. Drzewiecka-Matuszek, D. Rutkowska-Zbik, Application of TD-DFT Theory to Studying Porphyrinoid-Based Photosensitizers for Photodynamic Therapy: A Review, *Molecules*, **2021**, 26, 7176–7193.

[524] S. Lehtola, M. Dimitrova, H. Fliegl, D. Sundholm, Benchmarking Magnetizabilities with Recent Density Functionals, *J. Chem. Theory Comput.*, **2021**, 17, 1457–1468.

[525] E. Steiner, P. W. Fowler, L. W. Jenneskens, Counter-Rotating Ring Currents in Coronene and Corannulene, *Angew. Chem., Int. Ed. Engl.*, **2001**, 40, 362–366.

[526] A. Kumar, M. Duran, M. Solà, Is Coronene Better Described by Clar's Aromatic π-Sextet Model or by the AdNDP Representation?, *J. Comput. Chem.*, **2017**, 38, 1606–1611.

[527] M. A. Dobrowolski, M. K. Cyrański, Z. Wróbel, Cyclic π-Electron Delocalization in Non-Planar Linear Acenes, *Phys. Chem. Chem. Phys.*, **2016**, 18, 11813–11820.

[528] F. Feixas, E. Matito, J. Poater, M. Solà, Aromaticity of Distorted Benzene Rings: Exploring the Validity of Different Indicators of Aromaticity, *J. Phys. Chem. A*, **2007**, 111, 4513–4521.

[529] A. G. Papadopoulos, N. D. Charistos, M. P. Sigalas, Aromaticity Variation in BN Substituted Triphenylene: A Theoretical Study, *AIP Conf. Proc.*, **2012**, 1504, 1223–1226.

[530] J. A. Wunderlich, W. N. Lipscomb, Structure of $B_{12}H_{12}^{-2}$ Ion, *J. Am. Chem. Soc.*, **1960**, 82, 4427–4428.

[531] J. Poater, C. Viñas, I. Bennour, S. Escayola, M. Solà, F. Teixidor, Too Persistent to Give Up: Aromaticity in Boron Clusters Survives Radical Structural Changes, *J. Am. Chem. Soc.*, **2020**, 142, 9396–9407.

[532] G. Wilkinson, M. Rosenblum, M. C. Whiting, R. B. Woodward, The Structure of Iron *bis*-Cyclopentadienyl, *J. Am. Chem. Soc.*, **1952**, 74, 2125–2126.

[533] J. Warneke, S. Z. Konieczka, G.-L. Hou, E. Aprà, C. Kerpen, F. Keppner, T. C. Schäfer, M. Deckert, Z. Yang, E. J. Bylaska, G. E. Johnson, J. Laskin, S. S. Xantheas, X.-B. Wang, M. Finze, Properties of Perhalogenated *closo*-B_{10} and *closo*-B_{11} Multiply Charged Anions and a Critical Comparison with *closo*-B_{12} in the Gas and the Condensed Phase, *Phys. Chem. Chem. Phys.*, **2019**, 21, 5903–5915.

[534] J. Warneke, G.-L. Hou, E. Aprà, C. Jenne, Z. Yang, Z. Qin, K. Kowalski, X.-B Wang, S. S. Xantheas, Electronic Structure and Stability of $[B_{12}X_{12}]^{2-}$ (X= F–At): A Combined Photoelectron Spectroscopic and Theoretical Study, *J. Am. Chem. Soc.*, **2017**, 139, 14749–14756.

[535] R. T. Boeré, J. Derendorf, C. Jenne, S. Kacprzak, M. Keßler, R. Riebau, S. Riedel, T. L. Roemmele, M. Rühle, H. Scherer, T. Vent-Schmidt, J. Warneke, S. Weber, On the Oxidation of the Three-Dimensional Aromatics $[B_{12}X_{12}]^{2-}$ (X= F, Cl, Br, I), *Chem. Eur. J.*, **2014**, 20, 4447–4459.

A   Summarized Supplemental Data

Section 4.1: Guidelines for Tuning the Excited State Hückel–Baird Hybrid Aromatic Character of Pro-Aromatic Quinoidal Compounds: Key Supplemental Data

This is the list of elements reported in the supplemental material of Section 4.1. The complete set of supplemental material associated with this paper can be accessed at 4.1-SI DOI:10.1002/ange.202100261.

- Computational Details
- Choice of Exchange-Correlation Functional
- DFT Functional and Solvent Dependence
- Relative Energies
- Molecular Orbitals
- Vertical Excitations
- Structural Analysis
- Charge and Spin Densities
- Theoretical Vibrational Frequency $\tilde{v}(\mathrm{C}^{\equiv}\mathrm{N})$
- Delocalization Indices
- Study of the Aromaticity
- Constrained DFT
- Baird contribution from QTAIM charge/spin
- Aromaticity of Reference Molecules

Additionally, this section explicitly includes selected tables and figures to complement the detailed discussions of the results.

Table A.1 Modified version of Table S18 in 4.1-SI. KS- and TD-B3LYP/6-311+G(d,p) relative energies (in eV); adiabatic (adia) and vertical (denoted as KS, TD, or TDA, depending on the DFT approximation used) for T_1 and S_1 excited states. T_1 (adia) correspond to KS-B3LYP/6-311+G(d,p) energies on geometries optimized at the same level of theory. S_1 (adia) correspond to TDDFT energies on geometries optimized at the same level of theory unless otherwise specified.

	T_1 (adia)	S_1 (adia)	T_1 (KS)	T_1 (TD)	S_1 (TD)	T_1 (TDA)	S_1 (TDA)
5R	0.85	1.60	1.11	0.96	2.06	1.10	2.31
6R	0.78	2.84	1.11	0.68	2.98	1.16	3.40
9R	1.16	0.95	1.36	1.26	2.53	1.37	2.87
10R	0.80	2.12	1.33	1.03	2.37	1.30	2.64
cis-**5RT**	0.33	1.27	0.42	—	1.50	0.43	1.92
cis'-**5RT**	0.47	1.50	0.55	0.32	1.70	0.55	2.11
trans-**5RT**	0.40	1.38	0.49	0.22	1.60	0.50	2.01
cis-**6RT**	0.11	1.80	0.36	—	1.89	0.43	2.44
trans-**6RT**	0.11	1.82	0.36	—	1.90	0.43	2.44
cis-**9RT**	0.60	1.68^b	0.66	0.53	1.73	0.67	2.16
cis'-**9RT**	0.65	1.73^b	0.71	0.58	1.76	0.71	2.18
trans-**9RT**	0.63	1.70^b	0.69	0.55	1.74	0.69	2.16
cis-**10RT**	0.20	1.63	0.75	0.40	1.78	0.75	2.1
trans-**10RT**	0.21	1.65	0.75	0.39	1.81	0.75	2.12
4RN-5	1.81	2.43^b	2.35	2.16	3.06	2.3	3.16
4RO-5	2.12	2.15	2.44	2.14	3.11	2.33	3.22
5R-5	0.72	1.53^a	0.90	0.77	1.90	0.89	2.15
5R-5b	0.47	1.09^b	0.73	0.57	1.58	0.73	1.75
5R-5c	0.33	0.78^a	0.57	0.40	1.24	0.57	1.41
6Ra	0.65	2.19	1.01	0.53	2.64	1.06	2.70
6R-5a	0.70	1.13^a	0.99	0.58	1.89	1.02	1.96
6R-5b	-0.78	0.48^b	0.03	—	1.03	0.13	1.09
6R-5c	-0.44	0.92^b	0.13	—	0.93	0.22	0.99
6R-3a	1.01	1.38^a	1.95	1.71	2.19	1.81	2.25
6R-3b	1.35	1.14	1.70	1.55	1.57	1.55	1.57
6R-3c	0.95	2.03^b	1.93	1.78	2.47	1.90	2.47
7Ra	0.41	—	—	—	—	—	—
7Rb	0.35	—	—	—	—	—	—
5R-2H$^+$	0.62	1.10^a	1.12	0.84	1.72	0.97	1.90
5R-4H$^+$	0.52	0.93^a	1.01	0.77	1.57	0.93	1.71
6R-2H$^+$	0.77	2.13	1.04	0.66	2.56	1.04	2.63
10R-2H$^+$	0.85	1.89	1.18	0.98	2.14	1.15	2.42

^{a} TDA optimized geometry.

^{b} T_1-KS optimized geometry.

Table A.2 Aromaticity of the reference systems according to HOMA, FLU, MCI, and $MCI^{1/n}$ in the S_0 and T_1 states. Values obtained at the B3LYP/6-311+G(d,p) level of theory, adapted from Table S104 in 4.1-SI.

system	state	symm.	HOMA	FLU	MCI	$MCI^{1/n}$
$C_3H_3^+$	S_0	D_{3h}	1.168	0.0008	0.3945	0.7334
$C_3H(NH_2)_2^+$	S_0	C_{2v}	0.948	0.0104	0.2918	0.6633
C_4H_4	T_1	D_{4h}	0.301	0.0100	0.1241	0.5935
$C_5H_5^-$	S_0	D_{5h}	0.810	0.0002	0.0676	0.5833
	T_1	C_s	0.325	0.0188	0.0247	0.4770
$C_5H_5^+$	S_0	C_{2v}	−1.344	0.0474	−0.0382	−0.5204
	T_1	D_{5h}	0.668	0.0085	0.0976	0.6279
$C_5H_3(CN)_2^-$	S_0	C_{2v}	0.736	0.0075	0.0496	0.5483
$C_5H_2Cl_3^+$	S_0	C_{2v}	−0.913	0.0422	−0.0115	−0.4092
	T_1	C_{2v}	0.664	0.0169	0.0604	0.5704
C_6H_6	S_0	D_{6h}	0.989	0.0000	0.0717	0.6445
	T_1	D_{2h}	−0.491	0.0238	0.0000	0.0000
$C_6H_6^{2+}$	S_0	D_{2h}	−0.947	0.0281	−0.0126	0.4827^a
	T_1	D_{6h}	0.554	0.0099	0.0786	0.6545
$C_6H_2(CH_3)_4^{2+}$	S_0	C_s	−0.417	0.0267	−0.0013	0.3300^a
	T_1	C_s	0.486	0.0155	0.0487	0.6043
$C_6H_2Cl_4^{2+}$	S_0	D_{2h}	−0.327	0.0277	0.0039	0.3965
	T_1	D_{2h}	0.649	0.0156	0.0343	0.5700
$C_7H_7^-$	S_0	C_2	0.163	0.0279	−0.0016	−0.3991
	T_1	D_{7h}	0.826	0.0013	0.0309	0.6085
$C_9H_9^-$	S_0	D_{9h}	0.947	0.0000	0.0148	0.6263
	T_1^b	C_s	0.822	0.0014	−0.0101	−0.5999
$C_9H_9^+$	S_0^b	C_s	0.885	0.0016	−0.0174	−0.6376
	T_1	C_2	0.935	0.0013	0.0196	0.6459
$C_{11}H_{10}$	S_0	C_{2v}	0.887	0.0036	0.0093	0.6265
	T_1	C_{2v}	0.441	0.0180	—	—
$C_{11}H_{10}^{2+}$	S_0	C_{2v}	0.603	0.0146	−0.0034	0.5661^a
	T_1	C_{2v}	0.761	0.0058	—	—

^{a} The $MCI^{1/n}$ has been calculated taking the absolute value of the MCI index.
^{b} In these cases, the optimized structure presents Möbius topology.

Table A.3 Dissection of normalized MCI ($MCI^{1/n}$, where n is the number of atoms in the ring) into spin parts for various molecules. Adapted from Table S95 in 4.1-SI.

Molecule	$MCI^{1/n}$	$MCI\text{-}\alpha^{1/n}$	$MCI\text{-}\beta^{1/n}$	$\Delta MCI^{1/n}$	$\Delta MCI^{1/n}/MCI^{1/n}$
5R	0.5100	0.5487	0.4540	0.0948	0.1858
6R	0.5999	0.6171	0.5798	0.0373	0.0622
9R	0.5617	0.5948	0.4957	0.0991	0.1764
10R	0.5782	0.6023	0.5390	0.0633	0.1095
5RT	0.5077	0.5449	0.4547	0.0902	0.1777
6RT	0.6075	0.6107	0.6042	0.0065	0.0107
9RT	0.4782	0.4985	0.4472	0.0513	0.1072
10RT	0.6016	0.6064	0.5964	0.0100	0.0166
5R-5a	0.5086	0.5497	0.4473	0.1024	0.2013
5R-5b	0.5035	0.5411	0.4493	0.0917	0.1822
5R-5c	0.5011	0.5361	0.4521	0.0840	0.1677
6R-5a	0.6009	0.6094	0.5917	0.0177	0.0294
6R-5b	0.6097	0.6098	0.6097	0.0001	0.0002
6R-5c	0.5979	0.5997	0.5961	0.0036	0.0060
6R-3a	0.5606	0.5156	0.5926	−0.0770	−0.1374
6R-3b	0.5556	0.4726	0.6022	−0.1296	−0.2333
6R-3c	0.5773	0.5359	0.6077	−0.0719	−0.1245
4RN-5	0.3203	0.2919	0.3427	−0.0508	−0.1587
4RO-5	0.3508	0.3759	0.3188	0.0571	0.1627
7Ra	0.5748	0.4636	0.6240	−0.1604	−0.2791
7Rb	0.5753	0.4698	0.6236	−0.1538	−0.2673
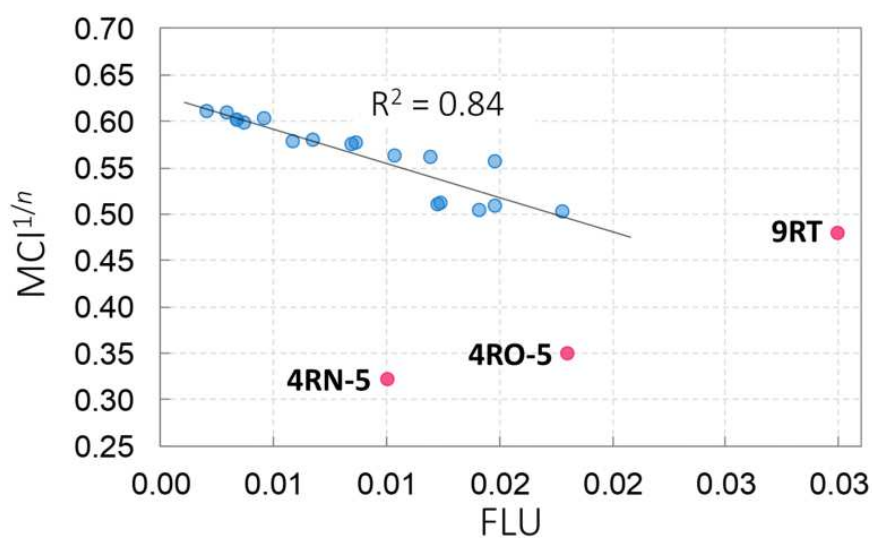
Figure A.1 Correlation of FLU vs. $MCI^{1/n}$ across different molecules in 4.1.

Baird and Hückel Character Assessment using Charges, Spin Densities, and C-DFT Energies

The Baird character, as discussed in Sections 4.1 and 6.1, is calculated based on how closely the charge and spin density in the central ring of a compound match the expected value in a system with 100% Baird character. This value is defined by the specific charge of the central ring: for neutral rings in the non-aromatic GS (*e.g.* **6R**(**T**) and **10R**(**T**)), the Baird excited state would have a central ring charge of $+2$. Similarly, if the ring in the ground state has a charge of -1 (**5R**(**T**) and **9R**(**T**)), then in the Baird excited state, it would have a charge of $+1$. Conversely, if the ring in the ground state has a charge of $+1$ (**7R**), the corresponding Baird excited state would have a charge of $+1$. For the spin density, in all cases, the expected value for the central ring in the Baird excited state is 2. Thus, the %Baird(spin) is calculated as the ratio of the computed spin density in the central ring to this reference value of 2. The %Baird based on charges can be computed for both S_1 and T_1, while the one based on spin density can only be obtained for the T_1 state (these %Baird based on QTAIM charges and spin densities are reported in Figure 8b,c in Section 4.1).

To compare the Baird contribution of all studied systems, in the T_1 state, we considered the minimum value between %Baird from QTAIM charges and spins at the central ring:

$$\%\mathrm{Baird}(\mathrm{T}_1) = \min[\%\mathrm{Baird}(\mathrm{T}_1, \mathrm{charge}), \%\mathrm{Baird}(\mathrm{T}_1, \mathrm{spin})] \tag{A.1}$$

For the singlet state S_1, for which only the %Baird(charge) can be obtained, we considered an 'spin correction' derived from the T_1 analysis:

$$\%\mathrm{Baird}(\mathrm{S}_1) = \%\mathrm{Baird}(\mathrm{S}_1, \mathrm{charge}) + \Delta \tag{A.2}$$

$$\Delta = \begin{cases} 0 & \text{if} \quad \%\mathrm{Baird}(\mathrm{T}_1, \mathrm{charge}) \leq \%\mathrm{Baird}(\mathrm{T}_1, \mathrm{spin}) \\ \%\mathrm{Baird}(\mathrm{T}_1, \mathrm{spin}) - \%\mathrm{Baird}(\mathrm{T}_1, \mathrm{charge}) & \text{otherwise} \end{cases} \tag{A.3}$$

Furthermore, an energetic index has been used to determine the Baird contribution. This index involves the construction of an artificial triplet state wavefunction (applicable to S_1 as well) as outlined in Eq. (1) in Section 4.1. The wavefunction is a linear combination of constrained Hückel and Baird forms, calculated using constrained-DFT (C-DFT) [517]. This technique imposes the required charge and spin on the central ring and exocyclic groups, as detailed in 4.1. Then, the weights of each configuration (c_H and c_B amplitudes), described in Eq. (2) in Section 4.1, provide the basis for estimating the Baird characters presented in Figure 8a in Section 4.1.

The evaluation for the singlet state is more complex, owing to the potential contribution of the ground state quinoidal form in addition to the Hückel and Baird forms. This adds a layer of complexity to the analysis. Alternatively, to measure the proximity of our systems to Baird-like behavior, we computed the energies of the constrained Baird and Hückel forms for both T_1 and S_1 excited states. The differences in these energies are depicted in Figure A.2. Here, positive energy differences signify a more stable Hückel form, while negative differences indicate a dominance of the Baird form, thereby suggesting the most probable description of the relaxed state. In most cases, particularly in 6- and 10-MR systems, the Hückel form exhibits greater stability, often exceeding 5 eV. However, in certain 5- and 7-MR systems, the Baird form demonstrates notable stabilization.
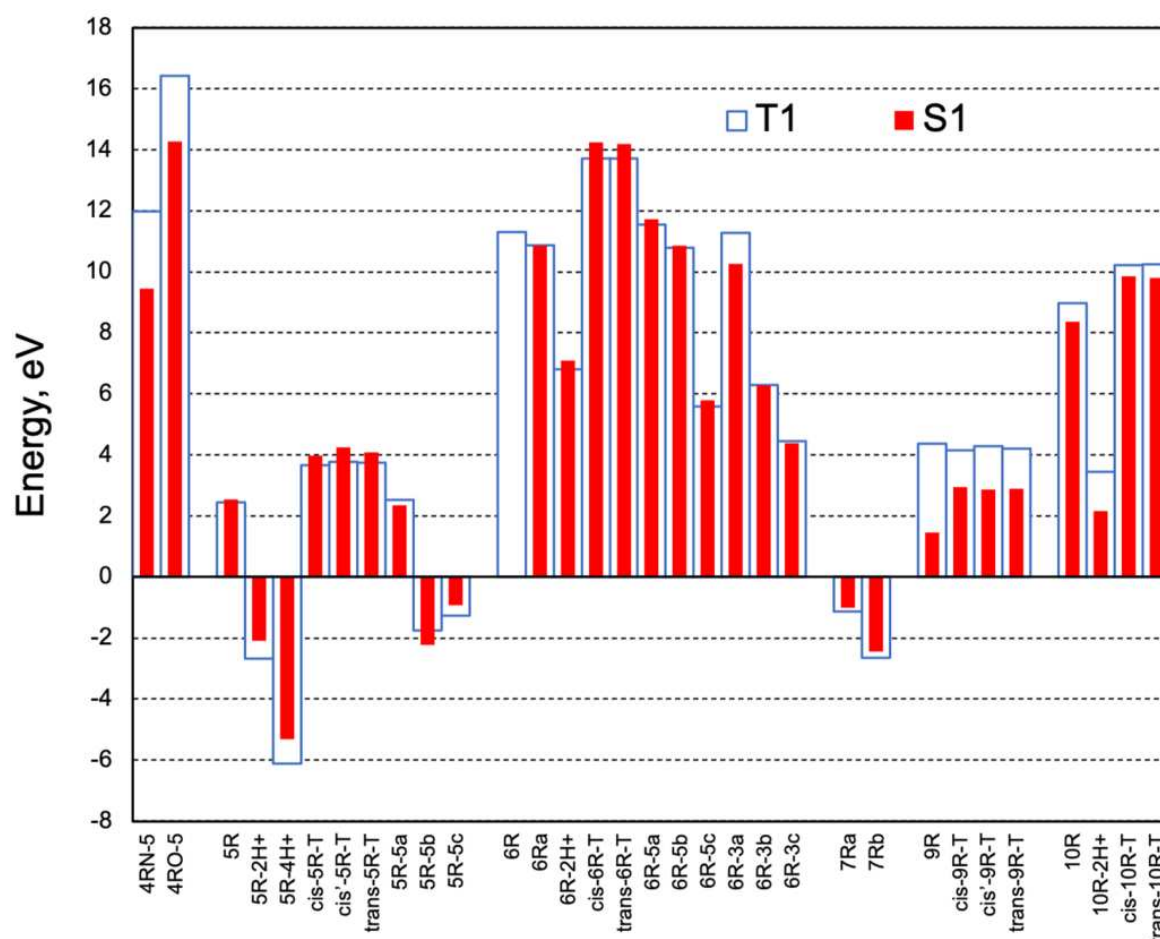
Figure A.2 Energy differences between Baird and Hückel energies for the singlet and triplet states of all studied molecules in Section 4.1 computed using C-DFT B3LYP/6-311G(d,p). Note: S_1 Hückel energy of **6R** has not been converged, hence we only show the value for the T_1 state. Adapted from Figure S41 in 4.1-SI.

Section 4.2: Effect of Exocyclic Substituents and π-System Length on the Electronic Structure of Chichibabin Diradical(oid)s: Key Supplemental Data

The content of the supporting information for Section 4.2 is listed below and can be accessed at 4.2-SI DOI:10.1021/acsomega.9b00916.

- Selection of the Computational Approach
- Analysis of the different conformations
- Structural parameters, energy, $\left\langle \hat{S}^2 \right\rangle$, diradical character (y), Mulliken populations, and aromaticity results

This section also includes one specific table to complement the results discussed.

Table A.4 Relative energies (in eV), at the OPBE/cc-pVTZ level of theory, for the OSS and T states. $\Delta E_{CSX} = E_X - E_{CS}$ where X refers to OS or T, of all studied systems in Section 4.2. Adapted from Table S17 in 4.2-SI.

systems 1-6				systems 7-11			
substituent	m	OSS	T	substituent	m	OSS	T
1	1	—	1.39	**7**	1	—	0.70
	2	—	0.44		2	—	0.19
	3	−0.09	−0.02		3	−0.14	−0.12
	4	−0.31	−0.30		4	−0.27	−0.26
	5	−0.43	−0.43		5	−0.31	−0.31
2	1	—	1.32	**8**	1	—	0.70
	2	—	0.54		2	—	0.19
	3	−0.02	0.10		3	−0.13	−0.11
	4	−0.17	−0.16		4	−0.26	−0.25
	5	−0.29	−0.29		5	−0.30	−0.30
3	1	—	1.32	**9**	1	—	0.58
	2	—	0.61		2	—	0.12
	3	—	0.19		3	−0.13	−0.12
	4	−0.09	−0.06		4	−0.22	−0.22
	5	−0.19	−0.18		5	−0.25	−0.25
4	1	—	0.40	**10**	1	—	0.87
	2	—	0.16		2	—	0.28
	3	−0.07	−0.02		3	−0.11	−0.07
	4	−0.21	−0.21		4	−0.25	−0.25
	5	−0.26	−0.26		5	−0.32	−0.31
5	1	—	0.84	**11**	1	—	0.51
	2	—	0.27		2	—	0.13
	3	−0.08	−0.02		3	−0.46	−0.43
	4	−0.19	−0.18		4	−0.53	−0.52
	5	−0.26	−0.25		5	−0.21	−0.21
6	1	—	0.30				
	2	−0.06	−0.02				
	3	−0.19	−0.19				
	4	−0.26	−0.26				
	5	−0.29	−0.29				

Section 5.1.1: From (Sub)Porphyrin to (Sub)Phthalocyanine: Aromaticity Signatures in the UV-Vis Absorption Spectra: Key Supplemental Data

The elements listed below are included in the supplemental material for Section 5.1.1. The complete set of supplemental material associated with this paper can be accessed at 5.1.1-SI DOI:.

- Performance of Different Functionals
- UV-Vis Spectra and Frontier Molecular Orbitals
- Singlet-Triplet Energy Gap
- Electron Delocalization and Aromaticity Measures

Additionally, this section explicitly includes selected tables and figures to complement the detailed discussions of the results.
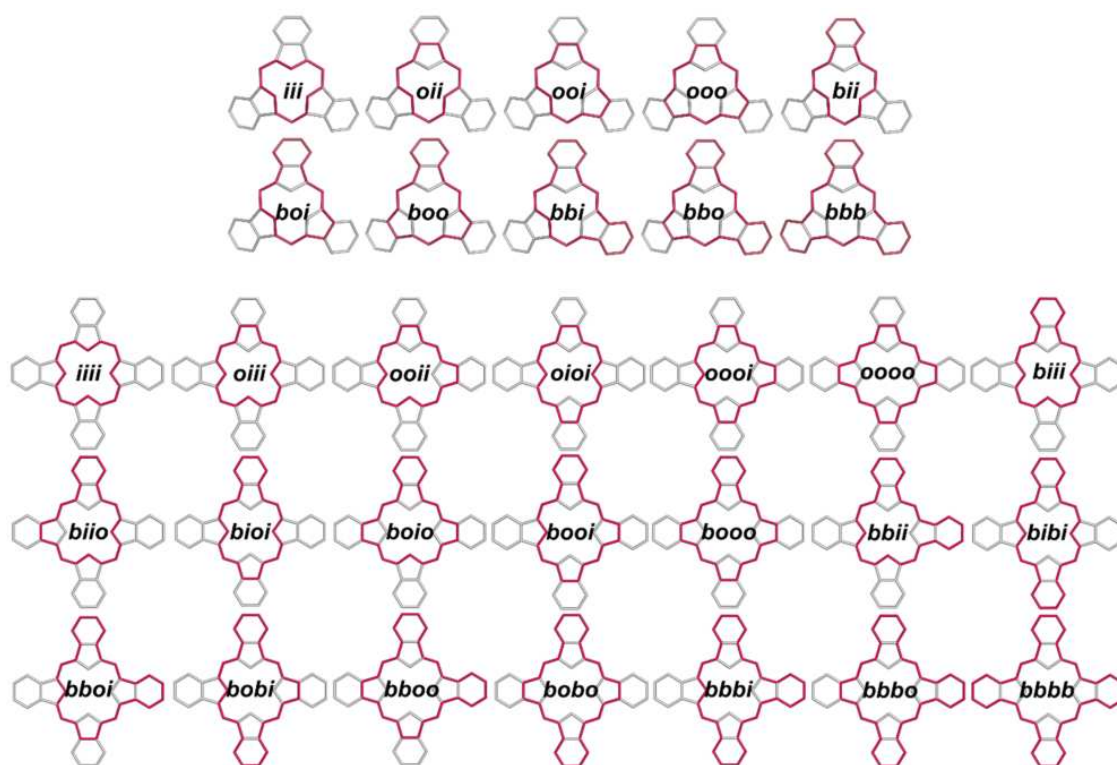
Figure A.3 Representation of the different pathways considered in (sub)phthalocyanine systems. Reproduced from Figure S11 in 5.1.1-SI.

Table A.5 Top part: experimental vs. computed geometries of **Pc** using different functionals. Bottom part: absolute error in absolute values compared to experimental values. Distances and angles in Å and degrees, respectively.

	ZnN_p	ZnN_pC_α	$N_pC_\alpha N_m$	$C_\alpha N_pC_\alpha$	$C_\alpha N_mC_\alpha$	$C_\alpha N_p$	$C_\alpha N_m$	$C_\alpha C_\beta$	$C_\beta C_\beta$	$C_\beta C_c$	C_cC_d	C_dC_d
X-Ray	1.980	125.4	127.8	109.1	123.5	1.369	1.331	1.455	1.400	1.393	1.391	1.396
B3LYP	2.000	125.0	127.4	110.0	125.1	1.367	1.326	1.459	1.406	1.390	1.388	1.402
CAM-B3LYP	1.988	125.0	127.4	109.9	125.1	1.360	1.319	1.456	1.396	1.385	1.381	1.398
ωB97X	1.989	125.0	127.6	110.0	124.8	1.360	1.322	1.459	1.395	1.388	1.383	1.401
M06-2X	1.997	124.9	127.6	110.2	124.9	1.361	1.324	1.460	1.399	1.387	1.385	1.401
TPSSH	1.993	125.2	127.5	109.6	124.6	1.370	1.328	1.457	1.407	1.392	1.390	1.403
LC-wHPBE	1.980	125.1	127.5	109.8	124.7	1.355	1.317	1.456	1.389	1.384	1.378	1.397
X-Ray	0.000	0.0	0.0	0.0	0.0	0.000	0.000	0.000	0.000	0.000	0.000	0.000
B3LYP	0.020	0.4	0.4	0.9	1.6	0.002	0.005	0.004	0.006	0.003	0.003	0.006
CAM-B3LYP	0.008	0.4	0.4	0.8	1.6	0.009	0.012	0.001	0.004	0.008	0.010	0.002
ωB97X	0.009	0.4	0.2	0.9	1.3	0.009	0.009	0.004	0.005	0.005	0.008	0.005
M06-2X	0.017	0.5	0.2	1.1	1.4	0.008	0.007	0.005	0.001	0.006	0.006	0.005
TPSSH	0.013	0.2	0.3	0.5	1.1	0.001	0.003	0.002	0.007	0.001	0.001	0.007
LC-wHPBE	0.000	0.3	0.3	0.7	1.2	0.014	0.014	0.001	0.011	0.009	0.013	0.001
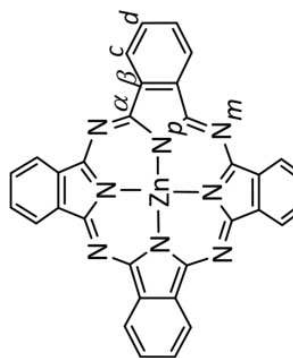
Figure A.4 Atom labels in **Pc**.

Table A.6 Top part: experimental vs. computed geometries of **SubPc** using different functionals. Bottom part: absolute error in absolute values compared to experimental values. Distances and angles in Å and degrees, respectively.

	BX	BN_p	N_pBN_p	N_pBX	$C_\alpha N_p$	$C_\alpha N_m$	$C_\alpha C_\beta$	$C_\beta C_\beta$	$C_\beta C_c$	$C_c C_d$	$C_d C_d$	P1[a]	P2[b]
X-Ray	1.863	1.467	105.2	113.3	1.369	1.344	1.46	1.427	1.391	1.370	1.394	0.58	2.47
B3LYP	1.879	1.486	105.1	113.6	1.367	1.336	1.453	1.427	1.391	1.386	1.403	0.59	2.57
CAM-B3LYP	1.863	1.482	104.8	113.8	1.357	1.330	1.451	1.416	1.387	1.379	1.398	0.60	2.57
ωB97X	1.853	1.487	104.5	114.1	1.357	1.332	1.454	1.414	1.391	1.380	1.402	0.61	2.60
M06-2X	1.854	1.486	104.6	114.0	1.359	1.333	1.454	1.418	1.390	1.382	1.402	0.60	2.60
TPSSH	1.868	1.488	104.8	113.8	1.366	1.339	1.452	1.428	1.393	1.388	1.404	0.60	2.57
LC-wHPBE	1.841	1.483	104.3	114.3	1.352	1.327	1.452	1.408	1.387	1.375	1.398	0.61	2.58
X-Ray	0.000	0.000	0.0	0.0	0.000	0.000	0.000	0.000	0.000	0.000	0.000	0.00	0.00
B3LYP	0.016	0.019	0.1	0.3	0.002	0.008	0.007	0.000	0.000	0.016	0.009	0.01	0.10
CAM-B3LYP	0.000	0.015	0.4	0.5	0.012	0.014	0.009	0.011	0.004	0.009	0.004	0.02	0.10
ωB97X	0.010	0.020	0.7	0.8	0.012	0.012	0.006	0.013	0.000	0.010	0.008	0.02	0.13
M06-2X	0.009	0.019	0.6	0.7	0.010	0.011	0.006	0.009	0.001	0.012	0.008	0.02	0.13
TPSSH	0.005	0.021	0.4	0.5	0.003	0.005	0.008	0.001	0.002	0.018	0.010	0.02	0.10
LC-wHPBE	0.022	0.016	0.9	1.0	0.017	0.017	0.008	0.019	0.004	0.005	0.004	0.03	0.11

Distance in Å between [a]the B and the plane containing the three N_p; and [b]the B and the plane containing the six C_d.
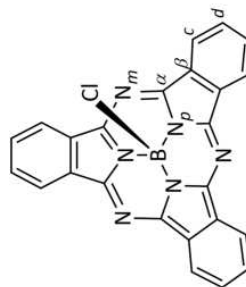
Figure A.5 Atom labels in **SubPc**.
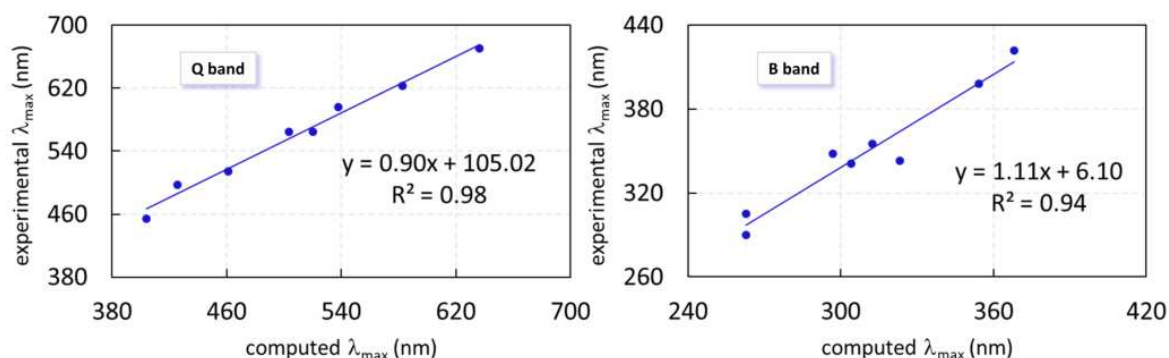
Figure A.6 Linear correlation of experimental and theoretical—CAM-B3LYP/cc-pVTZ level of theory—UV-Vis absorption maxima. Left Q band; right B band.

Figure A.7 Six frontier molecular orbitals of **P**, **TBP**, **Pz**, and **Pc** at CAM-B3LYP/cc-pVTZ level of theory. The isocontour is 0.02 a.u. and the energies of the orbitals are in eV.
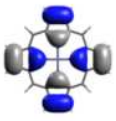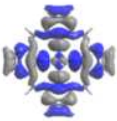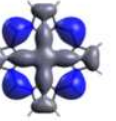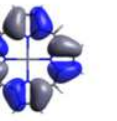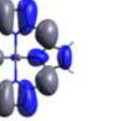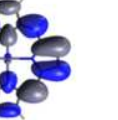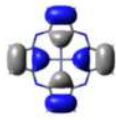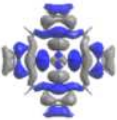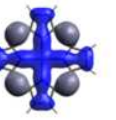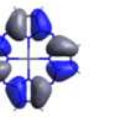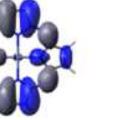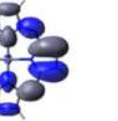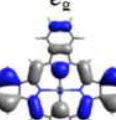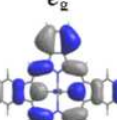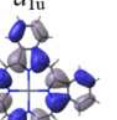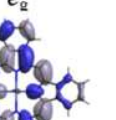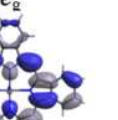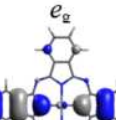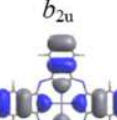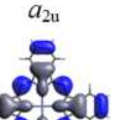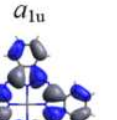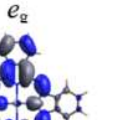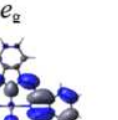
	HOMO-3	HOMO-2	HOMO-1	HOMO	LUMO	LUMO+1
ZnSubP	MO 72 e -8.133	MO 73 e -8.133	MO 74 a_1 -6.670	MO 75 a_2 -6.357	MO 76 a_1 -0.980	MO 77 e -0.736
SubP	MO 68 e -8.577	MO 69 e -8.577	MO 70 a_1 -7.208	MO 71 a_2 -7.009	MO 72 e -1.322	MO 73 e -1.322
SubPz	MO 68 e -9.19	MO 69 e -9.19	MO 70 a_1 -9.06	MO 71 a_2 -7.39	MO 72 e -2.13	MO 73 e -2.13
TBSubP	MO 107 e -8.335	MO 108 e -8.335	MO 109 a_1 -7.282	MO 110 a_2 -6.168	MO 111 e -1.252	MO 112 e -1.252
SubPc	MO 107 a_1 -8.71	MO 108 e -8.64	MO 109 e -8.64	MO 110 a_2 -6.409	MO 111 e -1.842	MO 112 e -1.842

Figure A.8 Six frontier molecular orbitals of **Zn-SubP**, **SubP**, **TBSubP**, **SubPz**, and **SubPc** at CAM-B3LYP/cc-pVTZ level of theory. Isocontour 0.02 a.u.; energies in eV.
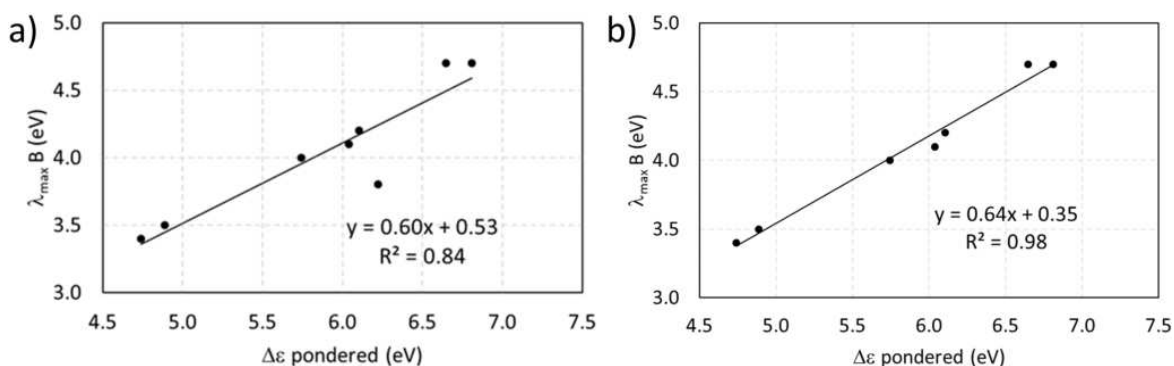
Figure A.9 Relationship between B band λ_{max} and pondered $\Delta\varepsilon$ in eV including a) all systems and b) including all systems but **Pz**.

Table A.7 Orbital transitions involved in the B band, $\Delta\varepsilon$ in eV of the corresponding orbitals, weighting factor, and pondered $\Delta\varepsilon$ in eV at CAM-B3LYP/cc-pVTZ level of theory considering the implicit solvent (scrf=(pcm,solvent=solvent used in the experiment—see experimental details in Section 5.1.1)).

| system	transition	$\Delta\varepsilon$	weighting factor	pondered $\Delta\varepsilon$
P	$94 \to 96$	4.93	0.52	4.89
	$95 \to 97$	4.84	0.48	
Pz	$88 \to 97$	6.97	0.18	6.22
	$91 \to 98$	6.54	0.11	
	$92 \to 97$	6.48	0.34	
	$93 \to 97$	6.03	0.26	
	$95 \to 96$	4.32	0.11	
TBP	$146 \to 148$	5.12	0.61	4.74
	$147 \to 149$	4.15	0.30	
	$147 \leftarrow 149$	4.15	0.10	
Pc	$138 \to 149$	6.57	0.13	6.11
	$139 \to 148$	6.56	0.10	
	$145 \to 149$	6.23	0.15	
	$146 \to 149$	6.20	0.44	
	$147 \to 148$	3.72	0.10	
	$136 \to 149$	7.13	0.07	
SubP	$67 \to 72$	7.87	0.10	6.04
	$70 \to 72$	5.93	0.50	
	$71 \to 73$	5.71	0.39	
SubPz	$67 \to 72$	7.60	0.22	6.81
	$70 \to 72$	6.98	0.61	
	$71 \to 73$	5.25	0.18	
TBSubP	$109 \to 111$	6.06	0.72	5.74
	$110 \to 112$	4.92	0.28	
SubPc	$104 \to 111$	7.41	0.13	6.65
	$107 \to 111$	6.83	0.55	
	$108 \to 111$	6.77	0.11	
	$109 \to 112$	6.77	0.11	
	$110 \to 112$	4.54	0.11	
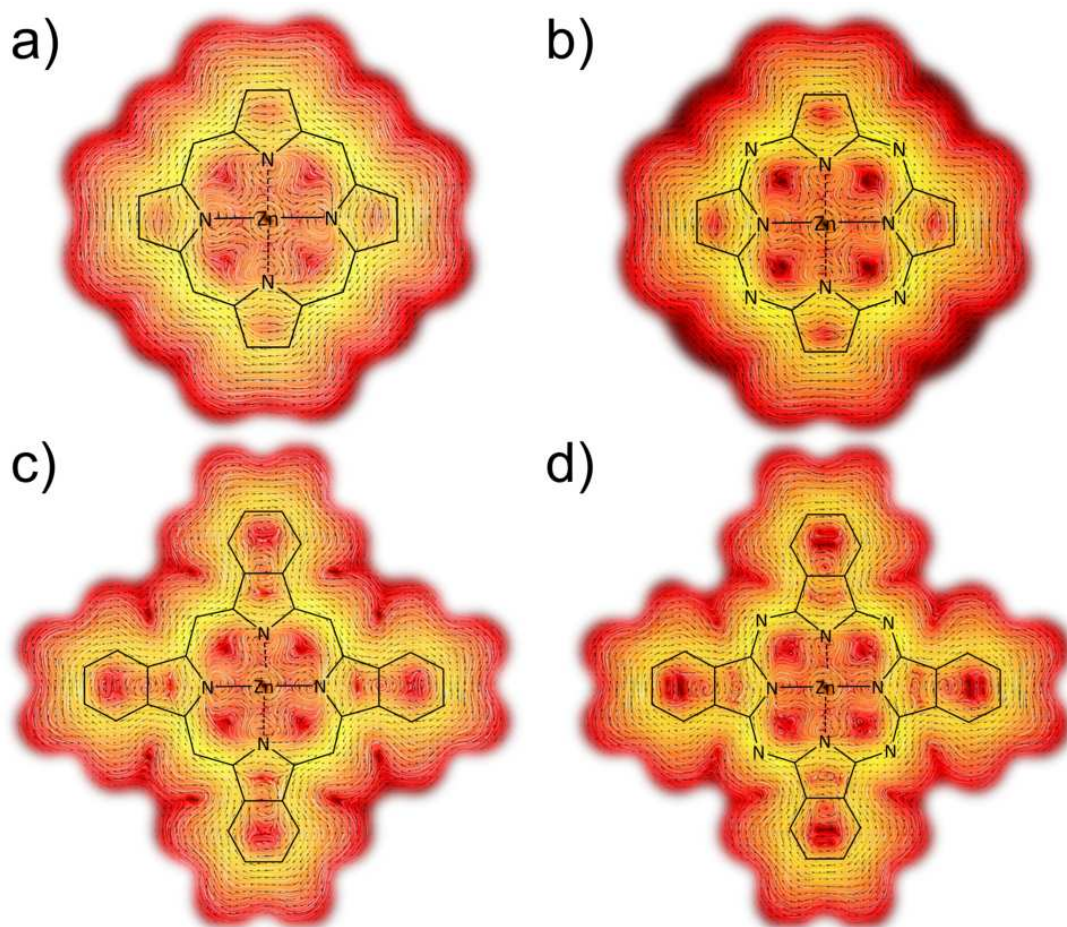
Figure A.10 Current density in the S_0 state visualized using the LIC representation. For **P**, **TBP**, **Pz**, and **Pc** the plane is 1 Å above the molecular plane. The color scale corresponds to the strength of the modulus of the current-density susceptibility in the range of 0.0001 (red) to 0.4 (white) nA/T/Å^2.

Summarized Supplemental Data

Section 5.2.1: An Unprecedented π-Electronic Circuit Involving an Odd Number of Carbon Atoms in a Grossly Warped Non-Planar Nanographene: Key Supplemental Data

The elements listed below are included in the supplemental material for Section 5.2.1. The complete set of supplemental material associated with this paper can be accessed at 5.2.1-SI DOI:10.1039/D1CC00593F.

- Methodology and Computational Details
- NICS Maps and Induced Magnetic Fields
- Reference Molecules
- EDDB Isosurfaces
- GIMIC Results—Current Density Pathways and Current Strengths
- Local Aromatic Descriptors
- Cartesian Coordinates

Section 5.3.1: In the Quest of Hückel–Hückel and Hückel–Baird Double Aromatic Tropylium (tri)Cation and Anion Derivatives: Key Supplemental Data

The content of the supporting information for Section 5.3.1 is listed below and can be accessed at 6.3.1-SI DOI:10.1002/poc.4447.

- Comparison of Different Functionals
- Aromaticity Values of Reference: $^1C_7H_7^+$, $^3C_7H_7^-$, and $^3C_7H_7^3+$
- Normal Mode Analysis
- Delocalization Indices
- Molecular Orbitals
- EDDB Results
- GIMIC Results
- Charges of the C and Br Rings of D_{7h} $^1C_7Br_7^+$ and $^1C_7Br_7^-$ Systems
- $^3C_7Br_7^3+$ Species Using Different Functionals

Additionally, this section includes selected figures to complement the discussed results.
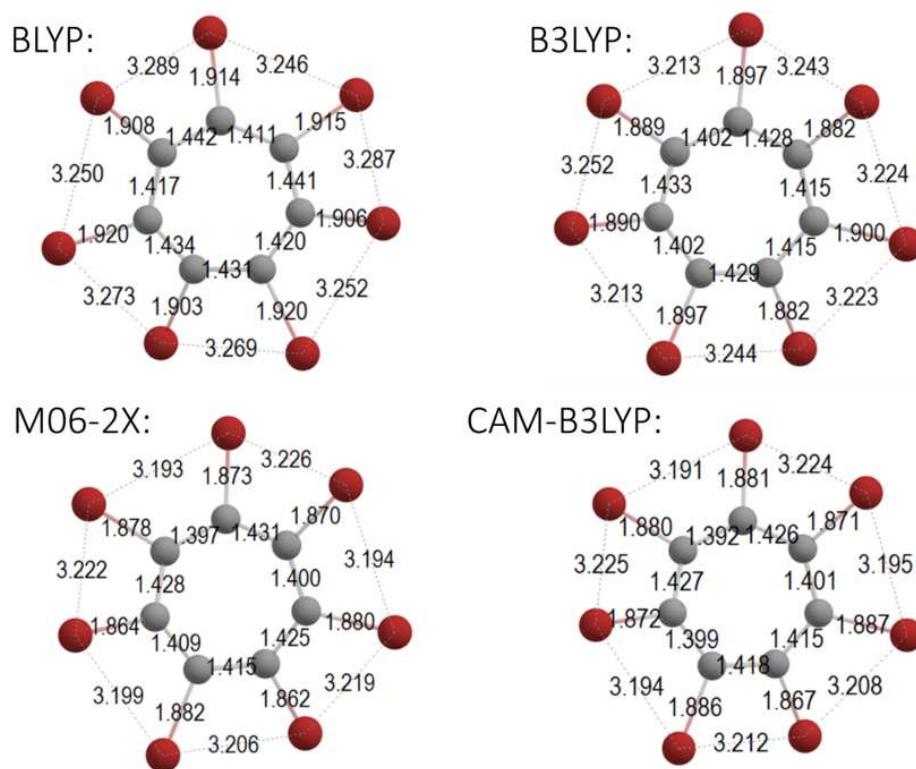
Figure A.11 Optimized geometries of $^1C_7Br_7^+$ using different DFAs/6-311+G(d,p).

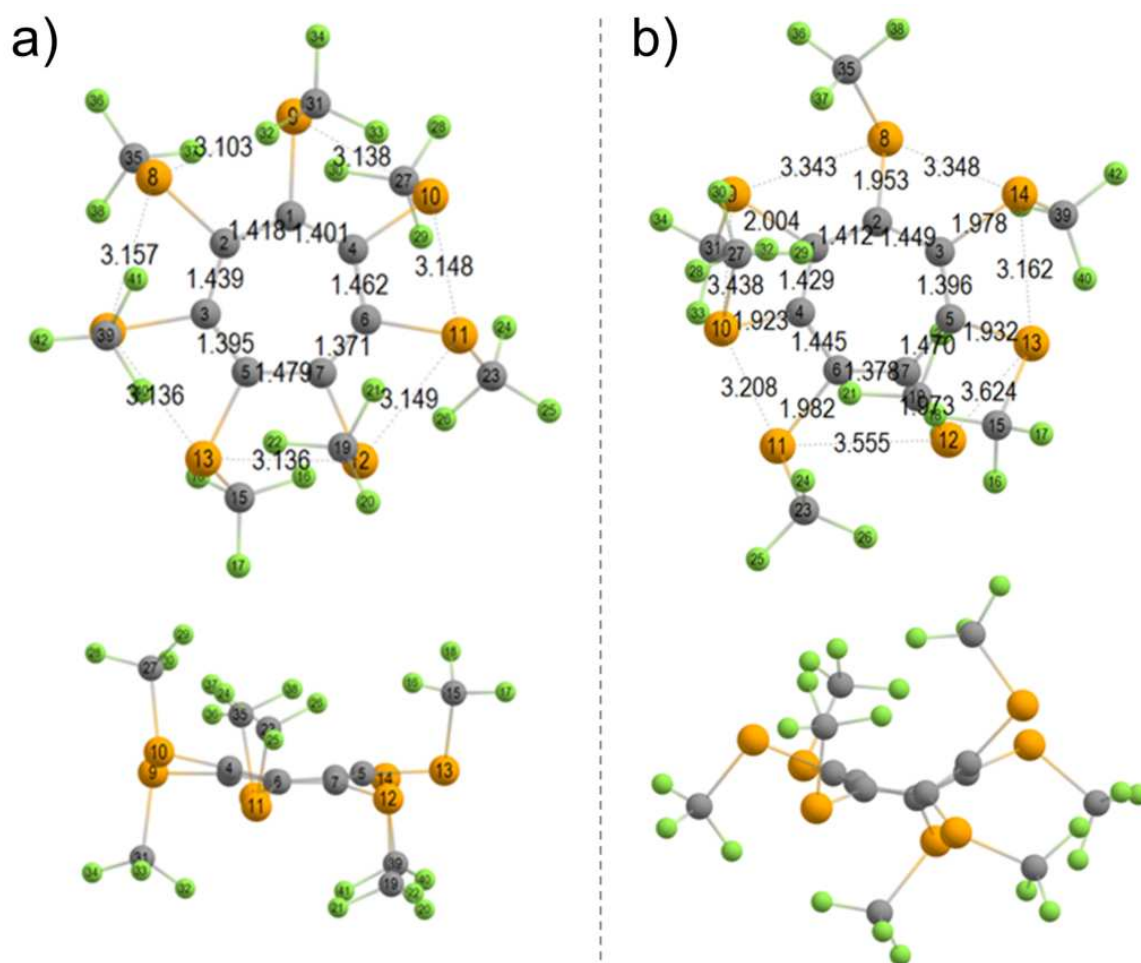**Figure A.12** Optimized geometries of $^1C_7(SeCF_3)_7^+$ using BLYP together with the a) 6-31G(d,p) or b) 6-311+G(d,p) basis set.
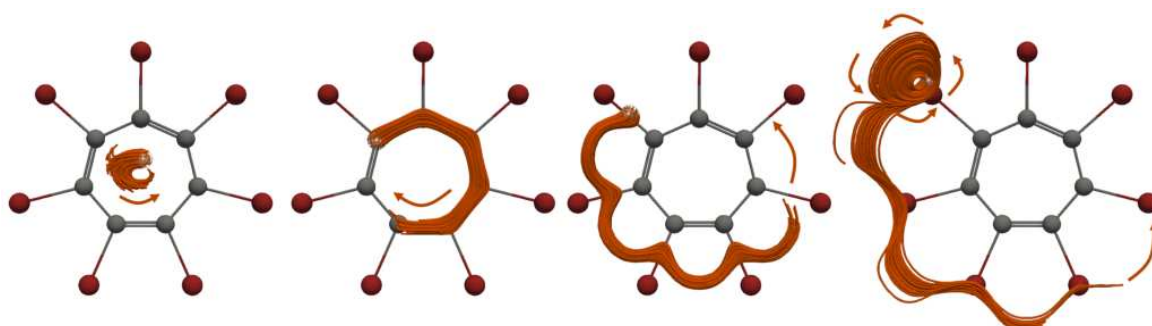

Figure A.13 Streamline representation of the concentric currents in $^3C_7Br_7^{3+}$.

Section 5.4.1: Too Persistent to Give Up: Aromaticity in Boron Clusters Survives Radical Structural Changes: Key Supplemental Data

The elements listed below are included in the supplemental material for Section 5.4.1. The complete set of supplemental material associated with this paper can be accessed at 6.4.1-SI DOI:10.1021/jacs.0c02228.

Experimental Section:

- Materials and Instrumentation
- Synthesis and Characterization of $[HNMe_3][7,9\text{-}nido\text{-}(C_2B_9H_{12})]$

Computational Section:

- Cartesian Coordinates
- Computational Details for the GIMIC Calculations
- Current Density Results

Additionally, this section includes selected tables and figures to complement the detailed discussions of the results.

Section 5.4.2: Pioneering the Power of Twin Bonds in a Revolutionary Double Bond Formation. Unveiling the True Identity of o-Carboryne as o-Carborene: Key Supplemental Data

The elements listed below are included in the supplemental material for Section 5.4.2. The complete set of supplemental material associated with this paper can be accessed at 5.4.2-SI DOI:10.1002/chem.202302448.

- Current-Density Vector Field of Benzene and o-Benzyne
- Current-Density Vector Field of o-Carborane and o-Carboryne
- Structures of Cyclotrimerization of o-Benzyne, Phenanthryne, and o-Carboryne
- Localized Molecular Orbitals of o-Benzyne and o-Carboryne
- HOMO and LUMO Orbitals of o-Carborane, o-Carboryne, Benzene, and o-Benzyne
- Cartesian Coordinates

Additionally, this section includes selected tables and figures to complement the detailed discussions of the results.

Section 5.4.3: Single—Not Double—3D-Aromaticity in Oxidized *Closo* Icosahedral Dodecaiodo-Dodecaborate Cluster: Key Supplemental Data

The elements listed below are included in the supplemental material for Section 5.4.3. The complete set of supplemental material associated with this paper can be accessed at 5.4.3-SI DOI:10.1021/jacs.3c07335.

- Frontier Molecular Orbitals of $[B_{12}I_{12}]^{2-}$
- GIMIC Calculation Parameters
- Experimental Structural Data
- NICS Scans and Current Density Results
- EDDB Results
- QTAIM Analysis
- Steric Maps—$\%V_{Bur}$
- Homodesmotic Reactions Results
- Cartesian Coordinates

Additionally, this section includes selected tables and figures to complement the detailed discussions of the results.

B Cover Art
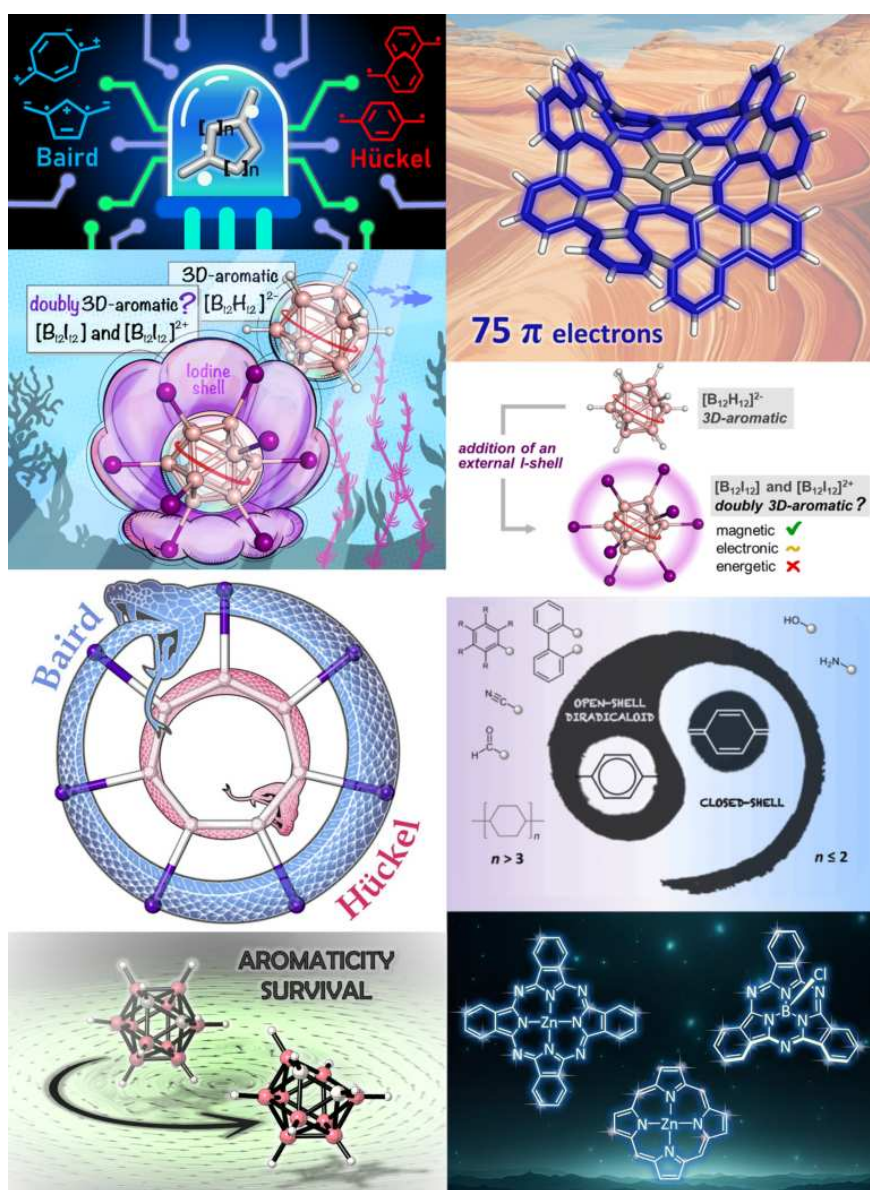
An Unprecedented π-Electronic Circuit Involving an Odd Number of Carbon Atoms in a Grossly Warped Non-Planar Nanographene

Showcasing research from Grupo de Química Inorgánica y Materiales Moleculares, Universidad Autónoma de Chile, Santiago de Chile, Chile and Institut de Química Computacional i Catàlisi, Universitat de Girona, Girona, Catalonia, Spain. Image designed and illustrated by Sílvia Escayola

An unprecedented π-electronic circuit involving an odd number of carbon atoms in a grossly warped non-planar nanographene

The most efficient circuits for π-electron delocalization in a grossly warped nanographene ($C_{80}H_{30}$) are a 50 π-electrons circuit that obeys Hückel's rule and a 75 π-electrons circuit that does not follow any of the known rules of aromaticity.
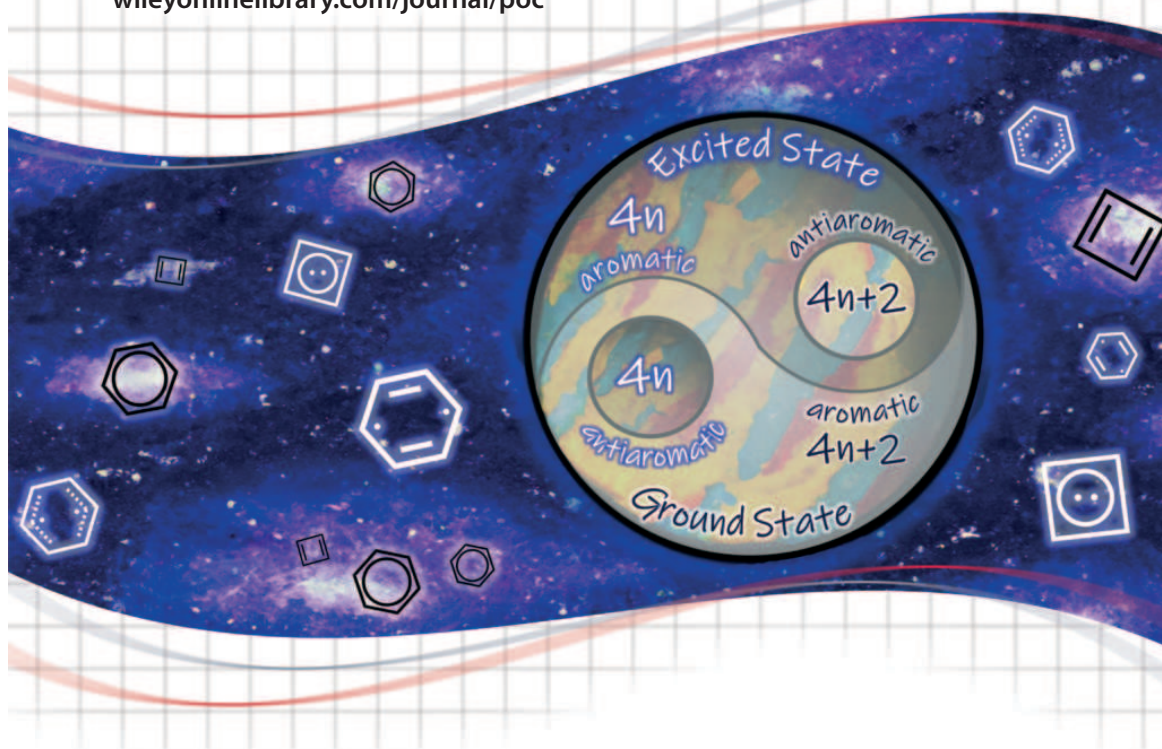
As featured in:

See Alvaro Muñoz-Castro, Miquel Solà *et al.*, *Chem. Commun.*, 2021, **57**, 3087.

ROYAL SOCIETY OF CHEMISTRY

rsc.li/chemcomm

JPOC Special Issue: Excited-state Aromaticity and Antiaromaticity

Journal of Physical Organic Chemistry

wileyonlinelibrary.com/journal/poc

IN THIS ISSUE:

The first fifty years have passed since Colin Baird's pioneering paper in 1972 - now starts the next fifty
by Henrik Ottosson, Bo Durbeej and Miquel Solà
Cover image by Sílvia Escayola

WILEY

Too Persistent to Give Up: Aromaticity in Boron Clusters Survives Radical Structural Changes

Single – Not Double – 3D-Aromaticity in Oxidized *Closo* Icosahedral Dodecaiodo-Dodecaborate Cluster